

nature

FILLING THE GAPS

Fossil skull of *Taytalura* illuminates major transition in reptile evolution



Coronavirus

Why children's immune systems are so good at fighting COVID

Personal touch

Look beyond genetics to predict disease risk and tailor treatment

Ground state

How much coal and gas must stay unextracted to meet climate targets?

Nature.2021.09.11

[Sat, 11 Sep 2021]

- [This Week](#)
- [News in Focus](#)
- [Books & Arts](#)
- [Opinion](#)
- [Work](#)
- [Research](#)
- [Amendments & Corrections](#)

This Week

- **[Indonesia's science super-agency must earn researchers' trust](#)** [08 September 2021]
Editorial • The drastic shake-up of the country's science system is intended to boost innovation, but there are concerns about political interference in the new centralized agency.
- **[License CRISPR patents for free to share gene editing globally](#)** [07 September 2021]
Editorial • Universities hold the majority of CRISPR patents. They are in a strong position to ensure that the technology is widely shared for education and research.
- **[How misconduct helped psychological science to thrive](#)** [07 September 2021]
World View • Grass-roots action against bad behaviour has spurred reform — and should keep going.
- **[Affluence buys a diet good for human health and bad for the planet](#)** [03 September 2021]
Research Highlight • Prosperous people in the United States tend to consume food that requires large amounts of land and water to produce.
- **[Origami robotic arm writhes like an octopus's](#)** [01 September 2021]
Research Highlight • A remote operator can use a magnetic system to control the highly capable limb.
- **[Victims of Mt Vesuvius reveal ancient Romans' gendered diets](#)** [31 August 2021]
Research Highlight • Skeletal remains suggest that men and women in Herculaneum, which was destroyed by the same eruption that buried Pompeii, had distinct diets.
- **[Broken skulls of children tell of an ancient massacre](#)** [01 September 2021]
Research Highlight • Even youngsters less than 10 years old were not spared in a spate of gruesome violence in central Europe more than 6,000 years ago.
- **[No hands, no problem: clever parrots craft and wield tools](#)** [03 September 2021]
Research Highlight • The Goffin's cockatoo joins chimpanzees and others in the small club of animals that can make implements.

- **A stellar explosion moves from theory to reality** [02

September 2021]

Research Highlight • Radio signals help to provide evidence for a type of supernova triggered by a black hole or neutron star on the rampage.

- **How to grow a long-sought wonder material: on a silver platter** [01 September 2021]

Research Highlight • Two sheets of boron, each only one atom thick, are coaxed to take shape on crystals of silver.

- EDITORIAL
- 08 September 2021

Indonesia's science super-agency must earn researchers' trust

The drastic shake-up of the country's science system is intended to boost innovation, but there are concerns about political interference in the new centralized agency.



Former president Megawati Soekarnoputri will chair Indonesia's science 'super-agency', BRIN. Credit: WF Sihardian/Pacific Press/LightRocket/Getty

For decades, Indonesia's leaders have watched as the nation's southeast Asian neighbours have become powerhouses for technology and innovation.

Indonesia lacks the tech multinationals on the scale of Singapore, Thailand or Malaysia. Its businesses contribute just 8% of expenditure on research and development (R&D), and technology exports comprise less than 10% of all exports. By contrast, Malaysia and Singapore's businesses account for around half of all R&D spending, and technology makes up half of exports.

Successive Indonesian governments have debated how the country can emulate its peers, and in 2017 the research ministry, Kemenristek, proposed that researchers and businesses should work more closely. But for reasons that are still not entirely clear, the government of President Joko Widodo decided it was time to shake up the entire science system. The cabinet-level research ministry has been merged with the education ministry, and a new 'science super-agency', BRIN, was inaugurated on 28 April.

BRIN is led by Laksana Tri Handoko, previously the head of the Indonesian Institute of Sciences, which was one of the country's oldest national research organizations, employing some 2,000 researchers in mostly applied fields. Funding data have not yet been released, but BRIN's budget is likely to be many multiples of the universities budget.

The move has proved unpopular with Indonesia's science community. Opposition to BRIN has united organizations spanning the generations, including both the Indonesian Academy of Sciences and the Indonesian Young Academy of Science.

Last week, BRIN absorbed the institute of sciences, along with other previously stand-alone research organizations, including the National Nuclear Energy Agency and the space and aeronautics agency. BRIN will eventually assume responsibility for R&D conducted in many — if not all — government departments. The agency will be overseen by a steering committee headed by Megawati Soekarnoputri, a former president of Indonesia and the chair of the governing Indonesian Democratic Party of Struggle.



India must protect the independence of its landmark science agency

Handoko told *Nature* that the changes are needed to bring coherence to a fragmented research system. He says grants will be awarded on the basis of independent peer review. Moreover, combining many different research and funding sources into one giant fund (including monies derived from a levy on businesses) will allow Indonesia to invest the sizeable sums needed to build research and technology infrastructure.

But researchers fear such a structure is a recipe for political interference in science funding. Furthermore, it isn't yet clear how BRIN will boost innovation. Satryo Brodjonegoro, head of the Indonesian Academy of Sciences, told *Nature* that BRIN's creation is a setback for Indonesian science.

Researchers are right to be concerned. Although Indonesia's government spends little of its national income on R&D (in 2018, spending accounted for just 0.23% of gross domestic product), in the past decade scientists in the country have recorded southeast Asia's highest rate of growth in scientific publications. This is partly because, since 2017, the nation's researchers have been evaluated according to their output in international journals.

Publications grew from 6,080 in 2013 to 37,513 in 2019, according to data compiled by the United Nations science agency UNESCO

(go.nature.com/3n4ky30). Of these, 24% are in physics and astronomy, and 27% are in strategic areas such as artificial intelligence, energy, materials science and nanotechnology. Indonesia has also recorded significant gains in publishing related to the UN Sustainable Development Goals, and the proportion of researchers in the population has been rising.

In the past, President Widodo has complained that researchers are not doing enough to boost innovation, but scientists fear that the country's top leadership does not understand or respect their achievements.

It is rare to see a country bring previously autonomous R&D agencies under the control of a single body. The United Kingdom's 2018 merger of nine funding agencies into UK Research and Innovation (UKRI) is an exception. Most countries in which R&D is organized more centrally — such as China — created this type of arrangement at the start. Meanwhile, some countries with relatively centralized systems, such as India and France, are on a path to decentralization by strengthening research and innovation in universities.



Egalité: France's research reforms must balance competitiveness with well-being

Other nations with a strong research tradition, such as Germany and the United States, spread responsibility for science funding, governance and accountability across multiple organizations. Accountability is particularly

important, because it helps to ensure that the autonomy of staff and grant recipients is protected. And that is where Indonesia's plans carry perhaps the greatest risk. This urgently needs to be mitigated.

BRIN's leadership should consult Indonesia's science and innovation policy-research community, in which these questions have long been studied. At the very least, BRIN should consider giving Indonesia's parliament some kind of oversight role. Parliamentarians could, for example, approve its budget and check that promises of non-interference are being kept. The United Kingdom chose not to have UKRI report to Parliament; compared with the previous arrangements, this move potentially increases government influence over science funding.

A science agency chaired by one of Indonesia's most powerful political figures, reporting directly to the president, does have its advantages — science will clearly be represented at the highest level of government. But there might come a time — as a result of a change in government, for example — when BRIN's leadership and Indonesia's president come from different political parties. The agency will need to function just as well in such a scenario. This is why safeguards against interference and potential conflicts of interest need to be put in place, and why parliament needs to have a stronger role.

The creation of BRIN is, without doubt, an ambitious reorganization, but it's not clear how the agency will help Indonesia with its technology ambitions. More clarity and better communication are needed, and governance architecture must be designed in such a way that it outlasts its founders. Only then will Indonesian science and innovation truly thrive.

Nature **597**, 151-152 (2021)

doi: <https://doi.org/10.1038/d41586-021-02419-4>

This article was downloaded by **calibre** from <https://www.nature.com/articles/d41586-021-02419-4>

- EDITORIAL
- 07 September 2021

License CRISPR patents for free to share gene editing globally

Universities hold the majority of CRISPR patents. They are in a strong position to ensure that the technology is widely shared for education and research.

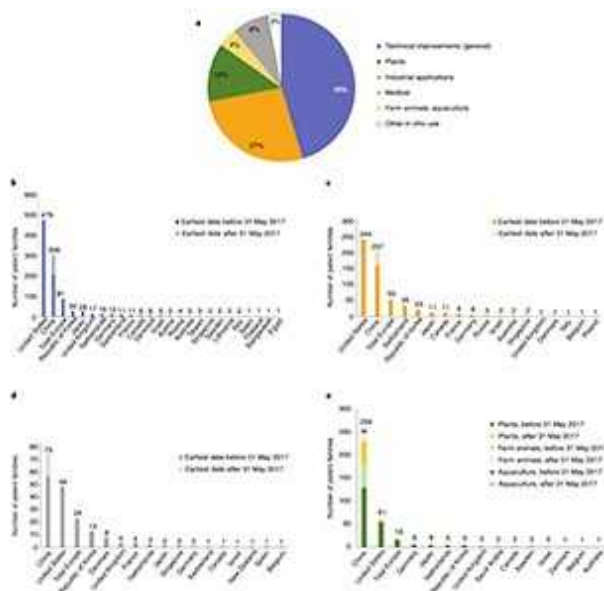


The library at Wageningen University and Research in the Netherlands. The university is providing free access to CRISPR patents for non-commercial use. Credit: Frans Sellies/Moment/Getty

This week, Wageningen University and Research in the Netherlands announced that it will allow non-profit organizations to [use its CRISPR-Cas9 gene-editing technology for free](#), for non-commercial applications in food and agriculture. It's an important development, and another step towards making a technology with untapped potential more accessible — especially for researchers in low- and middle-income countries.

Wageningen is one of a clutch of research institutions globally that hold patents on CRISPR, a technique that enables precise changes to be made to genomes, at specific locations. Other institutions — including the Broad Institute in Cambridge, Massachusetts, and the University of California, Berkeley, which have some of the largest portfolios of patents on the subject — also provide CRISPR tools and some intellectual property (IP) for free for non-profit use. But universities could do better to facilitate access to CRISPR technologies for research.

The field is snowballing. The US Patent and Trademark Office alone has around 6,000 CRISPR patents or patent applications, with 200 being added every month, mostly from China and the United States.



[Worldwide CRISPR patent landscape shows strong geographical biases](#)

But unusually, universities and publicly funded research organizations dominate the CRISPR patenting landscape. As of 2017, only one-third of

CRISPR patents came from the private sector, according to an analysis by Agnès Ricroch, a plant geneticist at the institute AgroParisTech, and her colleagues ([J. Martin-Laffon et al. Nature Biotechnol. 37, 613–620; 2019](#)). That means universities are in a strong position to influence change. And change begins with the licensing agreement — which is needed even when an organization is using IP for research.

Licensing agreements should be transparent, so that institutions offering access can be held accountable for the promises they make. But few publish these agreements, out of concern that it would give their competitors an advantage. However, if universities all agreed not to charge for IP used in research, they would no longer be in competition, and could collaborate to create model agreements.

Licensing agreements should also limit ‘reach-through clauses’. These allow patent holders to claim rights on commercialization of discoveries and inventions based on their IP, many years into the future. It’s a method of prolonging income, but has been likened to authors paying royalties to Google or Microsoft if they write a book on the companies’ word-processing software.

For centuries, patents have helped to protect inventors’ IP from competitors who would otherwise be able to copy and profit from someone else’s idea. Patents also incentivize the investment needed to develop or commercialize an idea, because they reassure investors that a technology cannot easily be copied.



A patent waiver on COVID vaccines is right and fair

But companies have been known to use patents to hinder competition. Moreover, when inappropriately applied, patents can be harmful. During a pandemic, for example, patents on vaccines could slow or reduce vaccine availability. That is why more than 100 countries, and many organizations (including *Nature*) are calling on members of the World Trade Organization to temporarily waive IP protection on COVID-19 vaccines.

Equitable access is crucial. Nearly two decades ago, international donors created the African Agricultural Technology Foundation in Nairobi as a platform to share know-how, tools and technology. Ecologist Gordon Conway, then president of the Rockefeller Foundation in New York City, promised it would “unjam the logjam” of IP in agricultural technology. In practice, concerns over genetic modification put the brakes on such technologies in low- and middle-income countries. But CRISPR is changing that, and universities that benefit from patents could help to establish an organization to facilitate access.

Two years ago, the Netherlands Federation of University Medical Centres proposed ten principles for “socially responsible licensing”. High on the list is that academic institutions should ensure that their research benefits societies, including allowing findings to be used freely for research or education.

It is fitting that a Dutch university is among those applying these principles for a technology that has world-changing potential. The time has come for all universities that hold CRISPR patents, along with public funders and international institutions such as the World Intellectual Property Organization, to consider how they might join forces so that IP on CRISPR can be more easily accessed free of charge for research, under clear and transparent rules.

Nature **597**, 152 (2021)

doi: <https://doi.org/10.1038/d41586-021-02420-x>

This article was downloaded by **calibre** from <https://www.nature.com/articles/d41586-021-02420-x>

| [Section menu](#) | [Main menu](#) |

- WORLD VIEW
- 07 September 2021

How misconduct helped psychological science to thrive



Grass-roots action against bad behaviour has spurred reform — and should keep going.

- [Jelte Wicherts](#) 9

Ten years ago this week, I was startled to see tweets saying that Dutch psychologist Diederik Stapel, a former colleague, had admitted to falsifying and fabricating data in dozens of articles. My inbox filled with e-mails from fellow methodologists, researchers who examine and refine research techniques and statistical tools. They expressed disbelief about the extent of the misconduct, but also a sense of inevitability. We all knew that sloppiness, low ethical standards and competitiveness were widespread.

What happened next was inspiring: an open debate that went far beyond misconduct and focused on improving research. Numerous researchers, many early in their careers, used social media to call for bias-countering practices, such as sharing data and plans for analysis. It changed the conversation. Before 2011, my applications for grants to study statistical errors and biases in psychology were repeatedly rejected as low priority. By 2012, I had received funding and set up my current research group.

This August, another incident of data fraud came to light, this time in a 2012 publication from behavioural-science superstar Dan Ariely, who agrees that the data are fabricated, but says he did not fabricate them. This case, ironically in a study assessing how to encourage honesty, is an invitation to examine how expectations for research practice have changed, and how much further reform must go.



[Research integrity: nine ways to move from talk to walk](#)

Publication bias — the tendency for findings that confirm hypotheses to be published more often than are null results — was documented clearly in the 1950s. The 1960s and 1970s brought warnings that decisions about how data were analysed could cause bias, such as the identification of spurious or overly strong effects. The widespread failure to share psychology data for verification purposes was also proclaimed in the 1960s and 1970s. (My group documented it in 2006.)

By the 1990s, methodologists had raised the alarm that most studies had unacceptably low statistical power — the probability that actual effects are being detected — and that researchers often misrepresented a study as being designed to test a specific hypothesis, when in fact they had spotted a trend in exploratory work. The high prevalence of statistical errors was not news, at least to methodologists. Nor was the practice of tweaking and repeating analyses until a statistical threshold (such as $P < 0.05$) was reached. In 2005, a modelling paper showed that, combined, these biases could mean that most published results were false ([J. P. A. Ioannidis *PLoS Med.* 2, e124; 2005](#)). This provocative message generated attention, but little practical change.

Despite this history, before Stapel, researchers were broadly unaware of these problems or dismissed them as inconsequential. Some months before the case became public, a concerned colleague and I proposed to create an archive that would preserve the data collected by researchers in our department, to ensure reproducibility and reuse. A council of prominent colleagues dismissed our proposal on the basis that competing departments had no similar plans. Reasonable suggestions that we made to promote data sharing were dismissed on the unfounded grounds that psychology data sets can never be safely anonymized and would be misused out of jealousy, to attack well-meaning researchers. And I learnt about at least one serious attempt by senior researchers to have me disinvited from holding a workshop for young researchers because it was too critical of suboptimal practices.



Institutions can retool to make research more rigorous

Around the time that the Stapel case broke, a trio of researchers coined the term *P* hacking and demonstrated how the practice could produce statistical evidence for absurd premises ([J. P. Simmons et al. *Psychol. Sci.* 22, 1359–1366; 2011](#)). Since then, others have tirelessly promoted study preregistration and organized large collaborative projects to assess the replicability of published findings.

Much of the advocacy and awareness has been driven by early-career researchers. Recent cases show how preregistering studies, replication, publishing negative results, and sharing code, materials and data can both empower the self-corrective mechanisms of science and deter questionable research practices and misconduct.

For these changes to stick and spread, they must become systemic. We need tenure committees to reward practices such as sharing data and publishing rigorous studies that have less-than-exciting outcomes. Grant committees and journals should require preregistration or explanations of why it is not warranted. Grant-programme officers should be charged with checking that data are made available in accordance with mandates, and PhD committees should demand that results are verifiable. And we need to strengthen a culture in which top research is rigorous and trustworthy, as well as creative and exciting.

The Netherlands is showing the way. In 2016, the Dutch Research Council allocated funds for replication research and meta-research aimed at improving methodological rigour. This year, all universities and major funders in the country are discussing how to include open research practices when they assess the track records of candidates for tenure, promotion and funding.

Grass-roots enthusiasm has created a fleet of researchers who want to improve practices. Now the system must assure them that they can build successful careers by following these methods. Never again can research integrity become a taboo topic: that would only create more untrustworthy research and, ultimately, misconduct.

Nature **597**, 153 (2021)

doi: <https://doi.org/10.1038/d41586-021-02421-w>

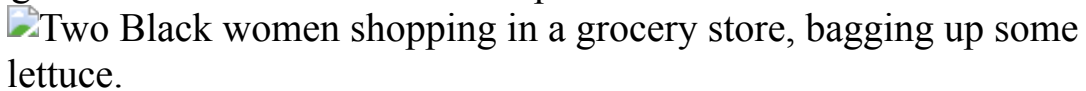
This article was downloaded by **calibre** from <https://www.nature.com/articles/d41586-021-02421-w>

| [Section menu](#) | [Main menu](#) |

- RESEARCH HIGHLIGHT
- 03 September 2021

Affluence buys a diet good for human health and bad for the planet

Prosperous people in the United States tend to consume food that requires large amounts of land and water to produce.



Vegetables are consumed more often by higher-income people in the United States than by those with fewer means. Credit: Granger Wootz/Getty

Wealthy Americans eat a better-balanced and more nutritious diet than do those in lower income groups, but their food habits are a bigger burden on the environment.

Access options

Subscribe to Journal

Get full journal access for 1 year

\$199.00

only \$3.90 per issue

[Subscribe](#)

All prices are NET prices.
VAT will be added later in the checkout.
Tax calculation will be finalised during checkout.

Rent or Buy article

Get time limited or full article access on ReadCube.

from \$8.99

[Rent or Buy](#)

All prices are NET prices.

Additional access options:

- [Log in](#)
- [Learn about institutional subscriptions](#)

Nature **597**, 154 (2021)

doi: <https://doi.org/10.1038/d41586-021-02404-x>

References

1. 1.

[Nature Food \(2021\)](#)

This article was downloaded by **calibre** from <https://www.nature.com/articles/d41586-021-02404-x>

- RESEARCH HIGHLIGHT
- 01 September 2021

Origami robotic arm writhes like an octopus's

A remote operator can use a magnetic system to control the highly capable limb.



A robotic arm modelled on the octopus's appendage is made of magnetic materials folded in origami patterns. Credit: Shuai Wu

An octopus-inspired robotic arm whose complex movements can be controlled remotely could lead to improved medical devices.

Access options

Subscribe to Journal

Get full journal access for 1 year

\$199.00

only \$3.90 per issue

[Subscribe](#)

All prices are NET prices.

VAT will be added later in the checkout.

Tax calculation will be finalised during checkout.

Rent or Buy article

Get time limited or full article access on ReadCube.

from \$8.99

[Rent or Buy](#)

All prices are NET prices.

Additional access options:

- [Log in](#)
- [Learn about institutional subscriptions](#)

Nature **597**, 154 (2021)

doi: <https://doi.org/10.1038/d41586-021-02384-y>

References

1. 1.

[Proc. Natl Acad. Sci. USA \(2021\)](#)

This article was downloaded by **calibre** from <https://www.nature.com/articles/d41586-021-02384-y>.

| [Section menu](#) | [Main menu](#) |

- RESEARCH HIGHLIGHT
- 31 August 2021

Victims of Mt Vesuvius reveal ancient Romans' gendered diets

Skeletal remains suggest that men and women in Herculaneum, which was destroyed by the same eruption that buried Pompeii, had distinct diets.



A mosaic in the ancient Roman town of Herculaneum depicts a man holding a fish, which was more commonly eaten by the community's men than by its women. Credit: REDA & CO srl/Alamy

The women of Herculaneum seem to have had different eating habits from the men who lived in this ancient Roman town.

Access options

Subscribe to Journal

Get full journal access for 1 year

\$199.00

only \$3.90 per issue

[Subscribe](#)

All prices are NET prices.

VAT will be added later in the checkout.

Tax calculation will be finalised during checkout.

Rent or Buy article

Get time limited or full article access on ReadCube.

from \$8.99

[Rent or Buy](#)

All prices are NET prices.

Additional access options:

- [Log in](#)
- [Learn about institutional subscriptions](#)

Nature **597**, 154 (2021)

doi: <https://doi.org/10.1038/d41586-021-02354-4>

Science Advances (2021)

References

1. 1.

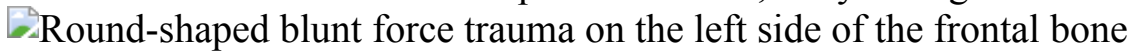
[Sci. Adv. \(2021\)](#)

This article was downloaded by **calibre** from <https://www.nature.com/articles/d41586-021-02354-4>

- RESEARCH HIGHLIGHT
- 01 September 2021

Broken skulls of children tell of an ancient massacre

Even youngsters less than 10 years old were not spared in a spate of gruesome violence in central Europe more than 6,000 years ago.



The skull of an 11-to-15-year-old boy was damaged by a club or similar weapon during his violent death some 6,000 years ago. Credit: I. Janković *et al./Am. J. Phys. Anthropol.*

The battered skulls of men, women and children interred in a prehistoric mass grave in what is now Croatia are evidence of an early incident of indiscriminate killing in Europe.

Access options

Subscribe to Journal

Get full journal access for 1 year

\$199.00

only \$3.90 per issue

[Subscribe](#)

All prices are NET prices.

VAT will be added later in the checkout.

Tax calculation will be finalised during checkout.

Rent or Buy article

Get time limited or full article access on ReadCube.

from \$8.99

[Rent or Buy](#)

All prices are NET prices.

Additional access options:

- [Log in](#)
- [Learn about institutional subscriptions](#)

Nature **597**, 154 (2021)

doi: <https://doi.org/10.1038/d41586-021-02372-2>

References

1. 1.

[Am. J. Phys. Anthropol. \(2021\)](#)

This article was downloaded by **calibre** from <https://www.nature.com/articles/d41586-021-02372-2>

- RESEARCH HIGHLIGHT
- 03 September 2021

No hands, no problem: clever parrots craft and wield tools

The Goffin's cockatoo joins chimpanzees and others in the small club of animals that can make implements.



Who're you calling a bird brain? Some wild Goffin's cockatoos can make a tool kit and put it to work to access tasty treats. Credit: Lynn M. Stone/Nature Picture Library/Alamy

Parrots are smart and social, and their parents care for them for a long time — all characteristics shared with tool-using primates. Goffin's cockatoos (*Cacatua goffiniana*), medium-sized parrots native to Indonesia, are known to create and use tools in captivity, but Mark O'Hara and Berenika Mioduszewska at the University of Vienna and their colleagues wanted to know if they also do so in the wild.

Access options

Subscribe to Journal

Get full journal access for 1 year

\$199.00

only \$3.90 per issue

[Subscribe](#)

All prices are NET prices.
VAT will be added later in the checkout.
Tax calculation will be finalised during checkout.

Rent or Buy article

Get time limited or full article access on ReadCube.

from \$8.99

[Rent or Buy](#)

All prices are NET prices.

Additional access options:

- [Log in](#)
- [Learn about institutional subscriptions](#)

Nature **597**, 155 (2021)

doi: <https://doi.org/10.1038/d41586-021-02381-1>

References

1. 1.

[Curr. Biol. \(2021\)](#)

This article was downloaded by **calibre** from <https://www.nature.com/articles/d41586-021-02381-1>

- RESEARCH HIGHLIGHT
- 02 September 2021

A stellar explosion moves from theory to reality

Radio signals help to provide evidence for a type of supernova triggered by a black hole or neutron star on the rampage.

A computer generated image of a compact object at the core of its massive stellar companion.

A black hole or other compact astronomical body (artist's impression) has spiralled into the heart of its companion star, which is about to explode as a supernova. Credit: Chuck Carter

It starts with a familiar tale. Two massive stars are born from a cloud of gas and dust. One eventually runs out of fuel, forming either a neutron star or a black hole. But then, in a fratricidal twist, this compact object spirals closer and closer to the other star, sweeps through its sibling's atmosphere and eventually tugs on its core so hard that it explodes.

Access options

Subscribe to Journal

Get full journal access for 1 year

\$199.00

only \$3.90 per issue

[Subscribe](#)

All prices are NET prices.
VAT will be added later in the checkout.
Tax calculation will be finalised during checkout.

Rent or Buy article

Get time limited or full article access on ReadCube.

from \$8.99

[Rent or Buy](#)

All prices are NET prices.

Additional access options:

- [Log in](#)
- [Learn about institutional subscriptions](#)

Nature **597**, 155 (2021)

doi: <https://doi.org/10.1038/d41586-021-02395-9>

References

1. 1.

[Science \(2021\)](#)

This article was downloaded by **calibre** from <https://www.nature.com/articles/d41586-021-02395-9>

- RESEARCH HIGHLIGHT
- 01 September 2021

How to grow a long-sought wonder material: on a silver platter

Two sheets of boron, each only one atom thick, are coaxed to take shape on crystals of silver.

 Black and white micrograph of bilayer borophene showing a honeycomb structure.

Double-layered borophene (pictured) is expected to have desirable magnetic or electronic traits. Credit: X. Liu *et al.*/*Nature Mater.*

Engineers have tamed the unruly element boron into a sheet precisely two atoms thick — achieving the first synthesis of a double layer of the wonder material borophene.

Access options

Subscribe to Journal

Get full journal access for 1 year

\$199.00

only \$3.90 per issue

[Subscribe](#)

All prices are NET prices.

VAT will be added later in the checkout.

Tax calculation will be finalised during checkout.

Rent or Buy article

Get time limited or full article access on ReadCube.

from \$8.99

[Rent or Buy](#)

All prices are NET prices.

Additional access options:

- [Log in](#)
- [Learn about institutional subscriptions](#)

Nature **597**, 155 (2021)

doi: <https://doi.org/10.1038/d41586-021-02380-2>

References

1. 1.

[Nature Mater. \(2021\)](#)

This article was downloaded by **calibre** from <https://www.nature.com/articles/d41586-021-02380-2>

| [Section menu](#) | [Main menu](#) |

News in Focus

- **[World's most northern island and climate change's role in floods](#)** [08 September 2021]
News Round-Up • The latest science news, in brief.
- **[US COVID origins report: researchers pleased with scientific approach](#)** [27 August 2021]
News • Intelligence investigation is inconclusive on virus's origins, but finds SARS-CoV-2 wasn't weaponized and is unlikely to have been engineered.
- **[India's DNA COVID vaccine is a world first – more are coming](#)** [02 September 2021]
News • The ZyCoV-D vaccine heralds a wave of DNA vaccines for various diseases that are undergoing clinical trials around the world.
- **[Rogue antibodies involved in almost one-fifth of COVID deaths](#)** [31 August 2021]
News • The self-targeting antibodies attack type 1 interferons that play a key role in fighting infection.
- **[US achieves laser-fusion record: what it means for nuclear-weapons research](#)** [27 August 2021]
News Explainer • Scientists are hopeful that the National Ignition Facility's recent success will advance understanding of thermonuclear reactions.
- **[Freak US winters linked to Arctic warming](#)** [03 September 2021]
News • Models suggest that distortions in polar-vortex winds can send chilly air hurtling southwards. But some climate scientists remain unconvinced.
- **[Kids and COVID: why young immune systems are still on top](#)** [07 September 2021]
News Feature • Innate immunity might be the key to why children have fared better with the virus. But the Delta variant poses fresh unknowns.
- **[Climate science is supporting lawsuits that could help save the world](#)** [08 September 2021]

News Feature • Governments have failed to slow climate change quickly enough, so activists are using courts to compel countries and companies to act — increasingly with help from forefront science.

| [Next section](#) | [Main menu](#) | [Previous section](#) |

- NEWS ROUND-UP
- 08 September 2021

World's most northern island and climate change's role in floods

The latest science news, in brief.



The island measures 60 by 30 metres and has a peak about 3 metres above sea level. Credit: Julian Charrière/VG Bild-Kunst, Bonn, Germany

Tiny island is world's northernmost

Shifting pack ice has uncovered what is thought to be the world's most northerly island, off the coast of Greenland. Scientists discovered the island

by accident while on an expedition to collect samples on an island called Oodaaq that was previously thought to be Earth's northernmost piece of land.

The researchers flew by helicopter to where they thought Oodaaq was located, but couldn't find it. While looking around, they came across another, previously undocumented, island almost 1 kilometre farther north.

The new island measures 60 by 30 metres and has a peak about 3 metres above sea level. There is no vegetation. The surface consists mainly of mud and moraine — rock and soil that is deposited by glaciers.

The researchers want the island to be named Qeqertaq Avannarleq, which means 'the northernmost island' in Greenlandic.



Record rainfall caused severe flooding in Germany, Belgium and the Netherlands (pictured) this year.Credit: Patrick van Katwijk/BSR Agency/Getty

Climate change implicated in deadly floods

Extraordinary downpours such as those responsible for this year's deadly flooding in Western Europe are becoming more frequent, and more intense, as a result of climate change. That's the finding of a study by researchers involved in the World Weather Attribution initiative, which assesses whether global warming is a factor in extreme weather events.

Record rainfall caused severe flooding in Germany, Belgium and the Netherlands in mid-July. The floods damaged the measurement stations that scientists normally use to collect data on water levels, so the study relied on rainfall data to assess the influence of climate change. The researchers poured these data into models that combined historical local weather and rainfall data with climate simulations for the wider region.

The models suggested that human-caused climate change had increased the rainfall intensity of such storms by 3–19%, relative to a pre-industrial climate that was 1.2 °C cooler than today's. They also estimated that similar events can now be expected to hit any part of Western Europe about once every 400 years.

The work is described in a preprint on the World Weather Attribution website. It has not yet been published in a peer-reviewed journal.

Nature **597**, 157 (2021)

doi: <https://doi.org/10.1038/d41586-021-02422-9>

This article was downloaded by **calibre** from <https://www.nature.com/articles/d41586-021-02422-9>

- NEWS
- 27 August 2021

US COVID origins report: researchers pleased with scientific approach

Intelligence investigation is inconclusive on virus's origins, but finds SARS-CoV-2 wasn't weaponized and is unlikely to have been engineered.

- [Amy Maxmen](#)



US Director of National Intelligence Avril Haines warned at the outset that the 90-day investigation into COVID-19's origins ordered by Joe Biden

might be inconclusive. Credit: Graeme Jennings/UPI/Shutterstock

When agents from the FBI and CIA flew to New Orleans, Louisiana, last month to talk to virologist Robert Garry about the origins of COVID-19, he was relieved by the depth of their scientific background. “These folks were really knowledgeable, had PhDs in molecular biology, they had read all of the papers in detail,” he says.

The visit was part of the 90-day US intelligence-community investigation into where the coronavirus SARS-CoV-2 came from, ordered by US President Joe Biden on 26 May. Like many researchers, Garry, at Tulane University, didn’t know what tack the confidential investigation would take, and felt that a scientific approach was essential. The agents spoke to him about studies, including his own, on coronavirus evolution.

Biden received the investigation’s classified report this week, on 24 August, and [an unclassified version](#) was made public today. The topline result is that the investigation was inconclusive. Intelligence agencies were divided on whether the pandemic most likely began because of a laboratory accident, or because of human contact with an infected animal. The only strong conclusion is that the coronavirus was not developed as a biological weapon; most agencies thought, with low confidence, that it was unlikely to have been genetically engineered. In a press statement, the intelligence community writes that it aims to issue more details on its investigation in the near future.



After the WHO report: what's next in the search for COVID's origins

Garry says the report exceeds his expectations. “It’s huge to mainly rule out that this is a product of engineering,” he says. He and other researchers aren’t surprised that the intelligence community hasn’t solved the mystery of COVID-19’s beginnings, because outbreak origin investigations are often complicated. The government’s senior intelligence officer, Avril Haines, warned of this outcome on 30 June, in an interview with Yahoo News. At the time, she said arguments could be made in favour of the two competing hypotheses. COVID-19 was first reported in Wuhan, China, where a leading institute studies coronaviruses, making a lab escape possible; and most emerging infectious diseases begin with a spillover from nature, lending weight to that scenario. She said the intelligence community would be working with experts, including scientists at national labs, collecting data and evaluating existing information, and trying to think about them in new ways. “I think the best thing I can do is to present the facts as we know them,” she said.

Many researchers welcome what seems to be a dispassionate investigation, after more than a year of politicization around how COVID-19 began. “I am glad to see us having a more nuanced discussion about this now,” says Stephen Morrison, director of global health policy at the Center for Strategic and International Studies in Washington DC. However, researchers also hope that the intelligence community will reveal more about its process, and are keen to hear about further investigations, either spearheaded by the World Health Organization (WHO) or independent of the agency. “This is an immensely complicated problem,” says David Relman, a microbiologist at Stanford University in California. “No one expected this to be figured out by summer.”

Scientific expertise

The US government has been considering COVID-19 origins ever since the pandemic began — but there have been disagreements between and within agencies, as made clear by recent reporting from Buzzfeed and other outlets. During the administration of former president Donald Trump, secretary of state Mike Pompeo and some other State Department officials argued that

the virus was the product of Chinese government manipulation, and a potential biological weapon. But in April last year, the intelligence community [issued a statement](#) that “the COVID-19 virus was not manmade or genetically modified”.

This June, Christopher Ford, who was a high-level state department official in the Trump administration, [posted an article on the website Medium](#) expressing discontent with what he felt were hasty conclusions that his colleagues had drawn without consulting scientific experts. The piece links to [a 4 January e-mail to his colleagues](#), now in the public domain, in which he writes: “Why hasn’t it been possible to get third-party experts together — folks with real bioscience chops … who can assess the worrying things you say you’ve found?” He adds, “We need to make sure what we say is solid and passes muster from real experts *before* we risk embarrassing and discrediting ourselves in public.”



[The COVID lab-leak hypothesis: what scientists do and don't know](#)

Biden asked the intelligence community to look into both the lab- and natural-origin hypotheses, while bringing scientists into the investigation. Today’s one-page report reveals that the National Intelligence Council and four intelligence groups leant towards COVID-19 stemming from a person naturally infected by an animal. One group leant towards a release from a lab accident, partly on the basis of the “inherently risky nature of work on

coronaviruses”, and three other groups were undecided. The report, which did not disclose the identities of the groups, says that more information is required. “China’s cooperation most likely would be needed to reach a conclusive assessment of the origins of COVID-19,” it reads, adding that Beijing resists sharing information.

Finer details of what the intelligence agencies assessed remain unknown to the public. According to an anonymous source [who spoke to CNN](#), some of the intelligence community’s probe was directed at a “trove” of genetic sequences from viruses associated with the Wuhan Institute of Virology. Garry has not seen such data, but speculates that the sequences could have been extracted from the cloud-based data systems. Typically, gene-sequencing machines automatically upload massive amounts of data to the cloud, which researchers can remotely access and analyse. That the report is inconclusive, says Garry, might indicate that investigators did not find a SARS-CoV-2 sequence dating from before the first cases of COVID-19 were reported, or a very similar sequence suggesting that researchers might have genetically tweaked an existing virus to create the pathogen circulating today.

Relman, however, says that it’s hard to draw conclusions without more information on the type of data the agents obtained, and their process.

Next steps

After the release of the public report on 27 August, Biden issued a statement that the United States would continue to trace the origins of COVID-19. He condemned China for its lack of cooperation, and pressed Chinese officials to cooperate fully with the WHO’s phase-two investigation. On 16 July, WHO director-general Tedros Adhanom Ghebreyesus outlined requests for that study, which would follow a probe supported by the agency [that was completed in March](#). Among other studies Tedros suggested were research into animals sold at markets in Wuhan, and an audit of the Wuhan Institute of Virology.

[At a news conference](#) soon afterwards, the vice-minister of China’s national health commission, Zeng Yixin, said that Chinese scientists were following

some leads suggested in the March report. He also welcomed a WHO-led phase-two investigation that includes tracing the history of the first people now known to have had COVID-19, and studies in multiple countries on animals that might have served as intermediary hosts, transferring the virus from, say, bats to humans. But Zeng rejected Tedros's call for a laboratory audit, saying: "From this point, I can feel that the plan showed disrespect for common sense and arrogance toward science."



[WHO report into COVID pandemic origins zeroes in on animal markets, not labs](#)

Since then, the WHO has [posted a notice](#) asking for scientists from about 20 fields, including laboratory security, veterinary medicine and virology, to apply to serve on a committee on the origins of emerging pathogens, ranging from SARS-CoV-2 to Ebola. This group, called the Scientific Advisory Group for Origins of Novel Pathogens (SAGO), would advise on the phase-two COVID-19 origins investigation, as well as those in the future.

Maria Van Kerkhove, head of the WHO's emerging-diseases unit, says she hopes that any relevant details from Biden's investigation will be shared with the organization. She reiterates that scientists who are curious about SAGO should not hesitate to apply, and emphasizes the importance of its work. "It's difficult to be a scientist who speaks publicly these days," she says. "We are all a bit battered, but I believe that we have a responsibility as scientists to move this forward."

Many researchers welcome the news of a standing scientific committee devoted to origins investigations, saying that it will help future studies to start sooner, when the early events of an outbreak are still fresh in bodies and in minds. However, Thomas Bollyky, director of the global health programme at the Council on Foreign Relations in Washington DC, says, “I think this sort of group would be better outside of the WHO, as a coalition of national scientific academies.”

Taking COVID-19 as an example, Bollyky explains that resolving where the pandemic came from requires cooperation from China. He says scientists — acting somewhat independently of governments — are well-placed to collaborate across borders. By contrast, the WHO is in a difficult position. It can’t force its member states to do anything, he says. And because the WHO is led and financed by its member states — two of the most powerful being the United States and China — it is ill-equipped to resolve the geopolitical differences between them.



[Divisive COVID ‘lab leak’ debate prompts dire warnings from researchers](#)

Meanwhile, investigations by US intelligence agencies are unlikely to achieve cooperation from China because their aim will be viewed as political, says Bollyky. “China and many other countries simply won’t accept the outcome, and that defeats the whole damn point of doing this origin investigation, which is to make us safer in the future.”

Relman also sees value in an international scientific committee outside of the WHO, and adds that members of it could promote transparency. For example, committee members could respond to people concerned about the involvement of the US National Institutes of Health in COVID-19's origins, by requesting that it publicly release all documents related to research it has funded on coronaviruses in China and at laboratories in Wuhan. “I personally doubt there’s much of substantive value in there,” he says, “but it serves the purpose of the scientific community to lead with openness.”

Nature **597**, 159-160 (2021)

doi: <https://doi.org/10.1038/d41586-021-02366-0>

This article was downloaded by **calibre** from <https://www.nature.com/articles/d41586-021-02366-0>

| [Section menu](#) | [Main menu](#) |

- NEWS
- 02 September 2021

India's DNA COVID vaccine is a world first – more are coming

The ZyCoV-D vaccine heralds a wave of DNA vaccines for various diseases that are undergoing clinical trials around the world.

- [Smriti Mallapaty](#)



ZyCoV-D is the first DNA vaccine for people to be approved anywhere in the world. Credit: Zydus Cadila

India has approved a new COVID-19 vaccine that uses circular strands of DNA to prime the immune system against the virus SARS-CoV-2.

Researchers have welcomed news of the first DNA vaccine for people to receive approval anywhere in the world, and say many other DNA vaccines might soon be hot on its heels.

ZyCoV-D, which is administered into the skin without an injection, has been found to be 67% protective against symptomatic COVID-19 in clinical trials, and will probably start to be administered in India this month. Although the efficacy is not particularly high compared to that of many other COVID-19 vaccines, the fact that it is a DNA vaccine is significant, say researchers.

It is proof of the principle that DNA vaccines work and can help in controlling the pandemic, says Peter Richmond, a paediatric immunologist at the University of Western Australia in Perth. “This is a really important step forward in the fight to defeat COVID-19 globally, because it demonstrates that we have another class of vaccines that we can use.”

Close to a dozen DNA vaccines against COVID-19 are in clinical trials globally, and at least as many again are in earlier stages of development. DNA vaccines are also being developed for many other diseases.

“If DNA vaccines prove to be successful, this is really the future of vaccinology” because they are easy to manufacture, says Shahid Jameel, a virologist at Ashoka University in Sonipat, India.

Fast-tracked development

The urgency of combating COVID-19 has fast-tracked the development of vaccines that use genetic technology, such as messenger RNA and DNA vaccines, says David Weiner, director of the Vaccine & Immunotherapy Center at the Wistar Institute in Philadelphia, Pennsylvania.

RNA vaccines were quicker to show strong immune responses in clinical trials; they have now been delivered to hundreds of millions of people around the world. But DNA vaccines have a number of benefits, because

they are easy to produce and the finished products are more stable than mRNA vaccines, which typically require storage at very low temperatures.

ZyCoV-D was developed by Indian pharmaceutical firm Zydus Cadila, headquartered in Ahmedabad. On 20 August, India's drug regulator [authorized the vaccine](#) for people aged 12 and older. The efficacy figure of 67% came from trials involving more than 28,000 participants, which saw 21 symptomatic cases of COVID-19 in the vaccinated group and 60 among people who received a placebo.

ZyCoV-D contains circular strands of DNA known as plasmids, which encode the spike protein of SARS-CoV-2, together with a promoter sequence for turning the gene on. Once the plasmids enter the nuclei of cells, they are converted into mRNA, which travels to the main body of the cell, the cytoplasm, and is translated into the spike protein itself. The body's immune system then mounts a response against the protein, and produces tailored immune cells that can clear future infections. Plasmids typically degrade within weeks to months, but the immunity remains.

Both DNA and mRNA vaccines have been under development since the 1990s, says Weiner. The challenge for DNA vaccines is that they need to make it all the way to the cell nucleus, unlike mRNA vaccines, which just need to get to the cytoplasm, says Jameel. So, for a long time, DNA vaccines struggled to induce potent immune responses in clinical trials, which is why they had been approved for use as [vaccines only in animals](#), such as horses, until now.

Injection-free vaccine

To solve this problem, ZyCoV-D is deposited under the skin, as opposed to deep in muscle tissue. The area under the skin is rich in immune cells that gobble up foreign objects, such as vaccine particles, and process them. "This helps capture the DNA far more efficiently than in the muscle," Jameel says. Unusually, the vaccine is delivered using a needle-free device pressed against the skin, which creates a fine, high-pressure stream of fluid that punctures the surface and is less painful than an injection.

But despite being more potent than previous DNA vaccines, ZyCoV-D requires a minimum of three doses to achieve its initial efficacy. This is likely to add to the logistical challenge of administering the vaccine during the current pandemic, says Jameel.

Although ZyCoV-D's efficacy seems to be lower than the 90% or higher achieved by some mRNA vaccines, the figures are not comparable, says Jameel. The ZyCoV-D trials in India earlier this year were conducted while the Delta variant of SARS-CoV-2 was the dominant variant in circulation, whereas earlier mRNA vaccine trials were conducted when less transmissible variants were circulating. "The efficacy is essentially against the Delta variant, so that is pretty good," he says.

Some researchers have criticized a lack of transparency in the approval process, because no late-stage trial results have yet been published. Zydus Cadila says the trial is still under way and it will submit the full analysis for publication shortly. The company says the first doses will start to be administered in India in September and it plans to produce up to 50 million doses by early next year.

DNA vaccines in clinical trials

Many DNA vaccines against COVID-19 are currently undergoing clinical trials around the world.

Vaccine	Developer	Location	Route	Stage of trial
ZyCoV-D	Zydus Cadila	India	Skin	Approved for emergency use
INO-4800	Inovio and partners	United States	Skin	Phase II/III
AG0302-	AnGes, Osaka	Japan	Muscle	Phase II/III

COVID19 University, Takara Bio

GX-19N	Genexine	South Korea	Muscle	Phase I/II
GLS-5310	GeneOne Life Science	South Korea	Skin	Phase I/II
COVID-eVax	Takis, Rottapharm Biotech	Italy	Muscle	Phase I/II
AG0301-COVID19	AnGes, Osaka University, Takara Bio	Japan	Muscle	Phase I/II
Covigenix VAX-001	Entos Pharmaceuticals	Canada	Muscle	Phase I
CORVax12	Oncosec, Providence Cancer Institute	United States	Skin	Phase I
bacTRL-Spike	Symvivo	Canada	Oral	Phase I
COVIGEN	BioNet, Technovalia, University of Sydney	Thailand, Australia	Skin or muscle	Phase I

Source: World Health Organization. [COVID-19 Vaccine Tracker and Landscape](#) (WHO, 2021).

Vaccine pipeline

Several other DNA vaccines are being developed against COVID-19, using a variety of antigens and delivery mechanisms (see ‘DNA vaccines in clinical trials’). Two have entered late-stage trials: one by Japanese company AnGes, based in Osaka; the other, which Weiner helped to develop, by Inovio Pharmaceuticals in Plymouth Meeting, Pennsylvania. Inovio is injected under the skin and uses a device that hits the skin with short electric pulses to form pores in the cells that the vaccine can slip through.

More than half a dozen DNA vaccines for COVID-19 are in early-stage trials, including one by the South Korean biotech company GeneOne Life Science in Seoul, and another that Richmond is involved in, developed by the Thai firm BioNet in Bangkok. This vaccine is undergoing a phase I trial in Australia.

But Richmond expects many more DNA vaccines to emerge, targeting diseases for which there are currently no vaccines — from cytomegalovirus, which can be passed on to babies during pregnancy, to respiratory syncytial virus. DNA vaccines are also being trialled or developed for influenza, human papillomavirus, HIV and Zika.

DNA vaccines can store lots of information, which means they can encode large, complex proteins or even multiple proteins. Weiner says that gives them promise as anti-cancer vaccines, a possibility he is exploring in his own research.

“It’s a very exciting time for genetic technologies. They have finally gotten a chance to show what they can do,” he says.

Nature **597**, 161-162 (2021)

doi: <https://doi.org/10.1038/d41586-021-02385-x>

This article was downloaded by **calibre** from <https://www.nature.com/articles/d41586-021-02385-x>

- NEWS
- 31 August 2021

Rogue antibodies involved in almost one-fifth of COVID deaths

The self-targeting antibodies attack type 1 interferons that play a key role in fighting infection.

- [Diana Kwon](#)

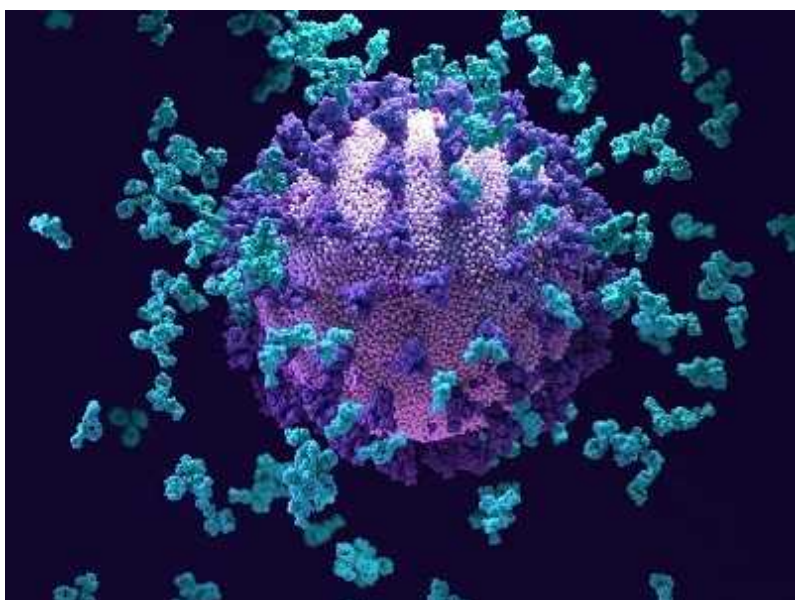


Physicians treat a person with COVID-19 at a hospital in Japan. Credit: Yasuyoshi Chiba/AFP via Getty

Antibodies that turn against elements of our own immune defences are a key driver of severe illness and death following SARS-CoV-2 infection in some people, according to a large international study. These rogue antibodies, known as autoantibodies, are also present in a small proportion of healthy, uninfected individuals — and their prevalence increases with age, which may help to explain why elderly people are at higher risk of severe COVID-19.

The findings, published on 19 August in *Science Immunology*¹, provide robust evidence to support an observation made by the same research team last October. Led by immunologist Jean-Laurent Casanova at the Rockefeller University in New York City, the researchers found that around 10% of people with severe COVID-19 had autoantibodies that attack and block type 1 interferons, protein molecules in the blood that have a critical role in fighting off viral infections².

“The initial report from last year was probably one of the most important papers in the pandemic,” says Aaron Ring, an immunologist at the Yale School of Medicine in New Haven, Connecticut, who was not involved in this work. “What they’ve done in this new study is really dig down to see just how common these antibodies are across the general population — and it turns out they’re astonishingly prevalent.”



[This ‘super antibody’ for COVID fights off multiple coronaviruses](#)

The international research team focused on detecting autoantibodies that could neutralize lower, more physiologically relevant concentrations of interferons. They studied 3,595 patients from 38 countries with critical COVID-19, meaning that the individuals were ill enough to be admitted to an intensive-care unit. Overall, 13.6% of these patients possessed autoantibodies, with the proportion ranging from 9.6% of those below the age of 40, up to 21% of those over 80. Autoantibodies were also present in 18% of people who had died of the disease.

Casanova and his colleagues suspected that these devious antibodies were a cause, rather than a consequence, of critical COVID-19. There were hints that this might be the case — the group had previously found that autoantibodies were present in around 4 in 1,000 healthy people whose samples had been collected before the pandemic². The team also found that individuals with genetic mutations that disrupt the activity of type 1 interferons are at higher risk of life-threatening disease^{3,4}.

To examine this link further, the researchers hunted for autoantibodies in a massive collection of blood samples taken from almost 35,000 healthy people before the pandemic. They found that 0.18% of those between 18 and 69 had existing autoantibodies against type 1 interferon, and that this proportion increased with age: autoantibodies were present in around 1.1% of 70- to 79-year-olds, and 3.4% of those over the age of 80.

“There is a massive increase in prevalence” with age, Casanova says. “This largely explains the high risk of severe COVID in people in the elderly population.” He adds that these findings have clear clinical implications, and suggests that hospitals should be checking patients for these autoantibodies, as well as mutations implicated in blocking type 1 interferons. This could identify people who are more likely to become critically ill from COVID-19, helping physicians to tailor their treatment appropriately.

A sample of more than 30,000 people is “too big to ignore”, according to Ring. “It just shows that this is something that we need to think about.” He adds that researchers should now consider whether autoantibodies play a part in driving other infectious diseases. Ring’s team has already found evidence⁵ of autoantibodies against various immune-system components in

people with COVID-19, and he and his colleagues are now investigating further. “I suspect that we’ve just started scratching the surface,” Ring says.

Nature **597**, 162 (2021)

doi: <https://doi.org/10.1038/d41586-021-02337-5>

References

1. 1.

Bastard, P. *et al.* *Science Immunol.* **6**, eabl4340 (2021).

2. 2.

Bastard, P. *et al.* *Science* **370**, eabd4585 (2020).

3. 3.

Asano, T. *et al.* *Science Immunol.* **6**, eabl4348 (2021).

4. 4.

Zhang, Q. *et al.* *Science* **370**, eabd4570 (2020).

5. 5.

Wang, E. Y. *et al.* *Nature* **595**, 283–288 (2021).

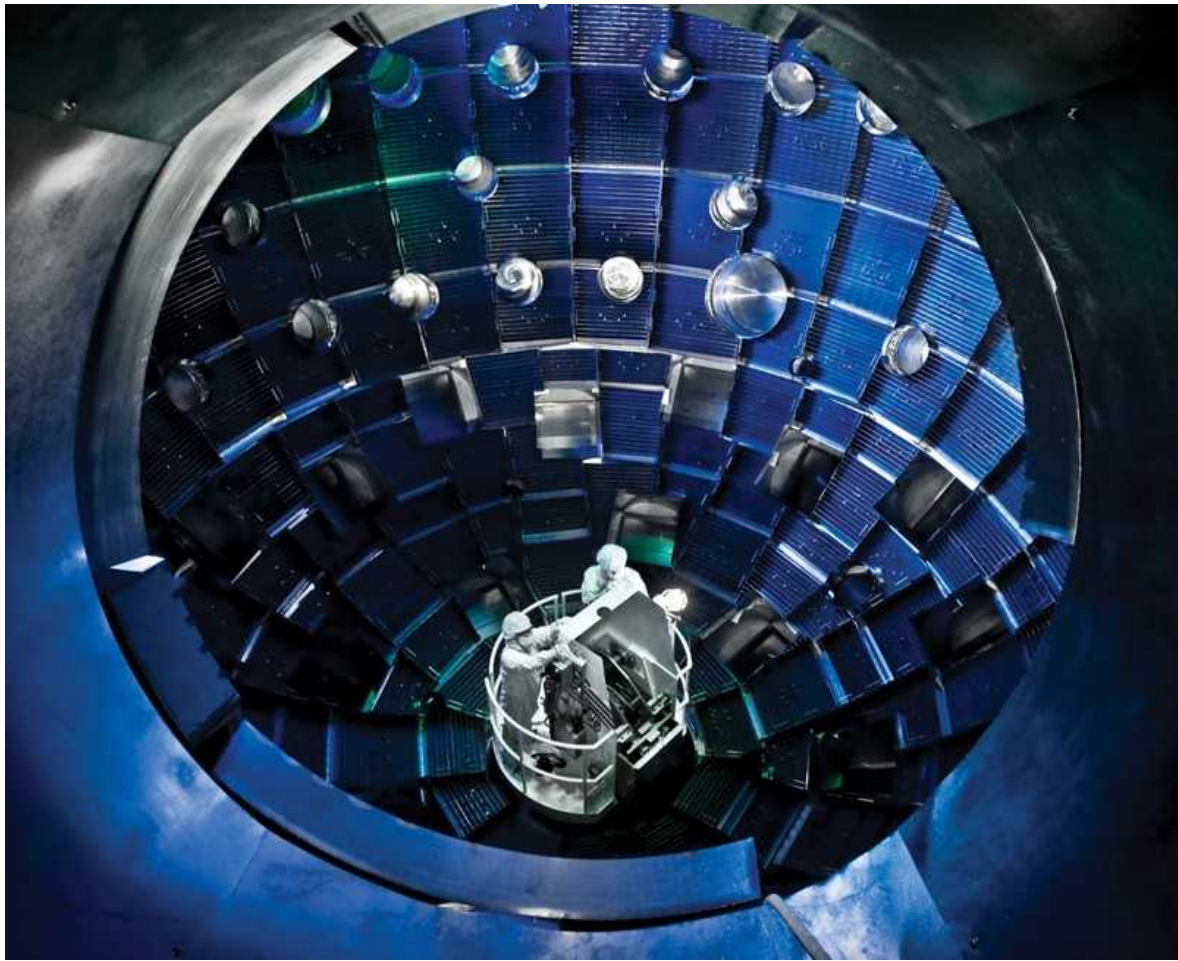
This article was downloaded by **calibre** from <https://www.nature.com/articles/d41586-021-02337-5>

- NEWS EXPLAINER
- 27 August 2021

US achieves laser-fusion record: what it means for nuclear-weapons research

Scientists are hopeful that the National Ignition Facility's recent success will advance understanding of thermonuclear reactions.

- [Jeff Tollefson](#)



The US National Ignition Facility (target chamber shown) is the size of three American football fields.Credit: Lawrence Livermore National Laboratory

Scientists at the US Department of Energy's flagship laser facility shattered their own record earlier this month by generating more than 10 quadrillion watts of fusion power for a fraction of a second — roughly 700 times the generating capacity of the entire US electrical grid at any given moment. News of the breakthrough has revived hopes that the long-troubled National Ignition Facility (NIF) might yet attain its goal of producing more energy than it consumes in a sustained fusion reaction.



[UK hatches plan to build world's first fusion power plant](#)

Housed at Lawrence Livermore National Laboratory in California, the US\$3.5-billion facility wasn't designed to serve as a power-plant prototype, however, but rather to probe fusion reactions at the heart of thermonuclear weapons. After the United States banned underground nuclear testing at the end of the cold war in 1992, the energy department proposed the NIF as part of a larger science-based Stockpile Stewardship Program, designed to verify the reliability of the country's nuclear weapons without detonating any of them.

With this month's laser-fusion breakthrough, scientists are cautiously optimistic that the NIF might live up to its promise, helping physicists to better understand the initiation of nuclear fusion — and thus the detonation of nuclear weapons. "That's really the scientific question for us at the moment," says Mark Herrmann, Livermore's deputy director for fundamental weapons physics. "Where can we go? How much further can we go?"

Here *Nature* looks at the NIF's long journey, what the advance means for the energy department's stewardship programme and what lies ahead.

How does the NIF achieve nuclear fusion?

Ten storeys high and spanning the area of three American football fields, the NIF houses an array of optics and mirrors that amplify and split an initial pulse of photons into 192 ultraviolet laser beams, ultimately focusing them on a target that is smaller than a pencil eraser. The beams hit the target — a gold cylinder — with around 1.9 megajoules of energy in less than 4 billionths of a second, creating temperatures and pressures seen only in stars and thermonuclear bombs.

Faced with this pulse power, the cylinder, which holds a frozen pellet of deuterium and tritium, collapses as the hydrogen isotopes at the pellet's core heat up, fuse and generate helium nuclei, neutrons and electromagnetic radiation. The goal is to unleash a cascade of particles that leads to more fusion and more particles, thus creating a sustained fusion reaction; by definition, ‘ignition’ occurs when the fusion reaction generates more energy than it consumes. Preliminary results from the experiment on 8 August indicate that fusion reactions generated a record-shattering 70% of the power that went into the experiment — nearly achieving ignition.

The NIF began operations in 2009. Why has it taken so long to (nearly) achieve ignition?

Nobody said it would be easy, but building the NIF proved to be a more complex endeavour than officials originally thought. Construction began in 1997 and ended more than a decade later, several years behind schedule and at least \$2.4 billion over budget.

The NIF missed its goal of achieving ignition by 2012; scientists have spent the years since fine-tuning the facility and introducing optimized targets into the reaction chamber. The recent success was achieved after multiple changes to the massive system, including new diagnostics, improved target-fabrication techniques and enhancements to the precision of the lasers.



The NIF focuses 192 laser beams onto a target, creating temperatures and pressures like those inside thermonuclear bombs. Credit: Lawrence Livermore National Laboratory

Long before the NIF fired its first shot, it was [surrounded by controversy](#). Independent scientists raised questions about both the design and the management of the facility. As recently as May 2016, the US National Nuclear Security Administration (NNSA), a branch of the Department of Energy (DOE) that oversees nuclear weapons and funds the NIF to the tune of around \$350 million per year, questioned whether the facility would ever achieve its ignition goal.

But even long-time critics of the facility have acknowledged the recent breakthrough as a significant step forward. Stephen Bodner, a plasma physicist who formerly worked at the US Naval Research Laboratory in Washington DC, said he is both “surprised and pleased” with the result — assuming it’s reproducible. “I look forward to reading the scientific report that explains it,” he says.

The Livermore team and its collaborators are just beginning to pore over results, but preliminary data suggest an 8-fold increase in energy yield compared with experiments conducted several months ago, and a 25-fold

increase compared with the previously reported record, set in 2018. Laboratory officials said they made the announcement about the experiment before peer-reviewed publication because news of the results was already spreading through the fusion community.

If the NIF achieves full ignition, what could the results teach scientists about nuclear weapons?

In theory, the NIF could offer a better understanding of the precise conditions necessary to initiate and sustain a fusion reaction — which is, in a sense, what the facility's scientists have been working out as they've optimized the system over the past 12 years. This question is also at the heart of the stockpile stewardship programme.



[The labs that forge distant planets here on Earth](#)

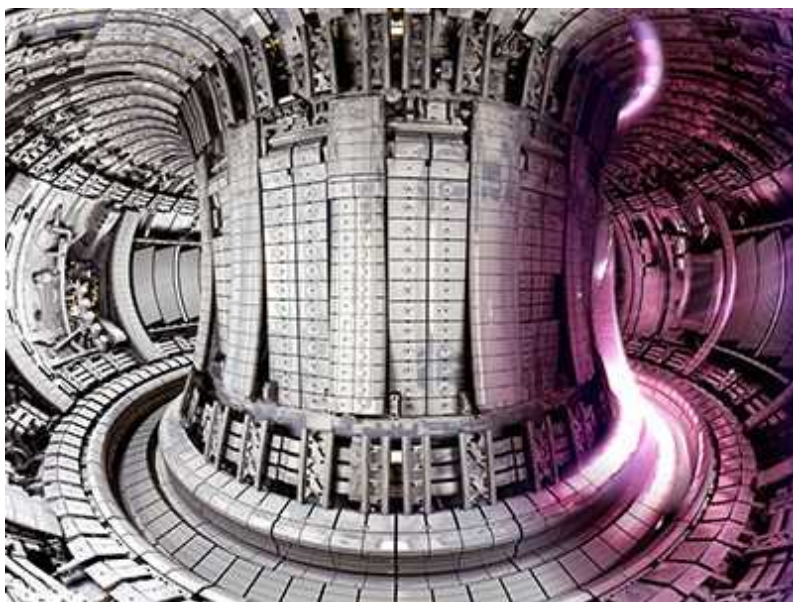
Since 1992, physicists [have been building a comprehensive programme to study the US nuclear arsenal](#) with increasingly powerful supercomputers and dozens of other research facilities designed to test everything from nuclear materials and components to explosives. Although the NIF is not detonating miniature bombs, says Herrmann, its experiments could help scientists improve the computer models they use to simulate how weapons will detonate, potentially reducing uncertainties. Other experiments might test

how the electronics and other components in a weapon hold up in the face of intense bursts of radiation expected in a hostile war environment.

Many scientists argue that the facility also bolsters confidence in the nation's weapons stockpile — and wards off external threats — by helping to attract young researchers to the nuclear field and maintaining a broader scientific enterprise. "There is an overall element of showing scientific prowess that is important as well," says Herrmann.

But is the NIF essential to the US stockpile stewardship programme?

Some critics have questioned whether scientists need the facility to maintain the United States' nuclear weapons. They say the stewardship programme has already bolstered confidence in the stockpile within the NNSA, and point out that the agency is now proposing to build what are effectively new nuclear weapons, rather than simply maintaining the current cache with minimal changes.



Fuel for world's largest fusion reactor ITER is set for test run

"That shows either an enormous amount of hubris, or an incredible confidence that you can build a lot of what we need for the next 50 years,

even without a functioning NIF,” says Hans Kristensen, who heads the nuclear information project at the Federation of American Scientists in Washington DC.

Herrmann argues that the NIF can still help, though. He says nuclear weapons scientists are constantly extrapolating from limited experimental data as they evaluate their computer simulations. Information gathered from more energetic fusion reactions at the NIF, he says, will allow them to test the models more directly, hopefully reducing uncertainties and making it easier for the NNSA to certify that weapons in the arsenal will detonate if needed, and not before.

So what happens next for the NIF?

The ultimate test — whether the team can replicate its 8 August success — could come as early as October, say laboratory officials. Meanwhile, scientists are rushing to understand and publish their findings. Because the facility is operating at the scientific edge of what is possible, even slight variations in the manufacture of the target capsule or the tuning of the lasers could cause the system to produce more, or less, energy than the earlier experiment, says Herrmann. “We can’t do the exact same target experiment, because we blew the target up,” he says. But with time, he adds, the science team should be able to repeat and build on this success — and push the facility even further.

Nature **597**, 163-164 (2021)

doi: <https://doi.org/10.1038/d41586-021-02338-4>

This article was downloaded by **calibre** from <https://www.nature.com/articles/d41586-021-02338-4>

- NEWS
- 03 September 2021

Freak US winters linked to Arctic warming

Models suggest that distortions in polar-vortex winds can send chilly air hurtling southwards. But some climate scientists remain unconvinced.

- [Quirin Schiermeier](#)



Unusually severe winter storms brought snow to Austin, Texas, in February. Credit: Montinique Monroe/Getty

Recent spells of unusually cold winter weather in the United States and other parts of the Northern Hemisphere could be a paradoxical consequence of the climate warming in the Arctic, according to a study based on decades of atmospheric observations. However, it is still unclear whether this represents a long-term trend that will persist as the world heats up.

The Arctic's rate of warming is twice that for Earth as a whole, and some climate researchers have long suspected that this rapid Arctic warming can trigger anomalies in the winds around the North Pole, with consequences for weather thousands of kilometres farther south.

"Conventional wisdom is that while global warming means more heatwaves, it will definitely lead to less cold spells and snowfall," says Judah Cohen, a climate scientist at the Massachusetts Institute of Technology in Cambridge, and lead author of the study. "But that's not quite true. There are mechanisms by which climate change can contribute to more severe winter weather too."

One dominant feature of the winter atmosphere above the Arctic is the polar vortex, a fast-flowing band of high-altitude winds. The vortex normally isolates the atmosphere over the Arctic from warmer air closer to the Equator. But when the polar vortex stretches and undulates, as it sometimes does, chilly air can leak out to latitudes that would otherwise rarely experience cold snaps. Such extreme weather can prove fatal in regions unprepared for frosty conditions — in February, at least 111 people died in Texas when cold Arctic air hit the state and parts of northern Mexico.



The Arctic is burning like never before — and that's bad news for climate change

In their study, published this week in *Science*¹, Cohen and his colleagues compared 40 years of satellite observations of atmospheric conditions over the Arctic with experiments based on computational climate models. The models probed how a decline in Arctic sea ice and snow cover would affect airstreams in the region. Since ice and snow reflect a large fraction of incoming sunlight back into space, whereas the darker ocean and land surface absorb more radiation, this decline is known to drive Arctic warming.

The researchers found that episodes of polar-vortex stretching have markedly increased in the past few decades, and that their models reproduced this behaviour well when they included the effects of Arctic warming.

“This is an insightful new analysis,” says Dim Coumou, a climate scientist at the Free University Amsterdam in the Netherlands, who was not involved in the study. “Its strength is that they have very carefully looked at a specific pattern of the polar vortex that is important for cold spells in particular places, and backed up their observational analyses with climate-modelling experiments.”

But the idea that Arctic warming might be responsible for cold spells in mid-latitude regions is still hotly debated among climate scientists. At first glance, it might seem obvious that winters will generally tend to get milder in a warming world. But climate models that are commonly used to study complex links between the different components of the climate system diverge on the issue of how strongly Arctic warming might influence mid-latitude winters, and state-of-the-art models do not accurately replicate observed trends in the behaviour of the polar vortex. It remains to be seen whether the models are missing something, or whether the observations of polar-vortex stretching merely reflect natural climate variability, says Daniela Matei, a climate modeller at the Max Planck Institute of Meteorology in Hamburg, Germany, who was not involved in the study.

The new analysis does not settle these questions, Matei says. Although changes in sea ice and snow cover do seem to have a role in wind anomalies high up above the Arctic, other factors such as decadal variability in sea surface temperatures could also drive wintertime anomalies in the Arctic atmosphere that can lead to unexpectedly cold weather elsewhere, she says. To complicate matters further, there are still significant uncertainties about how Earth's climate as a whole responds to snow and sea-ice changes.

For now, it remains unclear whether the recent examples of extreme winter cold are precedents for future weather. "Climate change isn't linear," Matei says. "What happens in one decade may not apply in the next one."

Nature **597**, 165 (2021)

doi: <https://doi.org/10.1038/d41586-021-02402-z>

References

1. 1.

Cohen, J., Agel, L., Barlow, M., Garfinkel, C. I. & White, I. *Science* **373**, 1116–1121 (2021).

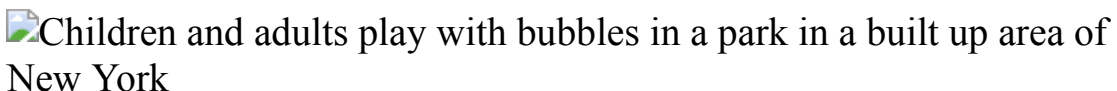
| [Section menu](#) | [Main menu](#) |

- NEWS FEATURE
- 07 September 2021

Kids and COVID: why young immune systems are still on top

Innate immunity might be the key to why children have fared better with the virus. But the Delta variant poses fresh unknowns.

- [Smriti Mallapaty](#)



After extremely low case rates in New York City early this summer, the number of children testing positive for SARS-CoV-2 has begun to rise.
Credit: Spencer Platt/Getty

Early last year, children's hospitals across New York City had to pivot to deal with a catastrophic COVID-19 outbreak. "We all had to quickly learn — or semi-learn — how to take care of adults," says Betsy Herold, a paediatric infectious-disease physician who heads a virology laboratory at the Albert Einstein College of Medicine. The reason: while hospitals across the city were bursting with patients, paediatric wards were relatively quiet. Children were somehow [protected from the worst of the disease](#).

Data collected by the US Centers for Disease Control and Prevention from hospitals across the country suggest that people under the age of 18 have accounted for less than 2% of hospitalizations due to COVID-19 — a total of 3,649 children between March 2020 and late August 2021. Some children do get very sick, and more than 420 have died in the United States, but the majority of those with severe illness have been adults — a trend that has been borne out in many parts of the world.

This makes SARS-CoV-2 somewhat anomalous. For most other viruses, from influenza to respiratory syncytial virus, young children and older adults are typically the most vulnerable; the risk of bad outcomes by age can be represented by a U-shaped curve. But with COVID-19, the younger end of that curve is largely chopped off. It's "absolutely remarkable", says Kawsar Talaat, an infectious-disease physician at the Johns Hopkins Bloomberg School of Public Health in Baltimore, Maryland. "One of the few silver linings of this pandemic is that children are relatively spared."

The phenomenon was not entirely surprising to immunologists, however. With other viruses, adults have the advantage of experience. Through prior infection or vaccination, their immune systems have been trained to deal with similar-looking pathogens. The novelty of SARS-CoV-2 levelled the playing field, and showed that children are naturally better at controlling viral infections. "We always think of children as germ factories," says Dusan Bogunovic, an immunologist and geneticist at the Icahn School of Medicine at Mount Sinai, in New York City. But it's not because their immune systems are ineffective; they're just inexperienced, he says.



[COVID and schools: the evidence for reopening safely](#)

Research is beginning to reveal that the reason children have fared well against COVID-19 could lie in the innate immune response — the body's crude but swift reaction to pathogens. Kids seem to have an innate response

that's "revved up and ready to go", says Herold. But she adds that more studies are needed to fully support that hypothesis.

The emergence of the Delta variant has made finding answers more urgent. Reports suggest that in the United States and elsewhere, children are starting to make up a [larger proportion of reported infections and hospitalizations](#). These trends might be due to Delta's high transmission rate and the fact that many adults are now protected by vaccines.

For now, there is no clear evidence that children are more vulnerable to or more affected by Delta compared with earlier variants. But SARS-CoV-2, like all viruses, is constantly mutating and becoming better at evading host defences, and that could make understanding childhood's protective benefits more important. "We haven't paid much attention to age-related differences in immune responses because it hasn't had huge clinical implications previously," says Lael Yonker, a paediatric pulmonologist at Massachusetts General Hospital in Boston. "COVID-19 highlights that we need to better understand these differences."

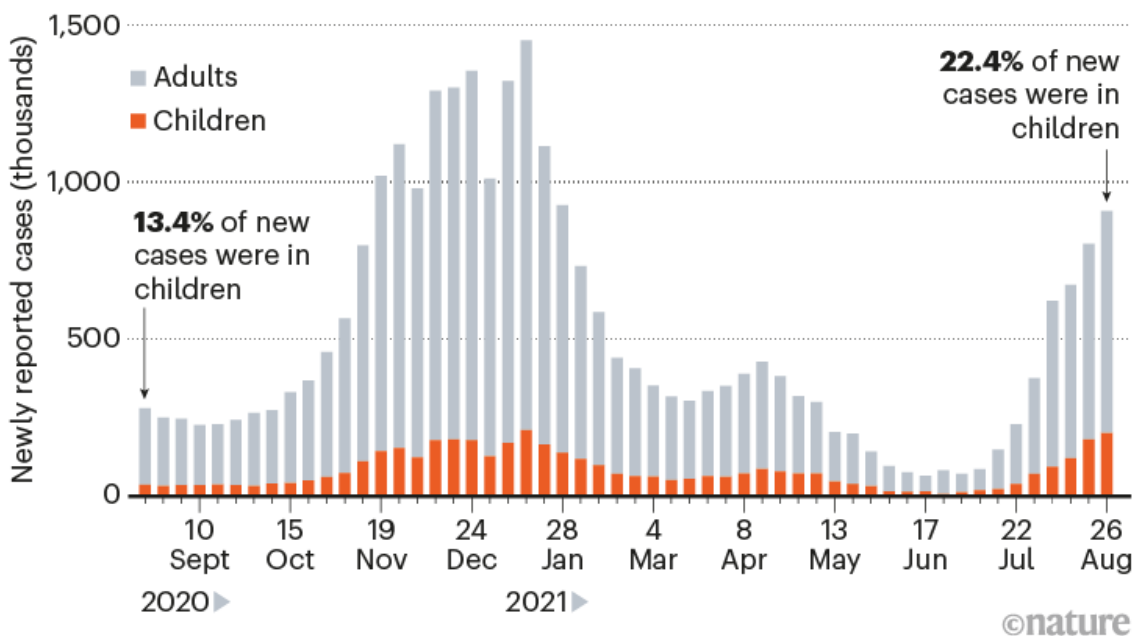
Brainstorming ideas

Why are children better than adults at controlling SARS-CoV-2? At first, researchers thought that children were simply not getting infected as often. But the data show that they are — at least nearly (children under age ten might be slightly less susceptible)¹.

The American Academy of Pediatrics found that, up until late last month, some 15% of all COVID-19 cases in the United States had been in individuals aged under 21 — that's more than 4.8 million young people (see 'Young and infected'). And a survey in India that tested people for antibodies against SARS-CoV-2, which are produced after infection or vaccination, found that more than half of children aged 6–17 — and two-thirds of the population overall — had detectable antibodies.

YOUNG AND INFECTED

Over the course of the COVID-19 pandemic, nearly 15% of all confirmed cases in the United States have been in children. In the last week of August 2021, just over 22% of weekly reported cases were in children, a rise that may be attributable to higher vaccination rates in adults.



Source: American Academy of Pediatrics and the Children's Hospital Association

Clearly, children are getting infected. So maybe the virus can't replicate in them as well as it does in adults. Some researchers proposed that children might have fewer ACE2 receptors, which the virus uses to enter and infect cells. There is conflicting evidence on age-related differences in ACE2 expression in the nose and lungs, but scientists who measured the 'viral load' — the concentration of viral particles — in people's upper airways have seen no clear difference between children and adults².

In one analysis³ of 110 children, posted as a preprint on 3 June, researchers found that infants through to teenagers could have high viral loads, especially soon after being infected. "Not only is the virus there and detectable, but it's live virus," which means these individuals are also infectious, says Yonker, who led the study.

Another proposal is that children, who seem to be sniffling all year round, might be more exposed to other coronaviruses that cause the common cold, and therefore have a squad of antibodies at the ready with some ability to latch on to the pandemic coronavirus. But the weight of evidence suggests that adults also have this immunity. Strikingly, these ‘cross-reactive’ antibodies don’t offer any special protection — if anything, they could lead to a misguided response.

Having largely discounted these hypotheses, Herold and her colleagues set out to look at whether there was something specific in children’s immune response that gave them a benefit.

Some clues were circulating in the blood of those who have been infected. In a study⁴ comparing 65 individuals aged under 24 with 60 older people, Herold and her colleagues found that, overall, the younger patients (who had milder symptoms) produced similar levels of antibodies to the older cohort. But they had reduced levels of specialized antibodies and cells related to the adaptive immune response, the arm of the immune system that learns about a pathogen and helps to quickly quash it if it ever returns. Specifically, kids had lower levels of ‘neutralizing’ antibodies that block SARS-CoV-2 from infecting cells; antibodies that label infected cells to be gobbled up and destroyed by other cells; and white blood cells known as regulatory and helper T cells.



Will COVID become a disease of the young?

By contrast, the children in the study had higher levels of the signalling proteins interferon- γ and interleukin-17, which alert the immune system to the arrival of a pathogen. These were probably produced by cells that line the airways, and are involved in mediating innate immunity. Herold suspected that the children mounted a less robust adaptive immune response because their innate response was more efficient at eliminating the threat. An overactive adaptive response in adults, she says, could be causing some of the complications in COVID-19.

Another study⁵, by researchers in Hong Kong, of adults and children infected with SARS-CoV-2 also found that the adaptive response — specifically that of T-cells — was less potent in children, suggesting that something was happening early on that triggered the difference, says study co-author Sophie Valkenburg at the University of Hong Kong.

But, she says, other factors such as reduced inflammation and a more targeted adaptive response could also be important. The researchers found that infected children had lower levels of cells known as monocytes, including inflammatory monocytes, which act as a bridge between the innate and adaptive immune systems. But these children did have higher levels of T follicular helper cells, which are important for making an early antibody response.

First responders

Herold and her colleagues have since tried to measure more directly the innate response in children. They took nose and throat swabs from people arriving at the emergency department, including 12 children with milder disease and 27 adults, some of whom died. The children had higher levels of signalling proteins such as interferons and interleukins, and higher expression of the genes that code for such proteins².

One broad category of immune cells that could be playing an important part in children, says Yonker, are innate lymphoid cells, which are among the first to detect tissue damage and secrete signalling proteins that help to

regulate the innate and adaptive immune responses. In one study⁶ posted as a preprint on 4 July, Yonker and her colleagues found that the number of innate lymphoid cells in the blood of people who did not have COVID-19 declined with age and was lower in men — mirroring the greater risk of severe disease observed in older men. Adults with severe disease and children with symptoms also had reduced levels of these cells.

Compared with adults, children recently infected with SARS-CoV-2 have also been found to have higher levels of activated neutrophils, cells that are on the front line in the response to unfamiliar invaders⁷. Neutrophils ingest viral particles before they have a chance to replicate, says Melanie Neeland, an immunologist at the Murdoch Children's Research Institute (MCRI) in Melbourne, who led the work. Furthermore, they become less effective with age.

Epithelial cells that line the insides of the nose could also be coordinating the quick response. In children, these cells are flush with receptors that can recognize molecules commonly found in pathogens; specifically, researchers have found that children have significantly higher expression of genes encoding MDA5, a receptor known to recognize SARS-CoV-2, than do adults⁸. After spotting the viral intruder, these cells immediately trigger the production of interferons. “For us adults, it takes two days to ramp up the viral defence system to a level that we see from day zero with children,” says study co-author Roland Eils, a scientist in computational genomics at the Berlin Institute of Health. “It’s the time lag which makes the difference between children and adults.”

Studies of rare, inherited, immune disorders also point to a predominant role for innate immunity in thwarting respiratory pathogens such as influenza.



A child receives treatment for COVID-19 in Istanbul, Turkey in April. Credit: Sebnem Coskun/Anadolu Agency/Getty

Isabelle Meyts, a paediatric immunologist and physician at the Catholic University of Leuven in Belgium, regularly sees children with immune disorders. When the pandemic hit, she prepared a plan to protect them. “The patients I was most scared for were actually the patients who have innate immune defects,” says Meyts.

Her hunch has so far proved correct. Children with disorders affecting their adaptive immune response — those who don’t produce antibodies or have faulty B-cell and T-cell production, for example — did not encounter problems when infected with SARS-CoV-2. Among those that became severely ill were children with shortcomings in their innate immune response, she says. “It’s not really the adaptive immune system that is helping you to beat this virus.”

A study in adults⁹ also found that a small number of people with severe COVID-19 have mutations that disrupt type 1 interferon activity, which plays a part in the innate immune response to viruses. Separate analyses

found that one in ten people with life-threatening COVID-19 produced antibodies that blocked the activity of these interferons^{[10](#)}, and that the prevalence of such antibodies increases with age in people who have not previously been infected with the coronavirus^{[11](#)}.

But, an overactive innate response might be detrimental as well. People with Down's syndrome, for example, are more at risk of severe COVID-19, which Meyts says could be because the extra chromosome they have contains several genes involved in the type 1 interferon response. There is an intriguing balance to be struck between a deficient initial response and an excessive one, says Meyts. "It needs to be exactly right on the spot, and the timing needs to be perfect."

Tickling bad memories

Innate immunity is hardly the whole story, say researchers, especially given how interconnected it is with the adaptive response.

"The idea that the immunologic tone is different in children seems likely," says Laura Vella, an immunologist and paediatric infectious-diseases researcher at the Children's Hospital of Philadelphia, Pennsylvania. "But what's contributing to that difference?" It could be many things working together, she says.

Some researchers propose that years of exposure to other human coronaviruses could mean that adult immune systems approach SARS-CoV-2 the way they would those other viruses, resulting in a less effective response — a concept known as [original antigenic sin](#). By contrast, kids could be producing a fresh, more finely tuned response to a brand-new virus.



COVID vaccines and kids: five questions as trials begin

Amy Chung, an immunologist at the Peter Doherty Institute for Infection and Immunity in Melbourne, Australia, has seen some evidence of this in an expansive study¹² of antibodies in the blood of a few hundred children and adults, including 50 infected with SARS-CoV-2. She and her colleagues found that adults had more cross-reactive antibodies targeted at parts of SARS-CoV-2 that were similar to bits of other coronaviruses, whereas children tended to produce a broader range of antibodies against all sections of the virus.

Researchers are also looking at other factors that are known to worsen with age, such as the ability to control inflammation and heal damaged tissue. Children are less prone to clots forming in blood vessels, and this could offer some protection, says Vera Ignjatovic, a biochemist who studies paediatric haematology at the MCRI.

Of course, not all children have asymptomatic or mild infection. Some, many of whom have underlying conditions such as chronic heart disease or cancer, get serious pneumonia. And estimates vary widely for the prevalence of ‘long COVID’, in which symptoms persist for months or more. A recent preprint suggested that up to 14% of young people who test positive for COVID-19 have multiple symptoms three months after the diagnosis¹³. And a small group of otherwise healthy children — some 3 out of 10,000 infected individuals aged under 21 — experience a condition known as multi-system inflammatory syndrome in children (MIS-C). They generally respond well to the initial infection, but about a month later are admitted to hospital with a

host of symptoms, from heart failure to abdominal pain and conjunctivitis, with minimal damage to the lungs. “It’s a sick group of kids,” says Vella.

Michael Levin, a paediatrician and infectious-diseases physician at Imperial College London, thinks MIS-C is probably the result of an outsized antibody or T-cell reaction to the infection. But despite hundreds of papers on the topic, “exactly what distinguishes children who get MIS-C from the rest of the child population is completely unknown”, says Levin.

As the pandemic wears on, researchers worry that the virus could evolve in ways that thwart some part of kids’ innate protection. Some researchers have found that the Alpha variant, which was dominant in some parts of the world for a time, developed tricks that allowed it to suppress the body’s innate immune response. They worry that Delta could do the same. For now, increased hospitalizations of children in regions where Delta is circulating seem to be the result of its enhanced infectivity across all ages, coupled with the fact that many adults are vaccinated or have already been infected with SARS-CoV-2. But researchers are watching carefully.

“Almost all viruses have developed ways of evading the innate immune system, and COVID-19 is no exception to that rule,” says Herold. “Right now — knock on wood — the kids are still winning with their innate immunity.” But for how much longer? “We don’t know.”

Nature **597**, 166-168 (2021)

doi: <https://doi.org/10.1038/d41586-021-02423-8>

References

1. 1.

Irfan, O., Li, J., Tang, K., Wang, Z. & Bhutta, Z. A. *J. Glob. Health* **11**, 05013 (2021).

2. 2.

Pierce, C. A. *et al. JCI Insight* **6**, e148694 (2021).

3. 3.

Yonker, L. M. *et al.* Preprint at medRxiv
<https://doi.org/10.1101/2021.05.30.21258086> (2021).

4. 4.

Pierce, C. A. *et al.* *Sci. Transl. Med.* **12**, eabd5487 (2021).

5. 5.

Cohen, C. A. *et al.* *Nature Commun.* **12**, 4678 (2021).

6. 6.

Silverstein, N. J. *et al.* Preprint at medRxiv
<https://doi.org/10.1101/2021.01.14.21249839> (2021).

7. 7.

Neeland, M. R. *et al.* *Nature Commun.* **12**, 1084 (2021).

8. 8.

Loske, J. *et al.* *Nature Biotechnol.* <https://doi.org/10.1038/s41587-021-01037-9> (2021).

9. 9.

Zhang, Q. *et al.* *Science* **370**, eabd4570 (2021).

10. 10.

Bastard, P. *et al.* *Science* **370**, eabd4585 (2021).

11. 11.

Bastard, P. *et al.* *Sci. Immunol.* **6**, eabl4340 (2021).

12. 12.

Selva, K. J. *et al.* *Nature Commun.* **12**, 2037 (2021).

13. 13.

Stephenson, T. *et al.* Preprint at Research Square
<https://doi.org/10.21203/rs.3.rs-798316/v1> (2021).

This article was downloaded by **calibre** from <https://www.nature.com/articles/d41586-021-02423-8>

| [Section menu](#) | [Main menu](#) |

- NEWS FEATURE
- 08 September 2021

Climate science is supporting lawsuits that could help save the world

Governments have failed to slow climate change quickly enough, so activists are using courts to compel countries and companies to act — increasingly with help from forefront science.

- [Quirin Schiermeier](#)



Thousands of people marched in Munich, Germany, in September 2019 to call for more urgency in fighting climate change. Credit: Sachelle Babbar/ZUMA Wire/Alamy

Friederike Otto hadn't really thought much about the legal world when she answered the phone one day in 2018. On the other end of the line was Petra Minnerop, a scholar of international law at the University of Durham, UK, who was exploring how the legal system might help to save the planet.

Minnerop had developed an interest in climate litigation — efforts to hold governments and companies legally responsible for contributing to global warming. Following the success of several climate lawsuits, she was seeking to get involved and thought Otto's research might help. Otto, a climate modeller at the University of Oxford, UK, is one of the world's leaders in attribution science — a field that has developed tools to assess how much human activities drive extreme weather events, including the heatwaves, fires and floods that have ravaged parts of the globe this year. In their

telephone call, the pair realized that they had similar aims and they set about thinking how science and environmental law might trigger more action to limit climate change.

Minnerop and Otto are in the vanguard of scientists and legal scholars who are assisting in lawsuits to force governments and companies [to take action against climate change](#). Over the past few decades, environmental groups and citizens around the world have filed more than 1,800 climate suits. Science has been central to supporting the arguments in these cases, but the vast majority have relied on the most basic conclusions of climate research. Now, Otto, Minnerop and others are seeking to bring in the latest science to improve lawsuits' chances of driving substantial reductions in greenhouse-gas pollution.

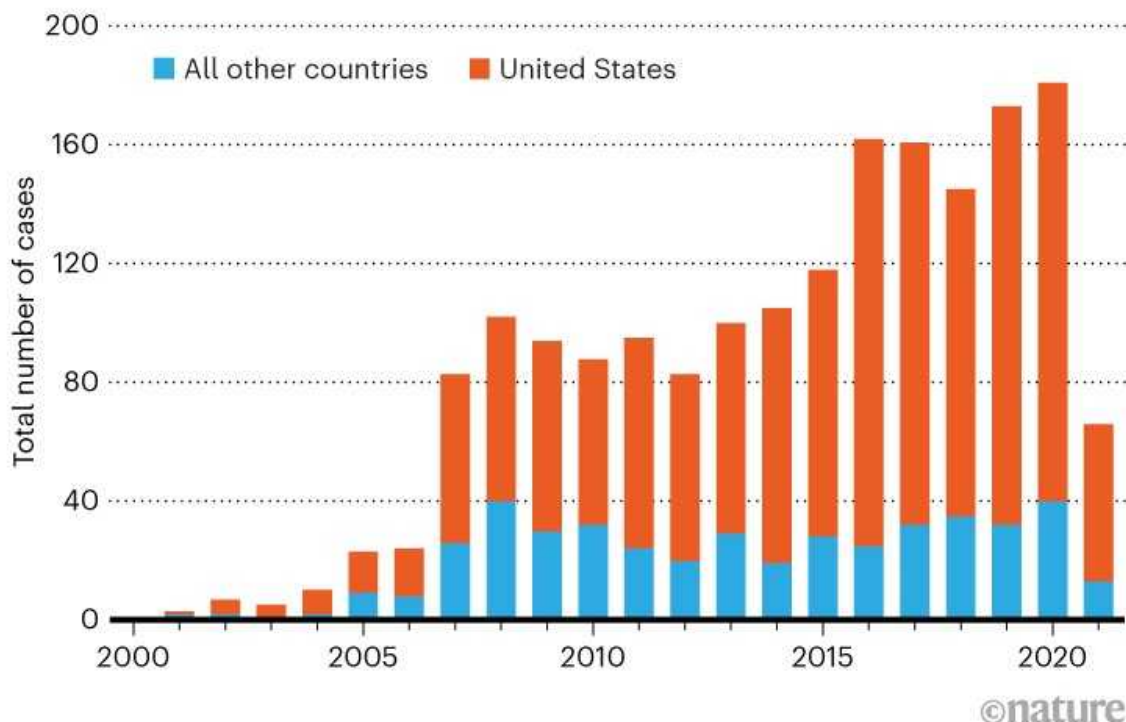
"There's a really big gap in many cases between what can be said scientifically and what is brought to courts," says Otto.

Court order

The number of climate suits has surged in recent years, thanks in part to a growing youth climate movement that has injected fresh energy into activism aimed at protecting the planet. Since 2015, plaintiffs, including children, have [filed more than 1,000 climate cases](#), according to an analysis¹ published in July by researchers at the Grantham Research Institute on Climate Change and the Environment in London (see 'Climate cases on the rise'). In 37 cases, lawsuits allege that governments have not lived up to their promises to lower the risks of climate change or to set goals that are ambitious enough. These cases, which target systemic problems, have generated the most attention, and could have some of the most far-reaching consequences if they are successful. Other cases focus on specific projects or practices, such as coal mining in Australia or deforestation in Brazil.

CLIMATE CASES ON THE RISE

There has been a sharp increase in the number of lawsuits related to climate change in the past five years.



©nature

Source: Ref. 1

Success at court was limited at first. But a string of wins in the past two years is raising hopes that the legal scales are tilting in favour of stronger climate action. In May, the District Court of The Hague ruled that the energy company Royal Dutch Shell must reduce its carbon emissions by 45% compared with 2019 levels over the next 9 years, arguing that the high level of current emissions by the group might contribute to imminent environmental harm to Dutch citizens.

A month earlier, the Federal Constitutional Court in Germany ordered the government to lay out a clearer strategy towards achieving its climate targets for the period after 2030. The country is the world's seventh-largest greenhouse-gas emitter. A similar court ruling last year compels the Irish government to flesh out its climate mitigation plan and explain how it intends to meet the goal of cutting emissions by 80% by 2050, relative to 1990 levels.



How scientists can help lawyers on climate action

These two cases follow a precedent set by a landmark decision in 2015 in the Netherlands — a few months before nations agreed in Paris to limit global warming to well below 2 °C relative to pre-industrial levels, and preferably to 1.5 °C. The [lawsuit had been filed in 2013](#) on behalf of almost 900 plaintiffs, including children. The court ordered the Dutch government to take action to lower domestic greenhouse-gas emissions by at least 25% by the end of 2020, compared with 1990 levels.

“People said we would have zero chance of winning,” says Jan Rotmans, a climate scientist at the Dutch Research Institute For Transitions in Rotterdam, who set up the Urgenda Foundation that filed the lawsuit. “But it turned out we were a catalyst.”

A court of appeal and the Supreme Court of the Netherlands [later upheld the ruling](#). Emissions in the Netherlands in 2020 were down by around 24%, but missed the target; the Urgenda Foundation announced in June, after a meeting with Dutch Prime Minister Mark Rutte, that it is considering suing the government for damages resulting from insufficient climate action.

Similarly to subsequent rulings, the Dutch court’s move was heavily based on the body of climate science compiled by the Intergovernmental Panel on Climate Change (IPCC). In its judgment, the court cited scientific consensus

that a global atmospheric concentration of carbon dioxide that was higher than 430 parts per million — the threshold to 1.5 °C warming — would mean “a serious degree of danger” for Dutch citizens, including extreme heat, drought, precipitation and sea-level rise.

“For the first time, a court had recognized that a government violates its duty of care for citizens if it doesn’t do enough to curb emissions,” says Joana Setzer, who specializes in climate litigation at the Grantham Institute and is a co-author of the July report. “This meant a lot from a legal point of view.”



[Climate lawsuits are breaking new legal ground to protect the planet](#)

Other cases have tended to follow the same scientific justification. Referring to IPCC science, judges in Ireland and Germany acknowledged that insufficient climate action might soon lead to disruptions — including wild weather or dangerous sea-level rises that would threaten the livelihood of future generations. In South Korea, a group of young people are challenging their government for human-rights violation on the same grounds. Judgments in that case and similar ones in the United States are still pending.

As signs of dangerous climate change are becoming more evident, pressure is mounting to hold governments and major carbon-emitting firms accountable. And this year has brought a string of weather extremes,

including record heat in July in parts of North America, wildfires raging in Siberia and severe rainfall and floods in Belgium, Germany and China. Studies by Otto's group and others have already demonstrated that climate change is at least [partly responsible for the North American heatwave](#) and the [central European floods](#). Extreme weather events worldwide [will become increasingly severe](#) as temperatures continue to rise, the IPCC said in August, in the first part of its latest assessment of the state of climate science².

Bigger picture

The new IPCC reports will add pressure for stronger climate action, but as climate litigation expands in scope, it will draw on a broader range of research, says Peter Frumhoff, chief climate scientist at the Union of Concerned Scientists in Cambridge, Massachusetts.

"It's a benefit to have the IPCC as a framework of accepted climate research," he says. "But IPCC science isn't all you need at court. There's a lot more to the picture." Future liability cases, says Frumhoff, could also incorporate the results of emerging attribution science, reviews of countries' compliance with national commitments to the Paris agreement and studies related to what companies are doing in terms of the climate risks of their products.

There's another reason that lawsuits might start to rely more on science that goes beyond what appears in IPCC reports. Those massive studies take years to compile, so the results can be out of date by the time the reports are released. Before this year, the last major IPCC report on the physical basis of climate science was published in 2013. Climate-change attribution was described as 'challenging' in a 2012 IPCC special report on managing the risks of extreme events and disasters³; but that science has matured to the point at which Otto and other researchers conduct attribution studies within days to weeks after major weather anomalies.

Yet judges are still reluctant to grant legal weight to attribution studies. A joint study by Minnerop, Otto and their colleagues, published in June⁴, found that such results are scarcely cited in climate lawsuits because of

lingering doubts over the robustness of the findings. [The IPCC's latest report](#) highlights that the methodology of climate-change attribution has matured since the last assessment, and that the results of state-of-the-art studies can now be considered robust.



Kelsey Juliana, lead plaintiff in the climate lawsuit *Juliana v. United States*. Credit: Terray Sylvester/VWPics/Redux/eyevine

This kind of statement by the IPCC in support of attribution science could make a difference, legally, as scientists and legal scholars start working together more. It will get harder for courts to ignore the relevant science that gets brought forward, including new work, says Frumhoff. The Union of Concerned Scientists [created a virtual rendezvous point](#) last year for scientists and legal experts who might want to team up. The hub, which provides legal scholars, lawyers and local officials with access to a broad range of science relevant in climate litigation, aims to catalyse legally relevant research across disciplines and make it easier for lawyers and legal scholars to use science in their cases.

One particularly relevant field is source attribution, a growing branch of attribution science that seeks to identify the relative contributions that different economic sectors and activities have made to climate change. For example, a 2020 assessment of the plastic industry's contribution to greenhouse gases found that the sector's emissions up to 2050 could total roughly 10–13% of what can be emitted if the world hopes to stay below 1.5 °C of warming⁵. Such studies could help courts considering lawsuits that allege that government agencies or companies have failed to prepare for the effects of climate change, or have contributed to it and should be held accountable.



US Supreme Court allows historic kids' climate lawsuit to go forward

“Causality is a key aspect in climate cases,” says Minnerop. “Any science that might convince judges that greenhouse-gas emitters are liable for their actions or inaction could be a game changer.”

Claiming financial damages from individual emitters might be tricky, however. “It is hard to see a judge accepting a damage claim and telling a company to pay compensation on the basis of source attribution,” she says. “It would open a flood gate.”

In the case against Royal Dutch Shell — and in climate suits against governments — plaintiffs chose a different strategy. Those lawsuits focus on

getting them to take responsibility for mitigating looming climate risks, rather than seeking compensation for harm suffered already.

A crucial piece of evidence in the Shell case was a set of expert reports on fossil-fuel economics, filed by the Dutch climate-action group Milieudefensie. During the case, Shell's lawyers had argued that if the company were to reduce its production of oil and gas, other firms would increase theirs, so that global production would remain the same. Milieudefensie asked Peter Erickson, the climate policy programme director at the Stockholm Environment Institute in Seattle, Washington, to respond to that substitution argument. The court agreed with Erickson that a reduction by Shell would not result in other firms making up the entire difference.

Expert opinion

Other science relevant to climate lawsuits includes studies about how climate change causes health problems; work that tracks environmental damage using satellite observations; and analyses of how financial flows from one country can increase fossil-fuel pollution in others.

“Too many environmental permits are given by local officials without adequately considering climate,” says Erickson. “I’m happy for my scholarship and science to be used where it is helpful. But it needs many more experts summarizing for courts the science in a clear and strong way.”

For all that, courts still tend to rely most on the scientific conclusions of the IPCC, says James Hansen, a climate scientist at Columbia University in New York who has advised or served as an expert witness in dozens of climate lawsuits since 2005. Hansen is currently both a plaintiff and a witness in the case of *Juliana v. United States*, which [21 young people brought forward in 2015 against the US federal government](#), demanding stronger emission cuts to help the world stay below 1.5 °C of global warming.

“As an expert witness I found the case to be frustrating,” Hansen says. “I spent months at a time preparing an expert report on climate change only to

see all that work buried in court proceedings and hardly considered by the judges.”



Dutch court rules that government must help stop climate change

A US court dismissed the original claim in January 2020, but the plaintiffs filed a motion this March to amend their suit and a judge ordered the United States and the plaintiffs to explore a settlement. Talks are ongoing and Hansen hopes that a settlement will include support from the Biden administration for a US carbon fee or tax.

Legal scholars foresee a range of other climate-related lawsuits coming up. One type could target financial entities that contribute to future climate change, such as companies trading in goods that can be linked to deforestation. These cases will rely on analyses of global trade and financial flows, says Setzer. Other types of lawsuit could involve ‘greenwashing’ — dubious claims that consumer products are environmentally friendly — and companies’ fiduciary duty to act in the best interests of business partners, she says. Research on whether countries meet their national contributions to the Paris agreement, and analysis of the costs of inaction, will also become increasingly relevant for future climate lawsuits, she adds.

Meanwhile, efforts are under way to support affected communities in poorer countries. ClientEarth, an international group of environmental lawyers, supports people affected by landslides in the Bududa district of Uganda who took the country’s government to court for failing to protect local villagers

from climate risks. ClientEarth is also training lawyers and public prosecutors in China with a view to bringing companies to court for polluting the air. If successful, such efforts could help to limit climate change because some air pollutants contribute to global warming. But it is unlikely in China's autocratic political system that a court would challenge the government for its climate policies, says Setzer.

Still, recent wins inspire hope that courts could help to tackle a planetary crisis — one that governments' legislative and executive branches have so far failed to avert. "The judiciary is less subject to political haggling and horse trade," says Hansen. "Court victories against governments are forcing them to think about and work on actual actions rather than promises for the distant future."

But law on its own won't be enough, cautions Rotmans. "Courts cannot force the global energy transition needed to stabilize the climate," he says. "Winning a lawsuit is one thing; getting rid of fossil fuels is another."

Nature **597**, 169-171 (2021)

doi: <https://doi.org/10.1038/d41586-021-02424-7>

References

1. 1.

Setzer, J. & Higham, C. *Global Trends in Climate Change Litigation: 2021 Snapshot* (London School of Economics and Political Science, 2021).

2. 2.

Intergovernmental Panel on Climate Change. *Climate Change 2021: The Physical Science Basis. Contribution of Working Group I to the Sixth Assessment Report* (eds Masson-Delmotte, V. et al.) Ch. 11 (IPCC, 2021).

3. 3.

Intergovernmental Panel on Climate Change. *Managing the Risks of Extreme Events and Disasters to Advance Climate Change Adaptation* (eds Field, C. B. *et al.*) Ch. 3 (IPCC, 2012).

4. 4.

Stuart-Smith, R. F. *et al.* *Nature Clim. Change* **11**, 651–655 (2021).

5. 5.

Shen, M. *et al.* *J. Cleaner Production* **254**, 120138 (2020).

This article was downloaded by **calibre** from <https://www.nature.com/articles/d41586-021-02424-7>

| [Section menu](#) | [Main menu](#) |

Books & Arts

- **[Dispatches from a world aflame](#)** [07 September 2021]

Book Review • From California's deadliest blaze to a new planetary fire regime, how wildfires are reshaping our climate-changed planet.

- BOOK REVIEW
- 07 September 2021

Dispatches from a world aflame

From California's deadliest blaze to a new planetary fire regime, how wildfires are reshaping our climate-changed planet.

- [Alexandra Witze](#)



The Camp Fire devastated the town of Paradise, California, in November 2018. Credit: Justin Sullivan/Getty

Paradise: One Town's Struggle to Survive an American Wildfire *Lizzie Johnson* Crown (2021)

The Pyrocene: How We Created an Age of Fire, and What Happens Next *Stephen J. Pyne* Univ. California Press (2021)

On the morning of 8 November 2018, an electrical-transmission tower in the foothills of northern California sent sparks raining into the bone-dry vegetation below. Strong winds fanned the flames and flung showers of embers ahead of the fire's ferocious advance. Within hours it had obliterated several mountain communities, including the town of Paradise. Eighty-five people died; it was the deadliest California wildfire so far.

The tale encapsulates many aspects of how wildfire is transforming lives around the globe. Ageing electrical-power infrastructure raises the risk of a fire igniting. Climate change brings drought, which transforms trees and grasses into kindling. Economic inequality pushes people out of overpriced cities and into more-affordable rural areas — in the path of wildfires. And poor municipal planning turns evacuation routes into death traps: roads become clogged with vehicles trying to flee a fire storm.

It is these many facets and scales that make grappling with the concept of wildfires challenging, as shown in two unforgettable books, *Paradise* and *The Pyrocene*. Wildfire is simultaneously a very local problem — what happens to a particular community when the flames reach it — and a very global one — what happens when climate change and humans fundamentally transform a fire-prone landscape.

Smoking ruin

Journalist Lizzie Johnson illuminates the local problem in her heartbreakng account of the Paradise inferno of 2018. A reporter at the *San Francisco Chronicle* when the fire broke out, she drove into the smoking remains to cover the story. She spent years following the aftermath, moving to the town part-time to embed herself in the community.

This unparalleled access infuses searing detail into Johnson's narrative. A mother and her hours-old baby find a lift in a stranger's car, only to be

trapped in the monstrous traffic jam heading out of Paradise. A maintenance man at a nursing home helps to lift its frail residents into the trucks of volunteers, even as his boss mulls whether they should wheel evacuees along the road in the hope of finding rides for more of them as the flames close in. A couple load their cat into a Tupperware container and seal it with duct tape, because they don't own a pet carrier.



The fire in Paradise was triggered by sparks from electrical lines.Credit: David Paul Morris/Bloomberg/Getty

After the fire, revelations unspooled. Community planners who had known that Paradise was at high risk of wildfire had never envisaged that the entire town would have to evacuate at once. Their emergency strategies utterly failed in the face of the scale of the disaster. Meanwhile, finger pointing continued at many levels of government, with the Pacific Gas and Electric company ultimately being held accountable, because it owned the transmission line that ignited the blaze.

The story has been told before, in media and film accounts and in *Fire in Paradise*, a 2020 book by Alastair Gee and Dani Anguiano, journalists at *The Guardian*. But Johnson's deep experience as a fire journalist makes her account the best of the bunch. Among other insights, she interweaves an oral history of fire from the Konkow (also known as Maidu) people, who live in the area. For more than 9,000 years, Indigenous peoples managed the region's landscape, intentionally setting low-intensity fires to clear brush, a practice that kept the forest healthy and reduced the fuel available to burn. Konkow knowledge includes the story of two wayward boys who threw pitch-pine sticks onto a camp fire, triggering a fire that killed most people in the area. Substitute 'transmission lines' for 'pitch-pine sticks', and you have the Paradise tragedy.

Ages of fire

Indigenous burning has shaped the planet for tens of thousands of years. In *The Pyrocene*, fire historian Stephen J. Pyne collects and expands on some of his previously published thoughts about the interaction between humanity and fire. Far from a narrow focus on one California town, he writes across landscape and time and planetary history.

Pyne's argument is framed around his long-standing concept of 'first fire' (primordial burning on early Earth, for instance from lightning or from volcanoes), 'second fire' (that lit by humans to cook food and provide warmth) and 'third fire' (that stemming from the combustion of fossil fuels). He repurposes his earlier writings on the Pleistocene epoch to draw comparisons between the past ice age and the new fire age. Readers accustomed to Pyne's oeuvre will find much familiar here.



The race to decipher how climate change influenced Australia's record fires

But *The Pyrocene* is his fullest elucidation yet of how humanity has entered a new age of fire, one that redefines the human-altered era of the Anthropocene. And Pyne, a former smoke-spotter who tracked blazes at Grand Canyon National Park in Arizona, is certainly the best writer to make this argument. His previous books documented cultural and political practices that led to Earth's current fire regime. One such is the '10 a.m.' policy (now mostly abandoned) of the US Forest Service, which held that fires ignited on federal land should be extinguished by that time the following morning. What sounded like a well-planned effort to prevent forest fires instead led to decades of fire suppression and the dangerous build-up of brush in landscapes that would have functioned much better with occasional low-intensity burns. Similar policies in Australia shifted the continent from a well-managed fire regime to a highly combustible one.

Fires are now outside of all norms. As the story of Paradise shows, ignitions become infernos; places that have always burnt are burning in new ways. Climate change has supercharged wildfires well beyond humanity's control. Extreme fire behaviour includes spirals of flame, dubbed firenadoes, and towering smoke clouds that spawn their own thunderstorms. The Bootleg megafire that burnt this July and August in southern Oregon created its own weather for weeks. Smoke from the devastating Australian bush fires of

2019–20 encircled the globe, having a bigger impact on global climate than the COVID-19 lockdowns. This is the new age of megafires.

Earth is the only planet with fire; the very fact that it burns at all is a quirk of atmospheric chemistry. But there is plenty to burn, and we are making it worse as we unlock the carbon laid down millions of years ago and release it into the atmosphere. There is no return from the Pyrocene.

Nature **597**, 172–173 (2021)

doi: <https://doi.org/10.1038/d41586-021-02426-5>

This article was downloaded by **calibre** from <https://www.nature.com/articles/d41586-021-02426-5>

| [Section menu](#) | [Main menu](#) |

Opinion

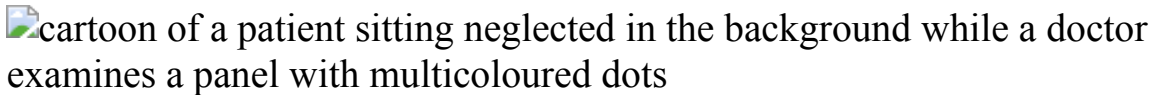
- **Personalized profiles for disease risk must capture all facets of health** [06 September 2021]
Comment • To provide individual care and prevent disease, we need to go beyond genetics in risk scores and include metrics that follow a person's changing environment and health.
- **Nicaragua: renewed call to defend human rights** [31 August 2021]
Correspondence •
- **COVID-19: release approved vaccines for trials of new ones** [07 September 2021]
Correspondence •
- **Spacefarers, protect our planet from falling debris** [07 September 2021]
Correspondence •
- **Waive CRISPR patents to meet food needs in low-income countries** [06 September 2021]
Correspondence •

- COMMENT
- 06 September 2021

Personalized profiles for disease risk must capture all facets of health

To provide individual care and prevent disease, we need to go beyond genetics in risk scores and include metrics that follow a person's changing environment and health.

- [Mark McCarthy](#) ⁰ &
- [Ewan Birney](#) ¹



Credit: David Parkins

Providing the best possible care for an individual means having a better understanding of their risks of developing disease. The goal is to have personalized answers when people need to know whether, for instance, preventive surgery makes sense, a given medicine is likely to be risky or a certain diet should be recommended.

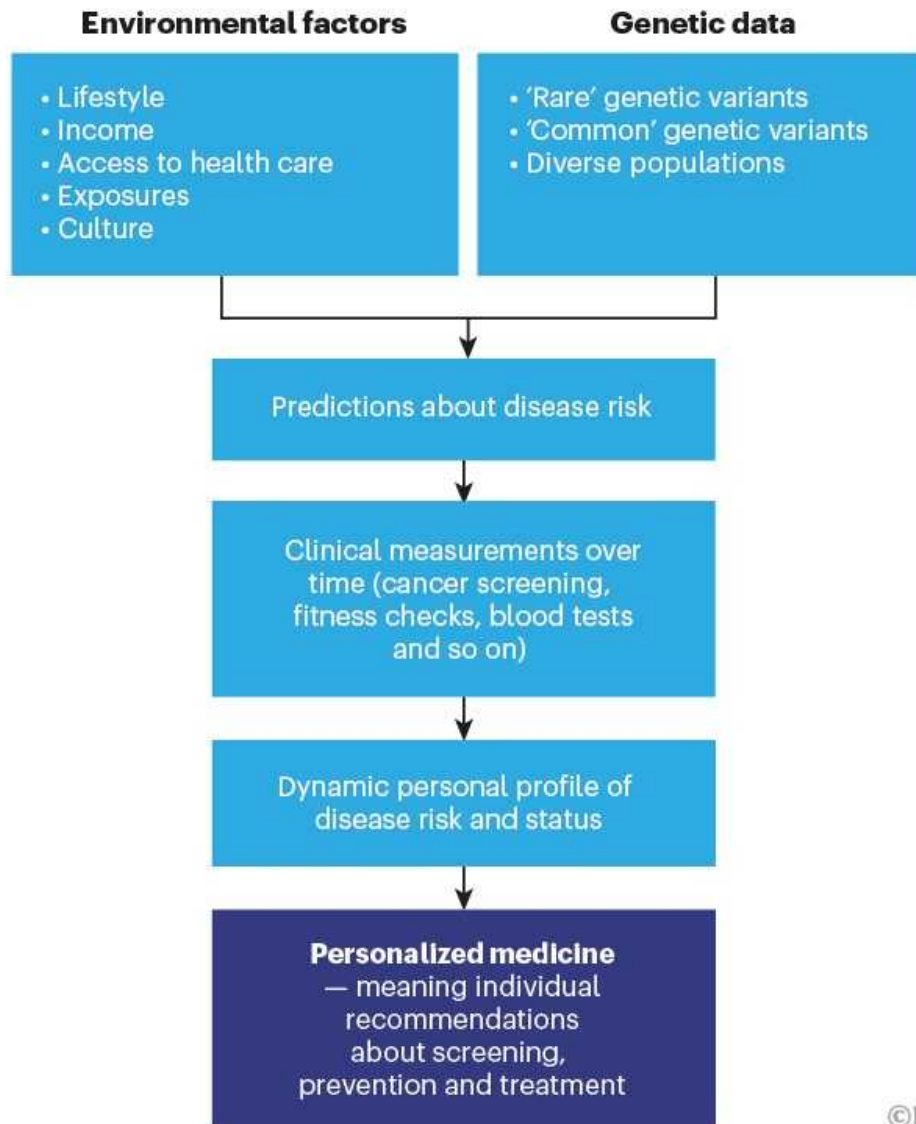
Information on genetic risk represents one promising approach to providing these answers. Genomic data, gathered across millions of individuals, have revealed thousands of DNA sequence variants associated with common diseases such as diabetes, heart disease, schizophrenia and cancer. These clues to disease risk can be combined to generate 'polygenic scores', which provide a measure of the degree to which an individual is genetically predisposed to developing each such disease¹.

A growing chorus of scientists and clinicians emphasize the value of such genetic profiling as an integral part of a person's medical record². Others argue that the clinical benefits have been massively overstated³. This debate often fails to recognize that the challenge is not merely to improve understanding of genetic risk, but to capture more about the interwoven, multifaceted factors that play into disease risk (see 'Path to personalization').

Here, we argue that clinical medicine must learn to develop more-holistic measures of individual risk, both genetic and non-genetic, and to combine these with clinical data over time to deliver better care.

PATH TO PERSONALIZATION

To tailor health care to individuals, information from various sources must be brought together. These data, both genetic and environmental, should be drawn from diverse populations.



©nature

Limited measures

Although current polygenic scores hold clinical promise, they come with several limitations. They leave out many sources of relevant data, and work best for the predominantly white, wealthy populations in which most genetic studies have been performed. The emphasis on genetic risk diverts attention away from non-genetic factors that might be equally important for disease.

risk and progression. Risk estimation on the basis of polygenic scores alone also fails to incorporate real-time measurements of clinical state that are especially important in diseases linked to ageing.

Both authors are strongly invested in the value of human genetics as a tool for understanding disease mechanisms, and are enthusiastic about the contribution that genetic profiling will make to personalizing care. M.M. is an endocrinologist who has focused on understanding the genetics of type 2 diabetes, and leads human genetic research at the biotechnology firm Genentech in South San Francisco, California. E.B. is the deputy director-general of the European Molecular Biology Laboratory (EMBL) and director of the EMBL European Bioinformatics Institute near Cambridge, UK, and has played a pivotal part in the design and analysis of multiple genome projects.

To gain a more accurate assessment of individual health risks (that is, to make medicine truly personalized), researchers and clinicians must integrate disparate types of data from a wider diversity of populations. First, researchers need to expand measures of genetic risk by embracing more-diverse populations, cataloguing the full spectrum of variants, and understanding the environmental context in which these variants act. Second, researchers and clinicians need to be able to consider both genetic and non-genetic risk factors (for type 2 diabetes, for example, these would encompass hundreds of genetic markers and measures of diet, exercise and socio-economic status alongside measures of current clinical state, such as glucose levels). Finally, the field needs to move away from its tendency to collapse all these rich, individual-level data into rigid clinical categories. Rather than classifying an individual as simply being at average or high risk for a condition such as coronary artery disease, researchers and clinicians should consider a gradation of risk. And instead of trying to categorize people into discrete subtypes of disease, we should appreciate that common disease typically involves several processes running in parallel⁴.

Inclusive genetics

Polygenic scores for late-onset diseases are mostly built around the common risk variants that have emerged from large-scale genetic studies. In contrast

to the rare, high-impact genetic variants that underlie diseases such as cystic fibrosis and sickle-cell anaemia, these generally have subtle effects that limit their clinical value when considered one at a time. However, when information from hundreds or thousands of relevant disease-risk variants is combined, we can capture a substantial slice of individual variation in disease risk^{1,5}. In European populations, for example, someone in the highest 1% of polygenic risk for coronary artery disease is at least ten times more likely to develop the disease than is someone in the lowest 1%⁵.

These polygenic scores have the potential to inform individual decisions about screening, lifestyle interventions and therapeutic choices. For example, rather than all women starting to have annual mammography screening at 45 years old (as currently recommended by the American Cancer Society), polygenic scores for breast cancer risk could be used to tailor schedules so that women with the highest genetic risk are screened earlier and more intensively than are those with below-average risk⁶.



Don't ignore data from minority populations

The reliability of these scores depends on the accuracy and inclusivity of the genetic information that goes into them. Most data currently used to construct polygenic scores come disproportionately from individuals of recent European descent. However, scores generated in one population typically perform poorly when deployed in another: a polygenic score for

body mass index (BMI) constructed from European individuals loses more than 60% of its predictive power when applied to individuals of more-recent African descent, for example⁷.

Another concern is that common genetic variants tell only part of the story of genetic risk. For many diseases, rare variants also contribute, often having a much greater impact on risk than any single common variant. Notable examples include effects of rare variants in the genes *BRCA1* and *BRCA2* on breast and ovarian cancer risk, and of those in *LDLR*, *APOB* and *PCSK9* on coronary artery disease (mediated through the effects of these variants on lipid levels). Polygenic scores that do not incorporate these rare, ‘high penetrance’ variants will provide misleading estimates of overall genetic risk for those who carry the high-impact version (or allele) of the genes responsible. Equally, the clinical consequences of inheriting a high-impact allele are modulated by an individual’s polygenic background: in some diseases, carriers of high-impact alleles who have a favourable polygenic background have a disease risk that is at or below the population average^{8,9}.

The solution is to integrate both common and rare variants into a single genetic risk score. Historically, research at the common and rare ends of the allele-frequency spectrum has involved different groups of researchers deploying distinct techniques (genotyping arrays and targeted sequencing, respectively). However, whole-genome sequencing is swiftly becoming the default genetic assay. This shift is eroding the artificial distinction between ‘rare’ and ‘common’ variants, and is making it much easier to consider the entire spectrum of genetic risk at once. This will, for example, allow carriers of high-risk alleles for breast cancer to make better decisions about screening and prophylactic surgery. Crucially, however, rare variants vary more between ancestries than do common variants, and the pursuit of equitable genetic information will depend even more on collecting inclusive global data on genetic variation and disease risk in diverse populations.

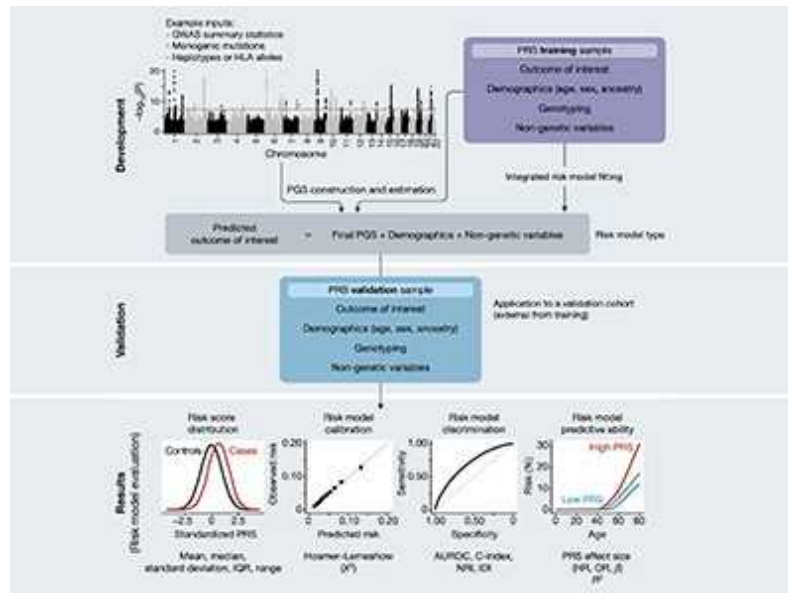
Getting holistic

There is more to disease risk than genetics. For most common, late-onset diseases, individual risk is heavily influenced by non-genetic factors. Often collectively labelled as environmental, these might include factors as varied

as diet, socio-economic status, access to health care, the status of personal relationships and gut-microbiome diversity.

It is not straightforward to measure and integrate these factors into risk estimates. Even for well-understood factors, such as smoking, diet and exercise, the lifelong impact on disease risk cannot easily be assembled from ‘snapshot’ measurements, such as steps walked or estimated calories consumed in the past week. What’s more, even when epidemiological associations are strong, it can be challenging to pin down the factors that are causal: consider ongoing debates about how dietary components, such as carbohydrate and fat intake, influence disease risk. Many exposures that might be relevant to disease are simply hard to reconstruct, for example prenatal nutrition and exposure to pathogens or antibiotics during infancy.

Complex societal factors, such as access to health care, education, effective sanitation or housing, have a profound impact on individual patterns of disease. As with genetic risk, data gathered from wealthier populations can translate poorly into disease prediction in disadvantaged communities¹⁰. Unless scientific leaders, funders, industry and societies work together to rebalance the populations involved in data generation and clinical validation, existing health disparities will be perpetuated and perhaps even amplified.



Improving reporting standards for polygenic scores in risk prediction studies

Genetic and non-genetic risk factors often interact in ways that can be hard to disentangle. For example, genetic variants that alter the function of nicotinic receptors influence smoking behaviour, and, as a consequence, are associated with individual risk of smoking-related diseases. The metabolic disease phenylketonuria is a striking example of how modifying the environment can modulate the consequence of genetic variation: the devastating consequences of inherited defects in the causative *PAH* gene can be mitigated by adopting a diet low in phenylalanine.

Clinical measurements, particularly when gathered over time, represent another route for improving risk estimation. Consider two people aged 50, both with polygenic scores in the top 10% of genetic risk for type 2 diabetes. One is sedentary and overweight, the other active and slim. One might reasonably expect the former to be at greater risk of diabetes than the latter. But now assume that yearly measurements of glycosylated haemoglobin (which reflect a person's glucose levels over the previous two to three months) have remained firmly in the normal range for the first individual for more than a decade, but show a steady increase towards the diabetic range for the second. That makes the second individual much more likely to become diabetic.

In general, clinical data collected repeatedly over time — from sources such as blood tests, imaging and wearable devices — reveal how broad-brush predictions derived from genetic and non-genetic risk factors are actually playing out in a given individual, and make it possible to chart personal trajectories from health to disease. The inclusion of real-time clinical data also helps to counter the fatalism that can seep into the interpretation of genetic risk. It emphasizes how, even in those with the highest genetic risk, interventions can mitigate disease progression. Such integrated assessments are also readily incorporated into clinical practice. For example, cholesterol measurements are already widely used to stratify cardiovascular risk precisely because they integrate diverse genetic and environmental factors, as well as dynamic measurements of current clinical state.

Preserving complexity

Medicine has historically focused on categorizing disease. Personalized medicine has often followed the same path, subdividing people into perceived disease subtypes, or establishing arbitrary divisions in continuous measurements (such as high and low risk). Such efforts assume that the highly variable manifestations of disease can best be explained by allocating individuals to distinct groups, and that each disease subtype has its own set of causes. However, most common diseases represent a confluence of disordered processes, several of which are likely to be at play in any given individual. For instance, premature coronary artery disease typically occurs amid a blend of abnormal processes, including disordered glucose metabolism, elevated lipids, high blood pressure and chronic inflammation. The precise mix will differ from one person to another, and even across a person's lifetime. Only in relatively few individuals (for example, those with familial hypercholesterolaemia) can premature disease be attributed to a single cause.

When many causes contribute to disease in an individual, it makes more sense to track each process involved, rather than collapsing rich quantitative information into a set of rigid, often-arbitrary, disease or risk categories. Even though clinical decision-making often demands binary decisions (such as to treat or not at a particular time point), these might not map neatly onto categories defined years previously. There is the danger that these become 'once-and-for-all' labels in the medical record that define future health care for that individual and divert attention away from personal differences in disease trajectory. A more quantitative approach would, for example, render moot unproductive debates about the most appropriate definition of metabolic syndrome, or how best to use ancestry to define which BMI thresholds constitute overweight and obese.

Tracking multiple measurements reveals the ebb and flow of each individual's status with respect to health and disease. Then, when it becomes necessary to make a binary clinical decision — whether or not to operate, or whether to try drug A or B — both the individual and the physician can rely on much richer and more up-to-date information than on categories assigned years previously.

Moving forward

How do we get there? Researchers should commit to adopting a more-holistic perspective in their work. Researchers, funders and industry need to embrace greater diversity in the design and implementation of studies, focusing not only on gender and ethnicity, but also on social, cultural and economic factors that influence disease risk and access to health care. Recent moves by major funders to encourage more-diverse participation in population cohorts and biobanks are welcome, but reducing the diversity of modern populations to census-defined categories does not do justice to the complex, admixed ancestries of so many.

Efforts to base personalized medicine on risk-factor prediction alone will fall short. All involved in this endeavour — researchers, industry, funders, governments and citizens — will need to come together to enable the collection of large, rich data sets that go beyond static one-time measurements and which capture individual health trajectories. Such efforts are, however, destined to fail unless the data are collected in standardized formats and shared in ways that allow information from different studies and populations to be combined and compared. This will inevitably bring the realms of research and clinical care together, and will require us to address fundamental questions about data ownership, privacy, equality of access, fairness and social responsibility. Global efforts to create such standards are in place, for example the [Global Alliance for Genomics and Health](#).

Achieving this more-holistic mindset will take time and effort. But the resulting understanding of disease and framing of personal risk will be deeper, broader and much better equipped to bring the promise of personalized medicine into routine health care.

Nature **597**, 175-177 (2021)

doi: <https://doi.org/10.1038/d41586-021-02401-0>

Disclaimer: M.M.'s views in this article are his own and not those of Genentech.

References

1. 1.

Torkamani, A., Wineinger, N. E. & Topol, E. J. *Nature Rev. Genet.* **19**, 581–590 (2018).

2. 2.

Lambert, S. A., Abraham, G. & Inouye, M. *Hum. Mol. Genet.* **28**, R133–R142 (2019).

3. 3.

Sud, A., Turnbull, C. & Houlston, R. *NPJ Precis. Oncol.* **5**, 40 (2021).

4. 4.

Erdmann, J., Kessler, T., Munoz Venegas, L. & Schunkert, H. *Cardiovasc. Res.* **114**, 1241–1257 (2018).

5. 5.

Khera, A. V. *et al.* *Nature Genet.* **50**, 1219–1224 (2018).

6. 6.

Mavaddat, N. *et al.* *Am. J. Hum. Genet.* **104**, 21–34 (2019).

7. 7.

Martin, A. R. *et al.* *Nature Genet.* **51**, 584–591 (2019).

8. 8.

Fahed, A. C. *et al.* *Nature Commun.* **11**, 3635 (2020).

9. 9.

Mars, N. *et al.* *Nature Commun.* **11**, 6383 (2020).

10. 10.

Mostafavi, H. *et al.* *eLife* **9**, e48376 (2020).

This article was downloaded by **calibre** from <https://www.nature.com/articles/d41586-021-02401-0>

| [Section menu](#) | [Main menu](#) |

- CORRESPONDENCE
- 31 August 2021

Nicaragua: renewed call to defend human rights

- [Martin Chalfie](#) ORCID: <http://orcid.org/0000-0002-9079-7046>⁰,
- [Edouard Brézin](#)¹ &
- [Belita Koiller](#) ORCID: <http://orcid.org/0000-0003-2939-0287>²

As scientists and leaders of the International Human Rights Network of Academies and Scholarly Societies (<https://www.internationalhrnetwork.org>) — an alliance to support at-risk colleagues — we are gravely concerned about ongoing governmental repression in Nicaragua. This alarming situation has important implications for science and health in the country.

Access options

Subscribe to Journal

Get full journal access for 1 year

\$199.00

only \$3.90 per issue

[Subscribe](#)

All prices are NET prices.

VAT will be added later in the checkout.

Tax calculation will be finalised during checkout.

Rent or Buy article

Get time limited or full article access on ReadCube.

from \$8.99

[Rent or Buy](#)

All prices are NET prices.

Additional access options:

- [Log in](#)
- [Learn about institutional subscriptions](#)

Nature **597**, 178 (2021)

doi: <https://doi.org/10.1038/d41586-021-02373-1>

This article was downloaded by **calibre** from <https://www.nature.com/articles/d41586-021-02373-1>

| [Section menu](#) | [Main menu](#) |

- CORRESPONDENCE
- 07 September 2021

COVID-19: release approved vaccines for trials of new ones

- [Melanie Saville](#) ✉

Scientists must develop the next generation of COVID-19 vaccines now, if the world is to meet the challenge of SARS-CoV-2 variants and reduce vaccine inequity by increasing global supply. This can be done only if comparator COVID-19 vaccines — those that have already been approved — are available to support clinical trials. Such comparator vaccines are almost impossible to secure; governments, developers and manufacturers must find a solution to unlock supplies.

So far, COVID-19 vaccines have received approval on the basis of data from unvaccinated participants in placebo-controlled efficacy trials. These trials become increasingly difficult to carry out as the number of people who are immunized rises. Comparator vaccines, essentially replacing placebos, are therefore needed for trials that assess whether new candidate vaccines provide comparable levels of protection, including against emerging variants.

The number of comparator-vaccine doses needed to support clinical trials is small. However, contracts between manufacturers and governments for approved vaccines restrict their use to improving public health. This must change if vital COVID-19 vaccine research and development are to progress.

Nature **597**, 178 (2021)

doi: <https://doi.org/10.1038/d41586-021-02398-6>

This article was downloaded by **calibre** from <https://www.nature.com/articles/d41586-021-02398-6>

| [Section menu](#) | [Main menu](#) |

- CORRESPONDENCE
- 07 September 2021

Spacefarers, protect our planet from falling debris

- [Dipshikha Chakravortty](#) ORCID: <http://orcid.org/0000-0002-7838-5145>⁰,
- [Saptarshi Basu](#) ORCID: <http://orcid.org/0000-0002-9652-9966>¹ &
- [K. S. Nandakumar](#) ORCID: <http://orcid.org/0000-0001-5802-7853>²

World cooperation can prevent collisions and the generation of debris in space ([Nature 596, 163; 2021](#)). In our view, international forums are also needed to monitor and deal with the uncontrolled fall of rockets and other debris from space. Such oversight would counter spacefaring nations' current negligence in protecting Earth's environment and ecology.

Access options

Subscribe to Journal

Get full journal access for 1 year

\$199.00

only \$3.90 per issue

[Subscribe](#)

All prices are NET prices.

VAT will be added later in the checkout.

Tax calculation will be finalised during checkout.

Rent or Buy article

Get time limited or full article access on ReadCube.

from \$8.99

[Rent or Buy](#)

All prices are NET prices.

Additional access options:

- [Log in](#)
- [Learn about institutional subscriptions](#)

Nature **597**, 178 (2021)

doi: <https://doi.org/10.1038/d41586-021-02396-8>

This article was downloaded by **calibre** from <https://www.nature.com/articles/d41586-021-02396-8>

| [Section menu](#) | [Main menu](#) |

- CORRESPONDENCE
- 06 September 2021

Waive CRISPR patents to meet food needs in low-income countries

- [John van der Oost](#)⁰ &
- [Louise O. Fresco](#)¹

Wageningen University & Research announced this week that it will provide non-profit organizations with free licences to use its CRISPR–Cas gene-editing technology for non-commercial applications. CRISPR tools can then be used, for instance, to help make food production sustainable, nutritious and safe. The university hopes that the move will inspire a worldwide change in CRISPR–Cas intellectual-property policy.

CRISPR–Cas offers an advantage over conventional plant breeding in that it can rapidly and efficiently modify plant traits — for example, to offset the impacts of climate change and pathogens. There have been thousands of CRISPR-related patent applications over the past decade, including by Wageningen University & Research and the Dutch Research Council.

Charging licence fees to protect intellectual property makes good business sense, but it can put technologies beyond the reach of non-profit organizations in low-income countries. These organizations are crucial to improving crops for local farmers and poor consumers. As the United Nations Food Systems Summit approaches, the importance of free access to CRISPR–Cas technologies in low-income nations must be recognized.

Nature **597**, 178 (2021)

doi: <https://doi.org/10.1038/d41586-021-02397-7>

This article was downloaded by **calibre** from <https://www.nature.com/articles/d41586-021-02397-7>

| [Section menu](#) | [Main menu](#) |

Work

- **[Five hundred days between pay cheques: the road I took to revive my career](#)** [26 August 2021]

Career Column • A global career move left one member of a scientist couple unemployed during the pandemic. Here's what he learnt.

- **[Five keys to writing a reproducible lab protocol](#)** [06 September 2021]

Technology Feature • Effective sharing of experimental methods is crucial to ensuring that others can repeat results. An abundance of tools is available to help.

- **[Who wants to be a polar bear?](#)** [06 September 2021]

Where I Work • Joel Berger braves freezing temperatures and charging musk oxen to learn how melting sea ice is affecting mammalian encounters.

- CAREER COLUMN
- 26 August 2021

Five hundred days between pay cheques: the road I took to revive my career

A global career move left one member of a scientist couple unemployed during the pandemic. Here's what he learnt.

- [Nuwan Bandara](#) 0



Credit: Getty

In February 2020, my wife Buddini Karawdeniya and I moved with our one-year-old son from the United States to Australia. We'd worked together as postdocs at Southern Methodist University (SMU) in Dallas, Texas, until Buddini, a nanopore researcher, accepted a research fellowship at the Australian National University (ANU) in Canberra. The move meant that we could be closer to our parents, who live in Sri Lanka. We visited them before leaving for Australia — and I never imagined that it would be the last time I would see my father, who passed away a year later, in February 2021. We planned for me to find a job in Australia and to visit our parents every year, but this never materialized: they are eagerly waiting to see us and our son, but with the pandemic still rampaging through Sri Lanka, that's a very distant dream.

In March 2020, the pandemic hit much of the world, and my prospects of being hired dwindled with each passing day. Being unemployed would have been much more challenging without Buddini's salary and some savings. But as the economy nosedived, I fought to keep my career alive and to stay employable, rather than looking for jobs that simply did not exist. It would not have been possible to hold out for a research job during that period without Buddini's support.

And although unemployment put my career back a few steps, I used the time to acquire skills and to lay the foundation for a strong return.

Keep up with the field

There is a steady stream of new techniques, methods, theories and approaches that embrace nanopore-based single-molecule sensing, which is my specialism. Supervisors prefer candidates to thoroughly understand both recent and past developments documented in the literature.

So I set up Google Alerts — which inform you when new content related to a particular topic appears on the web — and followed [@TheNanoporeSite](#) on Twitter — both of which I checked regularly to stay up to date in the field. Not having a university affiliation meant I could not access most papers. However, Buddini and my colleagues from my previous laboratory

(especially Jugal Saharia, another nanopore researcher) would share articles with me — and would often be keen to discuss them.

Most days, I used my son’s afternoon nap time to glance through a paper or two. I found this was enough to stay up to date with the most significant research developments.

Take all opportunities that come your way

Being a stay-at-home dad kept me much busier than my previous job did. But I also signed up for two courses (in machine learning and MATLAB, a programming tool for analysing data and modelling) through the online learning platform Coursera, which I undertook at night after signing off from toddler duties.

These skills were in high demand in my field because of the growing number of research papers that use machine learning and MATLAB techniques.

I also continued working on three projects I’d left behind at SMU — which involved problem-solving, manuscript writing and data analysis — and these are now published. And I contributed to the chapter called ‘Experimental approaches to solid-state nanopores’, of which I am the lead author, of a book tentatively titled *Single Molecule Sensing Beyond Fluorescence* (to be published by Springer).



Nuwan Bandara and his family.Credit: Nuwan Bandara

All of these achievements were not worth much individually, but together they strengthened my CV and showed that my time outside employment was not spent outside research.

Record your ideas

Jason Dwyer, who supervised me while I pursued my chemistry PhD at the University of Rhode Island in South Kingstown, suggested jotting down any epiphanies that might strike, to ensure that they were not forgotten. I started doing this during my unemployment by noting any ideas to pursue that I came up with while reading a paper or just thinking about science. When I took the machine-learning course, for example, a few ideas came to me around nanopore data analysis. I was constantly looking to use what I learnt through this course in my research involving some old data I had.

Doing this helped to keep my thinking on track, similarly to a researcher who had a regular job. I also documented some past ideas that I'd had but could not pursue at the time.

Rather than wallowing in unemployment, this helped me to think positively and to plan the next couple of steps in my career.

Volunteer

In July 2020, our son got a two-day-per-week slot at an early-learning centre.

The economic downturn meant universities could not hire as many people, but they could invite visiting researchers — and the 482 Temporary Skill Shortage visa I was on did not preclude me from volunteering.

I pitched the idea of helping ANU to develop nanopore-based single-molecule sensing to Patrick Kluth, one of the researchers Buddini is working for as part of her postdoc. He accepted, and I began visiting the lab twice per week.

Along with my wife and other colleagues, we drove technological advances to expand the scope of nanopore research at ANU. We initiated a collaboration on nanopore data analysis with Minjun Kim, our former supervisor at SMU, which has since been published in *Analytical Chemistry*¹.

I also accepted an invitation from Buddini's main supervisor, physicist Dragomir Neshev, to contribute to a review paper (which will be submitted to *Chemical Reviews*).

My CV now includes work experience at one of the best universities in Australia, and a couple more published papers (I hope).

Reach out to your network

By November 2020, I realized that finding a job in Australia would remain challenging because of the pandemic. Our expenses were mounting, especially because our son was to start attending the early-learning centre full-time from January 2021, and we were dipping further into our savings. We could afford to go on a single salary for only another 6–8 months before having to discontinue our son’s experience at the early-learning centre. This was disheartening to us as parents.

Buddini and I decided that, if I needed to move again for work — even back to the United States — we would be able to manage in our relationship and as parents. I reached out to my former supervisors and friends in the United States, in particular Kim and Dwyer, to ask whether they could help me to find a job. Both reached out to their network and forwarded various options to me.

Kim connected me to Kevin Freedman, a specialist in nanopore sensing at the University of California, Riverside (UCR), who hired me. So, in May 2021, I moved back to the United States and the preparation during those hard months for future employment is paying its dividends now. I now work as a postdoctoral researcher at UCR with a focus on using nanopipettes for single-molecule sensing. Having very close friends in California made the move smoother than it could have been, because I had to start life in the United States from ground zero.

Having a cousin and a family friend (fondly called Aunt Maya) in Canberra, and some close family in Sydney, made this move to the United States easier because I knew they would be there for my wife and our son to help support our family in Australia.

The personal challenges are far from over: my wife and I are now living the two-body problem, working on two continents (with a 17-hour time difference), with a child to think about. The inbound travel restrictions in Australia add an extra layer of complexity. I stay up well past midnight to talk to my son when he comes home from the early-learning centre. Long days have become the norm, and both of us try to stay positive. Every day, I tell myself, “You are doing this for your family,” and that keeps me going.

Although we are breaking even financially without saving, as parents, we are happy that we can provide our son with the best available education. He comes home babbling about his friends and what he did during the day, which is more than enough compensation for the uphill battle we are fighting currently.

Buddini has laid the groundwork to apply for jobs in the United States so that we can be reunited soon. But I'm certain our approach to my unemployment helped me to eventually get hired.

Nature **597**, 291-292 (2021)

doi: <https://doi.org/10.1038/d41586-021-02359-z>

This is an article from the Nature Careers Community, a place for Nature readers to share their professional experiences and advice. [Guest posts are encouraged.](#)

References

1. 1.

Nuwan, Y. M., Bandara, D. Y., Nuwan, Y. M. & Bandara, D. Y. *Anal. Chem.* <https://doi.org/10.1021/acs.analchem.1c01646> (2021).

This article was downloaded by **calibre** from <https://www.nature.com/articles/d41586-021-02359-z>

- TECHNOLOGY FEATURE
- 06 September 2021
- Correction [09 September 2021](#)

Five keys to writing a reproducible lab protocol

Effective sharing of experimental methods is crucial to ensuring that others can repeat results. An abundance of tools is available to help.

- [Monya Baker](#)



Illustration by The Project Twins

Every laboratory scientist has a horror story. The five-minute step they didn't know they needed, which ended up costing them five months — or five years. Maybe it was swirling the plate as crowded cells were split between culture dishes. Or maybe the published protocol said to wash your sample once and heat thrice but meant the opposite, so that following the printed instructions destroyed the sample.

More than 60% of respondents to a 2016 *Nature* survey said they had tried to repeat other scientists' experiments [and been unable to do so](#). A poll of members of the American Society for Cell Biologists similarly found that more than [70% had been unable to replicate](#) a published experimental result, with incomplete detail in the original protocol given as the most common explanation.

That's no surprise to Tim Errington, director of research at the Center for Open Science in Charlottesville, Virginia, who managed the Reproducibility Project: Cancer Biology (RP:CB), which launched in 2013 to replicate results of prominent cancer-biology papers. Errington sees two overarching reasons for poorly explained methods. One is a lack of incentives or training for better descriptions. The other is that researchers assume everyone works the same way and fail to recognize what details are crucial. The word 'standard' is a red flag for this type of thinking, he says. "There is no such thing as a standard protocol: it's only standard in your lab."



Share methods through visual and digital protocols

But things are improving, says Elizabeth Iorns, who helped to launch the RP:CB and is chief executive at Science Exchange in Palo Alto, California, which provides research-outsourcing services. “There’s a lot of progress in documentation and tools that are available to people to use.” A move towards automated experiments and data collection is also helping, she says, and people are more aware than ever about the need to describe reagents precisely.

Such tools will move the needle on reproducibility only if they are widely used, Errington warns. “Even though we have them, it’s not systemic yet, or rewarded.”

Communicating methods more accurately, research-improvement advocates say, requires changes to both mindset and workflow. Here are some strategies that can help.

Document as you go

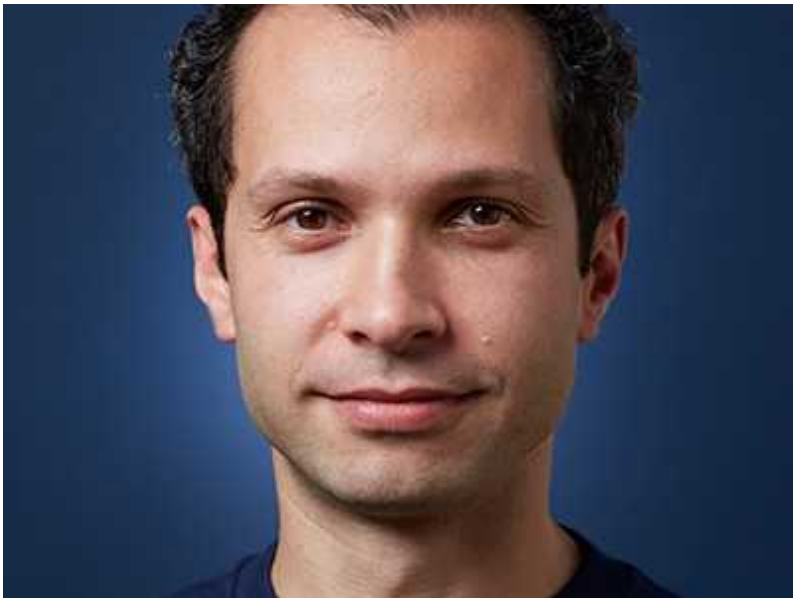
If nothing else, consider how you’ll share your experimental methods from day one. In the past five years, several publishers of high-profile journals, including *Nature*, have strengthened requirements for reporting experimental

details in their papers. And many publishers encourage depositing methods in a repository, such as Nature Portfolio's [Protocol Exchange](#), [protocols.io](#) or [Bio-protocol](#). But waiting to gather these details until manuscript submission will leave researchers scrambling to find information that could have been right at their fingertips, says Lenny Teytelman, chief executive at protocols.io in Berkeley, California. Logging information as the experiments are done, he says, "makes your life easier, rather than harder".

Write less, show more

In 2014, Kornelia Polyak, a breast-cancer researcher at the Dana-Farber Cancer Institute in Boston, Massachusetts, showed just how tricky sharing methods could be ([W. C. Hines et al. *Cell Rep.* 6, 779–781; 2014](#)). Her collaborators in California were getting flow cytometry results that were very different from hers, even when they shared samples and reagents and discussed their methods extensively. Visiting each other's labs revealed the reason: one group disaggregated tumour tissue by vigorous shaking for 6–8 hours, whereas the other used gentle rocking for 18–24 hours. When both teams switched to the same, slower method, results aligned. Now, Polyak's lab makes informal videos that new lab members can watch before certain experiments even start.

The [Journal of Visualized Experiments](#), based in Cambridge, Massachusetts, lets researchers submit text descriptions of methods for peer review. If accepted, the journal sends in a film crew for a day and then edits experiments into short videos, usually 8–15 minutes long. Researchers do this both to get credit for their work and to persuade others to adopt their methods and expand a field, says Moshe Pritsker, who founded the journal in 2006.



No more excuses for non-reproducible methods

Timelines and diagrams can also be valuable, says Errington. For one replication study that he coordinated, the original authors, reviewers and replicators consulted intensively using written documents to agree on a replication protocol, only to find that mice became too sick to complete the experiment ([K. Eaton et al. *eLife* 7, e34364; 2018](#)). It turned out that a vague description of time points meant that the replicators started taking measurements weeks later than the original experimenters had. A flow chart would have eliminated that confusion from the start, Errington says.

There are tools that can help, he says. For instance, [Experimental Design Assistant](#) from the UK National Centre for the Replacement, Refinement & Reduction of Animals in Research is a web-based platform to help researchers plan animal studies. It captures reporting requirements before work begins and displays them in a clear diagram. However, researchers tend to leave out the diagram and focus on written paragraphs, he says.

Errington urges researchers to think less about lengthy protocols and more about incorporating online tools while they plan and conduct experiments, so that the information can be shared. (A bonus, he says, is that this can show what didn't work, such as commercial reagents that failed to perform — information that is otherwise hard to come by.) Anything used to share data can also share methods, he notes: electronic lab notebooks, or

repositories such as Zenodo, GitHub or Figshare. It is just a matter of recognizing the need to do so.

Link, template, standardize

Electronic lab notebooks (ELNs), in particular, could be just the ticket for linking to lab protocols, reagent details, related experiments or other essential details as experiments proceed, says Ingo Przesdzing, the ELN programme leader at the Berlin Institute for Health. ELNs can be much more efficient at capturing crucial details than conventional written documentation is, he says, and tools to tag whether or not experiments worked can help with both sharing and troubleshooting. But the benefits come only if people are trained properly — otherwise, he says, they use the ELN like a paper book, without the advantages of a digital solution.

Electronic laboratory and research notebooks can also help to standardize methods and record-keeping while providing experimental flexibility, says Alastair Downie, head of information technology at the Gurdon Institute in Cambridge, UK, who helps lab groups there implement ELNs. Having appropriate templates at the ready makes it much easier to communicate what to do, he says. “It becomes a huge advantage; everyone talks the same language.”

Deposit and document reagents

Countless experiments go wrong when a colleague gives a scientist the wrong cell line or reagent. Now, organizations such as the [ATCC](#) in Manassas, Virginia; [Addgene](#) in Watertown, Massachusetts; and the [Jackson Laboratory](#) in Bar Harbor, Maine, can act as gatekeepers, supplying cell lines, plasmids and genetically engineered mice, respectively, that are quality checked and distributed to other researchers. Many journals (including *Nature*) ask researchers to deposit research materials in the repositories of such institutions. This spares labs the burden of distributing them and ensures that other scientists will receive quality materials in a reasonable time.



NatureTech hub

Also available are tools to document commercial reagents in a standardized way. The [Resource Identification Initiative](#), for instance, assigns reagents unique identifiers that persist even if a company goes out of business or modifies its catalogue numbers; more than 600 journals (including *Nature*) encourage their use. The identifiers can be used to populate fields in a lab notebook, for example, or exported into in-development manuscripts to ease study write-up, troubleshooting and reproducibility.

One often-overlooked strategy for enhancing reproducibility is to understand the rationale behind every step, says Polyak. That way, researchers can troubleshoot situations that might be unique to their lab. Off-the-shelf kits undermine this ability to reason, she says. When it comes to reproducibility, a good protocol “gives you enough details”, says Luciano Martelotto, director of the single-cell core facility at Harvard Medical School in Boston. But a better protocol, he continues, helps researchers understand every step, and why one RNA inhibitor, for instance, is used over another.

Communicate

One of the most powerful aspects of emerging methods-sharing tools is how they enable conversations that share tips and extensions, says Martelotto. He

uses protocols.io to host a group, called [Single Cell Ninjas](#), to help other researchers get single-cell studies working. Updating, correcting and interacting about methods is becoming a scientific norm, he says.

Perhaps because these protocols are seen as less formal than papers, other researchers are more likely to ask questions, says Benjamin Schwessinger, who studies plant–microbe interactions at the Australian National University in Canberra and helped to launch an initiative called [Reproducibility for Everyone](#) to help researchers share methods and data. Schwessinger says many more people approach him about his protocols than about his papers, even if only to thank him for posting them and explaining the modifications they've made for different organisms. He gets alerts when people comment on his protocols at protocols.io, and also on social media. “It comes naturally for people to interact,” Schwessinger says. “You just need to build a community around it.”

Nature **597**, 293–294 (2021)

doi: <https://doi.org/10.1038/d41586-021-02428-3>

Updates & Corrections

- **Correction 09 September 2021:** An earlier version of this Technology feature gave the wrong name for the Reproducibility Project: Cancer Biology.

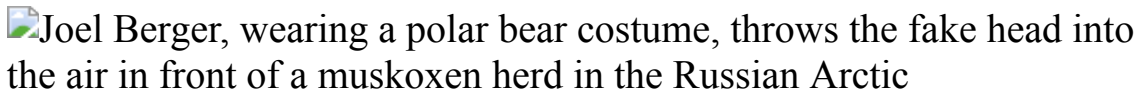
This article was downloaded by **calibre** from <https://www.nature.com/articles/d41586-021-02428-3>

- WHERE I WORK
- 06 September 2021

Who wants to be a polar bear?

Joel Berger braves freezing temperatures and charging musk oxen to learn how melting sea ice is affecting mammalian encounters.

- [Amber Dance](#) ⁰



Joel Berger studies wildlife conservation at Colorado State University in Fort Collins and is a senior scientist at the Wildlife Conservation Society in New York City. Credit: Sergei Abarok

As a wildlife-conservation biologist studying climate change, I want to understand the evolving environment through the eyes of large animals. My work — usually in cold, remote places — involves finding animals, and ways to eat, sleep and be warm. I might be miserable, but I get insights that others cannot into what animals are doing.

For about 15 years I've been interested in musk oxen (*Ovibos moschatus*), social herd animals that roamed with woolly mammoths. This picture was taken on Wrangel Island, off the northeast coast of Russia, when I was studying how musk oxen react to polar bears. Because polar ice is melting, more polar bears are hunting on land, and they're known to have killed musk oxen. These herd animals typically don't flee from predators such as grizzly bears. They tend to form huddles instead, and male musk oxen have killed grizzlies. Would they try to kill polar bears, too?

To find out, I dressed as a polar bear, pulling a bear head on and placing a cape over a range finder, camera and data books. I was cold and nervous. I

didn't want to be killed by a charging musk ox — or by anything else. If some oxen charged, I'd throw off my costume and stand up straight, as I'm doing here; so far, that had stopped them. I'd also encountered a female polar bear with newborn cubs, but she'd left me alone. This picture is from the end of a session, and I'd lived another day. Whew!

I learnt that musk oxen are more likely to flee from polar bears than from grizzlies. But during this trip to Russia, I was arrested — over a date error on my permits. In court, the only word I understood was 'CIA'. I was let go, but banned from returning for three years, so I'm now studying the huemul (*Hippocamelus bisulcus*), an endangered species of deer that lives in the shadows of glaciers at the tip of South America. As glaciers recede, how will huemul populations respond?

Nature **597**, 296 (2021)

doi: <https://doi.org/10.1038/d41586-021-02429-2>

This article was downloaded by **calibre** from <https://www.nature.com/articles/d41586-021-02429-2>

| [Section menu](#) | [Main menu](#) |

Research

- **[Chronically lonely flies overeat and lose sleep](#)** [18 August 2021]
News & Views • The fruit fly *Drosophila melanogaster* is a social animal. Flies kept in chronic social isolation have now been found to show dysregulated sleep and feeding patterns, casting light on how prolonged absence of social contact affects health.
- **[Fructose in the diet expands the surface of the gut and promotes nutrient absorption](#)** [18 August 2021]
News & Views • Feeding mice high-fructose corn syrup, a widely used sweetener in human diets, has been found to drive an increase in the surface area of the gut that is associated with enhanced absorption of dietary nutrients and weight gain.
- **[A stem-cell basis for skeletal ageing](#)** [11 August 2021]
News & Views • How ageing contributes to bone loss is unclear. In ageing mice, skeletal stem cells lose their ability to generate bone-forming cells called osteoblasts, and instead promote the generation of bone-resorbing cells called osteoclasts.
- **[Ubiquitin protein helps cells to recover from stress](#)** [16 August 2021]
News & Views • In stressed cells, proteins and RNA molecules cluster together to form stress granules. It emerges that the small protein modifier ubiquitin is needed to disassemble stress granules in recovering cells.
- **[Hybrid light–matter states formed in self-assembling cavities](#)** [08 September 2021]
News & Views • Tiny flakes of metal suspended in a solution have been observed to self-assemble into pairs separated by a narrow gap — offering a tunable system for studying combinations of light and matter known as polaritons.
- **[Interface nano-optics with van der Waals polaritons](#)** [08 September 2021]
Review Article • This Review discusses the state of the art of interface optics—including refractive optics, meta-optics and moiré engineering—for the control of van der Waals polaritons.
- **[A roadmap for the Human Developmental Cell Atlas](#)** [08 September 2021]
Perspective • This Perspective outlines the Human Developmental Cell Atlas initiative, which uses state-of-the-art technologies to map and model human development across gestation, and discusses the early milestones that have been achieved.

- **Large metallicity variations in the Galactic interstellar medium** [08 September 2021]

Article • The metallicity of the interstellar medium measured towards 25 stars relatively near the Sun shows large variations, suggesting that infalling pristine gas is not efficiently mixed in the interstellar medium.

- **High-fidelity laser-free universal control of trapped ion qubits** [08 September 2021]

Article • Laser-free universal control of two trapped-ion qubits using a combination of radiofrequency and microwave magnetic fields achieves some of the highest fidelities ever reported for two-qubit maximally entangled states.

- **Tunable self-assembled Casimir microcavities and polaritons** [08 September 2021]

Article • Gold nanoflake pairs form by self-assembly in an aqueous ligand solution and offer stable and tunable microcavities by virtue of equilibrium between attractive Casimir forces and repulsive electrostatic forces.

- **Transmembrane transport in inorganic colloidal cell-mimics** [08 September 2021]

Article • Hollow colloidal capsules, each with a single micropore, act as artificial cell-like structures that can capture and release payloads such as solid particles or bacteria from the external environment.

- **Widespread woody plant use of water stored in bedrock** [08 September 2021]

Article • Woody plants across the continental United States make extensive use of water stored in bedrock across diverse climates and biomes.

- **Unextractable fossil fuels in a 1.5 °C world** [08 September 2021]

Article • A global energy system model finds that planned fossil fuel extraction is inconsistent with limiting global warming to 1.5 °C, because the majority of fossil fuel reserves must stay in the ground.

- **A Triassic stem lepidosaur illuminates the origin of lizard-like reptiles** [25 August 2021]

Article • Taytalura alcoberi, represented by a three-dimensionally preserved skull from the Late Triassic epoch of Argentina, is phylogenetically inferred as the earliest known lepidosauromorph, and reveals that sphenodontian skull architecture is plesiomorphic for lepidosaurs.

- **Chronic social isolation signals starvation and reduces sleep in Drosophila** [18 August 2021]

Article • Behavioural and transcriptomic analyses show that chronic social isolation of Drosophila causes perturbed sleep and increased feeding, and induces a starvation-like brain state.

- **Hypothalamic dopamine neurons motivate mating through persistent cAMP signalling** [25 August 2021]

Article • A population of hypothalamic dopamine neurons sustains mating drive in male mice through a persistent mode of biochemical signalling in target neurons.

- **Cells of the human intestinal tract mapped across space and time** [08 September 2021]

Article • Cells from embryonic, fetal, paediatric and adult human intestinal tissue are analysed at different locations along the intestinal tract to construct a single-cell atlas of the developing and adult human intestinal tract, encompassing all cell lineages.

- **Aged skeletal stem cells generate an inflammatory degenerative niche** [11 August 2021]

Article • An analysis of skeletal stem cells in mice reveals that bone ageing occurs at the level of local niches affecting skeletal and haematopoietic lineage output, which may influence systemic aspects of multi-organ physiological ageing.

- **Dietary fructose improves intestinal cell survival and nutrient absorption** [18 August 2021]

Article • A high-fructose diet in mice improves the survival of intestinal epithelial cells, which leads to an increase in gut surface area, enhanced absorption of lipids and the promotion of tumour growth and obesity.

- **Rapid and stable mobilization of CD8+ T cells by SARS-CoV-2 mRNA vaccine** [28 July 2021]

Article • Longitudinal analyses of SARS-CoV-2 mRNA vaccine-elicited epitope-specific CD8+ T cell responses shows that CD8+ T cells are rapidly induced after prime vaccination and stably maintained after boost vaccination.

- **Defining HPV-specific B cell responses in patients with head and neck cancer** [18 November 2020]

Article • Detailed analyses of B cells in the tumour microenvironment of human papilloma virus (HPV)-linked head and neck cancers reveal strong humoral immune responses to HPV antigens and the secretion of HPV-specific antibodies in situ.

- **Functional HPV-specific PD-1+ stem-like CD8 T cells in head and neck cancer** [01 September 2021]

Article • An analysis of human papillomavirus (HPV)-specific CD8 T cells in patients with head and neck cancer identifies functional PD-1+TCF-1+CD8 T cells in the tumour with implications for therapeutic vaccination and PD-1 directed immunotherapy.

- **Structural basis for piRNA targeting** [01 September 2021]
Article • Cryo-electron microscopy structures of a PIWI–piRNA complex provide insight into how piRNAs recognise target RNAs and reveal differences from the target mechanisms of microRNAs.

| [Next section](#) | [Main menu](#) | [Previous section](#) |

- NEWS AND VIEWS
- 18 August 2021

Chronically lonely flies overeat and lose sleep

The fruit fly *Drosophila melanogaster* is a social animal. Flies kept in chronic social isolation have now been found to show dysregulated sleep and feeding patterns, casting light on how prolonged absence of social contact affects health.

- [Joel D. Levine](#) ⁰

The neuroscientist Bruce McEwen wrote¹ in 2002 that stress is the foremost public-health issue of our times, and that “when activated chronically it can cause damage and accelerate disease”. Many stressors are of a social nature, and McEwen¹ and others (see go.nature.com/3s3b4kw) noted with concern that certain social pressures, such as poverty, inadequate education and violent crime, can contribute to the development of illnesses such as cancer, diabetes and depression. However, little is understood about how these social pressures translate to disease. [Writing in Nature](#), Li *et al.*² present a fascinating and creative approach to modelling the effects of social context on an individual’s health, using the fruit fly *Drosophila melanogaster*.

Access options

Subscribe to Journal

Get full journal access for 1 year

\$199.00

only \$3.90 per issue

Subscribe

All prices are NET prices.

VAT will be added later in the checkout.

Tax calculation will be finalised during checkout.

Rent or Buy article

Get time limited or full article access on ReadCube.

from \$8.99

Rent or Buy

All prices are NET prices.

Additional access options:

- [Log in](#)
- [Learn about institutional subscriptions](#)

Nature **597**, 179–180 (2021)

doi: <https://doi.org/10.1038/d41586-021-02194-2>

References

1. 1.

McEwen, B. & Lasley, E. N. *The End of Stress As We Know It* (Dana, 2002).

2. 2.

Li, W. *et al.* *Nature* **597**, 239–244 (2021).

3. 3.

Bourassa, C., McKay-McNabb, K. & Hampton, M. *Can. Woman Stud.* **24**, 23–29 (2004).

4. 4.

Schneider, J., Atallah, J. & Levine, J. D. *Adv. Genet.* **77**, 59–78 (2012).

5. 5.

Dawson, E. H. *et al.* *Nature Commun.* **9**, 3574 (2018).

6. 6.

Sokolowski, M. B. *Neuron* **65**, 780–794 (2010).

7. 7.

Tomova, L. *et al.* *Nature Neurosci.* **23**, 1597–1605 (2020).

8. 8.

Hulse, B. K. *et al.* Preprint at bioRxiv
<https://doi.org/10.1101/2020.12.08.413955> (2020).

9. 9.

Donlea, J. M., Thimgan, M. S., Suzuki, Y., Gottschalk, L. & Shaw, P. J. *Science* **332**, 1571–1576 (2011).

10. 10.

Lee, G., Bahn, J. H. & Park, J. H. *Proc. Natl Acad. Sci. USA* **103**, 12580–12585 (2006).

11. 11.

Lee, C. R., Chen, A. & Tye, K. M. *Cell* **184**, 1500–1516 (2021).

12. 12.

Ramdy, P. *et al.* *Nature* **519**, 233–236 (2015).

13. 13.

Schneider, J., Dickinson, M. H. & Levine, J. D. *Proc. Natl Acad. Sci. USA* **109**, 17174–17179 (2012).

14. 14.

Danchin, E. *et al.* *Science* **362**, 1025–1030 (2018).

15. 15.

Bellen, H. J., Tong, C. & Tsuda, H. *Nature Rev. Neurosci.* **11**, 514–522 (2010).

This article was downloaded by **calibre** from <https://www.nature.com/articles/d41586-021-02194-2>

| [Section menu](#) | [Main menu](#) |

- NEWS AND VIEWS
- 18 August 2021

Fructose in the diet expands the surface of the gut and promotes nutrient absorption

Feeding mice high-fructose corn syrup, a widely used sweetener in human diets, has been found to drive an increase in the surface area of the gut that is associated with enhanced absorption of dietary nutrients and weight gain.

- [Patrícia M. Nunes](#)⁰ &
- [Dimitrios Anastasiou](#) ORCID: <http://orcid.org/0000-0002-1269-843X>¹

The incidence of obesity has been steadily increasing, tripling globally between 1975 and 2016, at a high cost to public health¹. Obesity predisposes individuals to various diseases, including cancer, and the number of obesity-associated deaths globally each year¹ (estimated at 2.8 million) is similar in scale to the reported COVID-19-associated deaths in the ongoing pandemic. Although fat-rich diets have taken much of the blame for the rise in obesity, excess consumption of processed sugars, and high-fructose corn syrup (HFCS) in particular, is strongly implicated in diet-induced obesity. Whether and how fructose causes obesity in humans remains a hotly debated question^{2,3}. In [a report in Nature](#) that should make one think twice before gulping down sugar-sweetened drinks with fatty snacks, Taylor *et al.*⁴ propose that HFCS promotes obesity by boosting the ability of the intestine to absorb nutrients.

Access options

[Subscribe to Journal](#)

Get full journal access for 1 year

\$199.00

only \$3.90 per issue

[Subscribe](#)

All prices are NET prices.

VAT will be added later in the checkout.

Tax calculation will be finalised during checkout.

Rent or Buy article

Get time limited or full article access on ReadCube.

from \$8.99

[Rent or Buy](#)

All prices are NET prices.

Additional access options:

- [Log in](#)
- [Learn about institutional subscriptions](#)

Nature **597**, 180-182 (2021)

doi: <https://doi.org/10.1038/d41586-021-02195-1>

References

1. 1.

Lancet Gastroenterol. Hepatol. **6**, 411 (2021).

2. 2.

van Buul, V. J., Tappy, L. & Brouns, F. J. *Nutr. Res. Rev.* **27**, 119–130 (2014).

3. 3.

Stanhope, K. L. *Crit. Rev. Clin. Lab. Sci.* **53**, 52–67 (2016).

4. 4.

Taylor, S. R. *et al.* *Nature* **597**, 263–267 (2021).

5. 5.

Jang, C. *et al.* *Cell Metab.* **27**, 351–361 (2018).

6. 6.

Andres-Hernando, A. *et al.* *Cell Metab.* **32**, 117–127 (2020).

7. 7.

Zhao, S. *et al.* *Nature* **579**, 586–591 (2020).

8. 8.

Todoric, J. *et al.* *Nature Metab.* **2**, 1034–1045 (2020).

9. 9.

Softic, S., Cohen, D. E. & Kahn, C. R. *Dig. Dis. Sci.* **61**, 1282–1293 (2016).

10. 10.

Goncalves, M. D. *et al.* *Science* **363**, 1345–1349 (2019).

11. 11.

Dayton, T. L., Jacks, T. & Vander Heiden, M. G. *EMBO Rep.* **17**, 1721–1730 (2016).

12. 12.

Luo, W. *et al.* *Cell* **145**, 732–744 (2011).

This article was downloaded by **calibre** from <https://www.nature.com/articles/d41586-021-02195-1>

| [Section menu](#) | [Main menu](#) |

- NEWS AND VIEWS
- 11 August 2021

A stem-cell basis for skeletal ageing

How ageing contributes to bone loss is unclear. In ageing mice, skeletal stem cells lose their ability to generate bone-forming cells called osteoblasts, and instead promote the generation of bone-resorbing cells called osteoclasts.

- [Matthew B. Greenblatt](#) ORCID: <http://orcid.org/0000-0001-9794-8532>⁰ &
- [Shawon Debnath](#)¹

Ageing is a key driver of bone-mass reductions and skeletal fragility. The bone loss that occurs with ageing reflects the confluence of many molecular and cellular processes, and it has therefore been more difficult to understand than the mechanistically distinct form of bone loss associated with the decline of oestrogen in women after menopause^{1–3}. However, insights into the identity of skeletal stem cells (SSCs) and other related progenitor cell populations that produce bone-forming cells called osteoblasts^{4,5} have facilitated investigation into how ageing affects skeletal cells. [Writing in Nature](#), Ambrosi *et al.*⁶ now determine how, with ageing, the function of SSCs changes, contributing to bone loss and impaired skeletal regeneration.

Access options

Subscribe to Journal

Get full journal access for 1 year

\$199.00

only \$3.90 per issue

Subscribe

All prices are NET prices.

VAT will be added later in the checkout.

Tax calculation will be finalised during checkout.

Rent or Buy article

Get time limited or full article access on ReadCube.

from \$8.99

Rent or Buy

All prices are NET prices.

Additional access options:

- [Log in](#)
- [Learn about institutional subscriptions](#)

Nature **597**, 182–183 (2021)

doi: <https://doi.org/10.1038/d41586-021-02118-0>

References

1. 1.

Manolagas, S. C. *J. Bone Miner. Res.* **33**, 371–385 (2018).

2. 2.

Ucer, S. *et al. J. Bone Miner. Res.* **32**, 560–574 (2017).

3. 3.

Farr, J. N. *et al.* *J. Bone Miner. Res.* **34**, 1407–1418 (2019).

4. 4.

Chan, C. K. F. *et al.* *Cell* **160**, 285–98 (2015).

5. 5.

Chan, C. K. F. *et al.* *Cell* **175**, 43–56.e21 (2018).

6. 6.

Ambrosi, T. H. *et al.* *Nature* **597**, 256–262 (2021).

7. 7.

Salazar, V. S., Gamer, L. W. & Rosen, V. *Nature Rev. Endocrinol.* **12**, 203–221 (2016).

8. 8.

Matsushita, Y. *et al.* *Nature Commun.* **11**, 332 (2020).

9. 9.

Seike, M., Omatsu, Y., Watanabe, H., Kondoh, G. & Nagasawa, T. *Genes Dev.* **32**, 359–372 (2018).

10. 10.

Zhou, B. O., Yue, R., Murphy, M. M., Peyer, J. G. & Morrison, S. J. *Cell Stem Cell* **15**, 154–168 (2014).

11. 11.

Farr, J. N. *et al.* *Nature Med.* **23**, 1072–1079 (2017).

12. 12.

This article was downloaded by **calibre** from <https://www.nature.com/articles/d41586-021-02118-0>

| [Section menu](#) | [Main menu](#) |

- NEWS AND VIEWS
- 16 August 2021

Ubiquitin protein helps cells to recover from stress

In stressed cells, proteins and RNA molecules cluster together to form stress granules. It emerges that the small protein modifier ubiquitin is needed to disassemble stress granules in recovering cells.

- [Titus Franzmann](#)⁰ &
- [Simon Alberti](#)¹

The biggest threat to a cell during exposure to environmental stress factors, such as high temperature, is the unfolding of its proteins. Two strategies prevent the accumulation of damaged proteins: refolding, which is assisted by chaperone proteins, and protein degradation. In one degradation pathway, ubiquitin molecules are attached to target proteins to signal that they are to be degraded by a protein complex called the proteasome. Early work showed that heat stress induces the ubiquitination and proteasomal degradation of cellular proteins¹. Now, writing in *Science*, [Maxwell et al.](#)² and [Gwon et al.](#)³ report that ubiquitination of a large set of proteins is required to recover normal cellular function when stress subsides.

Access options

Subscribe to Journal

Get full journal access for 1 year

\$199.00

only \$3.90 per issue

Subscribe

All prices are NET prices.

VAT will be added later in the checkout.

Tax calculation will be finalised during checkout.

Rent or Buy article

Get time limited or full article access on ReadCube.

from \$8.99

Rent or Buy

All prices are NET prices.

Additional access options:

- [Log in](#)
- [Learn about institutional subscriptions](#)

Nature **597**, 183-184 (2021)

doi: <https://doi.org/10.1038/d41586-021-02197-z>

References

1. 1.

Parag, H. A., Raboy, B. & Kulka, R. G. *EMBO J.* **6**, 55–61 (1987).

2. 2.

Maxwell, B. A. *et al. Science* **372**, eabc3593 (2021).

3. 3.

Gwon, Y. *et al.* *Science* **372**, eabf6548 (2021).

4. 4.

Xu, G. *et al.* *J. Cell Sci.* **129**, 1892–1901 (2016).

5. 5.

Aprile-Garcia, F., Tomar, P., Hummel, B., Khavaran, A. & Sawarkar, R. *Nature Struct. Mol. Biol.* **26**, 137–146 (2019).

6. 6.

Yang, P. *et al.* *Cell* **181**, 325–345 (2020).

7. 7.

Guillén-Boixet, J. *et al.* *Cell* **181**, 346–361 (2020).

8. 8.

Sanders, D. W. *et al.* *Cell* **181**, 306–324 (2020).

9. 9.

Ganassi, M. *et al.* *Mol. Cell* **63**, 796–810 (2016).

10. 10.

Seguin, S. J. *et al.* *Cell Death Differ.* **21**, 1838–1851 (2014).

11. 11.

Mateju, D. *et al.* *EMBO J.* **36**, 1669–1687 (2017).

12. 12.

Tolay, N. & Buchberger, A. *Life Sci. Alliance* **4**, e202000927 (2021).

13. 13.

Turakhiya, A. *et al.* *Mol. Cell* **70**, 906–919 (2018).

14. 14.

Buchan, J. R., Kolaitis, R.-M., Taylor, J. P. & Parker, R. *Cell* **153**, 1461–1474 (2013).

15. 15.

Alberti, S. & Hyman, A. A. *Nature Rev. Mol. Cell. Biol.* **22**, 196–213 (2021).

This article was downloaded by **calibre** from <https://www.nature.com/articles/d41586-021-02197-z>

| [Section menu](#) | [Main menu](#) |

- NEWS AND VIEWS
- 08 September 2021

Hybrid light–matter states formed in self-assembling cavities

Tiny flakes of metal suspended in a solution have been observed to self-assemble into pairs separated by a narrow gap — offering a tunable system for studying combinations of light and matter known as polaritons.

- [Johannes Feist](#) [ORCID: http://orcid.org/0000-0002-7972-0646](#) 0

Stable physical systems generally require a balance between attractive forces that pull their components together and repulsive forces that push them apart. For example, Earth's gravity pulls us down, but our feet do not sink through the floor because of the overall repulsive electrical forces between the electrons and nuclei that both we and the floor are made of. On a microscopic level, the stability of materials is due to the electrostatic interaction between charged electrons and nuclei, with like charges repelling and opposite charges attracting each other. [Writing in Nature](#), Munkhbat *et al.*¹ report that a different balance of attraction and repulsion can cause two or more microscopic metal flakes to form an optical cavity by self-assembly — generating a pair of mirrors that can trap light between them. Such cavities have a wide range of uses because they modify the interaction between light and matter within them.

Access options

Subscribe to Journal

Get full journal access for 1 year

\$199.00

only \$3.90 per issue

Subscribe

All prices are NET prices.

VAT will be added later in the checkout.

Tax calculation will be finalised during checkout.

Rent or Buy article

Get time limited or full article access on ReadCube.

from \$8.99

Rent or Buy

All prices are NET prices.

Additional access options:

- [Log in](#)
- [Learn about institutional subscriptions](#)

Nature **597**, 185–186 (2021)

doi: <https://doi.org/10.1038/d41586-021-02376-y>

References

1. 1.

Munkhbat, B., Canales, A., Küçüköz, B., Baranov, D. G. & Shegai, T. O. *Nature* **597**, 214–219 (2021).

2. 2.

Grzelczak, M., Vermant, J., Furst, E. M. & Liz-Marzán, L. M. *ACS Nano* **4**, 3591–3605 (2010).

3. 3.

Purcell, E. M. *Phys. Rev.* **69**, 681 (1946).

4. 4.

Haroche, S. & Kleppner, D. *Phys. Today* **42**, 24–30 (1989).

5. 5.

Ruggenthaler, M., Tancogne-Dejean, N., Flick, J., Appel, H. & Rubio, A. *Nature Rev. Chem.* **2**, 0118 (2018).

6. 6.

Carusotto, I. & Ciuti, C. *Rev. Mod. Phys.* **85**, 299–366 (2013).

7. 7.

Hutchison, J. A., Schwartz, T., Genet, C., Devaux, E. & Ebbesen, T. W. *Angew. Chem. Int. Edn* **51**, 1592–1596 (2012).

8. 8.

Galego, J., Garcia-Vidal, F. J. & Feist, J. *Phys. Rev. Lett.* **119**, 136001 (2017).

9. 9.

Coles, D. M. *et al.* *Nature Mater.* **13**, 712–719 (2014).

10. 10.

Zhong, X. *et al.* *Angew. Chem. Int. Edn* **56**, 9034–9038 (2017).

11. 11.

Xiang, B. *et al.* *Proc. Natl Acad. Sci. USA* **115**, 4845–4850 (2018).

This article was downloaded by **calibre** from <https://www.nature.com/articles/d41586-021-02376-y>.

| [Section menu](#) | [Main menu](#) |

- Review Article
- [Published: 08 September 2021](#)

Interface nano-optics with van der Waals polaritons

- [Qing Zhang¹ ✉nal](#),
- [Guangwei Hu](#) [ORCID: orcid.org/0000-0002-3023-9632¹](#) ✉nal,
- [Weiliang Ma²](#),
- [Peining Li](#) [ORCID: orcid.org/0000-0003-3836-3803²](#),
- [Alex Krasnok³](#),
- [Rainer Hillenbrand](#) [ORCID: orcid.org/0000-0002-1904-4551^{4,5}](#),
- [Andrea Alù](#) [ORCID: orcid.org/0000-0002-4297-5274^{3,6}](#) &
- [Cheng-Wei Qiu](#) [ORCID: orcid.org/0000-0002-6605-500X¹](#)

[Nature](#) volume **597**, pages 187–195 (2021)

- 2916 Accesses
- 24 Altmetric
- [Metrics details](#)

Subjects

- [Optical materials and structures](#)
- [Surfaces, interfaces and thin films](#)
- [Two-dimensional materials](#)

Abstract

Polaritons are hybrid excitations of matter and photons. In recent years, polaritons in van der Waals nanomaterials—known as van der Waals polaritons—have shown great promise to guide the flow of light at the nanoscale over spectral regions ranging from the visible to the terahertz. A vibrant research field based on manipulating strong light–matter interactions in the form of polaritons, supported by these atomically thin van der Waals nanomaterials, is emerging for advanced nanophotonic and opto-electronic applications. Here we provide an overview of the state of the art of exploiting interface optics—such as refractive optics, meta-optics and moiré engineering—for the control of van der Waals polaritons. This enhanced control over van der Waals polaritons at the nanoscale has not only unveiled many new phenomena, but has also inspired valuable applications—including new avenues for nano-imaging, sensing, on-chip optical circuitry, and potentially many others in the years to come.

Access options

Subscribe to Journal

Get full journal access for 1 year

\$199.00

only \$3.90 per issue

[Subscribe](#)

All prices are NET prices.

VAT will be added later in the checkout.

Tax calculation will be finalised during checkout.

Rent or Buy article

Get time limited or full article access on ReadCube.

from \$8.99

[Rent or Buy](#)

All prices are NET prices.

Additional access options:

- [Log in](#)
- [Access through your institution](#)
- [Learn about institutional subscriptions](#)

Fig. 1: Interface optics with vdW polaritons.



Fig. 2: Refractive optics based on planar polaritonic elements.



Fig. 3: Meta-optics based on polaritonic vdW nanostructures and heterostructures.



Fig. 4: Interlayer effects and moiré engineering for extreme polariton dispersion.

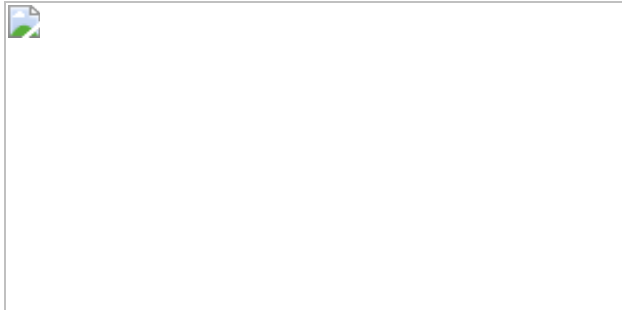
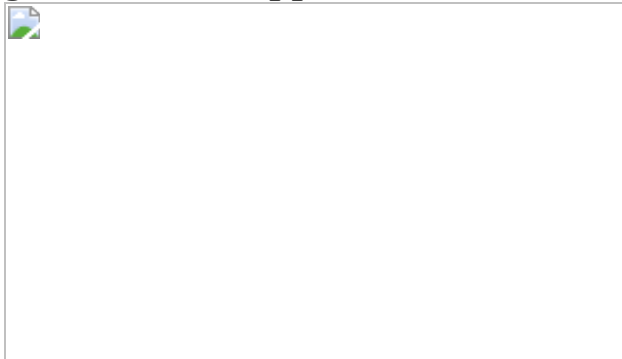


Fig. 5: Potential applications and future developments.



References

1. 1.

Basov, D. N., Fogler, M. M. & García de Abajo, F. J. Polaritons in van der Waals materials. *Science* **354**, aag1992 (2016).

2. 2.

Low, T. et al. Polaritons in layered two-dimensional materials. *Nat. Mater.* **16**, 182–194 (2017). **Refs.^{1,2} are two comprehensive reviews of early-stage research on polaritons in natural vdW materials—including monolayers, thin slabs and hybrid heterostructures—summarizing the unique physical features of different types of vdW polariton.**

3. 3.

Dai, Z. et al. Artificial metaphotonics born naturally in two dimensions. *Chem. Rev.* **120**, 6197–6246 (2020).

4. 4.

Rodrigo, D. et al. Mid-infrared plasmonic biosensing with graphene. *Science* **349**, 165–168 (2015).

5. 5.

Hu, H. et al. Far-field nanoscale infrared spectroscopy of vibrational fingerprints of molecules with graphene plasmons. *Nat. Commun.* **7**, 12334 (2016).

6. 6.

Autore, M. et al. Boron nitride nanoresonators for phonon-enhanced molecular vibrational spectroscopy at the strong coupling limit. *Light Sci. Appl.* **7**, 17172 (2018).

7. 7.

Alfaro-Mozaz, F. J. et al. Nanoimaging of resonating hyperbolic polaritons in linear boron nitride antennas. *Nat. Commun.* **8**, 15624 (2017).

8. 8.

Li, P. et al. Hyperbolic phonon-polaritons in boron nitride for near-field optical imaging and focusing. *Nat. Commun.* **6**, 7507 (2015).

9. 9.

Dai, S. et al. Subdiffractive focusing and guiding of polaritonic rays in a natural hyperbolic material. *Nat. Commun.* **6**, 6963 (2015).

10. 10.

Liu, M. et al. A graphene-based broadband optical modulator. *Nature* **474**, 64–67 (2011).

11. 11.

Ni, G. et al. Ultrafast optical switching of infrared plasmon polaritons in high-mobility graphene. *Nat. Photonics* **10**, 244–247 (2016).

12. 12.

Yao, B. et al. Broadband gate-tunable terahertz plasmons in graphene heterostructures. *Nat. Photonics* **12**, 22–28 (2018).

13. 13.

Phare, C. T., Lee, Y.-H. D., Cardenas, J. & Lipson, M. Graphene electro-optic modulator with 30 GHz bandwidth. *Nat. Photonics* **9**, 511–514 (2015).

14. 14.

Ansell, D. et al. Hybrid graphene plasmonic waveguide modulators. *Nat. Commun.* **6**, 8846 (2015).

15. 15.

Wu, S. et al. Monolayer semiconductor nanocavity lasers with ultralow thresholds. *Nature* **520**, 69–72 (2015).

16. 16.

Chakraborty, S. et al. Gain modulation by graphene plasmons in aperiodic lattice lasers. *Science* **351**, 246–248 (2016).

17. 17.

Kurman, Y. et al. Control of semiconductor emitter frequency by increasing polariton momenta. *Nat. Photonics* **12**, 423–429 (2018).

18. 18.

Brar, V. W. et al. Hybrid surface-phonon-plasmon polariton modes in graphene/monolayer h-BN heterostructures. *Nano Lett.* **14**, 3876–3880 (2014).

19. 19.

Dai, S. et al. Graphene on hexagonal boron nitride as a tunable hyperbolic metamaterial. *Nat. Nanotechnol.* **10**, 682–686 (2015).

20. 20.

Woessner, A. et al. Highly confined low-loss plasmons in graphene–boron nitride heterostructures. *Nat. Mater.* **14**, 421–425 (2015).

21. 21.

Dubrovkin, A. M., Qiang, B., Krishnamoorthy, H. N. S., Zheludev, N. I. & Wang, Q. J. Ultra-confined surface phonon polaritons in molecular layers of van der Waals dielectrics. *Nat. Commun.* **9**, 1762 (2018).

22. 22.

Chaudhary, K. et al. Engineering phonon polaritons in van der Waals heterostructures to enhance in-plane optical anisotropy. *Sci. Adv.* **5**, eaau7171 (2019).

23. 23.

Caldwell, J. D. et al. Atomic-scale photonic hybrids for mid-infrared and terahertz nanophotonics. *Nat. Nanotechnol.* **11**, 9–15 (2016).

24. 24.

Yan, H. et al. Damping pathways of mid-infrared plasmons in graphene nanostructures. *Nat. Photonics* **7**, 394–399 (2013).

25. 25.

Alcaraz Iranzo, D. et al. Probing the ultimate plasmon confinement limits with a van der Waals heterostructure. *Science* **360**, 291–295 (2018).

26. 26.

Epstein, I. et al. Far-field excitation of single graphene plasmon cavities with ultracompressed mode volumes. *Science* **368**, 1219–1223 (2020).

27. 27.

Chen, J. et al. Optical nano-imaging of gate-tunable graphene plasmons. *Nature* **487**, 77–81 (2012).

28. 28.

Fei, Z. et al. Gate-tuning of graphene plasmons revealed by infrared nano-imaging. *Nature* **487**, 82–85 (2012). **Refs.^{27,28} independently demonstrated real-space imaging of surface plasmon polaritons in graphene.**

29. 29.

Alonso-González, P. et al. Controlling graphene plasmons with resonant metal antennas and spatial conductivity patterns. *Science* **344**, 1369–1373 (2014).

30. 30.

Yoxall, E. et al. Direct observation of ultraslow hyperbolic polariton propagation with negative phase velocity. *Nat. Photonics* **9**, 674 (2015).

31. 31.

Nikitin, A. et al. Real-space mapping of tailored sheet and edge plasmons in graphene nanoresonators. *Nat. Photonics* **10**, 239–243 (2016).

32. 32.

Ni, G. X. et al. Plasmons in graphene moiré superlattices. *Nat. Mater.* **14**, 1217–1222 (2015).

33. 33.

Sunku, S. S. et al. Photonic crystals for nano-light in moiré graphene superlattices. *Science* **362**, 1153–1156 (2018).

34. 34.

Chaudhary, K. et al. Polariton nanophotonics using phase-change materials. *Nat. Commun.* **10**, 4487 (2019).

35. 35.

Zheng, Z. et al. A mid-infrared biaxial hyperbolic van der Waals crystal. *Sci. Adv.* **5**, eaav8690 (2019).

36. 36.

Li, P. et al. Infrared hyperbolic metasurface based on nanostructured van der Waals materials. *Science* **359**, 892–896 (2018).

37. 37.

Lundeberg, M. B. et al. Thermoelectric detection and imaging of propagating graphene plasmons. *Nat. Mater.* **16**, 204–207 (2017).

38. 38.

Woessner, A. et al. Electrical detection of hyperbolic phonon-polaritons in heterostructures of graphene and boron nitride. *npj 2D Mater. Appl.* **1**, 25 (2017).

39. 39.

Alonso-González, P. et al. Acoustic terahertz graphene plasmons revealed by photocurrent nanoscopy. *Nat. Nanotechnol.* **12**, 31–35 (2017).

40. 40.

Ambrosio, A. et al. Mechanical detection and imaging of hyperbolic phonon polaritons in hexagonal boron nitride. *ACS Nano* **11**, 8741–8746 (2017).

41. 41.

Tamagnone, M. et al. Ultra-confined mid-infrared resonant phonon polaritons in van der Waals nanostructures. *Sci. Adv.* **4**, eaat7189 (2018).

42. 42.

Govyadinov, A. A. et al. Probing low-energy hyperbolic polaritons in van der Waals crystals with an electron microscope. *Nat. Commun.* **8**, 95 (2017).

43. 43.

Li, N. et al. Direct observation of highly confined phonon polaritons in suspended monolayer hexagonal boron nitride. *Nat. Mater.* **20**, 43–48 (2021).

44. 44.

Dong, W. et al. Broad-spectral-range sustainability and controllable excitation of hyperbolic phonon polaritons in α -MoO₃. *Adv. Mater.* **32**, 2002014 (2020).

45. 45.

Folland, T. G. et al. Reconfigurable infrared hyperbolic metasurfaces using phase change materials. *Nat. Commun.* **9**, 4371 (2018).

46. 46.

Woessner, A. et al. Electrical 2π phase control of infrared light in a 350-nm footprint using graphene plasmons. *Nat. Photonics* **11**, 421–424 (2017).

47. 47.

Vakil, A. & Engheta, N. Transformation optics using graphene. *Science* **332**, 1291–1294 (2011).

48. 48.

Lin, X. et al. All-angle negative refraction of highly squeezed plasmon and phonon polaritons in graphene-boron nitride heterostructures. *Proc. Natl Acad. Sci. USA* **114**, 6717–6721 (2017).

49. 49.

Zhang, Q. et al. Negative refraction inspired polariton lens in van der Waals lateral heterojunctions. *Appl. Phys. Lett.* **114**, 221101 (2019).

50. 50.

Hu, F. et al. Imaging the localized plasmon resonance modes in graphene nanoribbons. *Nano Lett.* **17**, 5423–5428 (2017).

51. 51.

Dai, Z. et al. Edge-oriented and steerable hyperbolic polaritons in anisotropic van der Waals nanocavities. *Nat. Commun.* **11**, 6086 (2020).

52. 52.

Dolado, I. et al. Nanoscale guiding of infrared light with hyperbolic volume and surface polaritons in van der Waals material ribbons. *Adv. Mater.* **32**, 1906530 (2020).

53. 53.

Kloppstech, K. et al. Giant heat transfer in the crossover regime between conduction and radiation. *Nat. Commun.* **8**, 14475 (2017).

54. 54.

Dias, E. J. C., Yu, R. & García de Abajo, F. J. Thermal manipulation of plasmons in atomically thin films. *Light Sci. Appl.* **9**, 87 (2020).

55. 55.

Gomez-Diaz, J. S., Tymchenko, M. & Alù, A. Hyperbolic plasmons and topological transitions over uniaxial metasurfaces. *Phys. Rev. Lett.* **114**, 233901 (2015).

56. 56.

Hu, G. et al. Topological polaritons and photonic magic angles in twisted α -MoO₃ bilayers. *Nature* **582**, 209–213 (2020).

57. 57.

Li, P. et al. Collective near-field coupling and nonlocal phenomena in infrared-phononic metasurfaces for nano-light canalization. *Nat. Commun.* **11**, 3663 (2020).

58. 58.

Cortes, C. L. & Jacob, Z. Super-Coulombic atom–atom interactions in hyperbolic media. *Nat. Commun.* **8**, 14144 (2017).

59. 59.

Alfaro-Mozaz, F. J. et al. Deeply subwavelength phonon-polaritonic crystal made of a van der Waals material. *Nat. Commun.* **10**, 42 (2019).

60. 60.

Xiong, L. et al. Photonic crystal for graphene plasmons. *Nat. Commun.* **10**, 4780 (2019).

61. 61.

Li, P. et al. Reversible optical switching of highly confined phonon-polaritons with an ultrathin phase-change material. *Nat. Mater.* **15**, 870–875 (2016).

62. 62.

Cao, Y. et al. Unconventional superconductivity in magic-angle graphene superlattices. *Nature* **556**, 43–50 (2018).

63. 63.

Cao, Y. et al. Correlated insulator behaviour at half-filling in magic-angle graphene superlattices. *Nature* **556**, 80–84 (2018).

64. 64.

Tran, K. et al. Evidence for moiré excitons in van der Waals heterostructures. *Nature* **567**, 71–75 (2019).

65. 65.

Seyler, K. L. et al. Signatures of moiré-trapped valley excitons in MoSe₂/WSe₂ heterobilayers. *Nature* **567**, 66–70 (2019).

66. 66.

Jin, C. et al. Observation of moiré excitons in WSe₂/WS₂ heterostructure superlattices. *Nature* **567**, 76–80 (2019).

67. 67.

Alexeev, E. M. et al. Resonantly hybridized excitons in moiré superlattices in van der Waals heterostructures. *Nature* **567**, 81–86 (2019).

68. 68.

Aoki, M. & Amawashi, H. Dependence of band structures on stacking and field in layered graphene. *Solid State Commun.* **142**, 123–127 (2007).

69. 69.

Zhang, F., Jung, J., Fiete, G. A., Niu, Q. & MacDonald, A. H. Spontaneous quantum Hall states in chirally stacked few-layer graphene systems. *Phys. Rev. Lett.* **106**, 156801 (2011).

70. 70.

Ju, L. et al. Topological valley transport at bilayer graphene domain walls. *Nature* **520**, 650–655 (2015).

71. 71.

Jiang, L. et al. Manipulation of domain-wall solitons in bi- and trilayer graphene. *Nat. Nanotechnol.* **13**, 204–208 (2018).

72. 72.

Jiang, L. et al. Soliton-dependent plasmon reflection at bilayer graphene domain walls. *Nat. Mater.* **15**, 840–844 (2016).

73. 73.

Hu, F. et al. Real-space imaging of the tailored plasmons in twisted bilayer graphene. *Phys. Rev. Lett.* **119**, 247402 (2017).

74. 74.

Ni, G. X. et al. Soliton superlattices in twisted hexagonal boron nitride. *Nat. Commun.* **10**, 4360 (2019).

75. 75.

Luo, Y. et al. In situ nanoscale imaging of moiré superlattices in twisted van der Waals heterostructures. *Nat. Commun.* **11**, 4209 (2020).

76. 76.

Chen, X. et al. Moiré engineering of electronic phenomena in correlated oxides. *Nat. Phys.* **16**, 631–635 (2020).

77. 77.

Sunku, S. S. et al. Nano-photocurrent mapping of local electronic structure in twisted bilayer graphene. *Nano Lett.* **20**, 2958–2964 (2020).

78. 78.

McGilly, L. J. et al. Visualization of moiré superlattices. *Nat. Nanotechnol.* **15**, 580–584 (2020).

79. 79.

Lewandowski, C. & Levitov, L. Intrinsically undamped plasmon modes in narrow electron bands. *Proc. Natl Acad. Sci. USA* **116**, 20869–20874 (2019).

80. 80.

Khaliji, K., Stauber, T. & Low, T. Plasmons and screening in finite-bandwidth two-dimensional electron gas. *Phys. Rev. B* **102**, 125408 (2020).

81. 81.

Brey, L., Stauber, T., Slipchenko, T. & Martín-Moreno, L. Plasmonic Dirac cone in twisted bilayer graphene. *Phys. Rev. Lett.* **125**, 256804 (2020).

82. 82.

Woods, C. et al. Commensurate–incommensurate transition in graphene on hexagonal boron nitride. *Nat. Phys.* **10**, 451–456 (2014).

83. 83.

Kennes, D. M. et al. Moiré heterostructures as a condensed-matter quantum simulator. *Nat. Phys.* **17**, 155–163 (2021).

84. 84.

Hu, G., Krasnok, A., Mazor, Y., Qiu, C.-W. & Alù, A. Moiré hyperbolic metasurfaces. *Nano Lett.* **20**, 3217–3224 (2020).

85. 85.

Kotov, O. & Lozovik, Y. E. Hyperbolic hybrid waves and optical topological transitions in few-layer anisotropic metasurfaces. *Phys. Rev. B* **100**, 165424 (2019).

86. 86.

Zheng, Z. et al. Phonon polaritons in twisted double-layers of hyperbolic van der Waals crystals. *Nano Lett.* **20**, 5301–5308 (2020).

87. 87.

Duan, J. et al. Twisted nano-optics: manipulating light at the nanoscale with twisted phonon polaritonic slabs. *Nano Lett.* **20**, 5323–5329 (2020).

88. 88.

Ma, W. et al. In-plane anisotropic and ultra-low-loss polaritons in a natural van der Waals crystal. *Nature* **562**, 557–562 (2018).

89. 89.

Pendry, J. B., Schurig, D. & Smith, D. R. Controlling electromagnetic fields. *Science* **312**, 1780–1782 (2006).

90. 90.

Schurig, D. et al. Metamaterial electromagnetic cloak at microwave frequencies. *Science* **314**, 977–980 (2006).

91. 91.

Alù, A. & Engheta, N. Achieving transparency with plasmonic and metamaterial coatings. *Phys. Rev. E* **72**, 016623 (2005).

92. 92.

Jin, D. et al. Infrared topological plasmons in graphene. *Phys. Rev. Lett.* **118**, 245301 (2017).

93. 93.

Liu, W. et al. Generation of helical topological exciton-polaritons. *Science* **370**, 600–604 (2020).

94. 94.

Kumar, A. et al. Chiral plasmon in gapped Dirac systems. *Phys. Rev. B* **93**, 041413 (2016).

95. 95.

Song, J. C. & Rudner, M. S. Chiral plasmons without magnetic field. *Proc. Natl Acad. Sci. USA* **113**, 4658–4663 (2016).

96. 96.

Kaminer, I. et al. Efficient plasmonic emission by the quantum Čerenkov effect from hot carriers in graphene. *Nat. Commun.* **7**, ncomms11880 (2016).

97. 97.

Tao, J., Wu, L. & Zheng, G. Graphene surface-polariton in-plane Cherenkov radiation. *Carbon* **133**, 249–253 (2018).

98. 98.

Tao, J., Wu, L., Zheng, G. & Yu, S. Cherenkov polaritonic radiation in a natural hyperbolic material. *Carbon* **150**, 136–141 (2019).

99. 99.

Rivera, N., Kaminer, I., Zhen, B., Joannopoulos, J. D. & Soljačić, M. Shrinking light to allow forbidden transitions on the atomic scale. *Science* **353**, 263–269 (2016).

100. 100.

Lin, X. et al. Splashing transients of 2D plasmons launched by swift electrons. *Sci. Adv.* **3**, e1601192 (2017).

101. 101.

Shentcis, M. et al. Tunable free-electron X-ray radiation from van der Waals materials. *Nat. Photonics* **14**, 686–692 (2020).

102. 102.

Wong, L. J., Kaminer, I., Ilic, O., Joannopoulos, J. D. & Soljačić, M. Towards graphene plasmon-based free-electron infrared to X-ray sources. *Nat. Photonics* **10**, 46–52 (2016).

103. 103.

Rosolen, G. et al. Metasurface-based multi-harmonic free-electron light source. *Light Sci. Appl.* **7**, 64 (2018).

104. 104.

Li, Y., Ferreyra, P., Swan, A. K. & Paiella, R. Current-driven terahertz light emission from graphene plasmonic oscillations. *ACS Photonics* **6**, 2562–2569 (2019).

105. 105.

Yang, Y. et al. Maximal spontaneous photon emission and energy loss from free electrons. *Nat. Phys.* **14**, 894–899 (2018).

106. 106.

Farmer, D. B., Avouris, P., Li, Y., Heinz, T. F. & Han, S.-J. Ultrasensitive plasmonic detection of molecules with graphene. *ACS Photonics* **3**, 553–557 (2016).

107. 107.

Hu, H. et al. Gas identification with graphene plasmons. *Nat. Commun.* **10**, 1131 (2019).

108. 108.

Tamagnone, M. et al. High quality factor polariton resonators using van der Waals materials. Preprint at <https://arxiv.org/abs/1905.02177> (2019).

109. 109.

Lee, I.-H., Yoo, D., Avouris, P., Low, T. & Oh, S.-H. Graphene acoustic plasmon resonator for ultrasensitive infrared spectroscopy. *Nat. Nanotechnol.* **14**, 313–319 (2019).

110. 110.

Lee, I.-H. et al. Anisotropic acoustic plasmons in black phosphorus. *ACS Photonics* **5**, 2208–2216 (2018).

111. 111.

Yuan, Z. et al. Extremely-confined acoustic phonon polaritons in monolayer-hBN/metal heterostructures for strong light-matter interactions. *ACS Photonics* **7**, 2610–2617 (2020).

112. 112.

Francescato, Y., Giannini, V., Yang, J., Huang, M. & Maier, S. A. Graphene sandwiches as a platform for broadband molecular spectroscopy. *ACS Photonics* **1**, 437–443 (2014).

113. 113.

Bylinkin, A. et al. Real-space observation of vibrational strong coupling between propagating phonon polaritons and organic molecules. *Nat. Photonics* **15**, 197–202 (2021).

114. 114.

Lin, X. et al. Chiral plasmons with twisted atomic bilayers. *Phys. Rev. Lett.* **125**, 077401 (2020).

115. 115.

Stauber, T., Low, T. & Gómez-Santos, G. Plasmon-enhanced near-field chirality in twisted van der Waals heterostructures. *Nano Lett.* **20**, 8711–8718 (2020).

116. 116.

Lin, J. et al. Polarization-controlled tunable directional coupling of surface plasmon polaritons. *Science* **340**, 331–334 (2013).

117. 117.

Rodríguez-Fortuño, F. J. et al. Near-field interference for the unidirectional excitation of electromagnetic guided modes. *Science* **340**, 328–330 (2013).

118. 118.

Nemilentsau, A., Stauber, T., Gómez-Santos, G., Luskin, M. & Low, T. Switchable and unidirectional plasmonic beacons in hyperbolic two-dimensional materials. *Phys. Rev. B* **99**, 201405 (2019).

119. 119.

Huber, M. A. et al. Femtosecond photo-switching of interface polaritons in black phosphorus heterostructures. *Nat. Nanotechnol.* **12**, 207–211 (2017).

120. 120.

Klein, M. et al. 2D semiconductor nonlinear plasmonic modulators. *Nat. Commun.* **10**, 3264 (2019).

121. 121.

Guerrero-Becerra, K. A., Tomadin, A. & Polini, M. Electrical plasmon injection in double-layer graphene heterostructures. *Phys. Rev. B* **100**, 125434 (2019).

122. 122.

Ni, G. X. et al. Fundamental limits to graphene plasmonics. *Nature* **557**, 530–533 (2018).

123. 123.

Giles, A. J. et al. Ultralow-loss polaritons in isotopically pure boron nitride. *Nat. Mater.* **17**, 134–139 (2018).

124. 124.

Weiliang, M. G. et al. Ghost hyperbolic surface polaritons in bulk anisotropic crystals. *Nature* **596**, 362–366 (2021). **This reference reports the first observation of ghost polaritons and the first real-space mapping of the hyperbolic polaritons in bulk anisotropic crystals, which demonstrates approximately 20-μm long-range propagation at room temperature and large-scale production readiness for polaritonic on-chip devices.**

125. 125.

Dai, S. et al. Tunable phonon polaritons in atomically thin van der Waals crystals of boron nitride. *Science* **343**, 1125–1129 (2014).

126. 126.

Hu, F. et al. Imaging exciton–polariton transport in MoSe₂ waveguides. *Nat. Photonics* **11**, 356–360 (2017).

127. 127.

Low, T. et al. Plasmons and screening in monolayer and multilayer black phosphorus. *Phys. Rev. Lett.* **113**, 106802 (2014).

128. 128.

Nemilentsau, A., Low, T. & Hanson, G. Anisotropic 2D materials for tunable hyperbolic plasmonics. *Phys. Rev. Lett.* **116**, 066804 (2016).

129. 129.

Wang, C. et al. Van der Waals thin films of WTe₂ for natural hyperbolic plasmonic surfaces. *Nat. Commun.* **11**, 1158 (2020).

130. 130.

Zheng, Z. et al. Highly confined and tunable hyperbolic phonon polaritons in van der Waals semiconducting transition metal oxides. *Adv. Mater.* **30**, 1705318 (2018).

131. 131.

Álvarez-Pérez, G. et al. Infrared permittivity of the biaxial van der Waals semiconductor α -MoO₃ from near- and far-field correlative studies. *Adv. Mater.* **32**, 1908176 (2020).

132. 132.

Taboada-Gutiérrez, J. et al. Broad spectral tuning of ultra-low-loss polaritons in a van der Waals crystal by intercalation. *Nat. Mater.* **19**, 964–968 (2020).

133. 133.

Álvarez-Pérez, G., Voronin, K. V., Volkov, V. S., Alonso-González, P. & Nikitin, A. Y. Analytical approximations for the dispersion of electromagnetic modes in slabs of biaxial crystals. *Phys. Rev. B* **100**, 235408 (2019).

134. 134.

Sun, F. et al. Polariton waveguide modes in two-dimensional van der Waals crystals: an analytical model and correlative nano-imaging. *Nanoscale* **13**, 4845–4854 (2021).

Acknowledgements

This project was supported by the National Research Foundation, Prime Minister's Office, Singapore under Competitive Research Program Award NRF-CRP22-2019-0006; the Vannevar Bush Faculty Fellowship program; the Simons Foundation; and the Air Force Office of Scientific Research MURI program. R.H. acknowledges financial support from the Spanish Ministry of Science, Innovation and Universities (national project RTI2018-094830-B-100 and the project MDM-2016-0618 of the Marie de Maeztu Units of Excellence Program) and the Basque Government (grant no. IT1164-19). P.L. acknowledges the National Natural Science Foundation of

China (grant no. 62075070). G.H. acknowledges the support from A*STAR AME Young Individual Research Grants (YIRG, No. A2084c0172).

Author information

Author notes

1. These authors contributed equally: Qing Zhang, Guangwei Hu

Affiliations

1. Department of Electrical and Computer Engineering, National University of Singapore, Singapore, Singapore

Qing Zhang, Guangwei Hu & Cheng-Wei Qiu

2. Wuhan National Laboratory for Optoelectronics and School of Optical and Electronic Information, Huazhong University of Science and Technology, Wuhan, China

Weiliang Ma & Peining Li

3. Advanced Science Research Center, City University of New York, New York, NY, USA

Alex Krasnok & Andrea Alù

4. CIC nanoGUNE BRTA and Department of Electricity and Electronics, UPV/EHU, Donostia-San Sebastián, Spain

Rainer Hillenbrand

5. IKERBASQUE, Basque Foundation for Science, Bilbao, Spain

Rainer Hillenbrand

6. Physics Program, Graduate Center, City University of New York, New York, NY, USA

Andrea Alù

Contributions

Q.Z., G.H. and W.M. wrote the manuscript; P.L., A.K. and R.H. contributed to the discussion of content; and A.A. and C.-W.Q. supervised the project. All authors contributed to the editing of the paper.

Corresponding authors

Correspondence to [Andrea Alù](#) or [Cheng-Wei Qiu](#).

Ethics declarations

Competing interests

The authors declare no competing interests.

Additional information

Peer review information *Nature* thanks Tony Low and the other, anonymous, reviewer(s) for their contribution to the peer review of this work.

Publisher's note Springer Nature remains neutral with regard to jurisdictional claims in published maps and institutional affiliations.

Rights and permissions

[Reprints and Permissions](#)

About this article

Cite this article

Zhang, Q., Hu, G., Ma, W. *et al.* Interface nano-optics with van der Waals polaritons. *Nature* **597**, 187–195 (2021). <https://doi.org/10.1038/s41586-021-03581-5>

- Received: 07 June 2020
- Accepted: 23 April 2021
- Published: 08 September 2021
- Issue Date: 09 September 2021
- DOI: <https://doi.org/10.1038/s41586-021-03581-5>

This article was downloaded by **calibre** from <https://www.nature.com/articles/s41586-021-03581-5>

| [Section menu](#) | [Main menu](#) |

- Perspective
- [Published: 08 September 2021](#)

A roadmap for the Human Developmental Cell Atlas

- [Muzlifah Haniffa](#) [ORCID: orcid.org/0000-0002-3927-2084](https://orcid.org/0000-0002-3927-2084)^{1,2,3 nA1},
- [Deanne Taylor](#) [ORCID: orcid.org/0000-0002-3302-4610](https://orcid.org/0000-0002-3302-4610)^{4,5 nA1},
- [Sten Linnarsson](#) [ORCID: orcid.org/0000-0002-3491-3444](https://orcid.org/0000-0002-3491-3444)^{6 nA1},
- [Bruce J. Aronow](#) [ORCID: orcid.org/0000-0001-5109-6514](https://orcid.org/0000-0001-5109-6514)⁷,
- [Gary D. Bader](#) [ORCID: orcid.org/0000-0003-0185-8861](https://orcid.org/0000-0003-0185-8861)⁸,
- [Roger A. Barker](#)^{9,10},
- [Pablo G. Camara](#)¹¹,
- [J. Gray Camp](#) [ORCID: orcid.org/0000-0003-3295-1225](https://orcid.org/0000-0003-3295-1225)¹²,
- [Alain Chédotal](#) [ORCID: orcid.org/0000-0001-7577-3794](https://orcid.org/0000-0001-7577-3794)¹³,
- [Andrew Copp](#) [ORCID: orcid.org/0000-0002-2544-9117](https://orcid.org/0000-0002-2544-9117)¹⁴,
- [Heather C. Etchevers](#) [ORCID: orcid.org/0000-0003-0201-3799](https://orcid.org/0000-0003-0201-3799)¹⁵,
- [Paolo Giacobini](#) [ORCID: orcid.org/0000-0002-3075-1441](https://orcid.org/0000-0002-3075-1441)¹⁶,
- [Berthold Göttgens](#) [ORCID: orcid.org/0000-0001-6302-5705](https://orcid.org/0000-0001-6302-5705)^{9,17},
- [Guoji Guo](#) [ORCID: orcid.org/0000-0002-1716-4621](https://orcid.org/0000-0002-1716-4621)¹⁸,
- [Ania Hupalowska](#)¹⁹,
- [Kylie R. James](#)²,
- [Emily Kirby](#)²⁰,
- [Arnold Kriegstein](#) [ORCID: orcid.org/0000-0001-5742-2990](https://orcid.org/0000-0001-5742-2990)²¹,
- [Joakim Lundeberg](#) [ORCID: orcid.org/0000-0003-4313-1601](https://orcid.org/0000-0003-4313-1601)²²,
- [John C. Marioni](#) [ORCID: orcid.org/0000-0001-9092-0852](https://orcid.org/0000-0001-9092-0852)²³,
- [Kerstin B. Meyer](#) [ORCID: orcid.org/0000-0001-5906-1498](https://orcid.org/0000-0001-5906-1498)²,
- [Kathy K. Niakan](#) [ORCID: orcid.org/0000-0003-1646-4734](https://orcid.org/0000-0003-1646-4734)^{24,25},
- [Mats Nilsson](#) [ORCID: orcid.org/0000-0001-9985-0387](https://orcid.org/0000-0001-9985-0387)²⁶,
- [Bayanne Olabi](#)¹,
- [Dana Pe'er](#) [ORCID: orcid.org/0000-0002-9259-8817](https://orcid.org/0000-0002-9259-8817)²⁷,
- [Aviv Regev](#) [ORCID: orcid.org/0000-0003-3293-3158](https://orcid.org/0000-0003-3293-3158)^{19,28 nAff44},
- [Jennifer Rood](#)¹⁹,
- [Orit Rozenblatt-Rosen](#) [ORCID: orcid.org/0000-0001-6313-3570](https://orcid.org/0000-0001-6313-3570)^{19 nAff44},
- [Rahul Satija](#) [ORCID: orcid.org/0000-0001-9448-8833](https://orcid.org/0000-0001-9448-8833)²⁹,

- [Sarah A. Teichmann](#) ORCID: orcid.org/0000-0002-6294-6366^{2,30},
- [Barbara Treutlein](#) ORCID: orcid.org/0000-0002-3299-5597³¹,
- [Roser Vento-Tormo](#) ORCID: orcid.org/0000-0002-9870-8474²,
- [Simone Webb](#) ORCID: orcid.org/0000-0003-3058-8952¹ &
- [Human Cell Atlas Developmental Biological Network](#)

Nature volume 597, pages 196–205 (2021)

- 5941 Accesses
- 198 Altmetric
- [Metrics details](#)

Subjects

- [Developmental biology](#)
- [Embryology](#)

Abstract

The Human Developmental Cell Atlas (HDCA) initiative, which is part of the Human Cell Atlas, aims to create a comprehensive reference map of cells during development. This will be critical to understanding normal organogenesis, the effect of mutations, environmental factors and infectious agents on human development, congenital and childhood disorders, and the cellular basis of ageing, cancer and regenerative medicine. Here we outline the HDCA initiative and the challenges of mapping and modelling human development using state-of-the-art technologies to create a reference atlas across gestation. Similar to the Human Genome Project, the HDCA will integrate the output from a growing community of scientists who are mapping human development into a unified atlas. We describe the early milestones that have been achieved and the use of human stem-cell-derived cultures, organoids and animal models to inform the HDCA, especially for prenatal tissues that are hard to acquire. Finally, we provide a roadmap towards a complete atlas of human development.

[Download PDF](#)

Main

Most modern developmental biology research has historically focused on model organisms. Owing to practical challenges, human development—from a fertilized

ovum to a fully formed fetus at birth—has remained a poorly understood ‘black box’. The implications of a human developmental cell atlas for understanding human development are far-reaching, as many congenital disorders and childhood cancers may originate during susceptible windows of development^{1,2,3}. The clinical relevance of the atlas extends into adulthood for ageing, cancer and applications in regenerative medicine and stem cell therapies^{4,5,6}. Furthermore, embryonic and fetal stem cells^{7,8} and developmental trajectories provide an essential reference and guide for engineering human stem-cell-derived models^{9,10,11,12,13}, organoids¹⁴ and cellular therapies.

Human development begins with a fertilized oocyte that divides and differentiates through preimplantation, embryonic and fetal stages (Fig. 1). Early studies began with morphometric and qualitative assessments of human embryos, leading to development of the Carnegie staging system¹⁵ (Fig. 1). Advances in imaging, cytometry and genomics technologies have provided further insights into the complex spatiotemporal changes during organogenesis¹⁶. Recent progress in single-cell profiling technologies has revolutionized our ability to study human development at an unprecedented resolution¹⁷. Leveraging these advances to build a comprehensive atlas of human development (from the fertilized oocyte to birth) at cellular resolution is an ambitious endeavour that is similar in scale to the Human Genome Project, which required multidisciplinary scientific expertise from disparate fields working together collaboratively. Such a community has arisen from the grassroots assembly of global researchers who are working as part of the Human Cell Atlas (HCA)¹⁸ initiative. As with the Human Genome Project, the HCA will be a foundational scientific resource, composed of diverse data types and available freely through browsable and searchable web portals that visualize cells across anatomical space and developmental time.

Fig. 1: Human embryo development and model systems.

 **figure1**

a, Timeline of human development from fertilization to birth. CT, cytotrophoblast; ESC, embryonic stem cell; EPI, epiblast; PrE, primitive endoderm; pcw, post-conception weeks; SCT, syncytiotrophoblast; TE, trophectoderm; TSC, trophoblast stem cell; XEN, extraembryonic endoderm; YSE, yolk sac endoderm. **b**, Models derived from human stem cells, and associated studies. In vitro model systems to study early embryonic development. A–P, anterior–posterior. **c**, Experimental model systems to study development, including *Drosophila melanogaster*, *Danio rerio*, *Xenopus*

Xenopus laevis, *Gallus gallus*, *Mus musculus*, cell culture and organoids, and their amenability to facilitating various aspects of scientific study.

The HDCA is a strategic focus of HCA¹⁹, and is pursued by scientists from individual laboratories as well as large national and international research consortia (Supplementary Table 1); the HDCA is open to all who adhere to its mission and open science values²⁰. The HDCA aims for equity, inclusivity and diversity both in terms of scientific participation and the representation of human tissue samples. We encourage any interested researcher to become a member, participate, register their study and contribute their data and publications to the HDCA and HCA²¹.

Building a developmental cell atlas

The successful construction of a HDCA poses substantial scientific challenges in terms of experimental measurement technologies, computational analysis and visualization algorithms (Fig. 2). In particular, the dynamic nature of gestation creates challenges for designing a sampling strategy, especially to capture transient morphological changes in the first eight weeks. A major endeavour for the HDCA will be to develop the conceptual and computational framework to capture development with respect to cellular and morphological changes. The HDCA, through coordination with the HCA Organoid Network²², will incorporate data from in vitro culture model and organoid systems²³ to cautiously infer development between seven days and four weeks after conception (a period in which samples are difficult to obtain) (Fig. 1b,c).

Fig. 2: Building the HDCA.

 **figure2**

a, ‘How to build an atlas’ modules, including an interdisciplinary team (biological disciplines, clinical specialities, computational scientists and technology engineers), multimodal technologies and integration of data across platforms. **b**, Key features of the HDCA. Single-cell measurements across three-dimensional space (alongside a fourth dimension of time) allow for the capture of dynamic developmental processes, including cell proliferation, migration and regulation. Spatial extension captures cell proliferation (changes in organ size and shape), and the sensing and control of

morphogenesis; spatio-temporal events include cell differentiation and replication, and changes in cellular composition and gene expression. Permutations and variabilities outline the spatial determinants of cell differentiation, mechanical adhesive feedback and heterocellular signalling by ligands. Time series trajectories reveal fate-biased migrating progenitors, lineage specifications and cell migration. **c**, Utility and applications of the HDCA: cellular and molecular biological insights into the coordination of organ development across the whole embryo (left) are applied to advance regenerative medicine, tissue engineering and therapeutic strategies (right).

The successful delivery of the HDCA will leverage the Human Genome Project-initiated restructuring of how large science projects are funded, conducted, coordinated and shared (based on the Fort Lauderdale Principles²⁴) that forms the basis for the HCA, its committees (for example, computation and ethics) and ‘Biological Networks’²⁰. This organizational framework has enabled researchers to form large-scale coordinated collaborations across technologies and biological disciplines: developmental biology, embryology, genetics and model systems, computational biology, clinical specialities (including in vitro fertilization), clinical genetics and pathology, as well as coordination with funders. Partnerships with allied biological networks, including organoid and paediatric atlas projects, will facilitate clinical applications.

Ethics, resources and data sharing

Accessing human developmental samples is constrained by general and geographically specific ethical and legal challenges. These include issues relating to donation, access to and research use of legally defined developing human tissue material, regulatory approvals processes and cultural sensitivities. Research on human embryos and fetuses is supported within European and national regulations, such as the UK National Research Ethics Service (NRES) and the French Agence de Biomédecine. In the UK, studies on preimplantation human embryos (up to 14 days after conception) are governed by the Human Fertilisation and Embryology Authority and a research ethics committee (such as NRES). However, in the USA, research on donated human embryonic and fetal materials has increasingly been restricted over the past two decades, despite the existence of similar regulatory oversight.

Nonetheless, resources to support research in human development (such as the UK’s Human Developmental Biology Resource (HDBR)²⁵) provide material to researchers. Recipients of HDBR tissue who are not based in the UK require their own project-specific ethics approval, before receipt of material. The HDBR provides embryonic and fetal samples from 4 to 20 weeks after conception with karyotype information and, increasingly, with anonymized maternal DNA and clinical history. Material from fetuses with prenatally diagnosed disorders is also available. The French Human

Developmental Cell Atlas (HuDeCA) (<https://hudeca.genouest.org>) has recently been established, and aspires to constitute a comprehensive European resource of human embryonic or early fetal samples.

The international sharing of genomic sequencing and clinical data derived from prenatal or paediatric tissue samples is subject to data protection regulation that considers live versus deceased status, consent regarding research data use and confidentiality. Data from living donors are shared under appropriate access controls. The HCA Ethics Working Group is developing tools, guidance notes²⁶, consent-form templates and sampling information for embryonic, fetal and paediatric tissue material, and international data-sharing guidance for the HDCA.

Mapping development across space and time

Development is intricately orchestrated in three spatial dimensions and gestation time. Human embryogenesis cannot be easily assessed at high resolution *in vivo*²⁷. Time-lapse studies are limited to in vitro preimplantation embryos. The application of high-throughput genomics technologies to dissociated cells and tissue sections *in situ* is beginning to provide data of unprecedented resolution (Fig. 3, Table 1).

Fig. 3: Multi-omics profiling and data integration.



a, Organ or anatomical unit profiling of a prenatal embryo derived from multiple germ layers. **b**, Single-cell atlas technologies by relative resolution and genome scale. CODEX, co-detection by indexing; H&E, haematoxylin and eosin staining; IF, immunofluorescence; ISS, in situ sequencing; MERFISH, multiplexed error-robust FISH; MIBI, multiplexed ion beam imaging; seqFISH, sequential FISH; smFISH, single-molecule FISH; STARmap, spatially resolved transcript annotation readout mapping. **c**, Integration of datasets from different technologies (for example, spatial transcriptomics, scRNA-seq and targeted ISS) to profile organs or whole embryos.

Table 1 Publications registered with the HDCA

Cellular and molecular heterogeneity

Single-cell molecular profiles based on RNA, chromatin accessibility, methylation or select protein signatures have enabled a more nuanced definition of cell types and states. The data underpinning such definitions are increasingly derived from single-cell RNA sequencing (scRNA-seq), barcoded antibodies and accessible chromatin

sequencing of dissociated cells^{28,29}. Resolving cell types and trajectories at high granularity is aided by full-length scRNA-seq, but is primarily performed by profiling large numbers of cells. Cell-type definition is currently guided by existing knowledge from model organisms and adult cellular profiles, which may not faithfully reflect prenatal cell types, transient cell types that are present only during development and transitional states of differentiation.

To overcome these challenges, many time points need to be profiled and defined cell states need to be mapped back into their 3D space over time and functionally characterized. High levels of multiplexing can attain this level of granularity at an affordable cost for a complete human developmental cell atlas^{30,31}. Molecular profiles, morphology, functional assessment and other features can reflect the multifaceted state of a cell. For example, the transcriptome reflects the present and potential future of a cell; protein expression captures the immediate past and present state of a cell; chromatin profiles reveal its invariant type and potential for future differentiation; and ontogeny reveals its history.

The field of developmental biology has traditionally drawn on ontogenic relationships to define cell types, but this is challenging in humans for whom information is captured as snapshots across gestation. CRISPR scarring is applicable only in stem cells, organoid systems and short-term explants^{32,33}. The tracking of somatic mutations is the only available technology to definitively determine ontogeny, but is limited by its current lack of scalability^{34,35}. Recent methods that rely on the simultaneous measurement of mitochondrial DNA and RNA, transcriptome and open chromatin may overcome this challenge^{36,37}. We anticipate the field moving towards a consensus cell ontology that integrates multimodal single-cell profiling data as well as legacy knowledge of embryonic cell-type definitions augmented by information from diverse animal models.

Mapping cells in 2D and 3D

Spatial genomics methods to measure RNA in tissue sections typically offer a trade-off: high-resolution (single-cell and subcellular) methods that typically measure hundreds of transcripts or whole transcriptome profiles at a multicellular level^{38,39}. This trade-off can be mitigated by integration with single-cell profiles from dissociated cells, expanding the genomic coverage by predicting the spatial expression of unmeasured genes or enhancing resolution by deconvolution of multicellular measurements. Tissue clearing methods to render organs transparent⁴⁰, combined with whole-mount protein immunostaining and RNA single-molecule fluorescence in situ hybridization (FISH)^{41,42}, can now provide 3D molecular profiling at cellular or subcellular resolution using light-sheet microscopy^{43,44,45}. Increasing multiplex

capacity and use of artificial intelligence and machine learning algorithms to overcome data analytical challenges have successfully been deployed to image whole-organismal vasculature following tissue clearing^{46,47}.

Biophysical methods and live imaging

Mounting evidence from *Drosophila* and other models shows that mechanical forces have a key role in development processes and tissue morphogenesis⁴⁸. Surface tension and pressure can be measured in single cells of preimplantation mouse embryos⁴⁹. Adapting these technologies to human preimplantation embryos and stem-cell-based embryo models⁵⁰ can build a spatiotemporal mechanical atlas.

Positional landmarks in development

A standard coordinate system for locations in the human body (a common coordinate framework (CCF)) is crucial for the HCA and HDCA⁵¹. Two types of systems are useful: absolute (similar to postcode or zip code addresses) and relative (similar to a landmark-based address system). CCF anatomical ‘postcodes’ enable the integration of multimodal datasets of different spatial and longitudinal resolution. The Allen Mouse Brain Reference Atlas version 3 provides a CCF of 3D anatomical features and local features grouped in a hierarchy to facilitate multilevel analysis of the mouse brain. Efforts are currently underway to establish CCFs for adult human organs within the Human Biomolecular Atlas Program of the National Institutes of Health (NIH). The HDCA will need to develop a CCF that incorporates space and time, as well as cell movement and patterns during organogenesis on the basis of existing macro-level 3D coordinates for human embryos (such as the HDBR atlas (<http://hdbratlas.org/>) and the Transparent Human Embryo (<https://transparent-human-embryo.com/>)).

Computation and data visualization

Among the key algorithmic challenges to integrating data into a developmental atlas are (1) mapping cells with more intermediate states compared to adult counterparts; (2) inferring time orderings and lineage relations, including branching lineages and multiple paths converging on the same outcome; (3) inferring spatial movement of cells; (4) building a temporal series of CCFs, each as a probabilistic model for a time window as well as a model for their morphing along space and time⁵²; (5) mapping across modalities and time points (for example, chromatin states in one time window to RNA and protein levels of another); and (6) regulatory and molecular network inference within and across cells. Theories and insights from multiple fields will be required to model the mechanisms that underpin tissue formation and growth. It is

likely that additional emergent properties of cells and their ecosystems will be discovered using interdisciplinary approaches. These will need new vocabularies, ontologies and modelling approaches to be understood. The HDCA community must also apply FAIR (findability, accessibility, interoperability and reusability) principles to help to ensure reproducibility and data accessibility⁵³.

Computational integration of multi-omics data for visualizations similar to that of Google Maps, such as the Open Microscopy Environment (<https://www.openmicroscopy.org/>), will enable zooming to the single-cell level from a large-volume tissue view. Additional complexity will combine visualizations from imaging and sequencing data. A sophisticated abstraction of raw data and integration across modalities, anchored by a developmental CCF, will be essential. Links to clinical relevance and applications will enhance the utility of the atlas.

Emerging cell atlases of human development

The advantages of whole tissue or organ profiling compared to lineage-centric analysis include comprehensive cellular analysis and the discovery of emergent biological properties. For example, the developing liver functions as a haematopoietic organ during early gestation until the middle of the second trimester, before it functionally transitions into a metabolic organ similar to the adult liver⁵⁴. To meet the high demand for erythropoiesis during development, the human skin and adrenal glands can also support erythrocyte maturation during the first trimester^{54,55}.

In contrast to our terrestrial postnatal life, the human embryo and fetus exist in an aquatic environment: our lung, gut and skin are exposed to amniotic fluid. In contrast to the postnatal lung, the developing lung does not perform oxygen transfer or receive the same volume of blood through the pulmonary veins. The effect of these physiological factors on individual tissues and the role of the placenta and maternal decidua in supporting human embryogenesis and fetal life are emerging^{56,57}.

Current organ atlases of brain, gut, heart, liver, kidney, placenta, thymus and skin (Table 1) underscore the importance of studying human samples and have revealed unique aspects of human development that are not conserved with animal model systems^{58,59,60,61}. These include timelines of development during gestation, cell-type markers and the expression pattern of transcription factors between mouse and human organs^{62,63}.

The specification of functional tissue niches occurs during both prenatal and postnatal life. Studies of the fetal gut have highlighted the importance of interactions between the epithelial and mesenchymal compartments in allowing the formation of villi, and have identified fetal gut transcription factors that are aberrantly activated in

individuals with paediatric Crohn's disease⁶⁴. Comparison between the developing and adult kidney have demonstrated the establishment of a dedicated spatial zonation pattern that protects against uropathogenic bacterial challenges postnatally^{61,65}. Single-cell transcriptomics of germ cells during development have provided important insights into the main pathways that control their differentiation^{66,67}, with ongoing studies focused on exploring the regulatory mechanisms of sex determination (<https://hugodeca-project.eu>).

Early developmental studies of the brain have focused on human and primate cortical development^{68,69,70}. The developing human and rodent midbrain, which contains the clinically relevant dopaminergic cell groups that are lost in individuals with Parkinson's disease, has also extensively been studied^{63,71,72}, as have the developing mouse spinal cord and cerebellum^{73,74}, the hypothalamic arcuate nucleus and the diencephalon⁷⁵.

Atlases of distributed systems (such as the immune system) have been initiated, detailing haematopoietic organs such as the yolk sac^{76,77} and liver⁵⁴, lymphoid tissues such as thymus (in which T cells differentiate)⁷⁸ and non-lymphoid tissues such as skin and kidney, in which immune cells reside. These studies have revealed an intrinsic change in the differentiation potential of haematopoietic stem progenitor cells with gestational time, together with the importance of the local tissue microenvironment for blood and immune-cell development.

Model organisms and culture systems

Our understanding of human development has largely been inferred from studies on animal model systems that are not always conserved across species⁷⁹ (Fig. 1). Two recent studies contrast the kinetics of development between human and mouse, highlighting the need for caution in interpreting heterospecific graft studies and findings from nonprimate preclinical models^{80,81}. However, the feasibility of perturbation and in-depth mechanistic studies using animal models and culture systems provide a valuable scaffold and complement the HDCA, particularly for the immediate weeks after implantation during which human samples are inaccessible.

Single-cell molecular profiling has transformed many aspects of developmental biology research across all major model organisms^{82,83,84,85,86}, providing mechanistic insights into fundamental biological processes (including the early specification of germ layers and diversification of early cardiovascular cells)^{29,87}. Comparative biology has the potential to make major contributions to cell ontology. The availability of parallel human and model species data will support expanded cross-species analyses. Computational analysis can align cells and inferred lineages across species to

extrapolate findings from nonprimate models and help to optimize animal models of normal and pathological human development. From a computational perspective, it will be important to develop tools for better annotation of 3' and 5' untranslated regions of animal model data, as most scRNA-seq technologies capture only these regions. The development of computational tools that can robustly map developmental trajectories across species and that can account for different developmental kinetics between cell types within and between species will be required. Comparative studies of human and mouse preimplantation and gastrulation embryos have revealed conserved and divergent transcriptional programs. For example, *Klf2* expression in mouse embryo-fated epiblast progenitor cells is not observed in humans; by contrast, *KLF17* is enriched in human, but not mouse, epiblast⁸⁸.

The self-organization of human embryonic tissue can be captured from the earliest moments in vitro^{50,89}, and extended to gastrulation, anterior–posterior embryonic patterning and the early phases of somitogenesis¹¹. The recent human gastrulation embryo dataset will be informative as a benchmark to further refine in vitro directed differentiation of human cells, including gastruloid models¹¹. Other processes during organogenesis can also be monitored, including the clock control of somite segmentation^{90,91}, boundary formations during hepato-biliary–pancreatic organ budding⁹² and patterning of the neural tube. Protocols are now established to mimic the development of diverse human tissues that exhibit morphologies and physiological functionalities of developing human tissues. These organoid systems include hair-bearing skin⁹³; the small intestine with a crypt–villus axis⁹⁴; region-specific⁹⁵ and multiregion⁹⁶ brain tissue that models neurogenesis, neural migration and synapse formation; multilayered neural retina with photoreception responses⁹⁷; and arterio-venous specification during blood vessel development⁹⁸.

A comprehensive reference atlas of the cell types and states that are present during human development will be critical to benchmark stem-cell-derived organoids. Such roadmap comparisons will highlight similarities⁶⁹ and deficiencies⁹⁹, and define strategies for improving organoids for disease modelling. In the future, high-fidelity human stem-cell-derived human organoids and single-cell multi-omic modalities will be powerful tools to understand the mechanisms that control human organogenesis.

Clinical relevance and applications

The interaction of genotype and environment that leads to phenotype underlies developmental disorders. A range of childhood and adult disorders have their origins in prenatal life (Fig. 4). These include structural birth defects¹⁰⁰, neurodevelopmental disorders (including schizophrenia)¹⁰¹, childhood cancers^{2,65}, inborn errors of immunity¹⁰², infertility and differences of sex development¹⁰³, as well as many

paediatric disorders¹⁰⁴. Thousands of rare genetic diseases can each present a spectrum of perturbed developmental sequelae at birth, and sometimes differ widely in medical presentation even when classified as the same disease or condition¹⁰⁵. As examples, Down syndrome (trisomy 21)¹⁰⁶ and 22q11.2 deletion syndrome¹⁰⁷ separately present substantial risks for schizophrenia, Alzheimer's disease and hypothyroidism starting in adolescence¹⁰⁸. Identifying the aetiology of developmental disorders and the effects of maternal genotype, paternal age and other external risk factors (such as diet, alcohol, toxins, endocrine disruptors and pathogens) has been hampered by our limited understanding of normal development in humans.

Fig. 4: Clinical relevance and applications of the HDCA.



- a**, Diseases related to brain development, across lifespan. A timeline of brain development across human life, with examples of diseases with onset at different gestational stages and ages. **b**, Disease state compared to developmental atlas, showing how a single-cell atlas with temporal and spatial information can be used as a reference to understand disease states.

Development atlases are also revealing the pathogenesis of childhood cancers (Fig. 4). Paediatric and adult brain tumours in their early stages often present impaired developmental programs within tumour cells^{109,110}. Comparing the expression profile of tumour cells with the HDCA can identify the cancer cell of origin and its oncogenic pathways. For example, a single-cell atlas of the developing mouse cerebellum has been used to investigate subtypes of human medulloblastoma (a paediatric brain tumour)^{2,111}, and cell states during nephrogenesis revealed the developmental cellular origin of Wilms' tumour⁶⁵. High-resolution mapping of developing immune cells will inform the molecular basis and extent of disease phenotypes of childhood leukaemias and primary immunodeficiencies.

Many adult cancers also recapitulate a dysregulated version of human developmental programs¹¹². The acquisition of early developmental molecular programs is characteristic of malignant pathology, and is a previously unrecognized hallmark of immunological disease and the cancer immune environment^{113,114}. HDCA data have also facilitated our understanding of the differential susceptibility of adult and prenatal cells to SARS-CoV-2 through examination of viral entry receptor and protease expression in a wide range of organs¹¹⁵.

Cell and tissue engineering for clinical therapies and regenerative medicine are areas with considerable potential for the direct utility of the HDCA. Cell therapies derived from human pluripotent stem cells are now entering early clinical trials for the treatment of Parkinson's disease¹¹⁶, using protocols that were refined on the basis of developmental studies of midbrain dopaminergic neurons⁷². Similar approaches are being followed to develop a range of other stem cell products for human trials¹¹⁷. Haematopoietic stem cell transplantation is an established and widely used treatment for many haematological, and increasingly non-haematological, disorders. Leveraging the potency factors of fetal haematopoietic stem cells could have a substantial benefit for patients who receive transplants of haematopoietic stem cells.

Towards a whole embryo atlas

The initial HCA white paper emphasized 12 distinct organ systems within the human body and highlighted the importance of a developmental cell atlas. Integrated multi-organ analyses will provide insights into the tissue microenvironment that shapes resident epithelial, stroma and immune cells and the cellular heterogeneity of innervating blood vessels, lymphatics and peripheral nerves. Eventually, this may illuminate system-level lineage development and cell fate decisions across an entire organism. The datasets from profiling based on human developmental organs have been critical in interpreting recent multi-organ developmental atlases^{55,118}.

There are several large-scale organ-based studies being undertaken by HDCA researchers. These include the NIH ‘Brain Research through Advancing Innovative Neurotechnologies’ (BRAIN) initiative (including the BRAIN Initiative Cell Census Network (BICCN) consortium) focusing on the developing human cortex; the Swedish Human Cell Atlas consortium performing large-scale scRNA-seq, assay for transposase-accessible chromatin using sequencing (ATAC-seq) and spatial-omic analyses of the developing human brain, heart¹¹⁹ and lung during the first trimester; the French HuDeCA consortium mapping eight first-trimester human organs using 3D imaging and scRNA-seq; the European Union (EU) Horizon 2020-funded developing brain (Braintime) and gonad (HUGODECA) projects; the NIH Developmental Genotype-Tissue Expression (dGTEX)¹²⁰ project; and UK consortia funded by the Wellcome Trust and Medical Research Council. The logical next step will be to coordinate these efforts and extend the current approach to contextualize the development of different cell lineages across all organs.

However, multi-organ approaches do not permit the analysis of distributed tissue networks as a continuum from a single donor sample. Whole-embryo analysis has been limited to very early preimplantation samples^{88,121,122} and one gastrulation-stage embryo¹²³. Multi-omics suspension and spatial-genomics profiling of anatomically dissected units from whole human embryos at six to seven weeks after conception are being undertaken by the HDCA researchers based in the UK. We anticipate a first whole human embryo profiling within the next two years. On the basis of existing HDCA data and the rapid changes during early development, we propose a minimum of three replicates for each biologically relevant gestation period (for example, each week from six weeks after conception). All such data produced and shared by the global research community (formally registered with the HCA or not) contributes to the HDCA. Defining a universal organizing framework for these data will enable them to be unified into a complete atlas that will be a transformative resource for the research and clinical communities.

References

1. 1.

Behjati, S., Lindsay, S., Teichmann, S. A. & Haniffa, M. Mapping human development at single-cell resolution. *Development* **145**, dev152561 (2018).

2. 2.

Vladoiu, M. C. et al. Childhood cerebellar tumours mirror conserved fetal transcriptional programs. *Nature* **572**, 67–73 (2019).

3. 3.

Velmeshev, D. et al. Single-cell genomics identifies cell type-specific molecular changes in autism. *Science* **364**, 685–689 (2019).

4. 4.

Gulsuner, S. et al. Spatial and temporal mapping of de novo mutations in schizophrenia to a fetal prefrontal cortical network. *Cell* **154**, 518–529 (2013).

5. 5.

Simmons, R. A. Developmental origins of adult disease. *Pediatr. Clin. North Am.* **56**, 449–466 (2009).

6. 6.

Laughney, A. M. et al. Regenerative lineages and immune-mediated pruning in lung cancer metastasis. *Nat. Med.* **26**, 259–269 (2020).

7. 7.

Sozen, B., Jorgensen, V., Zhu, M., Cui, T. & Zernicka-Goetz, M. Reconstructing human early embryogenesis in vitro with pluripotent stem cells. Preprint at <https://doi.org/10.1101/2021.03.12.435175> (2021).

8. 8.

Yu, L. et al. Blastocyst-like structures generated from human pluripotent stem cells. *Nature* **591**, 620–626 (2021).

9. 9.

Liu, X. et al. Modelling human blastocysts by reprogramming fibroblasts into iBlastoids. *Nature* **591**, 627–632 (2021).

10. 10.

Simunovic, M. et al. A 3D model of a human epiblast reveals BMP4-driven symmetry breaking. *Nat. Cell Biol.* **21**, 900–910 (2019).

11. 11.

Moris, N. et al. An in vitro model of early anteroposterior organization during human development. *Nature* **582**, 410–415 (2020).

12. 12.

Shao, Y. et al. A pluripotent stem cell-based model for post-implantation human amniotic sac development. *Nat. Commun.* **8**, 208 (2017).

13. 13.

Warmflash, A., Sorre, B., Etoc, F., Siggia, E. D. & Brivanlou, A. H. A method to recapitulate early embryonic spatial patterning in human embryonic stem cells. *Nat. Methods* **11**, 847–854 (2014).

14. 14.

Camp, J. G., Wollny, D. & Treutlein, B. Single-cell genomics to guide human stem cell and tissue engineering. *Nat. Methods* **15**, 661–667 (2018). **This review highlights the potential utility of single-cell genomics to optimize cell and tissue engineering, with a focus on emerging methodologies that can guide this process (such as transcription factor combinatorics, spatial reconstruction, CRISPR–Cas9 screens and lineage-coupled transcriptomics).**

15. 15.

Morgan, L. *Icons of Life: A Cultural History of Human Embryos* (Univ. California Press, 2009).

16. 16.

Blonder, L. X. Morphogenesis: The cellular and molecular processes of developmental anatomy. By Jonathan Bard. xi 313 pp. New York: Cambridge University Press. 1990. \$37.95. (paper). *Am. J. Hum. Biol.* **5**, 245–246 (1993).

17. 17.

Aldridge, S. & Teichmann, S. A. Single cell transcriptomics comes of age. *Nat. Commun.* **11**, 4307 (2020).

18. 18.

Human Cell Atlas. Home, <https://www.humancellatlas.org/> (2021).

19. 19.

Regev, A. et al. Science forum: the human cell atlas. *eLife* **6**, e27041 (2017).

20. 20.

The HCA Consortium. *The Human Cell Atlas White Paper*,
https://www.humancellatlas.org/wp-content/uploads/2019/11/HCA_WhitePaper_18Oct2017-copyright.pdf (2019).

21. 21.

Human Cell Atlas. Register, <https://www.humancellatlas.org/register> (2021).

22. 22.

Bock, C. et al. The organoid cell atlas. *Nat. Biotechnol.* **39**, 13–17 (2021).

23. 23.

Subbaraman, N. Lab-grown structures mimic human embryo's earliest stage yet. *Nature* **591**, 510–511 (2021).

24. 24.

Wellcome Trust. *Sharing Data from Large-scale Biological Research Projects: A System of Tripartite Responsibility*,
<http://www.genome.gov/Pages/Research/WellcomeReport0303.pdf> (Wellcome Trust, 2003).

25. 25.

Gerrelli, D., Lisgo, S., Copp, A. J. & Lindsay, S. Enabling research with human embryonic and fetal tissue resources. *Development* **142**, 3073–3076 (2015). **The HDBR is a biobank that collects and distributes material for research from human embryos (from 4 weeks after conception) and fetuses (up to 22 weeks after conception); <https://www.hdbr.org/> shows the range of facilities offered by the HDBR and provides access for prospective users.**

26. 26.

Human Cell Atlas. Ethics, <https://www.humancellatlas.org/ethics/> (2021).

27. 27.

Huang, Q. et al. Intravital imaging of mouse embryos. *Science* **368**, 181–186 (2020).

28. 28.

Mereu, E. et al. Benchmarking single-cell RNA-sequencing protocols for cell atlas projects. *Nat. Biotechnol.* **38**, 747–755 (2020).

29. 29.

Argelaguet, R. et al. Multi-omics profiling of mouse gastrulation at single-cell resolution. *Nature* **576**, 487–491 (2019).

30. 30.

Cao, J. et al. Comprehensive single-cell transcriptional profiling of a multicellular organism. *Science* **357**, 661–667 (2017).

31. 31.

McGinnis, C. S. et al. MULTI-seq: sample multiplexing for single-cell RNA sequencing using lipid-tagged indices. *Nat. Methods* **16**, 619–626 (2019).

32. 32.

Fujii, M., Clevers, H. & Sato, T. Modeling human digestive diseases with CRISPR-Cas9-modified organoids. *Gastroenterology* **156**, 562–576 (2019).

33. 33.

Artegiani, B. et al. Fast and efficient generation of knock-in human organoids using homology-independent CRISPR–Cas9 precision genome editing. *Nat. Cell Biol.* **22**, 321–331 (2020).

34. 34.

Lee-Six, H. et al. Population dynamics of normal human blood inferred from somatic mutations. *Nature* **561**, 473–478 (2018).

35. 35.

D’Gama, A. M. & Walsh, C. A. Somatic mosaicism and neurodevelopmental disease. *Nat. Neurosci.* **21**, 1504–1514 (2018).

36. 36.
Ludwig, L. S. et al. Lineage tracing in humans enabled by mitochondrial mutations and single-cell genomics. *Cell* **176**, 1325–1339 (2019).
37. 37.
Lareau, C. A. et al. Massively parallel single-cell mitochondrial DNA genotyping and chromatin profiling. *Nat. Biotechnol.* **39**, 451–461 (2021).
38. 38.
Ståhl, P. L. et al. Visualization and analysis of gene expression in tissue sections by spatial transcriptomics. *Science* **353**, 78–82 (2016).
39. 39.
Wang, X. et al. Three-dimensional intact-tissue sequencing of single-cell transcriptional states. *Science* **361**, eaat5691 (2018).
40. 40.
Ueda, H. R. et al. Tissue clearing and its applications in neuroscience. *Nat. Rev. Neurosci.* **21**, 61–79 (2020).
41. 41.
Yang, B. et al. Single-cell phenotyping within transparent intact tissue through whole-body clearing. *Cell* **158**, 945–958 (2014).
42. 42.
Sylwestrak, E. L., Rajasethupathy, P., Wright, M. A., Jaffe, A. & Deisseroth, K. Multiplexed intact-tissue transcriptional analysis at cellular resolution. *Cell* **164**, 792–804 (2016).
43. 43.
Casoni, F. et al. Development of the neurons controlling fertility in humans: new insights from 3D imaging and transparent fetal brains. *Development* **143**, 3969–3981 (2016).
44. 44.

Belle, M. et al. Tridimensional visualization and analysis of early human development. *Cell* **169**, 161–173 (2017). **A 3D map of first-trimester human development by tissue clearing and light-sheet imaging, providing high-resolution images of the developing cardiopulmonary, vascular, peripheral nervous, muscular and urogenital systems, as well as insights into complex processes such as skin innervation and the differential vascularization of male and female genital systems.**

45. 45.

Zhao, S. et al. Cellular and molecular probing of intact human organs. *Cell* **180**, 796–812 (2020).

46. 46.

Todorov, M. I. et al. Machine learning analysis of whole mouse brain vasculature. *Nat. Methods* **17**, 442–449 (2020).

47. 47.

Kirst, C. et al. Mapping the fine-scale organization and plasticity of the brain vasculature. *Cell* **180**, 780–795 (2020).

48. 48.

Gracia, M. et al. Mechanical impact of epithelial-mesenchymal transition on epithelial morphogenesis in *Drosophila*. *Nat. Commun.* **10**, 2951 (2019).

49. 49.

Dumortier, J. G. et al. Hydraulic fracturing and active coarsening position the lumen of the mouse blastocyst. *Science* **365**, 465–468 (2019).

50. 50.

Shahbazi, M. N., Siggia, E. D. & Zernicka-Goetz, M. Self-organization of stem cells into embryos: a window on early mammalian development. *Science* **364**, 948–951 (2019).

51. 51.

Rood, J. E. et al. Toward a common coordinate framework for the human body. *Cell* **179**, 1455–1467 (2019).

52. 52.

Bonneel, N. *Optimal Transport for Computer Graphics and Temporal Coherence of Image Processing Algorithms*. PhD thesis, Sorbonne Univ. (2018).

53. 53.

Wilkinson, M. D. et al. The FAIR guiding principles for scientific data management and stewardship. *Sci. Data* **3**, 160018 (2016).

54. 54.

Popescu, D.-M. et al. Decoding human fetal liver haematopoiesis. *Nature* **574**, 365–371 (2019). **A detailed single-cell characterization of fetal liver blood and immune-cell development, revealing inferred differentiation trajectories from haematopoietic stem cells and gestation-specific potential for the differentiation of haematopoietic stem cells.**

55. 55.

Cao, J. et al. A human cell atlas of fetal gene expression. *Science* **370**, eaba7721 (2020). **One of a set of two studies focusing on integrating single-cell gene expression⁵⁵ and chromatin accessibility¹¹⁸ from 15 first- and second-trimester human organs.**

56. 56.

Vento-Tormo, R. et al. Single-cell reconstruction of the early maternal-fetal interface in humans. *Nature* **563**, 347–353 (2018). **A detailed scRNA-seq analysis of first-trimester decidua and placenta, highlighting the cell–cell interactions that take place at the maternal–fetal interface during human development using a receptor–ligand database (CellPhoneDB).**

57. 57.

Suryawanshi, H. et al. A single-cell survey of the human first-trimester placenta and decidua. *Sci. Adv.* **4**, eaau4788 (2018).

58. 58.

Holloway, E. M. et al. Mapping development of the human intestinal niche at single-cell resolution. *Cell Stem Cell* **28**, 568–580 (2021).

59. 59.

Pollen, A. A. et al. Low-coverage single-cell mRNA sequencing reveals cellular heterogeneity and activated signaling pathways in developing cerebral cortex. *Nat. Biotechnol.* **32**, 1053–1058 (2014).

60. 60.

Han, X. et al. Construction of a human cell landscape at single-cell level. *Nature* **581**, 303–309 (2020). **A single-cell gene expression study of multiple organs during first- and second-trimester human development, with comparative analyses between human and mouse to identify conserved genetic networks.**

61. 61.

Stewart, B. J. et al. Spatiotemporal immune zonation of the human kidney. *Science* **365**, 1461–1466 (2019).

62. 62.

Cui, Y. et al. Single-cell transcriptome analysis maps the developmental track of the human heart. *Cell Rep.* **26**, 1934–1950 (2019).

63. 63.

La Manno, G. et al. Molecular diversity of midbrain development in mouse, human, and stem cells. *Cell* **167**, 566–580 (2016).

64. 64.

Elmentait, R., Ross, A., James, K. R., Ortmann, D. & Gomes, T. Single-cell sequencing of developing human gut reveals transcriptional links to childhood Crohn’s disease. *Dev. Cell* **55**, 771–783 (2020).

65. 65.

Young, M. D. et al. Single-cell transcriptomes from human kidneys reveal the cellular identity of renal tumors. *Science* **361**, 594–599 (2018). **Comparative single-cell analyses of fetal, paediatric and adult kidneys and of Wilms’ tumours, demonstrating the origin of Wilms’ tumour as aberrant nephron development.**

66. 66.

Vértesy, Á. et al. Parental haplotype-specific single-cell transcriptomics reveal incomplete epigenetic reprogramming in human female germ cells. *Nat.*

Commun. **9**, 1873 (2018).

67. 67.

Li, L. et al. Single-cell RNA-seq analysis maps development of human germline cells and gonadal niche interactions. *Cell Stem Cell* **20**, 858–873 (2017).

68. 68.

Nowakowski, T. J. et al. Spatiotemporal gene expression trajectories reveal developmental hierarchies of the human cortex. *Science* **358**, 1318–1323 (2017).

69. 69.

Camp, J. G. et al. Human cerebral organoids recapitulate gene expression programs of fetal neocortex development. *Proc. Natl Acad. Sci. USA* **112**, 15672–15677 (2015).

70. 70.

Lu, Y. et al. Single-cell analysis of human retina identifies evolutionarily conserved and species-specific mechanisms controlling development. *Dev. Cell* **53**, 473–491 (2020).

71. 71.

Tiklová, K. et al. Single-cell RNA sequencing reveals midbrain dopamine neuron diversity emerging during mouse brain development. *Nat. Commun.* **10**, 581 (2019).

72. 72.

Kee, N. et al. Single-cell analysis reveals a close relationship between differentiating dopamine and subthalamic nucleus neuronal lineages. *Cell Stem Cell* **20**, 29–40 (2017).

73. 73.

Rosenberg, A. B., Roco, C. M., Muscat, R. A. & Kuchina, A. Single-cell profiling of the developing mouse brain and spinal cord with split-pool barcoding. *Science* **360**, 176–182 (2018).

74. 74.

Carter, R. A. et al. A single-cell transcriptional atlas of the developing murine cerebellum. *Curr. Biol.* **28**, 2910–2920 (2018).

75. 75.

Huisman, C. et al. Single cell transcriptome analysis of developing arcuate nucleus neurons uncovers their key developmental regulators. *Nat. Commun.* **10**, 3696 (2019).

76. 76.

Utz, S. G. et al. Early fate defines microglia and non-parenchymal brain macrophage development. *Cell* **181**, 557–573 (2020).

77. 77.

Ginhoux, F. & Jung, S. Monocytes and macrophages: developmental pathways and tissue homeostasis. *Nat. Rev. Immunol.* **14**, 392–404 (2014).

78. 78.

Park, J.-E. et al. A cell atlas of human thymic development defines T cell repertoire formation. *Science* **367**, eaay3224 (2020).

79. 79.

Rossant, J. & Tam, P. P. L. New insights into early human development: lessons for stem cell derivation and differentiation. *Cell Stem Cell* **20**, 18–28 (2017).

80. 80.

Rayon, T. et al. Species-specific pace of development is associated with differences in protein stability. *Science* **369**, eaba7667 (2020).

81. 81.

Matsuda, M. et al. Species-specific segmentation clock periods are due to differential biochemical reaction speeds. *Science* **369**, 1450–1455 (2020).

82. 82.

Pijuan-Sala, B. et al. A single-cell molecular map of mouse gastrulation and early organogenesis. *Nature* **566**, 490–495 (2019). **A densely sampled time-course analysis covering mouse gastrulation and early organogenesis provides an**

scRNA-seq reference atlas, which is then exploited to provide insights into early blood and endothelial development through parallel analysis of mouse chimeras that lack the key regulator TAL1 (also known as SCL).

83. 83.

Wagner, D. E. et al. Single-cell mapping of gene expression landscapes and lineage in the zebrafish embryo. *Science* **360**, 981–987 (2018).

84. 84.

Briggs, J. A. et al. The dynamics of gene expression in vertebrate embryogenesis at single-cell resolution. *Science* **360**, eaar5780 (2018).

85. 85.

Cao, J. et al. The single-cell transcriptional landscape of mammalian organogenesis. *Nature* **566**, 496–502 (2019).

86. 86.

Cusanovich, D. A. et al. The *cis*-regulatory dynamics of embryonic development at single-cell resolution. *Nature* **555**, 538–542 (2018).

87. 87.

Lescroart, F. et al. Defining the earliest step of cardiovascular lineage segregation by single-cell RNA-seq. *Science* **359**, 1177–1181 (2018).

88. 88.

Blakeley, P. et al. Defining the three cell lineages of the human blastocyst by single-cell RNA-seq. *Development* **142**, 3151–3165 (2015).

89. 89.

Deglincerti, A. et al. Self-organization of the in vitro attached human embryo. *Nature* **533**, 251–254 (2016).

90. 90.

Matsuda, M. et al. Recapitulating the human segmentation clock with pluripotent stem cells. *Nature* **580**, 124–129 (2020).

91. 91.

Diaz-Cuadros, M. et al. In vitro characterization of the human segmentation clock. *Nature* **580**, 113–118 (2020).

92. 92.

Koike, H. et al. Modelling human hepato-biliary-pancreatic organogenesis from the foregut-midgut boundary. *Nature* **574**, 112–116 (2019).

93. 93.

Lee, J. et al. Hair-bearing human skin generated entirely from pluripotent stem cells. *Nature* **582**, 399–404 (2020).

94. 94.

Spence, J. R. et al. Directed differentiation of human pluripotent stem cells into intestinal tissue in vitro. *Nature* **470**, 105–109 (2011).

95. 95.

Marton, R. M. & Pašca, S. P. Organoid and assembloid technologies for investigating cellular crosstalk in human brain development and disease. *Trends Cell Biol.* **30**, 133–143 (2020).

96. 96.

Lancaster, M. A. et al. Cerebral organoids model human brain development and microcephaly. *Nature* **501**, 373–379 (2013).

97. 97.

Quadrato, G. et al. Cell diversity and network dynamics in photosensitive human brain organoids. *Nature* **545**, 48–53 (2017).

98. 98.

Wimmer, R. A. et al. Human blood vessel organoids as a model of diabetic vasculopathy. *Nature* **565**, 505–510 (2019).

99. 99.

Bhaduri, A. et al. Cell stress in cortical organoids impairs molecular subtype specification. *Nature* **578**, 142–148 (2020).

100. 100.

Homsy, J. et al. De novo mutations in congenital heart disease with neurodevelopmental and other congenital anomalies. *Science* **350**, 1262–1266 (2015).

101. 101.

Barnat, M. et al. Huntington’s disease alters human neurodevelopment. *Science* **369**, 787–793 (2020).

102. 102.

Zhang, S.-Y. et al. Human inborn errors of immunity to infection affecting cells other than leukocytes: from the immune system to the whole organism. *Curr. Opin. Immunol.* **59**, 88–100 (2019).

103. 103.

Croft, B. et al. Human sex reversal is caused by duplication or deletion of core enhancers upstream of *SOX9*. *Nat. Commun.* **9**, 5319 (2018).

104. 104.

Taylor, D. M. et al. The pediatric cell atlas: defining the growth phase of human development at single-cell resolution. *Dev. Cell* **49**, 10–29 (2019).

105. 105.

Haendel, M. et al. How many rare diseases are there? *Nat. Rev. Drug Discov.* **19**, 77–78 (2020).

106. 106.

Ly, A. et al. DSCAM is a netrin receptor that collaborates with DCC in mediating turning responses to netrin-1. *Cell* **133**, 1241–1254 (2008).

107. 107.

Yamagishi, H. & Srivastava, D. Unraveling the genetic and developmental mysteries of 22q11 deletion syndrome. *Trends Mol. Med.* **9**, 383–389 (2003).

108. 108.

Biswas, A. B. & Furniss, F. Cognitive phenotype and psychiatric disorder in 22q11.2 deletion syndrome: a review. *Res. Dev. Disabil.* **53-54**, 242–257 (2016).

109. 109.

Jessa, S. et al. Stalled developmental programs at the root of pediatric brain tumors. *Nat. Genet.* **51**, 1702–1713 (2019).

110. 110.

Tirosh, I. et al. Single-cell RNA-seq supports a developmental hierarchy in human oligodendrogloma. *Nature* **539**, 309–313 (2016).

111. 111.

Hovestadt, V. et al. Medulloblastomics revisited: biological and clinical insights from thousands of patients. *Nat. Rev. Cancer* **20**, 42–56 (2020).

112. 112.

Phillips, H. S. et al. Molecular subclasses of high-grade glioma predict prognosis, delineate a pattern of disease progression, and resemble stages in neurogenesis. *Cancer Cell* **9**, 157–173 (2006).

113. 113.

Sharma, A. et al. Onco-fetal reprogramming of endothelial cells drives immunosuppressive macrophages in hepatocellular carcinoma. *Cell* **183**, 377–394 (2020).

114. 114.

Reynolds, G. et al. Developmental cell programs are co-opted in inflammatory skin disease. *Science* **371**, eaba6500 (2021). **Comparative analyses of fetal skin with healthy and diseased adult skin, revealing the co-option of developmental cell programs in two common inflammatory skin conditions (atopic dermatitis and psoriasis).**

115. 115.

Sungnak, W. et al. SARS-CoV-2 entry factors are highly expressed in nasal epithelial cells together with innate immune genes. *Nat. Med.* **26**, 681–687

(2020).

116. 116.

Barker, R. A., Parmar, M., Studer, L. & Takahashi, J. Human trials of stem cell-derived dopamine neurons for Parkinson's disease: dawn of a new era. *Cell Stem Cell* **21**, 569–573 (2017).

117. 117.

Takahashi, J. Preparing for first human trial of induced pluripotent stem cell-derived cells for Parkinson's disease: an interview with Jun Takahashi. *Regen. Med.* **14**, 93–95 (2019).

118. 118.

Domcke, S. et al. A human cell atlas of fetal chromatin accessibility. *Science* **370**, eaba7612 (2020).

119. 119.

Asp, M. et al. A spatiotemporal organ-wide gene expression and cell atlas of the developing human heart. *Cell* **179**, 1647–1660 (2019). **A temporal and 3D spatial map of the developing human heart from the first trimester by using a combination of transcriptome-wide scRNA-seq and spatial transcriptomics methods with cellular validation by in situ sequencing.**

120. 120.

NHGRI & NICHD. Developmental Genotype-Tissue Expression (dGTEX).
<https://www.genome.gov/Funded-Programs-Projects/Developmental-Genotype-Tissue-Expression> (2020).

121. 121.

Yan, L. et al. Single-cell RNA-seq profiling of human preimplantation embryos and embryonic stem cells. *Nat. Struct. Mol. Biol.* **20**, 1131–1139 (2013). **A comprehensive scRNA-seq analysis of human oocytes to blastocyst-stage embryos that has widely been used to investigate lineage-associated gene expression and as a comparative analysis to human pluripotent stem cell lines.**

122. 122.

Petropoulos, S. et al. Single-cell RNA-seq reveals lineage and X chromosome dynamics in human preimplantation embryos. *Cell* **165**, 1012–1026 (2016).

123. 123.

Tyser, R. C. V. et al. A spatially resolved single cell atlas of human gastrulation. Preprint at <https://doi.org/10.1101/2020.07.21.213512> (2020).

124. 124.

Elmentait, R. et al. Cells of the human intestinal tract mapped across space and time. *Nature*, <https://doi.org/10.1038/s41586-021-03852-1> (2021).

Acknowledgements

The HDCA initiative receives funding from Wellcome, the UK Research and Innovation Medical Research Council, EU Horizon 2020, INSERM (HuDeCA) and the Knut and Alice Wallenberg and Erling-Persson foundations. We thank the HCA Executive Office and T. Andrews for their support. This publication is part of the Human Cell Atlas - <https://www.humancellatlas.org/publications/>

Author information

Author notes

1. Aviv Regev & Orit Rozenblatt-Rosen

Present address: Genentech, South San Francisco, CA, USA

2. These authors jointly supervised this work: Muzlifah Haniffa, Deanne Taylor, Sten Linnarsson

Affiliations

1. Biosciences Institute, Newcastle University, Newcastle upon Tyne, UK

Muzlifah Haniffa, Bayanne Olabi, Simone Webb, Deborah Henderson & Steven Lisgo

2. Wellcome Sanger Institute, Hinxton, UK

Muzlifah Haniffa, Kylie R. James, Kerstin B. Meyer, Sarah A. Teichmann, Roser Vento-Tormo, Omer Bayraktar & Sam Behjati

3. Department of Dermatology and NIHR Newcastle Biomedical Research Centre, Newcastle Hospitals NHS Foundation Trust, Newcastle upon Tyne, UK

Muzlifah Haniffa

4. Department of Biomedical and Health Informatics (DBHi), The Children's Hospital of Philadelphia, Philadelphia, PA, USA

Deanne Taylor

5. Department of Pediatrics, University of Pennsylvania Perelman School of Medicine, Philadelphia, PA, USA

Deanne Taylor

6. Division of Molecular Neurobiology, Department of Medical Biochemistry and Biophysics, Karolinska Institutet, Stockholm, Sweden

Sten Linnarsson

7. Division of Developmental Biology and Biomedical Informatics, Cincinnati Children's Hospital Medical Centre, Cincinnati, OH, USA

Bruce J. Aronow

8. The Donnelly Centre, University of Toronto, Toronto, Ontario, Canada

Gary D. Bader

9. Wellcome and MRC Cambridge Stem Cell Institute, University of Cambridge, Cambridge, UK

Roger A. Barker & Berthold Göttgens

10. Department of Clinical Neurosciences, University of Cambridge, Cambridge, UK

Roger A. Barker

11. Department of Genetics, University of Pennsylvania Perelman School of Medicine, Philadelphia, PA, USA

Pablo G. Camara

12. Institute of Molecular and Clinical Ophthalmology Basel (IOB), University of Basel, Basel, Switzerland

J. Gray Camp

13. INSERM, CNRS, Institut de la Vision, Sorbonne Université, Paris, France

Alain Chédotal & Yorick Gitton

14. Developmental Biology and Cancer Programme, UCL Great Ormond Street Institute of Child Health, London, UK

Andrew Copp

15. MMG, INSERM, U1251, Aix Marseille Université, Marseille, France

Heather C. Etchevers & Stéphane Zaffran

16. Laboratory of Development and Plasticity of the Neuroendocrine Brain, Inserm, CHU Lille, Lille Neuroscience and Cognition, UMR-S 1172, Université Lille, Lille, France

Paolo Giacobini

17. Department of Haematology, University of Cambridge, Cambridge, UK

Berthold Göttgens

18. Center for Stem Cell and Regenerative Medicine, Zhejiang University School of Medicine, Hangzhou, China

Guoji Guo

19. Klarman Cell Observatory, Broad Institute of Harvard and MIT, Cambridge, MA, USA

Ania Hupalowska, Aviv Regev, Jennifer Rood & Orit Rozenblatt-Rosen

20. Centre of Genomics and Policy, McGill University, Montreal, Quebec, Canada

Emily Kirby

21. Department of Neurology, University of California San Francisco (UCSF), San Francisco, CA, USA

Arnold Kriegstein

22. Science for Life Laboratory, KTH Royal Institute of Technology, Solna, Sweden

Joakim Lundeberg & Emma Lundberg

23. Cancer Research Institute UK Cambridge Institute, University of Cambridge, Cambridge, UK

John C. Marioni

24. Francis Crick Institute, London, UK

Kathy K. Niakan

25. Centre for Trophoblast Research, Department of Physiology, Development and Neuroscience, University of Cambridge, Cambridge, UK

Kathy K. Niakan

26. Science for Life Laboratory, Department of Biochemistry and Biophysics, Stockholm University, Stockholm, Sweden

Mats Nilsson

27. Computational and Systems Biology Program, Sloan Kettering Institute, Memorial Sloan Kettering Cancer Center, New York, NY, USA

Dana Pe'er

28. Department of Biology, Massachusetts Institute of Technology, Cambridge, MA, USA

Aviv Regev

29. New York Genome Center, New York University, New York, NY, USA

Rahul Satija

30. Cavendish Laboratory, Department of Physics, University of Cambridge, Cambridge, UK

Sarah A. Teichmann

31. Department of Biosystems Science and Engineering, Eidgenössische Technische Hochschule (ETH) Zurich, Basel, Switzerland

Barbara Treutlein

32. Institut de Pharmacologie Moléculaire et Cellulaire, UMR7275, CNRS/UNS, Université Côte d'Azur, Valbonne, France

Pascal Barbry

33. Miltenyi Biotec B.V. & Co. KG, Bergisch Gladbach, Germany

Andreas Bosio

34. Laboratoire Développement du Système Immunitaire, Ecole Pratique des Hautes Etudes, INSERM U976, Institut de Recherche Saint Louis, Centre Hayem, Hôpital Saint Louis 1, Paris, France

Bruno Canque

35. Inserm, EHESP, Irset (Institut de recherche en santé, environnement et travail)
UMR_S 1085, Université Rennes, Rennes, France

Frédéric Chalmel, Séverine Mazaud-Guittot & Antoine Rolland

36. University Department of Growth and Reproduction, EDMaRC, Rigshospitalet, University of Copenhagen, Copenhagen, Denmark

Anne Jorgensen

37. Genome Institute of Singapore, Singapore, Singapore

Jinyue Liu

38. Institut Curie, Paris, France

Jean-Léon Maitre

39. Sir William Dunn School of Pathology, University of Oxford, Oxford, UK

Elizabeth Robertson

40. U1016 INSERM Institut Cochin, Groupe Hospitalier Cochin Port Royal, Paris, France

Raphael Scharfmann

41. INSERM UMRS 1131, Institut de Recherche Saint Louis, Paris, France

Michèle Souyri

42. Division of Neurobiology, Care Sciences and Society, Karolinska Institutet, Stockholm, Sweden

Erik Sundström & Matthias Zilbauer

43. University of Cambridge, Cambridge, UK

Matthias Zilbauer

Consortia

Human Cell Atlas Developmental Biological Network

- Pascal Barbry
- , Omer Bayraktar
- , Sam Behjati
- , Andreas Bosio
- , Bruno Canque
- , Frédéric Chalmel
- , Yorick Gitton
- , Deborah Henderson
- , Anne Jorgensen
- , Steven Lisgo
- , Jinyue Liu
- , Emma Lundberg
- , Jean-Léon Maitre
- , Séverine Mazaud-Guittot
- , Elizabeth Robertson
- , Antoine Rolland
- , Raphael Scharfmann
- , Michèle Souyri
- , Erik Sundström
- , Stéphane Zaffran
- & Matthias Zilbauer

Contributions

M.H., D.T. and S. Linnarsson are coordinators of the HCA Developmental Biological Network. M.H., S.A.T. and A. Regev conceived the idea, co-ordinated the writing process, wrote parts of the paper and edited all sections. A.H. designed and created the figures. All other authors wrote parts of the paper and provided feedback on all parts.

Corresponding author

Correspondence to [Muzlifah Haniffa](#).

Ethics declarations

Competing interests

A. Regev is a co-founder and equity holder of Celsius Therapeutics, an equity holder in Immunitas, and was a Scientific Advisory Board member of Thermo Fisher Scientific, Syros Pharmaceuticals, Neogene Therapeutics and Asimov until 31 July 2020. From 1 August 2020, A. Regev and O.R-R. are employees of Genentech. S.A.T. has consulted for Genentech and Roche, and is a remunerated member of Scientific Advisory Boards for GlaxoSmithKline, Biogen and Foresite Labs. J. Lundeberg is a scientific advisor for 10x Genomics. All other authors declare no competing interests.

Additional information

Peer review information *Nature* thanks Oliver Pourquié, Susana Chuva de Sousa Lopes and the other, anonymous, reviewer(s) for their contribution to the peer review of this work.

Publisher's note Springer Nature remains neutral with regard to jurisdictional claims in published maps and institutional affiliations.

Supplementary information

[Supplementary Table 1](#)

HDCA consortia listed are funded HDCA projects that have been registered with the HCA. Any researcher, including those not part of existing HDCA consortia, can contribute to HDCA.

Rights and permissions

[Reprints and Permissions](#)

About this article

Cite this article

Haniffa, M., Taylor, D., Linnarsson, S. *et al.* A roadmap for the Human Developmental Cell Atlas. *Nature* **597**, 196–205 (2021).
<https://doi.org/10.1038/s41586-021-03620-1>

- Received: 08 September 2020
- Accepted: 07 May 2021
- Published: 08 September 2021
- Issue Date: 09 September 2021
- DOI: <https://doi.org/10.1038/s41586-021-03620-1>

This article was downloaded by **calibre** from <https://www.nature.com/articles/s41586-021-03620-1>

| [Section menu](#) | [Main menu](#) |

- Article
- [Published: 08 September 2021](#)

Large metallicity variations in the Galactic interstellar medium

- [Annalisa De Cia](#) [ORCID: orcid.org/0000-0003-2082-1626](#)¹,
- [Edward B. Jenkins](#) [ORCID: orcid.org/0000-0003-1892-4423](#)²,
- [Andrew J. Fox](#) [ORCID: orcid.org/0000-0003-0724-4115](#)³,
- [Cédric Ledoux](#) [ORCID: orcid.org/0000-0002-7864-3327](#)⁴,
- [Tanita Ramburth-Hurt](#) [ORCID: orcid.org/0000-0003-2597-2415](#)¹,
- [Christina Konstantopoulou](#) [ORCID: orcid.org/0000-0002-4690-0157](#)¹,
- [Patrick Petitjean](#)⁵ &
- [Jens-Kristian Krogager](#) [ORCID: orcid.org/0000-0002-4912-9388](#)¹

[Nature](#) volume **597**, pages 206–208 (2021)

- 765 Accesses
- 408 Altmetric
- [Metrics details](#)

Subjects

- [Astrophysical dust](#)
- [Galaxies and clusters](#)
- [Interstellar medium](#)

Abstract

The interstellar medium (ISM) comprises gases at different temperatures and densities, including ionized, atomic and molecular species, and dust particles¹. The neutral ISM is dominated by neutral hydrogen² and has ionization fractions of up to eight per cent³. The concentration of chemical elements heavier than helium (metallicity) spans orders of magnitudes in Galactic stars⁴, because they formed at different times. However, the gas in the vicinity of the Sun is assumed to be well mixed and to have a solar metallicity in traditional chemical evolution models⁵. The ISM chemical abundances can be accurately measured with ultraviolet absorption-line spectroscopy. However, the effects of dust depletion^{6,7,8,9}—which removes part of the metals from the observable gaseous phase and incorporates it into solid grains—have prevented, until recently, a deeper investigation of the ISM metallicity. Here we report the dust-corrected metallicity of the neutral ISM measured towards 25 stars in our Galaxy. We find large variations in metallicity over a factor of ten (with an average of 55 ± 7 per cent solar metallicity and a standard deviation of 0.28 dex), including many regions of low metallicity, down to about 17 per cent solar metallicity and possibly below. Pristine gas falling onto the Galactic disk in the form of high-velocity clouds can cause the observed chemical inhomogeneities on scales of tens of parsecs. Our results suggest that this low-metallicity accreting gas does not efficiently mix into the ISM, which may help us understand metallicity deviations in nearby coeval stars.

Access options

Subscribe to Journal

Get full journal access for 1 year

\$199.00

only \$3.90 per issue

[Subscribe](#)

All prices are NET prices.

VAT will be added later in the checkout.

Tax calculation will be finalised during checkout.

Rent or Buy article

Get time limited or full article access on ReadCube.

from \$8.99

[Rent or Buy](#)

All prices are NET prices.

Additional access options:

- [Log in](#)
- [Access through your institution](#)
- [Learn about institutional subscriptions](#)

Fig. 1: Location of our targets on the Galactic plane.

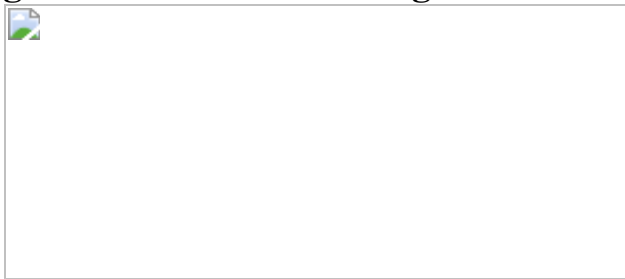


Fig. 2: Dust-corrected abundances in the neutral ISM.

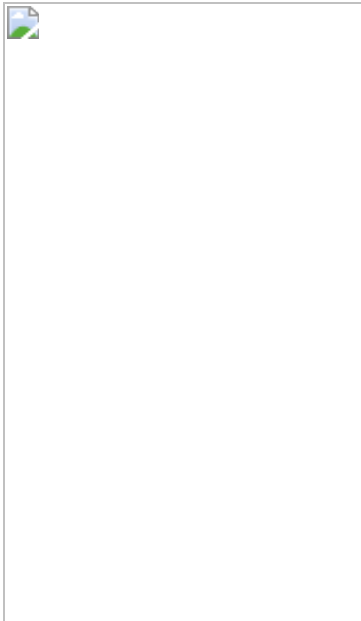
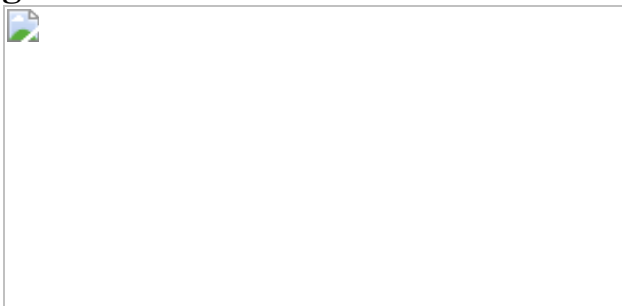


Fig. 3: Metalicities in the neutral ISM.



Data availability

The observational data used in this work are publicly available in the Mikulski Archive for Space Telescope (HST/STIS data, programme ID 15335, principal investigator A.D.C., <https://doi.org/10.17909/t9-r14v-tp03>) and the ESO Science Archive Facility (VLT/UVES data http://archive.eso.org/wdb/wdb/adp/phase3_spectral/form?). The data used in the figures and tables are available as electronically readable source data files, except for the publicly available observational data (Extended Data Fig. 1). [Source data](#) are provided with this paper.

Code availability

The VoigtFit software is publicly available on GitHub at
<https://github.com/jkrogager/VoigtFit>.

References

1. 1.
Draine, B. T. *Physics of the Interstellar and Intergalactic Medium* (Princeton Univ. Press, 2011).
2. 2.
Viegas, S. M. Abundances at high redshift: ionization correction factors. *Mon. Not. R. Astron. Soc.* **276**, 268–272 (1995).
3. 3.
Jenkins, E. B. The fractional ionization of the warm neutral interstellar medium. *Astrophys. J.* **764**, 25 (2013).
4. 4.
McWilliam, A. Abundance ratios and galactic chemical evolution. *Annu. Rev. Astron. Astrophys.* **35**, 503-556 (1997).
5. 5.
Matteucci, F. *Chemical Evolution of Galaxies* (Astronomy and Astrophysics Library, Springer, 2012).
6. 6.
Field, G. B. Interstellar abundances: gas and dust. *Astrophys. J.* **187**, 453–459 (1974).
7. 7.

Savage, B. D. & Sembach, K. R. Interstellar abundances from absorption-line observations with the Hubble Space Telescope. *Annu. Rev. Astron. Astrophys.* **34**, 279–330 (1996).

8. 8.

Jenkins, E. B. A unified representation of gas-phase element depletions in the interstellar medium. *Astrophys. J.* **700**, 1299–1348 (2009).

9. 9.

De Cia, A. et al. Dust-depletion sequences in damped Lyman- α absorbers. A unified picture from low-metallicity systems to the Galaxy. *Astron. Astrophys.* **596**, A97 (2016).

10. 10.

Arellano-Córdova, K. Z., Esteban, C., Garca-Rojas, J. & Méndez-Delgado, J. E. The Galactic radial abundance gradients of C, N, O, Ne, S, Cl, and Ar from deep spectra of H II regions. *Mon. Not. R. Astron. Soc.* **496**, 1051–1076 (2020).

11. 11.

Edmunds, M. G. Is the Galactic Disk well mixed? *Astrophys. Space Sci.* **32**, 483–491 (1975).

12. 12.

Tosi, M. The effect of metal-rich infall on galactic chemical evolution. *Astron. Astrophys.* **197**, 47–51 (1988).

13. 13.

Chiappini, C., Matteucci, F. & Gratton, R. The chemical evolution of the Galaxy: the two-infall model. *Astrophys. J.* **477**, 765–780 (1997).

14. 14.

Edvardsson, B. et al. The chemical evolution of the Galactic disk. I. Analysis and results. *Astron. Astrophys.* **275**, 101–152 (1993).

15. 15.

Pilyugin, L. S. & Edmunds, M. G. Chemical evolution of the Milky Way Galaxy. II. On the origin of scatter in the age–metallicity relation. *Astron. Astrophys.* **313**, 792–802 (1996).

16. 16.

White, S. D. M. & Audouze, J. Stochastic effects in the chemical evolution of galaxies. *Mon. Not. R. Astron. Soc.* **203**, 603–618 (1983).

17. 17.

de Avillez, M. A. & Mac Low, M. M. Mixing timescales in a supernova-driven interstellar medium. *Astrophys. J.* **581**, 1047–1060 (2002).

18. 18.

Andrews, S. M., Meyer, D. M. & Lauroesch, J. T. Small-scale interstellar Na I structure toward M92. *Astrophys. J. Lett.* **552**, L73–L76 (2001).

19. 19.

Nasoudi-Shoar, S., Richter, P., de Boer, K. S. & Wakker, B. P. Interstellar absorptions towards the LMC: small-scale density variations in Milky Way disc gas. *Astron. Astrophys.* **520**, A26 (2010).

20. 20.

Fox, A. J. & Davé, R. *Gas Accretion onto Galaxies* (Astrophysics and Space Science Library 430, Springer, 2017).

21. 21.

Wright, R. J., Lagos, C. P., Power, C. & Correa, C. A. Revealing the physical properties of gas accreting to haloes in the EAGLE simulations. *Mon. Not. R. Astron. Soc.* **504**, 5702–5725 (2021).

22. 22.

Gritton, J. A., Shelton, R. L. & Kwak, K. Mixing between high velocity clouds and the Galactic halo. *Astrophys. J.* **795**, 99 (2014).

23. 23.

Heitsch, F. & Putman, M. E. The fate of high-velocity clouds: warm or cold cosmic rain? *Astrophys. J.* **698**, 1485–1496 (2009).

24. 24.

Putman, M. E., Peek, J. E. G. & Joung, M. R. Gaseous galaxy halos. *Annu. Rev. Astron. Astrophys.* **50**, 491–529 (2012).

25. 25.

Richter, P. *Gas Accretion onto the Milky Way* (Astrophysics and Space Science Library 430, Springer, 2017).

26. 26.

Lehner, N. & Howk, J. C. A reservoir of ionized gas in the Galactic halo to sustain star formation in the Milky Way. *Science* **334**, 955–958 (2011).

27. 27.

Fox, A. J. et al. The mass inflow and outflow rates of the Milky Way. *Astrophys. J.* **884**, 53 (2019).

28. 28.

Cheng, J. Y. et al. Metallicity gradients in the Milky Way disk as observed by the SEGUE survey. *Astrophys. J.* **746**, 149 (2012).

29. 29.

Wendt, M., Bouché, N. F., Zabl, J., Schroetter, I. & Muzahid, S. MUSE gas flow and wind V. The dust/metallicity-anisotropy of the circum-galactic medium. *Mon. Not. R. Astron. Soc.* **502**, 3733–3745 (2021).

30. 30.

Welty, D. E. & Crowther, P. A. Interstellar Ti II in the Milky Way and Magellanic Clouds. *Mon. Not. R. Astron. Soc.* **404**, 1321–1348 (2010).

31. 31.

Diplas, A. & Savage, B. D. An IUE survey of interstellar H i Ly α absorption. I. Column densities. *Astrophys. J. Suppl. Ser.* **93**, 211–228 (1994).

32. 32.

Savage, B. D., Bohlin, R. C., Drake, J. F. & Budich, W. A survey of interstellar molecular hydrogen. I. *Astrophys. J.* **216**, 291–307 (1977).

33. 33.

Gaia Collaboration et al. The Gaia mission. *Astron. Astrophys.* **595**, A1 (2016).

34. 34.

Gaia Collaboration et al. Gaia Data Release 2. Summary of the contents and survey properties. *Astron. Astrophys.* **616**, A1 (2018).

35. 35.

Welty, D. E., Sonnentrucker, P., Snow, T. P. & York, D. G. HD 62542: probing the bare, dense core of a translucent interstellar cloud. *Astrophys. J.* **897**, 36, (2020).

36. 36.

Valencic, L. A., Clayton, G. C. & Gordon, K. D. Ultraviolet extinction properties in the Milky Way. *Astrophys. J.* **616**, 912–924 (2004).

37. 37.

Savage, B. D. & Sembach, K. R. The analysis of apparent optical depth profiles for interstellar absorption lines. *Astrophys. J.* **379**, 245–259 (1991).

38. 38.

Jenkins, E. B. A procedure for correcting the apparent optical depths of moderately saturated interstellar absorption lines. *Astrophys. J.* **471**, 292–301 (1996).

39. 39.

Sembach, K. R. & Savage, B. D. Observations of highly ionized gas in the Galactic halo. *Astrophys. J. Suppl. Ser.* **83**, 147–201 (1992).

40. 40.

Bowen, D. V. et al. The Far Ultraviolet Spectroscopic Explorer Survey of O VI absorption in the disk of the Milky Way. *Astrophys. J. Suppl. Ser.* **176**, 59–163 (2008).

41. 41.

Krogager, J.-K. VoigtFit: a Python package for Voigt profile fitting. Preprint at <https://arxiv.org/abs/1803.01187> (2018).

42. 42.

Price, R. J., Crawford, I. A., Barlow, M. J. & Howarth, I. D. An ultra-high-resolution study of the interstellar medium towards Orion. *Mon. Not. R. Astron. Soc.* **328**, 555–582 (2001).

43. 43.

Phillips, A. P., Gondhalekar, P. M. & Pettini, M. A study of element depletions in interstellar gas. *Mon. Not. R. Astron. Soc.* **200**, 687–703 (1982).

44. 44.

Jenkins, E. B., Savage, B. D. & Spitzer, L. Jr Abundances of interstellar atoms from ultraviolet absorption lines. *Astrophys. J.* **301**, 355–379 (1986).

45. 45.

Roman-Duval, J. et al. METAL: The Metal Evolution, Transport, and Abundance in the Large Magellanic Cloud Hubble program. II. Variations of interstellar depletions and dust-to-gas ratio within the LMC. *Astrophys. J.* **910**, 95 (2021).

46. 46.

De Cia, A. Metals and dust in the neutral ISM: the Galaxy, Magellanic Clouds, and damped Lyman- α absorbers *Astron. Astrophys.* **613**, L2 (2018).

47. 47.

Jenkins, E. B. A closer look at some gas-phase depletions in the ISM: trends for O, Ge, and Kr versus F^* , $f(H_2)$, and starlight intensity. *Astrophys. J.* **872**, 55 (2019).

48. 48.

De Cia, A., Ledoux, C., Petitjean, P. & Savaglio, S. The cosmic evolution of dust-corrected metallicity in the neutral gas. *Astron. Astrophys.* **611**, A76 (2018).

49. 49.

Simón-Díaz, S. The chemical composition of the Orion star forming region. I. Homogeneity of O and Si abundances in B-type stars. *Astron. Astrophys.* **510**, A22 (2010).

50. 50.

Rubin, R. H., Dufour, R. J. and Walter, D. K. Silicon and carbon abundances in the Orion nebula. *Astrophys. J.* **413**, 242–250 (1993).

51. 51.

Garnett, D. R. et al. Si/O abundance ratios in extragalactic H II regions from Hubble Space Telescope UV spectroscopy. *Astrophys. J.* **449**, L77–L81 (1995).

52. 52.

Simón-Díaz, S. & Stasińska, G. The chemical composition of the Orion star forming region. II. Stars, gas, and dust: the abundance discrepancy conundrum. *Astron. Astrophys.* **526**, A48 (2011).

53. 53.

Esteban, C. et al. A reappraisal of the chemical composition of the Orion nebula based on Very Large Telescope echelle spectrophotometry. *Mon. Not. R. Astron. Soc.* **355**, 229–247 (2004).

54. 54.

Esteban, C. & García-Rojas, J. Revisiting the radial abundance gradients of nitrogen and oxygen of the Milky Way. *Mon. Not. R. Astron. Soc.* **478**, 2315–2336 (2018).

55. 55.

Balser, D. S., Wenger, T. V., Anderson, L. D. and Bania, T. M. Azimuthal metallicity structure in the Milky Way Disk. *Astrophys. J.* **806**, 199 (2015).

56. 56.

Wang, E. & Lilly, S. J. Gas-phase metallicity as a diagnostic of the drivers of star-formation on different scales. *Astrophys. J.* **910**, 137 (2021).

57. 57.

Kreckel, K. et al. Mapping metallicity variations across nearby Galaxy disks. *Astrophys. J.* **887**, 80 (2019).

58. 58.

Kreckel, K. et al. Measuring the mixing scale of the ISM within nearby spiral galaxies. *Mon. Not. R. Astron. Soc.* **499**, 193–209 (2020).

59. 59.

McMillan, P. J. Mass models of the Milky Way. *Mon. Not. R. Astron. Soc.* **414**, 2446–2457 (2011).

60. 60.

Cashman, F. H., Kulkarni, V. P., Kisielius, R., Ferland, G. J. & Bogdanovich, P. Atomic data revisions for transitions relevant to observations of interstellar, circumgalactic, and intergalactic matter. *Astrophys. J. Suppl. Ser.* **230**, 8 (2017).

61. 61.

Morton, D. C. Atomic data for resonance absorption lines. III. Wavelengths longward of the Lyman limit for the elements hydrogen to gallium. *Astrophys. J. Suppl. Ser.* **149**, 205–238 (2003).

62. 62.

Boissé, P. & Bergeron, J. Improved Ni II oscillator strengths from quasar absorption systems. *Astron. Astrophys.* **622**, A140 (2019).

63. 63.

Kisielius, R. et al. Atomic data for Zn II: improving spectral diagnostics of chemical evolution in high-redshift galaxies. *Astrophys. J.* **804**, 76 (2015).

64. 64.

Jenkins, E. B. & Tripp, T. M. Measurements of the f -values of the resonance transitions of Ni II at 1317.217 and 1370.132 Å. *Astrophys. J.* **637**, 548–552 (2006).

65. 65.

Wiseman, P. et al. Evolution of the dust-to-metals ratio in high-redshift galaxies probed by GRB-DLAs. *Astron. Astrophys.* **599**, A24 (2017).

Acknowledgements

A.D.C. thanks C. Chiosi and the ‘Galaxies and the Universe’ group at the University of Geneva for discussions, and B. Holl for help with navigating the Gaia archive. A.D.C., T.R.-H., C.K. and J.-K.K. acknowledge support by the Swiss National Science Foundation under grant 185692. Based on observations with the NASA/ESA Hubble Space Telescope obtained at the Space Telescope Science Institute (STScI), which is operated by the Association of Universities for Research in Astronomy, Incorporated, under NASA contract NAS5-26555. E.B.J. was supported by grant number HST-GO-15335.002-A from STScI to Princeton University. Based on data obtained from the ESO Science Archive Facility. This work has made use of data from the European Space Agency (ESA) mission Gaia (<https://www.cosmos.esa.int/gaia>), processed by the Gaia Data Processing and Analysis Consortium (DPAC, <https://www.cosmos.esa.int/web/gaia/dpac/consortium>). Funding for the DPAC has been provided by national institutions, in particular the institutions participating in the Gaia Multilateral Agreement. The background image in Fig. 1 is courtesy of NASA/JPL-Caltech/R. Hurt (SSC/Caltech).

Author information

Affiliations

1. Department of Astronomy, University of Geneva, Versoix, Switzerland

Annalisa De Cia, Tanita Ramburth-Hurt, Christina
Konstantopoulou & Jens-Kristian Krogager

2. Princeton University Observatory, Princeton, NJ, USA

Edward B. Jenkins

3. AURA for ESA, Space Telescope Science Institute, Baltimore, MD,
USA

Andrew J. Fox

4. European Southern Observatory, Vitacura, Chile

Cédric Ledoux

5. Institut d’Astrophysique de Paris, Sorbonne Universités & CNRS,
Paris, France

Patrick Petitjean

Contributions

A.D.C. initiated, designed and directed the project, is the principal investigator of the HST data, analysed and interpreted the data, developed and applied the main methodology, and wrote the bulk of the manuscript. E.B.J. reduced the HST data and retrieved the UVES data, analysed and interpreted the data, measured the column densities, developed and applied one of the two methods to measure the metallicity, contributed to the writing and produced Fig. 3. A.J.F. contributed to the writing and scientific design of the paper. C.L. checked the consistency of the analysis, helped

interpret the data and contributed to the writing. E.B.J., C.L., A.J.F. and P.P. are co-investigators of the HST data. T.R.-H. measured the position of our targets within the Galaxy and produced Fig. 1 and Extended Data Fig. 4. C.K. reviewed the depletion methods and assumptions, and collected data from Galactic extinction maps. P.P. contributed to the prioritization of the scientific goals and the writing. J.-K.K. assessed the ionization effects and contributed to the writing. J.-K.K., T.R.-H., C.K., C.L. and A.D.C. measured the column densities towards eight targets with an independent method for a cross-check of the results. All authors participated in the scientific interpretation, edited the manuscript and contributed to its revision.

Corresponding author

Correspondence to [Annalisa De Cia](#).

Ethics declarations

Competing interests

The authors declare no competing interests.

Additional information

Peer review information *Nature* thanks the anonymous reviewers for their contribution to the peer review of this work.

Publisher's note Springer Nature remains neutral with regard to jurisdictional claims in published maps and institutional affiliations.

Extended data figures and tables

[Extended Data Fig. 1 Line profiles of Zn ii \$\lambda\$ 2026 \(black\), Cr ii \$\lambda\$ 2056 \(blue\) and Fe ii \$\lambda\$ 2260 \(green\) in our sample.](#)

The Mg i λ 2026 line is separated by \sim 50 km s $^{-1}$ from Zn ii. Vertical lines mark the zero-velocity central wavelength of the Zn ii line. The yellow curve shows the 1σ uncertainties.

Extended Data Fig. 2 Determination of the metallicity and strength of depletion with the relative method.

The variables and coefficients of the linear relation are defined in equations (4) to (7), where the y intercept gives the $[M/H]_{tot}$ and the slope of the relation the strength of depletion $[Zn/Fe]_{fit}$. The error bars show the 1σ uncertainties.

[Source data](#)

Extended Data Fig. 3 Determination of $[M/H]_{tot}$ and F^* with the F^* method.

The variables are described in equation (8). The most volatile elements (red) are taken from the literature (Extended Data Table 6) and shown for reference: their discrepancy with respect to the more refractory elements suggests a mix between high-metallicity and pristine gas, see Methods. The error bars show the 1σ uncertainties.

[Source data](#)

Extended Data Fig. 4 Metallicity towards our targets and their Galactic location.

a, Metallicities towards our targets and their Galactic radii. The green dotted line shows the metallicity gradient measured in H ii regions by ref. 10, although without dust corrections. The solar Galactic radius (red cross) is assumed at 8.29 kpc 59. The error bars show the 1σ uncertainties. **b**, Metallicities towards our targets and their height above the Galactic Disk. The error bars show the 1σ uncertainties.

[Source data](#)

Extended Data Table 1 Target sample characteristics

Extended Data Table 2 Column densities

Extended Data Table 3 Metallicities of the neutral ISM

Extended Data Table 4 Absorption lines that we use in this work and their oscillator strengths

Extended Data Table 5 Coefficients used in equations (6) and (7)

Extended Data Table 6 Column densities of the volatile elements

Supplementary information

[**Source Data Fig. 1**](#)

[**Source Data Fig. 2**](#)

[**Source Data Fig. 3**](#)

[**Source Data Extended Data Fig. 2**](#)

[**Source Data Extended Data Fig. 3**](#)

[**Source Data Extended Data Fig. 4**](#)

[**Source Data Extended Data Table 1**](#)

[**Source Data Extended Data Table 2**](#)

[**Source Data Extended Data Table 3**](#)

[**Source Data Extended Data Table 4**](#)

[**Source Data Extended Data Table 5**](#)

[**Source Data Extended Data Table 6**](#)

Rights and permissions

[Reprints and Permissions](#)

About this article

Cite this article

De Cia, A., Jenkins, E.B., Fox, A.J. *et al.* Large metallicity variations in the Galactic interstellar medium. *Nature* **597**, 206–208 (2021).
<https://doi.org/10.1038/s41586-021-03780-0>

- Received: 19 December 2020
- Accepted: 29 June 2021
- Published: 08 September 2021
- Issue Date: 09 September 2021
- DOI: <https://doi.org/10.1038/s41586-021-03780-0>

This article was downloaded by **calibre** from <https://www.nature.com/articles/s41586-021-03780-0>

| [Section menu](#) | [Main menu](#) |

- Article
- [Published: 08 September 2021](#)

High-fidelity laser-free universal control of trapped ion qubits

- [R. Srinivas](#) [ORCID: orcid.org/0000-0002-8462-6072](#)^{1,2 nAff8},
- [S. C. Burd](#)^{1,2 nAff9},
- [H. M. Knaack](#)^{1,2},
- [R. T. Sutherland](#) [ORCID: orcid.org/0000-0001-5583-5150](#)^{3,4,5},
- [A. Kwiatkowski](#)^{1,2},
- [S. Glancy](#)¹,
- [E. Knill](#)^{1,6},
- [D. J. Wineland](#)^{1,2,7},
- [D. Leibfried](#)¹,
- [A. C. Wilson](#) [ORCID: orcid.org/0000-0003-4172-4710](#)¹,
- [D. T. C. Allcock](#)^{1,2,7} &
- [D. H. Slichter](#) [ORCID: orcid.org/0000-0002-1228-0631](#)¹

[Nature](#) volume **597**, pages 209–213 (2021)

- 1122 Accesses
- [Metrics details](#)

Subjects

- [Atomic and molecular physics](#)
- [Quantum information](#)

Abstract

Universal control of multiple qubits—the ability to entangle qubits and to perform arbitrary individual qubit operations¹—is a fundamental resource for quantum computing², simulation³ and networking⁴. Qubits realized in trapped atomic ions have shown the highest-fidelity two-qubit entangling operations^{5,6,7} and single-qubit rotations⁸ so far. Universal control of trapped ion qubits has been separately demonstrated using tightly focused laser beams^{9,10,11,12} or by moving ions with respect to laser beams^{13,14,15}, but at lower fidelities. Laser-free entangling methods^{16,17,18,19,20} may offer improved scalability by harnessing microwave technology developed for wireless communications, but so far their performance has lagged the best reported laser-based approaches. Here we demonstrate high-fidelity laser-free universal control of two trapped-ion qubits by creating both symmetric and antisymmetric maximally entangled states with fidelities of $\langle\{1\}_{-0.0017}\rangle^{+0}$ and $\langle\{0.9977\}_{-0.0013}\rangle^{+0.0010}$, respectively (68 per cent confidence level), corrected for initialization error. We use a scheme based on radiofrequency magnetic field gradients combined with microwave magnetic fields that is robust against multiple sources of decoherence and usable with essentially any trapped ion species. The scheme has the potential to perform simultaneous entangling operations on multiple pairs of ions in a large-scale trapped-ion quantum processor without increasing control signal power or complexity. Combining this technology with low-power laser light delivered via trap-integrated photonics^{21,22} and trap-integrated photon detectors for qubit readout^{23,24} provides an opportunity for scalable, high-fidelity, fully chip-integrated trapped-ion quantum computing.

Access options

Subscribe to Journal

Get full journal access for 1 year

\$199.00

only \$3.90 per issue

[Subscribe](#)

All prices are NET prices.
VAT will be added later in the checkout.
Tax calculation will be finalised during checkout.

Rent or Buy article

Get time limited or full article access on ReadCube.

from \$8.99

[Rent or Buy](#)

All prices are NET prices.

Additional access options:

- [Log in](#)
- [Access through your institution](#)
- [Learn about institutional subscriptions](#)

Fig. 1: Experimental setup.

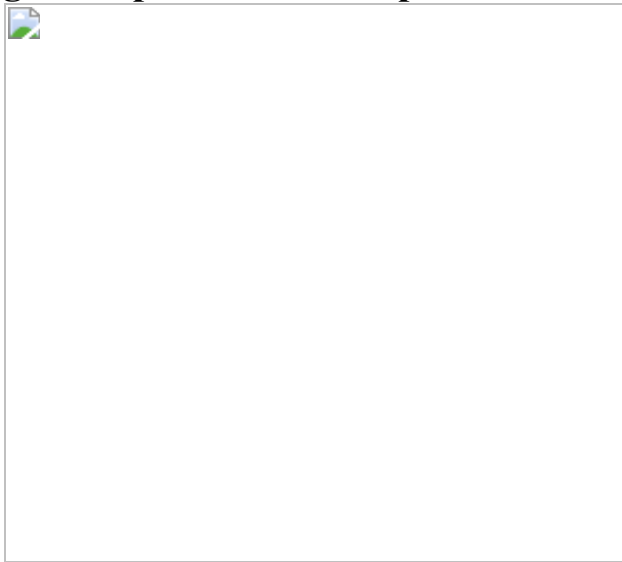


Fig. 2: Robustness of entangling operation.

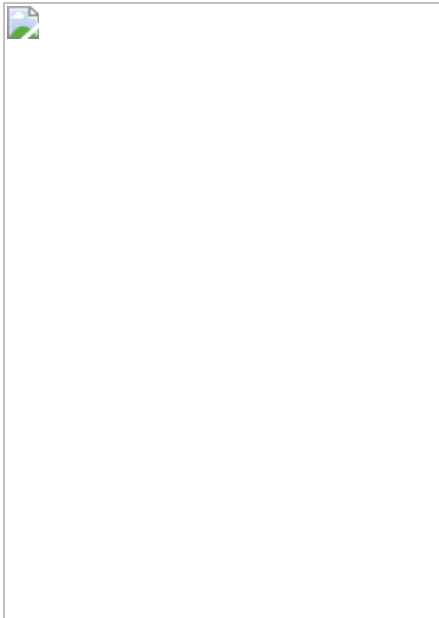
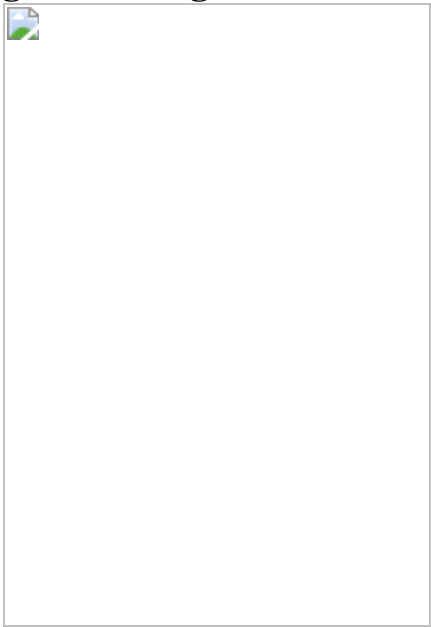


Fig. 3: Entangled-state fidelity analysis.



Data availability

Source data are provided with this paper. All other data that support the plots within this paper and other findings of this study are available from the corresponding authors upon reasonable request.

Code availability

All simulation code or analysis code that support the plots within this paper and other findings of this study are available from the corresponding authors upon reasonable request.

References

1. 1.

Barenco, A. et al. Elementary gates for quantum computation. *Phys. Rev. A* **52**, 3457–3467 (1995).

2. 2.

Jozsa, R. in *The Geometric Universe: Science, Geometry, and the work of Roger Penrose* (eds Huggett, S. A, Mason, L. J., Tod, K. P., Tsou, S. T. & Woodhouse, N. M. J.) 369 (Oxford Univ. Press, 1998).

3. 3.

Georgescu, I. M., Ashhab, S. & Nori, F. Quantum simulation. *Rev. Mod. Phys.* **86**, 153–185 (2014).

4. 4.

Kimble, H. J. The quantum internet. *Nature* **453**, 1023–1030 (2008).

5. 5.

Ballance, C. J., Harty, T. P., Linke, N. M., Sepiol, M. A. & Lucas, D. M. High-fidelity quantum logic gates using trapped-ion hyperfine qubits. *Phys. Rev. Lett.* **117**, 060504 (2016).

6. 6.

Gaebler, J. P. et al. High-fidelity universal gate set for ${}^9\text{Be}^+$ ion qubits. *Phys. Rev. Lett.* **117**, 060505 (2016).

7. 7.

Clark, C. R. et al. High-fidelity Bell-state preparation with $^{40}\text{Ca}^+$ optical qubits. Preprint at <https://arxiv.org/abs/2105.05828> (2021).

8. 8.

Harty, T. P. et al. High-fidelity preparation, gates, memory, and readout of a trapped-ion quantum bit. *Phys. Rev. Lett.* **113**, 220501 (2014).

9. 9.

Schmidt-Kaler, F. et al. Realization of the Cirac–Zoller controlled-NOT quantum gate. *Nature* **422**, 408–411 (2003).

10. 10.

Debnath, S. et al. Demonstration of a small programmable quantum computer with atomic qubits. *Nature* **536**, 63–66 (2016).

11. 11.

Wright, K. et al. Benchmarking an 11-qubit quantum computer. *Nat. Commun.* **10**, 5464 (2019).

12. 12.

Erhard, A. et al. Characterizing large-scale quantum computers via cycle benchmarking. *Nat. Commun.* **10**, 5347 (2019).

13. 13.

Barrett, M. D. et al. Deterministic quantum teleportation of atomic qubits. *Nature* **429**, 737–739 (2004).

14. 14.

Ruster, T. et al. Entanglement-based dc magnetometry with separated ions. *Phys. Rev. X* **7**, 031050 (2017).

15. 15.

Pino, J. M. et al. Demonstration of the trapped-ion quantum CCD computer architecture. *Nature* **592**, 209–213 (2021).

16. 16.

Wineland, D. J. et al. Experimental issues in coherent quantum-state manipulation of trapped atomic ions. *J. Res. Natl Inst. Stand. Technol.* **103**, 259–328 (1998).

17. 17.

Mintert, F. & Wunderlich, C. Ion-trap quantum logic using long-wavelength radiation. *Phys. Rev. Lett.* **87**, 257904 (2001).

18. 18.

Ospelkaus, C. et al. Trapped-ion quantum logic gates based on oscillating magnetic fields. *Phys. Rev. Lett.* **101**, 090502 (2008).

19. 19.

Harty, T. P. et al. High-fidelity trapped-ion quantum logic using near-field microwaves. *Phys. Rev. Lett.* **117**, 140501 (2016).

20. 20.

Zarantonello, G. et al. Robust and resource-efficient microwave near-field entangling ${}^9\text{Be}^+$ gate. *Phys. Rev. Lett.* **123**, 260503 (2019).

21. 21.

Mehta, K. K. et al. Integrated optical multi-ion quantum logic. *Nature* **586**, 533–537 (2020).

22. 22.

Niffenegger, R. J. et al. Integrated multi-wavelength control of an ion qubit. *Nature* **586**, 538–542 (2020).

23. 23.

Todaro, S. L. et al. State readout of a trapped ion qubit using a trap-integrated superconducting photon detector. *Phys. Rev. Lett.* **126**, 010501 (2021).

24. 24.

Setzer, W. et al. Fluorescence detection of a trapped ion with a monolithically integrated single-photon-counting avalanche diode. Preprint at <https://arxiv.org/abs/2105.01235> (2021).

25. 25.

Cirac, J. I. & Zoller, P. Quantum computations with cold trapped ions. *Phys. Rev. Lett.* **74**, 4091 (1995).

26. 26.

Milburn, G. J., Schneider, S. & James, D. F. V. Ion trap quantum computing with warm ions. *Fortschr. Phys.* **48**, 801–810 (2000).

27. 27.

Sørensen, A. & Mølmer, K. Quantum computation with ions in thermal motion. *Phys. Rev. Lett.* **82**, 1971–1974 (1999).

28. 28.

Sørensen, A. & Mølmer, K. Entanglement and quantum computation with ions in thermal motion. *Phys. Rev. A* **62**, 022311 (2000).

29. 29.

Leibfried, D., Blatt, R., Monroe, C. & Wineland, D. Quantum dynamics of single trapped ions. *Rev. Mod. Phys.* **75**, 281–324 (2003).

30. 30.

Nägerl, H. C. et al. Laser addressing of individual ions in a linear ion trap. *Phys. Rev. A* **60**, 145 (1999).

31. 31.

Monroe, C., Meekhof, D. M., King, B. E., Itano, W. M. & Wineland, D. J. Demonstration of a fundamental quantum logic gate. *Phys. Rev. Lett.* **75**, 4714–4717 (1995).

32. 32.

Leibfried, D. et al. Experimental demonstration of a robust, high-fidelity geometric two ion-qubit phase gate. *Nature* **422**, 412–415 (2003).

33. 33.

Ozeri, R. et al. Errors in trapped-ion quantum gates due to spontaneous photon scattering. *Phys. Rev. A* **75**, 042329 (2007).

34. 34.

Ospelkaus, C. et al. Microwave quantum logic gates for trapped ions. *Nature* **476**, 181–184 (2011).

35. 35.

Hahn, H. et al. Integrated ${}^9\text{Be}^+$ multi-qubit gate device for the ion-trap quantum computer. *npj Quantum Inf.* **5**, 70 (2019).

36. 36.

Khromova, A. et al. Designer spin pseudomolecule implemented with trapped ions in a magnetic gradient. *Phys. Rev. Lett.* **108**, 220502 (2012).

37. 37.

Weidt, S. et al. Trapped-ion quantum logic with global radiation fields. *Phys. Rev. Lett.* **117**, 220501 (2016).

38. 38.

Leibfried, D. Individual addressing and state readout of trapped ions utilizing rf micromotion. *Phys. Rev. A* **60**, R3335 (1999).

39. 39.

Johanning, M. et al. Individual addressing of trapped ions and coupling of motional and spin states using rf radiation. *Phys. Rev. Lett.* **102**, 073004 (2009).

40. 40.

Warring, U. et al. Individual-ion addressing with microwave field gradients. *Phys. Rev. Lett.* **110**, 173002 (2013).

41. 41.

Sutherland, R. T. et al. Versatile laser-free trapped-ion entangling gates. *New J. Phys.* **21**, 033033 (2019).

42. 42.

Hayes, D. et al. Coherent error suppression in multiqubit entangling gates. *Phys. Rev. Lett.* **109**, 020503 (2012).

43. 43.

Srinivas, R. et al. Trapped-ion spin-motion coupling with microwaves and a near-motional oscillating magnetic field gradient. *Phys. Rev. Lett.* **122**, 163201 (2019).

44. 44.

Sackett, C. A. et al. Experimental entanglement of four particles. *Nature* **404**, 256–259 (2000).

45. 45.

Sutherland, R. T. et al. Laser-free trapped-ion entangling gates with simultaneous insensitivity to qubit and motional decoherence. *Phys. Rev. A* **101**, 042334 (2020).

46. 46.

Emerson, J., Alicki, R. & Życzkowski, K. Scalable noise estimation with random unitary operators. *J. Opt. B* **7**, S347–S352 (2005).

47. 47.

Knill, E. et al. Randomized benchmarking of quantum gates. *Phys. Rev. A* **77**, 012307 (2008).

48. 48.

Piltz, C., Sriarunothai, T., Varón, A. F. & Wunderlich, C. A trapped-ion-based quantum byte with 10^{-5} next-neighbour cross-talk. *Nat. Commun.* **5**, 4679 (2014).

49. 49.

Aude Craik, D. P. L. et al. High-fidelity spatial and polarization addressing of $^{43}\text{Ca}^+$ qubits using near-field microwave control. *Phys. Rev. A* **95**, 022337 (2017).

50. 50.

Leibfried, D., Knill, E., Ospelkaus, C. & Wineland, D. J. Transport quantum logic gates for trapped ions. *Phys. Rev. A* **76**, 032324 (2007).

51. 51.

Kielpinski, D., Monroe, C. & Wineland, D. J. Architecture for a large-scale ion-trap quantum computer. *Nature* **417**, 709 (2002).

52. 52.

Stuart, J. et al. Chip-integrated voltage sources for control of trapped ions. *Phys. Rev. Appl.* **11**, 024010 (2019).

53. 53.

Chou, C.-W. et al. Preparation and coherent manipulation of pure quantum states of a single molecular ion. *Nature* **545**, 164–165 (2017).

54. 54.

Kozlov, M. G., Safranova, M. S., Crespo López-Urrutia, J. R. & Schmidt, P. O. Highly charged ions: optical clocks and applications in fundamental physics. *Rev. Mod. Phys.* **90**, 045005 (2018).

55. 55.

Matthiesen, C., Yu, Q., Guo, J., Alonso, A. M. & Häffner, H. Trapping electrons in a room-temperature microwave Paul trap. *Phys. Rev. X* **11**, 011019 (2021).

Acknowledgements

We thank C. J. Ballance, T. P. Harty, J. P. Gaebler, S. B. Libby, D. M. Lucas, V. M. Schäfer and T. R. Tan for helpful discussions. We thank M. Affolter and A. L. Collopy for insightful comments on the manuscript. At the time the work was performed, R.S., S.C.B., H.M.K., A.K., and D.T.C.A. were supported as associates in the Professional Research Experience Program (PREP) operated jointly by the National Institute of Standards and Technology (NIST) and the University of Colorado Boulder under award number 70NANB18H006 from the US Department of Commerce, NIST. This work was supported by the NIST Quantum Information Program and ONR.

Author information

Author notes

1. R. Srinivas

Present address: Department of Physics, Clarendon Laboratory,
University of Oxford, Oxford, UK

2. S. C. Burd

Present address: Department of Physics, Stanford University, Stanford,
CA, USA

Affiliations

1. National Institute of Standards and Technology, Boulder, CO, USA

R. Srinivas, S. C. Burd, H. M. Knaack, A. Kwiatkowski, S. Glancy, E. Knill, D. J. Wineland, D. Leibfried, A. C. Wilson, D. T. C. Allcock & D. H. Slichter

2. Department of Physics, University of Colorado, Boulder, CO, USA

R. Srinivas, S. C. Burd, H. M. Knaack, A. Kwiatkowski, D. J. Wineland & D. T. C. Allcock

3. Physics Division, Physical and Life Sciences, Lawrence Livermore National Laboratory, Livermore, CA, USA

R. T. Sutherland

4. Department of Electrical and Computer Engineering, University of Texas at San Antonio, San Antonio, TX, USA

R. T. Sutherland

5. Department of Physics and Astronomy, University of Texas at San Antonio, San Antonio, TX, USA

R. T. Sutherland

6. Center for Theory of Quantum Matter, University of Colorado,
Boulder, CO, USA

E. Knill

7. Department of Physics, University of Oregon, Eugene, OR, USA

D. J. Wineland & D. T. C. Allcock

Contributions

R.S. and H.M.K. carried out the experiments, assisted by S.C.B., D.T.C.A and D.H.S.; D.H.S., R.S., H.M.K., A.K. and R.T.S. analysed the data and performed numerical simulations, with support from E.K. and S.G.; D.T.C.A., D.H.S., R.S., S.C.B. and H.M.K. built and maintained the experimental apparatus; R.S. wrote the manuscript with input from all authors; A.C.W., D.L., D.H.S. and D.J.W. secured funding for the work; and D.H.S. and D.T.C.A. supervised the work with support from A.C.W., D.L., S.G., E.K. and D.J.W.

Corresponding authors

Correspondence to [R. Srinivas](#) or [D. H. Slichter](#).

Ethics declarations

Competing interests

The authors declare no competing interests.

Additional information

Peer review information *Nature* thanks Tracy Northup, Christian Roos and the other, anonymous, reviewer(s) for their contribution to the peer review of this work. Peer reviewer reports are available.

Publisher's note Springer Nature remains neutral with regard to jurisdictional claims in published maps and institutional affiliations.

Supplementary information

Supplementary Information

This file contains Supplementary Sections 1–4, including Supplementary Figs. 1–5, Table 1 and References.

Source Data

This file contains source data for Supplementary Fig. 3.

Source Data

This file contains source data for Supplementary Fig. 4.

Source Data

This file contains source data for Supplementary Fig. 5.

Peer Review File

Rights and permissions

Reprints and Permissions

About this article

Cite this article

Srinivas, R., Burd, S.C., Knaack, H.M. *et al.* High-fidelity laser-free universal control of trapped ion qubits. *Nature* **597**, 209–213 (2021). <https://doi.org/10.1038/s41586-021-03809-4>

- Received: 01 April 2021
- Accepted: 07 July 2021
- Published: 08 September 2021
- Issue Date: 09 September 2021
- DOI: <https://doi.org/10.1038/s41586-021-03809-4>

Laser-free qubit control

- Giulia Pacchioni

In Brief 10 Sept 2021

This article was downloaded by **calibre** from <https://www.nature.com/articles/s41586-021-03809-4>

| [Section menu](#) | [Main menu](#) |

- Article
- [Published: 08 September 2021](#)

Tunable self-assembled Casimir microcavities and polaritons

- [Battulga Munkhbat](#) ORCID: [orcid.org/0000-0002-1923-0960¹](https://orcid.org/0000-0002-1923-0960),
- [Adriana Canales¹](#),
- [Betül Küçüköz¹](#),
- [Denis G. Baranov](#) ORCID: [orcid.org/0000-0002-8071-1587^{1,2}](https://orcid.org/0000-0002-8071-1587) &
- [Timur O. Shegai](#) ORCID: [orcid.org/0000-0002-4266-3721¹](https://orcid.org/0000-0002-4266-3721)

Nature volume **597**, pages 214–219 (2021)

- 2213 Accesses
- 46 Altmetric
- [Metrics details](#)

Subjects

- [Nanocavities](#)
- [Nanoparticles](#)
- [Nanophotonics and plasmonics](#)
- [Quantum mechanics](#)

Abstract

Spontaneous formation of ordered structures—self-assembly—is ubiquitous in nature and observed on different length scales, ranging from atomic and molecular systems to micrometre-scale objects and living matter¹. Self-

ordering in molecular and biological systems typically involves short-range hydrophobic and van der Waals interactions^{2,3}. Here we introduce an approach to micrometre-scale self-assembly based on the joint action of attractive Casimir and repulsive electrostatic forces arising between charged metallic nanoflakes in an aqueous solution. This system forms a self-assembled optical Fabry–Pérot microcavity with a fundamental mode in the visible range (long-range separation distance about 100–200 nanometres) and a tunable equilibrium configuration. Furthermore, by placing an excitonic material in the microcavity region, we are able to realize hybrid light–matter states (polaritons^{4,5,6}), whose properties, such as coupling strength and eigenstate composition, can be controlled in real time by the concentration of ligand molecules in the solution and light pressure. These Casimir microcavities could find future use as sensitive and tunable platforms for a variety of applications, including opto-mechanics⁷, nanomachinery⁸ and cavity-induced polaritonic chemistry⁹.

Access options

Subscribe to Journal

Get full journal access for 1 year

\$199.00

only \$3.90 per issue

[Subscribe](#)

All prices are NET prices.

VAT will be added later in the checkout.

Tax calculation will be finalised during checkout.

Rent or Buy article

Get time limited or full article access on ReadCube.

from \$8.99

[Rent or Buy](#)

All prices are NET prices.

Additional access options:

- [Log in](#)
- [Access through your institution](#)
- [Learn about institutional subscriptions](#)

Fig. 1: The self-assembled microcavity system and the physical mechanism behind its operation.

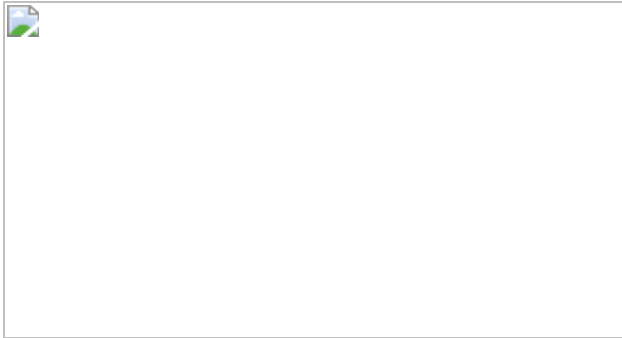


Fig. 2: Self-assembled trimer cavities.



Fig. 3: Self-assembled cavities in nanoflake-on-static-mirror configuration and the formation of polaritons.

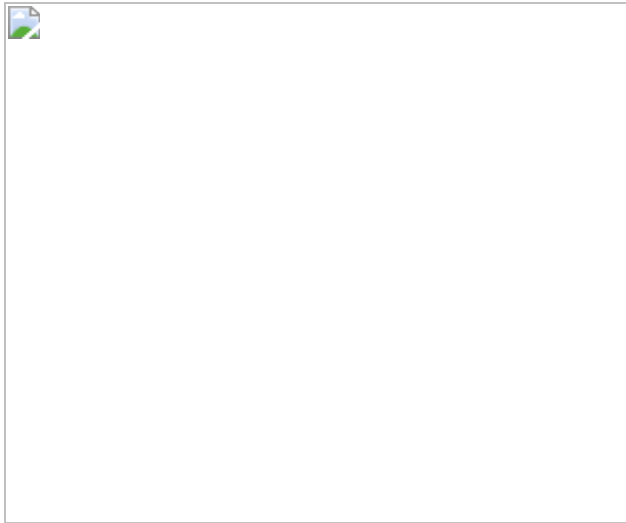


Fig. 4: Actively tunable microcavities and polaritons.



Data availability

The set of experimental and calculated optical spectra, SEM images, optical images and numerical codes are available through figshare.com with the identifier <https://doi.org/10.6084/m9.figshare.14883024.v2>. Additional data are available from T.O.S. upon request.

References

1. 1.

- Whitesides, G. M. & Grzybowski, B. Self-assembly at all scales. *Science* **295**, 2418–2421 (2002).

2. 2.

Min, Y., Akbulut, M., Kristiansen, K., Golan, Y. & Israelachvili, J. in *Nanoscience and Technology: a Collection of Reviews from Nature Journals* (ed. Rodgers, P.) 38–49 (World Scientific/Nature Publishing Group, 2010).

3. 3.

Batista, C. A. S., Larson, R. G. & Kotov, N. A. Nonadditivity of nanoparticle interactions. *Science* **350**, 1242477 (2015).

4. 4.

Khitrova, G., Gibbs, H., Kira, M., Koch, S. W. & Scherer, A. Vacuum Rabi splitting in semiconductors. *Nat. Phys.* **2**, 81–90 (2006).

5. 5.

Törmä, P. & Barnes, W. L. Strong coupling between surface plasmon polaritons and emitters: a review. *Rep. Prog. Phys.* **78**, 013901 (2015).

6. 6.

Baranov, D. G., Wersäll, M., Cuadra, J., Antosiewicz, T. J. & Shegai, T. Novel nanostructures and materials for strong light-matter interactions. *ACS Photon.* **5**, 24–42 (2018).

7. 7.

Eichenfield, M., Camacho, R., Chan, J., Vahala, K. J. & Painter, O. A picogram- and nanometre-scale photonic-crystal optomechanical cavity. *Nature* **459**, 550–555 (2009).

8. 8.

Zhao, R. et al. Stable Casimir equilibria and quantum trapping. *Science* **364**, 984–987 (2019).

9. 9.

Thomas, A. et al. Ground-state chemical reactivity under vibrational coupling to the vacuum electromagnetic field. *Angew. Chem. Int. Edn* **55**, 11462–11466 (2016).

10. 10.

Casimir, H. B. G. On the attraction between two perfectly conducting plates. *Kon. Ned. Akad. Wetensch. Proc.* **51**, 793–795 (1948).

11. 11.

Rodriguez, A. W. et al. Classical and fluctuation-induced electromagnetic interactions in micron-scale systems: designer bonding, antibonding, and Casimir forces. *Ann. Phys.* **527**, 45–80 (2015).

12. 12.

Derjaguin, B. V. & Landau, L. D. Theory of the stability of strongly charged lyophobic sols and of the adhesion of strongly charged particles in solutions of electrolytes. *Acta Physicochim. URSS* **14**, 633–662 (1941).

13. 13.

Verwey, E. J. W. Theory of the stability of lyophobic colloids. *J. Phys. Chem.* **51**, 631–636 (1947).

14. 14.

Lifshitz, E. M. The theory of molecular attractive forces between solids. *Sov. Phys. JETP* **2**, 73–83 (1956).

15. 15.

Dzyaloshinskii, I. E., Lifshitz, E. M. & Pitaevskii, L. P. The general theory of van der Waals forces. *Adv. Phys.* **10**, 165–209 (1961).

16. 16.

van Blokland, P. H. & Overbeek, J. T. G. Van der Waals forces between objects covered with a chromium layer. *J. Chem. Soc. Faraday Trans. I* **74**, 2637–2651 (1978).

17. 17.

Lamoreaux, S. K. Demonstration of the Casimir force in the 0.6 to 6 μm range. *Phys. Rev. Lett.* **78**, 5–8 (1997).

18. 18.

Bressi, G., Carugno, G., Onofrio, R. & Ruoso, G. Measurement of the Casimir force between parallel metallic surfaces. *Phys. Rev. Lett.* **88**, 041804 (2002).

19. 19.

Munday, J. N., Capasso, F. & Parsegian, V. A. Measured long-range repulsive Casimir–Lifshitz forces. *Nature* **457**, 170–173 (2009).

20. 20.

Munday, J. & Capasso, F. Repulsive Casimir and van der Waals forces: from measurements to future technologies. *Int. J. Mod. Phys. A* **25**, 2252–2259 (2010).

21. 21.

Tang, L. et al. Measurement of non-monotonic Casimir forces between silicon nanostructures. *Nat. Photon.* **11**, 97–101 (2017).

22. 22.

Cho, Y. K., Wartena, R., Tobias, S. M. & Chiang, Y.-M. Self-assembling colloidal-scale devices: selecting and using short-range surface forces between conductive solids. *Adv. Funct. Mater.* **17**, 379–389 (2007).

23. 23.

Biggs, S. & Mulvaney, P. Measurement of the forces between gold surfaces in water by atomic force microscopy. *J. Chem. Phys.* **100**, 8501–8505 (1994).

24. 24.

Israelachvili, J. N. *Intermolecular and Surface Forces* (Academic, 2015).

25. 25.

Chen, S. et al. Rapid seedless synthesis of gold nanoplates with microscaled edge length in a high yield and their application in SERS. *Nano-Micro Lett.* **8**, 328–335 (2016).

26. 26.

Li, R. et al. Study on the assembly structure variation of cetyltrimethylammonium bromide on the surface of gold nanoparticles. *ACS Omega* **5**, 4943–4952 (2020).

27. 27.

Liu, Y., Tourbin, M., Lachaize, S. & Guiraud, P. Silica nanoparticles separation from water: aggregation by cetyltrimethylammonium bromide (CTAB). *Chemosphere* **92**, 681–687 (2013).

28. 28.

Chen, F., Mohideen, U., Klimchitskaya, G. & Mostepanenko, V. Demonstration of the lateral Casimir force. *Phys. Rev. Lett.* **88**, 101801 (2002).

29. 29.

Chen, F., Mohideen, U., Klimchitskaya, G. & Mostepanenko, V. Experimental and theoretical investigation of the lateral Casimir force

between corrugated surfaces. *Phys. Rev. A* **66**, 032113 (2002).

30. 30.

Rodrigues, R. B., Neto, P. A. M., Lambrecht, A. & Reynaud, S. Lateral Casimir force beyond the proximity-force approximation. *Phys. Rev. Lett.* **96**, 100402 (2006).

31. 31.

Meyer, M., Le Ru, E. & Etchegoin, P. Self-limiting aggregation leads to long-lived metastable clusters in colloidal solutions. *J. Phys. Chem. B* **110**, 6040–6047 (2006).

32. 32.

Junginger, A. et al. Tunable strong coupling of two adjacent optical $\lambda/2$ Fabry-Pérot microresonators. *Opt. Express* **28**, 485–493 (2020).

33. 33.

Berkhout, A., Wolterink, T. A. & Koenderink, A. F. Strong coupling to generate complex birefringence: metasurface in the middle etalons. *ACS Photon.* **7**, 2799 (2020).

34. 34.

Li, Y. et al. Measurement of the optical dielectric function of monolayer transition-metal dichalcogenides: MoS₂, MoSe₂, WS₂, and WSe₂. *Phys. Rev. B* **90**, 205422 (2014).

35. 35.

Gatemala, H., Pienpinijtham, P., Thammacharoen, C. & Ekgasit, S. Rapid fabrication of silver microplates under an oxidative etching environment consisting of O₂/Cl⁻, NH₄OH/H₂O₂, and H₂O₂. *CrystEngComm* **17**, 5530–5537 (2015).

36. 36.

Castellanos-Gomez, A. et al. Deterministic transfer of two-dimensional materials by all-dry viscoelastic stamping. *2D Mater.* **1**, 011002 (2014).

37. 37.

Shegai, T., Brian, B., Miljkovic, V. D. & Käll, M. Angular distribution of surface-enhanced Raman scattering from individual au nanoparticle aggregates. *ACS Nano* **5**, 2036–2041 (2011).

38. 38.

Lifshitz, E. M. et al. in *Perspectives in Theoretical Physics* (ed. Pitaevski, L. P.) 329–349 (Elsevier, 1992).

39. 39.

Johnson, P. B. & Christy, R.-W. Optical constants of the noble metals. *Phys. Rev. B* **6**, 4370 (1972).

40. 40.

Segelstein, D. *The Complex Refractive Index of Water*. MSc thesis, Univ. Missouri (1981).

41. 41.

Kadirov, M. K., Litvinov, A. I., Nizameev, I. R. & Zakharova, L. Y. Adsorption and premicellar aggregation of CTAB molecules and fabrication of nanosized platinum lattice on the glass surface. *J. Phys. Chem. C* **118**, 19785–19794 (2014).

Acknowledgements

The authors acknowledge K. Eliasson for help with Raman measurements, as well as E. Tornéus, A. B. Yankovich, P. Erhart and M. Käll for

stimulating discussions. The authors acknowledge financial support from the Swedish Research Council (under the VR Miljö project, grant no. 2016-06059 to T.O.S; and the VR project, grant no. 2017-04545 to T.O.S), the Knut and Alice Wallenberg Foundation (project no. 2019.0140 to T.O.S.), and the Chalmers Excellence Initiative Nano.

Author information

Affiliations

1. Department of Physics, Chalmers University of Technology, Gothenburg, Sweden

Battulga Munkhbat, Adriana Canales, Betül Küçüköz, Denis G. Baranov & Timur O. Shegai

2. Center for Photonics and 2D Materials, Moscow Institute of Physics and Technology, Dolgoprudny, Russia

Denis G. Baranov

Contributions

B.M. and T.O.S. conceived the idea. B.M. fabricated the samples. B.M. and A.C. performed optical measurements. B.M. and B.K. investigated active tuning of the structures. D.G.B. performed theoretical analysis of the experimental data. B.M., D.G.B. and T.O.S. wrote the manuscript with input from all co-authors. T.O.S. supervised the study.

Corresponding author

Correspondence to [Timur O. Shegai](#).

Ethics declarations

Competing interests

The authors declare no competing interests.

Additional information

Peer review information *Nature* thanks Jeremy Munday and the other, anonymous, reviewer(s) for their contribution to the peer review of this work. Peer reviewer reports are available.

Publisher's note Springer Nature remains neutral with regard to jurisdictional claims in published maps and institutional affiliations.

Supplementary information

Supplementary Information

This file contains Supplementary Notes 1 – 5, Supplementary Text, Supplementary Figures 1 – 25, Supplementary Tables 1 – 3, legends for Supplementary Videos 1 – 6 and Supplementary References.

Supplementary Video 1

A stable gold nanoflake dimer as well as formation of a dimer.

Supplementary Video 2

Relative displacement of top and bottom nanoflakes within a self-assembled dimer along x and y directions as a function of time. Note that while flakes can move and rotate with respect to each other, their relative displacement is always small in comparison to the lateral size of the flakes. This indicated the dimer stability not only in vertical, but also in lateral directions.

Supplementary Video 3

A stable gold nanoflake trimer.

Supplementary Video 4

Relative displacement of top, middle, and bottom nanoflakes within a trimer along x and y directions as a function of time. This video shows that the self-assembled trimer exhibits an equilibrium not only in vertical direction, but also in lateral directions.

Supplementary Video 5

Additional examples of stable self-assembled multi-stacks of gold nanoflakes.

Supplementary Video 6

Additional examples of stable self-assembled multi-stacks of gold nanoflakes.

Peer Review File

Rights and permissions

Reprints and Permissions

About this article

Cite this article

Munkhbat, B., Canales, A., Küçüköz, B. *et al.* Tunable self-assembled Casimir microcavities and polaritons. *Nature* **597**, 214–219 (2021).
<https://doi.org/10.1038/s41586-021-03826-3>

- Received: 16 March 2021
- Accepted: 15 July 2021
- Published: 08 September 2021
- Issue Date: 09 September 2021

- DOI: <https://doi.org/10.1038/s41586-021-03826-3>

Hybrid light–matter states formed in self-assembling cavities

- Johannes Feist

News & Views 08 Sept 2021

This article was downloaded by **calibre** from <https://www.nature.com/articles/s41586-021-03826-3>

| [Section menu](#) | [Main menu](#) |

- Article
- [Published: 08 September 2021](#)

Transmembrane transport in inorganic colloidal cell-mimics

- [Zhe Xu ORCID: orcid.org/0000-0002-8599-079X¹](#),
- [Theodore Hueckel¹](#),
- [William T. M. Irvine ORCID: orcid.org/0000-0002-4925-2060²](#) &
- [Stefano Sacanna ORCID: orcid.org/0000-0002-8399-3524¹](#)

[Nature](#) volume 597, pages 220–224 (2021)

- 2678 Accesses
- 342 Altmetric
- [Metrics details](#)

Subjects

- [Colloids](#)
- [Self-assembly](#)

Abstract

A key aspect of living cells is their ability to harvest energy from the environment and use it to pump specific atomic and molecular species in and out of their system—typically against an unfavourable concentration gradient¹. Active transport allows cells to store metabolic energy, extract waste and supply organelles with basic building blocks at the submicrometre scale. Unlike living cells, abiotic systems do not have the

delicate biochemical machinery that can be specifically activated to precisely control biological matter^{2,3,4,5}. Here we report the creation of microcapsules that can be brought out of equilibrium by simple global variables (illumination and pH), to capture, concentrate, store and deliver generic microscopic payloads. Borrowing no materials from biology, our design uses hollow colloids serving as spherical cell-membrane mimics, with a well-defined single micropore. Precisely tunable monodisperse capsules are the result of a synthetic self-inflation mechanism and can be produced in bulk quantities. Inside the hollow unit, a photoswitchable catalyst⁶ produces a chemical gradient that propagates to the exterior through the membrane's micropore and pumps target objects into the cell, acting as a phoretic tractor beam⁷. An entropic energy barrier^{8,9} brought about by the micropore's geometry retains the cargo even when the catalyst is switched off. Delivery is accomplished on demand by reversing the sign of the phoretic interaction. Our findings provide a blueprint for developing the next generation of smart materials, autonomous micromachinery and artificial cell-mimics.

Access options

Subscribe to Journal

Get full journal access for 1 year

\$199.00

only \$3.90 per issue

[Subscribe](#)

All prices are NET prices.

VAT will be added later in the checkout.

Tax calculation will be finalised during checkout.

Rent or Buy article

Get time limited or full article access on ReadCube.

from \$8.99

[Rent or Buy](#)

All prices are NET prices.

Additional access options:

- [Log in](#)
- [Access through your institution](#)
- [Learn about institutional subscriptions](#)

Fig. 1: Self-inflating droplets.

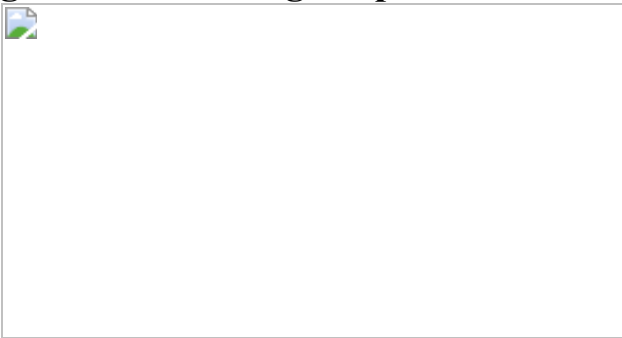


Fig. 2: Tunable mechanical properties.

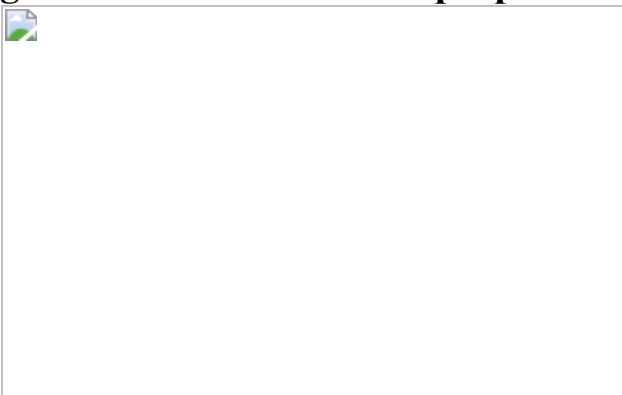


Fig. 3: Micropore fabrication.

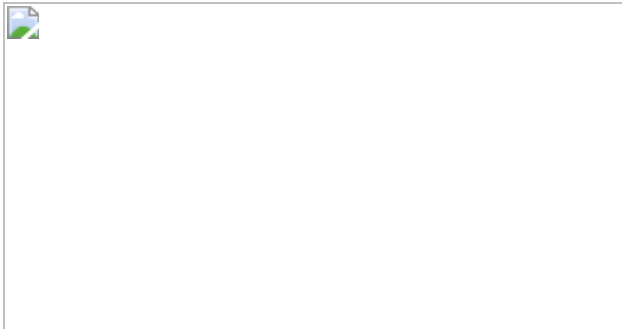
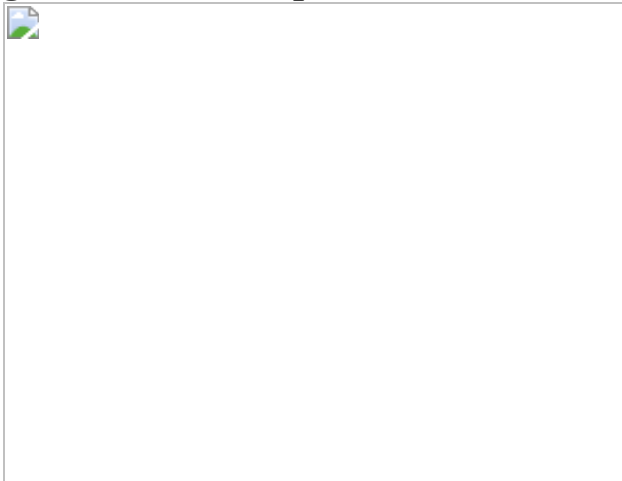


Fig. 4: Active transport.



Data availability

The data that support the findings of this study are available from the corresponding authors on request.

References

1. 1.

Skou, J. C. & Esmann, M. The Na,K-ATPase. *J. Bioenerg. Biomembr.* **24**, 249–261 (1992).

2. 2.

Shang, L. & Zhao, Y. Droplet-templated synthetic cells. *Matter* **4**, 95–115 (2021).

3. 3.

Rodríguez-Arco, L., Li, M. & Mann, S. Phagocytosis-inspired behaviour in synthetic protocell communities of compartmentalized colloidal objects. *Nat. Mater.* **16**, 857–863 (2017).

4. 4.

Rideau, E., Dimova, R., Schwille, P., Wurm, F. R. & Landfester, K. Liposomes and polymersomes: a comparative review towards cell mimicking. *Chem. Soc. Rev.* **47**, 8572–8610 (2018).

5. 5.

Dinsmore, A. D. et al. Colloidosomes: selectively permeable capsules composed of colloidal particles. *Science* **298**, 1006–1009 (2002).

6. 6.

Sugimoto, T., Khan, M. M. & Muramatsu, A. Preparation of monodisperse peanut-type α -Fe₂O₃ particles from condensed ferric hydroxide gel. *Colloids Surf. A* **70**, 167–169 (1993).

7. 7.

Palacci, J. et al. Light-activated self-propelled colloids. *Philos. Trans. R. Soc. A* **372**, 20130372 (2014).

8. 8.

Cheng, K. L., Sheng, Y. J. & Tsao, H. K. Brownian escape and force-driven transport through entropic barriers: particle size effect. *J. Chem. Phys.* **129**, 184901 (2008).

9. 9.

Grigoriev, I. V., Makhnovskii, Y. A., Berezhkovskii, A. M. & Zitserman, V. Y. Kinetics of escape through a small hole. *J. Chem. Phys.* **116**, 9574–9577 (2002).

10. 10.

Wadhams, G. H. & Armitage, J. P. Making sense of it all: bacterial chemotaxis. *Nat. Rev. Mol. Cell Biol.* **5**, 1024–1037 (2004).

11. 11.

Tweedy, L. et al. Seeing around corners: cells solve mazes and respond at a distance using attractant breakdown. *Science* **369**, eaay9792 (2020).

12. 12.

Taylor, J. W., Eghtesadi, S. A., Points, L. J., Liu, T. & Cronin, L. Autonomous model protocell division driven by molecular replication. *Nat. Commun.* **8**, 237 (2017).

13. 13.

Zhu, T. F., Adamala, K., Zhang, N. & Szostak, J. W. Photochemically driven redox chemistry induces protocell membrane pearling and division. *Proc. Natl Acad. Sci. USA* **109**, 9828–9832 (2012).

14. 14.

Zhu, T. F. & Szostak, J. W. Coupled growth and division of model protocell membranes. *J. Am. Chem. Soc.* **131**, 5705–5713 (2009).

15. 15.

Yewdall, N. A., Mason, A. F. & van Hest, J. C. M. The hallmarks of living systems: towards creating artificial cells. *Interface Focus* **8**, 20180023 (2018).

16. 16.

Yang, Z., Wei, J., Sobolev, Y. I. & Grzybowski, B. A. Systems of mechanized and reactive droplets powered by multi-responsive surfactants. *Nature* **553**, 313–318 (2018).

17. 17.

Qiao, Y., Li, M., Booth, R. & Mann, S. Predatory behaviour in synthetic protocell communities. *Nat. Chem.* **9**, 110–119 (2017).

18. 18.

Yin, Y. et al. Non-equilibrium behaviour in coacervate-based protocells under electric-field-induced excitation. *Nat. Commun.* **7**, 10658 (2016).

19. 19.

Fujii, S., Matsuura, T., Sunami, T., Kazuta, Y. & Yomo, T. In vitro evolution of α -hemolysin using a liposome display. *Proc. Natl Acad. Sci. USA* **110**, 16796–16801 (2013).

20. 20.

Li, G., Wang, L., Ni, H. & Pittman, C. U. Polyhedral oligomeric silsesquioxane (POSS) polymers and copolymers: a review. *J. Inorg. Organomet. Polym. Mater.* **11**, 123–154 (2001).

21. 21.

van der Wel, C. et al. Preparation of colloidal organosilica spheres through spontaneous emulsification. *Langmuir* **33**, 8174–8180 (2017).

22. 22.

Okubo, M., Kobayashi, H., Huang, C., Miyanaga, E. & Suzuki, T. Water absorption behavior of polystyrene particles prepared by emulsion polymerization with nonionic emulsifiers and innovative easy synthesis of hollow particles. *Langmuir* **33**, 3468–3475 (2017).

23. 23.

Shi, H., Huang, C., Liu, X. & Okubo, M. Role of osmotic pressure for the formation of sub-micrometer-sized, hollow polystyrene particles by

heat treatment in aqueous dispersed systems. *Langmuir* **35**, 12150–12157 (2019).

24. 24.

Kim, S. H., Park, J. G., Choi, T. M., Manoharan, V. N. & Weitz, D. A. Osmotic-pressure-controlled concentration of colloidal particles in thin-shelled capsules. *Nat. Commun.* **5**, 3068 (2014).

25. 25.

Sillett, E. V., Xu, Z., Youssef, M., Sacanna, S. & Jerschow, A. Monitoring molecular transport across colloidal membranes. *J. Phys. Chem. B* **122**, 4931–4936 (2018).

26. 26.

Datta, S. S. et al. Delayed buckling and guided folding of inhomogeneous capsules. *Phys. Rev. Lett.* **109**, 134302 (2012).

27. 27.

Opdam, J., Tuinier, R., Hueckel, T., Snoeren, T. J. & Sacanna, S. Selective colloidal bonds via polymer-mediated interactions. *Soft Matter* **16**, 7438–7446 (2020).

28. 28.

Kim, S. H., Shim, J. W., Lim, J. M., Lee, S. Y. & Yang, S. M. Microfluidic fabrication of microparticles with structural complexity using photocurable emulsion droplets. *New J. Phys.* **11**, 075014 (2009).

29. 29.

Hyuk Im, S., Jeong, U. & Xia, Y. Polymer hollow particles with controllable holes in their surfaces. *Nat. Mater.* **4**, 671–675 (2005).

30. 30.

Qiu, J. et al. Encapsulation of a phase-change material in nanocapsules with a well-defined hole in the wall for the controlled release of drugs. *Angew. Chem. Int. Edn Engl.* **58**, 10606–10611 (2019).

31. 31.

Sacanna, S. et al. Shaping colloids for self-assembly. *Nat. Commun.* **4**, 1688 (2013).

32. 32.

Kar, A., Chiang, T. Y., Ortiz Rivera, I., Sen, A. & Velegol, D. Enhanced transport into and out of dead-end pores. *ACS Nano* **9**, 746–753 (2015).

33. 33.

Kuijk, A., van Blaaderen, A. & Imhof, A. Synthesis of monodisperse, rodlike silica colloids with tunable aspect ratio. *J. Am. Chem. Soc.* **133**, 2346–2349 (2011).

Acknowledgements

This research was primarily supported by the US Army Research Office under award number W911NF2010117. S.S. acknowledges additional support from Kairos Ventures. W.T.M.I. acknowledges additional support from the Packard Foundation and the Brown Science Foundation. We thank T. Islam, M. Youssef, R. Bahn and M. Weigl for exploratory synthetic work, and L. Mahal for providing the *E. coli* sample.

Author information

Affiliations

1. Molecular Design Institute, Department of Chemistry, New York University, New York, NY, USA

Zhe Xu, Theodore Hueckel & Stefano Sacanna

2. James Franck Institute, Enrico Fermi Institute, Department of Physics,
University of Chicago, Chicago, IL, USA

William T. M. Irvine

Contributions

Z.X. designed the cell-mimic synthetic protocol, synthesized all the colloidal systems and performed the active transport experiments. T.H. discovered the self-inflation mechanism and performed the preliminary synthetic work. S.S. conceived the study. S.S. and W.T.M.I. supervised and directed research. All authors analysed data, discussed the results and commented on the manuscript.

Corresponding authors

Correspondence to [William T. M. Irvine](#) or [Stefano Sacanna](#).

Ethics declarations

Competing interests

The authors declare no competing interests.

Additional information

Peer review information *Nature* thanks Yuanjin Zhao and the other, anonymous, reviewer(s) for their contribution to the peer review of this work.

Publisher's note Springer Nature remains neutral with regard to jurisdictional claims in published maps and institutional affiliations.

Extended data figures and tables

Extended Data Fig. 1 Functional emulsions.

a, Silsesquioxanes-based emulsions form via hydrolytic condensation of functionalized trialkoxysilane molecules (oil precursor). **b**, Monodispersed droplets nucleate upon the addition of ammonia and grow over time until the precursor is fully consumed. The cross-linking density of the newly formed oil-phase increases with the emulsion age τ , which is defined as the time passed from the addition of ammonia to the sample (nucleation). Ageing manifests with an increase of the oil-air contact angle formed by oil droplets resting on a clean silicon substrate (SEM images, right). **c**, The droplets can be fully cured by UV polymerization, resulting in a suspension of solid microspheres. Scale bars, 1 μm .

Extended Data Fig. 2 Self-inflation process.

a, b, Chemically induced osmotic pressure Π_i transforms primed emulsion droplets (**a**) into expanding vesicles (**b**). The osmotic pressure is generated by charged monomers produced by the reaction between NaOH and the TPM oil phase. **c**, Expanding vesicles can be fixed via UV polymerization, resulting in solid capsules. Scale bars, 2 μm .

Extended Data Fig. 3 Full synthetic roadmap to self-inflating microcapsules.

a, b, The schematic shows an overview of the microcapsule fabrication process and highlights key steps. NaOH can be added to the emulsion droplets at any time τ during their ageing process (**b**). The droplets' response, however, depends on both τ and the NaOH concentration, as shown in Fig. [1c](#). Panels **a** and **b** are described in detail in Extended Data Figs. [1](#) and [2](#), respectively.

Extended Data Fig. 4 Buckling behaviour.

a–c, SEM images showing the three characteristic responses that we observed during the osmotic stress experiments in Fig. [2e](#). In Fig. [2](#), we refer to these responses as (**a**) intact, (**b**) mode 2 and (**c**) mode 1. We studied

11 different capsule geometries each tested against 9 different osmotic pressures. Within each sample, >90% of the capsules responded in the same manner. Scale bars, 2 μm .

Extended Data Fig. 5 Tunable micropores.

SEM images of cell-mimics displaying micropores in a wide range of sizes. Scale bar, 2 μm .

Extended Data Fig. 6 Growth and ageing of TPM droplets.

We characterize the emulsions by measuring the diameter of the droplets and the oil–air contact angle θ of the droplets on a silicon substrate. The graph shows a typical emulsion behaviour where θ increases monotonically with the droplet age τ , while their diameter reaches a maximum within 1 h from nucleation. Error bars, ± 1 s.d.

Extended Data Fig. 7 Quantitative model of self-inflation.

The extent of the inflation for a forming vesicle can be predicted by balancing osmotic pressure and surface tension (solid line). The model is built assuming that the vesicle have a constant volume of oil and a fixed number of molecular species inside contributing to Π_i . The experimental points are measurements of the vesicles size at different external osmotic pressures Π_e . Radii are measured by SEM after polymerization and corrected for the relative density change (7% increase after polymerization²¹). Π_e is adjusted using NaCl. R_0 , radius of the oil droplets measured before inflation. Error bars, ± 1 s.d. Scale bars, 3 μm .

Extended Data Fig. 8 Ingestion of nanoparticles.

Optical microscopy time-lapse showing cell-mimics ingesting 450 nm (**a**) and 300 nm (**b**) PS tracers. In both experiments, the cell-mimic has a micropore of 1.1 μm . Scale bars are 1 μm .

Supplementary information

Self-inflation of emulsion droplets

SI Video 1: . Video microscopy illustrating the self-inflation process. TPM emulsion droplets transform into vesicles upon exposure to NaOH

Ingestion of PS spheres

SI Video 2: . Video microscopy showing cell mimics ingesting, holding and expelling PS tracers. (The video has been sped up by ~2 times)

Ingestion of E.coli

SI Video 3: . Video microscopy showing cell mimics ingesting E.coli. (The video has been sped up by ~2 times)

Ingestion of silica rods

SI Video 4: . Video microscopy showing cell mimics ingesting silica rods. (The video has been sped up by ~2 times)

Rights and permissions

Reprints and Permissions

About this article

Cite this article

Xu, Z., Hueckel, T., Irvine, W.T.M. *et al.* Transmembrane transport in inorganic colloidal cell-mimics. *Nature* **597**, 220–224 (2021).
<https://doi.org/10.1038/s41586-021-03774-y>

- Received: 21 January 2021

- Accepted: 28 June 2021
 - Published: 08 September 2021
 - Issue Date: 09 September 2021
 - DOI: <https://doi.org/10.1038/s41586-021-03774-y>
-

This article was downloaded by **calibre** from <https://www.nature.com/articles/s41586-021-03774-y>.

| [Section menu](#) | [Main menu](#) |

- Article
- [Published: 08 September 2021](#)

Widespread woody plant use of water stored in bedrock

- [Erica L. McCormick](#) ORCID: [orcid.org/0000-0002-7160-398X¹](https://orcid.org/0000-0002-7160-398X),
- [David N. Dralle](#) ORCID: [orcid.org/0000-0002-1944-2103²](https://orcid.org/0000-0002-1944-2103),
- [W. Jesse Hahm³](#),
- [Alison K. Tune](#) ORCID: [orcid.org/0000-0003-1870-4981¹](https://orcid.org/0000-0003-1870-4981),
- [Logan M. Schmidt¹](#),
- [K. Dana Chadwick](#) ORCID: [orcid.org/0000-0002-5633-4865¹](https://orcid.org/0000-0002-5633-4865) &
- [Daniella M. Rempe¹](#)

[Nature](#) volume 597, pages 225–229 (2021)

- 845 Accesses
- 58 Altmetric
- [Metrics details](#)

Subjects

- [Forest ecology](#)
- [Hydrology](#)

Abstract

In the past several decades, field studies have shown that woody plants can access substantial volumes of water from the pores and fractures of bedrock^{1,2,3}. If, like soil moisture, bedrock water storage serves as an

important source of plant-available water, then conceptual paradigms regarding water and carbon cycling may need to be revised to incorporate bedrock properties and processes^{4,5,6}. Here we present a lower-bound estimate of the contribution of bedrock water storage to transpiration across the continental United States using distributed, publicly available datasets. Temporal and spatial patterns of bedrock water use across the continental United States indicate that woody plants extensively access bedrock water for transpiration. Plants across diverse climates and biomes access bedrock water routinely and not just during extreme drought conditions. On an annual basis in California, the volumes of bedrock water transpiration exceed the volumes of water stored in human-made reservoirs, and woody vegetation that accesses bedrock water accounts for over 50% of the aboveground carbon stocks in the state. Our findings indicate that plants commonly access rock moisture, as opposed to groundwater, from bedrock and that, like soil moisture, rock moisture is a critical component of terrestrial water and carbon cycling.

Access options

Subscribe to Journal

Get full journal access for 1 year

\$199.00

only \$3.90 per issue

[Subscribe](#)

All prices are NET prices.

VAT will be added later in the checkout.

Tax calculation will be finalised during checkout.

Rent or Buy article

Get time limited or full article access on ReadCube.

from \$8.99

[Rent or Buy](#)

All prices are NET prices.

Additional access options:

- [Log in](#)
- [Access through your institution](#)
- [Learn about institutional subscriptions](#)

Fig. 1: Over 45% of the wooded land area across the CONUS is underlain by shallow (<1.5 m deep) bedrock.

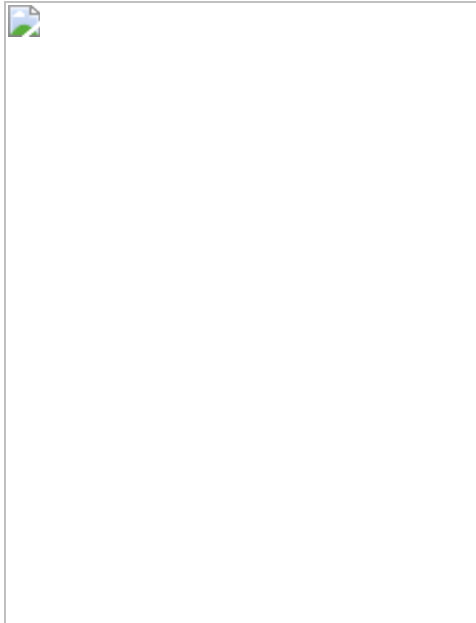


Fig. 2: Bedrock water use by woody plants is spatially extensive and can be routine.

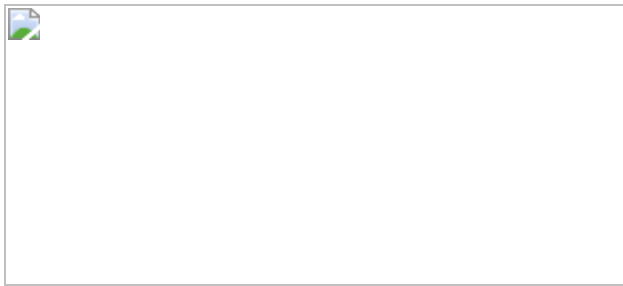


Fig. 3: Magnitude of bedrock water contribution to ET across Texas, California and field studies.

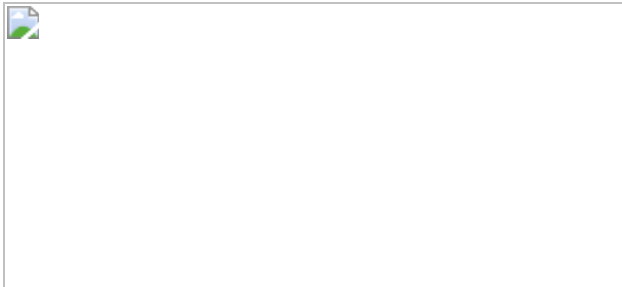


Fig. 4: Bedrock hosts a large fraction of root-zone water storage capacity.



Data availability

All of the datasets generated in this study are available in the Hydroshare repository at

[https://doi.org/10.4211/hs.a2f0d5fd10f14cd189a3465f72cba6f3⁵¹](https://doi.org/10.4211/hs.a2f0d5fd10f14cd189a3465f72cba6f3). The precipitation data are available from the PRISM Climate Group⁵⁶ at <https://prism.oregonstate.edu/>. The evapotranspiration data are available from Penman–Monteith–Leuning Evapotranspiration V2 (PML_V2)⁵⁸ at https://github.com/gee-hydro/gee_PML. The snow cover data are available from NASA’s MODIS/Terra Snow Cover Daily⁶⁴ at <https://nsidc.org/data/MOD10A1/versions/6>. The soil data are available from the USDA’s gNATSGO⁴¹ database at <https://www.nrcs.usda.gov/wps/portal/nrcs/detail/soils/survey/geo/?cid=nrcseprd1464625> and in the Hydroshare repository. The landcover data are available from the USGS’s National Land Cover Database⁴⁰ at

https://www.usgs.gov/centers/eros/science/national-land-cover-database?qt-science_center_objects=0#qt-science_center_objects. The biome data are available from NASA's MODIS/Terra+Aqua Land Cover Type Yearly⁶⁵ at <https://lpdaac.usgs.gov/products/mcd12q1v006/>. The Köppen⁶⁶ climate data are available at <https://people.eng.unimelb.edu.au/mpeel/koppen.html>. The above ground biomass¹⁹ data are available at https://daac.ornl.gov/VEGETATION/guides/Global_Maps_C_Density_2010.html. With the exception of the gNATSGO and aboveground biomass data, all of the raster datasets are accessible via Google Earth Engine⁶². Google Earth Engine access URLs can be found in the code accompanying this study (see Code Part 2, Section 1). [Source data](#) are provided with this paper.

Code availability

Codes are available from <https://github.com/erica-mccormick/widespread-bedrock-water-use> or <https://doi.org/10.5281/zenodo.4904036>.

References

1. 1.
Schwinning, S. The ecohydrology of roots in rocks. *Ecohydrology* **3**, 238–245 (2010).
2. 2.
Rose, K., Graham, R. & Parker, D. Water source utilization by *Pinus jeffreyi* and *Arctostaphylos patula* on thin soils over bedrock. *Oecologia* **134**, 46–54 (2003).
3. 3.
Rempe, D. M. & Dietrich, W. E. Direct observations of rock moisture, a hidden component of the hydrologic cycle. *Proc. Natl Acad. Sci. USA* **115**, 2664–2669 (2018).

4. 4.

Schwinning, S. A critical question for the critical zone: how do plants use rock water? *Plant Soil* **454**, 49–56 (2020).

5. 5.

Fan, Y. et al. Hillslope hydrology in global change research and Earth system modeling. *Wat. Resour. Res.* **55**, 1737–1772 (2019).

6. 6.

Brantley, S. L. et al. Reviews and syntheses: on the roles trees play in building and plumbing the critical zone. *Biogeosciences* **14**, 5115–5142 (2017).

7. 7.

Chaney, N. W. et al. POLARIS soil properties: 30-m probabilistic maps of soil properties over the contiguous United States. *Wat. Resour. Res.* **55**, 2916–2938 (2019).

8. 8.

Uhlig, D., Schuessler, J. A., Bouchez, J., Dixon, J. L. & Blanckenburg, F. V. Quantifying nutrient uptake as driver of rock weathering in forest ecosystems by magnesium stable isotopes. *Biogeosciences* **14**, 3111–3128 (2017).

9. 9.

Wald, J. A., Graham, R. C. & Schoeneberger, P. J. Distribution and properties of soft weathered bedrock at 1 m depth in the contiguous United States. *Earth Surf. Process. Landf.* **38**, 614–626 (2013).

10. 10.

Nimmo, J. R., Creasey, K. M., Perkins, K. S. & Mirus, B. B. Preferential flow, diffuse flow, and perching in an interbedded

fractured-rock unsaturated zone. *Hydrogeol. J.* **25**, 421–444 (2017).

11. 11.

Leshem, B. Resting roots of *Pinus halepensis*: structure, function, and reaction to water stress. *Bot. Gaz.* **131**, 99–104 (1970).

12. 12.

Hahm, W. J. et al. Low subsurface water storage capacity relative to annual rainfall decouples Mediterranean plant productivity and water use from rainfall variability. *Geophys. Res. Lett.* **46**, 6544–6553 (2019).

13. 13.

Hahm, W. J. et al. Lithologically controlled subsurface critical zone thickness and water storage capacity determine regional plant community composition. *Wat. Resour. Res.* **55**, 3028–3055 (2019).

14. 14.

Eggemeyer, K. D. & Schwinnig, S. Biogeography of woody encroachment: why is mesquite excluded from shallow soils? *Ecohydrology* **2**, 81–87 (2009).

15. 15.

Madakumbura, G. D. et al. Recent California tree mortality portends future increase in drought-driven forest die-off. *Environ. Res. Lett.* **15**, 124040 (2020).

16. 16.

McDowell, N. G. et al. Mechanisms of a coniferous woodland persistence under drought and heat. *Environ. Res. Lett.* **14**, 045014 (2019).

17. 17.

McEvoy, D. J., Pierce, D. W., Kalansky, J. F., Cayan, D. R. & Abatzoglou, J. T. Projected changes in reference evapotranspiration in California and Nevada: implications for drought and wildland fire danger. *Earth's Future* **8**, e2020EF001736 (2020).

18. 18.

Hauwert, N. M. & Sharp, J. M. Measuring autogenic recharge over a karst aquifer utilizing eddy covariance evapotranspiration. *J. Water Resour. Prot.* **6**, 869–879 (2014).

19. 19.

Spawn, S. A., Sullivan, C. C., Lark, T. J. & Gibbs, H. K. Harmonized global maps of above and belowground biomass carbon density in the year 2010. *Sci. Data* **7**, 112 (2020).

20. 20.

Goulden, M. L. & Bales, R. C. California forest die-off linked to multi-year deep soil drying in 2012–2015 drought. *Nat. Geosci.* **12**, 632–637 (2019).

21. 21.

Hahm, W. J. et al. Oak transpiration drawn from the weathered bedrock vadose zone in the summer dry season. *Wat. Resour. Res.* **56**, e2020WR027419 (2020).

22. 22.

Cannon, W. A. *The Root Habits of Desert Plants* 131 (Carnegie Institute of Washington, 1911).

23. 23.

Daily reservoir storage summary. *California Department of Water Resources* <https://info.water.ca.gov/cgi-progs/reservoirs/RES> (2020).

24. 24.

USGS water use data for California. *United States Geological Society* https://waterdata.usgs.gov/ca/nwis/water_use/ (2020).

25. 25.

David, T., Ferreira, M., Cohen, S., Pereira, J. & David, J. Constraints on transpiration from an evergreen oak tree in southern Portugal. *Agric. For. Meteorol.* **122**, 193–205 (2004).

26. 26.

Querejeta, J. I., Estrada-Medina, H., Allen, M. F. & Jimenez-Osornio, J. J. Water source partitioning among trees growing on shallow karst soils in a seasonally dry tropical climate. *Oecologia* **152**, 26–36 (2007).

27. 27.

Carrière, S. D. et al. The role of deep vadose zone water in tree transpiration during drought periods in karst settings—insights from isotopic tracing and leaf water potential. *Sci. Total Environ.* **699**, 134332 (2020).

28. 28.

Rambal, S. Water balance and pattern of root water uptake by a *Quercus coccifera* L. evergreen scrub. *Oecologia* **62**, 18–25 (1984).

29. 29.

Montaldo, N. et al. Rock water as a key resource for patchy ecosystems on shallow soils: digging deep tree clumps subsidize surrounding surficial grass. *Earths Future* **9**, e2020EF001870 (2021).

30. 30.

Corona, R. & Montaldo, N. On the transpiration of wild olives under water-limited conditions in a heterogeneous ecosystem with shallow soil over fractured rock. *J. Hydrol. Hydromech.* **68**, 338–350 (2020).

31. 31.

Nardini, A. et al. Water ‘on the rocks’: a summer drink for thirsty trees? *New Phytol.* **229**, 199–212 (2021).

32. 32.

Ruiz, L. et al. Water balance modelling in a tropical watershed under deciduous forest (Mule Hole, India): regolith matric storage buffers the groundwater recharge process. *J. Hydrol.* **380**, 460–472 (2010).

33. 33.

Ding, Y., Nie, Y., Chen, H., Wang, K. & Querejeta, J. I. Water uptake depth is coordinated with leaf water potential, water-use efficiency and drought vulnerability in karst vegetation. *New Phytol.* **229**, 1339–1353 (2021).

34. 34.

Dawson, T. E., Hahm, W. J. & Crutchfield-Peters, K. Digging deeper: what the critical zone perspective adds to the study of plant ecophysiology. *New Phytol.* **226**, 666–671 (2020).

35. 35.

Salve, R., Rempe, D. M. & Dietrich, W. E. Rain, rock moisture dynamics, and the rapid response of perched groundwater in weathered, fractured argillite underlying a steep hillslope. *Wat. Resour. Res.* **48**, W11528 (2012).

36. 36.

Harsch, M. A., Hulme, P. E., McGlone, M. S. & Duncan, R. P. Are treelines advancing? A global meta-analysis of treeline response to

climate warming. *Ecol. Lett.* **12**, 1040–1049 (2009).

37. 37.

Kapnick, S. & Hall, A. Causes of recent changes in western North American snowpack. *Clim. Dyn.* **38**, 1885–1899 (2012).

38. 38.

Tune, A. K., Druhan, J. L., Wang, J., Bennett, P. C. & Rempe, D. M. Carbon dioxide production in bedrock beneath soils substantially contributes to forest carbon cycling. *J. Geophys. Res. Biogeosci.* **125**, e2020JG005795 (2020).

39. 39.

Hasenmueller, E. A. et al. Weathering of rock to regolith: the activity of deep roots in bedrock fractures. *Geoderma* **300**, 11–31 (2017).

40. 40.

Yang, L. et al. A new generation of the United States National Land Cover Database: requirements, research priorities, design, and implementation strategies. *ISPRS J. Photogramm. Remote Sens.* **146**, 108–123 (2018).

41. 41.

Soil Survey Staff *Gridded National Soil Survey Geographic (gNATSGO) Database for the Conterminous United States* (USDA, 2019); <https://nrcs.app.box.com/v/soils>

42. 42.

QGIS Development Team *QGIS Geographic Information System* (Open Source Geospatial Foundation, 2019); <http://qgis.org>

43. 43.

O'Geen, A. T. et al. Southern Sierra Critical Zone Observatory and Kings River Experimental Watersheds: a synthesis of measurements, new insights, and future directions. *Vadose Zone J.* **17**, 180081 (2018).

44. 44.

Anderson, M. A., Graham, R. C., Alyanakian, G. J. & Martynn, D. Z. Late summer water status of soils and weathered bedrock in a giant sequoia grove. *Soil Sci.* **160**, 415–422 (1995).

45. 45.

Hubbert, K. R., Graham, R. C. & Anderson, M. A. Soil and weathered bedrock: components of a Jeffrey pine plantation substrate. *Soil Sci. Soc. Am. J.* **65**, 1255–1262 (2001).

46. 46.

Bornyasz, M., Graham, R. & Allen, M. Ectomycorrhizae in a soil-weathered granitic bedrock regolith: linking matrix resources to plants. *Geoderma* **126**, 141–160 (2005).

47. 47.

Sternberg, P., Anderson, M., Graham, R., Beyers, J. & Tice, K. Root distribution and seasonal water status in weathered granitic bedrock under chaparral. *Geoderma* **72**, 89–98 (1996).

48. 48.

Graham, R. C., Sternberg, P. D. & Tice, K. R. Morphology, porosity, and hydraulic conductivity of weathered granitic bedrock and overlying soils. *Soil Sci. Soc. Am. J.* **61**, 516–522 (1997).

49. 49.

McCole, A. A. & Stern, L. A. Seasonal water use patterns of *Juniperus ashei* on the Edwards Plateau, Texas, based on stable isotopes in water. *J. Hydrol.* **342**, 238–248 (2007).

50. 50.

Schwinning, S. The water relations of two evergreen tree species in a karst savanna. *Oecologia* **158**, 373–383 (2008).

51. 51.

McCormick, E. L. et al. Dataset for “Evidence for widespread woody plant use of water stored in bedrock”. *Hydroshare* <https://doi.org/10.4211/hs.a2f0d5fd10f14cd189a3465f72cba6f3> (2021).

52. 52.

Jackson, R. B. et al. A global analysis of root distributions for terrestrial biomes. *Oecologia* **108**, 389–411 (1996).

53. 53.

Schenk, H. J. & Jackson, R. B. The global biogeography of roots. *Ecol. Monogr.* **72**, 311–328 (2002).

54. 54.

Schenk, H. J. & Jackson, R. B. Rooting depths, lateral root spreads and below-ground/above-ground allometries of plants in water-limited ecosystems. *J. Ecol.* **90**, 480–494 (2002).

55. 55.

Fan, Y., Miguez-Macho, G., Jobbagy, E. G., Jackson, R. B. & Otero-Casal, C. Hydrologic regulation of plant rooting depth. *Proc. Natl Acad. Sci. USA* **114**, 10572–10577 (2017).

56. 56.

Daly, C. et al. Physiographically sensitive mapping of climatological temperature and precipitation across the conterminous United States. *Int. J. Climatol.* **28**, 2031–2064 (2008).

57. 57.

Daly, C., Smith, J. I. & Olson, K. V. Mapping atmospheric moisture climatologies across the conterminous United States. *PLoS ONE* **10**, e0141140 (2015).

58. 58.

Zhang, Y. et al. Coupled estimation of 500 m and 8-day resolution global evapotranspiration and gross primary production in 2002–2017. *Remote Sens. Environ.* **222**, 165–182 (2019).

59. 59.

Gan, R. et al. Use of satellite leaf area index estimating evapotranspiration and gross assimilation for Australian ecosystems. *Ecohydrology* **11**, e1974 (2018).

60. 60.

Dralle, D. N., Hahm, W. J., Chadwick, K. D., McCormick, E. L. & Rempe, D. M. Technical note: accounting for snow in the estimation of root-zone water storage capacity from precipitation and evapotranspiration fluxes. *Hydrol. Earth Syst. Sci.* **25**, 2861–2867 (2021).

61. 61.

Wang-Erlandsson, L. et al. Global root zone storage capacity from satellite-based evaporation. *Hydrol. Earth Syst. Sci.* **20**, 1459–1481 (2016).

62. 62.

Gorelick, N. et al. Google Earth Engine: planetary-scale geospatial analysis for everyone. *Remote Sens. Environ.* **202**, 18–27 (2017).

63. 63.

Singh, C., Wang-Erlandsson, L., Fetzer, I., Rockstrom, J. & van der Ent, R. Rootzone storage capacity reveals drought coping strategies along rainforest savanna transitions. *Environ. Res. Lett.* **15**, 124021 (2020).

64. 64.

Hall, D., Riggs, G. & Salomonson, V. *MODIS/Terra Snow Cover Daily L3 Global 500m Grid, Version 6 [Data set]* (NASA National Snow and Ice Data Center Distributed Active Archive Center, 2016).

65. 65.

Friedl, M. & Sulla-Menashe, D. *MCD12Q1 MODIS/Terra+ Aqua Land Cover Type Yearly L3 Global 500m SIN Grid V006 [Data set]* (NASA EOSDIS Land Processes DAAC, 2015).

66. 66.

Peel, M. C., Finlayson, B. L. & McMahon, T. A. Updated world map of the Koppen–Geiger climate classification. *Hydrol. Earth Syst. Sci. Discuss.* **4**, 439–473 (2007).

67. 67.

Harris, I., Jones, P. D., Osborn, T. J. & Lister, D. H. Updated high-resolution grids of monthly climatic observations—the CRU TS3.10 dataset. *Int. J. Climatol.* **34**, 623–642 (2014).

68. 68.

Funk, C. et al. The climate hazards infrared precipitation with stations—a new environmental record for monitoring extremes. *Sci. Data* **2**, 150066 (2015).

69. 69.

Niemeyer, R. J. et al. Spatiotemporal soil and saprolite moisture dynamics across a semi-arid woody plant gradient. *J. Hydrol.* **544**, 21–

35 (2017).

70. 70.

Pedrazas, M. A. et al. The relationship between topography bedrock weathering and water storage across a sequence of ridges and valleys. *J. Geophys. Res. Earth Surf.* **126**, e2020JF005848 (2021).

71. 71.

Arkley, R. J. Soil moisture use by mixed conifer forest in a summer-dry climate. *Soil Sci. Soc. Am. J.* **45**, 423–427 (1981).

72. 72.

Zwieniecki, M. A. & Newton, M. Water-holding characteristics of metasedimentary rock in selected forest ecosystems in southwestern Oregon. *Soil Sci. Soc. Am. J.* **60**, 1578–1582 (1996).

73. 73.

Hellmers, H., Horton, J. S., Juhren, G. & O'Keefe, J. Root systems of some chaparral plants in southern California. *Ecology* **36**, 667–678 (1955).

74. 74.

Cardella Dammeyer, H., Schwinnig, S., Schwartz, B. F. & Moore, G. W. Effects of juniper removal and rainfall variation on tree transpiration in a semi-arid karst: evidence of complex water storage dynamics. *Hydrol. Process.* **30**, 4568–4581 (2016).

75. 75.

Twidwell, D. et al. Drought-induced woody plant mortality in an encroached semi-arid savanna depends on topoedaphic factors and land management. *Appl. Veg. Sci.* **17**, 42–52 (2013).

76. 76.

Davis, E. A. Root system of shrub live oak in relation to water yield by chaparral. Proceedings of the 1977 Meetings of the Arizona Section of the American Water Resources Association and the Hydrology Section of the Arizona Academy of Sciences. *Hydrol. Water Resour. Ariz. Southwest* **7**, 241–248 (1977).

77. 77.

West, A. G., Hultine, K. R., Burtch, K. G., & Ehleringer, J. R. Seasonal variations in moisture use in a piñon–juniper woodland. *Oecologia* **153**, 787–798 (2007).

78. 78.

Seyfried, M. S. & Wilcox, B. P. Soil water storage and rooting depth: key factors controlling recharge on rangelands. *Hydrol. Process.* **20**, 3261–3275 (2006).

79. 79.

Dietrich, W. E. & Dunne, T. Sediment budget for a small catchment in mountainous terrain. *Zeitschrift Für Geomorphologie* **29**, 191–206 (1978).

80. 80.

Litvak, M. E., Schwinnig, S. & Heilman, J. L. in *Ecosystem Function in Savannas* (eds Hill, M. J. & Hanan, N. P.) 117–134 (2010).

Acknowledgements

We thank R. Breunig. We acknowledge funding support from the USDA Forest Service Pacific Southwest Research Station, the National Science Foundation Graduate Research Fellowship Program and the US Department of Energy, Office of Science, Office of Biological Environmental Research under award number DESC0018039.

Author information

Affiliations

1. Department of Geological Sciences, Jackson School of Geosciences, University of Texas at Austin, Austin, TX, USA

Erica L. McCormick, Alison K. Tune, Logan M. Schmidt, K. Dana Chadwick & Daniella M. Rempe

2. Pacific Southwest Research Station, United States Forest Service, Davis, CA, USA

David N. Dralle

3. Department of Geography, Simon Fraser University, Burnaby, British Columbia, Canada

W. Jesse Hahm

Contributions

E.L.M. led the data acquisition and analysis and coordinated the manuscript preparation. E.L.M. and D.M.R. drafted the initial manuscript. D.N.D., K.D.C. and W.J.H. contributed to writing and data analysis. A.K.T. contributed to data acquisition. All authors contributed to the interpretation and presentation of the results, editing and review process, and approved the final version. D.M.R. conceptualized and led the study.

Corresponding author

Correspondence to [Erica L. McCormick](#).

Ethics declarations

Competing interests

The authors declare no competing interests.

Additional information

Peer review information *Nature* thanks Ying Fan, Huade Guan and the other, anonymous, reviewer(s) for their contribution to the peer review of this work. Peer reviewer reports are available.

Publisher's note Springer Nature remains neutral with regard to jurisdictional claims in published maps and institutional affiliations.

Extended data figures and tables

[Extended Data Fig. 1 Flow chart of the methodology for bedrock storage deficit and capacity calculations.](#)

Workflow for the calculation of total and annual bedrock water storage deficits (S_{bedrock} and $D_{\text{bedrock},Y}$, respectively). Data products (solid thick border) are reported with their spatial resolution. Calculations and thresholds are reported in white boxes (Methods). Masking procedures exclude areas where output fluxes significantly exceed input fluxes (top right) and include areas where woody vegetation is established on shallow soils (middle right). These masks are applied to the water budget calculation (left and bottom) to arrive at conservative estimates of S_{bedrock} and $D_{\text{bedrock},Y}$ at the CONUS scale.

[Extended Data Fig. 2 Maps of soil and aboveground carbon input products used in this study.](#)

a, Aboveground carbon sourced from Spawn et al.¹⁹ (Mg ha^{-1}). **b**, Soil available water storage capacity (mm) for the CONUS. Soil available water storage sourced at 90-m resolution from the USDA gNATSGO⁴¹ product and provided for the upper 1.5 m (Methods).

Extended Data Fig. 3 Annual bedrock water storage deficit for four years across the CONUS.

a–d, Annual bedrock water storage deficit, $D_{\text{bedrock},Y}$, for 2011 (**a**), 2014 (**b**), 2015 (**c**) and 2017 (**d**).

Extended Data Fig. 4 Median annual bedrock water storage deficit constitutes more than a quarter of mean annual precipitation in some places.

The magnitude of median D_{bedrock} divided by mean annual precipitation shown as a percent for California (left) and Texas (right). Mean annual precipitation was calculated in Google Earth Engine⁶² in the Google Colaboratory environment using the PRISM Daily Spatial Climate Data set AN81d data product^{56,57}.

Extended Data Fig. 5 Bedrock water storage capacity across the CONUS, California and Texas.

The distribution of bedrock water storage capacity, S_{bedrock} , for locations meeting masking and calculation criteria. Where S_{bedrock} is greater than zero, bedrock water storage is needed to explain observed ET (Methods).

Extended Data Fig. 6 Distribution of bedrock water storage capacity varies by Köppen climate type and biome.

a, Boxplots show median, interquartile range and 1.5 times the interquartile range of S_{bedrock} across Köppen climate type⁶⁶ (left) and biome (MODIS landcover classifications⁶⁵) (right) for locations which meet analysis criteria (Methods). The number of pixels in each category is given above each box. The 25th percentile is non-zero for many biomes and climates. **b**, Maps indicating the locations associated with each climate (left) and biome (right). Biome and climate subgroups with less than 2,000 km² are excluded. Summary statistics of groupings are presented in Extended Data

Table 1. Post hoc tests (Kruskal–Wallis and Dunn’s tests) reveal statistically significant differences ($P = <0.001$) of median S_{bedrock} between all climate group pairings and between all biome group pairings. Boxplots and statistical analyses were processed using the Google Earth Engine⁶² Python API.

Extended Data Fig. 7 Soil and bedrock water storage capacity at locations where rock moisture use by plants has been documented.

Soil water storage capacity S_{soil} (brown) and median $D_{\text{bedrock},2004–2017}$ (blue) for locations with documented plant use of rock moisture, that is, bedrock water storage from the unsaturated zone. Superscripts denote locations that are masked, for not being classified as woody vegetation (‡), having soil depth greater than 1.5 m (*) or because the cumulative 2003–2017 evapotranspiration exceeds precipitation (†) (Methods, Extended Data Fig. 1). Data were sourced from the literature review (Methods). References for field studies: refs. [20](#),[69](#),[70](#),[71](#),[72](#),[73](#),[74](#),[75](#),[76](#),[77](#),[78](#),[79](#),[80](#)

Source data.

Extended Data Fig. 8 Comparison of S_{bedrock} and median D_{bedrock} to calculations using double the published soil water storage capacity values.

a, Bedrock water storage capacity (S_{bedrock}) assuming soil water storage capacity (S_{soil}) is double that reported by gNATSGO⁴¹ to account for the possibility of soils providing water to ET at saturation, which is commonly estimated as double field capacity. **b**, S_{bedrock} without doubling of S_{soil} . **c, d**, Median annual bedrock water storage deficit, $D_{\text{bedrock},2003–2017}$, with doubled (**c**) and original (**d**) S_{soil} .

Extended Data Fig. 9 Bedrock water storage capacity calculated with published values of root-zone storage capacity.

a, b, Two versions of bedrock water storage capacity (S_{bedrock}) are calculated using root-zone storage capacity (S_r) published by Wang-Erlundsson et al. ⁶¹ at a 0.5° (roughly 50 km) resolution with input and output fluxes from Climatic Research Unit Time Series version 3.22 (CRU TS3.22)⁶⁷ (a) and Climate Hazards Group InfraRed Precipitation with Stations (CHIRPS)⁶⁸ (b). To arrive at S_{bedrock} , S_{soil} is subtracted from the maximum S_r reported in Wang-Erlundsson et al. ⁶¹.

Extended Data Table 1 Median bedrock water storage capacity for combinations of biomes and Köppen climate types

Supplementary information

[Peer Review File](#)

Source data

[Source Data Fig. 2](#)

[Source Data Fig. 3](#)

[Source Data Extended Data Fig. 7](#)

Rights and permissions

[Reprints and Permissions](#)

About this article

Cite this article

McCormick, E.L., Dralle, D.N., Hahm, W.J. *et al.* Widespread woody plant use of water stored in bedrock. *Nature* **597**, 225–229 (2021).

<https://doi.org/10.1038/s41586-021-03761-3>

- Received: 30 December 2020
- Accepted: 22 June 2021
- Published: 08 September 2021
- Issue Date: 09 September 2021
- DOI: <https://doi.org/10.1038/s41586-021-03761-3>

This article was downloaded by **calibre** from <https://www.nature.com/articles/s41586-021-03761-3>

| [Section menu](#) | [Main menu](#) |

- Article
- [Published: 08 September 2021](#)

Unextractable fossil fuels in a 1.5 °C world

- [Dan Welsby](#) [ORCID: orcid.org/0000-0002-8800-0229¹](#),
- [James Price²](#),
- [Steve Pye](#) [ORCID: orcid.org/0000-0003-1793-2552²](#) &
- [Paul Ekins¹](#)

Nature volume **597**, pages 230–234 (2021)

- 16k Accesses
- 1 Citations
- 3673 Altmetric
- [Metrics details](#)

Subjects

- [Energy modelling](#)
- [Fossil fuels](#)

Abstract

Parties to the 2015 Paris Agreement pledged to limit global warming to well below 2 °C and to pursue efforts to limit the temperature increase to 1.5 °C relative to pre-industrial times¹. However, fossil fuels continue to dominate the global energy system and a sharp decline in their use must be realized to keep the temperature increase below 1.5 °C (refs. [2](#),[3](#),[4](#),[5](#),[6](#),[7](#)). Here we use a global energy systems model⁸ to assess the amount of fossil fuels that would need to be left in the ground, regionally and globally, to allow for a 50 per cent probability of limiting warming to 1.5 °C. By 2050, we find that nearly 60 per cent of oil and fossil methane gas, and 90 per cent of coal must remain unextracted to keep within a 1.5 °C carbon budget. This is a large

increase in the unextractable estimates for a 2 °C carbon budget⁹, particularly for oil, for which an additional 25 per cent of reserves must remain unextracted. Furthermore, we estimate that oil and gas production must decline globally by 3 per cent each year until 2050. This implies that most regions must reach peak production now or during the next decade, rendering many operational and planned fossil fuel projects unviable. We probably present an underestimate of the production changes required, because a greater than 50 per cent probability of limiting warming to 1.5 °C requires more carbon to stay in the ground and because of uncertainties around the timely deployment of negative emission technologies at scale.

[Download PDF](#)

Main

In 2015, McGlade and Ekins⁹ set out the limits to fossil fuel extraction under stringent climate targets. They estimated that one-third of oil reserves, almost half of fossil methane gas reserves and over 80% of current coal reserves should remain in the ground in 2050 to limit warming to 2 °C. They also highlighted that some countries would need to leave much higher proportions of fossil fuel reserves in the ground than others. Since 2015, the Paris Agreement and the Intergovernmental Panel on Climate Change (IPCC) have helped to refocus the debate on warming limits of 1.5 °C (refs. [1,10](#)). Multiple scenarios have been published, showing the additional effort required to limit global CO₂ emissions to net zero by around 2050 to meet this target¹¹. In this Article, we extend the earlier 2015 work to estimate the levels of unextractable fossil fuel reserves out to 2100 under a 1.5 °C scenario (50% probability), using a 2018–2100 carbon budget of 580 GtCO₂ (ref. [3](#)). We also provide insights into the required decline of fossil fuel production at a regional level, which will necessitate a range of policy interventions. We define unextractable fossil fuels as the volumes that need to stay in the ground, regardless of end use (that is, combusted or non-combusted), to keep within our 1.5 °C carbon budget.

Paris Agreement-compliant fossil fuel prospects

Fossil fuels continue to dominate the global energy system, accounting for 81% of primary energy demand¹². After decades of growth, their rate of production and use will need to reverse and decline rapidly to meet internationally agreed climate goals. There are some promising signs, with global coal production peaking in 2013, and oil output estimated to have peaked in 2019 or be nearing peak demand, even by some industry commentators¹³.

The plateauing of production and subsequent decline will mean that large amounts of fossil fuel reserves, prospects that are seen today as economic, will never be extracted. This has important implications for producers who may be banking on monetizing those reserves in the future, and current and prospective investors. Investments made today in fossil fuel energy therefore risk being stranded¹⁴. However, there continues to be a disconnect between the production outlook of different countries and corporate entities and the necessary pathway to limit average temperature increases².

A number of analyses have explored how fossil fuels fit into an energy system under a 1.5 °C target. The IPCC's *Special Report on Global Warming of 1.5 °C* estimates coal use only representing 1–7% of primary energy use in 2050, while oil and fossil methane gas see declines relative to 2020 levels by 39–77% and 13–62%, respectively³. Despite strong declines, the use of fossil fuels continues at lower levels, reflecting the assumed inertia in the system and continued use of fossil fuels in hard-to-mitigate sectors. Luderer et al.⁴ estimate that, despite large-scale efforts, CO₂ emissions from fossil fuels will probably exceed the 1.5 °C carbon budget and require high levels of carbon dioxide removals (CDR). Grubler et al.⁵ explored efforts to reduce energy demand, substantially reducing the role of fossil fuels and removing the need for CDR deployment.

The extent of fossil fuel decline in the coming decades remains uncertain, influenced by factors such as the rapidity of the rollout of clean technologies and decisions about the retirement of (and new investment in) fossil fuel infrastructure. Indeed, while dependent on lifetimes and operating patterns, existing fossil fuel infrastructure already places a 1.5 °C target at risk owing to implied 'committed' future CO₂ emissions⁶. The possible extent of CDR further complicates this picture. At high levels, this may allow for more persistent use of fossil fuels, but such assumptions have attracted considerable controversy⁷.

Although a number of studies have explored fossil fuel reductions under a 1.5 °C target, none have estimated the fossil fuel reserves and resources that have to remain in the ground. Here, using global energy systems model TIAM-UCL, we assess the levels of fossil fuels that would remain unextractable in 2050 and 2100.

Unextractable reserves under a 1.5 °C target

Unextractable oil, fossil methane gas and coal reserves are estimated as the percentage of the 2018 reserve base that is not extracted to achieve a 50% probability of keeping the global temperature increase to 1.5 °C. We estimate this to be 58% for oil, 59% for fossil methane gas and 89% for coal in 2050. This means that very high shares of reserves considered economic today would not be extracted under a global 1.5 °C

target. These estimates are considerably higher than those made by McGlade and Ekins⁹, who estimated unextractable reserves at 33% and 49% for oil and fossil methane gas, respectively (Supplementary Fig. 3). This reflects the stronger climate ambition assumed in this analysis, plus a more positive outlook for low-carbon technology deployment, such as zero-emission vehicles and renewable energy.

Continued use of fossil fuels after 2050 sees these estimates reduce by 2100. For oil, the global estimate drops to 43% in 2100. The reduction is smaller for fossil methane gas, reducing from 59% to 50%. The majority of fossil fuels extracted after 2050 are used as feedstocks in the petrochemical sector, and as fuel in the aviation sector in the case of oil. Feedstock use, which has a substantially lower carbon intensity than combustion, accounts for 65% and 68% of total oil and fossil methane gas use, respectively, in 2100 under a 1.5 °C carbon budget. However, it also reflects limited consideration of targeted actions to reduce feedstock use that, if available, would limit the dependence on CDR.

Unextractable shares vary substantially by region, relative to the global estimates (Fig. 1, Table 1). The largest reserve holders, such as the Middle East (MEA) (for oil and fossil methane gas) and Russia and other former Soviet states (FSU) (for fossil methane gas) have the strongest influence on the global picture, and therefore have estimates close to or marginally above the global average. For oil, Canada has much higher unextractable estimates than in other regions, at 83%. This includes 84% of the 49 billion barrels (Gb) of Canadian oil sands we estimate as proven reserves. By contrast, the FSU region has a relatively low unextractable share of total oil reserves (38% in 2050), reflecting their cost-effectiveness.

Fig. 1: Unextractable reserves of fossil fuels by region in 2050 and 2100 under a 1.5 °C scenario.

 **figure1**

Left, 2050. Right, 2100. Top, Maps of the percentage of unextractable reserves of oil, fossil methane gas and coal (from top to bottom) disaggregated into the model regions. We note that 13 out of 16 TIAM regions are plotted with the Western and Eastern EU aggregated together, and South Korea and Japan are not shown owing to their

negligible reserves. Bottom, The absolute amount of each fossil fuel reserve that must remain unextracted. In some cases the order of regions on the x axis changes between 2050 and 2100 owing to similar levels of unextractable reserves in 2050 and small differences in cumulative production after 2050 leading to regions switching places. Reserves are defined as both technically and economically proven given current market conditions. They can be further subcategorized: currently producing, undeveloped but post/pending final investment decision and undeveloped but sufficient field appraisal to meet SPE definition of technically and economically proven²⁷. Additional detail on the definition of reserves in this work is provided in the Methods. The mapping software used was Python version 3.8 (Python Software Foundation). The y -axis units are billion barrels (Gb), trillion m³ (Tcm) and billion tonnes (Gt) for oil, gas and coal, respectively.

[Source data](#).

Table 1 Unextractable reserves of fossil fuels by region under the 1.5 °C scenario

Given its role as a key exporter and with the lowest-cost reserve base, MEA sees unextractable reserves of 62% in 2050, reducing to 38% by 2100. As previously mentioned, oil consumption after 2050 is dominated by non-combustible feedstocks and therefore action to reduce demand for oil-based products, such as plastics¹⁵, would substantially change this picture for producers¹⁶ including MEA. It is evident that large incumbent producers dominate the production picture going forwards, with the vast majority of undeveloped (particularly unconventional) oil remaining unused.

Unextractable estimates for coal show less regional variation, although they are lowest in those regions that utilize most coal in the next 30 years, notably India, China and other parts of Asia (ODA). However, coal consumption declines rapidly even in these regions (see Supplementary Information section [6](#) for additional detail on coal decline).

A sensitivity analysis on key model assumptions was undertaken to explore the effect on unextractable reserve estimates (Supplementary Information section [3](#)). These include the rate of carbon capture and storage (CCS) deployment, availability of bioenergy, and growth in future energy service demands in aviation and the chemical sector given the challenges in their decarbonization. We find that the sensitivities do not affect the unextractable estimates substantially, suggesting that the headline results are relatively robust to uncertainties across key assumptions. Of the sensitivities, the availability of biomass (and therefore negative emissions potential from bioenergy with CCS (BECCS)) has the most impact on unextractable estimates. Where higher biomass availability is assumed, unextractable estimates in 2050 for oil, fossil methane gas and coal are 55% (-3%), 56% (-3%), and 87% (-2%), respectively (change relative to central scenario in brackets).

Broadening out unextractable estimates to resources is important because a share of non-reserve resources will come online in future years, and contribute to overall production and eventual emissions (Supplementary Information section 1). For unconventional oil, their large size (as well as less-favourable economics and higher carbon intensity) means that 99% of these resources remain unextractable. A higher share of unconventional gas also remains unextractable (86%), relative to conventional resources (74%), again due to higher extraction costs in most regions, with the exception of North America. Arctic oil and fossil methane gas resources across all regions where these are located remain undeveloped.

Production decline of major producing regions

Underlying the regional unextractable estimates of both reserves and the wider resource base are regional production trajectories. Figure 2 shows the outlook to 2050 for the five largest oil-and fossil methane gas-producing regions. The outlook is one of decline, with 2020 marking both global peak oil and fossil methane gas production, with decline thereafter to 2050 of 2.8% and 3.2%, respectively (Supplementary Fig. 1).

Fig. 2: Production profiles for regions producing major oil and fossil methane gas for 2020–2050.

 figure2

a, Total oil production. **b**, Total fossil methane gas production. The left-hand *y* axis shows the production from each of the five largest oil (**a**) and gas (**b**)-producing regions, whereas the right-hand *y* axis shows the global share captured by these

incumbent producers. The legend shows the year and volume of peak production for each region in parentheses.

Source data

Apart from the USA, all oil producing regions see strong declines to 2050 (Fig. 2a). The USA sees production growth to 2025, peaking at 16.9 million barrels per day, before constant decline out to 2050. This initial increase is due to several factors including falling imports of oil into the USA, the continued use of oil in the transport sector before strong growth in low-emission vehicles and the flexibility of light tight oil due to its production dynamics (that is, high production growth and decline rates from tight oil wells).

For CSA, production shows modest decline of 1.1% per year to 2025, before a more rapid rate of decline of 3.5% out to 2050. The early slow decline reflects Brazilian fields with final investment decisions offsetting production decline in mature producing assets¹⁷. MEA, the largest oil producer, sees a decline of over 50% by 2050 (relative to 2020). Given the huge reserves in the region, most production to 2050 is from designated reserves (85–91% in any given year). Elsewhere, oil production in Africa and the FSU exhibits constant decline from 2020 out to 2050 at rates of 3.5% and 3.1%, respectively, driven by declining domestic demand and oil demand destruction in key importing regions (for example, Europe).

Regional fossil methane gas production is a more complex story owing to its use to meet demand growth in emerging markets, and as an alternative to coal use in the industrial sector, notably in China and ODA (Fig. 2b). Production in the USA peaks in 2020 and sees rapid decline through 2050, with an annual derived decline rate of 8.1%. This mirrors a rapid decline in the domestic market, with complete phase out of use in the power sector by 2040. In addition, the high share of unconventional gas in the production mix exhibits faster decline than for other major producers. This has important implications for US liquefied fossil methane gas exports, with prospects of low utilization rates of infrastructure, and limited prospect for future additional liquefaction capacity. The FSU region sees peak gas production in 2020, but with production decline across legacy gas fields in Western Siberia and Central Asia moderated by the production increases from export projects to predominantly Asian (and particularly Chinese) markets and a shift of production to the Yamal Peninsula and East Siberia.

Three of the regions in Fig. 2b see fossil methane gas production growth out to the 2030s, before decline. For the Middle East, this reflects the competitiveness of exporters in the region. For Africa, this growth is driven by increased demand for electricity, higher industrial demand (partially displacing oil) and modest growth in exports to 2035. For ODA, fossil methane gas gains domestic market share as coal is

rapidly phased out of industry. However, there is considerable uncertainty around the geological and economic feasibility of undeveloped resources, particularly for the two largest producers in ODA: Indonesia and Malaysia. The profiles for Africa and ODA also suggest substantial transition risk, particularly as post-2035 production rapidly declines at rates of 5.7% and 6.6%, respectively. This decline is due to the ramp-up in renewables crowding fossil methane gas out of the power sector and the increasing electrification of industry. This transition risk also extends to large exporters, given rapidly changing import dynamics in regions such as China. For example, Chinese gas demand peaks at 700 billion m³ (60% of which is imported) in 2035, before reverting to 2018 levels by 2050.

Reassessing fossil fuel production

The need to forgo future production means country producers, fossil energy companies and their investors need to seriously reassess their production outlooks. This is particularly true for countries that are fiscally reliant on fossil fuels, to allow for a managed diversification of their economies. Many regions are facing peak production now or over the next decade, and the development of new low-carbon sectors of their economies that will provide employment and revenues will therefore be key. For regions that are heavily dependent on fossil fuels for fiscal revenue, this analysis echoes recent work suggesting huge transition risk unless economies diversify rapidly¹⁸. For example, Middle Eastern oil production needs to peak in 2020, which in combination with lower oil prices from demand destruction signifies large reductions in fiscal revenue, with Iraq, Bahrain, Saudi Arabia and Kuwait relying on fossil fuels for 65–85% of total government revenues at present.

Central to pushing this transition forwards will be the domestic policy measures required to both restrict production and reduce demand¹⁹. Increasing attention is being focused on supply-side policies that can complement carbon pricing and regulatory instruments that focus on demand²⁰. Such policies act to curtail the extraction of fossil fuels and can include subsidy removal, production taxes, penalties for regulatory non-compliance and bans on new exploration and production²¹. The development of international initiatives, such as the proposed non-proliferation treaty on fossil fuels²², is also key as they could serve to foster global action, as could existing frameworks such as the United Nations Framework Convention on Climate Change²³.

The recent downturn in oil and fossil methane gas demand due to COVID-19 provides an opportune moment for governments to shift strategy². The crisis has further exposed the vulnerability of the oil and gas sector in particular, and raised concerns about its profitability in the future^{24,25}. With many fossil fuel energy companies revising their outlooks downwards in 2020, this makes new investments risky. These

risks are compounded by the momentum towards low-carbon technologies, with continued falls in renewable energy costs and battery technology. Governments who have historically benefited should take the lead, with other countries that have a high dependency on fossil fuels but low capacity for transition—or those forgoing extractive activities—needing to be supported to follow this lead²⁶.

The bleak picture painted by our scenarios for the global fossil fuel industry is very probably an underestimate of what is required and, as a result, production would need to be curtailed even faster. This is because our scenarios use a carbon budget associated with a 50% probability of limiting warming to 1.5 °C, which does not consider uncertainties around, for example, Earth system feedbacks³; therefore, to ensure more certainty of stabilizing at this temperature, more carbon needs to stay in the ground. Furthermore, it relies on CDR of approximately 4.4 (5.9) GtCO₂ per year by 2050 (2100). Given the substantial uncertainties around the scaling of CDR, this dependency risks underestimating the required rate of emissions reduction.

Methods

We first describe the TIAM-UCL model, before presenting our approach to modelling scenarios. The remainder of the Methods focuses on key issues of definition around geological categories and techno-economic classifications of fossil fuels.

Description of TIAM-UCL

To explore the question of unextractable fossil fuel reserves and resources under a 1.5 °C carbon budget, we used the TIMES Integrated Assessment Model at University College London (TIAM-UCL)^{8,9,28,29}. This model provides a representation of the global energy system, capturing primary energy sources (oil, fossil methane gas, coal, nuclear, biomass and renewables) from production through to their conversion (electricity production, hydrogen and biofuel production, oil refining), transport and distribution, and their eventual use to meet energy service demands across a range of economic sectors. Using a scenario-based approach, the evolution of the system over time to meet future energy service demands can be simulated, driven by a least-cost objective. The model uses the TIMES modelling framework, which is described in detail in Supplementary Information section 7.

The model represents the countries of the world as 16 regions (Supplementary Table 26), allowing for more detailed characterization of regional energy sectors and the trade flows between regions. Upstream sectors within regions that contain members of OPEC are modelled separately, for example, the upstream sector in the Central and South America (CSA) region will be split between OPEC (Venezuela) and non-OPEC

countries. Regional coal, oil and fossil methane gas prices are generated within the model. These incorporate the marginal cost of production, scarcity rents (for example, the benefit forgone by using a resource now as opposed to in the future, assuming discount rates), rents arising from other imposed constraints (such as depletion rates) and transportation costs, but not fiscal regimes. This means that the full price formation, which includes taxes and subsidies, is not captured in TIAM-UCL, and remains a contested limitation of this type of model³⁰.

A key strength of TIAM-UCL is the representation of the regional fossil resource base (Supplementary Information section 5). For oil reserves and resources, these are categorized into current conventional proved (1P) reserves in fields that are in production or are scheduled to be developed, reserve growth, undiscovered oil, Arctic oil, light tight oil, gas liquids, natural bitumen and extra-heavy oil. The latter two categories represent unconventional oil resources. For fossil methane gas, these resources are categorized into current conventional 1P reserves that are in fields in production or are scheduled to be developed, reserve growth, undiscovered gas, Arctic gas, associated gas, tight gas, coal-bed methane and shale gas. The categorization of resources and associated definitions are described later in the Methods. For oil and fossil methane gas, individual supply cost curves for each of the categories are estimated for each region (Extended Data Fig. 1a, b). These supply cost curves in TIAM-UCL refer to all capital and operating expenditure associated with exploration through production, but do not include fiscal regimes or additional transportation costs³¹. Crucially, the upstream emissions associated with the extraction of different fossil fuels are also captured in the model.

The model has various technological options to remove emissions from the atmosphere via negative emissions, including a set of bioenergy with carbon capture and storage (BECCS) technologies, in power generation, industry, and H₂ and biofuel production. The primary limiting factor on this suite of technologies is the global bioenergy resource potential, set at a maximum 112 EJ per year, in line with the recent UK Committee on Climate Change (CCC) biomass report³². This is a lower level than the biomass resource available in many other integrated assessment scenarios for 1.5 °C (which can be up to 400 EJ per year)^{33,34}, and is more representative of an upper estimate of the global resource of truly low-carbon sustainable biomass based on many ecological studies³⁵ (Supplementary Table 20). In addition to technological solutions for capturing carbon from the atmosphere, TIAM-UCL also models CO₂ emissions from land use, land-use change and forestry (LULUCF) at the regional level on the basis of exogenously defined data from the IMAGE model³⁶. Here we use a trajectory based on that model's Shared Socio-economic Pathway 2 (SSP2) RCP2.6 scenario, which leads to global net negative CO₂ emissions from LULUCF from 2060 onwards.

In TIAM-UCL, exogenous future demands for energy services (including mobility, lighting, residential, commercial and industrial heat and cooling) drive the evolution of the system so that energy supply meets the energy service demands across the whole time horizon (that is, 2005–2100), which have increased through population and economic growth. For this Article, we use energy service demands derived from SSP2³⁷. The model was also run with an elastic demand function, with energy service demands reducing as the marginal price of satisfying the energy service increases. Decisions around what energy sector investments to make across regions are determined using the cost-effectiveness of investments, taking into account the existing system today, energy resource potential, technology availability and, crucially, policy constraints such as emissions reduction targets. The model time horizon runs to 2100, in line with the timescale typically used for climate stabilization.

In conjunction with a cumulative CO₂ budget, an upper limit is placed on annual CH₄ and N₂O emissions based on pathways from the IPCC's *Special Report on Global Warming of 1.5 °C* scenario database¹¹. We select all pathways that have a warming at or below 1.5 °C in 2100 and take an average across these scenarios to derive a CH₄ and N₂O emissions trajectory that is in line with a 1.5 °C world. Further information on key assumptions used in the model is provided in Supplementary Information section 6. The TIAM-UCL model version used for this analysis was 4.1.1, and was run using TIMES code 4.2.2 with GAMS 27.2. The model solver used was CPLEX 12.9.0.0.

Scenario specification

Extended Data Table 1 describes the scenarios used in this work and some key sensitivities to explore the effect on unextractable fossil fuels under a 1.5 °C-consistent carbon budget. For a 50% probability, this is estimated at 580 GtCO₂ (from 2018)³. With regard to sensitivities, three key parameters were varied; (1) the rate at which carbon capture and storage technologies can deploy; (2) the availability of bioenergy and therefore the potential for negative emissions through BECCS; and (3) the future energy service demands in aviation and the chemical sector, which provide a considerable challenge to decarbonize given their current total reliance on fossil fuels.

The lower level of bioenergy on sustainability grounds, compared with other IAM models³⁸, combined with a constrained role for direct air capture (DAC), puts the global emissions trajectory in our central scenario between the P2 and P3 archetypes set out in the IPCC's special report on 1.5 °C. Here, in our central case, BECCS sequesters 287 GtCO₂ cumulatively out to 2100, compared with 151 and 414 GtCO₂ for P2 and P3 scenarios, respectively. Annually, BECCS use is 5 GtCO₂ in 2100 with a further 0.9 GtCO₂ being captured by DAC. This scale of engineered removals mean

the central 1.5D scenario is on the edge of what is feasible (that is, it does not require a backstop to remove CO₂) within the current version of TIAM-UCL.

As such, while CDR has an important role in our scenarios, aside from 1.5D-HiBio, we do not see cases in which global net negative emissions are in the range of 10–20 GtCO₂ per year in the second half of the century, which would enable a large carbon budget exceedance before net zero. This in turn inherently limits the amount that global surface temperatures can exceed or overshoot 1.5 °C before 2100 and, to some extent, reduces exposure to the sizable long-term risks associated with reliance on extensive negative emissions after 2050 as envisaged by P3 and P4 type scenarios³⁹.

For the low-demand scenarios, we derived an exponential annual growth rate for aviation (domestic and international) and the chemical sector using Grubler et al.⁵, considering regional variation between OECD and non-OECD regions. These growth rates were then applied to the calibrated historical data in TIAM-UCL and extrapolated forwards to 2050 and 2100. These two sub-sectors were chosen due to relatively high residual emissions, and because the specific policy direction can influence consumer demand (for example, passenger demand for aviation and demand for plastics). More detail on the low-energy-service demand trajectories, and how these differ from our central 1.5 °C scenario, can be found in Supplementary Information section 3.

Defining geological categories and techno-economic classifications of fossil fuel resources

It is crucial that definitions for reporting are clearly set out, given the regular use of both geological and techno-economic terminology in previous sections, and their differing use in the literature.

Conventional and unconventional oil and fossil methane gas

Conventional oil in TIAM-UCL is defined as having an American Petroleum Institute (API) index greater than 10°; this reflects the ‘density’ of the oil and therefore its flow characteristics in the hydrocarbon-bearing reservoir³¹. Conventional oil also includes light tight oil, gas liquids and Arctic oil. Unconventional oil, which includes ultra-heavy oil and bitumen, generally has an API < 10° and therefore is extremely viscous with a very high density, typically requiring additional processing and upgrading to produce synthetic crude oil (SCO), which is comparable to conventional crude oil. The additional energy required for upgrading results in a more carbon-intensive product and often at higher costs than conventional oils (shown in Extended Data Fig. 1a).

TIAM-UCL also includes shale oil (kerogen), which we classify as unconventional. However, none of this is produced in any scenario conducted for this work, and therefore we have not included it within our unextractable resource estimates.

Conventional fossil methane gas refers to those resources in well-defined reservoirs, which do not require additional stimulation to recover economical volumes. It can be found in both gas-only reservoirs and associated with oil (associated fossil methane gas, either forming a gas cap or dissolved in the oil stream). Unconventional fossil methane gas refers to the gas-bearing reservoir, and whether additional technologies are required to initiate commercial flow rates such as hydraulic fracturing. In TIAM-UCL, this includes shale (low-permeability shale source rock), tight (sandstone reservoirs with extremely low permeability) and coal bed methane (absorbed within coal matrices).

Conventional oil and fossil methane gas are split further into four main production categories, with (1) providing the bulk of our reserve estimates, and the other three categories (2–4) included as resources.

- (1) Reserves. These include resources technically and economically proven at prevailing market rates. If the field is not developed, sufficient appraisal needs to have occurred to satisfy the condition of technically and economically proven. As described below, oil and gas reserves are considered on a 1P basis.
- (2) Reserve additions. These are discovered but undeveloped accumulations that are either sub-economic, abandoned or reservoirs in producing fields that have not yet been developed due to technical constraints or insufficient geological testing. Therefore, these can become reserves through improved efficiency, technical improvements, fossil fuel price increases and additional geological testing.
- (3) New discoveries. These resources of conventional oil and fossil methane gas can be geologically inferred to be recoverable (usually under different probabilities) without taking costs into account.
- (4) Arctic oil and fossil methane gas. These include undiscovered and undeveloped conventional resources in the Arctic region. As discussed by McGlade³¹, the categorization of Arctic resources is based on economic viability (that is, whether the field has been developed or any interest in development has been indicated), with the geographical extent defined by the USGS⁴⁰.

Unconventional oil and gas do not have the same disaggregation in terms of resource steps, with no distinct ‘proved reserves’ step for unconventional oil and gas as with conventional reserves, but instead three different cost steps for the overall resource base. Therefore, we have identified volumes of unconventional oil and gas that we

categorize as reserves, with the relevant cumulative production from these steps accounted for in the calculation of unextractable fossil fuel reserves.

Coal

Unlike oil and fossil methane gas production, which naturally decline through time, coal is not susceptible to the same geological cost–depletion characteristics. Although considerably more attention is paid in this paper to oil and fossil methane gas, coal reserve levels were compared with recent data from the BGR⁴¹. Given the rapid phase-out of coal across our 1.5 °C scenarios, a systematic review of uncertainties in the availability and cost of coal reserves and resources was not undertaken. However, static reserve and resource numbers were cross-checked with the BGR as mentioned.

Reserve estimates for oil and fossil methane gas

Oil and fossil methane gas reserves are assumed to be recoverable with current technologies at current market prices or are now producing. They are typically provided with a given probability of the reported volume being recovered at current market prices: the notation for this is 1P, 2P and 3P, reflecting proved, probable and possible reserves. 1P reserves would be the most conservative, with a 90% probability of at least the reported volume being recovered. 2P reserves have a 50% probability, whereas 3P are the most speculative with a 10% probability of the reported volume being recovered.

In this Article, for reserve estimates we use the methods described by D.W. (manuscript in preparation) for fossil methane gas and used a combination of publicly available data and the methods set out by McGlade³¹ for oil (described in further detail in Supplementary Information section 5). Both used discrete estimates of proven reserves, and combined these (assuming various degrees of correlation) using Monte Carlo simulations. For fossil methane gas, using a 1P basis, outputs from the reserve uncertainty distributions were then combined with a field-level cost database, which was extended to non-producing fields using linear regression models. For oil, we have updated and recalibrated McGlade’s study using 1P estimates from public sources given that these are the most up-to-date available. This allows us to account for reserves of light tight oil in the USA⁴², while maintaining the robust assessment of uncertainty conducted by McGlade³¹. The definitions follow SPE guidelines on what constitutes proved reserves to the greatest possible extent²⁷. For example, McGlade³¹ identified several key examples (the Middle East, Venezuela and Canada) where publicly reported estimates of oil reserves are probably exaggerated, including due to countries booking reserves for political leverage⁴³, and which provide the bulk of the variation between our 1P estimates and those reported by public sources^{12,44,45,46}.

D.W. (manuscript in preparation) also identified the example of Russia, where publicly reported ‘proved’ gas reserves (under an SPE definition) actually seem in reality to refer to Russian reporting standards where field economics are not considered within the definition of reserves^{47,48}. The bottom-up assessment of reserves, using field-level data and accounting for the inherent volumetric uncertainty using probability distributions, is the main driver behind the systematically lower reserve numbers in this work compared with other publicly reporting sources. A detailed explanation of the method used to estimate reserves is provided in Supplementary Information section 5.

Resource estimates for oil and fossil methane gas

Resource estimates used in TIAM-UCL are based on the category of technically recoverable resources. These are a subset of ultimately recoverable resources, in that technologies assumed to be used in recovery are relatively static (that is, do not evolve). Oil resources were originally defined on an ultimately recoverable resources basis. Owing to the sensitivity of resource estimates to the recovery factor, a Monte Carlo simulation method was used that combined uncertainty distributions of recovery factors with in-place unconventional volumes to generate aggregated country- and region-level volumes of ultimately recoverable unconventional oil^{9,31}. Since their original estimation, updates have been undertaken to consider historical production (since 2010) and changes in both estimates of recoverable volumes and costs. For example, the revised volumes of ultimately recoverable extra-heavy oil and bitumen (EHOB) have been reconciled with recent technically recoverable resource estimates from the IEA¹².

For unconventional gas, there is a wide range of literature now estimating technically recoverable resources at individual play levels (at least for shale gas). Therefore, play-level uncertainty ranges of technically recoverable shale resources were constructed and combined using a Monte Carlo simulation to generate regional estimates of technically recoverable shale gas (D.W., manuscript in preparation). These were then combined with cost–depletion curves derived from statistically significant drivers of field supply costs for individual shale plays. This process is illustrated in Supplementary Fig. 12. For tight-gas and coal-bed methane, country-level ranges were combined in a similar manner to generate regional estimates of technically recoverable resources.

Estimation approach for unextractable reserves and resources

The representation of fossil fuels in TIAM-UCL is driven by detailed bottom-up analysis of both the cost and availability of different geological categories of oil and

fossil methane gas. McGlade³¹ and D.W. (manuscript in preparation) constructed supply cost curves for each region and resource category in TIAM-UCL using robust statistical methods to estimate the availability and cost of oil and fossil methane gas.

The supply cost curves of different fossil fuel resources in TIAM-UCL are shown in Extended Data Fig. 1, with oil, fossil methane gas and coal split into the regions of TIAM-UCL. Additional information is provided in Supplementary Information section 5. These supply costs represent costs associated with getting the fossil fuels out of the ground, but do not include transportation costs or taxes under different fiscal regimes. Therefore, they should not be considered as break-even prices. The oil supply cost curve (Extended Data Fig. 1a) reflects the supply cost for a representative barrel of oil energy equivalent (boe), as the mining processes yield different energy commodities. For example, conventional oil reserves output a barrel of crude oil, whereas oil sand production processes output a barrel of bitumen, which may then have to be upgraded if it is to be used for certain downstream uses. This requires additional energy inputs and technology processes, the additional costs of which are not included in the supply curve although are captured in the processing sector of TIAM-UCL.

To provide full transparency and flexibility across the full hydrocarbon resource base, we extended our analysis in this study to unextractable fossil fuel resources (that is, not just reserves), taking into account production from across the supply cost curves shown in Extended Data Fig. 1. Crucially, fossil fuels are not necessarily extracted in cost order along the supply curve because additional constraints (at a region and resource category level) are included, which control both the rate of production expansion and decline.

Constraints are based on McGlade³¹, McGlade and Ekins⁹ and D.W. (manuscript in preparation), with each constructed from bottom-up databases of oil and gas fields (and individual wells for US shale gas), and allow TIAM-UCL to provide an empirically robust representation of the ‘depletion’ characteristics of oil and fossil methane gas production. The decline and growth constraints are used to model both geological and techno-economic characteristics of oil and gas mining technologies, as well as some degree of inertia within the system. Additional information on how these constraints function, as well as underlying data assumptions, is provided in Supplementary Information section 5.

In this Article, resources beyond reserves are considered when estimating unextractable fossil fuels for a number of reasons. First, the dynamic nature of reserves means that resources can shift across the techno-economic feasibility matrix in either direction (that is, resources can become reserves and vice versa). Therefore, considering the whole resource base allows us to expand away from the relatively restrictive definition of reserves, albeit necessarily increasing the uncertainty range

away from the most certain recoverable volumes. Second, not all fossil fuel production, particularly when moving out to 2100, is from the reserves base, due to constraints on production growth and decline, and trade. The full resource base needs consideration to capture non-reserve volumes. Finally, when analysing fossil fuel extraction under a 1.5-°C-consistent carbon budget, it is not just the supply cost hierarchy of different reserves and resources that drives the regional distribution of production, but also the volume of CO₂ (and other greenhouse gases) associated with those resources, and therefore the potential emissions from extraction and consumption.

Data availability

The results data and key source data in the figures (including in the [Supplementary Information](#)) are available via Zenodo at <https://doi.org/10.5281/zenodo.5118971>. [Source data](#) are provided with this paper.

Code availability

The underlying code (mathematical equations) for the model is available via GitHub (https://github.com/etsap-TIMES/TIMES_model). The full model database is also available via Zenodo (<https://doi.org/10.5281/zenodo.5118971>). Given the complexity of the model, further guidance will be provided on model assumptions upon reasonable request from the corresponding author.

References

1. 1.

Adoption of the Paris Agreement

<https://unfccc.int/resource/docs/2015/cop21/eng/l09r01.pdf> (United Nations, 2015).

2. 2.

The Production Gap Report: 2020 Special Report

<http://productiongap.org/2020report> (SEI, IISD, ODI, E3G & UNEP, 2020).

3. 3.

Rogelj, J. et al. in *Special Report on Global Warming of 1.5 °C* (eds Masson-Delmotte, V. et al.) (IPCC, WMO, 2018).

4. 4.

Luderer, G. et al. Residual fossil CO₂ emissions in 1.5–2 °C pathways. *Nat. Clim. Change* **8**, 626–633 (2018).

5. 5.

Grubler, A. et al. A low energy demand scenario for meeting the 1.5 °C target and sustainable development goals without negative emission technologies. *Nat. Energy* **3**, 515–527 (2018).

6. 6.

Tong, D. et al. Committed emissions from existing energy infrastructure jeopardize 1.5 °C climate target. *Nature* **572**, 373–377 (2019).

7. 7.

Anderson, K. & Peters, G. The trouble with negative emissions. *Science* **354**, 182–183 (2016).

8. 8.

Pye, S. et al. An equitable redistribution of unburnable carbon. *Nat. Commun.* **11**, 3968 (2020).

9. 9.

McGlade, C. & Ekins, P. The geographical distribution of fossil fuels unused when limiting global warming to 2 °C. *Nature* **517**, 187–190 (2015).

10. 10.

Masson-Delmotte, V. et al. (eds) *Special Report on Global Warming of 1.5 °C* (IPCC, WMO, 2018).

11. 11.

Rogelj, J. et al. Scenarios towards limiting global mean temperature increase below 1.5 °C. *Nat. Clim. Change* **8**, 325–332 (2018).

12. 12.

World Energy Outlook 2019 (IEA, 2019).

13. 13.

BP Energy Outlook: 2020 Edition <https://www.bp.com/content/dam/bp/business-sites/en/global/corporate/pdfs/energy-economics/energy-outlook/bp-energy-outlook-2020.pdf> (BP, 2020).

14. 14.

Unburnable Carbon 2013: Wasted Capital and Stranded Assets (Carbon Tracker & Grantham Research Institute of Climate Change and the Environment, 2013).

15. 15.

Lau, W. W. Y. et al. Evaluating scenarios toward zero plastic pollution. *Science* **369**, 1455–1461 (2020).

16. 16.

The Future's Not in Plastics: Why Plastics Demand Won't Rescue the Oil Sector <https://carbontracker.org/reports/the-futures-not-in-plastics/> (Carbon Tracker Initiative, 2020).

17. 17.

Godoi, J. M. A. & dos Santos Matai, P. H. L. Enhanced oil recovery with carbon dioxide geosequestration: first steps at Pre-salt in Brazil. *J. Petrol. Explor. Prod.* **11**, 1429–1441 (2021).

18. 18.

Beyond Petrostates: The Burning Need to Cut Oil Dependence in the Energy Transition <https://carbontracker.org/reports/petrostates-energy-transition-report/> (Carbon Tracker Initiative, 2021).

19. 19.

Green, F. & Denniss, R. Cutting with both arms of the scissors: the economic and political case for restrictive supply-side climate policies. *Clim. Change* **150**, 73–87 (2018).

20. 20.

Erickson, P., Lazarus, M. & Piggot, G. Limiting fossil fuel production as the next big step in climate policy. *Nat. Clim. Change* **8**, 1037–1043 (2018).

21. 21.

Lazarus, M. & van Asselt, H. Fossil fuel supply and climate policy: exploring the road less taken. *Clim. Change* **150**, 1–13 (2018).

22. 22.

Newell, P. & Simms, A. Towards a fossil fuel non-proliferation treaty. *Clim. Policy* **20**, 1043–1054 (2020).

23. 23.

Piggot, G., Erickson, P., van Asselt, H. & Lazarus, M. Swimming upstream: addressing fossil fuel supply under the UNFCCC. *Clim. Policy* **18**, 1189–1202 (2018).

24. 24.

World Energy Outlook 2020 (IEA, 2020).

25. 25.

Decline and Fall: The Size & Vulnerability of the Fossil Fuel System
<https://carbontracker.org/reports/decline-and-fall/> (Carbon Tracker Initiative, 2020).

26. 26.

Muttitt, G. & Kartha, S. Equity, climate justice and fossil fuel extraction: principles for a managed phase out. *Clim. Policy* **20**, 1024–1042 (2020).

27. 27.

Petroleum Resources Management System
http://info.speccommunications.org/rs/833-LLT-087/images/PRMgmtSystem_V1.01Nov27.pdf?mkt_tok=ODMzLUxMVC0wODcAAAF9dSrG2UNYnY2eBC7yyN17I25FkaA9i2XvL5kjWdgP6mXak-NSn63rWtB1NFtduvqTfPhyTxIcU92WlXrHa762rjyWID3PytxB3BUUJLfhomzKAA (Society of Petroleum Engineers, 2018).

28. 28.

McCollum, D. L. et al. Interaction of consumer preferences and climate policies in the global transition to low-carbon vehicles. *Nat. Energy* **3**, 664–673 (2018).

29. 29.

Marangoni, G. et al. Sensitivity of projected long-term CO₂ emissions across the Shared Socioeconomic Pathways. *Nat. Clim. Change* **7**, 113–117 (2017).

30. 30.

Erickson, P. et al. Why fossil fuel producer subsidies matter. *Nature* **578**, E1–E4 (2020).

31. 31.

McGlade, C. *Uncertainties in the Outlook for Oil and Gas*. PhD thesis, UCL (2013).

32. 32.

Biomass in a Low-Carbon Economy

<https://www.theccc.org.uk/publication/biomass-in-a-low-carbon-economy/> (CCC, 2018).

33. 33.

Huppmann, D., Rogelj, J., Kriegler, E., Krey, V. & Riahi, K. A new scenario resource for integrated 1.5 °C research. *Nat. Clim. Change* **8**, 1027–1030 (2018).

34. 34.

Fuss, S. et al. Negative emissions—part 2: costs, potentials and side effects. *Environ. Res. Lett.* **13**, 063002 (2018).

35. 35.

Creutzig, F. et al. Bioenergy and climate change mitigation: an assessment. *Glob. Change Biol. Bioenergy* **7**, 916–944 (2015).

36. 36.

Integrated Assessment of Global Environmental Change with IMAGE 3.0: Model Description and Policy Applications

<https://www.pbl.nl/en/publications/integrated-assessment-of-global-environmental-change-with-IMAGE-3.0> (PBL, 2014).

37. 37.

Fricko, O. et al. The marker quantification of the Shared Socioeconomic Pathway 2: a middle-of-the-road scenario for the 21st century. *Glob. Environ. Change* **42**, 251–267 (2017).

38. 38.

Bauer, N. et al. Global energy sector emission reductions and bioenergy use: overview of the bioenergy demand phase of the EMF-33 model comparison. *Clim. Change* **163**, 1553–1568 (2020).

39. 39.

Fuss, S. et al. Betting on negative emissions. *Nat. Clim. Change* **4**, 850–853 (2014).

40. 40.

Gautier, D. & Moore, T. in *The 2008 Circum-Arctic Resource Appraisal* Professional Paper No. 1824 (eds Gautier, D. & Moore, T.) (USGS, 2017).

41. 41.

BGR Energy Study 2019: Data and Developments Concerning German and Global Energy Supplies
https://www.bgr.bund.de/EN/Themen/Energie/Downloads/energiestudie_2019_en.pdf;jsessionid=A73E36C969C2253E194ADF4E2484C95A.1_cid321?__blob=publicationFile&v=6 (BGR, 2020).

42. 42.

Assumptions to the Annual Energy Outlook 2020: Oil and Gas Supply Module
<https://www.eia.gov/outlooks/aoe/assumptions/pdf/oilgas.pdf> (EIA, 2020).

43. 43.

Laherrère, J. Future of oil supplies. *Energy Explor. Exploit.* **21**, 227–267 (2003).

44. 44.

OPEC Annual Statistical Bulletin 2019
https://www.opec.org/opec_web/static_files_project/media/downloads/publications/ASB_2019.pdf (OPEC, 2019).

45. 45.

Statistical Review of World Energy <https://www.bp.com/content/dam/bp/business-sites/en/global/corporate/pdfs/energy-economics/statistical-review/bp-stats-review-2020-full-report.pdf> (BP, 2020).

46. 46.

Energy Study 2016: Reserves, Resources and Availability of Energy Resources (BGR, 2016).

47. 47.

Russian Energy 2015 <https://ac.gov.ru/files/publication/a/10205.pdf> (Analytical Centre for the Government of the Russian Federation, 2016).

48. 48.

Natural Gas Information 2019 <https://www.iea.org/reports/natural-gas-information-2019> (2019).

Acknowledgements

We thank P. Erickson (SEI), G. Muttitt (IISD) and C. McGlade (IEA) for commenting on a draft version of this paper. This work has been supported by the European Climate Foundation (ECF) and the UK Energy Research Centre Phase 4 (grant number EP/S029575/1).

Author information

Affiliations

1. Institute for Sustainable Resources, University College London, London, UK

Dan Welsby & Paul Ekins

2. UCL Energy Institute, University College London, London, UK

James Price & Steve Pye

Contributions

All authors were involved in the design approach to the research. D.W. and J.P. undertook the scenario modelling and analysed the results. All authors contributed to the development of early drafts of the paper, and to writing the final paper.

Corresponding author

Correspondence to [Dan Welsby](#).

Ethics declarations

Competing interests

The authors declare no competing interests.

Additional information

Peer review information *Nature* thanks Dieter Franke, Gang He and Michael Lazarus for their contribution to the peer review of this work. Peer reviewer reports are available.

Publisher's note Springer Nature remains neutral with regard to jurisdictional claims in published maps and institutional affiliations.

Extended data figures and tables

[**Extended Data Fig. 1 Supply cost curves split by region in TIAM-UCL.**](#)

a–c, Curves for oil (**a**), fossil methane gas (**b**) and coal (**c**). Costs are given on an energy-content basis (barrel of oil equivalent for oil, British thermal units for gas and joules for coal), on a US\$₂₀₀₅ basis. For oil, different mining processes output different commodities (for example, oil sands mining initially (pre-upgrading) outputs a barrel of bitumen) hence the use of the energy-content cost basis. For gas, associated gas is not included in Extended Data Fig. [1b](#) as it is a by-product of oil production

[Source data](#).

Extended Data Table 1 Description of the scenarios explored in this work

Supplementary information

Supplementary Information

This file contains supplementary text, supplementary table 1 – 26, supplementary equations, supplementary figures 1 – 17 and supplementary references.

Peer Review File

Source data

Source Data Fig. 1

Source Data Fig. 2

Source Data Extended Data Fig. 1

Rights and permissions

Reprints and Permissions

About this article

Cite this article

Welsby, D., Price, J., Pye, S. *et al.* Unextractable fossil fuels in a 1.5 °C world. *Nature* **597**, 230–234 (2021). <https://doi.org/10.1038/s41586-021-03821-8>

- Received: 25 February 2021
- Accepted: 09 July 2021
- Published: 08 September 2021
- Issue Date: 09 September 2021
- DOI: <https://doi.org/10.1038/s41586-021-03821-8>

Further reading

- **Most fossil-fuel reserves must remain untapped to hit 1.5 °C warming goal**

- Bianca Nogrady

Nature (2021)

This article was downloaded by **calibre** from <https://www.nature.com/articles/s41586-021-03821-8>

| [Section menu](#) | [Main menu](#) |

- Article
- [Published: 25 August 2021](#)

A Triassic stem lepidosaur illuminates the origin of lizard-like reptiles

- [Ricardo N. Martínez](#) ORCID: [orcid.org/0000-0002-6013-1139¹](https://orcid.org/0000-0002-6013-1139),
- [Tiago R. Simões](#) ORCID: [orcid.org/0000-0003-4716-649X^{2,3}](https://orcid.org/0000-0003-4716-649X),
- [Gabriela Sobral](#) ORCID: [orcid.org/0000-0002-5001-4406⁴](https://orcid.org/0000-0002-5001-4406) &
- [Sebastián Apesteguía⁵](#)

Nature volume **597**, pages 235–238 (2021)

- 2619 Accesses
- 413 Altmetric
- [Metrics details](#)

Subjects

- [Palaeontology](#)
- [Phylogenetics](#)

Abstract

The early evolution of diapsid reptiles is marked by a deep contrast between our knowledge of the origin and early evolution of archosauromorphs (crocodiles, avian and non-avian dinosaurs) to that of lepidosauromorphs (squamates (lizards, snakes) and sphenodontians (tuataras)). Whereas the

former include hundreds of fossil species across various lineages during the Triassic period¹, the latter are represented by an extremely patchy early fossil record comprising only a handful of fragmentary fossils, most of which have uncertain phylogenetic affinities and are confined to Europe^{1,2,3}. Here we report the discovery of a three-dimensionally preserved reptile skull, assigned as *Taytalura alcoberi* gen. et sp. nov., from the Late Triassic epoch of Argentina that is robustly inferred phylogenetically as the earliest evolving lepidosauromorph, using various data types and optimality criteria. Micro-computed tomography scans of this skull reveal details about the origin of the lepidosaurian skull from early diapsids, suggesting that several traits traditionally associated with sphenodontians in fact originated much earlier in lepidosauromorph evolution. *Taytalura* suggests that the strongly evolutionarily conserved skull architecture of sphenodontians represents the plesiomorphic condition for all lepidosaurs, that stem and crown lepidosaurs were contemporaries for at least ten million years during the Triassic, and that early lepidosauromorphs had a much broader geographical distribution than has previously been thought.

Access options

Subscribe to Journal

Get full journal access for 1 year

\$199.00

only \$3.90 per issue

[Subscribe](#)

All prices are NET prices.

VAT will be added later in the checkout.

Tax calculation will be finalised during checkout.

Rent or Buy article

Get time limited or full article access on ReadCube.

from \$8.99

[Rent or Buy](#)

All prices are NET prices.

Additional access options:

- [Log in](#)
- [Access through your institution](#)
- [Learn about institutional subscriptions](#)

Fig. 1: Holotype of *T. alcoberi* (PVSJ 698).

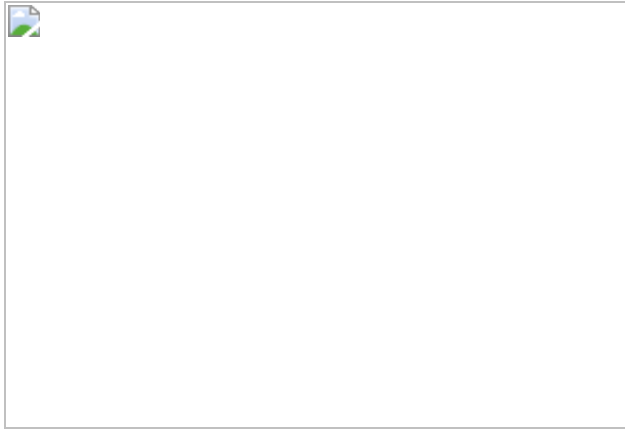
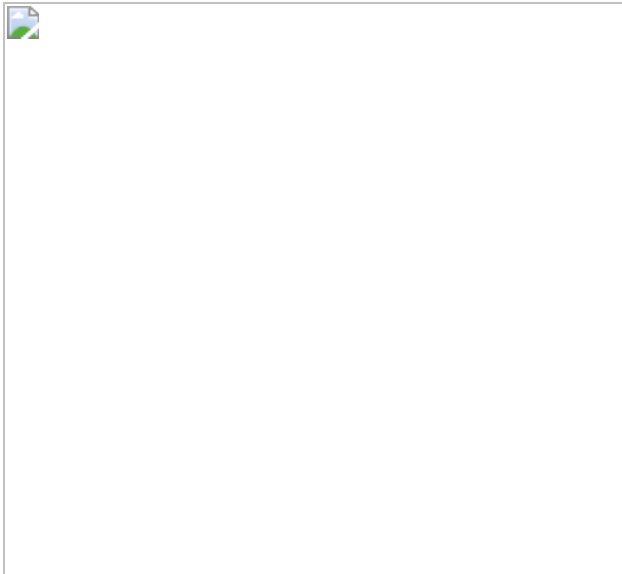


Fig. 2: Combined-evidence Bayesian-inference phylogenetic analysis and morphospace occupation.



Data availability

Computed tomography scan data, including surface volume files of the holotype, all morphological and molecular data generated and analysed, along with trees and log files described in the Article are available online as 'Supplementary Data 1' at Harvard Dataverse (<https://doi.org/10.7910/DVN/G5EOOC>)⁴³.

Code availability

The MrBayes commands for Bayesian analyses are provided as 'Supplementary Data 2' and R scripts for reproducing the morphospace analyses and figures are available as the file 'Supplementary Data 3', both at Harvard Dataverse (<https://doi.org/10.7910/DVN/G5EOOC>)⁴³.

References

1. 1.

Sues, H. D. *The Rise of Reptiles: 320 Million Years of Evolution* (John Hopkins Univ. Press, 2019).

2. 2.

Simões, T. R. & Caldwell, M. W. in *Encyclopedia of Geology* 2nd ed., vol. 3 (eds Alderton, D. & Elias, S. A.) 165–174 (Academic, 2021).

3. 3.

Simões, T. R. & Pyron, R. A. The squamate tree of life. *Bull. Mus. Comp. Zool.* **163**, 47–95 (2021).

4. 4.

Uetz, P. & Hošek, J. *The Reptile Database* <http://www.reptile-database.org> (2021).

5. 5.

Gill, F., Donsker, D. & Rasmussen, F. *IOC World Bird List (v.11.1)* (2021).

6. 6.

Simões, T. R., Pesteguía, S., Hsiou, A. S. & Daza, J. D. Lepidosauromorphs from Gondwana: an introduction. *J. Herpetol.* **51**, 297–299 (2017).

7. 7.

Sues, H.-D. & Kligman, B. T. A new lizard-like reptile from the Upper Triassic (Carnian) of Virginia and the Triassic record of Lepidosauromorpha (Diapsida, Sauria). *J. Vert. Paleontol.* **40**, e1879102 (2021).

8. 8.

Schoch, R. R. & Sues, H.-D. A new lepidosauromorph reptile from the Middle Triassic (Ladinian) of Germany and its phylogenetic relationships. *J. Vertebr. Paleontol.* **38**, e1444619 (2018).

9. 9.

Evans, S. E. & Borsuk-Białyńicka, M. A small lepidosauromorph reptile from the Early Triassic of Poland. *Palaeontol. Pol.* **65**, 179–202 (2009).

10. 10.

Romo De Vivar, P. R., Martinelli, A. G., Fonseca, P. H. M. & Soares, M. B. To be or not to be: the hidden side of *Cargninia enigmatica* and other puzzling remains of Lepidosauromorpha from the Upper Triassic of Brazil. *J. Vert. Paleontol.* **40**, e1828438 (2020).

11. 11.

Cavicchini, I., Zaher, M. & Benton, M. J. An enigmatic neodiapsid reptile from the Middle Triassic of England. *J. Vertebr. Paleontol.* **40**, e1781143 (2020).

12. 12.

Sobral, G., Simões, T. R. & Schoch, R. R. A tiny new Middle Triassic stem-lepidosauromorph from Germany: implications for the early evolution of lepidosauromorphs and the Vellberg fauna. *Sci. Rep.* **10**, 2273 (2020).

13. 13.

Simões, T. R. et al. The origin of squamates revealed by a Middle Triassic lizard from the Italian Alps. *Nature* **557**, 706–709 (2018).

14. 14.

Simões, T. R., Vernygora, O., Caldwell, M. W. & Pierce, S. E. Megaevolutionary dynamics and the timing of evolutionary innovation in reptiles. *Nat. Commun.* **11**, 3322 (2020).

15. 15.

Simões, T. R., Caldwell, M. W. & Pierce, S. E. Sphenodontian phylogeny and the impact of model choice in Bayesian morphological

clock estimates of divergence times and evolutionary rates. *BMC Biol.* **18**, 191 (2020).

16. 16.

Scheyer, T. M. et al. *Colobops*: a juvenile rhynchocephalian reptile (Lepidosauromorpha), not a diminutive archosauromorph with an unusually strong bite. *R. Soc. Open Sci.* **7**, 192179 (2020).

17. 17.

Hsiou, A. S., De França, M. A. G. & Ferigolo, J. New data on the *Clevosaurus* (Sphenodontia: Clevosauridae) from the Upper Triassic of Southern Brazil. *PLoS ONE* **10**, e0137523 (2015).

18. 18.

Fraser, N. C. The osteology and relationships of *Clevosaurus* (Reptilia: Sphenodontida). *Phil. Trans. R. Soc. Lond. B* **321**, 125–178 (1988).

19. 19.

Martinez, R. N. et al. A basal dinosaur from the dawn of the dinosaur era in southwestern Pangaea. *Science* **331**, 206–210 (2011).

20. 20.

Garberoglio, F. F. et al. New skulls and skeletons of the Cretaceous legged snake *Najash*, and the evolution of the modern snake body plan. *Sci. Adv.* **5**, eaax5833 (2019).

21. 21.

Bittencourt, J. S., Simões, T. R., Caldwell, M. W. & Langer, M. C. Discovery of the oldest South American fossil lizard illustrates the cosmopolitanism of early South American squamates. *Commun. Biol.* **3**, 201 (2020).

22. 22.

Bertin, T. J. C., Thivichon-Prince, B., LeBlanc, A. R. H., Caldwell, M. W. & Viriot, L. Current perspectives on tooth implantation, attachment, and replacement in Amniota. *Front. Physiol.* **9**, 1630 (2018).

23. 23.

Fraser, N. C. A new rhynchocephalian from the British Upper Trias. *Palaeontology* **25**, 709–725 (1982).

24. 24.

Evans, S. E. The skull of a new eosuchian reptile from the Lower Jurassic of South Wales. *Zool. J. Linn. Soc.* **70**, 203–264 (1980).

25. 25.

Whiteside, D. I. The head skeleton of the Rhaetian sphenodontid *Diphydontosaurus avonis* gen. et sp. nov. and the modernizing of a living fossil. *Phil. Trans. R. Soc. Lond. B* **312**, 379–430 (1986).

26. 26.

Herrera-Flores, J. A., Stubbs, T. L. & Benton, M. J. Macroevolutionary patterns in Rhynchocephalia: is the tuatara (*Sphenodon punctatus*) a living fossil? *Palaeontology* **60**, 319–328 (2017).

27. 27.

Gemmell, N. J. et al. The tuatara genome reveals ancient features of amniote evolution. *Nature* **584**, 403–409 (2020).

28. 28.

Jones, M. E. H. et al. Integration of molecules and new fossils supports a Triassic origin for Lepidosauria (lizards, snakes, and tuatara). *BMC Evol. Biol.* **13**, 208 (2013).

29. 29.

Hsiou, A. S. et al. A new clevosaurid from the Triassic (Carnian) of Brazil and the rise of sphenodontians in Gondwana. *Sci. Rep.* **9**, 11821 (2019).

30. 30.

Vernygora, O. V., Simões, T. R. & Campbell, E. O. Evaluating the performance of probabilistic algorithms for phylogenetic analysis of big morphological datasets: a simulation study. *Syst. Biol.* **69**, 1088–1105 (2020).

31. 31.

Maddison, W. P. & Maddison, D. R. Mesquite: a modular system for evolutionary analysis, version 3.04, <http://mesquiteproject.org> (2015).

32. 32.

Goloboff, P. A., Farris, J. S. & Nixon, K. C. TNT, a free program for phylogenetic analysis. *Cladistics* **24**, 774–786 (2008).

33. 33.

Ronquist, F. et al. MrBayes 3.2: efficient Bayesian phylogenetic inference and model choice across a large model space. *Syst. Biol.* **61**, 539–542 (2012).

34. 34.

Miller, M. A., Pfeiffer, W. & Schwartz, T. Creating the CIPRES Science Gateway for inference of large phylogenetic trees in *Gateway Computing Environments Workshop (GCE)* 1–8 (IEEE, 2010).

35. 35.

Lanfear, R., Frandsen, P. B., Wright, A. M., Senfeld, T. & Calcott, B. PartitionFinder 2: new methods for selecting partitioned models of evolution for molecular and morphological phylogenetic analyses. *Mol. Biol. Evol.* **34**, 772–773 (2017).

36. 36.

Lewis, P. O. A likelihood approach to estimating phylogeny from discrete morphological character data. *Syst. Biol.* **50**, 913–925 (2001).

37. 37.

Hughes, M., Gerber, S. & Wills, M. A. Clades reach highest morphological disparity early in their evolution. *Proc. Natl Acad. Sci. USA* **110**, 13875–13879 (2013).

38. 38.

Sutherland, J., Flannery, T., Moon, B. C., Stubbs, T. L. & Benton, M. J. Does exceptional preservation distort our view of disparity in the fossil record? *Proc. R. Soc. Lond. Biol. Sci.* **286**, 20190091 (2019).

39. 39.

Lloyd, G. T. Estimating morphological diversity and tempo with discrete character-taxon matrices: implementation, challenges, progress, and future directions. *Biol. J. Linn. Soc.* **118**, 131–151 (2016).

40. 40.

Gerber, S. Use and misuse of discrete character data for morphospace and disparity analyses. *Palaeontology* **62**, 305–319 (2019).

41. 41.

Cisneros, J. C. & Ruta, M. Morphological diversity and biogeography of procolophonids (Amniota: Parareptilia). *J. Syst. Palaeontology* **8**, 607–625 (2010).

42. 42.

Ciampaglio, C. N., Kemp, M. & McShea, D. W. Detecting changes in morphospace occupation patterns in the fossil record: characterization

and analysis of measures of disparity. *Paleobiology* **27**, 695–715 (2001).

43. 43.

Martinez, R., Simões, T. R., Sobral, G. & Apesteguía, S. Supplementary Data for “A Triassic stem lepidosaur illuminates the origin of lizard-like reptiles” *Harvard Dataverse* (2021).

Acknowledgements

R.N.M. thanks the Secretaría de Ciencia, Técnica e Innovación of San Juan (SECITI) and the field crew and EarthWatch volunteers of 2001 fieldwork. T.R.S. thanks the Natural Sciences and Engineering Research Council of Canada (NSERC) for providing a postdoctoral fellowship. We thank J. Antonio González for his line reconstruction of *Taytalura* skull and jaw and J. Blanco for his artwork of *Taytalura*.

Author information

Affiliations

1. Instituto y Museo de Ciencias Naturales, Centro de Investigaciones de la Geósfera y la Biósfera, Universidad Nacional de San Juan, San Juan, Argentina

Ricardo N. Martínez

2. Department of Organismic and Evolutionary Biology, Harvard University, Cambridge, MA, USA

Tiago R. Simões

3. Museum of Comparative Zoology, Harvard University, Cambridge, MA, USA

Tiago R. Simões

4. Department of Palaeontology, Staatliches Museum für Naturkunde Stuttgart, Stuttgart, Germany

Gabriela Sobral

5. Área de Paleontología, Fundación de Historia Natural Félix de Azara, Universidad Maimónides, Buenos Aires, Argentina

Sebastián Apesteguía

Contributions

R.N.M. led the project, and conducted fieldwork and specimen preparation. T.R.S. conducted phylogenetic and morphospace analyses. G.S. performed CT scan data segmentation. T.R.S., G.S. and S.A. produced the figures. All authors contributed to interpretation of the results, discussions and manuscript writing.

Corresponding authors

Correspondence to [Ricardo N. Martínez](#) or [Tiago R. Simões](#).

Ethics declarations

Competing interests

The authors declare no competing interests.

Additional information

Peer review information *Nature* thanks Hans-Dieter Sues and the other, anonymous, reviewer(s) for their contribution to the peer review of this work. Peer reviewer reports are available.

Publisher's note Springer Nature remains neutral with regard to jurisdictional claims in published maps and institutional affiliations.

Extended data figures and tables

Extended Data Fig. 1 Location and geology of the Ischigualasto–Villa Unión Basin.

a, Geologic map of the southern outcrops of the Ischigualasto–Villa Unión Basin. **b**, Stratigraphic section of the Ischigualasto Formation. Black star indicates the type locality of PVSJ 698. Black line indicates the location of the stratigraphic section.

Extended Data Fig. 2 Cranial anatomy of *T. alcoberi* on the basis of segmented micro-computed tomography scan data.

a, b, Three-dimensional model of *Taytalura* with segmented bones in right lateral and ventral views. **c**, Segmented right squamosal and quadrate in lateral view (left) and corresponding line drawing (right). **d**, Segmented left quadrate in posterior view. **e, f**, Line drawings of the left jaw in medial and dorsal views. af, adductor fossa; ap, anterior process; ar, articular; bc, braincase; co, coronoid; dp, dorsal process; fr, frontal; gf, glenoid fossa; hy, hyoid arch; ju, jugal; lc, lateral condyle; lj, lower jaw; mc, medial condyle; mf, medial flange; mx, maxilla; na, nasal; oc, otic conch; pa, parietal; pm, pre-maxilla; pl, palate; po, post-orbital; pof, post-frontal; pr, pre-artciular; prf, pre-frontal; qd, quadrate; qj, quadrato-jugal; sp., splenial; sq, squamosal; vp, ventral process. Scale bars, 3.5 mm.

Extended Data Fig. 3 Further details of cranial anatomy of *T. alcoberi* on the basis of segmented micro-computed tomography scan data.

a, b, Segmented palate in right lateral and left dorsolateral views. **c**, Segmented right posterior half of the braincase with stapes in red in lateral view. **d**, Segmented left posterior half of the braincase in lateral view. **e, f**, Segmented anterior region of the braincase in left lateral and anterior views. ap, ascending process; bc, braincase; bp, basipterygoid process; CN, cranial nerve; cp, cultriform process; cr, raised crest formed by the pterygoids

meeting medially; clp, clinoid process; crp, crista prootica; ds, dorsum sella; ec, ectopterygoid; ep, epipterygoid; fo, fenestra ovalis; hf, hypophyseal fossa; lf, lateral flange; oc, otic conch; os, orbitosphenoid; pa, palatine; pp, paroccipital process; qw, quadrate wing; rc, recess; st, stapes. Roman numerals indicate corresponding cranial nerves. Scale bars, 3.5 mm (**a, b**), 1.5 mm (**c–f**).

Extended Data Fig. 4 Cranial anatomy of *T. alcoberi* on the basis of 2D cross-sectional slices from micro-computed tomography scan data.

a–c, Transverse cross sections of the skull showing the paired nasals (**a**), frontals (**b**) and parietales (**c**). **d**, Longitudinal cross-section of the paired frontals. **e**, Transverse cross section of the left lower and upper jaws in anterior view, showing labial and lingual walls of the tooth grooves of the maxilla and dentary. **f**, Transverse cross section of the posterior region of the skull through the braincase and the left lower jaw in anterior view. **g**, Transverse cross section of the left maxilla, showing the replacement tooth going into position. **h**, Longitudinal cross-section of the left dentary in occlusal view. **i, j**, Longitudinal cross section of the anterior (**i**) and posterior (**j**) sectors of the right maxilla in occlusal view. In **h–i**, the absence of the interdental ridges and less dense attachment tissue (alveolar bone and/or cementum) in the interdental space of the anterior dentition is shown, whereas **j** shows the direct contact between the posterior teeth and the absence of interdental space. Planes of the sections in the corresponding details. ac, adductor crest; alv.t., alveolar tissue; de, dentary; mx, maxilla; na, nasals; f-f, inter-frontal suture; fr, frontals; la, labial wall; li, lingual wall; ot, otolith; pa, parietales; pof, post-frontal; prf, pre-frontal; rp, resorption pit; rt, replacement tooth; to, tooth. Scale bars, 1.5 mm (**a**), 1 mm (**b–e, h–j**), 2.5 mm (**f**), 2 mm (**g**).

Extended Data Fig. 5 Skull and jaw of *T. alcoberi*.

a–d, Photographs of PVSJ 698 in dorsal (**a**), ventral (**b**), left lateral (**c**) and right lateral (**d**) views. **e–h**, Reconstruction of the skull of *T. alcoberi* in dorsal (**e**), ventral (**f**), anterior (**g**) and left lateral (**h**) views (reconstructed

on the basis of information from both sides). **i–k**, Reconstruction of the lower jaw of *T. alcoberi* in lateral (**i**), medial (**j**) and occlusal (**k**) views. d, dentary; ec, ectopterygoid; fr, frontal; ju, jugal; mx, maxilla; na, nasal; pa, parietal; pm, pre-maxilla; pl, palatine; po, post-orbital; pof, post-frontal; prf, pre-frontal; pt, pterygoid; qd, quadrate; qj, quadrato-jugal; sq, squamosal; Scale bar, 10 mm.

Extended Data Fig. 6 Phylogenetic analyses using morphological data only, including data from all species.

a, Equal weights maximum parsimony analysis. Strict consensus of 602 most parsimonious trees (2,481 steps each). **b**, Bayesian inference analysis. Majority rule consensus tree. Numbers at nodes indicate posterior probabilities.

Extended Data Fig. 7 Bayesian inference phylogenetic analysis of combined morphological and molecular data, including data from all species.

Maximum compatibility tree (illustrating all nodes, including those with very low support). Numbers at nodes indicate posterior probabilities.

Extended Data Fig. 8 Phylogenetic analyses using morphological data only, with data from the rogue taxon (*Vellbergia*) removed.

a, Equal weights maximum parsimony analysis. Strict consensus of 572 most parsimonious trees (2,480 steps each). **b**, Bayesian inference analysis. Majority rule consensus tree. Numbers at nodes indicate posterior probabilities.

Extended Data Fig. 9 Bayesian inference phylogenetic analysis of combined morphological and molecular data, with data from the rogue taxon (*Vellbergia*) removed.

Majority rule consensus tree. Numbers at nodes indicate posterior probabilities.

[Extended Data Fig. 10 Morphospace occupation by early diapsid reptiles and lepidosauromorphs, with the first 10 pairwise principal coordinate comparisons illustrated.](#)

PC1 distinguishes squamates from all other groups when contrasted against all other principal coordinates (red), whereas PC3 distinguishes sphenodontians from all other groups when contrasted against all other principal coordinates (cyan). Major clades of interest are highlighted within convex hulls: squamatans (yellow), sphenodontians (light green), early lepidosaurs of uncertain placement (blue), all other diapsids (purple) and *Taytalura* (turquoise). For individual taxon names for each data point and relative contribution of each principal coordinate, see supplementary data files at Harvard Dataverse ('Data availability' in Methods).

Supplementary information

[Supplementary Information](#)

This file contains Geological and paleontological settings, Description of *Taytalura alcoberi*, Historical overview of lepidosauromorph classification, Additional taxa added to phylogenetic dataset, Synapomorphies Supplementary References.

[Reporting Summary](#)

[Peer Review File](#)

Rights and permissions

[Reprints and Permissions](#)

About this article

Cite this article

Martínez, R.N., Simões, T.R., Sobral, G. *et al.* A Triassic stem lepidosaur illuminates the origin of lizard-like reptiles. *Nature* **597**, 235–238 (2021). <https://doi.org/10.1038/s41586-021-03834-3>

- Received: 31 May 2021
- Accepted: 19 July 2021
- Published: 25 August 2021
- Issue Date: 09 September 2021
- DOI: <https://doi.org/10.1038/s41586-021-03834-3>

This article was downloaded by **calibre** from <https://www.nature.com/articles/s41586-021-03834-3>

| [Section menu](#) | [Main menu](#) |

- Article
- [Published: 18 August 2021](#)

Chronic social isolation signals starvation and reduces sleep in *Drosophila*

- [Wanhe Li](#) [ORCID: orcid.org/0000-0001-5682-5173¹](#),
- [Zikun Wang¹](#),
- [Sheyum Syed](#) [ORCID: orcid.org/0000-0002-4642-6678²](#),
- [Cheng Lyu³](#),
- [Samantha Lincoln¹](#),
- [Jenna O'Neil¹](#),
- [Andrew D. Nguyen¹](#),
- [Irena Feng](#) [ORCID: orcid.org/0000-0001-7740-9793¹](#) &
- [Michael W. Young](#) ¹

[Nature](#) volume 597, pages 239–244 (2021)

- 8992 Accesses
- 590 Altmetric
- [Metrics details](#)

Subjects

- [Emotion](#)
- [Sleep](#)

Abstract

Social isolation and loneliness have potent effects on public health^{1,2,3,4}. Research in social psychology suggests that compromised sleep quality is a key factor that links persistent loneliness to adverse health conditions^{5,6}. Although experimental manipulations have been widely applied to studying the control of sleep and wakefulness in animal models, how normal sleep is perturbed by social isolation is unknown. Here we report that chronic, but not acute, social isolation reduces sleep in *Drosophila*. We use quantitative behavioural analysis and transcriptome profiling to differentiate between brain states associated with acute and chronic social isolation. Although the flies had uninterrupted access to food, chronic social isolation altered the expression of metabolic genes and induced a brain state that signals starvation. Chronically isolated animals exhibit sleep loss accompanied by overconsumption of food, which resonates with anecdotal findings of loneliness-associated hyperphagia in humans. Chronic social isolation reduces sleep and promotes feeding through neural activities in the peptidergic fan-shaped body columnar neurons of the fly. Artificial activation of these neurons causes misperception of acute social isolation as chronic social isolation and thereby results in sleep loss and increased feeding. These results present a mechanistic link between chronic social isolation, metabolism, and sleep, addressing a long-standing call for animal models focused on loneliness⁷.

Access options

Subscribe to Journal

Get full journal access for 1 year

\$199.00

only \$3.90 per issue

[Subscribe](#)

All prices are NET prices.

VAT will be added later in the checkout.

Tax calculation will be finalised during checkout.

Rent or Buy article

Get time limited or full article access on ReadCube.

from \$8.99

[Rent or Buy](#)

All prices are NET prices.

Additional access options:

- [Log in](#)
- [Access through your institution](#)
- [Learn about institutional subscriptions](#)

Fig. 1: Sleep is reduced by chronic but not acute social isolation in *Drosophila*.

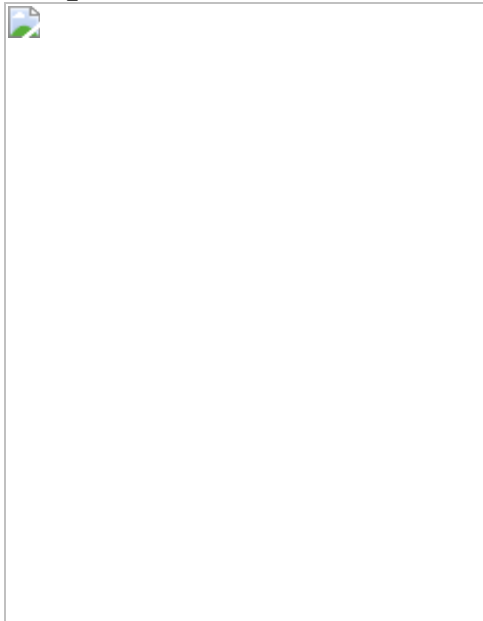


Fig. 2: Chronic social isolation induces a starvation gene expression program and results in excessive feeding.

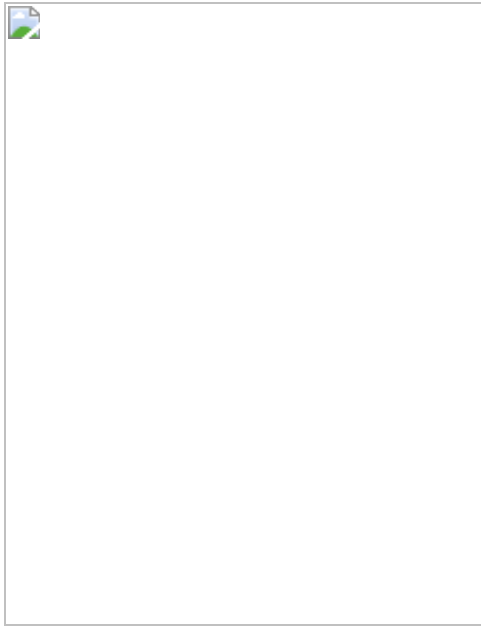


Fig. 3: P2 neurons are required for sleep loss induced by chronic social isolation.

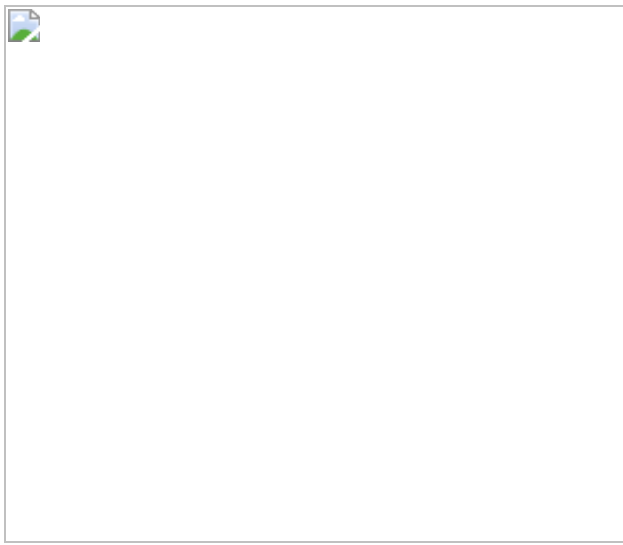
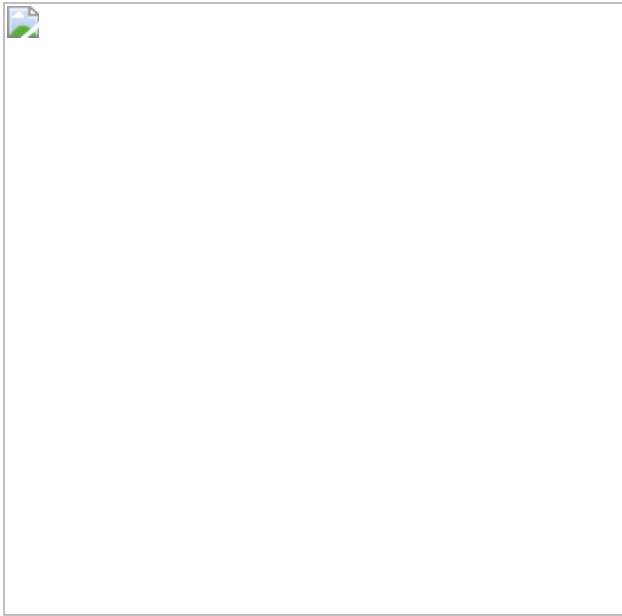


Fig. 4: Activation of P2 neurons during acute social isolation induces sleep loss and over-consumption of food.



Data availability

The RNA-seq data sets generated in this study have been deposited in NCBI's Gene Expression Omnibus⁴³ and are accessible through GEO series accession number [GSE137498](#). [Source data](#) are provided with this paper.

Code availability

Customized R script based on the R/rethomics package is available upon request.

References

1. 1.

Cacioppo, J. T. & Cacioppo, S. The growing problem of loneliness. *Lancet* **391**, 426 (2018).

2. 2.

Steptoe, A., Shankar, A., Demakakos, P. & Wardle, J. Social isolation, loneliness, and all-cause mortality in older men and women. *Proc. Natl*

Acad. Sci. USA **110**, 5797–5801 (2013).

3. 3.

Holt-Lunstad, J., Smith, T. B. & Layton, J. B. Social relationships and mortality risk: a meta-analytic review. *PLoS Med.* **7**, e1000316 (2010).

4. 4.

Holt-Lunstad, J., Smith, T. B., Baker, M., Harris, T. & Stephenson, D. Loneliness and social isolation as risk factors for mortality: a meta-analytic review. *Perspect. Psychol. Sci.* **10**, 227–237 (2015).

5. 5.

Cacioppo, J. T. et al. Loneliness and health: potential mechanisms. *Psychosom. Med.* **64**, 407–417 (2002).

6. 6.

Kurina, L. M. et al. Loneliness is associated with sleep fragmentation in a communal society. *Sleep* **34**, 1519–1526 (2011).

7. 7.

Cacioppo, J. T. et al. Loneliness across phylogeny and a call for comparative studies and animal models. *Perspect. Psychol. Sci.* **10**, 202–212 (2015).

8. 8.

Anderson, D. J. & Adolphs, R. A framework for studying emotions across species. *Cell* **157**, 187–200 (2014).

9. 9.

Sokolowski, M. B. Social interactions in “simple” model systems. *Neuron* **65**, 780–794 (2010).

10. 10.

Ramdy, P., Schneider, J. & Levine, J. D. The neurogenetics of group behavior in *Drosophila melanogaster*. *J. Exp. Biol.* **220**, 35–41 (2017).

11. 11.

Danchin, E. et al. Cultural flies: Conformist social learning in fruitflies predicts long-lasting mate-choice traditions. *Science* **362**, 1025–1030 (2018).

12. 12.

Ganguly-Fitzgerald, I., Donlea, J. & Shaw, P. J. Waking experience affects sleep need in *Drosophila*. *Science* **313**, 1775–1781 (2006).

13. 13.

Alfa, R. W. et al. Suppression of insulin production and secretion by a decretin hormone. *Cell Metab.* **21**, 323–334 (2015).

14. 14.

Söderberg, J. A. E., Carlsson, M. A. & Nässel, D. R. Insulin-producing cells in the *Drosophila* brain also express satiety-inducing cholecystokinin-like peptide, drosulfakinin. *Front. Endocrinol.* **3**, 109 (2012).

15. 15.

Buch, S., Melcher, C., Bauer, M., Katzenberger, J. & Pankratz, M. J. Opposing effects of dietary protein and sugar regulate a transcriptional target of *Drosophila* insulin-like peptide signaling. *Cell Metab.* **7**, 321–332 (2008).

16. 16.

Sonn, J. Y. et al. Serine metabolism in the brain regulates starvation-induced sleep suppression in *Drosophila melanogaster*. *Proc. Natl*

Acad. Sci. USA **115**, 7129–7134 (2018).

17. 17.

Murphy, K. R., Park, J. H., Huber, R. & Ja, W. W. Simultaneous measurement of sleep and feeding in individual *Drosophila*. *Nat. Protocols* **12**, 2355–2366 (2017).

18. 18.

Kume, K., Kume, S., Park, S. K., Hirsh, J. & Jackson, F. R. Dopamine is a regulator of arousal in the fruit fly. *J. Neurosci.* **25**, 7377–7384 (2005).

19. 19.

Liu, S. et al. WIDE AWAKE mediates the circadian timing of sleep onset. *Neuron* **82**, 151–166 (2014).

20. 20.

Stavropoulos, N. & Young, M. W. insomniac and Cullin-3 regulate sleep and wakefulness in *Drosophila*. *Neuron* **72**, 964–976 (2011).

21. 21.

Davis, F. P. et al. A genetic, genomic, and computational resource for exploring neural circuit function. *eLife* **9**, e50901 (2020).

22. 22.

Shao, L. et al. Dissection of the *Drosophila* neuropeptide F circuit using a high-throughput two-choice assay. *Proc. Natl Acad. Sci. USA* **114**, E8091–E8099 (2017).

23. 23.

Donlea, J. M., Pimentel, D. & Miesenböck, G. Neuronal machinery of sleep homeostasis in *Drosophila*. *Neuron* **81**, 860–872 (2014).

24. 24.

Jenett, A. et al. A GAL4-driver line resource for *Drosophila* neurobiology. *Cell Rep.* **2**, 991–1001 (2012).

25. 25.

Nern, A., Pfeiffer, B. D. & Rubin, G. M. Optimized tools for multicolor stochastic labeling reveal diverse stereotyped cell arrangements in the fly visual system. *Proc. Natl Acad. Sci. USA* **112**, E2967–E2976 (2015).

26. 26.

Scheffer, L. K. et al. A connectome and analysis of the adult *Drosophila* central brain. *eLife* **9**, e57443 (2020).

27. 27.

Hulse, B. K. et al. A connectome of the *Drosophila* central complex reveals network motifs suitable for flexible navigation and context-dependent action selection. Preprint at <https://doi.org/10.1101/2020.12.08.413955> (2020).

28. 28.

Baines, R. A., Uhler, J. P., Thompson, A., Sweeney, S. T. & Bate, M. Altered electrical properties in *Drosophila* neurons developing without synaptic transmission. *J. Neurosci.* **21**, 1523–1531 (2001).

29. 29.

Donlea, J. M. et al. Recurrent circuitry for balancing sleep need and sleep. *Neuron* **97**, 378–389.e4 (2018).

30. 30.

Pimentel, D. et al. Operation of a homeostatic sleep switch. *Nature* **536**, 333–337 (2016).

31. 31.

Kempf, A., Song, S. M., Talbot, C. B. & Miesenböck, G. A potassium channel β -subunit couples mitochondrial electron transport to sleep. *Nature* **568**, 230–234 (2019).

32. 32.

Ertekin, D., Kirszenblat, L., Faville, R. & van Swinderen, B. Down-regulation of a cytokine secreted from peripheral fat bodies improves visual attention while reducing sleep in *Drosophila*. *PLoS Biol.* **18**, e3000548 (2020).

33. 33.

de Bono, M. & Bargmann, C. I. Natural variation in a neuropeptide Y receptor homolog modifies social behavior and food response in *C. elegans*. *Cell* **94**, 679–689 (1998).

34. 34.

Li, W. et al. Activation of transposable elements during aging and neuronal decline in *Drosophila*. *Nat. Neurosci.* **16**, 529–531 (2013).

35. 35.

Serrano Negron, Y. L., Hansen, N. F. & Harbison, S. T. The sleep inbred panel, a collection of inbred *Drosophila melanogaster* with extreme long and short sleep duration. *G3* **8**, 2865–2873 (2018).

36. 36.

Harbison, S. T., Serrano Negron, Y. L., Hansen, N. F. & Lobell, A. S. Selection for long and short sleep duration in *Drosophila melanogaster* reveals the complex genetic network underlying natural variation in sleep. *PLoS Genet.* **13**, e1007098 (2017).

37. 37.

Geissmann, Q., Garcia Rodriguez, L., Beckwith, E. J. & Gilestro, G. F. Rethomics: an R framework to analyse high-throughput behavioural data. *PLoS One* **14**, e0209331 (2019).

38. 38.

Dobin, A. et al. STAR: ultrafast universal RNA-seq aligner. *Bioinformatics* **29**, 15–21 (2013).

39. 39.

Liao, Y., Smyth, G. K. & Shi, W. featureCounts: an efficient general purpose program for assigning sequence reads to genomic features. *Bioinformatics* **30**, 923–930 (2014).

40. 40.

Love, M. I., Huber, W. & Anders, S. Moderated estimation of fold change and dispersion for RNA-seq data with DESeq2. *Genome Biol.* **15**, 550 (2014).

41. 41.

Huang, W., Sherman, B. T. & Lempicki, R. A. Systematic and integrative analysis of large gene lists using DAVID bioinformatics resources. *Nat. Protocols* **4**, 44–57 (2009).

42. 42.

Green, J. et al. A neural circuit architecture for angular integration in *Drosophila*. *Nature* **546**, 101–106 (2017).

43. 43.

Edgar, R., Domrachev, M. & Lash, A. E. Gene Expression Omnibus: NCBI gene expression and hybridization array datarepository. *Nucleic Acids Res.* **30**, 207–210 (2002).

44. 44.

Johard, H. A. et al. Peptidergic clock neurons in *Drosophila*: ion transport peptide and short neuropeptide F in subsets of dorsal and ventral lateral neurons. *J. Comp. Neurol.* **516**, 59–73 (2009).

45. 45.

Liu, W. et al. Neuropeptide F regulates courtship in *Drosophila* through a male-specific neuronal circuit. *eLife* **8**, e49574 (2019).

Acknowledgements

We thank G. Maimon for advice on $[Ca^{2+}]$ imaging experiments and quantitative analysis of the hemibrain connectome; J. Park, W. Ja, L. Shao, U. Heberlein, S. Park, S. Kim, A. Sehgal, M. Wu and H. Steller for sharing fly stocks, reagents, protocols, and equipment; B. McEwen, L. Vosshall, A. Patke, L. Zhao, N. Svetec, Y. Shuai, S. Axelrod and D. Top for comments on the manuscript; the Resource Center of Precision Instrumentation Technologies and the Resource Center of Genomics at the Rockefeller University for technical support; the Bloomington *Drosophila* Stock Center for fly stocks; and the Developmental Studies Hybridoma Bank for antibodies. This work was supported by NIH grants 5R37 NS053087 and 5R35 GM136237 to M.W.Y. W.L. was supported by fellowships from the Leon Levy Foundation, the Jane Coffin Childs Memorial Fund, and the Grass Foundation. S.S. was partially supported by NSF IOS no. 1656603. C.L. was supported by a seed grant from the Kavli Foundation.

Author information

Affiliations

1. Laboratory of Genetics, The Rockefeller University, New York, NY, USA

Wanhe Li, Zikun Wang, Samantha Lincoln, Jenna O’Neil, Andrew D. Nguyen, Irena Feng & Michael W. Young

2. Department of Physics, University of Miami, Coral Gables, FL, USA

Sheyum Syed

3. Laboratory of Integrative Brain Function, The Rockefeller University, New York, NY, USA

Cheng Lyu

Contributions

W.L. conceived the project, designed experiments, analysed data, and wrote the manuscript. W.L., Z.W., S.L., J.O., A.D.N. and I.F. performed experiments. C.L. performed $[Ca^{2+}]$ imaging experiments and analysed the data. S.S. supervised statistical analyses. M.W.Y supervised the project and wrote the manuscript. All authors discussed the results and contributed to the manuscript.

Corresponding authors

Correspondence to [Wanhe Li](#) or [Michael W. Young](#).

Ethics declarations

Competing interests

The authors declare no competing interests.

Additional information

Peer review information *Nature* thanks Jason Rihel and the other, anonymous, reviewer(s) for their contribution to the peer review of this work.

Publisher's note Springer Nature remains neutral with regard to jurisdictional claims in published maps and institutional affiliations.

Extended data figures and tables

Extended Data Fig. 1 Social isolation reduces sleep in *Drosophila*.

a, Schematic of social isolation paradigm. Adult fruit flies with social experience were subjected to social isolation or group enrichment for 7 days before sleep was measured using *Drosophila* activity monitors. Social isolation consists of housing one fly per vial. Group enrichment consists of housing 2, 5, 25 or 100 flies per vial. **b**, Sleep profiles (mean \pm s.e.m.) proportion of time spent sleeping in consecutive 30-min segments during a 24-h LD cycle) of flies after social isolation or group enrichment with different group sizes for 7 days. **c–g**, Raster plots of sleep bouts of 20 individual animals after social isolation (**c**), group enrichment in a group of 2 animals (**d**), group enrichment in a group of 5 animals (**e**), group enrichment in a group of 25 animals (**f**) or group enrichment in a group of 100 animals (**g**). Each row is an individual fly, with each coloured bar representing a sleep bout in a 24-h LD cycle. **h–k**, Quantification (mean \pm s.e.m. with individual data points) of daily total sleep (**h**), daytime sleep (**i**), ZT0–4 sleep (**j**) and nighttime sleep (**k**) for flies after social isolation (Iso) or group enrichment (Grp) with different group sizes. For **b** and **h–k**, $n = 23\text{--}30$ flies. Ordinary one-way ANOVA followed by Tukey's multiple comparison tests; means sharing the same letter are not significantly different. For n and P values, see Source Data

[Source data.](#)

Extended Data Fig. 2 Chronic social isolation does not alter nighttime sleep in wild-type *Drosophila*.

a–d, Density plots for distribution of daytime sleep bouts for flies after 1, 3, 5 or 7 days of group enrichment or social isolation. All daytime sleep bouts collected from all animals in each condition were combined. **e**, Quantification (mean \pm s.e.m. with individual data points) of daily nighttime sleep for wild-type flies after group enrichment or social isolation for 7 days. **f–i**, Density plots for distribution of nighttime sleep bouts for

flies after 1, 3, 5 or 7 days of group enrichment or social isolation. All nighttime sleep bouts collected from all animals in each condition were combined. **j–m**, Plots of cumulative relative frequency for distributions of nighttime sleep bouts for flies after 1, 3, 5 or 7 days of group enrichment or social isolation. Kolmogorov–Smirnov tests were used to compare distributions. For **e**, $n = 29\text{--}32$ animals, two-sided unpaired t -test with Welch's correction; $*P < 0.05$, $**P < 0.01$, $***P < 0.001$, $****P < 0.0001$. n.s., not significant. For n and P values, see Source Data

[Source data](#).

Extended Data Fig. 3 Social isolation reduces *Drosophila* sleep in age-matched flies, in various isogenic strains, and in aged wild-type animals.

a, Schematics of measuring sleep using *Drosophila* activity monitors after 1 or 7 days of group enrichment or social isolation in age-matched flies. **b–e**, Sleep profile and quantification of daily total sleep, daytime sleep and ZT0–4 sleep after 1 day (**b**, **c**, $n = 55\text{--}64$ flies) or 7 days of group enrichment or social isolation (**d**, **e**, $n = 61\text{--}64$ flies). **f, g**, Sleep profile and quantification of daily total sleep, daytime sleep and ZT0–4 sleep of the *Canton-S* isogenic strain after social isolation or group enrichment with different group sizes for 7 days ($n = 30\text{--}47$ flies). **h**, A 7-day-long sleep profile of flies after group enrichment or social isolation for 7 days. **i, j**, Sleep profile and quantification of daily total sleep, daytime sleep and ZT0–4 sleep for *Berlin-K* flies after social isolation or group enrichment (25 flies in a group) for 7 days ($n = 22\text{--}31$ flies). **k, l**, Sleep profile and quantification of daily total sleep, daytime sleep and ZT0–4 sleep of aged wild-type flies after group enrichment or social isolation (25 flies in a group) for 7 days ($n = 52\text{--}54$ animals). **m, n**, Sleep profile and quantification of daily total sleep, daytime sleep and ZT0–4 sleep of male wild-type flies after group enrichment in a male-only group (30 flies in a group) or in a mixed-sex group (15 male and 15 female flies in a group) for 7 days ($n = 32$ animals). Sleep profiles are displayed as the average proportion of time spent sleeping in consecutive 30-min segments during a 24-h LD cycle (mean \pm s.e.m.). Quantifications are displayed as mean \pm s.e.m. with individual data points. For **g**, ordinary one-way ANOVA followed by Tukey's multiple comparison

test; means sharing the same letter are not significantly different. For **c**, **e**, **j**, **l** and **n**, two-sided unpaired *t*-tests with Welch's correction; **P* < 0.05, ***P* < 0.01, ****P* < 0.001, *****P* < 0.0001; n.s., not significant. For *n* and *P* values, see Source Data

[Source data](#).

Extended Data Fig. 4 Social isolation reduces sleep in *Drosophila* SIP lines.

a–d, Sleep profiles of long-sleeping flies: SIP-L1-3 (**a**), SIP-L1-4 (**b**), SIP-L2-1 (**c**), and SIP-L2-6 (**d**) after group enrichment or social isolation (25 flies in a group for group treatment) for 7 days. **e–h**, Sleep profiles of short-sleeping flies: SIP-S1-1 (**e**), SIP-S1-9 (**f**), SIP-S2-3 (**g**), and SIP-S2-9 (**h**) after group enrichment or social isolation (25 flies in a group for group treatment) for 7 days. Sleep profiles are displayed as the mean ± s.e.m. proportion of time spent sleeping in consecutive 30-min segments during a 24-h LD cycle. The long-sleeping and short-sleeping fly lines were randomly selected from the SIP, a panel of inbred *Drosophila melanogaster* strains with extreme long or short sleep-duration phenotypes^{35,36}.

Extended Data Fig. 5 RNA-seq reveals changes in gene expression during chronic social isolation.

a, b, Volcano plots of differential gene expression from RNA-seq results. **a**, Comparison between chronic isolation and group conditions (Iso_7D vs Grp). **b**, Comparison between chronic isolation and acute isolation conditions (Iso_7D vs Iso_1D). Red dots indicate genes with significant adjusted *P* values in both comparisons. Differential gene expression analyses were conducted using DESeq2, which uses a two-sided Wald test and Benjamini–Hochberg correction. **c**, Venn diagram showing the intersection of the above two comparisons. **d**, Heatmap of the 274 intersected genes showing significant differential gene expression changes in both comparisons. **e**, Gene ontology of the 214 candidate genes from categories II and IV in **d**. Black bar, counts of genes in each GO term; white

bar, $-\log_{10}P$ values for each GO term. See [Methods](#) and [Supplementary Information](#) for details on RNA-seq data analyses.

Extended Data Fig. 6 Chronic social isolation results in reduced sleep and excessive feeding, whereas food consumption is not altered in sleep mutants or after acute social isolation.

a, Sleep profiles and matching feeding profiles of three representative individual flies after seven days of group enrichment. **b**, Sleep profiles and matching feeding profiles of three representative individual flies after seven days of social isolation. Sleep profile is presented as sleep amount (min) in consecutive 30-min segments during a 24-h LD cycle. Matching feeding profile is presented as food consumption (μl) in consecutive 30-min segments during a 24-h LD cycle. **c**, Quantification of daily total food consumption, daytime food consumption, nighttime food consumption and ZT0–4 food consumption for wild-type and sleep mutant *inc*¹ flies ($n = 25$ –29 flies). **d**, Quantification of daily total food consumption, daytime food consumption, nighttime food consumption and ZT0–4 food consumption for wild-type and sleep mutant *fmn* flies ($n = 25$ –29 animals). **e**, Quantification of daily total food consumption, daytime food consumption, nighttime food consumption and ZT0–4 food consumption for wild-type and sleep mutant *wake*^{D2} flies ($n = 23$ –30 flies). **f**, Feeding profile measured by ARC assay in flies following 1 day of group enrichment or social isolation (mean \pm s.e.m.). **g**, Quantification of daily total food consumption, daytime food consumption, nighttime food consumption and ZT0–4 food consumption for flies after 1 day of group enrichment or social isolation (**f**, $n = 49$ –50 flies). All quantifications are displayed as mean \pm s.e.m. with individual data points. Unpaired *t*-tests with Welch's correction. For n and P values, see Source Data

[Source data](#).

Extended Data Fig. 7 Limostatin transcripts are detected in fly head RNA-seq sample libraries; *NPF-GAL4* expression pattern; feeding profile of flies in experiments silencing P2

neurons; and silencing P2 neurons with *UAS-shibire^{ts1}* during social isolation is insufficient to block chronic social isolation-induced sleep loss.

a, Reads from RNA-seq sample libraries (Grp, Iso_1D, and Iso_7D) align to the gene region of *Lst* (CG8317). **b**, *Akh* and *Lst* are known to be co-expressed in the corpora cardiaca¹³. No reads were detected or aligned to the gene region of *Akh*, suggesting that the RNA-seq samples were free of corpora cardiaca materials and that the measured *Lst* transcripts come from sources in the brain. **c**, Expression pattern of *NPF-GAL4*-labelled neurons revealed by *UAS-myr::GFP* and NPF antibody staining. NPF⁺ cells overlap with GFP⁺ cells. P1, P2, DM, L1-l (or LNd)²², s-LNv⁴⁴ and NPF^M (ref. ⁴⁵) neurons are labelled. **d**, An additional brain imaged from the posterior end to show NPF⁺ and GFP⁺ cell bodies of P2 neurons (dashed circle). Magenta, NPF; green, GFP; blue, N-cadherin; scale bars, 50 μm. **e–g**, Feeding profiles measured by ARC assay for parental control flies (**e**, **f**) and flies expressing *UAS-Kir2.1* with *P2-GAL4* (**g**) following 7 days of group enrichment or social isolation (mean ± s.e.m.; $n = 27\text{--}30$ flies). **h–m**, Sleep profiles for parental control flies (**h–k**) and flies expressing *UAS-shibire^{ts}* with *P2-GAL4* (**l**, **m**) following 7 days of group enrichment or social isolation at 22 °C (**h**, **j**, **l**) or 29 °C (**i**, **k**, **m**). All sleep behaviour was tested at 22 °C. **n**, Quantification (mean ± s.e.m. with individual data points) of daily total sleep, daytime sleep and ZT0–4 sleep for parental control flies and flies expressing *UAS-shibire^{ts}* with *P2-GAL4* following 7 days of group enrichment or social isolation at 22 °C or 29 °C. Sleep profiles are displayed as the mean ± s.e.m. proportion of time spent sleeping in consecutive 30-min segments during a 24-h LD cycle. For **h–n**, $n = 31\text{--}32$ flies; two-way ANOVAs were used for detecting interactions between temperature treatment and group/isolation status; Šidák multiple comparisons tests were used for post hoc analyses between group-treated and isolated animals of the same genotype and temperature treatment; * $P < 0.05$, ** $P < 0.01$, *** $P < 0.001$, **** $P < 0.0001$. For n and P values, see Source Data

[Source data](#).

Extended Data Fig. 8 P2 neurons show similar activity patterns after chronic social isolation or group enrichment and P2 neurons synapse onto cell types labelled by R23E20-GAL4.

a, Tethered, walking, $[Ca^{2+}]$ -imaging setup with an infrared-sensitive camera that tracks the rotation of the ball. **b**, The anatomy of hDeltaK cells from neuPrint²⁶ (left), compared with time-averaged z -projection of GCaMP7f signals driven by *P2-GAL4* (right). Both images show two separate layers (higher layer and lower layer) of fan-shaped body neuropils. **c**, Cross-correlation analysis of the lower-layer GCaMP7f activity and the fly's forward walking velocity. Thin lines, individual fly data; thick lines, population means. **d**, Cross-correlation analysis of the higher-layer GCaMP7f activity and the fly's forward walking velocity. Thin lines, individual fly data; thick lines, population means. **e**, Quantification (mean \pm s.e.m. with individual data points) of GCaMP7f activity during standing moments of flies after 7 days of group enrichment or social isolation. Identical two-photon acquisition parameters were used in all experiments (**c–e**, $n = 5$ –6 flies). **f**, The anatomy of FB6A cells from neuPrint. FB6A has been identified as one of the few cell types labelled by *R23E10-GAL4*²⁷. **g**, Synapse-number matrix for detected synapses from P2 neurons (named hDeltaK cells in neuPrint) to FB6A cells. Connectivity data and cell-type names are based on those in neuPrint, hemibrain: v1.1²⁶.

Extended Data Fig. 9 Sleep profiles and feeding profiles of flies in which P2 neurons were thermally activated by expressing UAS-dTPRA1 during acute (1 day) group enrichment or social isolation; parental and temperature controls are included.

a, Schematics of activating P2 neurons for 1 day of group enrichment or social isolation. Treatment at 22 °C (no thermoactivation) was used as control. Flies in group enrichment or social isolation were kept at 28 °C for 1 day to thermally activate P2 neurons. After 1 day of thermal activation (or no activation), sleep behaviour was measured at 22 °C. **b, c**, Sleep profiles of *UAS-dTRPA1*/+ heterozygous control flies after group enrichment or social isolation at 22 °C for 1 day or at 28 °C for 1 day. **d, e**, Sleep profiles of *P2-GAL4*/+ heterozygous control flies after group enrichment or social

isolation at 22 °C for 1 day or at 28 °C for 1 day. **f, g**, Sleep profiles of flies expressing *UAS-dTRPA1* under the control of *P2-GAL4* after group enrichment or social isolation at 22 °C for 1 day or at 28 °C for 1 day. **h**, Schematics of activating P2 neurons for 1 day of group enrichment or social isolation. Treatment at 22 °C (no thermoactivation) was used as control. Flies in group enrichment or social isolation were kept at 28 °C for 1 day to thermally activate P2 neurons. After 1 day of thermal activation (or no activation), feeding behaviour was measured at 22 °C. **i, j**, Feeding profiles of *UAS-dTRPA1*/+ heterozygous control flies after group enrichment or social isolation at 22 °C for 7 days or at 28 °C for 7 days. **k, l**, Feeding profiles of *P2-GAL4*/+ heterozygous control flies after group enrichment or social isolation at 22 °C for 7 days or at 28 °C for 7 days. **m, n**, Feeding profiles of flies expressing *UAS-dTRPA1* under the control of *P2-GAL4* after group enrichment or social isolation at 22 °C for 7 days or at 28 °C for 7 days. Sleep profiles are displayed as the mean ± s.e.m. proportion of time spent sleeping in consecutive 30-min segments during a 24-h LD cycle. Feeding profiles are presented as mean ± s.e.m. food consumption (μ l) in consecutive 30-min segments during a 24-h LD cycle. **b–e, i–n**, $n = 28\text{--}32$ flies.

Extended Data Fig. 10 Sleep profiles of flies in which P2 neurons were thermally activated by expressing *UAS-dTRPA1* during chronic (7 days) group enrichment or social isolation; parental and temperature controls are included.

a, Schematics of activating P2 neurons for 7 days of group enrichment or social isolation. Treatment at 22 °C (no thermoactivation) was used as control. Flies in group enrichment or social isolation were kept at 28 °C for 7 days to thermally activate P2 neurons. After 7 days of thermal activation (or no activation), sleep behaviour was measured at 22 °C. **b, c**, Sleep profiles of *UAS-dTRPA1*/+ heterozygous control flies after group enrichment or social isolation at 22 °C for 7 days or at 28 °C for 7 days. **d**, **e**, Sleep profiles of *P2-GAL4*/+ heterozygous control flies after group enrichment or social isolation at 22 °C for 7 days or at 28 °C for 7 days. **f, g**, Sleep profiles of flies expressing *UAS-dTRPA1* under the control of *P2-GAL4* after group enrichment or social isolation at 22 °C for 7 days or at

28 °C for 7 days. **h**, Quantification (mean ± s.e.m. with individual data points) of daily total sleep, daytime sleep and ZT0–4 sleep for experimental and heterozygous control flies grouped or isolated for 7 days with (28 °C) or without (22 °C) thermal activation of *P2-GAL4*-labelled neurons. Sleep profiles are displayed as the mean ± s.e.m. proportion of time spent sleeping in consecutive 30-min segments during a 24-h LD cycle. For **h**, two-way ANOVAs were used for detecting interactions between temperature treatment and group/isolation status. Šidák multiple comparisons tests were used for post hoc analyses between group-treated and isolated animals of the same genotype and temperature treatment. * $P < 0.05$, ** $P < 0.01$, *** $P < 0.001$, **** $P < 0.0001$; **b–h**, $n = 29\text{--}32$ animals. For n and P values, see Source Data

[Source data](#)

Supplementary information

[Supplementary Information](#)

This file contains Supplementary Sections 1-6 and Supplementary References.

[Reporting Summary](#)

[Supplementary Table](#)

This file contains Supplementary Table 1, a list of candidate Genes.

[Supplementary Table](#)

This file contains Supplementary Table 2.

Source data

[Source Data Fig. 1](#)

[**Source Data Fig. 2**](#)

[**Source Data Fig. 3**](#)

[**Source Data Fig. 4**](#)

[**Source Data Extended Data Fig. 1**](#)

[**Source Data Extended Data Fig. 2**](#)

[**Source Data Extended Data Fig. 3**](#)

[**Source Data Extended Data Fig. 6**](#)

[**Source Data Extended Data Fig. 7**](#)

[**Source Data Extended Data Fig. 10**](#)

Rights and permissions

[**Reprints and Permissions**](#)

About this article

Cite this article

Li, W., Wang, Z., Syed, S. *et al.* Chronic social isolation signals starvation and reduces sleep in *Drosophila*. *Nature* **597**, 239–244 (2021).
<https://doi.org/10.1038/s41586-021-03837-0>

- Received: 01 May 2020
- Accepted: 20 July 2021
- Published: 18 August 2021

- Issue Date: 09 September 2021
- DOI: <https://doi.org/10.1038/s41586-021-03837-0>

Chronically lonely flies overeat and lose sleep

- Joel D. Levine

News & Views 18 Aug 2021

This article was downloaded by **calibre** from <https://www.nature.com/articles/s41586-021-03837-0>

| [Section menu](#) | [Main menu](#) |

- Article
- [Published: 25 August 2021](#)

Hypothalamic dopamine neurons motivate mating through persistent cAMP signalling

- [Stephen X. Zhang](#)¹,
- [Andrew Lutas](#)¹,
- [Shang Yang](#) [ORCID: orcid.org/0000-0001-6671-7571](#)²,
- [Adriana Diaz](#)¹,
- [Hugo Fluhr](#)¹,
- [Georg Nagel](#)²,
- [Shiqiang Gao](#) [ORCID: orcid.org/0000-0001-6190-9443](#)² &
- [Mark L. Andermann](#) [ORCID: orcid.org/0000-0002-9882-933X](#)¹

[Nature](#) volume 597, pages 245–249 (2021)

- 8398 Accesses
- 213 Altmetric
- [Metrics details](#)

Subjects

- [Molecular neuroscience](#)
- [Motivation](#)
- [Neural circuits](#)
- [Sexual behaviour](#)
- [Social behaviour](#)

Abstract

Transient neuromodulation can have long-lasting effects on neural circuits and motivational states^{1,2,3,4}. Here we examine the dopaminergic mechanisms that underlie mating drive and its persistence in male mice. Brief investigation of females primes a male's interest to mate for tens of minutes, whereas a single successful mating triggers satiety that gradually recovers over days⁵. We found that both processes are controlled by specialized anteroventral and preoptic periventricular (AVPV/PVpo) dopamine neurons in the hypothalamus. During the investigation of females, dopamine is transiently released in the medial preoptic area (MPOA)—an area that is critical for mating behaviours. Optogenetic stimulation of AVPV/PVpo dopamine axons in the MPOA recapitulates the priming effect of exposure to a female. Using optical and molecular methods for tracking and manipulating intracellular signalling, we show that this priming effect emerges from the accumulation of mating-related dopamine signals in the MPOA through the accrual of cyclic adenosine monophosphate levels and protein kinase A activity. Dopamine transients in the MPOA are abolished after a successful mating, which is likely to ensure abstinence. Consistent with this idea, the inhibition of AVPV/PVpo dopamine neurons selectively demotivates mating, whereas stimulating these neurons restores the motivation to mate after sexual satiety. We therefore conclude that the accumulation or suppression of signals from specialized dopamine neurons regulates mating behaviours across minutes and days.

Access options

Subscribe to Journal

Get full journal access for 1 year

\$199.00

only \$3.90 per issue

Subscribe

All prices are NET prices.
VAT will be added later in the checkout.
Tax calculation will be finalised during checkout.

Rent or Buy article

Get time limited or full article access on ReadCube.

from \$8.99

Rent or Buy

All prices are NET prices.

Additional access options:

- [Log in](#)
- [Access through your institution](#)
- [Learn about institutional subscriptions](#)

Fig. 1: Motivational regulation of male mating behaviours across minutes and days.



Fig. 2: Specialized hypothalamic dopamine neurons control mating drive.

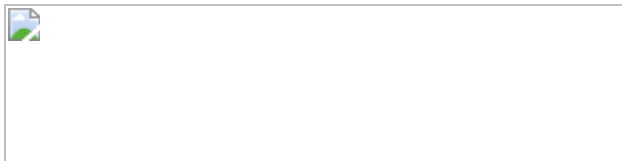


Fig. 3: Dopaminergic input to the MPOA builds up a persistent motivation to mate.

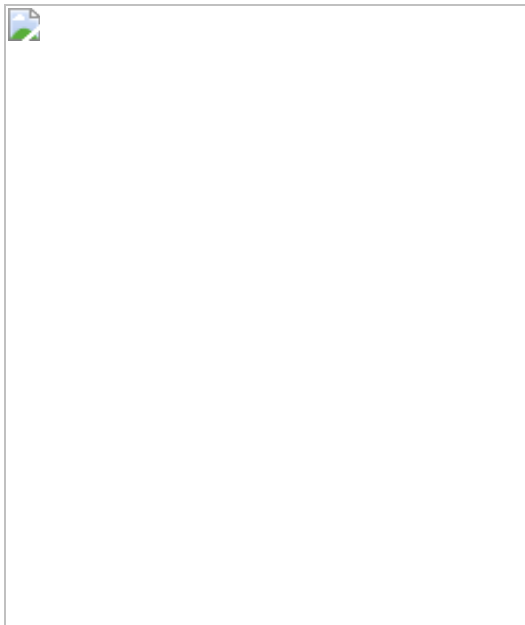
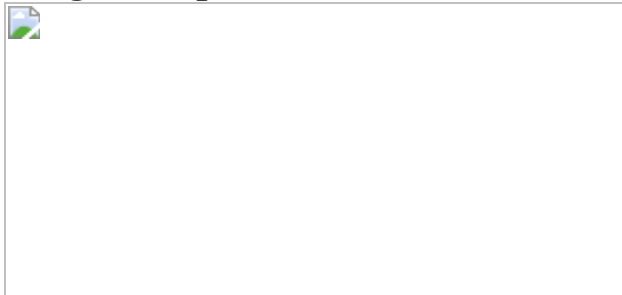


Fig. 4: Increased cAMP levels and PKA activity in the MPOA underlie mating drive persistence.



Data availability

Plasmids and sequences related to biPAC and PDE4D3-Cat have been deposited to Addgene under accession numbers 169127 for biPAC and 169128 for PDE4D3-Cat. The data that support the findings in this study are available from the corresponding author upon request.

Code availability

The custom analysis code and designs in this paper are publicly available on GitHub (<https://github.com/xzhang03/Code-for-Zhang-et-al-2021>).

References

1. 1.

Chen, Y. et al. Sustained NPY signaling enables AgRP neurons to drive feeding. *eLife* **8**, e46348 (2019).

2. 2.

Lahiri, A. K. & Bevan, M. D. Dopaminergic transmission rapidly and persistently enhances excitability of D1 receptor-expressing striatal projection neurons. *Neuron* **106**, 277–290 (2020).

3. 3.

Cohn, R., Morantte, I. & Ruta, V. Coordinated and compartmentalized neuromodulation shapes sensory processing in *Drosophila*. *Cell* **163**, 1742–1755 (2015).

4. 4.

Marlin, B. J., Mitre, M., James, A. D., Chao, M. V. & Froemke, R. C. Oxytocin enables maternal behaviour by balancing cortical inhibition. *Nature* **520**, 499–504 (2015).

5. 5.

McGill, T. E. Sexual behavior of the mouse after long-term and short-term postejaculatory recovery periods. *J. Genet. Psychol.* **103**, 53–57 (1963).

6. 6.

Bowers, M. B., Van Woert, M. & Davis, L. Sexual behavior during l-DOPA treatment for Parkinsonism. *Am. J. Psychiatry* **127**, 1691–1693 (1971).

7. 7.

Bitran, D. & Hull, E. M. Pharmacological analysis of male rat sexual behavior. *Neurosci. Biobehav. Rev.* **11**, 365–389 (1987).

8. 8.

Hull, E. M. et al. Dopaminergic control of male sex behavior in rats: effects of an intracerebrally-infused agonist. *Brain Res.* **370**, 73–81 (1986).

9. 9.

McHenry, J. A., Bell, G. A., Parrish, B. P. & Hull, E. M. Dopamine D1 receptor signaling in the medial preoptic area facilitates experience-induced enhancement of mating behavior in male rats. *Behav. Neurosci.* **126**, 523–529 (2012).

10. 10.

Zhang, S. X., Rogulja, D. & Crickmore, M. A. Dopaminergic circuitry underlying mating drive. *Neuron* **91**, 168–181 (2016).

11. 11.

Beach, F. A. & Jordan, L. Sexual exhaustion and recovery in the male rat. *Q. J. Exp. Psychol.* **8**, 121–133 (1956).

12. 12.

McGill, T. E. & Blight, W. C. Effects of genotype on the recovery of sex drive in the male mouse. *J. Comp. Physiol. Psychol.* **56**, 887–888 (1963).

13. 13.

Patriarchi, T. et al. Ultrafast neuronal imaging of dopamine dynamics with designed genetically encoded sensors. *Science* **360**, eaat4422 (2018).

14. 14.

Howe, M. W., Tierney, P. L., Sandberg, S. G., Phillips, P. E. M. & Graybiel, A. M. Prolonged dopamine signalling in striatum signals proximity and value of distant rewards. *Nature* **500**, 575–579 (2013).

15. 15.

Yeung, M. Y. et al. A mesoscale connectome of the mouse brain. *Nature* **15**, 942–953 (2016).

16. 16.

Gunaydin, L. A. et al. Natural neural projection dynamics underlying social behavior. *Cell* **157**, 1535–1551 (2014).

17. 17.

Menegas, W., Babayan, B. M., Uchida, N. & Watabe-Uchida, M. Opposite initialization to novel cues in dopamine signaling in ventral and posterior striatum in mice. *eLife* **6**, e21886 (2017).

18. 18.

Sheng, M. & Greenberg, M. E. The regulation and function of c-fos and other immediate early genes in the nervous system. *Neuron* **4**, 477–485 (1990).

19. 19.

Klapoetke, N. C. et al. Independent optical excitation of distinct neural populations. *Nat. Methods* **11**, 338–346 (2014).

20. 20.

Wei, D., Talwar, V. & Lin, D. Neural circuits of social behaviors: innate yet flexible. *Neuron* **109**, 1600–1620 (2021).

21. 21.

Xu, X. et al. Modular genetic control of sexually dimorphic behaviors. *Cell* **148**, 596–607 (2012).

22. 22.

Armbruster, B. N., Li, X., Pausch, M. H., Herlitze, S. & Roth, B. L. Evolving the lock to fit the key to create a family of G protein-coupled receptors potently activated by an inert ligand. *Proc. Natl Acad. Sci. USA* **104**, 5163–5168 (2007).

23. 23.

Thompson, K. J. et al. DREADD agonist 21 Is an effective agonist for muscarinic-based DREADDs in vitro and in vivo. *ACS Pharmacol. Transl. Sci.* **72**, 61–72 (2018).

24. 24.

Beaulieu, J.-M. & Gainetdinov, R. R. The physiology, signaling, and pharmacology of dopamine receptors. *Pharmacol. Rev.* **63**, 182–217 (2011).

25. 25.

Tewson, P. H., Martinka, S., Shaner, N. C., Hughes, T. E. & Quinn, A. M. New DAG and cAMP sensors optimized for live-cell assays in automated laboratories. *J. Biomol. Screen.* **21**, 298–305 (2016).

26. 26.

Chen, Y., Saulnier, J. L., Yellen, G. & Sabatini, B. L. A PKA activity sensor for quantitative analysis of endogenous GPCR signaling via 2-photon FRET-FLIM imaging. *Front. Pharmacol.* **5**, 56 (2014).

27. 27.

McHenry, J. A. et al. Hormonal gain control of a medial preoptic area social reward circuit. *Nat. Neurosci.* **20**, 449–458 (2017).

28. 28.

Wei, Y.-C. et al. Medial preoptic area in mice is capable of mediating sexually dimorphic behaviors regardless of gender. *Nat. Commun.* **9**, 279 (2018).

29. 29.

Karigo, T. et al. Distinct hypothalamic control of same- and opposite-sex mounting behaviour in mice. *Nature* **589**, 258–263 (2020).

30. 30.

Goto, A. et al. Circuit-dependent striatal PKA and ERK signaling underlies rapid behavioral shift in mating reaction of male mice. *Proc. Natl. Acad. Sci. USA* **112**, 6718–6723 (2015).

31. 31.

Lee, S. J. et al. Cell-type-specific asynchronous modulation of PKA by dopamine in learning. *Nature* **590**, 451–456 (2021).

32. 32.

Yagishita, S. et al. A critical time window for dopamine actions on the structural plasticity of dendritic spines. *Science* **345**, 1616–1620 (2014).

33. 33.

Sar, M. Estradiol is concentrated in tyrosine hydroxylase-containing neurons of the hypothalamus. *Science* **223**, 938–940 (1984).

34. 34.

Simerly, R. B., Zee, M. C., Pendleton, J. W., Lubahn, D. B. & Korach, K. S. Estrogen receptor-dependent sexual differentiation of dopaminergic neurons in the preoptic region of the mouse. *Neurobiology* **94**, 14077–14082 (1997).

35. 35.

Scott, N., Prigge, M., Yizhar, O. & Kimchi, T. A sexually dimorphic hypothalamic circuit controls maternal care and oxytocin secretion. *Nature* **525**, 519–522 (2015).

36. 36.

Montejo, A. L., Montejo, L. & Navarro-Cremades, F. Sexual side-effects of antidepressant and antipsychotic drugs. *Curr. Opin. Psychiatry* **28**, 418–423 (2015).

37. 37.

Bala, A., Nguyen, H. M. T. & Hellstrom, W. J. G. Post-SSRI sexual dysfunction: a literature review. *Sex. Med. Rev.* **6**, 29–34 (2018).

38. 38.

Moffitt, J. R. et al. Molecular, spatial, and functional single-cell profiling of the hypothalamic preoptic region. *Science* **362**, eaau5324 (2018).

39. 39.

Lin, D. et al. Functional identification of an aggression locus in the mouse hypothalamus. *Nature* **470**, 221–226 (2011).

40. 40.

Krashes, M. J. et al. Rapid, reversible activation of AgRP neurons drives feeding behavior in mice. *J. Clin. Invest.* **121**, 1424–1428 (2011).

41. 41.

Lutas, A. et al. State-specific gating of salient cues by midbrain dopaminergic input to basal amygdala. *Nat. Neurosci.* **22**, 1820–1833 (2019).

42. 42.

Bayless, D. W. et al. Limbic neurons shape sex recognition and social behavior in sexually naive males. *Cell* **176**, 1190–1205 (2019).

43. 43.

Inoue, S. et al. Periodic remodeling in a neural circuit governs timing of female sexual behavior. *Cell* **179**, 1393-1408.e16 (2019).

44. 44.

Chen, J. et al. Flexible scaling and persistence of social vocal communication. *Nature* **593**, 108–113 (2021).

45. 45.

Lein, E. S. et al. Genome-wide atlas of gene expression in the adult mouse brain. *Nature* **445**, 168–176 (2007).

46. 46.

Remedios, R. et al. Social behaviour shapes hypothalamic neural ensemble representations of conspecific sex. *Nature* **550**, 388–392 (2017).

47. 47.

Swaney, W. T., Dubose, B. N., Curley, J. P. & Champagne, F. A. Sexual experience affects reproductive behavior and preoptic androgen receptors in male mice. *Horm. Behav.* **61**, 472–478 (2012).

48. 48.

Li, Y. et al. Neuronal representation of social information in the medial amygdala of awake behaving mice. *Cell* **171**, 1176–1190 (2017).

49. 49.

Valente, S., Marques, T. & Lima, S. Q. No evidence for prolactin's involvement in the post-ejaculatory refractory period. *Commun. Biol.* **4**, 10 (2021).

50. 50.

Boyden, E. S., Zhang, F., Bamberg, E., Nagel, G. & Deisseroth, K. Millisecond-timescale, genetically targeted optical control of neural activity. *Nat. Neurosci.* **8**, 1263–1268 (2005).

51. 51.

Tan, C. L. & Knight, Z. A. Regulation of body temperature by the nervous system. *Neuron* **98**, 31–48 (2018).

52. 52.

Burgess, C. R. et al. Hunger-dependent enhancement of food cue responses in mouse postrhinal cortex and lateral amygdala. *Neuron* **91**, 1154–1169 (2016).

53. 53.

Garfield, A. S. et al. Dynamic GABAergic afferent modulation of AgRP neurons. *Nat. Neurosci.* **19**, 1628–1635 (2016).

54. 54.

Diaz-Carcia, C. M. et al. Quantitative in vivo imaging of neuronal glucose concentrations with a genetically encoded fluorescence lifetime sensor. *J. Neurosci. Res.* **97**, 946–960 (2019).

55. 55.

Ball, G. F. & Balthazart, J. How useful is the appetitive and consummatory distinction for our understanding of the neuroendocrine control of sexual behavior? *Horm. Behav.* **53**, 307–318 (2008).

56. 56.

Petreanu, L. et al. Activity in motor-sensory projections reveals distributed coding in somatosensation. *Nature* **489**, 299–303 (2012).

57. 57.

Mathis, A. et al. DeepLabCut: markerless pose estimation of user-defined body parts with deep learning. *Nat. Neurosci.* **21**, 1281–1289 (2018).

58. 58.

Liang, L. et al. A fine-scale functional logic to convergence from retina to thalamus. *Cell* **173**, 1343–1355.e24 (2018).

59. 59.

Bonin, V., Histed, M. H., Yurgenson, S. & Reid, R. C. Local diversity and fine-scale organization of receptive fields in mouse visual cortex. *J. Neurosci.* **31**, 18506–18521 (2011).

60. 60.

Mukamel, E. A., Nimmerjahn, A. & Schnitzer, M. J. Automated analysis of cellular signals from large-scale calcium imaging data. *Neuron* **63**, 747–760 (2009).

61. 61.

Sun, F. et al. Next-generation GRAB sensors for monitoring dopaminergic activity in vivo. *Nat. Methods* **17**, 1156–1166 (2020).

62. 62.

Franklin, K. B. J. & Paxinos, G. *The mouse brain in stereotaxic coordinates*. (2007).

63. 63.

Stierl, M. et al. Light modulation of cellular cAMP by a small bacterial photoactivated adenylyl cyclase, bPAC, of the soil bacterium *Beggiatoa*. *J. Biol. Chem.* **286**, 1181–1188 (2011).

64. 64.

Lim, J., Pahlke, G. & Conti, M. Activation of the cAMP-specific phosphodiesterase PDE4D3 by phosphorylation: Identification and function of an inhibitory domain. *J. Biol. Chem.* **274**, 19677–19685 (1999).

Acknowledgements

We thank M. Baum, B. Lowell, M. Crickmore, D. Rogulja, Y. Livneh, Y. Chen, O. Yizhar, V. Ruta, R. Froemke, L. Stowers, D. Lin, M. Frank, O. Amsalem, D. Tingley and members of the Andermann laboratory for feedback. H. Lauterwasser, C. McHugh, D. Fleharty, H. Kaul and K. Fernando assisted with animal care, behavioural experiments and histology. J. Madara and B. Lowell assisted with brain-slice imaging and A. Verstegen shared *Esrl*-Cre mice. B. Lowell and G. Yellen provided the hybrid PMT and time-correlated single photon counting board, respectively. S. Thornquist informed us of the lifetime properties of cADDIs. S. Gupta, M. Lehtinen, Boston Children's Hospital Viral Core, BIDMC Histology Core and HMS Research Instrumentation Core provided technical services. Authors were supported by a Lefler Fellowship (S.X.Z.), an NIH F32 DK112589 and a Davis Family Foundation Award (A.L.), a Bertarelli Fellowship (H.F.), NIH R01 DK109930, DP1 AT010971, DP1 AT010971-02S1, the McKnight Foundation, the Klarman Family Foundation, and the Harvard Brain Science Initiative Bipolar Disorder Seed Grant, supported by Kent and Liz Dauten (M.L.A), and by the Deutsche Forschungsgemeinschaft Projektnummer 374031971 TRR 240/A04 and Projektnummer 417451587 (G.N.).

Author information

Affiliations

1. Division of Endocrinology, Diabetes and Metabolism, Beth Israel Deaconess Medical Center, Harvard Medical School, Boston, MA, USA

Stephen X. Zhang, Andrew Lutas, Adriana Diaz, Hugo Fluhr & Mark L. Andermann

2. Institute of Physiology, Department of Neurophysiology, Biocenter, Julius-Maximilians-University of Würzburg, Würzburg, Germany

Shang Yang, Georg Nagel & Shiqiang Gao

Contributions

S.X.Z. and M.L.A. conceived the project and wrote the manuscript. S.X.Z. designed and performed the behavioural experiments, fibre photometry recording, Fos-related experiments, and *in vivo* two-photon FLIM imaging. A.D. helped to conduct behavioural and photometry experiments. H.F. tracked mice in photometry experiments. A.L. designed and built the FLIM system. S.X.Z. and A.L. performed two-photon imaging experiments of acute brain slices. S.X.Z., A.L., A.D., H.F. and M.L.A. analysed all data except for the biochemical characterizations of biPAC. S.Y., S.G. and G.N. developed biPAC and PDE4D3-Cat, designed and performed all initial biochemical characterizations, and analysed related data.

Corresponding author

Correspondence to [Mark L. Andermann](#).

Ethics declarations

Competing interests

The authors declare no competing interests.

Additional information

Peer review information *Nature* thanks Zachary Knight, Garret Stuber and Ofer Yizhar for their contribution to the peer review of this work. Peer reviewer reports are available.

Publisher's note Springer Nature remains neutral with regard to jurisdictional claims in published maps and institutional affiliations.

Extended data figures and tables

[Extended Data Fig. 1 Males suppress non-mating behaviours and gradually increase their sexual arousal during mating epochs.](#)

a, In the pre-mating epoch (after female entry and before the first mount), males engaged in feeding, digging, or trying to escape during ~25% of the “available” time (defined as the time not spent in sniffing the female, mounting the female, or lower-body grooming). In trials where males gained intromission at least once, they became hyper-engaged in mating. In the subsequent mating epoch (i.e. in the time between the first mount and the transfer of reproductive fluids), males spent almost no available time feeding, digging, or trying to escape. After transferring fluids, these males re-engaged in these non-mating behaviours. In trials where males never gained intromission (defined as the male’s thrusting movements becoming deeper and slower), they did not demonstrate a similarly hyper-engaged mode restricted to mating-related behaviours ($n = 7, 6, 5, 6$ males). **b**, We defined the appetitive sniffing metric as the fraction of pre-mounting time (i.e. the time from introduction of the female to up to 5 min later or to the first mount, whichever came first) spent in sniffing females. This metric was not significantly correlated with mounting latency ($n = 47$ first mounts from 20 males). **c**, About 80% of the first mounts were immediately preceded by a bout of sniffing (black arrows). This fraction gradually dropped across subsequent mounts, to about 5% for the fourth and fifth

mounts (1st mounts: n = 48; 2nd and 3rd mounts: n = 52; 4th and 5th mounts: n = 49 mounts; 20 males). ***p<0.001. See Supplementary Table 1 for statistics.

Extended Data Fig. 2 Specialized dopamine release in the MPOA during appetitive mating behaviours.

a–d, Optogenetically stimulating all dopaminergic inputs to the MPOA (in TH-Cre males, **a**) increased appetitive sniffing behaviour (**b**: n = 6 males) and decreased mounting latency (**c**: n = 5 males). The same stimulation did not further increase the fraction of males that mount in the first 15 min after introduction of the female (**d**), as this fraction was already near ceiling in the absence of stimulation (n = 6 trials from 6 males, mean ± 95% c.i.). **e**, dLight1.1 expression and fibre location in the MPOA (scale bar: 200 μm). **f**, The average dLight1.1 signal remained largely flat when a male mouse approached another male (n = 7 males). **g–i**, Normalizing the durations of different bouts of approach to the female to a fixed “stretched” time across bouts (**g**) still results in a ramp-and-drop profile in the dLight1.1 signal (**h**). This suggests that ramps are not the result of averaging of square-shaped signals of varying durations. For illustration purposes, we set this fixed stretched time to 10 s, the approximate median length of a sniffing bout. Normalizing the bout lengths of sniffs in a similar manner did not reveal any increase in dopamine release either during or after the sniffs (**i**) (n = 6 males). dLight1.1 signal is calculated as the difference between the signal at 465-nm excitation and the signal at the isosbestic excitation wavelength of 405 nm, after the 405-nm trace has been linearly scaled to fit the 465-nm trace. See also Fig. 2b. **j–n**, Quantification of the magnitude of the ramp and of the drop in the dLight1.1 signal (**j**) shows greatly diminished dopamine ramps (**k**) and drops (**l**) after satiety. The differences between baseline and post-satiety magnitudes of the ramp and of the drop persisted even after we sub-selected all pairs of sniffs (one per condition) with matching latencies to sniff onset (i.e. with latencies that differed by <2 s; 81% of the sniffs were matched) (**m,n**). Latency to sniff onset was defined as the number of minutes since female entry (n = 8 baseline and 6 satiated males). **o**, Overlay of changes in MPOA dLight1.1 signal and male speed surrounding each sniff. **p, q**, Scatter plots of dLight1.1 signal and male speed (both in 1-s bins) in the 5-s window surrounding the sniffs in two

example males (Pearson correlation; **p**: n = 80 trials; **q** = 50 trials). **r**, Moment-to-moment dLight1.1 signal in the MPOA is more correlated with male speed than with male-female distance, which also depends on female movements (n = 6 males). Correlation coefficients are calculated as in **p** and **q**. **s–u**, Same as **o–q** but for correlation between dLight1.1 signal and male-female distance (Pearson correlation; **t**: n = 80 trials; **u** = 50 trials). Mean ± s.e.m. unless otherwise specified. ***p<0.001. See Supplementary Table 1 for statistics.

Extended Data Fig. 3 Anatomically and functionally separable sources of dopamine in MPOA and NAc.

a, b, VTA and SNc dopamine neurons (which can be labeled by either DAT-Cre or VMAT2-Cre following injection of a Cre-dependent reporter virus) send few or no axons to the MPOA. The right panels of **a** and **b** only show the GFP (green) channel. Scale bar: 200 μm. Data from Allen Institute¹⁵. **c**, Cre-dependent expression of AAV8-EF1a-DIO-synaptophysin-mCherry in VTA of a DAT-Cre (*Slc6a3*-Cre) mouse shows dopamine terminals in the dorsal striatum (dSTR), the ventral striatum (vSTR, NAc), and the olfactory tubercle (OT). Some axons terminate in lateral preoptic area (LPOA). Almost no axons terminate in the MPOA. Scale bar: 200 μm. **d**, In the NAc, dLight1.1 photometry shows dopamine release after sniff onsets (n = 7 males). **e–g**, When males sniffed a novel, inanimate object (**d**), photometry recordings of dLight1.1 showed dopamine transients in the NAc (**e**) but not in the MPOA (**f**) (**e**: n = 7 males; **f**: n = 6). Mean ± s.e.m. for this figure.

Extended Data Fig. 4 Dopamine neurons in the AVPV and PVpo nuclei of the hypothalamus.

a, b, Data acquisition and analysis steps for quantifying TH and Fos co-localization. Brief description (see [Supplementary Methods](#) for details): high-redundancy volumes of 60-μm thick brain slices (50 volumes of 15-30 steps, 2-4 μm/step) that have been stained for TH and Fos were collected using a two-photon microscope. To segment dopaminergic somas, we first identified independent components of the TH volume along the z-axis through standard PCA/ICA analysis⁶⁰. We then applied a morphological

filter to the independent components, each usually containing a few closely located cells, to separate the individual somas. The preliminary segmentation results (see **b** for a sample; scale bar: 200 µm) were then manually corrected and validated before the regions-of-interest (ROIs) were applied to the Fos channel. An ROI was considered positive for both TH and Fos only if the two intensity profiles (along the z-axis) contained co-localized peaks. **c**, Representative images of co-localization of TH and Fos in AVPV, PVpo, and ADP. Cells positive for both TH and Fos are highlighted with dashed circles (Scale bars: 200 µm). **d**, Brain regions that did not show differences in fos expression in dopamine neurons ($n = 8$ males for ADP; 4-5 for all other brain regions; mean ± s.e.m.). ADP, anterior dorsal preoptic area; PVa, anterior periventricular nucleus; PVi, intermediate periventricular nucleus; Arc, arcuate nucleus; ZI, zona incerta; SNC, substantia nigra pars compacta; VTA, ventral tegmental area. **e–i**, Projections of AVPV/PVpo dopamine neurons (identified by injecting Cre-dependent axon-GCaMP6s in unilateral AVPV/PVpo of a TH-Cre male). Note that no axons were observed in the basolateral amygdala, which receives strong mesolimbic dopamine inputs. 3V, third ventricle; ac, anterior commissure; Arc, arcuate hypothalamic nucleus; BLA, basolateral amygdala nucleus; BMA, basomedial amygdala nucleus; BNST, bed nucleus of stria terminalis; BNSTa, anterior bed nucleus of the stria terminalis; CEA, central amygdala nucleus; COA, cortical amygdala area; DMH, dorsomedial nucleus of the hypothalamus; fx, column of fornix; LPOA, lateral preoptic area; LSc, caudal lateral septum; LSr, rostral lateral septum; MEAad, anterodorsal medial amygdala nucleus; MEAav, anteroventral medial amygdala; PIR, piriform area; PVH, paraventricular nucleus of the hypothalamus; PVT, paraventricular nucleus of the thalamus; sm, stria medullaris; Tu, tuberal nucleus; VMH, ventromedial nucleus of the hypothalamus. Scale bars: 200 µm.

Extended Data Fig. 5 AVPV/PVpo TH-Cre+ neurons release dopamine in the MPOA and promote mating behaviours.

a, Co-localization of TH-Cre+ cells (i.e., expressing EYFP) in the AVPV/PVpo with TH staining. Both EYFP and TH proteins were visualized with antibody staining. Scale bar: 200 µm. **b, c**, Optogenetic stimulation of TH-Cre+ AVPV/PVpo axonal projections to the MPOA in

awake, head-fixed males triggers robust local dopamine release that can be measured with the dopamine sensor dLight1.1 ($n = 5$ males). Note that the mean amplitude of the optogenetically evoked dLight1.1 transient is similar to the magnitude of transients evoked by female approach behaviours in Fig. 2b, c. **d–h**, Unilateral chemogenetic inhibition of AVPV/PVpo dopamine (**d**) neurons largely suppressed the ramp and drop of dopamine (surrounding sniffs) in the MPOA after injecting the agonist C21 (**f**) but not saline (**e**). Quantifications are shown in panels **g** and **h**, which use the same definitions of ramping and dropping as Extended Data Fig. 2j ($n = 5$ males). **i, j**, Bilateral chemogenetic inhibition of male AVPV/PVpo dopamine neurons did not suppress ingestive behaviours ($n = 10$ males). **k, l**, Optogenetic stimulation of AVPV/PVpo dopamine neuron cell bodies ('Soma') or axons in the MPOA reinvigorates both appetitive sniffing (**k**: $n = 7, 9, 9$ males) and consummatory mounting behaviours (**l**: $n = 7, 9, 9$, mean \pm 95% c.i.) in sexually sated mice. **m**, Optogenetic pre-stimulation of all dopamine axons in the MPOA (in TH-Cre males) did not further increase the fraction of males that mount in the first 15 min after introduction of the female, as this fraction was already near ceiling in the absence of stimulation ($n = 10, 8, 10, 9, 12, 12$ trials from 7 males, mean \pm 95% c.i.). **n–p**, Optogenetic pre-stimulation of all dopamine axons in the MPOA led to a sustained increase in male appetitive sniffing behaviour towards dioestrus females (**n**: $n = 6$ males) and a decrease in the latency to onset of the consummatory mounting behaviour (**o**: $n = 6$ males) at 10 min and 30 min after the stimulation. This stimulation did not further increase the fraction of males that mount in the first 15 min after introduction of the female, as this fraction was already near ceiling in the absence of stimulation (**p**: $n = 13, 14, 14, 14, 14, 14$ trials from 6 males, mean \pm 95% c.i.). **q–s**, Brief optogenetic pre-stimulation of dopaminergic somas in the AVPV/PVpo led to a sustained increase in male appetitive sniffing behaviour (**q**: $n = 6$ males) and a decrease in the latency to onset of the consummatory mounting behaviour (**r**: $n = 6$ males). This stimulation did not further increase the fraction of males that mount in the first 15 min after introduction of the female, as this fraction was already near ceiling in the absence of stimulation (**s**: $n = 9, 8, 7, 8$ trials from 6 males, mean \pm 95% c.i.). **t**, Brief optogenetic pre-stimulation of AVPV/PVpo dopamine axons in the MPOA did not further increase the fraction of males that mount in the first 15 min after introduction of the female, as this fraction was already

near ceiling in the absence of stimulation ($n = 22, 12, 18, 18, 18, 18$ trials from 6 males, mean \pm 95% c.i.). **u**, Female priming followed by pre-stimulation of all dopamine axons in the MPOA did not further increase the fraction of males that mount in the first 15 min after introduction of the female, as this fraction was already near ceiling in the absence of stimulation ($n = 10, 7, 7, 8$ trials from 5 males, mean \pm 95% c.i.). Mean \pm s.e.m. unless otherwise specified. * $p < 0.05$, ** $p < 0.01$, *** $p < 0.001$. See Supplementary Table 1 for statistics.

Extended Data Fig. 6 Measuring cAMP production with the sensor cADDIs in brain slices and *in vivo*.

a, b, Application of forskolin (an activator of adenylyl cyclase) to brain slices of NAc (**a**) and MPOA (**b**) induces cAMP production, as measured using the cAMP sensor cADDIs. cAMP production can be measured from changes either in fluorescence intensity or in fluorescence lifetime of cADDIs (**a**: $n = 6$ slices from 3 mice; **b**: $n = 2$ slices from 2 mice). Photobleaching is only observed in the intensity traces (e.g., prior to application of forskolin). The y-axes are flipped to make the plots more intuitive, as cADDIs fluorescence intensity and fluorescence lifetime both decrease with increasing cAMP. **c**, Experimental design for cADDIs photometry in the MPOA with Chrimson stimulation of AVPV/PVpo dopamine neurons. **d**, Histology of cADDIs expression, dopamine axons, and fibre location in the MPOA (scale bar: 200 μ m). **e**, Raw photometry measurements of cADDIs fluorescence intensity in the MPOA of awake, head-fixed males (during two example trials) show a persistent, downward deflection (increase in cAMP) after stimulating dopamine axons in the MPOA (red). Grey traces are mono-exponential fits of the pre-stimulation photometry data (fitted using the first 5 min of the traces), in order to estimate and account for the effects of photobleaching. A.U., arbitrary units. **f**, Experimental design for GRABDA_{2m}⁶¹ (a D2-based dopamine sensor) photometry in the MPOA, together with Chrimson stimulation of AVPV/PVpo dopamine neurons. **g**, Blocking D1/D5 transmission with SCH23390 (0.6 mg/kg, i.p.) did not affect optogenetically evoked dopamine release ($n = 5$ males). **h–j**, Repeated optogenetic stimulation of AVPV/PVpo dopamine axons in the MPOA (from data collected from the same experiments as in c-e) increased male appetitive sniffing behaviour (**h**:

$n = 7$ males) and decreased mounting latency (**i**: $n = 7$ males). But this stimulation did not further increase the fraction of males that mount in the first 15 min after introduction of the female, as this fraction was already at ceiling in the absence of stimulation (**j**: $n = 14$ trials from 7 males each, mean \pm 95% c.i.). Mean \pm s.e.m. unless otherwise specified. See Supplementary Table 1 for statistics.

Extended Data Fig. 7 Persistent PKA activity in the MPOA.

a, b, Application of forskolin to brain slices containing the NAc (**a**) or the MPOA (**b**) induces PKA activity, which can be measured with the PKA sensor FLIM-AKAR. PKA activity can be measured from changes either in fluorescence intensity or in fluorescence lifetime of FLIM-AKAR (**a**: $n = 3$ slices from 2 mice; **b**: $n = 4$ slices from 2 mice). Photobleaching is only seen in the fluorescence intensity traces. The y-axes are flipped to make the plots more intuitive, as FLIM-AKAR fluorescence intensity and fluorescence lifetime decrease with increasing PKA activity. **c–e**, cell body ROIs and corresponding neuropil rings for two representative cells (**c, d**), segmented from the intensity frames (top) and applied to the lifetime frames (bottom) during *in vivo* two-photon FLIM imaging via a GRIN lens inserted in the MPOA. The ROIs and corresponding rings are shaded red in left and right panels, respectively, and also displayed in insets at higher magnification. The purpose of calculating lifetime changes in both ROIs and in surrounding neuropil rings was to subtract lifetime changes in the neuropil rings from those in the ROIs, thereby isolating changes in cell body PKA activity above and beyond contributions from nearby neuropil. Samples traces of the ROI, neuropil ring, and ROI after neuropil ring subtraction are shown in **e** (same plotting format as in Fig. 4c; red horizontal bar: Chrimson stimulation). The cell highlighted in **c** (Cell 1) showed increased PKA activity following stimulation in the ROI but not in the surrounding neuropil. See [Methods](#) for detailed descriptions of ROI segmentation and neuropil ring calculation. Scalebar: 200 μ m. **f–h**, Average lifetime traces per mouse (**f**: $n = 3$ mice), per field-of-view (**g**: $n = 8\text{--}9$ fields of view, with fields of view from the same mouse spaced a minimum of 80 μ m apart along the Z-axis), and per cell (**h**: $n = 121, 86$ cells) show persistent increases in PKA activity in the MPOA after optogenetically stimulating AVPV/PVpo dopamine axons in the MPOA. Thin lines:

individual traces. Thick lines: means across traces. No change in PKA activity is seen in the no-stimulation controls. Neuropil changes were subtracted for all traces. Individual traces in **f** and **g** were obtained by averaging changes in fluorescence lifetime across all cells in each mouse (**f**) or in each field of view (**g**). **i, j**, K-means clustering (**i**, $k = 2$) reveals a sub-population of 36% of the MPOA neurons that show strong responses to dopamine stimulation (**j**, left). The other cluster includes cells that did not respond to the stimulation and cells in the no-stimulation control experiments (**j**, right; $n = 43$, 164 cells). We used this clustering method to identify responsive cells because each field of view was only imaged once per experimental condition. Neuropil changes were subtracted for all traces. **k**, Mean traces of cells analyzed in **j** ($n = 43$ responsive and 78 unresponsive cells from 3 males). **l**, Across responsive cells, the magnitude of change in FLIM-AKAR lifetime with dopamine stimulation was positively correlated with baseline lifetime, indicating that cells that show the strongest stimulation-evoked increases in PKA activity also exhibited lower initial PKA activity (Pearson correlation; $n = 43$ cells from 3 males). Mean \pm s.e.m. unless otherwise specified. * $p < 0.05$, *** $p < 0.001$. See Supplementary Table [1](#) for statistics.

Extended Data Fig. 8 Persistent cAMP elevation in the MPOA.

a, Setup and protocol for optogenetic Chrimson stimulation of dopamine axons in the MPOA in awake, head-fixed males while measuring PKA activity using two-photon fluorescence lifetime imaging (FLIM) of the cAMP sensor, cADDis, via a GRIN lens. Stimulation protocol: 10-ms pulses at 10 Hz for 5 s, repeated every 30 s. FLIM frames were collected 10 min before stimulation as well as 30, 60, and 120 min after stimulation. **b**, *Left*: mean cADDis fluorescence intensity image. Brighter regions: cell bodies. Scale bar: 200 μm . *Right*: dopamine stimulation (red dashed line) induced a persistent decrease in cADDis lifetime (increase in cAMP concentration) that gradually returned to baseline over tens of minutes. Scale bar: 200 μm . **c, d**, Average lifetime changes across fields-of-view (**c**: $n = 8$, 6 fields of view) and across mice (**d**: $n = 4$ mice) demonstrated a persistent decrease in lifetime following stimulation (segmentation and neuropil ring subtraction were performed as in FLIM-AKAR imaging, cf. Extended Data Fig. [7c, d](#)). **e**, *Left*: experimental design. *Right*: head-fixed

two-photon FLIM imaging sessions prior to priming ('A') and after priming ('B') show increased baseline cAMP concentration in the MPOA following priming ($n = 6$ fields of view from 3 mice, each value is the average of all cells in a field of view). Mean \pm s.e.m. *** $p < 0.001$. See Supplementary Table 1 for statistics.

Extended Data Fig. 9 AVPV/PVpo dopamine neurons signal to ESR1 neurons in the MPOA through D1/D5 transmission.

a, b, Fluorescence *in situ* hybridization (using the RNAscope kit) demonstrates high co-localization of DRD1 and ESR1 expression in the MPOA (a), with an average of ~2 DRD1 puncta per ESR1 cell ($n = 3$ mice). The masks were selected based on ESR1 puncta. A cropped subregion of these images is shown in Fig. 4f. Scale bars: 100 μm . **c**, In the LPOA, 39% of the ESR1 neurons also express DRD1 (average ~2 DRD1 puncta per ESR1 cell), and 68% of the DRD1 puncta are found in the ESR1 cells. **d**, Sample field of view of cADDIs expression in the ESR1 neurons in the MPOA (defined as the subregion of the preoptic area within 600 μm from the midline) and the LPOA (defined as the subregion beyond 600 μm from the midline). The definition of the boundary at 600 μm is derived from a standard mouse atlas⁶². Experimental designs are replotted here. In Experiment 1, we first used a concentric bipolar electrode to locally stimulate the AVPV/PVpo area for 20 rounds (20 Hz trains, 75 μA pulses for 1 s every 20 s) and then washed on the D1/D5 agonist SKF81297 (2 μM ; diluted from 100 mM stock solution in dimethyl sulfoxide). In Experiment 2, we first used a minimal stimulation protocol to identify the MPOA ESR1 neurons that responded to AVPV/PVpo stimulations, washed on the D1/D5 antagonist SCH23390 (300 nM; diluted from 50 mM stock solution in saline), and then performed 20 more rounds of AVPV/PVpo stimulation in the presence of the antagonist. **e**, Heatmaps showing the cell-by-cell cADDIs response in the MPOA to both AVPV/PVpo stimulation (left) and D1/D5 agonist wash-on (right). Stimulation responses are averages of 20 trials, following baseline subtraction of the pre-stimulation means, while the agonist response is a single-trial response following baseline subtraction of the pre-agonist value. ESR1 neurons are divided into those that responded to the agonist (above the horizontal blue line) and those that did not (below the horizontal blue line) using a classifier

(see [Methods](#)). Cells are sorted based on their agonist response and the same order is used for both panels. Grey lines on the top denote the windows that are used for quantification and classification. The colour of the ‘Slide ID’ indicates the identity of the slice ($n = 983$ neurons from 4 slices, 3 mice) from which the cell was recorded. **f, g**, In the agonist-responsive group (orange), neurons show persistent cAMP elevations (decreases in cADDIs intensity) that accumulate after each AVPV/PVpo stimulation (**f**). The cAMP elevations are not seen in the agonist-unresponsive group (grey in **f**; $n = 4$ slices from 3 males). Panel **g** summarizes agonist responses ($n = 4$ slices from 3 males). **h**, Heatmaps showing the cell-by-cell cADDIs response of MPOA ESR1 neurons to AVPV/PVpo stimulation both before (left) and after washing on the D1/D5 antagonist (right). Stimulation responses are averages of 3 and 20 trials, following baseline subtraction of the pre-stimulation means. MPOA ESR1 neurons are divided into those that responded to the pre-antagonist stimulation (above the horizontal blue line) and those that did not (below the horizontal blue line) using a classifier (see [Methods](#)). Cells are sorted based on their stimulation response, and the same order is used for both panels. Grey lines on the top denote the windows that are used for quantification and classification. The colour of the ‘Slide ID’ indicates the identity of the slice ($n = 947$ cells from 4 slices, 3 mice) from which the cell was recorded. **i, j**, In the stimulation-responsive group (red), neurons show persistent cAMP elevations that are accumulated after each AVPV/PVpo stimulation (**i**: $n = 4$ slices from 3 males). The cAMP elevations are not seen after the antagonist wash-on (**j**: $n = 4$ slices from 3 males). **k**, Same as **e** but for LPOA ESR1 neurons ($n = 192$ cells from 4 slices, 3 mice). **l, m**, Same as **f, g** but for LPOA neurons. Note that LPOA ESR1 neurons (including those in the agonist-responsive group) did not respond to AVPV/PVpo stimulation ($n = 4$ slices from 3 males). **n, o**, Same as **l–m** but for fluorescence lifetime measurements (a bleaching-insensitive way of analyzing fluorescence data; see [Methods](#)). Note that LPOA ESR1 neurons did not respond to AVPV/PVpo stimulation, including those in the agonist-responsive group ($n = 4$ slices from 3 males). **p–r**, In Experiment 2, we again observed only very few AVPV/PVpo stimulation-responsive neurons in the LPOA, before or after antagonist application ($n = 198$ cells from 4 slices, 3 mice). Plotting conventions are the same as above. Note that we did not plot average responses of the stimulation-responsive group due to its

small size. **s**, In combined data from Experiments 1 and 2, the fraction of cells that responded to AVPV/PVpo stimulation gradually dropped off over distance from the midline (**t**; n = 2320 cells from 8 slices, 6 mice). Axon fields of AVPV/PVpo dopamine neurons shown here for comparison (**s**). Scale bars: 200 μ m. **u**, In the agonist-responsive group (orange), MPOA ESR1 neurons show persistent elevations in PKA activity (decreases in FLIM-AKAR lifetime) that accumulate across repeated trials of AVPV/PVpo stimulation. The cAMP elevations are not seen in the agonist-unresponsive group (grey; n = 4 slices from 3 males). The right panel summarizes agonist responses (n = 4 slices from 3 males). **v**, In the stimulation-responsive group (red), MPOA ESR1 neurons show persistent elevations in PKA activity that accumulate after each AVPV/PVpo stimulation (left: n = 4 slices from 3 males). The elevations in PKA activity are not seen after antagonist wash-on (right: n = 4 slices from 3 males). **w**, Same as **u** but for LPOA ESR1 neurons. Note that LPOA ESR1 neurons did not respond to AVPV/PVpo stimulation, including those in the agonist-responsive group (n = 4 slices from 3 males). **x**, In Experiment 2, we again only recorded very few numbers of AVPV/PVpo stimulation-responsive ESR1 neurons in the LPOA, before or after antagonist. See above for plotting conventions. Note that we did not plot average responses of the stimulation-responsive group due to its small size. Mean \pm s.e.m. *p<0.05, **p<0.01, ***p<0.001. See Supplementary Table 1 for statistics.

Extended Data Fig. 10 Novel optogenetic and molecular tools to manipulate intracellular cAMP *in vivo*.

a, Peptide sequences of bPAC⁶³ and an improved variant, biPAC. **b**, cAMP production by bPAC and biPAC in *Xenopus laevis* oocytes. Measurement was performed 3 days after injection of 30 ng cRNA of Venus-bPAC or Venus-biPAC in the dark ('Dark', non-shaded bars) or after 1 min illumination with 473 nm, 0.3 mW/mm² light ('Light', shaded bars). The control bar shows uninjected oocytes (n = 3 groups of 5 oocytes). For comparison, the mean value of the uninjected oocytes is also noted with a horizontal dashed line. The Y-axis is on the log scale. Note that, in contrast to bPAC, biPAC does not exhibit increased enzymatic activity in darkness, above levels observed in baseline control conditions. **c**, Enzymatic activity of Venus-biPAC in dark and light conditions (n = 4, mean \pm s.d.). **d**, Light

intensity-dependent cAMP production of Venus-biPAC at 473 nm. After fitting with the Michaelis-Menten function, the Km value was determined to be $32 \mu\text{W/mm}^2$ ($n = 4$, mean \pm s.d.). Venus tag was used here for protein-quantification purpose (same below). **e**, cAMP concentrations at different time points in the dark after 500 ms of light stimulation. Fitting a mono-exponential function yielded an off time constant $\tau_{\text{off}} = 8.9 \pm 2.2 \text{ s}$ ($n = 4$, mean \pm s.d.). **f, g**, Brief optogenetic stimulation of biPAC expressed in Esr1-Cre cells in the MPOA did not further increase the fraction of males that mount in the first 15 min after subsequent introduction of the female, as this fraction was already near ceiling in the absence of stimulation (ns, non-significant; Fisher's exact test, $n = 35, 36$ trials from 12 males, mean \pm 95% c.i.). **h–j**, In mice that did not express biPAC, the same stimulation protocol failed to increase appetitive sniffing (**h**: $n = 6$ males), failed to decrease the latency to consummatory mounting behaviours (**i**: $n = 6$ males), and failed to increase the fraction of males that mounted (**j**: $n = 18$ trial from 6 males, mean \pm 95% c.i.). **k, l**, Design (**k**) and sequence (**l**) of PDE4D3-Cat. Upstream conserved regions (UCRs) are inhibitory, regulatory domains in the endogenous hPDE4D3⁶⁴. Replacement of these UCRs with mKate2 substantially increased the enzymatic activity of PDE4D3-Cat over hPDE4D3. **m**, Enzymatic activity of Venus-PDE4D3-Cat ($n = 3$, mean \pm s.d.). After fitting with the Michaelis-Menten function, the Km value was determined to be $3.1 \pm 0.4 \mu\text{M}$ and the Vmax value was $35.3 \pm 2.9 \text{ s}^{-1}$. This enzyme is much faster than the endogenous protein (Vmax = $5-9 \text{ s}^{-1}$)⁶⁴. ***p<0.001. See Supplementary Table 1 for statistics.

Supplementary information

Supplementary Information

This file contains Supplementary Methods, a Supplementary Discussion and Supplementary References.

Reporting Summary

Supplementary Table 1

Statistical details for Fig. 1-4 and Extended Data Figs. 1-10.

Peer Review File

Supplementary Video 1

Sniffing of female mice by males. After a female mouse enters the home cage of a male mouse, the male starts to investigate the new animal by following and sniffing her.

Supplementary Video 2

Male mounting and lower-body grooming. After investigating a female mouse, a male mouse decides to mount the female. Initially, the male's lower body thrusting is rapid and shallow. After the female intromits the male, the male's thrusting movements become deeper and slower. When the mounting bout ends, the male starts to clean his lower body.

Supplementary Video 3

Transfer of reproductive fluids. In the beginning of this video, a male mouse mounts a female and gains intromission a few seconds after. The repeated thrusting ends with the male transferring reproductive fluids, during which he shakes, falls on his side, and becomes temporarily immobilized. After the female moves away, the male stands up and cleans himself.

Supplementary Video 4

Priming of male mating drive by female interaction and dopamine stimulation. In this video, the male mouse's mating drive has been primed by 1) interacting with a female and then 2) stimulating dopamine axons in the MPOA. The priming steps were done 15 minutes before the start of this video, and the male has been alone in his cage since then. After a new female (i.e., different from the female that the male was primed with) enters

the cage, the male only briefly investigates her (~7 seconds) before initiating mounting behavior.

Rights and permissions

[Reprints and Permissions](#)

About this article

Cite this article

Zhang, S.X., Lutas, A., Yang, S. *et al.* Hypothalamic dopamine neurons motivate mating through persistent cAMP signalling. *Nature* **597**, 245–249 (2021). <https://doi.org/10.1038/s41586-021-03845-0>

- Received: 11 September 2020
- Accepted: 21 July 2021
- Published: 25 August 2021
- Issue Date: 09 September 2021
- DOI: <https://doi.org/10.1038/s41586-021-03845-0>

This article was downloaded by **calibre** from <https://www.nature.com/articles/s41586-021-03845-0>

- Article
- Open Access
- [Published: 08 September 2021](#)

Cells of the human intestinal tract mapped across space and time

- [Rasa Elmentaitė](#) [ORCID: orcid.org/0000-0001-7366-5466¹](#),
- [Natsuhiko Kumasaka](#) [ORCID: orcid.org/0000-0002-3557-0375¹](#),
- [Kenny Roberts](#) [ORCID: orcid.org/0000-0001-6155-0821¹](#),
- [Aaron Fleming²](#),
- [Emma Dann](#) [ORCID: orcid.org/0000-0002-7400-7438¹](#),
- [Hamish W. King](#) [ORCID: orcid.org/0000-0001-5972-8926³](#),
- [Vitalii Kleshchevnikov¹](#),
- [Monika Dabrowska¹](#),
- [Sophie Pritchard¹](#),
- [Liam Bolt](#) [ORCID: orcid.org/0000-0001-7293-0774¹](#),
- [Sara F. Vieira](#) [ORCID: orcid.org/0000-0002-1021-3021¹](#),
- [Lira Mamanova](#) [ORCID: orcid.org/0000-0003-1463-8622¹](#),
- [Ni Huang¹](#),
- [Francesca Perrone⁴](#),
- [Issac Goh Kai'En⁵](#),
- [Steven N. Lisgo⁵](#),
- [Matilda Katan](#) [ORCID: orcid.org/0000-0001-9992-8375⁶](#),
- [Steven Leonard¹](#),
- [Thomas R. W. Oliver](#) [ORCID: orcid.org/0000-0003-4306-0102^{1,7}](#),
- [C. Elizabeth Hook⁷](#),
- [Komal Nayak⁴](#),
- [Lia S. Campos¹](#),
- [Cecilia Domínguez Conde](#) [ORCID: orcid.org/0000-0002-8684-4655¹](#),
- [Emily Stephenson⁵](#),
- [Justin Engelbert⁵](#),
- [Rachel A. Botting](#) [ORCID: orcid.org/0000-0001-9595-4605⁵](#),
- [Krzysztof Polanski](#) [ORCID: orcid.org/0000-0002-2586-9576¹](#),
- [Stijn van Dongen¹](#),

- [Minal Patel¹](#),
- [Michael D. Morgan](#) ORCID: [orcid.org/0000-0003-0757-0711](#)^{8,9},
- [John C. Marioni](#) ORCID: [orcid.org/0000-0001-9092-0852](#)^{1,8,9},
- [Omer Ali Bayraktar](#) ORCID: [orcid.org/0000-0001-6055-277X](#)¹,
- [Kerstin B. Meyer](#) ORCID: [orcid.org/0000-0001-5906-1498](#)¹,
- [Xiaoling He¹⁰](#),
- [Roger A. Barker¹⁰](#),
- [Holm H. Uhlig](#) ORCID: [orcid.org/0000-0002-6111-7355](#)^{11,12,13},
- [Krishnaa T. Mahbubani](#) ORCID: [orcid.org/0000-0002-1327-2334](#)¹⁴,
- [Kourosh Saeb-Parsy](#) ORCID: [orcid.org/0000-0002-0633-3696](#)¹⁴,
- [Matthias Zilbauer](#) ORCID: [orcid.org/0000-0002-7272-0547](#)^{14,15,16},
- [Menna R. Clatworthy^{1,2}](#),
- [Muzlifah Haniffa](#) ORCID: [orcid.org/0000-0002-3927-2084](#)^{1,5,17},
- [Kylie R. James](#) ORCID: [orcid.org/0000-0002-7107-0650](#)¹ nAff¹⁹ &
- [Sarah A. Teichmann](#) ORCID: [orcid.org/0000-0002-6294-6366](#)^{1,18}

Nature volume 597, pages 250–255 (2021)

- 7064 Accesses
- 1 Citations
- 118 Altmetric
- [Metrics details](#)

Subjects

- [Cellular signalling networks](#)
- [Crohn's disease](#)
- [Developmental biology](#).

Abstract

The cellular landscape of the human intestinal tract is dynamic throughout life, developing in utero and changing in response to functional requirements and environmental exposures. Here, to comprehensively map cell lineages, we use single-cell RNA sequencing and antigen receptor analysis of almost half a million cells from up to 5 anatomical regions in the developing and up to 11 distinct anatomical regions in the healthy paediatric and adult human gut. This reveals the existence of transcriptionally distinct BEST4 epithelial cells throughout the human intestinal tract.

Furthermore, we implicate IgG sensing as a function of intestinal tuft cells. We describe neural cell populations in the developing enteric nervous system, and predict cell-type-specific expression of genes associated with Hirschsprung's disease. Finally, using a systems approach, we identify key cell players that drive the formation of secondary lymphoid tissue in early human development. We show that these programs are adopted in inflammatory bowel disease to recruit and retain immune cells at the site of inflammation. This catalogue of intestinal cells will provide new insights into cellular programs in development, homeostasis and disease.

[Download PDF](#)

Main

Intestinal tract physiology relies on the integrated contribution of multiple cell lineages, the relative abundance and cell networking of which fluctuate from embryonic development to adulthood. Further complexity is added because the intestinal tract is formed of distinct anatomical regions that develop at different rates and carry out diverse roles in digestion, nutrient absorption, metabolism and immune regulation.

The analysis of rare fetal tissues has resolved the formation of villi–crypt structures and the seeding of immune cells into the gut environment^{1,2,3}. Similarly, our understanding of the cellular landscape of the adult gut is benefiting from single-cell technologies. Regional differences in immune-cell activation and microbiome composition in the healthy human colon have previously been reported⁴. Studies that compare inflammatory bowel disease samples to healthy tissues have enabled the identification of disease-relevant stromal^{5,6}, tissue-resident CD8 T cell^{7,8,9} populations and correlation between cellular response and clinical treatment¹⁰. Although extensive work has been carried out to profile the intestinal tract at single-cell resolution (Supplementary Table 1), a holistic analysis of the gut through space (anatomical location) and time (lifespan) is lacking. Building such a developmental roadmap would be invaluable for the scientific community¹¹.

Here we create a single-cell census of the healthy human gut, encompassing around 428,000 cells from the small and the large intestines as well as associated lymph nodes during in utero development, childhood and adulthood.

Integrated map of human intestinal cells

To investigate cellular dynamics across the intestinal tract, we performed single-cell RNA sequencing (scRNA-seq) on distinct tissue regions of second-trimester (12–17

post-conception weeks (PCW)) and adult (29–69 years) intestines and draining mesenteric lymph nodes (mLN) (Fig. 1a, Extended Data Fig. 1a). Additionally, we integrated results from the scRNA-seq analysis of tissues from first-trimester (6–11 PCW) intestine, paediatric Crohn’s disease and healthy ileum¹.

Fig. 1: Intestinal cellular census throughout life.

 figure1

a, Schematic of human gut tissue sampling. Number of donors sampled for scRNA-seq is given. Mid., middle; prox., proximal; term., terminal; mLN, mesenteric lymph node; jej., jejunum; duo., duodenum; trans., transverse; asc., ascending; desc., descending; sig., sigmoid. **b**, Relative proportions of cell lineages at each developmental stage. NK, natural killer; CD, inflammatory bowel disease. **c**, Proportions of *BEST4*-expressing enterocytes among epithelial cells in scRNA-seq data of each tissue region and at each developmental stage. Ile., ileum; app., appendix; cae., caecum; rec., rectum. **d**, Expression of *BEST4* in histological sections, from <https://proteinatlas.org>⁴⁸ (Supplementary Table 8, $n = 2$ biologically independent samples for each region). Scale bars, 50 μm. **e**, Dot plot with relative expression of selected genes within *BEST4* epithelial cells from different locations and ages. Key genes are highlighted in red, and the full Milo analysis can be found in Extended Data Fig. 3d.

[Source data](#)

The dataset comprised more than 428,000 high-quality cells (Extended Data Fig. 1b, Supplementary Table 2). Leiden clustering and marker-gene analysis revealed major clusters of epithelial, mesenchymal, endothelial, immune, neural and erythroid cells (Fig. 1b, Extended Data Fig. 1c). Fetal gut samples were enriched for mesenchymal and neural cells, with increased abundance of immune cells from the second trimester onwards in gut and mLN (Fig. 1b, Extended Data Fig. 1d–f). Further sub-clustering of

the cellular lineages enabled the identification of 133 cell types and states with specific transcriptional identities (Extended Data Fig. 2a, Supplementary Tables 3–7).

BEST4 epithelial cells, which have been previously observed in human small and large intestines^{6,12,13}, varied in abundance between intestinal regions (Fig. 1c, d). Using differential cell-type abundance analysis¹⁴, we identified their region-specific expression signatures (Fig. 1e, Extended Data Fig. 3a–d). Notably, small-intestinal BEST4 cells were marked by high expression of the gene *CFTR*, which encodes a chloride channel and is mutated in cystic fibrosis (Fig. 1e); such high expression was also observed at the protein level (Extended Data Fig. 3e). In this staining and in previous work, BEST4 cells were in close proximity to cells that resembled goblet cells¹² (Extended Data Fig. 3f). Our analysis highlights a possible role of BEST4 enterocytes of the small intestine in aiding mucus production by goblet cells and biosynthesis of acids, in contrast to the functions of colonic BEST4 cells in the metabolism of small molecules (Extended Data Figs. 3g, 4a, b).

Diversity of intestinal epithelial cells

In the epithelial compartment, secretory cells consisted of goblet, tuft, Paneth and microfold cells, as well as precursor states. Absorptive and goblet cells showed regional separation at all life stages (Fig. 2a, b, Extended Data Figs. 5a–c, 6a, b). Given that the gut epithelium represents an entry point for SARS-CoV-2¹⁵, we also report that both *ACE2* and *TMPRSS2*—which encodes transmembrane serine protease 2—were expressed by enterocytes in early development (Fig. 2c, Extended Data Fig. 6c).

Fig. 2: Epithelial cells and FCGR2A signalling in tuft cells.

 **figure2**

a, b, Uniform manifold approximation and projection (UMAP) of fetal (**a**) and postnatal (**b**) epithelial cell types. Key cell types are circled with a dashed line and arrows depict paths of differentiation towards secretory and absorptive enterocytes as determined by scVelo. M cells, microfold cells; TA, transit-amplifying. **c**, Dot plot of

TMPRSS2 and *ACE2* expression in epithelial cells in the fetal intestine as in **a, d**, UMAP of enteroendocrine (EEC) and enterochromaffin (EC) cell subsets. Arrows depict summarised scVelo differentiation trajectories. *C9orf16* is also known as *BBLN*. **e**, Heat map of genes that change along the differentiation trajectory from *NEUROG3*-expressing progenitors to enterochromaffin cells (red arrow in **d**). Arrows indicate genes that have known associations with enterochromaffin cell differentiation. **f**, Dot plot with expression of molecules upstream or downstream of the *PLCG2* pathway in tuft cells and pooled absorptive (TA and enterocytes) and secretory (Paneth, goblet and EEC) cells. **g**, Per cent expression of Fc γ receptor by SiglecF $^+$ EpCAM $^+$ and SiglecF $^-$ EpCAM $^+$ cells in wild-type mice determined by flow cytometry (individual points represent biological replicates; $n = 4$). Using a two-way ANOVA we observe significant interaction between Fc γ receptor expression ($F(3, 39) = 42.29, P = 3.05 \times 10^{-11}$). Post-hoc analysis showed significant differences between non-Tuft epithelial cells and Tuft cells for Fc γ RIIB (mean difference = 2.80, 95% CI [1.80, 3.81], $P < 0.0001$) and Fc γ RIIB/III (mean difference = 4.88, 95% CI [3.88, 5.89], $P < 0.0001$) expression. *** $P_{adj} < 0.0001$ values corrected with Tukey's test for multiple comparisons. **h**, Schematic of proposed signalling pathways in tuft cells. RTK, receptor tyrosine kinases.

Source data

Subclustering of enteroendocrine cells (EECs) revealed *NEUROG3*-expressing precursor cells enriched in the first-trimester fetal gut, and multiple mature subsets resembling populations described in intestinal organoids¹⁶ (Fig. 2d, Extended Data Fig. 6d). Although neuropeptide W (encoded by *NPW*) is known to stimulate food intake¹⁷ and is broadly expressed by EECs^{16,18}, we found a subpopulation of *NPW*-expressing enterochromaffin cells that are also specific for *PRAC1* and *RXFP4* (Extended Data Fig. 4d). We delineated genes involved in the differentiation of *NEUROG3* precursors to enterochromaffin cells, including recently described genes (marked by arrows) such as *FEV*^{19,20} (Fig. 2e, Extended Data Fig. 6e, f).

Notably, among the top differentially expressed genes in tuft cells was *PLCG2* (Extended Data Fig. 6g, h), a phospholipase that is typically associated with haematopoietic cells. To explore the relevance of *PLCG2* in tuft cells, we screened for the expression of upstream receptors (Fig. 2f, Extended Data Fig. 6i). FCGR2A, which is activated in response to IgG and expressed by selected epithelial cells in immunized mice²¹, was specifically expressed by approximately 2.75% of tuft cells (Fig. 2f). We confirmed the expression of the protein FCGR3 (the mouse orthologue of human FCGR2A) by approximately 5% of small intestinal tuft cells in mice (Fig. 2g, Extended Data Fig. 6j). Receptor tyrosine kinases were expressed across tuft cells and other epithelial cell types. Because these are known to be mainly linked to PLCG1 activation, whether they are also responsible for PLCG2 activation in tuft cells is

difficult to delineate (Fig. 2h). *PLCG2* expression by tuft cells was at higher levels than in B and myeloid lineages, and was confirmed in both in vivo and in vitro models (Extended Data Fig. 7a–f) and—together with downstream signalling mediators including *RAC2*, *ITPR2*, *PRKCA* and *TRPM5* (Fig. 2f,h)—suggested the ability of tuft cells to respond to immune-cell signalling.

Development of the enteric nervous system

Next we investigated the differentiation of neural cells from enteric neural crest cell (ENCC) progenitors (Fig. 3a,b) that were present in the dataset from 6.5 PCW (Extended Data Fig. 8a). ENCCs balance proliferation and differentiation into glia and neurons, while maintaining a progenitor reserve. To capture discrete processes of ENCC differentiation, we analysed early (6–11 PCW) and late (12–17 PCW) development separately (Extended Data Fig. 8b). In early development, ENCCs differentiated primarily to neurons via neuroblasts, giving rise to two distinct branches: branch A (*ETV1*) and branch B (*BNC2*) (Fig. 3a, Extended Data Figs. 8c, 9a–d), as has been observed in mice²². At this stage, branch A further differentiated to inhibitory motor neurons (iMN, resembling ENC8–ENC9²²) and two subsets that had characteristics of intrinsic primary afferent neurons (IPANs) or interneurons (resembling ENC12²²) with similarity to cells observed in the human fetal gut³ (Extended Data Fig. 8d). Branch B further differentiated to immature excitatory motor neuron (eMN) subsets (branches B1 and B2, resembling ENC1–ENC3²²) (Fig. 3a).

Fig. 3: Cells of the developing enteric nervous system.

 **figure3**

a, b, UMAP of enteric neural crest cells (ENCC) and their progeny at 6–11 (**a**) and 12–17 (**b**) PCW. Overlaid arrows depict scVelo trajectories, with major neuronal branches shown as A and B. Marker genes for populations are listed. Branch A2 and A3 subsets were not observed at 12–17 PCW, possibly because they were

outnumbered by the glial populations. **c, d**, Multiplex smFISH staining of *SCGN* branch A1, *GRP* branch A2/A3 and *BNC2* branch B1/2 developing *ELAVL4* neurons (arrows, $n = 2$) in the 15 PCW ileum (scale bars, 100 μm) (**c**) and glia 1 (*DHH*, *MPZ*, *SOX10*) cells in the mesentery (scale bars: main, 100 μm ; expansion, 30 μm . $n = 2$) (**d**). n represents the number of biological replicates across regions. **e**, Heat map showing the mean expression of genes associated with HSCR across intestinal regions and developmental stages. iMN, inhibitory motor neuron; IPAN, primary afferent neurons; IN, interneurons, int., intestine.

[Source data](#)

At later development, branch A differentiated into *NEUROD6*-expressing interneurons (resembling ENC10²²), whereas branch B differentiated into IPANs (Fig. 3**b**, Extended Data Figs. 8**c**, 9**a–d**) similar to previously described adult human IPAN A cells²³. We visualize opposing expression of *SCGN* (branch A1) and *GRP* (branch A2 and A3) and *BNC2* (branch B1 and B2) in the developing and adult human myenteric plexus (Fig. 3**c**, Extended Data Fig. 8**e**). The expression of transcription factors, such as ETV1, was previously validated *in situ* in a complementary resource of the human gut²⁴.

Although differentiated neurons were abundant at 6–11 PCW, glial cells were enriched at later development. Three types of enteric neural and a subset of differentiating glia (*COL20A1*) were present at 12–17 PCW (Fig. 3**b**, Extended Data Fig. 9**a–d**). Colonic glia 1 cells expressed posterior HOX genes and *TFAP2B*, which suggests that they originated in the sacrum or trunk (Extended Data Fig. 8**g**). We visualized *BMP8B*-expressing cells in the myenteric plexus, whereas *DHH*-expressing cells were found both in the mesentery and the myenteric plexus (Fig. 3**d**, Extended Data Fig. 8**f**).

To identify neural cells involved in Hirschsprung's disease (HSCR), we screened for the expression of known HSCR-associated genes^{25,26,27}. The majority of HSCR-associated genes were expressed across multiple differentiating populations with varying intensity (Fig. 3**e**), and varied between neuron branches A and B. For example, *RET* was highly expressed by branch A, but not by branch B, neurons. Notably, *ZEB2* and *EDNRB* were more highly expressed across colonic glia and neuroblast subsets compared to equivalent small intestinal subsets (Fig. 3**e**). Any differences in expression between regions might also be due to the developmental lag of the large intestines. In addition, key ligands that are implicated in HSCR—including *GDNF*, *NRTN* and *EDN3*—were primarily expressed by mesothelium, smooth muscle cells and interstitial cells of Cajal (ICC) (Extended Data Fig. 8**h**).

Formation of secondary lymphoid organs

Gut-associated lymphoid tissues and mLN are key sites of gut immune surveillance. We observed mLN emergence at around 12 PCW, with structures disectable from 15 PCW (Extended Data Fig. 10a)—consistent with previous observations²⁸. Interactions between mesenchymal and endothelial lymphoid tissue organizers (mLTo and eLTo, respectively) and lymphoid tissue inducers (LTi) are central to initiating the formation of secondary lymphoid organs²⁹. To better understand this process in humans, we assessed our dataset for the key cell types involved.

Sub-clustering of fetal and adult T and innate lymphoid cells revealed three clusters that matched published characteristics of LTi cells (Fig. 4a, b). This included high expression of *RORC*, *KIT*, *TNF*, *LTA*, *LTB*, *IL7R* and *ITGB7* (beta chain of gut-specific $\alpha 4\beta 7$ integrin) as well as the absence of productive $\alpha\beta$ TCR (Extended Data Figs. 10b–d, 11a–c). Innate lymphoid cell progenitors (ILCPs) were transcriptionally comparable to fetal liver ILCPs³⁰ (Extended Data Fig. 10e), and were found both in fetal mLN and in embryonic gut, whereas NCR⁺ and NCR⁻ type 3 innate lymphoid cells (ILC3s) were expanded across gut regions throughout 6–17 PCW (Extended Data Fig. 10f). This suggests that LTi-like ILC3 subsets are expanded during the development of gut-associated lymphoid tissues, but not during the development of mLN. Single-molecule fluorescence in situ hybridization (smFISH) staining identified all three LTi-like subtypes (Extended Data Fig. 10g) and placed *CXCR5* and *RORC*-expressing LTi cells adjacent to *CXCL13*-expressing LTo cells in proximal gut mucosa (Fig. 4c), supporting the concept of congregation of these cells in the developing gut. These observations— together with the expression of genes that encode key chemokines (*CXCR5*, *CCR7* and *CCR6*) and RNA velocity analysis (Extended Data Fig. 10h)—suggests that ILCPs are the first LTi-like cells in the developing gut, and represent a progenitor state to ILC3s.

Fig. 4: Lymphoid tissue organogenesis programs adopted in Crohn’s disease.

 figure4

- a**, UMAP of T and innate cells in scRNA-seq data across development. Dotted line denotes LTi-like cells and listed are characteristic genes. **b**, Schematic showing expression signatures of identified LTi-like states. **c**, Multiplex smFISH of 15 PCW

ileum showing proximity of *RORC* *CXCR5*-expressing LTi-like cells to *CXCL13*-expressing mLTo cells ($n = 2$ biological replicates across regions). Arrows highlight cells of interest. Scale bars: main, 100 μm ; expansion, 50 μm . **d**, UMAP of stromal cell types across development. The dotted line highlights key lineages. **e**, Spatial mapping of cell types from the scRNA-seq data to spatial transcriptomics data of 17 PCW terminal ileum using cell2location³⁴. Estimated abundance for cell types (colour intensity) across locations (dots) is overlaid on a histology image for LEC2 (left), LTi-like ILC3 (middle) and microfold (right) cells. **f**, Heat map showing top cell types across fetal, paediatric (healthy and Crohn's disease) and adult data that are enriched for gene expression associated with either Crohn's disease or ulcerative colitis (UC). All cell types listed are FDR < 10% for Crohn's disease. Asterisks denote cell types with FDR < 10% for ulcerative colitis. CLP, common lymphoid progenitor.

Source data

We observed arterial, venous, capillary and lymphatic endothelial cells (LECs) (Extended Data Figs. 2a, 12a, b). LECs separated into six clusters (labelled LEC1–LEC6; Extended Data Fig. 12c). LEC2 cells expressed *TNFRSF9*, *THY1*, *CXCL5* and *CCL20*—as described in human lymph nodes³¹—as well as targets of the NF- κ B pathway and adhesion molecules including *MADCAMI*, *VCAMI* and *SELE*, suggesting their involvement in lymphocyte trafficking (Extended Data Fig. 12d, e). We confirmed that the presence of high endothelial venules was required for lymphocyte entry and for proximity of *PROXI*⁺ vessels to *CXCL13*⁺ mLTo and *RORC*⁺ LTi cells (Extended Data Fig. 12f, g).

Within the stromal compartment, we identified subtypes of myofibroblast, smooth muscle cells, pericyte, interstitial cells of Cajal, mesothelium and populations resembling stromal cells previously described in the colon⁵ (labelled as stromal 1–4) (Fig. 4d, Extended Data Fig. 2a). We further identified fibroblast populations typically defined in mouse lymph nodes³², including T reticular cells and follicular dendritic cells (Extended Data Fig. 13a). In the prenatal intestine and mLNs, we observed a stromal population—marked by the expression of *CCL19*, *CCL21* and *CXCL13* as well as adhesion and NF- κ B pathway molecules (Extended Data Fig. 13b–f)—that resembled the mLTo described in mouse lymph nodes³³. We further determined cell–cell interactions that governed early leukocyte recruitment across LEC2, mLTo and LTi-like cells (Extended Data Fig. 13g, h), and differences in B cell activation status between fetal and adult samples (Extended Data Fig. 14a–l).

To visualize the recruitment of naive immune cell subsets to activated mLTo, we used cell2location³⁴ to perform spatial mapping of single-cell transcriptomes to 10x Genomics Visium spatial zones in 17 PCW fetal ileums (Fig. 4e, Methods). In this analysis, we captured tissue zones with expression of mLTo marker genes (*CCL19*,

CCL21 and *CXCL13*) (Extended Data Fig. 15a–c) that were likely to correspond to developing secondary lymphoid organs. We found that LEC2, mLTo and LTi-like subsets mapped to the same tissue zones as naive immune subsets (for example, *SELL* CD4 T cells, T regulatory cells, immature B cells; tissue zone or fact_11 (Extended Data Fig. 15c)). M cells characteristic of secondary lymphoid organs were present in the adjacent zone (tissue zone or fact_5 (Extended Data Fig. 15c)).

Following our observations, we compared programs of lymphoid organogenesis with the formation of ectopic lymphoid structures that is observed in patients with Crohn’s disease³⁵. We found that ILC3s in tissues from patients with Crohn’s disease matched fetal NCR⁺ ILC3s with more than 60% probability, whereas T reticular cells and stromal 4 cells from patients with Crohn’s disease transcriptionally reassembled fetal mLTo (Extended Data Fig. 15d, e) and were expanded in four out of seven Crohn’s disease samples (Extended Data Fig. 13b). Finally, from a genome-wide association study across cell types in our dataset, we calculated the enrichment score for genes associated with Crohn’s disease and ulcerative colitis (with a false-discovery rate of 10%; Methods). Adult ILC3s and fetal ILCPs and NCR⁺ ILC3s were among the top cells that were enriched for the expression of genes associated with Crohn’s disease (Fig. 4f, Extended Data Fig. 15f).

Discussion

Here we present an integrated dataset of more than 428,000 single cells from multiple anatomical regions of the human gut throughout life. This dataset can be browsed at <https://gutcellatlas.org>.

We found that *FCGR2A*, which encodes a receptor activated by the Fc fragment of IgG upstream of *PLCG2*, is expressed by a subset of tuft cells. In the context of development, IgG has been shown to traverse the placenta, and so could provide a potential route for tuft cell activation in utero. Two missense variants of *PLCG2* have been linked to aberrant B cell responses in early-onset inflammatory bowel disease^{36,37} and primary immune deficiency³⁸. Here we show increased expression of FcγRIIB (human *FCGR2B*)—which encodes an inhibitory receptor—by tuft cells in a mouse model of colitis, suggesting another possible involvement for this pathway in inflammatory bowel disease through tuft cells. Overall, these data suggest a potentially impactful immune-sensing role for intestinal tuft cells, and a topic for further investigation in future.

Immune sensing in the intestines also occurs in secondary lymphoid organs, and although there are substantial differences in the size and location of secondary lymphoid organs between species³⁹, our understanding of the formation of these structures is mostly derived from animal models²⁹. Single-cell studies have begun to

elucidate the diversity and activation of immune cells in the developing human gut^{3,40,41}. Here we identify cell types in the developing intestines that have transcriptional signatures and signalling pathways matching LTi, mLTo and eLTo (LEC2) cells. In vitro studies have shown the ability of *RORC*-expressing CD56⁺CD127⁺IL17A⁺ cells⁴² and ILC3s⁴³ to activate mesenchymal cells. This leads us to propose that all three LTi-like subsets defined in this study act in the initiation of secondary lymphoid organs, but probably at different stages of the process. Future studies using complementary approaches will shed light on these cell states and their tissue architecture. Notably, we also observe two specialized fibroblast populations in paediatric Crohn's disease—follicular dendritic cells and T reticular cells—similar to cells described in mouse lymph nodes³², Peyer's patches^{44,45,46,47} and those expanded in patients with ulcerative colitis⁵ as well as patients with Crohn's disease^{1,10}.

Overall, our work provides clarity on the complex interplay between intestinal cell types throughout time and space, and has potential implications for disease and for the engineering of in vitro systems.

Methods

No statistical methods were used to predetermine sample size. The experiments were not randomized and the investigators were not blinded to allocation during experiments and outcome assessment.

Patient samples

The research complies with all relevant ethical regulations and guidelines. Informed consent was obtained from all human participants and includes consent to publish photographs included in figures. Maternal consent and fetal gut samples were obtained through Newcastle upon Tyne Hospitals NHS Foundation Trust, the Human Developmental Biology Resource (HDBR, <https://www.hdbr.org>), or through Addenbrooke's Hospital, Cambridge in collaboration with R. A. Barker. Procurement and study of fetal samples were approved by REC18/NE/0290- IRAS project ID: 250012, North East - Newcastle & North Tyneside 1 Research Ethics Committee and REC-96/085, East of England - Cambridge Central Research Ethics Committee.

Paediatric patient material used in intestinal organoid culture was obtained with informed consent from either parents and/or patients using age-appropriate consent and assent forms as part of the ethically approved research study (REC-12/EE/0482, NRES Committee East of England, Hertfordshire and REC-17/EE/0265- IRAS project ID: 222907, East of England - Cambridge South Research Ethics Committee).

Human adult tissue was obtained by the Cambridge Biorepository of Translational Medicine from deceased transplant organ donors after ethical approval (reference 15/EE/0152, East of England - Cambridge South Research Ethics Committee) and informed consent from the donor families. Details of the ages and genders of donors are included as Supplementary Table 2. Samples were collected from 11 distinct locations, including the duodenum (two locations, DUO1 and DUO2, which were pooled in the analysis), jejunum (JEJ), ileum (two locations, ILE1 and ILE2, which were pooled in the analysis), appendix (APD), caecum (CAE), ascending colon (ACL), transverse colon (TCL), descending colon (DCL), sigmoid colon (SCL), rectum (REC) and mesenteric lymph nodes (mLN). Fresh mucosal intestinal tissue and lymph nodes from the intestinal mesentery were excised within 1 h of circulatory arrest; intestinal tissue was preserved in University of Wisconsin organ-preservation solution (Belzer UW Cold Storage Solution; Bridge to Life) and mLN were stored in saline at 4 °C until processing. Tissue dissociation was conducted within 2 h of tissue retrieval.

Mouse samples

C57BL/6 mice were obtained from Jackson Laboratories and maintained in specific-pathogen-free conditions at a Home-Office-approved facility at the University of Cambridge. Female mice aged 10–14 weeks were used; the numbers of mice used are included in the relevant figure legends. All procedures were carried out in accordance with ethical guidelines with the United Kingdom Animals (Scientific Procedures) Act of 1986 and approved by The University of Cambridge Animal Welfare and Ethical Review Body.

Isolation of intestinal cells from fetal tissue

The fetal gut mesentery was cut to lengthen out the tissue and the gut was dissected into proximal ileum (PIL), middle ileum (MIL), terminal ileum (TIL), colon or large intestine (LI) and appendix. Samples, except appendix, were washed twice with Hanks Buffered Saline Solution (HBSS; Sigma-Aldrich, 55021C) and minced into pieces using a scalpel. The samples were incubated in 2 ml HBSS solution containing 0.21 mg ml⁻¹ Liberase TL (Roche, 5401020001) or DH (Roche, 5401089001) and 70 U ml⁻¹ hyaluronidase (Merck, 385931-25KU) for up to 50 min at 37 °C, shaking every 5 min, and homogenized every 15 min using a pipette. The single cells were passed through a 40–100 µm sieve and spun down at 400g at 4 °C for 10 min. Red cell lysis solution (eBioscience10X RBC Lysis Buffer (Multi-species)) was used according to the manufacturer's guidelines to remove red blood cells, and the remaining cells were collected in FACS buffer (1% (v/v) FBS in PBS) by centrifugation at 400g at 4 °C for 5 min. All gut region samples (except mLN) proceeded to enrichment by magnetic-activated cell sorting (MACS).

Isolation of intestinal cells from adult tissue

Adult tissue sections were weighed before being washed in cold D-PBS (Gibco, 14190094) and diced with a scalpel. Samples were dissociated in 1–2 ml of digestion mix (D-PBS, 250 µg ml⁻¹ Liberase TL (Roche, 5401020001), 0.1 mg ml⁻¹ DNaseI (Sigma, 11284932001)) or DH (Roche, 5401089001) and 70 U ml⁻¹ hyaluronidase (Merck, 385931-25KU) for up to 30 min at 37 °C. Digested lysates were then passed through a 70 µm cell strainer, followed by 10 ml of neutralization medium (RPMI 1640 medium with HEPES (Gibco, 42401042), 20% (v/v) FBS (Sigma, 25200-056)). The samples were then centrifuged at 700g for 5 min at 4 °C. Cells were resuspended in 1 ml 0.04% (w/v) BSA in D-PBS and counted using a NucleoCounter NC-200 and Vial1-Cassette (ChemoMetec). All gut region samples (except mLN) proceeded to MACS enrichment.

MACS enrichment

Samples with a cell yield of greater than 500,000 were enriched by MACS. Dissociated cells were centrifuged for 5 min at 300g at 4 °C and resuspended in 80 µl chilled MACS buffer (D-PBS, 0.5% (w/v) BSA (Sigma-Aldrich, A7906-10G), 2 mM EDTA (Thermo Fisher, 15575020)) with 20 µl CD45 MicroBeads (Miltenyi Biotech, 130-045-801) and incubated for 15 min at 4 °C. Cells were washed with 2 ml MACS buffer and centrifuged as above and resuspended in 500 µl MACS buffer. Cells were passed through a pre-wetted MS column (Miltenyi Biotech, 130-042-201) on a QuadroMACS Magnetic Cell Separator (Miltenyi Biotech) followed by four rounds of 500 µl of MACS buffer. Flow-through was collected as the CD45⁻ fraction. The column was removed from the magnet and the CD45⁺ fraction was eluted with 1 ml of MACS buffer. CD45⁻ and CD45⁺ fractions were centrifuged as above and resuspended in 0.5–1 ml of 0.04% (w/v) BSA in D-PBS. Cell count and viability was determined using a NucleoCounter NC-200 and Vial1-Cassette (ChemoMetec) or haemocytometer and resuspended in 0.04% (w/v) BSA in D-PBS. Fetal CD45⁺ and CD45⁻ fractions were combined at a 1:1 ratio.

Organoid culture

Intestinal organoids from paediatric patients were cultured in Matrigel (Corning). During organoid culture, the medium was replaced every 48–72 h. Organoids were passaged using mechanical disruption with a P1000 pipette and re-seeded in fresh growth-factor-reduced Matrigel (Corning). When comparing culture media, multiple wells were seeded from a single dissociated sample. The organoids were then allowed to grow for 5 days followed by 24 h treatment with recombinant human protein TNF (H8916, Sigma Aldrich) at 40 ng ml⁻¹ or IFNγ (PHC4031, Life Technologies) at 20 ng

ml^{-1} . Organoids were in vitro differentiated for 4 days by culturing in a differentiation medium⁴⁹ and then collected for RNA extraction. Bright-field images were taken using an EVOS FL system (Life Technologies).

Processing for single-cell sequencing analysis was performed by removing the organoids from Matrigel at passage 3–4 using incubation with Cell Recovery Solution at 4 °C for 20 min, pelleting the cells, and re-suspending in TrypLE enzyme solution (Thermo Fisher) for incubation at 37 °C for 10 min. Cells were pelleted again and re-suspended in DMEM/F12.

RNA extraction, reverse transcription and quantitative PCR

Total RNA was extracted with the GenElute Mammalian Total RNA Miniprep kit (Sigma) and 1 μg of RNA was reverse-transcribed using the QuantiTect Reverse Transcription Kit (Qiagen). Complementary DNA corresponding to 5 ng RNA was used for real-time PCR performed by QuantiFast SYBR Green PCR Master Mix (Qiagen) on the 7500 Fast real-time PCR system, 7500 software v.2.0.6 (Applied Biosciences by Thermo Fisher Scientific). Primers for the specific target amplification were: *FCGR2A* fwd 5'-CCATCCCACAAGCAAACCACAG-3' and rev 5'-AGCAGTCGCAATGACCACAG-3'; *FCGR2B* fwd 5'-CCATCCCACAAGCAAACCACAG-3' and rev 5'-ACAGCAATCCCAGTGACCACAG-3'; *PLCG2* fwd 5'-AACCCATCTGACCCTCCTCTTG-3' and rev 5'-AGACTGCTGTTCCCTGTGTTCC-3'; *POU2F3* fwd 5'-TTCAGCCAGACCACCACATCTCAC-3' and rev 5'-GGACTCTGCATCATTAGGCCAC-3'; *MUC2* fwd 5'-GATTGAAAGTGAAGAGCAAG-3' and rev 5'-CACTGGAGGAATAAACTGG-3'; *LGR5* fwd 5'-CTCCCAGGTCTGGTGTGTTG-3' and rev 5'-GAGGTCTAGGTAGGAGGTGAAG-3'. Relative quantifications were normalized against GAPDH and calculated applying the $\Delta\Delta C_t$ method.

Statistical analysis was performed using GraphPadPrism 7 software (GraphPad Software) by multiple *t*-test analysis.

10x Genomics Chromium GEX library preparation and sequencing

MACS-enriched and total cell fractions were loaded for droplet-based scRNA-seq according to the manufacturer's protocol for the Chromium Single Cell 5' gene expression v.2 (10x Genomics) to obtain 8,000–10,000 cells per reaction. Library preparation was carried out according to the manufacturer's protocol. Pools of 16

libraries were sequenced across both lanes of an Illumina NovaSeq 6000 S2 flow cell with 50 bp paired-end reads.

Intestinal organoids were prepared using Chromium Single Cell 3' gene expression v.2 (10x Genomics) to obtain 8,000 cells per reaction. Intestinal organoid cDNA libraries were sequenced on a single lane of an Illumina HiSeq 4000 with 50 bp paired-end reads.

V(D)J sample preparation

10x Genomics V(D)J libraries were generated from the 5' 10x Genomics Chromium complementary DNA (cDNA) libraries as detailed in the manufacturer's protocol. B cell receptor (BCR) and T cell receptor (TCR) libraries for relevant samples were pooled and sequenced on a single lane of an Illumina HiSeq 4000 with 150 bp paired-end reads.

Plate-based Smart-seq2

Plate-based scRNA-seq was performed with the NEBNext Single Cell/Low Input RNA Library Prep Kit for Illumina (E6420L; New England Biolabs). Total cell fractions from dissociated gut sections of donors BRC2033–2034, F67, F72, F78 were snap-frozen in 10% (v/v) DMSO in 90% (v/v) BSA. Cells were thawed rapidly in a 37 °C water bath and diluted slowly with a pre-warmed FACS buffer (2% (v/v) FBS in D-PBS). Cells were pelleted by centrifugation for 5 min at 300g, washed with 300 µl of D-PBS and pelleted as before. Cells were resuspended in 100 µl of Zombie Aqua Fixable Viability Kit (1:200 dilution; 423101) and incubated at room temperature for 15 min. Cells were washed with 2 ml of FACS buffer followed by 300 µl of FACS buffer and resuspended in a total of 100 µl of Brilliant Violet 650 mouse anti-human CD45 (dilution 1:200; BioLegend, 304043), Alexa Fluor 700 mouse anti-human CD4 (dilution 1:200; BioLegend, 300526) and APC-H7 mouse anti-human CD19 (dilution 1:200; BD Biosciences, 560727) and incubated for 20 min in the dark at room temperature. Cells were washed twice with 300 µl of FACS buffer. Single, live, CD45⁺ cells were sorted by fluorescence-activated cell sorting (FACS) into wells of a 384-well plate (0030128508; Eppendorf) containing 2 µl of 1× NEB Next Cell Lysis Buffer (New England Biolabs). FACS sorting was performed with a BD Influx sorter (BD Biosciences) with the indexing setting enabled. Plates were sealed and spun at 100g for 1 min then immediately frozen on dry ice and stored at –80 °C. cDNA and sequencing library generation was performed in an automated manner on the Bravo NGS Workstation (Agilent Technologies)⁴. The purified pool was quantified on an Agilent Bioanalyzer (Agilent Technologies) and sequenced on one lane of an Illumina HiSeq 4000. Raw reads were aligned to the human transcriptome v.GRCh38-3.0.0 using STAR aligner (v.2.5.1b).

Pre-processing of 10x Genomics scRNA-seq data

10x Genomics scRNA-seq gene expression raw sequencing data were processed using the CellRanger software v.3.0.0–v.3.0.2 and the 10X human transcriptome GRCh38-3.0.0 as the reference. The 10x Genomics V(D)J Ig heavy and light chains were processed using cellranger vdj v.3.1.0 and the reference cellranger-vdj-GRCh38-alts-ensembl-3.1.0 with default settings.

scRNA-seq quality control and processing of 10x sequencing data

Pandas (v.1.1.2), NumPy (v.0.25.2), Anndata (v.0.6.19), ScanPy (v.1.4) and Python (v.3) were used to pool single-cell counts and for downstream analyses. Single-cell transcript counts for fetal and adult samples were handled separately to control for anticipated differences in cell expression and sample quality. For each run, we apply the SoupX algorithm⁵⁰ with default parameters and function adjustCounts() to remove ambient mRNA from the count matrix. Cells for each dataset were filtered for more than 500 genes and less than 50% mitochondrial reads, and genes were filtered for expression in more than 3 cells. A Scrublet (v.0.2.1) score cut-off of 0.25 was applied to assist with doublet exclusion. Additional doublet exclusion was performed throughout downstream processing based on unexpected co-expression of canonical markers such as CD3D (component of the TCR) and EpCAM. Gene expression for each cell was normalized and log-transformed. Cell cycle score was calculated using the expression of 97 cell cycle genes listed in ref. ⁵¹. Cell cycle genes were then removed for initial clustering. Cell cycle score, the percentage of mitochondrial reads and unique molecular identifiers (UMIs) were regressed before scaling the data.

Cell-type annotation

Batch correction of fetal and adult datasets was performed with bbknn (v.1.3.9, neighbours=2-3, metric='euclidean', n_pcs=30-50, batch_key='donor_id' or 'batch'). Dimensionality reduction and Leiden clustering (resolution 0.3–1.5) was carried out and cell lineages were annotated on the basis of algorithmically defined marker gene expression for each cluster (sc.tl.rank_genes_groups, method='wilcoxon'). Cell lineages were then subclustered and batch correction and Leiden clustering were repeated for annotation of cell types and states. Annotated fetal and adult datasets were then merged and annotations adjusted for concordance. A brief description of cell-type annotation for each lineage is provided below.

Epithelial lineage cells

(*EPCAM*-positive) shared between fetal, paediatric and adult datasets were stem cells (*LGR5*, *ASCL2*, *SMOC2*, *RGMB*, *OLFM4*), Paneth (*DEFA5*, *DEFA6*, *REG3A*), transit-amplifying (TA; *MKI67*, *TOP2A*, *PCNA*), goblet cells (*CLCA1*, *SPDEF*, *FCGBP*, *ZG16*, *MUC2*), BEST4 enterocytes (*BEST4*, *OTOP2*, *CA7*), enterocytes (*RBP2*, *ANPEP*, *FABP2*) and colonocytes (*CA2*, *SLC26A2*, *FABP1*), enteroendocrine cells (*CHGA*, *CHGB*, *NEUROD1*), Microfold cells (*SPIB*, *CCL20*, *GP2*), Tuft cells (*POU2F3*, *LRMP* (also known as *IRAG2*), *TRPM5*), BEST2 goblet cells were observed in adult colonic samples (Extended Data Fig. 5). Amongst the genes enriched in BEST2 goblet cells were Kallikreins *KLK15* and *KLK3*, as well as protease inhibitors *WFDC2* and *WFDC3*. Among fetal epithelial cells, 43 large intestinal goblet cells expressed *BEST2*. Fetal BEST2-expressing cells clustered together with small intestinal goblet cells, possibly due to the small number of these cells present in the data. Enteroendocrine cells were further sub-clustered and annotated based on key hormones expressed (M/X cells (*MLN/GHRL*), D cells (*SST*), β cells (*INS*, possibly from developing pancreatic bud), L cells (*GCG*), N cells (*NTS*), K cells (*GIP*), I cells (*CCK*) and enterochromaffin cells (*TPHI*) either expressing neuropeptide W (*NPW*) or *TAC1*).

Fetal-specific subsets included proximal progenitors (*FGG*, *BEX5*) as described in refs. 1,2,3,52, distal progenitors enriched for colon genes (*CKB*, *AKAP7*, *GPC3*) and CLDN10 cells that are possibly pancreatic progenitors based on expression of *DLK1*, *PDX1*, *RBPJ*, *CPA1* and *SOX9*⁵³. This population also highly expressed *CLU*, a marker for intestinal revival stem cells that has previously been described⁵⁴.

Endothelial lineage cells

(*PECAMI*, *CDH5*) were subdivided into arterial (*GJA4*, *HEY1*, *HEY2*, *EFNB2*), venous (*ACKR1*, *VWF*) and lymphatic endothelium (*PROXI*, *LYVE1*, *CCL21*). Arterial and venous cells from fetal and adult donors formed separate clusters and differed in gene expression, possibly reflecting fetal cell immaturity. Among age-shared arterial genes were *GJA5*, *SEMA3G*, *HEY1*, *HEY2* and age-shared venous genes were *ACKR1*, *ADGRG6*, *CPE*, *APLNR*. Capillary clusters were defined based on expression of RGCC and VWA1. Arterial capillaries specifically expressed *CA4* and *FCN3*.

Lymphatic endothelium further separated into six clusters, including LEC1 (*ACKR4*, *OTC*), resembling cells lining the subcapsular sinus ceiling in the human lymph nodes;³¹ LEC2 (*GPIBA*, *UBD*, *ANO9*, *FIBIN*, *PAPLN*) and only LEC expressing MADCAM1 and reassembled LECs lining subcapsular sinus floor in human lymph nodes³¹. We further define LEC3 (*ADGRG3^{hi}*) present mostly in the paediatric and adult intestinal regions, and LEC4 (*SATB2^{hi}*, *PTX3^{hi}*, *CXADR^{hi}*) specific to developing gut (Extended Data Fig. 7c) that may represent differentiated and

immature lymphatic vessels, respectively. LEC5 (*CLDN11*, *DEGS2*, *SBSPOON*, *ANGPT2^{hi}*, *GJA4^{hi}*) reassembled collecting lymphatic valves in lymph nodes³¹.

Neural lineage cells

were defined on the basis of observations in mouse embryos⁵⁵. Neuronal branches were named branch A or B on the basis of expression of *ETV1* or *BNC2*, respectively. Subpopulations of the branches were named A1–A4 and B1–B3 and combinatorial gene markers are provided in Fig. 3a, b. Branch A1 was functionally named inhibitory motor neurons (iMN) based on expression of *GAL*, *NOS1* and *VIP*; branch A2 was a mixed IPAN/IN population based on *NTNG1* and *NXPH2*. Branch A3 was a second subset of IPAN/IN equivalent to adult PIN3 and PSN3.²² Branch A4 were annotated as interneurons (IN) based on *NEUROD6* expression²². Branch B1 were annotated as immature excitatory motor neurons (eMN) based on *NXPH4* and *NDUFA4L2*,²² branch B2 was a second cluster of eMN based on expression of *BNC2* and *PENK*,^{22,55} branch B3 (IPAN) was assigned the IPAN label based on *DLX3*, *ANO2*, *NOG* and *NTRK3*. Branch B3 also showed the expression of *CALB2* and *SST* described in the human IPAN A population²³.

All terminal glial cells expressed high levels of ENCC progenitor/terminal glial marker genes including *FOXD3*, *MPZ*, *CDH19*, *PLP1*, *SOX10*, *S100B* and *ERBB3*, but lacked *RET*. Three types of enteric glia (*S100B*, *CRYAB*, *MPZ*) were observed: glia 1 (*DHH*, *RXRG*, *NTRK2*, *MBP*), glia 2 (*ELN*, *TFAP2A*, *SOX8*, *BMP8B*), glia 3 (*BCAN*, *APOE*, *CALCA*, *HES5*, *FRZB*) and a subset of differentiating glia (*COL20A1*) were present at 12–17 PCW (Fig. 3b). Differentiating glia (*COL20A1*) cluster annotation was based on expression of glial markers, positioning in between differentiating subsets and scVelo results.

Mesenchymal lineage cells

included previously described mesodermal populations mesoderm 1 (*HAND1*, *HAND2*, *PITX2*) and mesoderm 2 (*ZEB2*);¹ stromal 1 (*ADAMDEC1*) subset either highly expressing *ADAM28* or *CCL11*, *CCL8*, *CCL13*; stromal 2 (*PDGFRA*, *BMP4*) either enriched for *F3*, *NPY* or *CH25H*, *MMPI* expression; stromal 3 (*C7*) expressing *KCNN3*, *LRRC3B* or *C3*, *CLEC3B*, *SEMA3E*. We also observe the stromal 4 population (*MMPI*, *MMP3*, *PDPN*, *COL7A1*, *CHI3L1*) most recently described in the fetal gut³. In addition, we observe populations consistent with lymph-node immune-organizing fibroblasts including T reticular cells (*CCL19*, *GREMI^{hi}*, *TNFSF13B*)³², follicular dendritic cells (*CXCL13*, *CRI*, *CR2*)³², a population of FMO2 stromal cells (*LMO3*, *RASDI*, *PODN^{hi}*) found in the mLN samples that may represent adipose stromal cell population based on the expression of *FOXO1*, *KLF15*, *ZBTB16*, *LMO3*,

HSD11BI^{56,57}. Myofibroblasts were identified on the basis of expression of actin (*ACTA2*) and transgelin (*TAGLN*), fibroblast characteristic decorin (*DCN*), but lacked smooth muscle marker desmin (*DES*). Myofibroblast populations further differed in the expression of *HHIP*, *NPNT*, *SYT10* or *RSPO2*, *SYT1*, *PTGER1*. Smooth muscle cells were annotated on the basis of high expression of *DES*, calponin (*CNN1*)⁵⁸ and actin/myosin chain expression (*ACTA2*, *MYH11*) and subsets were further characterized following the annotation in ref. ³. Interstitial cells of Cajal (ICC) were identified on the basis of expression of *KIT*, *ANO1* and *ETV1*^{32,59}. Other ICC genes included *DLK1*, *CDH8*, *CDH10* and *PRKCQ*. Cycling stromal cells were defined based on expression of *MKI67*, *TOP2A*, *CDK1* and other cell cycle genes. Fetal mLTo cells were defined as discussed in the text. Additionally, mLTo cells were high for *UBD*, *CLSTN3*, *SLC22A3*, *TNFSF11* and *APLNR* expression.

Pericytes were identified on the basis of expression of *NOTCH3*, *MCAM* (CD146) and *RGS5*. Immature pericytes were annotated based on high expression of *PDGFRB*, *CSPG4* (encoding NG2)⁵⁸ and was marked by high *NDUFA4L2* expression. We further annotate contractile pericytes (*ACTA2^{hi}*) that were specifically marked by expression of *PLN*, *RERGL*, *KCNA5*, *KCNABI*, *NRIP2*. Angiogenic pericytes were annotated based on high expression of *PRRX1* and *PROCR* among pericyte populations (also expressed in stromal cells) as described in ref. ³, and also more specifically marked by *ENPEP*, *ABCC8*, *COL25A1* and *TEX41*. We also observe a population of pericytes marked by *CD36*⁶⁰ (named ‘Pericyte’).

Mesothelial cells were defined on the basis of *KRT19*, *LRRN4* and *UPK3B* expression, as observed previously^{1,61}, and additionally observe the expression of *TNNT1*, *RASSF7* and *KLK11* in these cells. Mature pericytes captured in adult tissues highly expressed *PRG4*, *MTIF*, *MTIG*, *CP4BPA*, and *HASI*. In addition, we observe a population of mesothelial cells expressing *RGS5*, *TMEM235* and *SERPINE3*.

B lineage cells

were defined as the cluster having positive expression of *MS4A1* (encodes CD20) and *CD19*. Among fetal B cells, common lymphoid progenitor (CLP) cells were classified on the basis of minimal expression of the lineage markers and specific expression of *CD34*, *SPINK2* and *FLT3*. Pro-B cells had specific expression of *DNTT* (TdT), recombination-activating genes (RAG) 1 and 2, high expression of B lymphocyte antigen receptor *CD79B*, V-set pre-B cell surrogate light chains (*VPREB1*, *VPREB3*) and expression of immunoglobulin-lambda chain *IGLL1*. Pre-B cells specifically expressed *CD38* and had higher expression of *CD19* than pro-B cells. Immature B cells had the highest expression of *MS4A1* among B lineage cells and expression of immunoglobulin heavy chains M and D. Adult B lineage cells had distinct clusters of naive B cells (Fc fragment of IgM receptor- FCMR), memory B cells (*SELL* (encodes CD62L)) and a population of memory B cells that specifically expressed transmembrane immunoregulatory molecule *FCRL4* (encodes protein also known as FcRH4) that has been suggested to be tissue-restricted⁶². Class switch IgA and IgG plasma cells showed expression of the syndecan, *SDC1*, and immunoglobulin heavy chains A and G, respectively. Cycling B cells were characterized by specific expression of *MKI67* (encodes Ki67) and genes involved in DNA replication, *HMG2B*, *TUBA1B* and *UBE2C*.

T lineage cells

were determined as the cluster of fetal, paediatric and adult cells with expression of T cell receptor component *CD3D* and subpopulations were annotated as previously described⁴. CD4 T cells had expression of *CD4*, but not *CD8A*, and vice versa for CD8 T cells. For each of these T cell groups, a population of paediatric/adult *SELL* (encodes CD62L) naive/central memory cells and *CD69* activated cells was assigned. ‘Activated T’ are fetal cells that have productive TCR $\alpha\beta$ chains as determined by paired V(D)J sequencing. In addition, among postnatal CD4 T cells are *CXCR3*, *IFNG* T_H1 and *RORA^{hi}*, *IL22*, *CD20* T_H17 cells. Paediatric CD CD4 T cells labelled as T_H1 and T_H17 showed additional co-expression of

IL22 and *IL26*, matching previously reported expression of these molecules in dysfunctional CD8 T cells in ulcerative colitis⁸. T regulatory cells were defined by *FOXP3*, *CTLA4*, *TIGIT* expression and T follicular helper cells expressed *CXCR5* and *PDCD1*. Two subsets of CD8 T memory cells were observed: CD8 T_{mem} and *CX3CR1*-expressing CD8 T_{mem} cells that both expressed *FGFBP2*, *S1PR5*, *FCGR3A* and *TGFBR3*.

Adult gdT subsets differentially expressed gamma and delta variable chain genes. Paediatric gdT (*TRDC*) cells did not have TCR sequencing data and did not express specific variable chains (Extended Data Fig. 2a). Specific expression of *TRGV2*, *TGVG4* and *TRVG5/TRVG7*, which each encode a variable chain of the gamma TCR chain, further defined subpopulations respectively. We also observe a population of *TRDV2/TRGV9* gdT cells⁶³ in the fetal gut. NK T cells expressed *CD3D* as well as NK genes *GZMA*, *NKG7* and *PRF1*. MAIT cells expressed *TRAV1*, *TRAV2* and *SLC4A10*. ILC2 expressed *PTGDR2*, *HPGDS*, *IL1RL1* and *KRT1*⁶⁴ and were found in the fetal samples.

NK cells were defined on the basis of *EOMES*, *PRF1*, *NKG7* and KIR receptor expression. Adult ILC3s were defined based on the expression of *RORC*, *IL1RL1*, *IL23R*, *KIT*⁶⁴ and further expressed *TNFS4* and *PCDH9*. ILCP were defined as Lin⁻ *IL7R* (encodes CD127), *KIT* (CD117), *RORC* (ROR γ) cells that further express *CCR6*, *NRPI*, but not *NCR2* (encodes NKp44), as described in the liver⁶⁵. ILCPs also highly expressed chemokine receptors *CXCR5* and *CCR7*, cell adhesion molecule encoded by *SCNIB*⁶⁶ and serine protease encoded by *HPN*.

LTi-like NCR⁺ ILC3 cells had highest expression of *TNFRSF11A* (RANK) and its ligand *TNFSF11* (RANKL), as well as *NCR1* (NKp46) and *NCR2* (NKp44), whereas LTi-like NCR- ILC3s lacked *NCR2* (NKp44) and expressed *IL17A*, *ITGA6* and *CCR9*, and NK-associated genes including *NKG7*, *PRF1* and *GZMA*, consistent with NCR⁻ ILC3 cells described in mice⁶⁷. We observed the expression of *IL22* in the adult compared to fetal NRC2⁺ ILC3s, suggesting that fetal gut ILC3 represents an immature ILC3 counterpart. Reassuringly, the LTi-like subtypes were identifiable in full-length scRNA-seq data from fetal ileum (Extended Data Fig. 11).

Myeloid lineage cells

further sub-clustered to classical monocytes (*FCN1*, *S100A4*, *S100A6*), dendritic cells, macrophage, mast cells (*GATA2*, *CPA3*, *HPGDS*) and megakaryocytes (*GP9*, *LCN2*). Among dendritic cells (DCs) we observed cDC1 (*CLEC9A*) and cDC2 (*CLEC10A*), lymphoid DCs (*LAMP3*) and plasmacytoid DCs (pDCs; *CLEC4C*, *JCHAIN*). Among macrophage populations, we observe a subset of classical macrophages (*CD163*, *C1QB*, *C1QC*), LYVE1⁺ macrophages (*RNASE1*, *SPP1*) that have been previously observed in around heart vessels⁶⁸ and lung⁶⁹ and inflammatory macrophages (*MMP9*);¹⁰ we also observe a fetal-specific population of mono-neutrophil progenitors (*MPO*, *AZU1*, *ELANE*) previously described in human fetal liver³⁰ and CLC mast cells that could represent immature fetal states.

Cell-type scoring

For MHCII scoring of B cells we use the following genes: *SECTM1*, *CD320*, *CD3EAP* (also known as *POLR1G*) *CD177*, *CD74*, *CIITA*, *RELB*, *TAP2*, *HLA-DRA*, *HLA-DRB5*, *HLA-DRBI*, *HLA-DQAI*, *HLA-DQBI*, *HLA-DQBI-ASI*, *HLA-DQA2*, *HLA-DQB2*, *HLA-DOB*, *HLA-DMB*, *HLA-DMA*, *HLA-DOA*, *HLA-DPA1*, *HLA-DPB1*. Glial or neuronal cell signature score was calculated using the curated gene sets from ref. ⁷⁰ (glia: *ERBB3*, *PLP1*, *COL18A1*, *SOX10*, *GAS7*, *FABP7*, *NID1*, *QKI*, *SPARC*, *MEST*, *WWTR1*, *GPM6B*, *RASA3*, *FLRT1*, *ITPR1PL1*, *ITGA4*, *POSTN*, *PDPN*, *NRCAM*, *TSPAN18*, *RGCC*, *LAMA4*, *PTPRZ1*, *HMGAA2*, *TGFB2*, *ITGA6*, *SOX5*, *MTAP*, *HEYL*, *GPRI7*, *TTYH1*; neuronal: *ELAVL3*, *ELAVL4*, *TUBB2B*, *PHOX2B*, *RET*, *CHRNA3*). NF- κ B signalling pathway score was calculated using genes from <http://www.gsea-msigdb.org/gsea/msigdb/genesets.jsp> (*NFKB2*, *BIRC3*, *TNFAIP2*, *TNIP1*, *NOTCH2*, *TMEM173* (also known as *STING1*) *TIFA*, *PRDX4*, *CAMK4*, *BCL3*, *CHUK*, *IKBKB*, *IKBKE*, *NFKB1*, *NFKB2*, *NFKBIA*, *NFKBIB*, *NFKBIE*, *REL*, *RELA*, *RELB*). The scoring was done using `sc.tl.score_genes()` function with default parameters to calculate the average expression of selected genes substrated with the average expression of reference genes.

Intestinal organoid analysis

Single-cell count matrices from three organoid growth conditions were combined together using Pandas (v.1.1.2) and NumPy (v.0.25.2) packages. Cells with fewer than 8,000 genes and with less than 20% mitochondrial reads were included in the analysis. Genes with expression in fewer than 3 cells were also excluded. For *PLCG2* expression comparison we use normalized (`sc.pp.normalize_per_cell`) and log-transformed (`sc.pp.log1p`) counts. The data were plotted using Seaborn package bar plot and swarmplot functions (v.0.11.0).

Pre-processing and analysis of Smart-seq2 sequencing data

Cells with more than 6,000 genes and greater than 25% mitochondrial reads were excluded, before regression of ‘`n_counts`’, ‘`percent_mito`’ and ‘`G2M_score`’. Cells positive for *PTPRC* expression ($\log_{10} \text{TPM} + 1 >= 0.2$) were taken forward for downstream analysis. T cell receptor sequences generated using the Smart-seq2 scRNA-seq protocol were reconstructed using the TraCeR software (<https://hub.docker.com/r/teichlab/tracer/>) as described previously⁷¹.

Differential cell-state abundance analysis for BEST4 cells

To identify region-specific subpopulations, we performed compositional analysis between BEST4 enterocytes from small and large intestine tissue, using a tool for differential abundance testing on k -nearest neighbour (KNN) graph neighbourhoods, implemented in the R package miloR (v.0.99.8) <https://github.com/MarioniLab/miloR>¹⁴.

In brief, we performed PCA dimensionality reduction and KNN graph embedding on the BEST4 enterocytes. We define a neighbourhood as the group of cells that are connected to a sampled cell by an edge in the KNN graph. Cells are sampled for neighbourhood construction using the algorithm proposed previously⁷². For each neighbourhood we then perform hypothesis testing between conditions to identify differentially abundant cell states whilst controlling the FDR across the graph neighbourhoods.

We test for differences in abundance between the cells from small and large intestine tissue in adult samples and fetal samples. To identify markers of small-intestine-specific and large-intestine-specific subpopulations, we performed differential gene expression (DGE) analysis between adult cells in neighbourhoods enriched for small intestine cells and in neighbourhoods enriched for large intestine cells (10% FDR for the differential abundance test). The DGE test was performed using a linear model implemented in the package limma⁷³ (v.3.46.0), using 10% FDR, and aggregating expression profiles by sample(implemented in the function findNhoodGroupMarkers of the miloR package, with option aggregateSamples = TRUE). Gene Ontology enrichment analysis was performed using the R package clusterProfiler (v.3.18.1).

RNA velocity and diffusion map pseudotime analyses

For neural cell trajectory analysis we use scVelo 0.21 package implementation in Scanpy 1.5.1⁷⁴. The data were sub-clustered on fetal neural cells and pre-processed using functions for detection of minimum number of counts, filtering and normalization using scv.pp.filter_and_normalize and followed by scv.pp.moments function. The gene-specific velocities were obtained using scv.tl.velocity(mode = 'stochastic') and scv.tl.velocity_graph() by fitting a ratio between unspliced and spliced mRNA abundances. The gene specific velocities were visualized using scv.pl.velocity_graph() or scv.pl.velocity_embedding_grid() functions. To visualize genes that change along the pseudotime we use sc.pl.paga_path() function with pseudotime set to monocle3 pseudotime. This function required calculation of PAGA parameters and dpt_pseudotime with functions as follows: sc.tl.paga(), sc.pl.paga(), sc.tl.draw_graph(init_pos = 'paga'), sc.tl.dpt()⁷⁵.

BCR analysis

Single-cell BCR analyses were performed as described previously⁷⁶. In brief, poor quality or incomplete V(D)J contig sequences were discarded and all IgH sequences for each donor were combined together. IgH sequences were annotated with IgBLAST⁷⁷ before isotype reassignment

using AssignGenes.py (pRESTO⁷⁸). Ambiguous V gene calls were corrected using TIgGER v.03.1⁷⁹ before identifying clonally related sequences with DefineClones.py (ChangeO v.0.4.5⁷⁹) using a threshold of 0.2 for nearest-neighbour distances. The germline IgH sequence for each clonal family was determined using CreateGermlines.py (ChangeO v.0.4.5) followed by using observedMutations (Shazam v.0.1.11⁷⁹) to calculate somatic hypermutation frequencies for individual sequences. Finally, for integration with the single-cell gene expression object, the number of high quality and annotated contigs per Ig chain (IgH, IgK, IgL) was determined for each cell barcode. If multiple unique sequences for a given chain were detected, that cell was annotated as ‘Multi’ and not considered in further analysis. BCR metadata was combined with the scRNA object for downstream analysis and comparison of different B cell populations.

Cell–cell communication analysis

To infer cell–cell communication and screen for ligands and receptors involved we applied the CellPhoneDB v.2.0 Python package^{80,81} on the normalized raw counts and fine cell-type annotations from the second trimester intestinal samples (12–17 PCW). We use default parameters and set subsetting to 5,000 cells. To identify the most relevant interactions, we subset specific interactions on the basis of the ligand/receptor expression in more than 10% of cells within a cluster and where the \log_2 mean expression of the pair is greater than 0. The selected interactions were plotted as expression of both ligand and receptor in relevant cell types.

Gene expression linked to enteric nervous system disease

HSCR-related genes were curated from The Human Phenotype Ontology website (<https://hpo.jax.org/app/>, Aganglionic megacolon HP:0002251) and ref. ²⁵. We selected genes with expression greater than or equal to 0.1 in neural lineage single cells and calculated mean expression per cluster and organ. Expression was visualized using seaborn.clustermap() function (v.0.11.0).

Cell-type composition analysis using metadata

The number of cells for each sample ($n = 159$ samples in total with complete metadata) and coarse-grain cell type (9 different cell types in total) combination was modelled with a generalized linear mixed model with a Poisson outcome. The five clinical factors (age group, donor, biopsy, disease and gender) and the three technical factors (fraction, enzyme and 10x kit) were fitted as random effects to overcome the collinearity among the factors. The effect of each clinical or technical factor on cell-type composition was estimated by the interaction term with the cell type. The ‘glmer’ function in the lme4 package implemented on R was used to fit the model. The standard error of the standard deviation parameter for each factor was estimated using the numDeriv package. The effect size of each level of a clinical or technical factor was obtained by the posterior mean of the corresponding random effect coefficient and the local true sign rate (LTSR) was calculated from the posterior distribution. See Supplementary Note Section 1 for more details.

Cell-type enrichment analysis for IBD-GWAS genes

Inflammatory bowel disease genome-wide association study (IBD GWAS) summary statistics of Crohn’s disease and ulcerative colitis were obtained from the International Inflammatory Bowel Disease Genetics Consortium (IIBDGC) (<https://www.ibdgenetics.org/>). The GWAS enrichment analysis of 103 annotated gut cell types for Crohn’s disease and ulcerative colitis was performed using a fGWAS approach^{82,83}, often used for fine-mapping and enrichment analysis of various functional annotations for molecular quantitative trait and GWAS loci. The association statistics (log odds ratios and standard errors) were converted into the approximate Bayes factors using the Wakefield approach⁸⁴. A *cis*-regulatory region of 1 Mb centred at the transcription start site (TSS) was defined for each gene (Ensembl GRCh37 Release 101). The Bayes factors of variants existing in each *cis* region were weighted and averaged by the prior probability (an exponential function of TSS proximity) estimated from the distance distribution of regulatory interactions⁸⁵. The likelihood of an fGWAS model was given by the averaged Bayes factors across all genome-wide genes multiplied by the feature-level prior probability obtained from a linear combination of cell-type-specific expression and the averaged expression across all cell types as a baseline expression. The enrichment of each cell type was estimated as

the maximum likelihood estimator of the effect size for the cell-type-specific expression. The code of the hierarchical model (<https://github.com/natsuhiko/PHM>) was utilized for the enrichment analysis. The detailed model derivation is demonstrated in Supplementary Note section 2.

Visium spatial transcriptomics sample preparation

10x Genomics Visium protocol was applied on optimal cutting temperature medium (OCT)-embedded fresh frozen samples. All tissues were sectioned using the Leica CX3050S cryostat and were cut at 10 µm. The samples were selected on the basis of morphology, orientation (based on H&E) and RNA integrity number that was obtained using Agilent2100 Bioanalyzer. Tissue optimization was performed to obtain permeabilization time for fetal tissue (12 min) and after optimization the Visium spatial gene expression protocol from 10X Genomics was performed using Library Preparation slide and following the manufacturer's protocol. After transcript capture, Visium Library Preparation Protocol from 10x Genomics was performed. All images for this process were scanned at 40× on Hamamatsu NanoZoomer S60. Eight cDNA libraries were diluted and pooled to a final concentration of 2.25 nM (200 µl volume) and sequenced on 2× SP flow cells of Illumina NovaSeq 6000.

10x Genomics Visium data processing

10x Genomics Visium spatial sequencing samples were aligned to the human transcriptome GRCh38-3.0.0 reference (consistently with single-cell RNA-seq samples) using 10x Genomics SpaceRanger v.1.2.1 and exonic reads were used to produce mRNA count matrices for each sample. 10x Genomics SpaceRanger was also used to align paired histology images with mRNA capture spot positions in the Visium slide. The paired image was used to determine the average number of nuclei per Visium location in the tissue and used as a hyperparameter in the spatial mapping of cell types.

Spatial mapping of cell types with cell2location

To spatially map developing gut cell types *in situ*, 10x Genomics Visium mRNA count matrices were integrated with scRNA-seq data using the cell2location method as described in detail previously³⁴. In brief, the cell2location model estimates the abundance of each cell population in each location by decomposing mRNA counts in 10x Genomics Visium data using the transcriptional signatures of reference cell types. Reference signatures of 65 cell populations (neuronal and mesenchymal subtypes were grouped together where relevant to simplify interpretation of spatial mapping) from the 12–17 PCW small intestine samples were estimated using a negative binomial regression model provided in the cell2location package. We provide spatial cell abundance maps of all 65 cell subsets on GitHub (https://github.com/vitkl/fetal_gut_mapping/) and the distribution of all 65 cell subsets across tissue zones in Extended Data Fig. 9a–c.

Untransformed and unnormalized mRNA counts were used as input to both the regression model for estimating signatures (filtered to 13,904 genes and 124,049 cells) and the cell2location model for estimating spatial abundance of cell populations (filtered to 13,904 genes shared with scRNA-seq, 4,645 locations, 3 experiments analysed jointly).

Cell2location was used with the following settings (all other settings set to default values): training iterations: 40,000; cells per location \(\hat{N}=12\), estimated on the basis of comparison with histology image paired with 10x Genomics Visium; cell types per location \(\hat{A}=8\), assuming that most cells in a given location are of a different type; co-located cell type groups per location \(\hat{Y}=4\).

To identify tissue zones and groups of cell types that belong to them (Extended Data Fig. 15c, dot plot), conventional non-negative matrix factorization (NMF) was applied to cell abundance estimated by cell2location. The NMF model was trained for a range of factors and tissue zones $R = \{8, \dots, 35\}$ and the decomposition into 17 factors was selected as a balance between segmenting relevant tissue zones (lymphoid structures, blood vessel types) and over-separating known zones into several distinct factors. NMF weight for each factor and cell type is shown in Extended Data Fig. 15c.

Cryosectioning, single-molecule fluorescence *in situ* hybridization and confocal imaging

Fetal gut tissue was embedded in OCT and frozen on an isopentane-dry ice slurry at -60°C , and then cryosectioned onto SuperFrost Plus slides at a thickness of 10 μm . Before staining, tissue sections were post-fixed in 4% paraformaldehyde in PBS for 15 min at 4°C , then dehydrated through a series of 50%, 70%, 100% and 100% ethanol, for 5 min each. Staining with the RNAscope Multiplex Fluorescent Reagent Kit v2 Assay (Advanced Cell Diagnostics, Bio-Techne) was automated using a Leica BOND RX, according to the manufacturers' instructions. After manual pre-treatment, automated processing included epitope retrieval by protease digestion with Protease IV for 30 min prior to RNAscope probe hybridization and channel development with Opal 520, Opal 570, and Opal 650 dyes (Akoya Biosciences). Stained sections were imaged with a Perkin Elmer Opera Phenix High-Content Screening System, in confocal mode with 1 μm z-step size, using a 20 \times water-immersion objective (NA 0.16, 0.299 μm per pixel). Channels: DAPI (excitation 375 nm, emission 435–480 nm), Opal 520 (ex. 488 nm, em. 500–550 nm), Opal 570 (ex. 561 nm, em. 570–630 nm), Opal 650 (ex. 640 nm, em. 650–760 nm). The fourth channel was developed using TSA-biotin (TSA Plus Biotin Kit, Perkin Elmer) and streptavidin-conjugated Atto 425 (Sigma-Aldrich).

Flow cytometry validation of Fcgr on mice tuft cells

C57BL/6 mice received either normal drinking water or 2% (w/v) 36,000–50,000 MW dextran sodium sulfate (DSS) (MP Biomedicals) to induce colitis. For DSS treatment, mice received DSS water for 5 days followed by 14 days of normal drinking water, and then a final 5 days of 2% (w/v) DSS prior to being culled.

The small intestines of mice were flushed of faecal content with ice-cold PBS, opened longitudinally, cut into 0.5-cm pieces, and washed by vortexing three times with PBS with 10 mM HEPES. Tissue was then incubated with an epithelial stripping solution (RPMI-1640 with 2% (v/v) FCS, 10 mM HEPES, 1 mM DTT and 5 mM EDTA) at 37°C for two intervals of 20 min to remove epithelial cells. The epithelial fraction was

subsequently incubated at 37 °C for 10 min with dispase (0.3 U ml⁻¹, Sigma-Aldrich) and passed through a 100-µm filter to obtain a single-cell suspension. Cells were blocked for 20 min at 4 °C with 0.5% (v/v) heat-inactivated mouse serum followed by extracellular staining in PBS at 4 °C for 45 min with the following antibodies; EpCAM-FITC (1:400, G8.8, Invitrogen), CD45-Bv650 (1:200, 30-F11, BioLegend), CD11b-Bv421 (1:300, M1/70, BD Biosciences), Siglec-F-APC (1:200, 1RNM44N, Invitrogen), FcγRI-PE (1:200, X54-5/7.1, BioLegend), FcγRIIB-PE (1:200, AT130-2, Invitrogen), FcγRII/RIII-PE-Cy7 (1:200, 2.4G2, BD Biosciences), FcγRIV-PE (1:200, 9E9, BioLegend) and Rat IgG2b, κ isotype-PE-Cy7 (1:200, LOU/C, BD Biosciences). Cells were then stained with LIVE/DEAD Fixable Aqua Dead Cell Stain Kit (Thermo Fisher Scientific) for 20 min at room temperature, fixed with 2% PFA, and analysed on a CytoFLEX LX (Beckman Coulter) flow cytometer.

Reporting summary

Further information on research design is available in the [Nature Research Reporting Summary](#) linked to this paper.

Data availability

The expression data for fetal and adult regions is available on an interactive website: <https://www.gutcellatlas.org/>. Raw sequencing data are available at ArrayExpress (<https://www.ebi.ac.uk/arrayexpress>) with accession numbers E-MTAB-9543, E-MTAB-9536, E-MTAB-9532, E-MTAB-9533 and E-MTAB-10386. Previously published first trimester and paediatric data are available at ArrayExpress (E-MTAB-8901)¹. For the purpose of Open Access, the authors have applied a CC BY public copyright licence to any Author Accepted Manuscript version arising from this submission. [Source data](#) are provided with this paper.

Code availability

Processed single-cell RNA sequencing objects are available for online visualization and download at <https://www.gutcellatlas.org/>. The code

generated during this study is available at Github:
<https://github.com/Teichlab/SpaceTimeGut>,
https://github.com/vitkl/fetal_gut_mapping/
<https://github.com/natsuhiko/PHM>.

References

1. 1.
Elmentait, R. et al. Single-cell sequencing of developing human gut reveals transcriptional links to childhood Crohn's disease. *Dev. Cell* **55**, 771–783.e5 (2020).
2. 2.
Holloway, E. M. et al. Mapping development of the human intestinal niche at single-cell resolution. *Cell Stem Cell* **28**, 568–580.e4 (2021).
3. 3.
Fawkner-Corbett, D. et al. Spatiotemporal analysis of human intestinal development at single-cell resolution. *Cell* **184**, 810–826.e23 (2021).
4. 4.
James, K. R. et al. Distinct microbial and immune niches of the human colon. *Nat. Immunol.* **21**, 343–353 (2020).
5. 5.
Kinchen, J. et al. Structural remodeling of the human colonic mesenchyme in inflammatory bowel disease. *Cell* **175**, 372–386.e17 (2018).
6. 6.
Smillie, C. S. et al. Intra- and inter-cellular rewiring of the human colon during ulcerative colitis. *Cell* **178**, 714–730.e22 (2019).

7. 7.

Boland, B. S. et al. Heterogeneity and clonal relationships of adaptive immune cells in ulcerative colitis revealed by single-cell analyses. *Sci. Immunol.* **5**, eabb4432 (2020).

8. 8.

Corridoni, D. et al. Single-cell atlas of colonic CD8⁺ T cells in ulcerative colitis. *Nat. Med.* **26**, 1–11 (2020).

9. 9.

Huang, B. et al. Mucosal profiling of pediatric-onset colitis and ibd reveals common pathogenics and therapeutic pathways. *Cell* **179**, 1160–1176.e24 (2019).

10. 10.

Martin, J. C. et al. Single-cell analysis of Crohn's disease lesions identifies a pathogenic cellular module associated with resistance to anti-TNF therapy. *Cell* **178**, 1493–1508.e20 (2019).

11. 11.

Haniffa, M. et al. (2021) A roadmap for the Human Developmental Cell Atlas. *Nature*, <https://doi.org/10.1038/s41586-021-03620-1> (2021).

12. 12.

Ito, G. et al. Lineage-specific expression of bestrophin-2 and bestrophin-4 in human intestinal epithelial cells. *PLoS ONE* **8**, e79693 (2013).

13. 13.

Parikh, K. et al. Colonic epithelial cell diversity in health and inflammatory bowel disease. *Nature* **567**, 49–55 (2019).

14. 14.

Dann, E., Henderson, N. C., Teichmann, S. A., Morgan, M. D. & Marioni, J. C. Milo: differential abundance testing on single-cell data using k-NN graphs. Preprint at <https://doi.org/10.1101/2020.11.23.393769> (2020).

15. 15.

Lamers, M. M. et al. SARS-CoV-2 productively infects human gut enterocytes. *Science* **369**, 50–54 (2020).

16. 16.

Beumer, J. et al. High-resolution mRNA and secretome atlas of human enteroendocrine cells. *Cell* **181**, 1291–1306.e19 (2020).

17. 17.

Levine, A. S., Winsky-Sommerer, R., Huitron-Resendiz, S., Grace, M. K. & de Lecea, L. Injection of neuropeptide W into paraventricular nucleus of hypothalamus increases food intake. *Am. J. Physiol. Regul. Integr. Comp. Physiol.* **288**, R1727–R1732 (2005).

18. 18.

Roberts, G. P. et al. Comparison of human and murine enteroendocrine cells by transcriptomic and peptidomic profiling. *Diabetes* **68**, 1062–1072 (2019).

19. 19.

Gehart, H. et al. Identification of enteroendocrine regulators by real-time single-cell differentiation mapping. *Cell* **176**, 1158–1173.e16 (2019).

20. 20.

Beumer, J., Gehart, H. & Clevers, H. Enteroendocrine dynamics – new tools reveal hormonal plasticity in the gut. *Endocr. Rev.* **41**, 695–706 (2020).

21. 21.

Moreno-Fierros, L., Verdín-Terán, S. L. & García-Hernández, A. L. Intraperitoneal immunization with Cry1Ac protoxin from *Bacillus thuringiensis* provokes upregulation of Fc-gamma-II/and Fc-gamma-III receptors associated with IgG in the intestinal epithelium of mice. *Scand. J. Immunol.* **82**, 35–47 (2015).

22. 22.

Morarach, K. et al. Diversification of molecularly defined myenteric neuron classes revealed by single-cell RNA sequencing. *Nat. Neurosci.* **24**, 34–46 (2021).

23. 23.

May-Zhang, A. A. et al. Combinatorial transcriptional profiling of mouse and human enteric neurons identifies shared and disparate subtypes in situ. *Gastroenterology* **160**, 755–770.e26 (2021).

24. 24.

Memic, F. et al. Transcription and signaling regulators in developing neuronal subtypes of mouse and human enteric nervous system. *Gastroenterology* **154**, 624–636 (2018).

25. 25.

Tang, C. S.-M. et al. Identification of genes associated with Hirschsprung disease, based on whole-genome sequence analysis, and potential effects on enteric nervous system development. *Gastroenterology* **155**, 1908–1922.e5 (2018).

26. 26.

Zhang, Z. et al. Sporadic Hirschsprung disease: mutational spectrum and novel candidate genes revealed by next-generation sequencing. *Sci. Rep.* **7**, 14796 (2017).

27. 27.

Bondurand, N. & Southard-Smith, E. M. Mouse models of Hirschsprung disease and other developmental disorders of the enteric nervous system: old and new players. *Dev. Biol.* **417**, 139–157 (2016).

28. 28.

Hoorweg, K. & Cupedo, T. Development of human lymph nodes and Peyer's patches. *Semin. Immunol.* **20**, 164–170 (2008).

29. 29.

Krishnamurty, A. T. & Turley, S. J. Lymph node stromal cells: cartographers of the immune system. *Nat. Immunol.* **21**, 369–380 (2020).

30. 30.

Popescu, D.-M. et al. Decoding human fetal liver haematopoiesis. *Nature* **574**, 365–371 (2019).

31. 31.

Takeda, A. et al. Single-cell survey of human lymphatics unveils marked endothelial cell heterogeneity and mechanisms of homing for neutrophils. *Immunity* **51**, 561–572.e5 (2019).

32. 32.

Rodda, L. B. et al. Single-cell RNA sequencing of lymph node stromal cells reveals niche-associated heterogeneity. *Immunity* **48**, 1014–1028.e6 (2018).

33. 33.

Koning, J. J. et al. Nestin-expressing precursors give rise to both endothelial as well as nonendothelial lymph node stromal cells. *J. Immunol.* **197**, 2686–2694 (2016).

34. 34.

Kleshchevnikov, V. et al. Comprehensive mapping of tissue cell architecture via integrated single cell and spatial transcriptomics. Preprint at <https://doi.org/10.1101/2020.11.15.378125> (2020).

35. 35.

Sura, R., Colombel, J.-F. & Van Kruiningen, H. J. Lymphatics, tertiary lymphoid organs and the granulomas of Crohn's disease: an immunohistochemical study. *Aliment. Pharmacol. Ther.* **33**, 930–939 (2011).

36. 36.

de Lange, K. M. et al. Genome-wide association study implicates immune activation of multiple integrin genes in inflammatory bowel disease. *Nat. Genet.* **49**, 256–261 (2017).

37. 37.

Uhlig, H. H. Monogenic diseases associated with intestinal inflammation: implications for the understanding of inflammatory bowel disease. *Gut* **62**, 1795–1805 (2013).

38. 38.

Martín-Nalda, A. et al. Severe autoinflammatory manifestations and antibody deficiency due to novel hypermorphic *PLCG2* mutations. *J. Clin. Immunol.* **40**, 987–1000 (2020).

39. 39.

Haley, P. J. The lymphoid system: a review of species differences. *J. Toxicol. Pathol.* **30**, 111–123 (2017).

40. 40.

Li, N. et al. Memory CD4⁺ T cells are generated in the human fetal intestine. *Nat. Immunol.* **20**, 301–312 (2019).

41. 41.

Schreurs, R. R. C. E. et al. Human fetal TNF- α -cytokine-producing CD4⁺ effector memory T cells promote intestinal development and mediate inflammation early in life. *Immunity* **50**, 462–476.e8 (2019).

42. 42.

Cupedo, T. et al. Human fetal lymphoid tissue-inducer cells are interleukin 17-producing precursors to RORC⁺CD127⁺ natural killer-like cells. *Nat. Immunol.* **10**, 66–74 (2009).

43. 43.

Shikhagaie, M. M. et al. Neuropilin-1 is expressed on lymphoid tissue residing LTi-like group 3 innate lymphoid cells and associated with ectopic lymphoid aggregates. *Cell Rep.* **18**, 1761–1773 (2017).

44. 44.

Bannard, O. et al. Germinal center centroblasts transition to a centrocyte phenotype according to a timed program and depend on the dark zone for effective selection. *Immunity* **39**, 1182 (2013).

45. 45.

Rodda, L. B., Bannard, O., Ludewig, B., Nagasawa, T. & Cyster, J. G. Phenotypic and morphological properties of germinal center dark zone *Cxcl12*-expressing reticular cells. *J. Immunol.* **195**, 4781–4791 (2015).

46. 46.

Mesin, L., Ersching, J. & Victora, G. D. Germinal center B cell dynamics. *Immunity* **45**, 471–482 (2016).

47. 47.

Chang, J. E., Buechler, M. B., Gressier, E., Turley, S. J. & Carroll, M. C. Mechanosensing by Peyer's patch stroma regulates lymphocyte migration and mucosal antibody responses. *Nat. Immunol.* **20**, 1506–1516 (2019).

48. 48.

Uhlen M. et al. Tissue-based map of the human proteome. *Science* **347**, 1260419 (2015).

49. 49.

Kraiczy, J. et al. DNA methylation defines regional identity of human intestinal epithelial organoids and undergoes dynamic changes during development. *Gut* **68**, 49–61 (2019).

50. 50.

Young, M. D. & Behjati, S. SoupX removes ambient RNA contamination from droplet-based single-cell RNA sequencing data. *Gigascience* **9**, giaa151 (2020).

51. 51.

Tirosh, I. et al. Dissecting the multicellular ecosystem of metastatic melanoma by single-cell RNA-seq. *Science* **352**, 189–196 (2016).

52. 52.

Hung, Y.-H. et al. Chromatin regulatory dynamics of early human small intestinal development using a directed differentiation model. *Nucleic Acids Res.* **49**, 726–744 (2021).

53. 53.

Zaret, K. S. & Grompe, M. Generation and regeneration of cells of the liver and pancreas. *Science* **322**, 1490–1494 (2008).

54. 54.

Ayyaz, A. et al. Single-cell transcriptomes of the regenerating intestine reveal a revival stem cell. *Nature* **569**, 121–125 (2019).

55. 55.

Drokhlyansky, E. et al. The human and mouse enteric nervous system at single-cell resolution. *Cell* **182**, 1606–1622.e23 (2020).

56. 56.

Galitzky, J. & Bouloumié, A. Human visceral-fat-specific glucocorticoid tuning of adipogenesis. *Cell Metab.* **18**, 3–5 (2013).

57. 57.

Ambele, M. A., Dessels, C., Durandt, C. & Pepper, M. S. Genome-wide analysis of gene expression during adipogenesis in human adipose-derived stromal cells reveals novel patterns of gene expression during adipocyte differentiation. *Stem Cell Res.* **16**, 725–734 (2016).

58. 58.

Kumar, A. et al. Specification and diversification of pericytes and smooth muscle cells from mesenchymoangioblasts. *Cell Rep.* **19**, 1902–1916 (2017).

59. 59.

Lee, M. Y. et al. Transcriptome of interstitial cells of Cajal reveals unique and selective gene signatures. *PLoS ONE* **12**, e0176031 (2017).

60. 60.

Eom, J. et al. Distinctive subpopulations of stromal cells are present in human lymph nodes infiltrated with melanoma. *Cancer Immunol. Res.* **8**, 990–1003 (2020).

61. 61.

Kanamori-Katayama, M. et al. LRRN4 and UPK3B are markers of primary mesothelial cells. *PLoS ONE* **6**, e25391 (2011).

62. 62.

Ehrhardt, G. R. A. et al. Expression of the immunoregulatory molecule FcRH4 defines a distinctive tissue-based population of memory B cells. *J. Exp. Med.* **202**, 783–791 (2005).

63. 63.

Papadopoulou, M. et al. TCR sequencing reveals the distinct development of fetal and adult human V γ 9V δ 2 T cells. *J. Immunol.* **203**, 1468–1479 (2019).

64. 64.

Mazzurana, L. et al. Tissue-specific transcriptional imprinting and heterogeneity in human innate lymphoid cells revealed by full-length single-cell RNA-sequencing. *Cell Res.* **31**, 554–568 (2021).

65. 65.

Lim, A. I. et al. Systemic human ILC precursors provide a substrate for tissue ILC differentiation. *Cell* **168**, 1086–1100.e10 (2017).

66. 66.

Patino, G. A. et al. Voltage-gated Na⁺ channel β 1B: a secreted cell adhesion molecule involved in human epilepsy. *J. Neurosci.* **31**, 14577–14591 (2011).

67. 67.

Zeng, B. et al. ILC3 function as a double-edged sword in inflammatory bowel diseases. *Cell Death Dis.* **10**, 315 (2019).

68. 68.

Lim, H. Y. et al. Hyaluronan receptor LYVE-1-expressing macrophages maintain arterial tone through hyaluronan-mediated regulation of smooth muscle cell collagen. *Immunity* **49**, 1191 (2018).

69. 69.

Chakarov, S. et al. Two distinct interstitial macrophage populations coexist across tissues in specific subtissular niches. *Science* **363**, eaau0964 (2019).

70. 70.

Lasrado, R. et al. Lineage-dependent spatial and functional organization of the mammalian enteric nervous system. *Science* **356**, 722–726 (2017).

71. 71.

Stubbington, M. J. T. et al. T cell fate and clonality inference from single-cell transcriptomes. *Nat. Methods* **13**, 329–332 (2016).

72. 72.

Gut, G., Tadmor, M. D., Pe'er, D., Pelkmans, L. & Liberali, P. Trajectories of cell-cycle progression from fixed cell populations. *Nat. Methods* **12**, 951–954 (2015).

73. 73.

Ritchie, M. E. et al. limma powers differential expression analyses for RNA-sequencing and microarray studies. *Nucleic Acids Res.* **43**, e47 (2015).

74. 74.

Bergen, V., Lange, M., Peidli, S., Wolf, F. A. & Theis, F. J. Generalizing RNA velocity to transient cell states through dynamical

modeling. *Nat. Biotechnol.* **38**, 1408–1414 (2020).

75. 75.

Wolf, F. A. et al. PAGA: graph abstraction reconciles clustering with trajectory inference through a topology preserving map of single cells. *Genome Biol.* **20**, 59 (2019).

76. 76.

King, H. W. et al. Single-cell analysis of human B cell maturation predicts how antibody class switching shapes selection dynamics. *Sci. Immunol.* **6**, eabe6291 (2021).

77. 77.

Ye, J., Ma, N., Madden, T. L. & Ostell, J. M. IgBLAST: an immunoglobulin variable domain sequence analysis tool. *Nucleic Acids Res.* **41**, W34–W40 (2013).

78. 78.

Heiden, J. A. V. et al. pRESTO: a toolkit for processing high-throughput sequencing raw reads of lymphocyte receptor repertoires. *Bioinformatics* **30**, 1930–1932 (2014).

79. 79.

Gupta, N. T. et al. Change-O: a toolkit for analyzing large-scale B cell immunoglobulin repertoire sequencing data. *Bioinformatics* **31**, 3356–3358 (2015).

80. 80.

Efremova, M., Vento-Tormo, M., Teichmann, S. A. & Vento-Tormo, R. CellPhoneDB: inferring cell-cell communication from combined expression of multi-subunit ligand–receptor complexes. *Nat. Protocols* **15**, 1484–1506 (2020).

81. 81.

Vento-Tormo, R. et al. Single-cell reconstruction of the early maternal–fetal interface in humans. *Nature* **563**, 347–353 (2018).

82. 82.

Veyrieras, J.-B. et al. High-resolution mapping of expression-QTLs yields insight into human gene regulation. *PLoS Genet.* **4**, e1000214 (2008).

83. 83.

Pickrell, J. K. Joint analysis of functional genomic data and genome-wide association studies of 18 human traits. *Am. J. Hum. Genet.* **94**, 559–573 (2014).

84. 84.

Wakefield, J. A Bayesian measure of the probability of false discovery in genetic epidemiology studies. *Am. J. Hum. Genet.* **81**, 208–227 (2007).

85. 85.

Kumasaka, N., Knights, A. J. & Gaffney, D. J. High-resolution genetic mapping of putative causal interactions between regions of open chromatin. *Nat. Genet.* **51**, 128–137 (2019).

Acknowledgements

We acknowledge support from the Wellcome Sanger Cytometry Core Facility, Cellular Genetics Informatics team, Cellular Generation and Phenotyping (CGaP) and Core DNA Pipelines. This work was financially supported by the Wellcome Trust (WT206194, S.A.T.; 203151/Z/16/Z, R. A. Barker.); the European Research Council (646794, ThDefine, S.A.T.); an MRC New Investigator Research Grant (MR/T001917/1, M.Z.); and a project grant from the Great Ormond Street Hospital Children’s Charity,

Sparks (V4519, M.Z.). The human embryonic and fetal material was provided by the Joint MRC/Wellcome (MR/R006237/1) Human Developmental Biology Resource (<https://www.hdbr.org/>). K.R.J. holds a Non-Stipendiary Junior Research Fellowship from Christ's College, University of Cambridge. M.R.C. is supported by a Medical Research Council Human Cell Atlas Research Grant (MR/S035842/1) and a Wellcome Trust Investigator Award (220268/Z/20/Z). H.W.K. is funded by a Sir Henry Wellcome Fellowship (213555/Z/18/Z). A.F. is funded by a Wellcome PhD Studentship (102163/B/13/Z). K.T.M. is funded by an award from the Chan Zuckerberg Initiative. H.H.U. is supported by the Oxford Biomedical Research Centre (BRC) and the The Leona M. and Harry B. Helmsley Charitable Trust. We thank A. Chakravarti and S. Chatterjee for their contribution to the analysis of the enteric nervous system. We also thank R. Lindeboom and C. Talavera-Lopez for support with epithelium and Visium analysis, respectively; C. Tudor, T. Li and O. Tarkowska for image processing and infrastructure support; A. Wilbrey-Clark and T. Porter for support with Visium library preparation; A. Ross and J. Park for access to and handling of fetal tissue; A. Hunter for assistance in protocol development; D. Fitzpatrick for discussion on developmental intestinal disorders; and J. Eliasova for the graphical images. We thank the tissue donors and their families, and the Cambridge Biorepository for Translational Medicine and Human Developmental Biology Resource, for access to human tissue. This publication is part of the Human Cell Atlas: <https://www.humancellatlas.org/publications>.

Author information

Author notes

1. Kylie R. James

Present address: Garvan Institute of Medical Research, The Kinghorn Cancer Centre, Darlinghurst, New South Wales, Australia

Affiliations

1. Wellcome Sanger Institute, Wellcome Genome Campus, Hinxton, UK

Rasa Elmentaite, Natsuhiko Kumasaka, Kenny Roberts, Emma Dann, Vitalii Kleshchevnikov, Monika Dabrowska, Sophie Pritchard, Liam Bolt, Sara F. Vieira, Lira Mamanova, Ni Huang, Steven Leonard, Thomas R. W. Oliver, Lia S. Campos, Cecilia Domínguez Conde, Krzysztof Polanski, Stijn van Dongen, Minal Patel, John C. Marioni, Omer Ali Bayraktar, Kerstin B. Meyer, Menna R. Clatworthy, Muzlifah Haniffa, Kylie R. James & Sarah A. Teichmann

2. Molecular Immunity Unit, Department of Medicine, University of Cambridge, MRC Laboratory of Molecular Biology, Cambridge, UK

Aaron Fleming & Menna R. Clatworthy

3. Centre for Immunobiology, Blizard Institute, Queen Mary University of London, London, UK

Hamish W. King

4. Department of Paediatrics, University of Cambridge, Cambridge, UK

Francesca Perrone, Komal Nayak & Matthias Zilbauer

5. Biosciences Institute, Faculty of Medical Sciences, Newcastle University, Newcastle upon Tyne, UK

Issac Goh Kai’En, Steven N. Lisgo, Emily Stephenson, Justin Engelbert, Rachel A. Botting & Muzlifah Haniffa

6. Structural and Molecular Biology, Division of Biosciences, University College London, London, UK

Matilda Katan

7. Department of Histopathology, Cambridge University Hospitals NHS Foundation Trust, Cambridge, UK

Thomas R. W. Oliver & C. Elizabeth Hook

8. European Molecular Biology Laboratory, European Bioinformatics Institute, Wellcome Genome Campus, Cambridge, UK

Michael D. Morgan & John C. Marioni

9. Cancer Research UK Cambridge Institute, University of Cambridge, Cambridge, UK

Michael D. Morgan & John C. Marioni

10. John van Geest Centre for Brain Repair, Department of Clinical Neurosciences and Wellcome-MRC Cambridge Stem Cell Institute, University of Cambridge, Cambridge, UK

Xiaoling He & Roger A. Barker

11. Translational Gastroenterology Unit, John Radcliffe Hospital, University of Oxford, Oxford, UK

Holm H. Uhlig

12. Department of Paediatrics, University of Oxford, Oxford, UK

Holm H. Uhlig

13. NIHR Oxford Biomedical Research Centre, Oxford, UK

Holm H. Uhlig

14. Department of Surgery, University of Cambridge and NIHR Cambridge Biomedical Research Centre, Cambridge, UK

Krishnaa T. Mahbubani & Kourosh Saeb-Parsy

15. Department of Paediatric Gastroenterology, Hepatology and Nutrition, Cambridge University Hospitals Trust, Cambridge, UK

Matthias Zilbauer

16. Wellcome-MRC Cambridge Stem Cell Institute, Anne McLaren
Laboratory, University of Cambridge, Cambridge, UK

Matthias Zilbauer

17. Department of Dermatology and NIHR Newcastle Biomedical Research Centre, Newcastle Hospitals NHS Foundation Trust, Newcastle upon Tyne, UK

Muzlifah Haniffa

18. Theory of Condensed Matter Group, Cavendish
Laboratory/Department of Physics, University of Cambridge,
Cambridge, UK

Sarah A. Teichmann

Contributions

S.A.T., K.R.J. and M.H. initiated, designed and supervised the project; K.T.M. and K.S.-P. carried out adult tissue collection; K.R.J., R.E., M.D., S.P., L.B., S.F.V. and M.P. performed adult tissue processing and scRNA-seq experiments; R. A. Barker and X.H. supported collection of fetal tissue samples; S.N.L., R. A. Botting., I.G.K. 'E., J.E. and C.D.C. supported fetal tissue processing and scRNA-seq experiments; F.P. and K.N. conducted organoid experiments; L.M., L.B. and E.S. performed library preparation; A.F. performed flow cytometry validation in mice and data interpretation; T.R.W.O., C.E.H. and L.S.C. provided pathology support; K.R., S.P. and O.A.B. performed tissue sectioning, staining and imaging; K.R.J. and R.E. analysed single-cell data and generated figures; S.L., N.K., K.P., S.V.D. and N.H. provided analysis support; V.K. analysed 10x Genomics Visium data; H.W.K. performed BCR analysis and contributed to data visualization; E.D. performed differential abundance analysis; J.C.M., M.D.M., M.K., K.B.M., M.Z., H.U. and M.R.C. contributed to interpretation of the results; and K.R.J., R.E. and S.A.T. wrote the manuscript. All authors contributed to the discussion and interpretation of results, as well as editing of the manuscript.

Corresponding authors

Correspondence to [Kylie R. James](#) or [Sarah A. Teichmann](#).

Ethics declarations

Competing interests

In the past three years, S.A.T. has consulted for or been a member of scientific advisory boards at Roche, Qiagen, Genentech, Biogen, GlaxoSmithKline and ForeSite Labs. The remaining authors declare no competing interests.

Additional information

Peer review information *Nature* thanks Judy Cho, Gerard Eberl, Dominic Grun and Ulrika Marklund for their contribution to the peer review of this work. Peer reviewer reports are available.

Publisher's note Springer Nature remains neutral with regard to jurisdictional claims in published maps and institutional affiliations.

Extended data figures and tables

Extended Data Fig. 1 Data quality control.

a, Schematic showing tissue processing strategy for second trimester fetal, paediatric and adult scRNA-seq samples. After enzymatic dissociation, either total fraction was loaded onto a 10x Genomics Chromium chip or CD45⁺⁻ cell fractions were separated using magnetic cell sorting (MACS) and both fractions were loaded on the 10x Genomics Chromium chip separately. Lymph nodes were processed without enrichment. Second trimester fetal and adult cell samples were processed using 5' v2 10x Genomics Chromium kits (Methods). **b**, Pre-processing and quality control of single-cell RNA-seq data generated in this study and described previously¹. In short, four datasets—namely first trimester fetal, second trimester fetal, paediatric healthy and Crohn's disease, and adult—were pre-processed separately (including quality control, soupX analysis and scrublet

doublet removal). Firstly, dimension reduction, clustering and annotation by cell lineage was performed on each dataset separately. Each cell lineage was sub-clustered and a fine-grained cell type and cell state annotation was performed based on marker gene expression. The four datasets were then merged together and each lineage was sub-clustered to unify cell type labels where appropriate. UMAP visualizations show the combined dataset coloured by sample age, enrichment fraction and donor name. **c**, UMAP visualization of cellular landscape of the human intestinal tract coloured by cellular lineage. **d**, Forest plot showing the relative importance (explained standard deviation) of each technical/biological factor on the cell type proportion. The 95% confidence intervals were computed from $n = 1,431$ data points (9 cell types \times 159 samples). See Method section for more details. **e**, Dot plot in which the fold change represents the enrichment (or depletion, low fold change in blue) of cells compared with baseline. The LTSR value represents statistical significance of the fold change estimate ranging from 0 to 1, where 1 represents a confident estimate. See Method section for more details. **f**, Bar plots with relative proportion of cell lineages in each 10x Genomics Chromium run grouped by anatomical region within the scRNA-seq dataset as in Fig. [1b](#).

[Source data](#)

[Extended Data Fig. 2 Cell types defined in the study.](#)

a, Dot plot for expression of marker genes of cell types and states in each cell lineage in the scRNA-seq dataset. Relates to Supplementary Tables [3](#), [4](#).

[Extended Data Fig. 3 Region variability in BEST4 enterocytes.](#)

a, Expression of CSTE (antibody: CAB032687, $n = 3$ biologically independent samples for each region) in gut histological sections from proteinatlas.org. Scale bar = 50 μm . **b**, UMAP visualization of BEST4 enterocytes in scRNA-seq dataset coloured by key marker *BEST4/OTOP2* expression and region group (fetal and paediatric/adult). **c**, Volcano plot for differential abundance (DA) between cells from the small intestine and large intestine as in **b**. Each point represents a neighbourhood of BEST4

enterocytes (FDR: False Discovery Rate, logFC: log-Fold Change) for adult (red) and fetal samples (blue). The dotted line indicates the significance threshold of 10% FDR. **d**, Heat map showing the average neighbourhood expression of genes differentially expressed between DA neighbourhoods in adult BEST4 enterocytes (1,502 genes) as in **c**. Expression values for each gene are scaled between 0 and 1. Neighbourhoods are ranked by log-fold change in abundance between conditions. Positive log-fold change is small intestine neighbourhoods and negative is large intestine neighbourhoods. **e**, Expression of CFTR (antibody: CAB001951/HPA021939, $n = 3$ biologically independent samples for each region) in small intestinal (top) and colonic (bottom) histological sections from Human Protein Atlas (proteinatlas.org). Scale bar = 50 μm . **f**, Immunohistochemistry staining of BEST4 (HPA058564) and CFTR (HPA021939) in small intestinal sections as in **e**. Black arrows point to cells with goblet cell morphology and red arrows point to cells expressing either BEST4 or CFTR. Scale bar = 20 μm .

[Source data](#)

Extended Data Fig. 4 Function of BEST4 epithelial cells.

a, b, Gene ontology terms from genes upregulated in BEST4 enterocytes from adult small (**a**) versus large (**b**) intestines as determined from Milo analysis¹³.

[Source data](#)

Extended Data Fig. 5 BEST2⁺ goblet cells.

a, UMAP visualization of expression of *MUC2* (indicating goblet cells) and *BEST2* in paediatric/adult epithelial cells from scRNA-seq dataset. **b**, Bar plot of the number of goblet cells captured across paediatric/adult intestinal tissues. **c**, Dot plot of gene expression correlating with *BEST2* expression across epithelial cell types from scRNA-seq dataset calculated using Jaccard Similarity measure.

[Source data](#)

Extended Data Fig. 6 Epithelial cell types throughout intestinal life.

a, UMAP of fetal (top) and pooled paediatric and adult (bottom) epithelial cells as in Fig. [2a, b](#) coloured by gut region. **b**, Relative proportions of cell subtypes within total epithelial lineage as in Fig. [2a, b](#) separated by donor age (row). Unit of age is years unless specified as weeks. **c**, Dot plot of *TMPRSS2* and *ACE2* expression by epithelial cells of the paediatric (left) and adult (right) intestine. **d, e**, UMAP of enteroendocrine cells (subsetted from Fig. [2a, b](#)) coloured by **d**, (top) developmental age of donor and (bottom) normalised expression of key genes of NPW+ enterochromaffin cells and **e**, overlaid with calculated RNA velocity (arrows) and pseudotime (colour). **f**, Immunohistochemical staining of KLK12 (antibody: CAB025473, $n = 3$), AFP (antibody; HPA010607, $n = 4$), CES1 (antibody; HPA012023, $n = 10$), SLC18A1 (antibody; HPA063797, $n = 12$), GCH1 (antibody; HPA028612, $n = 8$), NPW (antibody; HPA064874, $n = 8$) in intestinal sections from Human Protein Atlas (proteinatlas.org). Red arrows highlight positive staining and n represents biological replicates across intestinal regions. **g**, Heat map of top differentially expressed genes in tuft cells across epithelial cell types in scRNA-seq dataset. The legend indicates whether the gene has a known association with tuft cells (purple) or are novel (orange). **h**, Immunohistochemical staining of HPGDS (antibody: HPA024035, $n = 8$), PSTPIP2 (antibody: HPA040944, $n = 8$), BMX (antibody: CAB032495, $n = 7$), MYO1B (antibody: HPA060144, $n = 6$), FYB1 (antibody: CAB025336, $n = 7$), SH2D7 (antibody: HPA076728, $n = 7$), PLCG2 (antibody: HPA020099, $n = 8$) protein expression in small intestine from Human Protein Atlas (proteinatlas.org). n represents biological replicates across intestinal regions. **i**, Dot plot showing expression of ITAM- and ITIM-linked receptors and receptor tyrosine kinases across tuft cells and pooled absorptive (TA and enterocytes) and secretory (Paneth, goblet and EECs) epithelial cells. **j**, Representative flow cytometry plots of Fc γ RII/III staining on EpCAM $^+$ SiglecF $^-$ (non-tuft epithelial cells) and EpCAM $^+$ SiglecF $^+$ (tuft cells) cells and isotype staining of EpCAM $^+$ SiglecF $^+$ cells. Numbers show the percentage of cells within the gate out of the total population.

[Source data](#)

Extended Data Fig. 7 Tuft cells and PLCG2 activation.

a, Heat map of expression of FCGR2A and downstream signalling molecules for epithelial cells with B and myeloid cell types included for reference. **b**, Representative brightfield images of paediatric intestinal organoid line (derived from healthy donors) in culture medium (undifferentiated) or differentiation medium (differentiated). Scale bar = 400 μ m. **c**, Bar plot of relative expression of *LGR5* and *MUC2* (left) ($n = 3$ from one patient) and other key mRNA (right) by intestinal organoids as in **b** ($n = 6$ from two patients). Mean with standard error of the mean (s.e.m.) is shown in bar plots, and statistics are calculated by multiple *t*-test analysis: * $P < 0.05$ and ** $P < 0.005$. **d**, Representative bright-field images of paediatric intestinal organoid line (derived from healthy donors) without (NT) or with stimulation with inflammatory recombinant human proteins IFN γ or TNF. **e**, Heat map of normalised gene expression in scRNA-seq data of organoids from Crohn's disease ($n = 1$) and control ($n = 3$) paediatric biopsies stimulated with inflammatory cytokines as in **d**. **f**, Per cent expression of indicated Fc γ receptors by SiglecF $^+$ EpCAM $^+$ small intestinal tuft cells in wild type ($n = 5$) and DSS-treated ($n = 3$) mice from a single experiment determined by flow cytometry. Mean with standard deviation is shown and statistics are calculated by multiple *t*-test analysis ** $P < 0.01$; NS = not significant.

Source data

Extended Data Fig. 8 Cell types in the developing enteric nervous system.

a, Multiplex smFISH images of *SOX10*, *ERBB3*, *MPZ*, *PLP1* expressing ENCCs in the human small and large intestine at 6.5 PCW (Scale bar panels: main = 100 μ m, zoom = 20 μ m, $n = 6$). n here and below are biological replicates across regions. **b**, UMAP visualization of neural lineage cells in 6–11 and 12–17 PCW timepoints coloured by glial or neuronal score (left), cell cycle phase (middle) or pseudotime (right). Arrows show differentiation trajectory inferred from scVelo arrows as in Fig. 3a, b. **c**, Bar plot with relative abundance of cell types among ENCC-lineage populations as described in (Figure 3a, b) across intestinal regions

and developmental timepoints. **d**, Heat map showing percentage of neural cells (6–17 PCW) described in this study (columns) matching with cells described in ref. ³ (rows). **e**, Multiplex smFISH imaging of *SCGN/BNC2*-expressing enteric neurons (left, scale bar = 50 μm) and *BMP8B*-expressing Glia 2 subtype (right, scale bar panels main = 100 μm, zoom = 50 μm) in the adult sample (55–60 years, terminal ileum, n=1) and **f**, Multiplex smFISH of *DHH*-expressing Glia 1 cells (n=2, left, scale bar panels main = 100 μm, zoom = 10 μm) and *BMP8B*-expressing Glia 2 subtype (n=2, right, scale bar panels main = 100 μm, zoom = 50 μm) in the fetal myenteric plexus from 15 PCW small intestines. The boxed area is shown at higher magnification below, and n represents biological replicates across regions. **g**, HOX gene expression across neural subsets in 6–11 PCW samples. In the red box are Glia 1 (*DHH*) cells from all regions. Genes highlighted in red are colon-specific. **h**, Dot plot of key HSCR-associated ligand-receptor genes across the entire fetal scRNA-seq dataset. FPIL, fetal proximal ileum; FMIL, fetal middle ileum; FTIL, fetal terminal ileum; FLI, fetal large intestine.

[Source data](#)

[Extended Data Fig. 9 Annotation of developing enteric neural cells.](#)

a, b, UMAP visualization of neural subsets combined from 6–17 PCW coloured by cell type annotation (**a**) or developmental stage (**b**). **c**, Bar plot showing regional distribution of neural subsets at 6–17 PCW. **d**, Dot plots with expression of key genes used to define enteric neuron subsets found at 6–11 PCW (above) and 12–17 PCW (middle) and glial cells across 6–17 PCW.

[Source data](#)

[Extended Data Fig. 10 Identification of LTi-cell-like subset.](#)

a, Photo images of human intestinal gut and developing lymph nodes (arrows) at 8–17 PCW. Scale bar = 1 cm. **b**, Heat map of relative expression of key LTi defining and marker genes expressed by LTi-like cell types, NK

cells and adult ILC3 as in Fig. 4a. Genes in red are highlighted in the schematic in Fig. 4b. c, Bar plot with productive TCR $\alpha\beta$ chain in fetal T and innate lymphoid cell types as determined by V(D)J sequencing paired with scRNA-seq data. d, Dot plot of scaled expression of selected differentially expressed genes in fetal immune subsets from scRNA-seq dataset. e, Dot plot of expression of selected LTi-like genes in fetal liver ILCPs compared to LTi-like subsets in the gut. f, Bar graph showing the relative proportion of cell types among total T and innate lymphocyte population across developmental and adult gut regions and ages. FPIL, fetal proximal ileum; FMIL, fetal middle ileum; FTIL, fetal terminal ileum; FLI, fetal large intestine; FMLN, fetal mesenteric lymph node; DUO, duodenum; JEJ, jejunum; ILE, ileum; APD, appendix; CAE, caecum; ACL, ascending colon; TCL, transverse colon; DCL, descending colon; SCL, sigmoid colon; REC, rectum; MLN, mesenteric lymph node. g, Representative multiplex smFISH staining of fetal ileum tissue at 15 PCW showing three LTi-like subsets: NCR 2^+ ILC3, IL17A-expressing NCR $-$ ILC3 and SCNI B-expressing ILCP cells (Scale bar panels: main = 20 μ m, zoom = 5 μ m, n = 2, biological replicates across regions). h, UMAP visualization of fetal T and innate lymphoid cells (subsetted from Fig. 4a) coloured by cell type and overlaid with RNA velocity arrows. Inset panel shows ILCP and LTi-like NCR $+$ ILC3 cells.

Source data

Extended Data Fig. 11 LTi-like cells in plate based single-cell sequencing data of sorted cells from the human fetal intestine.

a, UMAP visualization and feature plots of full-length Smart-seq2 data of flow cytometry-sorted CD45 $+$ cells from second-trimester fetal tissue coloured by intestinal region or Leiden clustering. b, Dot plot of key marker gene expression in T and innate lymphoid cell subsets captured in Smart-seq2 experiment as in a. c, Bar plot of productive TCR $\alpha\beta$ and TCR $\gamma\delta$ chain in fetal T and innate lymphoid cell types as in a.

Source data

Extended Data Fig. 12 Endothelial populations in the intestinal tract.

a, UMAP visualization of endothelial cell populations in fetal, paediatric and adult scRNA-seq data coloured by cell-cycle score (left) or annotation (right). Dashed line outlines lymphatic endothelial cell (LEC) subsets. **b**, Relative proportions of subtypes within total endothelial lineage separated by intestinal region (above) and intestinal region (below). Unit of age is years unless specified as weeks. Region names are: FPIL, fetal proximal ileum; FMIL, fetal middle ileum; FTIL, fetal terminal ileum; FLI, fetal large intestine; FMLN, fetal mesenteric lymph node; DUO, duodenum; JEJ, jejunum; ILE, ileum; APD, appendix; CAE, caecum; ACL, ascending colon; TCL, transverse colon; DCL, descending colon; SCL, sigmoid colon; REC, rectum; MLN, mesenteric lymph node. **c**, Heat map with top differentially expressed genes in the LEC subsets. **d**, Violin plot of NF- κ B signalling activation score across endothelial subpopulations. **e**, Dot plot with scaled expression of selected genes involved in lymphoid tissue organization and immune cell recruitment amongst lymphatic endothelial cell subsets and mLTo cells. **f**, H&E staining of cross-section of fetal colon (15 PCW). Magnified panels show developing vessels (Scale bar panels: main = 200 μ m, zoom = 20 μ m, n = 9). **g**, Representative multiplex smFISH of *PROX1* lymphatic vessels, *CXCR5* ILC3 subsets and *CXCL13*-expressing mLTo cells in the human fetal intestine at 15 PCW (scale bar = 100 μ m, n = 1). For **f**, **g**, n represents biological replicates across regions.

[Source data](#)

Extended Data Fig. 13 Stromal in the intestinal tract.

a, Heat map of top differentially expressed genes between follicular dendritic cells (FDCs) and T reticular cells (TRCs) and related stromal subsets. Each row is a cell. Arrows highlight key genes discussed in the text. **b**, Bar graph showing the relative proportion of cell types among the total stromal lineage across fetal and adult gut regions (top) and developmental ages (bottom). Unit of age is years unless specified as weeks. Region names are: FPIL, fetal proximal ileum; FMIL, fetal middle ileum; FTIL, fetal terminal ileum; FLI, fetal large intestine; FMLN, fetal

mesenteric lymph node; DUO, duodenum; JEJ, jejunum; ILE, ileum; APD, appendix; CAE, caecum; ACL, ascending colon; TCL, transverse colon; DCL, descending colon; SCL, sigmoid colon; REC, rectum; MLN, mesenteric lymph node. **c**, Dot plot comparing key defining genes expressed across populations in **a** and fetal mesenchymal lymphoid tissue organiser (mLTo) cells. **d**, Bar plot showing number of mLTo in scRNA-seq dataset and coloured by gut region. **e**, UMAP visualization of stromal cells as in Fig. 4d showing co-expression of *CXCL13*, *CCL19*, and *CCL21*. **f**, Heat map of top differentially expressed genes of mLTo cells between different intestinal regions. Each row is a cell. **g**, Heat map of mean expression of ligand-receptor pairs in mLTo, LTi-like and LEC subset from scRNA-seq dataset as identified using CellphoneDB. **h**, Heat maps showing mean expression of curated immune recruitment signal genes by selected fetal stromal, epithelial and endothelial cell types (top) and their receptor expression in the immune cell types of the fetal gut and mLNs. Red arrows in **f** and **h** link cognate ligand receptor pairs.

Source data

Extended Data Fig. 14 Intestinal B cells and BCR analysis.

a, UMAP visualizations of scRNA-seq of subsetted B lineage cells from fetal samples. CLP, common lymphoid progenitor. **b**, Heat map with mean expression of differentially expressed gene in fetal B cell populations as in **a**. **c**, Violin plot of MHCII expression score of fetal B cell subsets as in **a**. **c–e**, UMAP visualization of fetal B lineage cells as in **a** coloured by (**d**) BCR isotype retrieved from 10x Genomics Chromium V(D)J sequencing and (**e**) 10x Genomics technology. **f**, UMAP visualizations of subsetted B lineage cells from paediatric and adult scRNA-seq samples. LZ, light zone; DZ, dark zone; GC, germinal centre. **g**, Relative proportions of subtypes within total B cell fractions in the gut (above) and lymph nodes (below) separated by donor age (row) as in **a** and **f**. Unit of age is years unless specified as weeks. **h**, Estimated clonal abundances per donor for members of expanded B lineage cell clones in fetal and adult scRNA-seq datasets. **i**, Quantification of somatic hypermutation frequencies of IgH sequences from B lineage cells in fetal and adult scRNA-seq datasets as in **h**. **j, k**, Quantification of somatic hypermutation frequencies of IgH sequences (**j**)

and estimated clonal abundances per donor for members of expanded B lineage cell clones (**k**) across fetal and adult gut regions. FPIL, fetal proximal ileum; FMIL, fetal middle ileum; FTIL, fetal terminal ileum; FLI, fetal large intestine; FMLN, fetal mesenteric lymph node; DUO, duodenum; JEJ, jejunum; ILE, ileum; APD, appendix; CAE, caecum; ACL, ascending colon; TCL, transverse colon; DCL, descending colon; SCL, sigmoid colon; REC, rectum; MLN, mesenteric lymph node. **I**, Binary count of co-occurrence of expanded B cell clones identified by single-cell V(D)J analysis shared across gut regions and donors.

Source data

Extended Data Fig. 15 Ectopic lymphoid tissue formation in paediatric Crohn's disease.

a, Expression of mLTo gene markers by spatial coordinates in 10x Genomics Visium data (left) and abundance of mLTo and ILC3 cells as estimated by cell2location³⁴ (right) across 17 PCW (top) and 13 PCW fetal ileum (bottom). White boxes highlight predicted developing SLO tissue zones. **b**, Spatial mapping of scRNA-seq data to 10x Genomics Visium data showing estimated abundance (colour intensity) of cell subsets (colour) in fetal terminal ileum from 17 PCW (top), ileum from 13 PCW (bottom). **c**, Abundances of cell types as identified using non-negative matrix factorization (NMF) in tissue zones from Visium data as in **b**. Dot plot shows NMF weights of cell types (columns) across NMF factors (rows), which correspond to tissue zones (normalized across factors per cell type by dividing by maximum values). **d**, Heat map showing mean probability of immune and stromal cell types matching between fetal and Crohn's disease scRNA-seq datasets. **e**, Heat map with expression of cytokines and chemokines in cells involved in tertiary lymphoid organ development of fetal (black) and functionally related cell types in paediatric Crohn's disease (red). **f**, Forest plot of top cell types across fetal, paediatric (healthy and IBD), and adult data enriched for expression of genes associated with either Crohn's disease or ulcerative colitis. All cell types in red have FDR < 10%. The number of cells for each sample ($n = 159$ samples in total with complete metadata) and coarse-grain cell type (9 different cell types in total) combination was modelled with a generalised linear mixed model

with a Poisson outcome. Error bars show standard error for each factor as estimated using the numDeriv package.

[Source data](#)

Supplementary information

[Supplementary Information](#)

This file contains Supplementary Notes 1–4 and Supplementary References

[Reporting Summary](#)

[Supplementary Table 1 Single-cell datasets on the intestinal tract](#)

Summary table of current human and mouse gut single-cell datasets.

[Supplementary Table 2 Sample metadata](#)

Description of gene expression and V(D)J run ids, patient information and cell type enrichment in 164 10x Genomics scRNAseq data and 3 10x Visium samples described in this study.

[Supplementary Table 3 Cell type number by donor name](#)

Number of cells per donor in the scRNA-seq data.

[Supplementary Table 4 Cell type number by fraction](#)

Number of cells per enrichment fraction in the scRNA-seq data.

[Supplementary Table 5 Cell type number by age](#)

Number of cells per donor age in the scRNA-seq data.

Supplementary Table 6 Cell type number by intestinal region

Number of cells per intestinal region in the scRNA-seq data.

Supplementary Table 7 Marker genes

Differentially expressed genes with selected up to top 50 marker genes for each cluster. Statistical test used was Wilcoxon rank-sum implemented in Scanpy v.1.4. *P* value correction was performed using the Benjamini–Hochberg method.

Supplementary Table 8 Metadata of proteincellatlas.org image replicates

Information on replicates related to protein cell atlas images. The patient id information for images used as replicates are listed below and are browsable at proteinatlas.org.

Peer Review File

Source data

Source Data Fig. 1

Source Data Fig. 2

Source Data Fig. 3

Source Data Fig. 4

Source Data Extended Data Fig. 1

Source Data Extended Data Fig. 3

Source Data Extended Data Fig. 4

[**Source Data Extended Data Fig. 5**](#)

[**Source Data Extended Data Fig. 6**](#)

[**Source Data Extended Data Fig. 7**](#)

[**Source Data Extended Data Fig. 8**](#)

[**Source Data Extended Data Fig. 9**](#)

[**Source Data Extended Data Fig. 10**](#)

[**Source Data Extended Data Fig. 11**](#)

[**Source Data Extended Data Fig. 12**](#)

[**Source Data Extended Data Fig. 13**](#)

[**Source Data Extended Data Fig. 14**](#)

[**Source Data Extended Data Fig. 15**](#)

Rights and permissions

Open Access This article is licensed under a Creative Commons Attribution 4.0 International License, which permits use, sharing, adaptation, distribution and reproduction in any medium or format, as long as you give appropriate credit to the original author(s) and the source, provide a link to the Creative Commons licence, and indicate if changes were made. The images or other third party material in this article are included in the article's Creative Commons licence, unless indicated otherwise in a credit line to the material. If material is not included in the article's Creative Commons licence and your intended use is not permitted by statutory regulation or exceeds the permitted use, you will need to obtain

permission directly from the copyright holder. To view a copy of this licence, visit <http://creativecommons.org/licenses/by/4.0/>.

Reprints and Permissions

About this article

Cite this article

Elmentaita, R., Kumasaka, N., Roberts, K. *et al.* Cells of the human intestinal tract mapped across space and time. *Nature* **597**, 250–255 (2021). <https://doi.org/10.1038/s41586-021-03852-1>

- Received: 24 November 2020
- Accepted: 26 July 2021
- Published: 08 September 2021
- Issue Date: 09 September 2021
- DOI: <https://doi.org/10.1038/s41586-021-03852-1>

Further reading

- [**A roadmap for the Human Developmental Cell Atlas**](#)
 - Muzlifah Haniffa
 - , Deanne Taylor
 - , Sten Linnarsson
 - , Bruce J. Aronow
 - , Gary D. Bader
 - , Roger A. Barker
 - , Pablo G. Camara
 - , J. Gray Camp
 - , Alain ChÃ©dotal
 - , Andrew Copp

- , Heather C. Etchevers
- , Paolo Giacobini
- , Berthold GÄ¶ttgens
- , Guoji Guo
- , Ania Hupalowska
- , Kylie R. James
- , Emily Kirby
- , Arnold Kriegstein
- , Joakim Lundeberg
- , John C. Marioni
- , Kerstin B. Meyer
- , Kathy K. Niakan
- , Mats Nilsson
- , Bayanne Olabi
- , Dana Peær
- , Aviv Regev
- , Jennifer Rood
- , Orit Rozenblatt-Rosen
- , Rahul Satija
- , Sarah A. Teichmann
- , Barbara Treutlein
- , Roser Vento-Tormo
- , Simone Webb
- , Pascal Barbry
- , Omer Bayraktar
- , Sam Behjati
- , Andreas Bosio
- , Bruno Canque
- , FrÃ©dÃ©ric Chalmel
- , Yorick Gitton
- , Deborah Henderson
- , Anne Jorgensen
- , Steven Lisgo
- , Jinyue Liu
- , Emma Lundberg
- , Jean-LÃ©on Maitre
- , SÃ©verine Mazaud-Guittot

- , Elizabeth Robertson
- , Antoine Rolland
- , Raphael Scharfmann
- , MichÃ©le Souyri
- , Erik SundstrÃ¶m
- , StÃ©phane Zaffran
- & Matthias Zilbauer

Nature (2021)

This article was downloaded by **calibre** from <https://www.nature.com/articles/s41586-021-03852-1>

| [Section menu](#) | [Main menu](#) |

- Article
- [Published: 11 August 2021](#)

Aged skeletal stem cells generate an inflammatory degenerative niche

- [Thomas H. Ambrosi](#) ORCID: [orcid.org/0000-0002-7149-041X^{1,2 na1}](https://orcid.org/0000-0002-7149-041X),
- [Owen Marecic](#) ORCID: [orcid.org/0000-0002-1540-7191^{1,2 na1}](https://orcid.org/0000-0002-1540-7191),
- [Adrian McArdle^{1,2 na1}](#),
- [Rahul Sinha¹](#),
- [Gunsagar S. Gulati](#) ORCID: [orcid.org/0000-0003-2798-6220¹](https://orcid.org/0000-0003-2798-6220),
- [Xinming Tong³](#),
- [Yuting Wang^{1,2}](#),
- [Holly M. Steininger^{1,2}](#),
- [Malachia Y. Hoover^{1,2}](#),
- [Lauren S. Koepke^{1,2}](#),
- [Matthew P. Murphy](#) ORCID: [orcid.org/0000-0003-0885-4089^{1,2}](https://orcid.org/0000-0003-0885-4089),
- [Jan Sokol^{1,2}](#),
- [Eun Young Seo^{1,2}](#),
- [Ruth Tevlin^{1,2}](#),
- [Michael Lopez^{1,2}](#),
- [Rachel E. Brewer^{1,2}](#),
- [Shamik Mascharak^{2,4}](#),
- [Laura Lu^{2,4}](#),
- [Oyinkansola Ajanaku^{2,4}](#),
- [Stephanie D. Conley¹](#),
- [Jun Seita^{1,5}](#),
- [Maurizio Morri⁶](#),
- [Norma F. Neff](#) ORCID: [orcid.org/0000-0001-7141-5420⁶](https://orcid.org/0000-0001-7141-5420),
- [Debashis Sahoo](#) ORCID: [orcid.org/0000-0003-2329-8228⁷](https://orcid.org/0000-0003-2329-8228),

- [Fan Yang³](#),
- [Irving L. Weissman^{1,8}](#),
- [Michael T. Longaker](#) ORCID: [orcid.org/0000-0003-1430-8914^{1,2,4}](https://orcid.org/0000-0003-1430-8914)
 &
- [Charles K. F. Chan](#) ORCID: [orcid.org/0000-0001-6570-7574^{1,2,4}](https://orcid.org/0000-0001-6570-7574)

[Nature](#) volume **597**, pages 256–262 (2021)

- 10k Accesses
- 1 Citations
- 71 Altmetric
- [Metrics details](#)

Subjects

- [Ageing](#)
- [Haematopoietic stem cells](#)
- [Mesenchymal stem cells](#)

Abstract

Loss of skeletal integrity during ageing and disease is associated with an imbalance in the opposing actions of osteoblasts and osteoclasts¹. Here we show that intrinsic ageing of skeletal stem cells (SSCs)² in mice alters signalling in the bone marrow niche and skews the differentiation of bone and blood lineages, leading to fragile bones that regenerate poorly. Functionally, aged SSCs have a decreased bone- and cartilage-forming potential but produce more stromal lineages that express high levels of pro-inflammatory and pro-resorptive cytokines. Single-cell RNA-sequencing studies link the functional loss to a diminished transcriptomic diversity of SSCs in aged mice, which thereby contributes to the transformation of the bone marrow niche. Exposure to a youthful circulation through heterochronic parabiosis or systemic reconstitution with young haematopoietic stem cells did not reverse the diminished osteochondrogenic

activity of aged SSCs, or improve bone mass or skeletal healing parameters in aged mice. Conversely, the aged SSC lineage promoted osteoclastic activity and myeloid skewing by haematopoietic stem and progenitor cells, suggesting that the ageing of SSCs is a driver of haematopoietic ageing. Deficient bone regeneration in aged mice could only be returned to youthful levels by applying a combinatorial treatment of BMP2 and a CSF1 antagonist locally to fractures, which reactivated aged SSCs and simultaneously ablated the inflammatory, pro-osteoclastic milieu. Our findings provide mechanistic insights into the complex, multifactorial mechanisms that underlie skeletal ageing and offer prospects for rejuvenating the aged skeletal system.

Access options

Subscribe to Journal

Get full journal access for 1 year

\$199.00

only \$3.90 per issue

[Subscribe](#)

All prices are NET prices.

VAT will be added later in the checkout.

Tax calculation will be finalised during checkout.

Rent or Buy article

Get time limited or full article access on ReadCube.

from \$8.99

[Rent or Buy](#)

All prices are NET prices.

Additional access options:

- [Log in](#)
- [Access through your institution](#)
- [Learn about institutional subscriptions](#)

Fig. 1: Age-related bone loss coincides with altered skeletal stem-cell function.

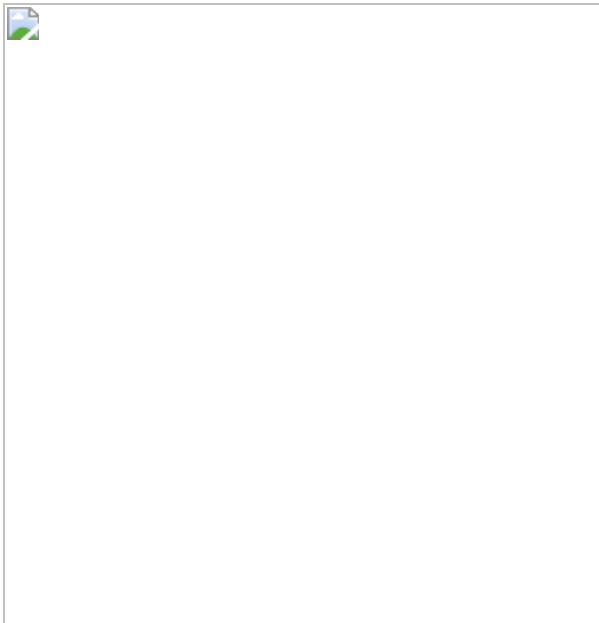


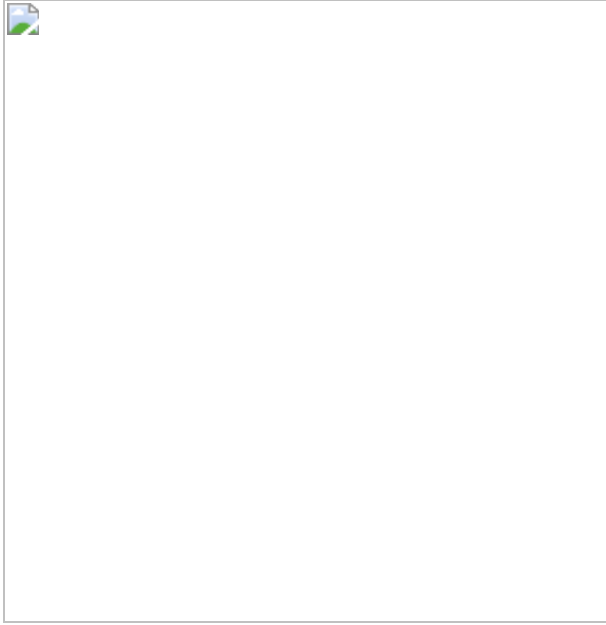
Fig. 2: The SSC lineage contributes to age-related skewing of the haematopoietic lineage.



Fig. 3: A pro-inflammatory aged skeletal lineage drives enhanced osteoclastic activity through CSF1.



Fig. 4: Combinatorial targeting of the aged skeletal niche restores youthful fracture regeneration.



Data availability

All sequencing data have been submitted to repositories and are available online. scRNA-seq data are available from the NCBI GEO under accession

numbers [GSE161946](#) and [GSE172149](#). Bulk RNA-sequencing data have been deposited under [GSE166441](#) and microarray data are publicly accessible as previously published under [GSE34723](#) as well as in the GEXC database under <https://gexc.riken.jp/models/2399> and <https://gexc.riken.jp/models/2400>. [Source data](#) are provided with this paper.

References

1. 1.
Boskey, A. L. & Coleman, R. Aging and bone. *J. Dent. Res.* **89**, 1333–1348 (2010).
2. 2.
Chan, C. K. F. et al. Identification and specification of the mouse skeletal stem cell. *Cell* **160**, 285–298 (2015).
3. 3.
Kenyon, C. J. The genetics of ageing. *Nature* **464**, 504–512 (2010).
4. 4.
Rossi, D. J., Jamieson, C. H. M. & Weissman, I. L. Stems cells and the pathways to aging and cancer. *Cell* **132**, 681–696 (2008).
5. 5.
Schmich, J. et al. Induction of reverse development in two marine hydrozoans. *Int. J. Dev. Biol.* **51**, 45–56 (2007).
6. 6.
Ermolaeva, M., Neri, F., Ori, A. & Rudolph, K. L. Cellular and epigenetic drivers of stem cell ageing. *Nat. Rev. Mol. Cell Biol.* **19**, 594–610 (2018).

7. 7.

de Haan, G. & Lazare, S. S. Aging of hematopoietic stem cells. *Blood* **131**, 479–487 (2018).

8. 8.

Pang, W. W. et al. Human bone marrow hematopoietic stem cells are increased in frequency and myeloid-biased with age. *Proc. Natl Acad. Sci. USA* **108**, 20012–20017 (2011).

9. 9.

Beerman, I. et al. Functionally distinct hematopoietic stem cells modulate hematopoietic lineage potential during aging by a mechanism of clonal expansion. *Proc. Natl Acad. Sci. USA* **107**, 5465–5470 (2010).

10. 10.

Ambrosi, T. H., Longaker, M. T. & Chan, C. K. F. A revised perspective of skeletal stem cell biology. *Front. Cell Dev. Biol.* **7**, 189 (2019).

11. 11.

Chan, C. K. F. et al. Identification of the human skeletal stem cell. *Cell* **175**, 43–56 (2018).

12. 12.

Halloran, B. P. et al. Changes in bone structure and mass with advancing age in the male C57BL/6J mouse. *J. Bone Miner. Res.* **17**, 1044–1050 (2002).

13. 13.

Ferguson, V. L., Ayers, R. A., Bateman, T. A. & Simske, S. J. Bone development and age-related bone loss in male C57BL/6J mice. *Bone*

33, 387–398 (2003).

14. 14.

Chan, C. K. F. et al. Clonal precursor of bone, cartilage, and hematopoietic niche stromal cells. *Proc. Natl Acad. Sci. USA* **110**, 12643–12648 (2013).

15. 15.

Marecic, O. et al. Identification and characterization of an injury-induced skeletal progenitor. *Proc. Natl Acad. Sci. USA* **112**, 9920–9925 (2015).

16. 16.

Ashapkin, V. V., Kutueva, L. I. & Vanyushin, B. F. in *Reviews on New Drug Targets in Age-Related Disorders* (ed. Guest, P. C.) 107–122 (Springer International Publishing, 2020).

17. 17.

Murphy, M. P. et al. Articular cartilage regeneration by activated skeletal stem cells. *Nat. Med.* **26**, 1583–1592 (2020).

18. 18.

Baht, G. S. et al. Exposure to a youthful circulation rejuvenates bone repair through modulation of β -catenin. *Nat. Commun.* **6**, 7131 (2015).

19. 19.

Pietras, E. M. Inflammation: a key regulator of hematopoietic stem cell fate in health and disease. *Blood* **130**, 1693–1698 (2017).

20. 20.

Wright, D. E., Wagers, A. J., Gulati, A. P., Johnson, F. L. & Weissman, I. L. Physiological migration of hematopoietic stem and progenitor

cells. *Science* **294**, 1933–1936 (2001).

21. 21.

Suda, T. et al. Modulation of osteoclast differentiation and function by the new members of the tumor necrosis factor receptor and ligand families. *Endocr. Rev.* **20**, 345–357 (1999).

22. 22.

Urist, M. R. Bone: formation by autoinduction. *Science* **150**, 893–899 (1965).

23. 23.

Mizuhashi, K. et al. Resting zone of the growth plate houses a unique class of skeletal stem cells. *Nature* **563**, 254–258 (2018).

24. 24.

Debnath, S. et al. Discovery of a periosteal stem cell mediating intramembranous bone formation. *Nature* **562**, 133–139 (2018).

25. 25.

Jaiswal, S. et al. Age-related clonal hematopoiesis associated with adverse outcomes. *N. Engl. J. Med.* **371**, 2488–2498 (2014).

26. 26.

Beerman, I. & Rossi, D. J. Epigenetic control of stem cell potential during homeostasis, aging, and disease. *Cell Stem Cell* **16**, 613–625 (2015).

27. 27.

Tevlin, R. et al. Pharmacological rescue of diabetic skeletal stem cell niches. *Sci. Transl. Med.* **9**, eaag2809 (2017).

28. 28.

Salazar, V. S. et al. Reactivation of a developmental *Bmp2* signaling center is required for therapeutic control of the murine periosteal niche. *eLife* **8**, e42386 (2019).

29. 29.

Ambrosi, T. H. et al. Adipocyte accumulation in the bone marrow during obesity and aging impairs stem cell-based hematopoietic and bone regeneration. *Cell Stem Cell* **20**, 771–784 (2017).

30. 30.

Shen, B. et al. A mechanosensitive peri-arteriolar niche for osteogenesis and lymphopoiesis. *Nature* **591**, 438–444 (2021).

31. 31.

Xie, M. et al. Schwann cell precursors contribute to skeletal formation during embryonic development in mice and zebrafish. *Proc. Natl Acad. Sci. USA* **116**, 15068–15073 (2019).

32. 32.

Schurman, C. A., Verbruggen, S. W. & Alliston, T. Disrupted osteocyte connectivity and pericellular fluid flow in bone with aging and defective TGF- β signaling. *Proc. Natl Acad. Sci. USA* **118**, e2023999118 (2021).

33. 33.

Sinha, P. et al. Loss of G_s α early in the osteoblast lineage favors adipogenic differentiation of mesenchymal progenitors and committed osteoblast precursors. *J. Bone Miner. Res.* **29**, 2414–2426 (2014).

34. 34.

Yamazaki, S. et al. Nonmyelinating Schwann cells maintain hematopoietic stem cell hibernation in the bone marrow niche. *Cell* **147**, 1146–1158 (2011).

35. 35.

Yue, R., Zhou, B. O., Shimada, I. S., Zhao, Z. & Morrison, S. J. Leptin receptor promotes adipogenesis and reduces osteogenesis by regulating mesenchymal stromal cells in adult bone marrow. *Cell Stem Cell* **18**, 782–796 (2016).

36. 36.

Worthley, D. L. et al. Gremlin 1 identifies a skeletal stem cell with bone, cartilage, and reticular stromal potential. *Cell* **160**, 269–284 (2015).

37. 37.

Newton, P. T. et al. A radical switch in clonality reveals a stem cell niche in the epiphyseal growth plate. *Nature* **567**, 234–238 (2019).

38. 38.

Bianco, P. & Robey, P. G. Skeletal stem cells. *Development* **142**, 1023–1027 (2015).

39. 39.

Gulati, G. S. et al. Isolation and functional assessment of mouse skeletal stem cell lineage. *Nat. Protocols* **13**, 1294–1309 (2018).

40. 40.

Chan, C. K. F. et al. Endochondral ossification is required for haematopoietic stem-cell niche formation. *Nature* **457**, 490–494 (2009).

41. 41.

Rossi, D. J. et al. Cell intrinsic alterations underlie hematopoietic stem cell aging. *Proc. Natl Acad. Sci. USA* **102**, 9194–9199 (2005).

42. 42.

Wilkinson, A. C., Ishida, R., Nakauchi, H. & Yamazaki, S. Long-term ex vivo expansion of mouse hematopoietic stem cells. *Nat. Protocols* **15**, 628–648 (2020).

43. 43.

Foster, D. S. et al. Elucidating the fundamental fibrotic processes driving abdominal adhesion formation. *Nat. Commun.* **11**, 4061 (2020).

44. 44.

Patro, R., Duggal, G., Love, M. I., Irizarry, R. A. & Kingsford, C. Salmon provides fast and bias-aware quantification of transcript expression. *Nat. Methods* **14**, 417–419 (2017).

45. 45.

Soneson, C., Love, M. I. & Robinson, M. D. Differential analyses for RNA-seq: transcript-level estimates improve gene-level inferences. *F1000Res.* **4**, 1521 (2015).

46. 46.

Jiang, H., Lei, R., Ding, S.-W. & Zhu, S. Skewer: a fast and accurate adapter trimmer for next-generation sequencing paired-end reads. *BMC Bioinformatics* **15**, 182 (2014).

47. 47.

Dobin, A. et al. STAR: ultrafast universal RNA-seq aligner. *Bioinformatics* **29**, 15–21 (2013).

48. 48.

Li, B. & Dewey, C. N. RSEM: accurate transcript quantification from RNA-seq data with or without a reference genome. *BMC Bioinformatics* **12**, 323 (2011).

49. 49.

Wolf, F. A., Angerer, P. & Theis, F. J. SCANPY: large-scale single-cell gene expression data analysis. *Genome Biol.* **19**, 15 (2018).

50. 50.

Nestorowa, S. et al. A single-cell resolution map of mouse hematopoietic stem and progenitor cell differentiation. *Blood* **128**, e20–e31 (2016).

51. 51.

Bergen, V. et al. Generalizing RNA velocity to transient cell states through dynamical modeling. *Nat. Biotechnol.* **38**, 1408–1414 (2020).

52. 52.

Gulati, G. S. et al. Single-cell transcriptional diversity is a hallmark of developmental potential. *Science* **367**, 405–411 (2020).

53. 53.

Chen, E. Y. et al. Enrichr: interactive and collaborative HTML5 gene list enrichment analysis tool. *BMC Bioinformatics* **14**, 128 (2013).

54. 54.

O’Flanagan, C. H. et al. Dissociation of solid tumor tissues with cold active protease for single-cell RNA-seq minimizes conserved collagenase-associated stress responses. *Genome Biol.* **20**, 210 (2019).

55. 55.

Denisenko, E. et al. Systematic assessment of tissue dissociation and storage biases in single-cell and single-nucleus RNA-seq workflows. *Genome Biol.* **21**, 130 (2020).

Acknowledgements

We thank A. McCarthy and C. Wang for mouse colony management; L. Quinn, V. Ford, C. McQuarrie, T. Naik and L. Jerabek for laboratory management; P. Lovelace, S. Weber and C. Carswell-Crumpton for FACS support; M. R. Eckart and the Stanford Gene Expression Facility (PAN Facility) as well as the Stanford Human Immune Monitoring Center (HIMC) for technical support, assistance and/or advice on this project; and L. Penland, B. Yu and M. Tan from the Chan Zuckerberg BioHub for support with scRNA-seq. This work was supported by NIH–NIA K99 R00 AG049958-01A1, the Heritage Medical Foundation, the American Federation for Aging Research (AFAR)–Arthritis National Research Foundation (ANRF) and an endowment from the DiGenova Family to C.K.F.C.; the German Research Foundation (DFG-Fellowship) 399915929 and NIH–NIA 1K99AG066963 to T.H.A.; NIH (R56 DE025597, R01 DE026730, R01 DE021683, R21 DE024230, R01 DE027323, U01 HL099776, U24 DE026914 and R21 DE019274), CIRMTR1-01249, the Oak Foundation, the Hagey Laboratory, the Pitch Johnson Fund and the Gunn/Olivier Research Fund to M.T.L.; NIDDK SHINE Award R01 DK115600 to I.L.W; and NIH UG3TR003355, UG3TR002968, R01AI155696, R01GM138385 and R00CA151673 and UCOP-RGPO (R01RG3780, R00RG2628 & R00RG2642) to D.S. Additional support came from NIH S10 RR02933801 to the Stanford University Stem Cell FACS core, and NIH S10 1S10OD02349701 to the Stanford University Clark Imaging Center (Principal Investigator: T. Doyle).

Author information

Author notes

1. These authors contributed equally: Thomas H. Ambrosi, Owen Marecic, Adrian McArdle

Affiliations

1. Institute for Stem Cell Biology and Regenerative Medicine, Stanford University School of Medicine, Stanford, CA, USA

Thomas H. Ambrosi, Owen Marecic, Adrian McArdle, Rahul Sinha, Gunsagar S. Gulati, Yuting Wang, Holly M. Steininger, Malachia Y. Hoover, Lauren S. Koepke, Matthew P. Murphy, Jan Sokol, Eun Young Seo, Ruth Tevlin, Michael Lopez, Rachel E. Brewer, Stephanie D. Conley, Jun Seita, Irving L. Weissman, Michael T. Longaker & Charles K. F. Chan

2. Department of Surgery, Stanford University School of Medicine, Stanford, CA, USA

Thomas H. Ambrosi, Owen Marecic, Adrian McArdle, Yuting Wang, Holly M. Steininger, Malachia Y. Hoover, Lauren S. Koepke, Matthew P. Murphy, Jan Sokol, Eun Young Seo, Ruth Tevlin, Michael Lopez, Rachel E. Brewer, Shamik Mascharak, Laura Lu, Oyinkansola Ajanaku, Michael T. Longaker & Charles K. F. Chan

3. Department of Bioengineering, Stanford University, Stanford, CA, USA

Xinming Tong & Fan Yang

4. Hagey Laboratory for Pediatric Regenerative Medicine, Stanford University School of Medicine, Stanford University, Stanford, CA, USA

Shamik Mascharak, Laura Lu, Oyinkansola Ajanaku, Michael T. Longaker & Charles K. F. Chan

5. Center for Integrative Medical Sciences and Advanced Data Science Project, RIKEN, Tokyo, Japan

Jun Seita

6. Chan Zuckerberg BioHub, San Francisco, CA, USA

Maurizio Morri & Norma F. Neff

7. Pediatrics, and Computer Science and Engineering, University of California San Diego, La Jolla, CA, USA

Debashis Sahoo

8. Ludwig Center for Cancer Stem Cell Biology and Medicine at Stanford University, Stanford, CA, USA

Irving L. Weissman

Contributions

T.H.A., O.M., A.M. and C.K.F.C. conceived the study, performed the majority of experiments, analysed the results and wrote the manuscript. R.S. helped to perform and analyse scRNA-seq experiments. G.S.G. conducted bulk RNA sequencing and S.M. analysed the data. X.T. and F.Y. provided hydrogels for factor delivery. Y.W., H.M.S., M.Y.H., L.S.K., M.P.M., E.S., R.T., M.L., S.D.C., R.E.B., L.L. and O.A. conducted cell culture, immunohistological, histological and bi-cortical fracture experiments. J. Seita, D.S. and J. Sokol analysed microarray and 10X scRNA-seq data. M.M. and N.F.N. provided expertise and resources for conducting scRNA-seq. I.L.W., M.T.L. and C.K.F.C. supervised the project.

Corresponding authors

Correspondence to [Michael T. Longaker](#) or [Charles K. F. Chan](#).

Ethics declarations

Competing interests

The authors declare no competing interests.

Additional information

Peer review information *Nature* thanks the anonymous reviewer(s) for their contribution to the peer review of this work. Peer reviewer reports are available.

Publisher's note Springer Nature remains neutral with regard to jurisdictional claims in published maps and institutional affiliations.

Extended data figures and tables

[Extended Data Fig. 1 Ageing alters bone physiology and fracture healing in mice.](#)

a, Representative haematoxylin and eosin (H&E) staining of proximal femurs from 2-month-old, 12-month-old and 24-month-old mice (representative of sections from three independent mice per age group). **b**, Three-dimensional μ CT reconstruction of femoral bone mass in 2-month-old, 12-month-old and 24-month-old mice. **c**, Quantification of bone parameters by μ CT measurements in the three age groups ($n = 3$ per age group). **d**, Bone formation rate (BFR) assessment by calcein labelling in 2-month-old and 24-month-old mice ($n = 3$ per age group). MS, mineralizing surface; BS, bone surface; MAR: mineral apposition rate. **e**, Radiograph, μ CT, and Movat's pentachrome staining images of fracture calluses at day 10 and day 21 after injury. **f**, Callus index measurements at day 10 and day 21 after fracture in femurs from 2-month-old, 12-month-old and 24-month-old mice (day 10 12-mo, $n = 5$; all other groups, $n = 3$). **g**, Mechanical strength test of fracture calluses at day 21 after fracture (2-mo, $n = 10$; 24-mo, $n = 8$). Box-and-whisker plots with centre line as median, box extending from 25th to 75th percentile and minimum to maximum values for whiskers. **h**, μ CT images of fracture calluses from 2-month-old, 12-month-old and 24-month-old mouse femurs at day 10 and day 21 after injury. **i**, Quantification of fracture callus parameters by μ CT measurements in the three age groups ($n = 3–6$). All scatter plot data are mean + s.e.m. One-sided Student's *t*-test for comparison of ageing groups to the 2-month-old group, adjusted for non-normality (Mann–Whitney test) or unequal

variances (Welch's test) where appropriate. For exact *P* values, see Source Data. Scale bars, 150 µm

[Source data](#).

Extended Data Fig. 2 Phenotypic SSCs are present in aged mice.

a, The mouse skeletal stem-cell lineage. A self-renewing SSC gives rise to a BCSP cell which is the precursor for committed cartilage, bone and stromal lineages. **b**, Schematic of experimental strategy to analyse intrinsic characteristics of highly purified SSC lineage cells from 2-month-old or 24-month-old mice. **c**, FACS gating strategy for the isolation of mouse SSC lineage cells. Representative FACS profiles for 2-month-old and 24-month-old mice are shown during the uninjured state and the day-10 fracture state. **d**, CD200 expression of SSC gated cells in 2-month-old (blue) and 24-month-old (red) mice. Isotype controls performed on SSCs from 2-month-old or 24-month-old mice are shown for gating of the CD200-positive fraction. **e**, Schematic representation of the experimental set-up investigating clonal activity in fractures of 2-month-old or 24-month-old Actin-Cre^{ERT} Rainbow mice (dpi, days post-injury). **f**, Flow cytometric quantification of BCSPs per uninjured femur (2-mo, *n* = 15; 24-mo, *n* = 7). **g**, Prevalence of BCSPs at different days after fracture injury in 2-month-old and 24-month-old mice (2-mo, *n* = 5-11; 24-mo, *n* = 3). **h**, Flow cytometric analysis of CD49f⁺ phenotypic SSCs and BCSPs under uninjured (uninj.) and fractured (fx; day 10) conditions in 2-month-old and 24-month-old mice (*n* = 4 per state, age and population). **i**, Proliferative activity within SSCs and BCSPs at day 10 after fracture as measured by EdU incorporation (2-mo, *n* = 7; 24-mo, *n* = 6). **j**, Assessment of apoptotic activity within SSCs and BCSPs at day 10 after fracture as measured by Annexin V staining (2-mo, *n* = 4; 24-mo, *n* = 3). **k**, Flow cytometric quantification of THY1+ and 6C3+ downstream cell population frequency in 2-month-old and 24-month-old mice in response to fracture at day 10 after injury (*n* = 4 per age). **l**, Flow cytometric analysis of the lineage output of BCSPs freshly isolated from 2-month-old and 24-month-old mice and cultured for six days (*n* = 3 per age). Comparison of 2-month-old and 24-month-old age groups by two-sided Student's *t*-test adjusted for non-

normality (Mann–Whitney test) or unequal variances (Welch’s test) where appropriate. Data are mean + s.e.m. For exact *P* values, see Source Data

[Source data](#).

Extended Data Fig. 3 SSCs and BCSPs show reduced functionality in vitro and in vivo.

a, Fibroblast colony forming unit (CFU-F) ability of 2-month-old and 24-month-old SSC-derived cell populations of long bones (2-mo, $n = 5\text{--}6$; 24-mo, $n = 9\text{--}10$). Two-way ANOVA with Bonferroni’s post-hoc test. **b**, SSC- and BCSP-derived colony size of cells derived from uninjured and day-10-fractured bones ($n = 7\text{--}120$). Statistical testing between age groups by unpaired Student’s *t*-test or Mann–Whitney test for non-normality. **c**, Representative images of colonies stained by Crystal Violet (representative of CFU-F from three independent experiments). **d**, In vitro osteogenic capacity of SSCs and BCSPs from 2-month-old and 24-month-old mice as determined by Alizarin Red S staining. Representative staining (left) and quantification of osteogenesis (right) ($n = 3$ per age). **e**, In vitro chondrogenic capacity of SSCs and BCSPs from 2-month-old and 24-month-old mice as determined by Alcan Blue staining. Representative staining (left) and quantification of chondrogenesis (right) ($n = 3$ per age). **f**, In vitro adipogenic capacity of SSCs and BCSPs from 2-month-old and 24-month-old mice as determined by Oil Red O staining. **g**, Renal capsule transplantation results of grafts excised 4 weeks after transplantation of GFP-labelled BCSPs derived from long bones of 2-month-old and 24-month-old mice. Representative gross images of kidneys and magnified graft as bright-field images and with GFP signal shown, for cells derived from 2-month-old (left) and 24-month-old (right) mice. Sectioned grafts stained by Movat’s pentachrome are displayed at the bottom. White and yellow arrows point at auto-fluorescent collagen sponge, which is not part of the graft (representative of 4 independent mice or experiments per age group). **h**, TRAP-staining images (top) and quantification (bottom) for osteoclast surfaces in sections derived from SSC-derived renal grafts ($n = 4$ per age group). Statistical testing by two-sided Student’s *t*-test adjusted for non-normality (Mann–Whitney test) or unequal variances (Welch’s test)

where appropriate. Data are mean + s.e.m. For exact *P* values, see Source Data. Scale bars, 50 µm

[Source data](#).

Extended Data Fig. 4 Exposure to a young circulation does not rejuvenate the SSC lineage.

a, THY1⁺ and 6C3+ cell frequency as assessed by flow cytometry at four weeks of parabiosis (IY, *n* = 6; HY, *n* = 3; HA, *n* = 3; IA, *n* = 3). **b**, Callus index (highest width of callus divided by bone shaft width next to fracture) for parabiosed mice at day 10 (IY, *n* = 9; HY, *n* = 9; HA, *n* = 6; IA, *n* = 5) and day 21 (IY, *n* = 4; HY, *n* = 5; HA, *n* = 3; IA, *n* = 3) after fracture injury. Statistical testing by two-way ANOVA with Bonferroni post-hoc test. **c**, SSC lineage frequencies as assessed by flow cytometry at day 10 after fracture (Fx) in parabionts (IY, *n* = 6; HY, *n* = 3; HA, *n* = 3; IA, *n* = 3). Statistical testing by one-way ANOVA analyses with Tukey's post-hoc test for all comparisons. **d**, Microarray-based inflammatory gene expression levels of purified SSCs from HA and HY mice. **e**, Blood serum concentration of RANKL in the circulation of four-week parabionts (*n* = 4 per group). **f**, Blood serum concentration of CTX1 in the circulation of four-week parabionts (*n* = 2 per group). **g**, Representative images of TRAP staining of fracture calluses of parabionts. **h**, Quantification of TRAP staining in fracture calluses of parabionts (IY, *n* = 4; HY, *n* = 4; HA, *n* = 3; IA, *n* = 4). **i**, Percentage of myeloid and lymphoid reconstitution from transplanted HSCs of parabionts into irradiated recipient mice (*n* = 4 per group). Statistical testing by one-way ANOVA analyses with Tukey's post-hoc test for all comparisons. All data are mean + s.e.m. For exact *P* values, see Source Data. Scale bar, 100 µm

[Source data](#).

Extended Data Fig. 5 The bone marrow microenvironment influences HSC lineage output.

a, Schematic of experimental approach for transplanting freshly isolated HSCs from fetal liver or 24-month-old mice into either 2-month-old or 24-

month-old lethally irradiated mice. **b**, BMD in 2-month-old and 24-month-old lethally irradiated mice transplanted with fetal liver (FL) HSCs or HSCs from 24-month-old mice 8 weeks after haematopoietic reconstitution (E15 FL into old mice, $n = 6$; $n = 5$, all other groups). BM, bone marrow. **c**, Callus index of recipient mice at day 14 after fracture induced at the 8-week time point after transplantation (E15 FL groups, $n = 5$; 24-mo BM groups, $n = 4$). **d**, Representative FACS-gating strategy for myeloid ($GR1^+$) and lymphoid (B and T cells) cells in peripheral blood after haematopoietic reconstitution with GFP-donor HSCs (gated from $TER119^-$, live cells). **e**, Representative bone marrow FACS-gating strategy of GFP^+ donor-derived cells for haematopoietic lineage tree populations. **f**, Peripheral blood analysis for donor chimerism after haematopoietic reconstitution of 2-month-old and 24-month-old mice with young HSCs. **g**, BM analysis of donor-derived (GFP^+) HSC lineage cell populations by flow cytometry. Two-way ANOVA with Bonferroni post-hoc test. **h**, Representative TRAP-staining and GFP-fluorescence images (same section) from day-10 fracture calluses of 2-month-old and 24-month-old mice reconstituted with GFP-labelled HSCs from 2-month-old mice. **i**, Quantification of the total area of $TRAP^+GFP^+$ regions in sections of fracture calluses of mice ($n = 3$ per age group). **j**, Flow cytometric analysis of lymphoid and myeloid cell types in 6-day co-cultures (no SSCs, $n = 4$; 2-mo, $n = 5$; 24-mo, $n = 5$). One-way ANOVA with Tukey's posthoc test for comparison of more than two groups. **k**, Peripheral blood analysis for donor chimerism after haematopoietic reconstitution with co-cultured haematopoietic cells. Two-way ANOVA with Bonferroni post-hoc test. **l**, Bone marrow analysis of co-cultured donor-derived (GFP^+) HSC lineage cell populations by flow cytometry (no SSCs, $n = 3$; 2-mo, $n = 4$; 24-mo, $n = 3$). One-way ANOVA with Tukey's post-hoc test for comparison of more than two groups. Comparison of 2-month-old versus 24-month-old groups by two-sided Student's *t*-test adjusted for non-normality (Mann–Whitney test) or unequal variances (Welch's test) where appropriate. One-way ANOVA with Tukey's post-hoc test. All data are mean + s.e.m. For exact *P* values, see Source Data. Scale bar, 100 μ m

[Source data](#).

Extended Data Fig. 6 Distinct transcriptomic signatures in SSCs of different ages.

a, Heat map of the top 150 differentially expressed genes in each age group by Leiden clusters. **b**, Gene count per single cell as violin plots grouped by age (left) and in a UMAP plot. Statistical testing by Mann–Whitney test. **c**, Heat map showing the expression of apoptosis-related genes in single-cell data grouped by age. **d**, Heat map showing the expression of senescence-associated genes in single-cell data grouped by age. **e**, Electrophoresis gel showing telomerase expression in freshly purified SSCs from 2-month-old and 24-month-old mice. For gel source data, see Supplementary Data 1. **f**, Heat map showing the expression of tissue digest and stress-associated response genes in single-cell data grouped by age. **g**, Heat map showing the expression of tissue digest and stress-associated response genes in single-cell data grouped by Leiden cluster. **h**, Total read count per single cell in UMAP plot. **i**, Cell-cycle status of single cells illustrated in UMAP plot. **j**, Proportion of cell-cycle state per age group. **k**, CytoTrace scores of single SSCs grouped by Leiden cluster (Early-osteо, $n = 48$; Osteо-1, $n = 19$; Chondro, $n = 48$; Root, $n = 51$; Stromal-1, $n = 19$; Osteо-2, $n = 56$; Stromal-2, $n = 33$; GABRA2⁺, $n = 28$ single cells). Data are shown as box-and-whisker plots with centre line as median, box extending from 25th to 75th percentile and minimum to maximum values for whiskers. **l**, Single-cell data of selected age-associated genes related to enhanced bone loss and support of osteoclastogenesis, shown as violin plots grouped by age. Statistical testing between age groups by two-sided Student’s *t*-test adjusted for non-normality (Mann–Whitney test) or unequal variances (Welch’s test) where appropriate. **m**, EnrichR GO analysis of differentially expressed genes of SSCs from 24-month-old versus 0-month-old or 2-month-old SSCs and their relation to cell function as determined by GO Biological Processes

[Source data.](#)

Extended Data Fig. 7 Skeletal-lineage-derived CSF1 promotes bone resorption with age.

a, Model of SSC-lineage-derived CSF1 actions as described in the literature for osteoclast function. **b**, Ligand (*Csf2* or *Csf3*) and receptor (*Csf2r* or *Csf3r*) bulk microarray gene expression (%) in the 2-month-old and 24-month-old SSC lineage and in the haematopoietic lineage, respectively. **c**, Quantification of the number of in-vitro-cultured osteoclasts derived from the bone marrow of 2-month-old and 24-month-old mice (2-mo, $n = 16$; 24-mo, $n = 18$, number per field of view, from three mice per age group). **d**, Number of nuclei per derived osteoclast ($n = 14$ per age group). **e**, Representative bright-field images of in-vitro-derived osteoclasts. **f**, Quantification of in vitro resorption activity of bone-marrow-derived osteoclasts from the bone marrow of 2-month-old and 24-month-old mice ($n = 5$ wells with cells from two different mice per age). **g**, Representative bright-field images in the same experiment. **h**, Luminex protein data of eotaxin1 and TGF β in the supernatant of SSC and BCSP cultures of 2-month-old and 24-month-old mice ($n = 4$ per age group). Statistical testing by two-sided Student's *t*-test. **i**, Blood serum concentrations of selected inflammatory markers in 2-month-old and 24-month-old mouse blood ($n = 4\text{-}5$ per age). Statistical testing by two-sided Student's *t*-test. **j**, Blood serum concentrations of CSF1, eotaxin1 and TGF β in the circulation of 2-month-old and 24-month-old mice ($n = 5$ per age). Statistical testing by two-sided Student's *t*-test. **k**, Gene expression of pro-haematopoietic or pro-osteoclastic and pro-osteogenic genes in bulk RNA-sequencing data of SSCs of day-10 fracture calluses from 2-month-old, 12-month-old and 24-month-old mice ($n = 3$ per age). One-sided Student's *t*-test of ageing groups versus 2-month-old group. All data in scatter plots are mean + s.e.m., except **c**, **d**, **f**, which show box-and-whisker plots with centre line as median, box extending from 25th to 75th percentile and minimum to maximum values for whiskers. For exact *P* values, see Source Data

[Source data](#).

Extended Data Fig. 8 CSF1 levels control skeletal maintenance and repair.

a, Representative μ CT images of day-10 fracture calluses at the time of surgery supplemented with hydrogel containing recombinant CSF1 (5 μ g) or PBS as control. **b**, BMD of day-10 fracture calluses treated with or

without rCSF1 (PBS, $n = 5$; rCSF1, $n = 4$). **c**, Total number of SSCs and BCSPs at day 10 assessed by FACS (PBS, $n = 4$; rCSF1, $n = 3$). **d**, Representative μ CT reconstructions of femur bones from uninjured wild-type or haplo-insufficient $Csf1^{KO}$ ($Csf1^{KO+/-}$) 15-month-old female and male mice. **e**, Trabecular BMD (top) and cortical total mineral density (TMD; bottom) of femur bones from female and male wild-type and $Csf1^{KO}$ mice ($n = 4$ per genotype and sex). **f**, Bone parameters quantified by μ CT from uninjured 15-month-old wild-type and $Csf1^{KO}$ female and male mice ($n = 4$ per genotype and sex). **g**, Bone parameters quantified by μ CT from 21-day fracture calluses of 15-month-old wild-type and $Csf1^{KO}$ female mice (WT, $n = 4$; $Csf1^{KO}$, $n = 7$). All comparison of 2-month-old versus 24-month-old groups by two-sided Student's *t*-test. Data are mean + s.e.m. For exact *P* values, see Source Data

[Source data](#).

Extended Data Fig. 9 Rejuvenating fracture healing in aged mice with defined factors.

a, Schematic representation of experimental set-up of rescue experiments with 24-month-old mice. **b**, Frequency of BCSPs, THY1 $^+$ and 6C3 $^+$ in 24-month-old mice at day 10 after fracture induction and application of factors (BMP2: 5 μ g; CSF1 $^{\text{low}}$: 2 μ g; CSF1 $^{\text{high}}$: 5 μ g) (2-mo PBS, $n = 6$; PBS, $n = 6$; CSF1 $^{\text{low}}$, $n = 5$; CSF1 $^{\text{high}}$, $n = 5$; BMP2, $n = 5$; Combo $^{\text{low}}$, $n = 9$; Combo $^{\text{high}}$, $n = 5$). **c**, μ CT analysis of newly formed mineralized bone volume of treated fracture calluses at day 21 (2-mo PBS, $n = 7$; PBS, $n = 9$; CSF1 $^{\text{low}}$, $n = 6$; CSF1 $^{\text{high}}$, $n = 7$; BMP2, $n = 12$; Combo $^{\text{low}}$, $n = 12$; Combo $^{\text{high}}$, $n = 8$). All two-sided Student's *t*-tests between the 2-month-old group and each 24-month-old group adjusted for non-normality (Mann–Whitney test) or unequal variances (Welch's test) where appropriate. **d**, CFU-F capacity of SSCs isolated from fracture calluses from the 2-mo-PBS, PBS and 'Combo $^{\text{low}}$ ' treatment groups at day 10 (2-mo PBS, $n = 6$; PBS, $n = 6$; Combo $^{\text{low}}$, $n = 5$). Two-sided Student's *t*-test between the 2-month-old PBS-treated group and each 24-month-old group adjusted for non-normality (Mann–Whitney test) where appropriate (n.s., not significant). Data are mean + s.e.m. For exact *P* values, see Source Data

[Source data](#).

Extended Data Fig. 10 Compositional and transcriptomic changes in fracture calluses of aged mice after rescue treatment.

a, Leiden clustering of 10X scRNA-seq experiment of 17,230 fracture callus cells from 24-month-old mice treated with PBS and from 24-month-old mice treated with aCSF1^{low} + BMP2 (Combo^{low}). **b**, UMAP plot showing expression of selected marker genes for Leiden clusters. **c**, UMAP plot showing distribution of cells from each treatment group. Red, 24-mo PBS; grey, 24-mo Combo^{low}. **d**, Percentual fraction of treatment group cells per Leiden cluster. **e**, Heat map showing positive and negative markers used to identify SSCs. **f**, Dot plot showing the absence of lymphoid gene expression in 10X datasets. **g**, UMAP plot with cells labelled by treatment group in 10X dataset subset for cells enriched for haematopoietic gene expression. **h**, Same UMAP plot showing expression of selected marker genes.

Extended Data Fig. 11 Graphical abstract of SSC-mediated skeletal ageing.

Loss of skeletal integrity with age owing to reduced bone formation and increased bone resorption is associated with reduced SSC frequency and activity. The 24-month-old skeleton is characterized by increased bone loss, impaired regeneration and lineage skewing of the SSC lineage towards osteoclast-supportive stroma. Skeletal regeneration can be rejuvenated by simultaneous application of recombinant BMP2 and a low dose of an antibody blocking the action of CSF1.

Supplementary information

Supplementary Data 1

Raw data for Extended Figure Data 6e. The uncropped electrophoresis gel comparing telomerase activity between ‘2-mo’ and ‘24-mo’ SSCs.

Reporting Summary

Supplementary Table 1

Excel sheet with results of single cell RNA-sequencing analysis of SSCs from newborn, young adult, and aged mice. Differentially expressed genes between leiden clusters.

Supplementary Table 2

Excel sheet with results of single cell RNA-sequencing analysis of SSCs from newborn, young adult, and aged mice. Differentially expressed genes between age groups.

Peer Review File

Source data

Source Data Fig. 1

Source Data Fig. 2

Source Data Fig. 3

Source Data Fig. 4

Source Data Extended Data Fig. 1

Source Data Extended Data Fig. 2

Source Data Extended Data Fig. 3

[**Source Data Extended Data Fig. 4**](#)

[**Source Data Extended Data Fig. 5**](#)

[**Source Data Extended Data Fig. 6**](#)

[**Source Data Extended Data Fig. 7**](#)

[**Source Data Extended Data Fig. 8**](#)

[**Source Data Extended Data Fig. 9**](#)

Rights and permissions

[Reprints and Permissions](#)

About this article

Cite this article

Ambrosi, T.H., Marecic, O., McArdle, A. *et al.* Aged skeletal stem cells generate an inflammatory degenerative niche. *Nature* **597**, 256–262 (2021).
<https://doi.org/10.1038/s41586-021-03795-7>

- Received: 06 May 2020
- Accepted: 05 July 2021
- Published: 11 August 2021
- Issue Date: 09 September 2021
- DOI: <https://doi.org/10.1038/s41586-021-03795-7>

Further reading

- [Ageing stem cells hold the key to age-related bone degeneration](#)

- Joanna Clarke

Nature Reviews Rheumatology (2021)

A stem-cell basis for skeletal ageing

- Matthew B. Greenblatt
- Shawon Debnath

News & Views 11 Aug 2021

[Ageing stem cells hold the key to age-related bone degeneration](#)

- Joanna Clarke

Research Highlight 01 Sept 2021

This article was downloaded by **calibre** from <https://www.nature.com/articles/s41586-021-03795-7>

- Article
- [Published: 18 August 2021](#)

Dietary fructose improves intestinal cell survival and nutrient absorption

- [Samuel R. Taylor](#)^{1,2,3,4},
- [Shakti Ramsamooj](#)^{1,2},
- [Roger J. Liang](#)^{1,2},
- [Alyna Katti](#)^{2,4},
- [Rita Pozovskiy](#)^{1,2},
- [Neil Vasan](#)^{2,5},
- [Seo-Kyoung Hwang](#) [ORCID: orcid.org/0000-0003-0866-5376](#)^{1,2},
- [Navid Nahyaan](#)⁶,
- [Nancy J. Francoeur](#)⁷,
- [Emma M. Schatoff](#)^{1,2,3},
- [Jared L. Johnson](#) [ORCID: orcid.org/0000-0003-1802-6527](#)²,
- [Manish A. Shah](#)²,
- [Andrew J. Dannenberg](#)²,
- [Robert P. Sebra](#)^{7,8},
- [Lukas E. Dow](#) [ORCID: orcid.org/0000-0001-7048-1418](#)²,
- [Lewis C. Cantley](#) [ORCID: orcid.org/0000-0002-1298-7653](#)²,
- [Kyu Y. Rhee](#) [ORCID: orcid.org/0000-0003-4582-2895](#)⁶ &
- [Marcus D. Goncalves](#) [ORCID: orcid.org/0000-0002-0784-9248](#)^{1,2}

Nature volume 597, pages 263–267 (2021)

- 15k Accesses

- 2 Citations
- 523 Altmetric
- [Metrics details](#)

Subjects

- [Cancer metabolism](#)
- [Fat metabolism](#)
- [Metabolomics](#)

Abstract

Fructose consumption is linked to the rising incidence of obesity and cancer, which are two of the leading causes of morbidity and mortality globally^{1,2}. Dietary fructose metabolism begins at the epithelium of the small intestine, where fructose is transported by glucose transporter type 5 (GLUT5; encoded by *SLC2A5*) and phosphorylated by ketohexokinase to form fructose 1-phosphate, which accumulates to high levels in the cell^{3,4}. Although this pathway has been implicated in obesity and tumour promotion, the exact mechanism that drives these pathologies in the intestine remains unclear. Here we show that dietary fructose improves the survival of intestinal cells and increases intestinal villus length in several mouse models. The increase in villus length expands the surface area of the gut and increases nutrient absorption and adiposity in mice that are fed a high-fat diet. In hypoxic intestinal cells, fructose 1-phosphate inhibits the M2 isoform of pyruvate kinase to promote cell survival^{5,6,7}. Genetic ablation of ketohexokinase or stimulation of pyruvate kinase prevents villus elongation and abolishes the nutrient absorption and tumour growth that are induced by feeding mice with high-fructose corn syrup. The ability of fructose to promote cell survival through an allosteric metabolite thus provides additional insights into the excess adiposity generated by a Western diet, and a compelling explanation for the promotion of tumour growth by high-fructose corn syrup.

Access options

Subscribe to Journal

Get full journal access for 1 year

\$199.00

only \$3.90 per issue

[Subscribe](#)

All prices are NET prices.

VAT will be added later in the checkout.

Tax calculation will be finalised during checkout.

Rent or Buy article

Get time limited or full article access on ReadCube.

from \$8.99

[Rent or Buy](#)

All prices are NET prices.

Additional access options:

- [Log in](#)
- [Access through your institution](#)
- [Learn about institutional subscriptions](#)

Fig. 1: Dietary fructose increases intestinal villus length and lipid absorption.

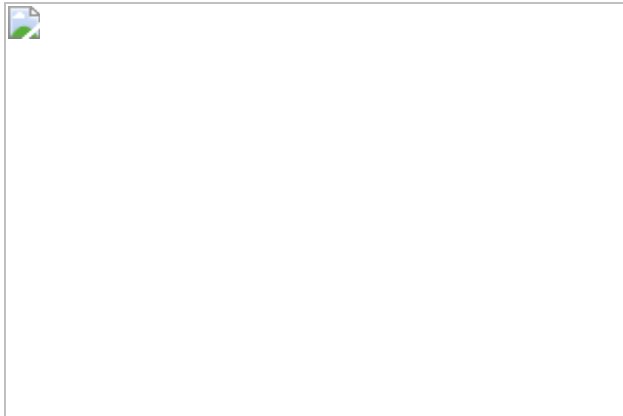


Fig. 2: Fructose metabolism enhances hypoxic cell survival and decreases pyruvate kinase activity.

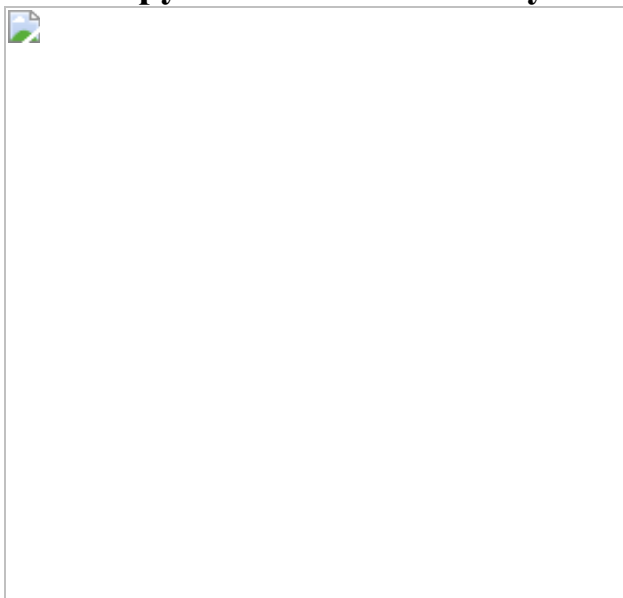
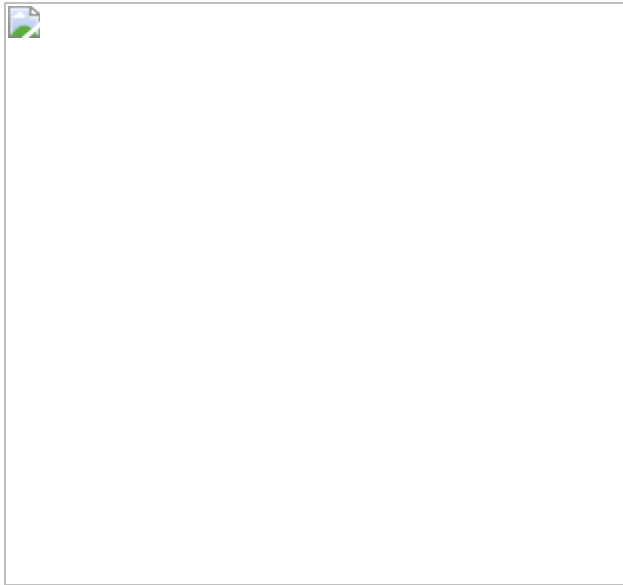


Fig. 3: PK activation diminishes the effect of fructose on hypoxia survival.



Data availability

Additional data that support the findings of this study are available from the corresponding author upon reasonable request. [Source data](#) are provided with this paper.

Code availability

Villi analysis code, licensing information, and instructions for use are available at <https://github.com/sam-taylor/VilliQuant>.

References

1. 1.

Bray, G. A., Nielsen, S. J. & Popkin, B. M. Consumption of high-fructose corn syrup in beverages may play a role in the epidemic of obesity. *Am. J. Clin. Nutr.* **79**, 537–543 (2004).

2. 2.

Joh, H.-K. et al. Simple sugar and sugar-sweetened beverage intake during adolescence and risk of colorectal cancer precursors. *Gastroenterology* **161**, 128–142 (2021).

3. 3.

Miller, M., Craig, J. W., Drucker, W. R. & Woodward, H. Jr. The metabolism of fructose in man. *Yale J. Biol. Med.* **29**, 335–360 (1956).

4. 4.

Jang, C. et al. The small intestine converts dietary fructose into glucose and organic acids. *Cell Metab.* **27**, 351–361 (2018).

5. 5.

Anastasiou, D. et al. Inhibition of pyruvate kinase M2 by reactive oxygen species contributes to cellular antioxidant responses. *Science* **334**, 1278–1283 (2011).

6. 6.

Nguyen, A. et al. PKLR promotes colorectal cancer liver colonization through induction of glutathione synthesis. *J. Clin. Invest.* **126**, 681–694 (2016).

7. 7.

Anastasiou, D. et al. Pyruvate kinase M2 activators promote tetramer formation and suppress tumorigenesis. *Nat. Chem. Biol.* **8**, 839–847 (2012).

8. 8.

Port, A. M., Ruth, M. R. & Istfan, N. W. Fructose consumption and cancer: is there a connection? *Curr. Opin. Endocrinol. Diabetes Obes.* **19**, 367–374 (2012).

9. 9.

Parikh, N. I. et al. Increasing trends in incidence of overweight and obesity over 5 decades. *Am. J. Med.* **120**, 242–250 (2007).

10. 10.

Liu, P. H. et al. Association of obesity with risk of early-onset colorectal cancer among women. *JAMA Oncol.* **5**, 37–44 (2019).

11. 11.

Siegel, R. L. et al. Colorectal cancer incidence patterns in the United States, 1974–2013. *J. Natl. Cancer Inst.* **109**, djw322 (2017).

12. 12.

Tasevska, N. et al. Sugars in diet and risk of cancer in the NIH-AARP Diet and Health Study. *Int. J. Cancer* **130**, 159–169 (2012).

13. 13.

Bostick, R. M. et al. Sugar, meat, and fat intake, and non-dietary risk factors for colon cancer incidence in Iowa women (United States). *Cancer Causes Control* **5**, 38–52 (1994).

14. 14.

Meyerhardt, J. A. et al. Dietary glycemic load and cancer recurrence and survival in patients with stage III colon cancer: findings from CALGB 89803. *J. Natl. Cancer Inst.* **104**, 1702–1711 (2012).

15. 15.

Goncalves, M. D. et al. High-fructose corn syrup enhances intestinal tumor growth in mice. *Science* **363**, 1345–1349 (2019).

16. 16.

Bu, P. et al. Aldolase B-mediated fructose metabolism drives metabolic reprogramming of colon cancer liver metastasis. *Cell Metab.*

27, 1249–1262 (2018).

17. 17.

Hall, P. A., Coates, P. J., Ansari, B. & Hopwood, D. Regulation of cell number in the mammalian gastrointestinal tract: the importance of apoptosis. *J. Cell Sci.* **107**, 3569–3577 (1994).

18. 18.

Israelsen, W. J. & Vander Heiden, M. G. Pyruvate kinase: Function, regulation and role in cancer. *Semin. Cell Dev. Biol.* **43**, 43–51 (2015).

19. 19.

Yang, H., Wang, X., Xiong, X. & Yin, Y. Energy metabolism in intestinal epithelial cells during maturation along the crypt-villus axis. *Sci. Rep.* **6**, 31917 (2016).

20. 20.

Christofk, H. R., Vander Heiden, M. G., Wu, N., Asara, J. M. & Cantley, L. C. Pyruvate kinase M2 is a phosphotyrosine-binding protein. *Nature* **452**, 181–186 (2008).

21. 21.

Luo, W. et al. Pyruvate kinase M2 is a PHD3-stimulated coactivator for hypoxia-inducible factor 1. *Cell* **145**, 732–744 (2011).

22. 22.

Schwitalla, S. et al. Intestinal tumorigenesis initiated by dedifferentiation and acquisition of stem-cell-like properties. *Cell* **152**, 25–38 (2013).

23. 23.

Schatoff, E. M. et al. Distinct colorectal cancer–associated APC mutations dictate response to tankyrase inhibition. *Cancer Discov.* **9**, 1358–1371 (2019).

24. 24.

Kucharzewska, P., Christianson, H. C. & Belting, M. Global profiling of metabolic adaptation to hypoxic stress in human glioblastoma cells. *PLoS ONE* **10**, e0116740 (2015).

25. 25.

Armitage, E. G. et al. Metabolic profiling reveals potential metabolic markers associated with hypoxia inducible factor-mediated signalling in hypoxic cancer cells. *Sci. Rep.* **5**, 15649 (2015).

26. 26.

Mirtschink, P. et al. HIF-driven SF3B1 induces KHK-C to enforce fructolysis and heart disease. *Nature* **522**, 444–449 (2015).

27. 27.

Park, T. J. et al. Fructose-driven glycolysis supports anoxia resistance in the naked mole-rat. *Science* **356**, 307–311 (2017).

28. 28.

Goran, M. I., Martin, A. A., Alderete, T. L., Fujiwara, H. & Fields, D. A. Fructose in breast milk is positively associated with infant body composition at 6 months of age. *Nutrients* **9**, 146 (2017).

29. 29.

Denyes, A. & Carter, J. D. Utilization of acetate-1-C-14 by hepatic tissue from cold-exposed and hibernating hamsters. *Am. J. Physiol.* **200**, 1043–1046 (1961).

30. 30.

Diggle, C. P. et al. Ketohexokinase: expression and localization of the principal fructose-metabolizing enzyme. *J. Histochem. Cytochem.* **57**, 763–774 (2009).

31. 31.

Macenko, M. et al. A method for normalizing histology slides for quantitative analysis. In *2009 IEEE International Symposium on Biomedical Imaging: From Nano to Macro* 1107–1110 (IEEE, 2009).

32. 32.

MATLAB v.9.7.0.1190202 (R2019b) (The MathWorks Inc., 2018).

33. 33.

Mystkowski, P. et al. Validation of whole-body magnetic resonance spectroscopy as a tool to assess murine body composition. *Int. J. Obes.* **24**, 719–724 (2000).

34. 34.

Millar, J. S., Cromley, D. A., McCoy, M. G., Rader, D. J. & Billheimer, J. T. Determining hepatic triglyceride production in mice: comparison of poloxamer 407 with Triton WR-1339. *J. Lipid Res.* **46**, 2023–2028 (2005).

35. 35.

Krisko, T. I. et al. Dissociation of adaptive thermogenesis from glucose homeostasis in microbiome-deficient mice. *Cell Metab.* **31**, 592–604 (2020).

36. 36.

Weir, J. B. New methods for calculating metabolic rate with special reference to protein metabolism. *J. Physiol.* **109**, 1–9 (1949).

37. 37.

Staffas, A. et al. Nutritional support from the intestinal microbiota improves hematopoietic reconstitution after bone marrow transplantation in mice. *Cell Host Microbe* **23**, 447–457 (2018).

38. 38.

Nalapareddy, K. et al. Canonical Wnt signaling ameliorates aging of intestinal stem cells. *Cell Rep.* **18**, 2608–2621 (2017).

39. 39.

Raleigh, J. A. & Koch, C. J. Importance of thiols in the reductive binding of 2-nitroimidazoles to macromolecules. *Biochem. Pharmacol.* **40**, 2457–2464 (1990).

40. 40.

O'Rourke, K. P., Dow, L. E. & Lowe, S. W. Immunofluorescent staining of mouse intestinal stem cells. *Bio Protoc.* **6**, e1732 (2016).

41. 41.

White, R., Yaeger, D. & Stavrianeas, S. Determination of blood lactate concentration: reliability and validity of a lactate oxidase-based method. *Int. J. Exerc. Sci.* **2**, 2 (2009).

42. 42.

Ashizawa, K., McPhie, P., Lin, K.-H. & Cheng, S.-Y. An in vitro novel mechanism of regulating the activity of pyruvate kinase M2 by thyroid hormone and fructose 1, 6-bisphosphate. *Biochemistry* **30**, 7105–7111 (1991).

43. 43.

Adelman, R. C., Ballard, F. J. & Weinhouse, S. Purification and properties of rat liver fructokinase. *J. Biol. Chem.* **242**, 3360–3365 (1967).

44. 44.

Al-Ani, A. et al. Oxygenation in cell culture: Critical parameters for reproducibility are routinely not reported. *PLoS ONE* **13**, e0204269 (2018).

45. 45.

Sullivan, M. R. et al. Quantification of microenvironmental metabolites in murine cancers reveals determinants of tumor nutrient availability. *eLife* **8**, e44235 (2019).

46. 46.

Smith, C. A., Want, E. J., O'Maille, G., Abagyan, R. & Siuzdak, G. XCMS: processing mass spectrometry data for metabolite profiling using nonlinear peak alignment, matching, and identification. *Anal. Chem.* **78**, 779–787 (2006).

47. 47.

Huang, X. et al. X13CMS: global tracking of isotopic labels in untargeted metabolomics. *Anal. Chem.* **86**, 1632–1639 (2014).

48. 48.

Fernandez-Martinez, J., Lacava, J. & Rout, M. P. Density gradient ultracentrifugation to isolate endogenous protein complexes after affinity capture. *Cold Spring Harb. Protoc.* <https://doi.org/10.1101/pdb.prot087957> (2016).

Acknowledgements

We acknowledge C. Gurbatri for her assistance in figure preparation, M. Lyashenko for his technical assistance with experiment replication and Y.-T. Chen for his pathological review of the primary human CRC tissue. We thank J. Yun for her discussions, which informed the early development of this work. *Khk*^{-/-} mice were provided by D. T. Bontron and R. J. Johnson.

Glut5^{-/-} mice were provided by R.P. Ferraris and St. Jude's Children's Research Hospital. S.R.T. and E.M.S. were supported by a Medical Scientist Training Program grant from the National Institute of General Medical Sciences of the National Institutes of Health under award number T32GM007739 to the Weill Cornell–Rockefeller–Sloan Kettering Tri-Institutional MD–PhD Program. This work was supported by NIH R35 CA197588 (L.C.C.), SU2C-AACR-DT22-17 (L.C.C.), NIH K08 CA230318 (M.D.G.), R25 AI140472 (K.Y.R.), a grant from the Lung Cancer Research Foundation and institutional funds from Weill Cornell Medicine.

Author information

Affiliations

1. Division of Endocrinology, Weill Department of Medicine, Weill Cornell Medicine, New York, NY, USA

Samuel R. Taylor, Shakti Ramsamooj, Roger J. Liang, Rita Pozovskiy, Seo-Kyoung Hwang, Emma M. Schatoff & Marcus D. Goncalves

2. Meyer Cancer Center, Weill Department of Medicine, Weill Cornell Medicine, New York, NY, USA

Samuel R. Taylor, Shakti Ramsamooj, Roger J. Liang, Alyna Katti, Rita Pozovskiy, Neil Vasan, Seo-Kyoung Hwang, Emma M. Schatoff, Jared L. Johnson, Manish A. Shah, Andrew J. Dannenberg, Lukas E. Dow, Lewis C. Cantley & Marcus D. Goncalves

3. Weill Cornell–Rockefeller–Sloan Kettering Tri-Institutional MD–PhD program, New York, NY, USA

Samuel R. Taylor & Emma M. Schatoff

4. Weill Cornell Graduate School of Medical Sciences, Weill Cornell Medicine, New York, NY, USA

Samuel R. Taylor & Alyna Katti

5. Breast Medicine Service, Memorial Sloan Kettering Cancer Center,
New York, NY, USA

Neil Vasan

6. Division of Infectious Diseases, Weill Department of Medicine, Weill
Cornell Medicine, New York, NY, USA

Navid Nahyaan & Kyu Y. Rhee

7. Department of Genetics and Genomic Sciences, Icahn School of
Medicine at Mount Sinai, New York, NY, USA

Nancy J. Francoeur & Robert P. Sebra

8. Sema4, Stamford, CT, USA

Robert P. Sebra

Contributions

S.R.T. and M.D.G. contributed to the conception and design of the study. S.R.T., A.J.D., L.E.D., K.Y.R., L.C.C. and M.D.G. contributed ideas that formulated the overarching research goals and aims. E.M.S. and L.E.D. generated and provided the *Apc^{Q1405X/+}* mouse model and guided its experimental use. S.R.T., N.V. and J.L.J. contributed to the structural and biochemical assays of pyruvate kinase. M.A.S. collected and provided the primary human tumour samples. A.J.D. provided the *Glut5^{-/-}* mouse model and ideas that guided the initial phenotyping of the wild-type mice that were fed fructose. S.R.T., S.R. and N.J.F. performed programming, software development and implementation of the computer code and supporting algorithms. S.R.T., S.R. and S.-K.H. conducted mouse physiology studies and performed necropsy and tissue analysis. S.R.T. and A.K. performed the mouse intestinal organoid experiments under the guidance of L.E.D. S.R.T. and N.N. performed and analysed the LC–MS metabolomics experiments under the guidance of K.Y.R. and M.D.G. R.J.L. performed mutagenesis

and generated recombinant pyruvate kinase. R.P. performed KHK activity assays. R.P.S. assisted with targeted isoform sequencing. S.R.T. performed all other experiments. S.R.T. and M.D.G. wrote the manuscript and verified the overall replication and reproducibility of results, experiments and other research outputs.

Corresponding author

Correspondence to [Marcus D. Goncalves](#).

Ethics declarations

Competing interests

L.C.C. is a founder, shareholder and member of the scientific advisory board of Agios Pharmaceuticals and a founder and former member of the scientific advisory board of Ravenna Pharmaceuticals (previously Petra Pharmaceuticals). These companies are developing therapies for cancer. L.C.C. has received research funding from Ravenna Pharmaceuticals. L.C.C. and M.D.G. are co-founders and shareholders of Faeth Therapeutics, which is developing therapies for cancer. M.D.G. has received speaking and/or consulting fees from Pfizer, Novartis, Petra Pharmaceuticals, Faeth Therapeutics and TruMacro Nutrition. The laboratory of M.D.G. has received financial support from Pfizer. All other authors report no competing interests.

Additional information

Peer review information *Nature* thanks Dimitrios Anastasiou, M. Mahmood Hussain and the other, anonymous, reviewer(s) for their contribution to the peer review of this work.

Publisher's note Springer Nature remains neutral with regard to jurisdictional claims in published maps and institutional affiliations.

Extended data figures and tables

Extended Data Fig. 1 Image segmentation avoids the pitfalls of manual villi measurement.

a, Stain-normalized H&E images of Swiss-rolled intestines were loaded into image-analysis software, which was used to manually measure the length of the gut section (dotted black line). **b**, Image segmentation isolates villi (white) while excluding other tissues such as lymph nodes, pancreas and intestinal crypts. **c**, Intra-operator variation is a source of measurement error in manual villi measurements. The *x* and *y* axes represent measurements taken by the same analyst at different times. **d**, Inter-operator variation is another source of measurement error in manual villi measurements. The *x* and *y* axes represent measurements taken by different analysts. **e**, **f**, Intra- and inter-operator variation are minimized when using the semi-automated protocol. The comparisons in **e**, **f** are the same as in **c**, **d**; however, the only manual measurement in the semi-automated method is the measurement of the whole gut section length. **g**, Automated and manual measurements correlate. The *x* and *y* axes represent measurements obtained from the manual and semi-automated protocols, respectively. **h**, Mice from various genetic backgrounds were fed HFCS and the mean villus length in the duodenal intestinal epithelium was measured using a custom analysis algorithm (mice per group: left to right ($H_2O|HFCS$): 4|5, 5|5, 10|10, 10|10, 9|5). **c–g**, Each point represents a distinct image; dotted line: unity; R_2 is displayed for the linear regression fit of the data. **h**, Two-way ANOVA followed by Holm–Sidak post-hoc test for multiple comparisons. * $P < 0.05$, ** $P < 0.01$, *** $P < 0.001$. Error bars represent \pm s.e.m. See Source Data for exact P values for all figures.

[Source data](#)

Extended Data Fig. 2 Dietary fructose promotes weight gain and adiposity independent of caloric intake.

a, Mice fed normal chow with or without 25% HFCS ad libitum were weighed weekly for six weeks. **b–d**, Total, lean and fat body mass were

measured before and five weeks after mice were placed on diets. **e–g**, Total consumption of chow and fluid was measured weekly to calculate caloric consumption ($n = 5$ serial measurements per group). **h, i**, Tissues from mice on the indicated diets were collected and weighed and the liver was assayed for triglyceride content. WAT, white adipose tissue from the left or right gonadal fat depot. **j**, After five weeks, mice were fasted and blood glucose was measured by glucometer (**a–j**, 5 mice per group). **k**, A lipid tolerance test was performed on wild-type female mice fed HFCS ($n = 3$ mice per group). **l**, Mice treated with water or HFCS were fasted and then given an intraperitoneal injection of poloxamer 407. One hour later, triglyceride levels were measured from the serum and the mice were given an oral olive oil bolus. Two hours later, serum triglyceride levels were measured again ($n = 7$ (H_2O) and $n = 5$ (HFCS) mice per group). **m**, Mice fed fructose-free control diets (control), high-fat diets consisting of 45% kcal from fat (HF), and high-fat diets with sucrose in place of glucose as the main sugar (HFHS) were monitored weekly for chow consumption by cage ($n = 3$ repeated measurements per group). **n**, Total, lean and fat body mass were measured after five weeks on the diet. Statistical comparisons are made against control fat mass ($n = 5$ mice per group). **o**, After four weeks on the diet, mice were fasted and blood glucose was measured with a glucometer ($n = 3$ mice per group). **p–r**, After euthanasia, tissues were collected and weighed, liver tissue was homogenized and assayed for triglyceride content, mouse intestines were excised en bloc and the intestinal length was measured using ImageJ software ($n = 5$ (**p, r**) and $n = 4$ (**q**) mice per group). **s**, Mice treated with high-fat or high-fat high-sucrose diets for two weeks were housed in metabolic cages and food intake over 24 h was measured. **t**, O_2 consumption and CO_2 production were measured to calculate the respiratory exchange ratio. **u, v**, Total distance travelled was also measured (**u**), as was hourly energy expenditure (**v**), which was calculated using the Weir equation⁸. **w–z**, Mice were individually housed and faecal matter was collected over a 24-h period (**w**), dried (**x**) and then analysed by bomb calorimetry to measure energy content and energy loss over the collection period (**y, z**) (**s–z**, 4 mice per group). **b, c, h, n**, Two-way ANOVA followed by Holm–Sidak post-hoc test for multiple comparisons; **d–g, i, j, l, s–u, w–z**, Student's two-sided *t*-test; **k, m, o, q**, one-way ANOVA followed by Holm–Sidak post-hoc test for multiple comparisons. NS, not significant;

* $P < 0.05$, ** $P < 0.01$, *** $P < 0.001$, **** $P < 0.0001$. All data are mean \pm s.e.m.

[Source data](#)

Extended Data Fig. 3 HFCS increases villus survival and expression of GLUT5 and HIF target proteins.

a, Model depicting the strategy of the BrdU tracing experiment. BrdU labels cells synthesizing DNA (brown). These cells transit up the length of the villus and away from richly oxygenated blood in 3–4 days. Unlabelled cells beyond the BrdU front at the time that mice were euthanized were thus generated before BrdU injection. **b**, Duodenal villus length was measured from H&E images from H₂O- and HFCS-treated mouse intestine ($n = 3$ mice per group, 40 villi per mouse). **c**, Mice were administered BrdU 72 h before euthanasia, and intestines were then examined by IHC. The length of BrdU-labelled regions of the villus was measured in both treatment groups and this length was divided by the interval between injection and euthanasia to yield migration rate ($n = 3$ mice per group, 15–20 duodenal villi per mouse). **d, e**, In a separate experiment, mice were treated with H₂O or HFCS and given BrdU (green) 48 h before and EdU (red) 24 h before euthanasia. Duodenal villi were then stained and imaged by immunofluorescence and analysed as in **c**. The difference between the BrdU and EdU lengths was divided by the interval between injections to yield the migration rate ($n = 3$ (H₂O) and $n = 4$ (HFCS) mice per group, 15–20 duodenal villi per mouse). Scale bars, 100 μ m. **f**, Mice treated with H₂O or 25% HFCS were euthanized and the intestines were examined by IHC against Ki-67, CC3 and TUNEL. Scale bars, 200 μ m. **g**, Before euthanasia, mice treated as in **f** were injected with pimonidazole to label tissue hypoxia. Intestines were then fixed and examined for pimonidazole intensity by IHC. Representative images are shown. Scale bars: 500 μ m. **h**, The pimonidazole-positive area was quantified and normalized to total small intestine (SI) area ($n = 5$ mice per group). **i**, Wild-type mice treated with H₂O or HFCS and total-body, constitutive *Glut5*^{-/-} mice treated with HFCS were euthanized and intestines were fixed and examined by IHC. Representative images are shown. Scale bars, 200 μ m (top); 50 μ m

(bottom). **j**, Wild-type mice treated with H₂O or 25% HFCS ad libitum for four weeks were euthanized and intestinal epithelium was collected for western blot for indicators of cell health including markers of energy homeostasis (pACC, pAMPK) and anti-apoptotic proteins (BCL2, BCL-XL, MCL-1). **k**, Mice treated as in **j** were also euthanized and the intestinal epithelium was examined by western blot for hypoxia response proteins (ENO1, LDHA) and KHK. **b, c, e, h**, two-sided Student's *t*-test. NS, not significant; ****P* < 0.001. All data are mean ± s.e.m. For gel source data, see Supplementary Fig. [1](#).

[Source data](#)

[Extended Data Fig. 4 Fructose enhances hypoxic cell survival.](#)

a, At the conclusion of the experiment depicted in Fig. [2a](#), HCT116 cells were collected and analysed by Trypan Blue exclusion assay. Total live cells per group were counted and normalized to the fructose-free group (*n* = 3 biological replicates per group). **b, c**, HCT116 cells were plated near confluence and cultured in hypoxia with or without 10 mM fructose in the medium. Every 48 h, as indicated, the medium was exchanged with fresh oxygen-equilibrated medium. Confluence was monitored and at the conclusion of the experiment cells were analysed by Trypan Blue exclusion assay as in **a** (*n* = 3 biological replicates per group). **d–f**, HCT116 (**d**) or DLD1 (**e, f**) cells were cultured with glucose and either staurosporin (Stau, 100 nM, apoptotic control) or fructose, in medium that also contained an Annexin V dye (**d, e**) and a nucleic-acid-binding cell death dye (CytoTox; **f**). Cells were incubated in normoxia (N) or hypoxia (H) and imaged daily by live-cell imaging. Stain intensity is reported as positive cell area per well normalized to the initial normoxic glucose control (*n* = 3 biological replicates per data point). **g**, Intestinal organoids were generated from adult B6J mice and cultured in hypoxia with or without fructose for 72 h. At experiment termination, organoids were pulsed with EdU, fixed *in situ*, stained for the indicated targets and examined by confocal microscopy. Representative images are shown. White arrows indicate regions with intra-organoid CC3 puncti. Scale bars, 50 µm. **h, i**, Organoids treated as in **g** were rapidly dissociated and stained for viability (via a membrane-impermeable dye) (**h**) and EdU (**i**). The resulting cell suspensions were analysed by flow

cytometry. Viability is expressed as viable cells recovered per culture well, normalized to the average of the normoxic glucose controls ($n = 3$ progenitor mice; each pair of points represents a different mouse progenitor). In these and other in vitro assays, unless otherwise noted, glucose was replenished daily as described in the Methods. **a, d, h**, One-way ANOVA followed by Holm–Sidak post-hoc test for multiple comparisons; **b, c**, two-sided Student’s *t*-test; * $P < 0.05$, ** $P < 0.01$, *** $P < 0.0001$. All data are mean \pm s.e.m.

[Source data](#)

Extended Data Fig. 5 Hypoxia increases GLUT5 expression and KHK-A transcription.

a, HCT116 and DLD1 cells cultured at the indicated O₂ concentrations with or without 10 mM fructose were lysed at 36 h and western blotted for the indicated targets. ‘+’ in the ‘%O₂’ row indicates that 100 μM cobalt chloride was added to the medium at time 0. **b**, RNA was extracted from HCT116 cells treated in normoxia or hypoxia for 24 h and analysed by IsoSeq. The relative proportion of the A and C isoforms of KHK are shown ($n = 1$ biological replicate per O₂ condition). **c**, HCT116 cells cultured in normoxia or hypoxia for 24 h were lysed and tested for KHK activity by enzymatic assay ($n = 3$ biological replicates). **c**, Two-sided student’s *t*-test. ** $P < 0.01$. Data in **c** are mean \pm s.e.m. For gel source data, see Supplementary Fig. 1.

[Source data](#)

Extended Data Fig. 6 F1P accumulates in cells and correlates with marked metabolic changes in hypoxia.

a, HCT116 cells cultured in hypoxia with fructose were labelled with various U-¹³C metabolites and intracellular metabolites were detected by LC–MS. The *y* axis reflects the fraction of the detected metabolite labelled with ¹³C on the number of carbons denoted by the colours to the right of each graph. The *x* axis denotes the labelled feed metabolite for that

particular group. The graph for fructose, for example, indicates that all detected fructose ions were labelled at all 6 carbons with ^{13}C when U- $^{13}\text{C}6$ fructose was provided in the medium ($n = 3$ biological replicates per unique label). **b**, HCT116 and DLD1 cells were cultured in hypoxia with 25 mM glucose with or without 10 mM fructose. At 48 h the growth medium was assayed for glucose and fructose content. Colours indicate the initial medium formulation for each group. The x axis denotes which sugar is being measured ($n = 3$ (Glc) and $n = 2$ (Glc + Fru) biological replicates per group). **c**, Mouse intestinal organoids were cultured in hypoxia with 10 mM glucose with or without 10 mM fructose for 72 h. Glucose in the 3-ml culture volume was increased by 5 mM daily to account for glucose depletion. After 72 h the growth medium was assayed for sugar content ($n = 3$ biological replicates per group, $n = 1$ from each progenitor mouse). **d**, HCT116 cells were treated with uniformly labelled ^{13}C -fructose or glucose and isotopologues for intracellular fructose were generated. Unless otherwise noted, each column represents an experimental group that received some form of glucose and fructose ($n = 3$ biological replicates per x -axis label). N, normoxia; H, hypoxia). **e, f**, Principal component analysis (PCA) (**e**) targeted heat map (**f**) of metabolomics data from HCT116 cells cultured at confluence in hypoxia for 36 h and then collected for LC–MS. PCA data are centred and unit-variance-scaled; heat map data are row-normalized ion abundances ($n = 3$ biological replicates per group; loading plots available in Supplementary Fig. 3). **g**, Pyruvate kinase activity was measured by enzymatic assay in lysates from HCT116 cells cultured in normoxia or hypoxia for 24 h with or without fructose. Assay wells were loaded with equal amounts of total protein for each group ($n = 3$ biological replicates per group). G6P, glucose 6-phosphate; G3P, glyceraldehyde 3-phosphate; 2PG, 2-phosphoglycerate; TCA: tri-carboxylic acid cycle; αKG , α -ketoglutarate; PA: phosphatidic acid; MG: monoacylglycerol; DG: diacylglycerol. **g**, Two-way ANOVA followed by Holm–Sidak post-hoc test for multiple comparisons. $*P < 0.05$. All error bars represent mean \pm s.e.m.

[Source data](#)

[Extended Data Fig. 7 The FBP-binding pocket of PKM2 is important for F1P inhibition.](#)

a, Simulated binding positions and residue interactions for FBP (left) and F1P (right) in the allosteric binding pocket of PKM2. Residues 482 and 489 are components of the FBP-activation loop that are predicted to interact with FBP but not F1P. **b**, Purified recombinant PKM2 (rPKM2) was incubated with the indicated metabolites and separated through a sucrose gradient (also containing the indicated metabolites). Fractions were removed from the gradients and analysed by SDS-PAGE and western blot for PKM2. FBP concentration, 100 μ M; F1P concentration, 500 μ M. **c**, Recombinant PKM2 incubated with the indicated metabolites was run on a gel filtration column and subjected to SDS-PAGE and Coomassie blue staining. FBP concentration during incubation and in the column, 100 μ M; F1P concentration, 500 μ M. **d, e**, The activity of recombinant PKL and the PKM2(R489L) mutant pre-incubated with the indicated metabolites was measured by enzymatic assay ($n = 3$ independent reaction wells per group). The residues responsible for PKM2 binding FBP are altered in these isoforms. **f–h**, Recombinant PKM2 mutants with alterations to the FBP-binding pocket were generated and assayed for PK activity with the indicated metabolites added at the incubation step. FBP concentration, 100 μ M; F1P concentration, 1 mM ($n = 2$ wells per data point). **i**, The activity of recombinant PK pre-incubated concurrently with the indicated metabolites or compounds was measured by enzymatic assay ($n = 3$ wells per group). **d, e**, One-way ANOVA followed by Holm–Sidak post-hoc test for multiple comparisons. * $P < 0.05$, ** $P < 0.01$, *** $P < 0.001$. Error bars represent mean \pm s.e.m. For gel source data, see Supplementary Fig. 1.

[Source data](#)

[**Extended Data Fig. 8 Fructose and pyruvate kinase activation modulate cell survival in hypoxia.**](#)

a, HCT116 cells were transduced with shRNA targeting a scrambled sequence (shScr) or PKM2 (shPKM2). Two weeks after transduction, parental cells as well as these modified lines were western blotted for the protein targets indicated on the left. Three separate shScr and shPKM2 subclones were analysed. Mouse gastrocnemius (gastroc.) muscle and liver tissue were used as PKM1 and PKLR controls, respectively. β -actin was used as a loading control. **b**, HCT116 cells expressing the indicated

shRNAs were cultured in normoxia or hypoxia with or without fructose and TEPP-46 (50 μ M) in the medium. Glucose was replenished daily, and confluence was monitored by live-cell imaging ($n = 3$ biological replicates per group). **c**, shScr or shPKM2-transduced HCT116 cells were cultured in hypoxia for 24 h with or without fructose or fructose and TEPP-46 (50 μ M). Total cell H₂O₂ was then measured using a luciferase-based assay ($n = 4$ biological replicates per group). **d**, Parental HCT116 cells were subjected to the same treatment as in **c**, but were cultured for 72 h in normoxia or hypoxia with daily glucose replenishment ($n = 4$ biological replicates per group). **e**, HCT116 cells cultured in hypoxia for 24 h were assayed for reduced thiols ($n = 5$ biological replicates per group). **f**, HCT116 cells cultured in hypoxia were provided with 10 mM glucose, 10 mM glucose with *N*-acetylcysteine (NAC) or 5 mM glucose and 5 mM fructose in the medium. After 144 h the viability of the adherent cells was measured ($n = 4$ biological replicates per group). **g**, HCT116 and DLD1 cells were subjected to varying levels of hypoxia for 24 h with fructose introduced in the medium either at the time the cells were placed in hypoxia ('+') or as pre-treatment ('PT+'), starting in the previous cell passage before plating the experiment and continuing through the hypoxic period (4 days total fructose exposure with the final 24 h in hypoxia). Cells were rapidly lysed at the conclusion of the experiment and analysed by western blot. **h**, HCT116 cells were exposed to hypoxia with or without fructose in the medium and LC-MS analysis was performed on the resulting polar extracts ($n = 3$ biological replicates per group). **i**, HCT116 cells were cultured in normoxia or hypoxia for 24 h with or without fructose. At the end of the experiment, medium samples were taken from each well and analysed by enzymatic assay for lactate content ($n = 3$ biological replicates per group). **c**, **d**, **i**, Two-way ANOVA followed by Holm–Sidak post-hoc test for multiple comparisons; **e**, Student's two-sided *t*-test; **f**, one-way ANOVA followed by Holm–Sidak post-hoc test for multiple comparisons. NS, not significant; * $P < 0.05$, ** $P < 0.01$, *** $P < 0.001$, **** $P < 0.0001$. All data are mean \pm s.e.m. where possible. For gel source data, see Supplementary Fig. 2.

[Source data](#)

Extended Data Fig. 9 Ablation of PKM2 in the villi results in upregulation of PKM1.

a, Representative intestines from 12-week-old mice examined by IHC for the indicated targets. Scale bar, 200 μ m. **b**, Mouse IEC lysates from wild-type mice, *Vil1*^{Cre/+}; *Pkm2*^{f/f} mice and wild-type mice treated with TEPP-46 were analysed by enzymatic assay for pyruvate kinase activity (mice per group: left to right: 5, 10, 5). Same final protein concentration in each reaction well. **c**, Wild-type and *Vil1*^{Cre/+}; *Pkm2*^{f/f} mice were euthanized and intestines were fixed and examined by IHC against PKM2 or PKM1, respectively. The left column shows proximal jejunum villi in each mouse, and the next two columns are high-magnification images of the distal and proximal villus in each mouse. The last column is colon epithelium. Blue arrows indicate nuclei with intense staining. Scale bars for each row are as indicated. **d**, Wild-type, *Khk*^{-/-} and *Vil1*^{Cre/+}; *Pkm2*^{f/f} mice were treated with H₂O or HFCS and the intestinal epithelium was examined by western blot. **e, f**, LDHA and ENO1 intensity were quantified relative to the β -actin loading control (mice per group: left to right: 3, 3, 3, 3, 2, 5). **g**, Serum triglyceride (T.G.) after a lipid challenge was measured in mice fed H₂O or 25% HFCS by daily oral gavage for two weeks. Units are normalized to the initial time point to highlight changes in blood triglyceride after the bolus (mice per group; top to bottom: 7, 6, 5, 5). **h**, After two weeks on the diet mice were euthanized, and the gonadal fat deposits were weighed. Units represent total gonadal depot fat mass as a percentage of total body mass, normalized to H₂O-treated mice (mice per group: left to right: 14, 14, 10, 5, 4, 5, 5). **i**, Liver was also collected and analysed for triglyceride content per gram of tissue (mice per group: left to right: 4, 4, 4, 5, 4, 5, 4). **b, h**, One-way ANOVA followed by Holm–Sidak post-hoc test for multiple comparisons; **e, f**, two-way ANOVA followed by Holm–Sidak post-hoc test for multiple comparisons. NS, not significant; * $P < 0.05$, ** $P < 0.01$; all data are mean \pm s.e.m. For gel source data, see Supplementary Fig. 2.

Source data

Extended Data Fig. 10 TEPP-46 ablates HFCS-induced villus elongation and tumour growth.

a, Wild-type mice provided with a daily oral gavage of HFCS or H₂O mixed with DMSO or TEPP-46 were euthanized after 10 days. Intestines were collected and analysed for mean villus length. **b**, Villi measurements for those same sections ($n = 5$ mice per group). **c**, Mice were treated with normal chow and water for two weeks, 25% HFCS by daily gavage for two weeks or HFCS for two weeks followed by HFCS with TEPP-46 (2 mg per kg per day) for another two weeks. At the conclusion of these treatments, the mice were euthanized and small intestine villus length was examined ($n = 5$ mice per group). **d**, Mice were fed the indicated diets by oral gavage for two weeks and serum triglyceride content was measured during the fasted state (mice per group: left to right: 8, 8, 5). **e**, Violin plot of gene expression data from GTEX (normal human colon epithelium) and TCGA (human colon adenocarcinoma) are shown for PKM. **f**, Samples of colon tumour (T) and matched normal epithelium (N) from patients with CRC were lysed and analysed by western blot for pyruvate kinase isoform expression and hypoxia markers. Mouse liver and gastrocnemius are included as controls. **g**, Pyruvate kinase activity was measured in lysates from patient samples before and after incubation with PK activator, and the ratio of initial versus activated activity is shown (tumour and adjacent normal tissue pairs from $n = 11$ individuals). **h–j**, Single channels and composite image of normal-diet-treated *Apc*^{Q1405X/+} intestinal tumours stained with DAPI, anti-CC3 and anti-pimonidazole and examined by immunofluorescence. **k–n**, Fly-out panels depicting areas of CC3 and pimonidazole colocalization both along the tumour periphery (**k**, **l**) and in the tumour core (**m**, **n**). Scale bars as indicated. **o**, Normal-diet-treated intestinal tumours were also examined by IHC using anti-GLUT5. Scale bar, 200 μ m. **p**, Representative H&E-stained Swiss-rolled intestines from *APC*^{Q1405X/+} mice treated with the indicated regimens. Arrows indicate tumours. Scale bars, 2 mm. **q**, **r**, H&E images of Swiss-rolled intestines were analysed for tumour burden. Each tumour in the section was counted and its cross-sectional area measured (mice per group: left to right: 6, 5, 4, 6). **b**, **q**, **r**, Two-way ANOVA followed by Holm–Sidak post-hoc test for multiple comparisons; **c**, **d**, one-way ANOVA followed by Holm–Sidak post-hoc test for multiple comparisons; **e**, **g**, two-sided Student’s *t*-test. NS, not significant; ** $P < 0.01$, *** $P < 0.001$, **** $P < 0.0001$. All error bars represent mean \pm s.e.m. For gel source data, see Supplementary Fig. 2.

Source data

Supplementary information

Supplementary Information

This file contains Supplementary Figures 1-4 and Supplementary Table 1.

Reporting Summary

Source data

Source Data Fig. 1

Source Data Fig. 2

Source Data Fig. 3

Source Data Extended Data Fig. 1

Source Data Extended Data Fig. 2

Source Data Extended Data Fig. 3

Source Data Extended Data Fig. 4

Source Data Extended Data Fig. 5

Source Data Extended Data Fig. 6

Source Data Extended Data Fig. 7

Source Data Extended Data Fig. 8

Source Data Extended Data Fig. 9

Source Data Extended Data Fig. 10

Rights and permissions

Reprints and Permissions

About this article

Cite this article

Taylor, S.R., Ramsamooj, S., Liang, R.J. *et al.* Dietary fructose improves intestinal cell survival and nutrient absorption. *Nature* **597**, 263–267 (2021). <https://doi.org/10.1038/s41586-021-03827-2>

- Received: 14 April 2020
- Accepted: 15 July 2021
- Published: 18 August 2021
- Issue Date: 09 September 2021
- DOI: <https://doi.org/10.1038/s41586-021-03827-2>

Fructose in the diet expands the surface of the gut and promotes nutrient absorption

- Patrícia M. Nunes
- Dimitrios Anastasiou

News & Views 18 Aug 2021

Dietary fructose acts on gut to increase nutrient uptake

- Olivia Tysoe

Research Highlight 27 Aug 2021

This article was downloaded by **calibre** from <https://www.nature.com/articles/s41586-021-03827-2>

| [Section menu](#) | [Main menu](#) |

- Article
- Open Access
- [Published: 28 July 2021](#)

Rapid and stable mobilization of CD8⁺ T cells by SARS-CoV-2 mRNA vaccine

- [Valerie Oberhardt](#)^{1,2 na1},
- [Hendrik Luxenburger](#) [ORCID: orcid.org/0000-0001-7182-8620](#)^{1,3 na1},
- [Janine Kemming](#)^{1,2 na1},
- [Isabel Schulien](#)^{1 na1},
- [Kevin Ciminski](#) [ORCID: orcid.org/0000-0001-5397-7497](#)⁴,
- [Sebastian Giese](#)⁴,
- [Benedikt Csernalabics](#)¹,
- [Julia Lang-Meli](#) [ORCID: orcid.org/0000-0003-0374-1093](#)^{1,3},
- [Iga Janowska](#)⁵,
- [Julian Staniek](#)^{2,5},
- [Katharina Wild](#)^{1,6},
- [Kristi Basho](#)¹,
- [Mircea Stefan Marinescu](#)¹,
- [Jonas Fuchs](#) [ORCID: orcid.org/0000-0003-1974-212X](#)⁴,
- [Fernando Topfstedt](#)⁵,
- [Ales Janda](#) [ORCID: orcid.org/0000-0001-5604-8378](#)⁷,
- [Oezlem Sogukpinar](#)¹,
- [Hanna Hilger](#)¹,
- [Katarina Stete](#)¹,
- [Florian Emmerich](#)⁸,
- [Bertram Bengsch](#) [ORCID: orcid.org/0000-0003-2552-740X](#)^{1,9},
- [Cornelius F. Waller](#) [ORCID: orcid.org/0000-0002-5777-0212](#)¹⁰,
- [Siegbert Rieg](#)¹,
- [Sagar](#)¹,
- [Tobias Boettler](#) [ORCID: orcid.org/0000-0002-1195-055X](#)^{1,11},
- [Katharina Zoldan](#)¹,
- [Georg Kochs](#) [ORCID: orcid.org/0000-0003-0187-559X](#)⁴,
- [Martin Schwemmle](#) [ORCID: orcid.org/0000-0002-2972-6855](#)⁴,

- [Marta Rizzi](#)⁵,
- [Robert Thimme](#) [ORCID: orcid.org/0000-0003-1417-4135](#)^{1 na2},
- [Christoph Neumann-Haefelin](#) [ORCID: orcid.org/0000-0001-7351-1387](#)^{1 na2} &
- [Maike Hofmann](#) [ORCID: orcid.org/0000-0001-8410-8833](#)^{1 na2}

[*Nature*](#) volume **597**, pages 268–273 (2021)

- 30k Accesses
- 822 Altmetric
- [Metrics details](#)

Subjects

- [Immunological memory](#)
- [Lymphocyte differentiation](#)
- [RNA vaccines](#)
- [SARS-CoV-2](#)
- [Viral infection](#)

Abstract

SARS-CoV-2 spike mRNA vaccines^{1,2,3} mediate protection from severe disease as early as ten days after prime vaccination³, when neutralizing antibodies are hardly detectable^{4,5,6}. Vaccine-induced CD8⁺ T cells may therefore be the main mediators of protection at this early stage^{7,8}. The details of their induction, comparison to natural infection, and association with other arms of vaccine-induced immunity remain, however, incompletely understood. Here we show on a single-epitope level that a stable and fully functional CD8⁺ T cell response is vigorously mobilized one week after prime vaccination with bnt162b2, when circulating CD4⁺ T cells and neutralizing antibodies are still weakly detectable. Boost vaccination induced a robust expansion that generated highly differentiated effector CD8⁺ T cells; however, neither the functional capacity nor the memory precursor T cell pool was affected. Compared with natural infection, vaccine-induced early memory T cells exhibited similar functional capacities but a different subset distribution. Our results indicate that CD8⁺ T cells are important effector cells, are expanded in the early protection window after prime vaccination, precede maturation of other effector arms of vaccine-induced immunity and are stably maintained after boost vaccination.

[Download PDF](#)

Main

The current SARS-CoV-2 vaccination campaign provides the unique opportunity to gain important insights into human CD8⁺ T cell biology in the context of prime or boost mRNA vaccination. Initial data revealed that all arms of adaptive immunity such as neutralizing antibodies, virus-specific CD4⁺ T cells with T helper 1 (T_H1) polarization and IFN γ -producing CD8⁺ T cells emerge after prime or boost vaccination^{4,5,9}. The onset of mRNA vaccine-mediated protection has been observed as early as 10–12 days after the first dose³. During this early phase, T cells and spike-specific antibodies are detectable^{7,8}, whereas neutralizing antibodies first appear after boost^{4,5,6,10,11}. These observations point towards a key role of vaccine-induced T cells in early protection after prime vaccination. Previous studies focused on the analysis of the overall vaccine-elicited spike-reactive T cell response^{4,5,7,8,12}; however, by this approach, the strength, dynamics and functional capacity are underestimated or even blurred in contrast to analyses performed at the single epitope level⁵. Here, we conducted continuous longitudinal analyses starting at baseline of prime vaccination until 3–4 months after boost on a single epitope level, to track the trajectories of bnt162b2 vaccine-elicited spike-specific CD8⁺ T cell responses in comparison to spike-specific CD4⁺ T cells, B cells, antibodies and their neutralizing activity.

Vaccine-elicited CD8⁺ T cells

We longitudinally collected peripheral blood mononuclear cells (PBMCs) and sera in 3–4-day intervals from 32 healthcare workers (Supplementary Table 1) that had not been previously infected with SARS-CoV-2, starting before prime until day 80–120 after boost (Extended Data Fig. 1a) and analysed the induction of spike-specific CD8⁺ T cells that target A*01/S₈₆₅, A*02/S₂₆₉ and A*03/S₃₇₈ epitopes in 4–5 individuals each (Extended Data Fig. 1b). All three epitopes are not highly conserved between SARS-CoV-2 and SARS-CoV-1, MERS or common cold coronaviruses (Extended Data Fig. 1c). Thus, the detected spike-specific CD8⁺ T cells indeed reflect a response to vaccination. The epitopes are not affected by the sequence variations present in the variants of concern (VOC) alpha, beta, gamma and delta (Extended Data Fig. 1c). The tested A*01-, A*02- and A*03-restricted CD8⁺ T cells that are part of a broader spike-specific CD8⁺ T cell response, however, proved to be dominant when analysing responses that span the whole S protein (Extended Data Fig. 1d). Ex vivo frequencies of A*01/S₈₆₅-, A*02/S₂₆₉- and A*03/S₃₇₈-specific CD8⁺ T cells were rather low after vaccination (Extended Data Fig. 2a). To increase the detection rate and to allow subsequent comprehensive profiling, we performed pMHC-I-tetramer enrichment (Extended Data Fig. 2b). We detected a rapid and substantial induction of spike-

specific CD8⁺ T cells that were present in 9 out of 13 tested donors already at days 6–8 and peaked in most donors 9–12 days post prime (dpp) (Fig. 1a). The strong CD8⁺ T cell activation was also reflected by high expression of CD38 and Ki-67 as early as days 6–8 in most cells (Fig. 1b,c and Extended Data Fig. 2c). Boost vaccination led to a further increase of CD8⁺ T cell frequencies that peaked 5–6 days post boost (dpb) with a subsequent slow contraction phase that reached nearly pre-boost frequencies at about 80–120 dpb (Fig. 1a). Post-boost and post-prime expansion were accompanied by effector T (T_{eff}) cell differentiation (high expression of Ki-67, CD38, granzyme B, PD-1, CD39, T-BET and TOX) (Fig. 1b and Extended Data Fig. 2c–e). However, *t*-distributed stochastic neighbour embedding (*t*-SNE) analysis revealed that CD8⁺ T_{eff} cells are qualitatively different at the peak expansion after boost (obtained at 5–6 dpb) compared with prime (obtained at 9–12 dpp) with a more consolidated cytotoxic effector cell phenotype (increased expression of T-BET, TOX and CD39) post boost (Extended Data Fig. 3a). This consolidated post-boost T_{eff} cell response is further supported by diffusion map analysis (Fig. 1c and Extended Data Fig. 3b). Specifically, diffusion map embedding revealed a continuous relationship of the longitudinally collected spike-specific CD8⁺ T cells after prime (depicted in reddish colours)/boost (depicted in grey colours) indicating a directed trajectory of the T_{eff} cell response.

Along the trajectory, CD8⁺ T cells exhibited the highest expression of PD-1, TOX, T-BET and CD38 after boost indicating profound activation and progressing differentiation (Fig. 1c and Extended Data Fig. 3b). Of note, a single vaccine dose also induced boost expansion and strong activation but lower TOX expression (Extended Data Fig. 4a–c) of spike-specific CD8⁺ T cells in individuals who recovered from mild to moderate infection approximately 12 months before vaccination (Supplementary Table 1).

Fig. 1: Vaccine-elicited epitope-specific CD8⁺ T cells.

 **figure1**

a, Calculated ex vivo frequency indicated at baseline (BL), dpp and dpb for spike-specific CD8⁺ T cells. Detection limit: 5×10^{-6} . **b**, Percentage of CD38, Ki-67 and T-BET^{hi} expressing spike-specific non-naive CD8⁺ T cells. **c**, Diffusion map showing flow cytometry data for A*02/S₂₆₉-specific CD8⁺ T cells in relation to dpp (shades of red) and dpb (shades of grey) in one individual. Expression levels of CD38, T-BET, TOX and BCL-2 are plotted on the diffusion map (blue denotes low expression; red denotes high expression). **d, e**, Calculated ex vivo frequencies of non-naive spike-specific CD8⁺ T cells expressing CD127 or TCF-1 for spike-specific CD8⁺ T cells. Line indicates median. *P* values determined by two-way ANOVA with main effects only comparing the effect of the different epitopes (P_e) and of time course (P_t).

Source data

We also assessed the induction of spike-specific memory precursor CD8⁺ T cells that are characterized by CD127, BCL-2 and TCF-1 expression and are relevant for maintaining the CD8⁺ T cell response^{13,14}. Roughly 20–30% of spike-specific CD8⁺ T cells expressed CD127 after prime followed by a transient reduction and subsequent strong increase after boost (Fig. 1d and Extended Data Fig. 4d). Expression dynamics of TCF-1 (Fig. 1e and Extended Data Fig. 4e) and BCL-2 (Extended Data Fig. 4f) were similar to CD127. However, the overall frequency of CD127⁺ (Fig. 1d) and TCF-1⁺ (Fig. 1e) spike-specific CD8⁺ T cells remained constant indicating a stable memory precursor pool induced already early after prime vaccination. Together, bnt162b2 vaccination vigorously induces a lasting spike-specific CD8⁺ T cell response rapidly after prime vaccination.

CD8⁺ T cell function after vaccination

After two weeks of peptide-specific in vitro expansion (Extended Data Fig. 5a, b), we detected higher frequencies of spike-specific CD8⁺ T cells after boost compared to prime vaccination (Extended Data Fig. 5c, d). However, the expansion index, a measure taking the input number of virus-specific CD8⁺ T cells into account was comparable for spike-specific CD8⁺ T cells after prime and boost vaccination, but differed between the A*01/S₈₆₅- A*02/S₂₆₉- and A*03/S₃₇₈-specific CD8⁺ T cell responses (Fig. 2a). Thus, the increased frequencies of spike-specific CD8⁺ T cells after peptide-specific expansion most probably result from the increased ex vivo frequencies after boost. We also assessed spike-specific production of IFNy and TNF (Extended Data Fig. 5e, f) and degranulation as indicated by CD107a expression (Extended Data Fig. 5g) in relation to the frequency of spike-specific CD8⁺ T cells after expansion as a measure of the effector function per cell. We observed reasonable effector capacity of circulating spike-specific CD8+ T cells obtained as early as 6–8 dpp (Fig. 2b–d). Similar to the expansion capacity, cytokine production and degranulation capacity remained nearly stable after boost compared to prime (Fig. 2b–e). Hence, functionally competent spike-specific CD8⁺ T cells that target different epitopes are substantially induced early after prime, and subsequent boost vaccination does not further increase their functional capacities in vitro.

Fig. 2: Functional capacities of vaccine-elicited spike-specific CD8⁺ T cells.



a, Expansion capacity of spike-specific CD8⁺ T cells after in vitro expansion. **b–d**, Percentage of CD8⁺ T cells producing effector molecules related to the frequency of spike-specific CD8⁺ T cells. **e**, Bar graphs depicting the polyfunctionality of spike-specific CD8⁺ T cells comparing 9–12 dpp and 5–6 dpb vaccination. Line indicates median. Bar charts show the median with interquartile range (IQR). *P* values

determined by two-way ANOVA with main effects only comparing the effect of the different epitopes and of time course (**a–d**) or by Mann–Whitney test with Holm–Šídák method (**e**).

[Source data](#)

CD4⁺ T cells, B cells and antibodies

Next, we longitudinally assessed circulating spike-specific CD4⁺ T cells that target DRB1*15:01/S₂₃₆ (Extended Data Fig. [6a](#)) after prime and boost vaccination in eight individuals (Supplementary Table [1](#)). The selected DRB1*15:01/S₂₃₆ epitope is unique for SARS-CoV-2 in comparison to SARS-CoV-1, MERS or common cold coronaviruses and conserved in circulating SARS-CoV-2 variants (B.1, alpha, gamma and delta) except for VOC beta (Extended Data Fig. [6c](#)). The frequencies of DRB1*15:01/S₂₃₆-specific CD4⁺ T cells were lower than CD8⁺ T cell responses but detectable after pMHCII tetramer-based enrichment (Extended Data Fig. [6b](#)). At baseline and in historic control samples (banked before August 2019), spike-specific CD4⁺ T cells were detectable with a primarily naive phenotype (Extended Data Fig. [6d,e](#)), which reflects the presence of antigen-unexperienced precursors. After vaccination, the proportion of naive spike-specific CD4⁺ T cells decreased, which suggests vaccine-induced activation (Extended Data Fig. [6e](#)). However, compared with CD8⁺ T cells, we observed a lower mobilization of circulating spike-specific CD4⁺ T cells indicated by a limited increase of frequencies (Fig. [3a](#)) and a smaller percentage of activated ICOS⁺CD38⁺⁺ or Ki-67⁺ subsets (Fig. [3b](#) and Extended Data Fig. [6f](#)). Most activated DRB1*15:01/S₂₃₆-specific CD4⁺ T cells exhibited a T_H1 cell phenotype (Fig. [3c](#)). In line with this observation, vaccine-induced spike-specific CD4⁺ T cells displayed a T_H1 cell rather than a follicular helper T (T_{FH}) cell phenotype (Extended Data Fig. [6g](#)).

Fig. 3: Circulating spike-specific CD4⁺ T cells, B cells and antibodies.

 **figure3**

a, Calculated ex vivo frequency of DRB1*15:01/S₂₃₆-specific CD4⁺ T cells ex vivo after pMHCII tetramer-based enrichment is indicated at baseline, dpp and dpb. Detection limit: 1.25×10^4 . **b**, ICOS⁺CD38⁺⁺ and Ki-67 expression within non-naive, DRB1*15:01/S₂₃₆-specific CD4⁺ T cells. **c**, ICOS⁺CD38⁺⁺ and Ki-67-expressing non-naive DRB1*15:01/S₂₃₆-specific CD4⁺ T cells on 9–12 dpp within T_{FH} (CXCR5⁺PD-1⁺) and T_H1-like (CXCR5[−]CXCR3⁺) cells. **d**, Anti-SARS-CoV-2 spike IgG at baseline and after vaccination (<35.2 binding antibody units (BAU) per ml: negative, ≥ 35.2 BAU ml⁻¹: positive; upper limit of quantification: 3,000 BAU ml⁻¹). **e**, Antibody neutralization activity is depicted as 50% plaque reduction neutralization tests (PRNT₅₀) at baseline, dpp and dpb vaccination for the SARS-CoV-2 variant B.1. Numbers indicate non-logarithmic median value. Detection limit: $5 \log_2$ PRNT₅₀. **f**, Percentage spike-specific B cells depicted at baseline, dpp and dpb as well as in natural infection for S1 and RBD. Detection limit: 0.05%. **g**, Secreted anti-SARS-CoV-2 spike IgG from PBMCs after in vitro stimulation with CpG and IL-2 (<35.2 BAU ml⁻¹: negative, ≥ 35.2 BAU ml⁻¹: positive). Line indicates median. Bar charts show the median and IQR. *P* values determined by one-way ANOVA with a mixed effects model comparing the effect of the time course (**a**, **b**, **f**), a Wilcoxon test (**c**) or a two-way ANOVA with main effects only comparing the effect of the different epitopes and of time course (**g**).

Source data

We then assessed the kinetics of the vaccine-induced humoral response. The distribution of peripheral B cell subpopulations was stable throughout prime or boost vaccination, with the exception of a progressively slight increase in antibody-secreting

cells (ASC) (Extended Data Fig. 7a, b). An increase in the frequency of CD95⁺ B cells was observed shortly after boost, which indicates ongoing B cell activation via CD40-mediated T cell help and/or B cell receptor activation within secondary lymphoid organs¹⁵ (Extended Data Fig. 7b). In line with the appearance of activated B cells in the periphery, we observed a progressive maturation of the serum antibody response with S1-specific IgM present after prime whereas S1-specific IgG reasonably detectable after boost (Fig. 3d and Extended Data Fig. 7c), coinciding with a high neutralization capacity in SARS-CoV-2 plaque reduction assays. More precisely, SARS-CoV-2 B.1 and VOC alpha were similarly well neutralized by post-boost sera, whereas the cross-neutralization activity against VOC beta was reduced approximately by a factor of 5 (Fig. 3e and Extended Data Fig. 7d). Neutralization capacity of post-boost sera was clearly increased compared with time point-matched mild infection (Extended Data Fig. 7e). In line with the progressive maturation of the antibody response, S1- and receptor-binding domain (RBD)-specific B cells (Extended Data Fig. 7f) largely remained below the ex vivo detection limit until the first week post boost (Fig. 3f). The delayed appearance of circulating S1-specific B cells was confirmed by polyclonal restimulation in vitro (Fig. 3g), which showed a limited presence of class-switched B cells that could produce S1-specific IgG before boost. S1-specific B cells were largely unswitched after prime (Extended Data Fig. 7g, h), also reflected by S1-specific IgM production upon polyclonal restimulation in vitro (Extended Data Fig. 7c), and acquired a memory phenotype after boost vaccination (Extended Data Fig. 7g, h). In addition, after boost vaccination, S1-specific B cells showed increased transferrin receptor (CD71) and CD95 expression (Extended Data Fig. 7g, h), which indicates their germinal centre origin¹⁶. Hence, bnt162b2 vaccination efficiently elicits a protective humoral immune response, composed of ASC and antigen-specific memory B cells that are mobilized to the periphery after boost.

Early memory CD8⁺ T cells

We compared vaccine-elicited spike-specific early memory CD8⁺ T cells (days post boost vaccination) with time point-matched T cells induced by natural infection (days post symptom onset) (Extended Data Fig. 8a). A*01/S₈₆₅-specific CD8⁺ T cell frequencies were similar after vaccination versus infection at all time points analysed. However, in comparison to vaccination, lower frequencies of A*02/S₂₆₉- and A*03/S₃₇₈-specific CD8⁺ T cells were detectable at days 80–120 (6 out of 30 (natural infected), 4 out of 28 (vaccinees) were obtained at days 120–200) after natural infection (Fig. 4a and Extended Data Fig. 8b). Phenotypic characteristics of early memory CD8⁺ T cells targeting A*01/S₈₆₅, A*02/S₂₆₉ and A*03/S₃₇₈ differed after vaccination versus natural infection as revealed by t-SNE analyses (Extended Data

Fig. 8c). Possible reasons for this include differences in their MHCI binding and presentation characteristics (Extended Data Fig. 1c). In addition, we also observed differences in T cell memory subset distribution (Fig. 4b and Extended Data Fig. 9a–c) of spike-specific early memory CD8⁺ T cells with higher fractions of more early differentiated subsets, for example, early differentiated (T_{ED}) and central memory (T_{CM}) T cells for A*01/S₈₆₅- and A*02/S₂₆₉-specific CD8⁺ T cells and transitional memory cells for A*03/S₃₇₈-specific CD8⁺ T cells after natural infection (80–120 dps). By contrast, higher frequencies of effector memory 1 T cells (T_{EM1}) were detectable after vaccination (80–120 dpb) (Fig. 4b). Spike-specific effector memory 2 and 3 T cells (T_{EM2} and T_{EM3}) and terminally differentiated effector memory T cells that expressed CD45RA (T_{EMRA}) were hardly detectable in the circulation (Extended Data Fig. 9c). Of note, the memory subset distribution of A*03/S₃₇₈-specific CD8⁺ T cells differed from A*01/S₈₆₅- and A*02/S₂₆₉-specific CD8⁺ T cells with only a minor fraction of T_{ED} and T_{CM} cells targeting A*03/S₃₇₈ reflecting an overall further differentiation towards effector memory subsets (Fig. 4b and Extended Data Fig. 9b). t-SNE analysis of concatenated expression data further supports qualitative differences of spike-specific CD8⁺ T cells obtained from the early memory phase (80–120 dpb/dps) after vaccination compared to natural infection being less pronounced for A*03/S₃₇₈-specific CD8⁺ T cells (Fig. 4c). For A*01/S₈₆₅-specific CD8⁺ T cells we also observed higher expression of TCF-1 and BCL-2 after natural infection (Extended Data Fig. 10a, b). Both t-SNE analysis and manual gating demonstrated a higher and prolonged CD38 expression on spike-specific CD8⁺ T cells after natural infection (Fig. 4c and Extended Data Fig. 10c). However, vaccine- and natural infection-associated expansion capacity and cytokine production of spike-specific CD8⁺ T cells were similar (Fig. 4d and Extended Data Fig. 10d, e). Hence, compared with natural infection, vaccine-associated spike-specific early memory CD8⁺ T cell populations exhibit similar functional capacities but a different subset distribution.

Fig. 4: Early memory CD8⁺ T cells after vaccination and natural infection.

 **figure4**

a, Calculated frequency of spike-specific CD8⁺ T cells 80–200 dpb vaccination or dps in natural infection. Detection limit: 5×10^{-6} . **b**, Distribution of spike-specific CD8⁺ T cell memory subsets 80–200 dpb/dps. **c**, t-SNE representation of flow cytometry data, depicting spike-specific CD8⁺ T cells more than 80 dpb vaccination and dps of natural infection (grey: vaccination, black: natural infection) for A*01/S₈₆₅- (vaccination $n = 9$, natural infection $n = 9$), A*02/S₂₆₉- (vaccination $n = 10$, natural infection $n = 8$) and A*03/S₃₇₈- (vaccination $n = 9$, natural infection $n = 9$) specific CD8⁺ T cells. **d**, Left, expansion index of spike-specific CD8⁺ T cells after in vitro expansion at 80–200 dpb/dps. Right, percentage of IFN γ -producing CD8⁺ T cells related to the frequency of spike-specific CD8⁺ T cells after in vitro expansion at 80–200 dpb/dps. T_{TM}, transitional memory T cells. Bar charts show the median with IQR. P values were determined by Mann–Whitney test with Holm–Šídák method.

[Source data](#)

Discussion

In summary, a robust, stable and fully functional spike-specific CD8⁺ T cell response is elicited already after prime vaccination at a time point when neutralizing antibodies were hardly detectable and coincides with the protective effect observed for mRNA vaccines that starts at 10–12 dpp^{2,3}. In contrast to CD8⁺ T cells, peak mobilization of neutralizing antibodies and antigen-specific B cells to the periphery was first detectable after boost. This is in line with previous reports^{4,7,11,12} and most probably

represents maturation of the response in secondary lymphoid organs¹⁷ with subsequent release to the circulation. After boost, highly cross-neutralizing antibodies are present in the sera, clearly adding a major protective effector mechanism on top of the early-mobilized spike-specific CD8⁺ T cell response. The humoral and CD8⁺ T cell response are potentially coordinated by early elicited spike-reactive CD4⁺ T cells⁸ that underwent a limited boost expansion after second dose mRNA vaccination supporting their coordinating role.

Fully functional vaccine-elicited early memory CD8⁺ T cells patrol the periphery for SARS-CoV-2 at least within the first months. The functional capacity of spike-specific early memory CD8⁺ T cells is similar after vaccination and natural infection up to 3–4 months after boost or symptom onset. Compared with natural infection, however, the early memory pool of spike-specific CD8⁺ T cells after vaccination exhibits a different memory T cell subset distribution that may affect long-term maintenance characteristics¹⁸. This difference may be caused by differential duration and location of antigen contact and different inflammatory responses after vaccination versus infection^{19,20}, as indicated by a lower CD38 expression on early memory spike-specific CD8⁺ T cells after vaccination compared with natural infection^{4,21}. Follow-up studies including larger cohorts of vaccinees and SARS-CoV-2 convalescent individuals are clearly required to assess longevity of CD8⁺ T cell immunity. Our study was limited to circulating spike-specific adaptive immunity, and did not address local immunity at the viral entry site, the respiratory tract. However, our data provide insights into the protective mechanisms that underlie bnt162b2 vaccination with implications for the development of vaccination strategies against emerging pathogens and cancer.

Methods

Study cohort

In total, 32 healthcare workers that received a prime and boost vaccination with the mRNA vaccine bnt162b2/Comirnaty, 59 convalescent individuals following a mild course of SARS-CoV-2 infection, 2 convalescent individuals given one dose of bnt162b2/Comirnaty 12 months after infection, and historic controls (sampled before August 2019) of 8 healthy individuals were recruited at the Freiburg University Medical Center, Germany. A mild course of infection was characterized by clinical symptoms without respiratory insufficiency. SARS-CoV-2 infection was confirmed by positive PCR testing from oropharyngeal swab and/or SARS-CoV-2 spike IgG positive antibody testing. Donor characteristics are summarized in Supplementary Table 1. HLA-typing was performed by next-generation sequencing and is listed in Supplementary Table 1.

Ethics

Written informed consent was obtained from all participants and the study was conducted according to federal guidelines, local ethics committee regulations (Albert-Ludwigs-Universität, Freiburg, Germany; vote: 322/20, 21-1135 and 315/20) and the Declaration of Helsinki (1975).

PBMC isolation

Venous blood samples were collected in EDTA-anticoagulated tubes. PBMCs were isolated with lymphocyte separation medium density gradients (Pancoll separation medium, PAN Biotech GmbH) and stored at -80°C . Frozen PBMCs were thawed in complete medium (RPMI 1640 supplemented with 10% fetal calf serum, 1% penicillin/streptomycin and 1.5% HEPES buffer 1 M (all additives from Thermo Scientific) containing 50 U ml $^{-1}$ benzonase (Sigma).

Sequence alignment

Sequence homology analyses were performed in Geneious Prime 2020.0.3 (<https://www.geneious.com/>) using Clustal Omega 1.2.2 alignment with default settings²². Reference genomes of human coronaviruses 229E (NC_002645), HKU1 (NC_006577), NL63 (NC_005831), OC43 (NC_006213), MERS (NC_019843), SARS-CoV-1 (NC_004718) and SARS-CoV-2 (MN908947.3) were downloaded from NCBI database. Spike proteins of human coronaviruses were aligned according to their homology (amino acid level). Analysed spike SARS-CoV-2 epitopes were then mapped to the corresponding protein alignment. Correspondingly mutation analyses were performed with the spike protein of VOC alpha, beta, gamma and delta.

In vitro expansion and intracellular IFN γ staining with overlapping peptides

A total of 182 overlapping peptides that spanned the SARS-CoV-2 spike sequence (Gene Bank Accession code MN908947.3) were synthesized as 18-mers overlapping by 11 amino acids with a free amine NH₂ terminus and a free acid COOH terminus with standard Fmoc chemistry and a purity of >70% (Genaxxon Bioscience). In vitro expansion with OLPs was performed as follows: 20% of the PBMCs were stimulated with a pool of all 181 SARS-CoV-2 spike OLPs (10 $\mu\text{g ml}^{-1}$) for 1 h at 37°C , washed and co-cultured with the remaining PBMCs in RPMI medium supplemented 20 U ml $^{-1}$ with recombinant IL-2. On day 10, intracellular IFN γ staining was performed with pooled OLPs (45 pools with 4 OLP each). Therefore, cells were re-stimulated with OLP pools (50 μM), DMSO as negative control or PMA and ionomycin as

positive control in the presence of brefeldin A and IL-2. After 5 h of incubation at 37 °C, cells were stained for surface markers (CD8⁺, CD4⁺; Viaprobe) and intracellular markers (IFNγ). Subsequently, on day 12 the single overlapping peptides of positive pools were tested by intracellular cytokine staining. Viral amino acid sequences of positive individual OLPs were analysed for pre-described minimal epitopes or the best HLA-matched predicted candidate using the Immune Epitope Database website (using two prediction algorithms ANN 4.0 and NetMHCpan EL 4.1²³ for 8-mer, 9-mer and 10-mer peptides with half-maximal inhibitory concentration (IC₅₀) of <500 nM).

Peptides and tetramers for T cell analysis

Peptides were synthesized with an unmodified N terminus and an amidated C terminus with standard Fmoc chemistry and a purity of >70% (Genaxxon Bioscience). Peptide was loaded on HLA class I easYmers (immunAware) according to manufacturer's instructions (A*01/S₈₆₅ LTDEMIAQY, A*02/S₂₆₉ YLQPRTFLL and A*03/S₃₇₈ KCYGVSPYK). SARS-CoV-2 peptide-loaded HLA class I tetramers were produced by conjugation of biotinylated peptide-loaded HLA class I easYmers with phycoerythrin (PE)-conjugated streptavidin (Agilent) according to the manufacturer's instructions. A SARS-CoV-2-specific HLA class II custom tetramer (DRB1*15:01/S₂₃₆ TRFQTLLALHRSYLT) was obtained from (MBL).

In vitro expansion of spike-specific CD8⁺ T cells and assessment of effector function

Approximately 1.5 × 10⁶ PBMCs were stimulated with A*01/S₈₆₅, A*02/S₂₆₉ or A*03/S₃₇₈-specific peptides (5 μM) and anti-CD28 monoclonal antibody (0.5 μg ml⁻¹, BD) and expanded for 14 days in complete RPMI culture medium containing rIL-2 (20 IU ml⁻¹, StemCell Technologies). Intracellular cytokine production and degranulation was assessed with spike-specific peptides (15 μM) in the presence of anti-CD107a (H4A3, 1:100) (BD Bioscience) for 1 h at 37 °C. Afterwards, brefeldin A (GolgiPlug, 0.5 μl ml⁻¹) and monensin (GolgiStop, 0.5 μl ml⁻¹) (all BD Biosciences) were added for additional 5 h, followed by surface and intracellular staining. The expansion capacity was calculated based on peptide-loaded HLA class I tetramer staining as previously described²⁴.

Magnetic bead-based enrichment of spike-specific CD8⁺ T cells

Spike-specific CD8⁺ T cells were enriched as previously described²⁵. In brief, 1 × 10⁷–2 × 10⁷ PBMCs (with an average of 15.7% CD8⁺ T cells) were labelled with

PE-coupled peptide-loaded HLA class I tetramers for 30 min. Enrichment was then performed using anti-PE beads with MACS technology (Miltenyi Biotec) according to the manufacturer's instructions. Subsequently, enriched spike-specific CD8⁺ T cells were analysed by multiparametric flow cytometry and frequencies of spike-specific CD8⁺ T cells were calculated as described before²⁵. Only enriched samples with ≥ 5 spike-specific CD8 T cells were included in further analyses, resulting in a detection limit of 5×10^{-6} .

Magnetic bead-based enrichment of spike-specific CD4⁺ T cells

Enrichment of spike-specific CD4⁺ T cells was adapted from the method described previously²⁵. In brief, 1.5×10^7 – 2×10^7 PBMCs of DRB1*15:01-positive donors were labelled with PE-coupled peptide-loaded MHC class II tetramers for 40 min. Then, 5 µl was taken from 1,000 µl pre-enriched sample (1:200) and used for subsequent flow cytometric staining. Subsequent enrichment was performed with anti-PE beads using MACS technology (Miltenyi Biotec) according to the manufacturer's protocol.

Enriched spike-specific CD4⁺ T cells and the pre-enriched sample were used for flow cytometric staining. The complete pre-enriched and enriched samples were recorded. Only enriched samples with ≥ 5 spike-specific CD4⁺ T cells were included in further analyses. The frequency of spike-specific CD4⁺ T cells was calculated as follows: Absolute number of spike-specific CD4⁺ T cells (enriched sample) divided by the absolute number of CD4⁺ T cells (pre-enriched sample) $\times 200$. The detection limit as a frequency was calculated as follows: 5 spike-specific CD4⁺ T cells (enriched sample) divided by the mean number of CD4⁺ T cells (pre-enriched sample) throughout all tested donors $\times 200$.

Multiparametric flow cytometry for T cell analysis

The following antibodies were used for multiparametric flow cytometry: anti-CCR7-PE-CF594 (150503, 1:50), anti-CCR7-BUV395 (3D12, 1:25), anti-CD4-BV786 (L200, 1:200), anti-CD8-BUV395 (RPA-T8, 1:400), anti-CD8-BUV510 (SK1, 1:100), anti-CD8-APC (SK-1, 1:200), anti-CD11a-BV510 (HI111, 1:25), anti-CD28-BV421 (CD28.2, 1:100), anti-CD38-APC-R700 (HIT2, 1:400), anti-CD38-BUV737 (HB7, 1:200), anti-CD39-BV650 (TU66, 33:1), anti-CD45RA-BUV496 (HI100, 1:800), anti-CD45RA-BUV737 (HI100, 1:200), anti-CD69-BUV395 (FN50, 1:50), anti-CD107a-APC (H4A3, 1:100), anti-CD127-BUV737 (HIL-7R-M21, 1:50), anti-CD127-BV421 (HIL-7R-M21, 3:100), anti-EOMES-PerCP-eF710 (WD1928, 1:50), anti-Granzyme B-PE-CF594 (GB11, 1:100), anti-ICOS-BV711 (DX29, 1:100), anti-IFN- γ -FITC (25723.11, 1:8), anti-IL-21-PE (3A3-N2.1, 1:25), anti-PD-1-BV605 (EH12.1, 1:50), anti-PD-1-PE-Cy7 (EH12.2H7, 1:200), anti-PD-1-BV786 (EH12.1, 1013122, 3:100), anti-T-BET-PE-CF594 (O4-46,93533305, 3:100), anti-TNF-PE-Cy7 (Mab11, 1:400)

(BD Biosciences), anti-BCL-2-BV421 (100, 1:200), anti-CCR7-BV785 (G043H7, 1:50), anti-CD4-AlexaFluor700 (RPA-T4, 300526, 1:200), anti-CD25-BV650 (BC96, 1:33), anti-CD57-BV605 (QA17A04, 1:100), anti-CD127-BV605 (A019D5, 3:100), anti-CXCR3-PerCP-Cy5.5 (G025H7, 1:33), anti-CXCR3-BV510 (G025H7, 3:100), anti-CXCR5-BV421 (J252D4, 1:100), anti-IL-2-PerCP-Cy5.5 (MQ1-17H12, 1:100), anti-Ki-67-BV711 (Ki-67, 1:200), anti-Ki-67-PE-Cy7 (Ki-67, 1:200) (BioLegend), anti-TCF-1-AlexaFluor488 (C63D9, 1:100) (Cell Signaling), anti-CD14-APC-eFluor780 (61D3, 1:400), anti-CD19-APC-eFluor780 (HIB19, 1:400), anti-CD27-FITC (0323, 1:100), anti-KLRG1-BV711 (13F12F2, 1:50), anti-T-BET-PE-Cy7 (4B10, 1:200), anti-TOX-eFluor660 (TRX10, 1:100) (Thermo Fisher), anti-CD45RA-PerCP-Cy5.5 (HI100, 3:100) (Invitrogen). For live/dead discrimination a fixable Viability Dye (APC-eFluor780 1:200, 1:400) (Thermo Fisher) or ViaProbe (7-AAD, 1:33) (BD Biosciences)) was used. FoxP3/Transcription Factor Staining Buffer Set (Thermo Fisher) and Fixation/Permeabilization Solution Kit (BD Biosciences) were used according to the manufacturer's protocol to stain for intranuclear and cytoplasmic molecules, respectively. After fixation of cells in 2% paraformaldehyde (PFA, Sigma), analyses were performed on FACSCanto II, LSRFortessa with FACSDiva software version 10.6.2 (BD) or CytoFLEX (Beckman Coulter) with CytExpert Software version 2.3.0.84. Data were analysed with FlowJo 10.6.2 (Treestar).

Dimensional reduction of multiparametric flow cytometry data

Dimensionality reduction of multiparametric flow cytometry data was done with R version 4.0.2 using the Bioconductor (release (3.11)) CATALYST package²³. The analyses were performed on gated virus-specific CD8+ T cells including the markers CD69, CD45RA, BCL-2, PD1, CD25, Ki-67, TCF-1, EOMES, CCR7, T-BET, TOX and CD38. Downsampling of cells to 100 or 200 cells (*t*-SNE or diffusion maps) was performed before dimensionality reduction to facilitate the visualization of different samples. Marker intensities were transformed by arcsinh (inverse hyperbolic sine) with a cofactor of 150. Dimensionality reduction on the transformed data was achieved by *t*-SNE and diffusion map visualization.

S1- and RBD-tetramerization for B cell analysis

A biotinylated form of recombinant S1 and RBD proteins (BioLegend) were tetramerized by addition of PE-conjugated or BV421-conjugated streptavidin (BioLegend) and used for B cell tetramer staining assays. In brief, streptavidin-PE or streptavidin-BV21 was added in an amount that equals one-fifth of the monomer substrate amount. The streptavidin was added in five equal portions to the monomer and incubated each time at 4 °C for 20 min on a shaker. The tetramers were filled up to 100 µl with 0.1% BSA in PBS and stored at 4 °C.

Multiparametric flow cytometry for B cell analysis

Phenotype of vaccinated individuals' PBMCs was determined by flow cytometry with the following antibodies: anti-CD20-BV510 (2H7, 1:80), anti-IgM-BV605 (MHM-88, 1:200), anti-CD71-FITC (CY1G4, 1:1000), anti-CD95-PE-Dazzle594 (DX2, 1:50), anti-CD24-FITC (ML5, 1:100), anti-CD38-PE-Cy7 (HB-7, 1:300), anti-BAFF-R-AF647 (11C1, 1:100), anti-CD19-APC-Cy7 (HIB19, 1:150) (BioLegend); anti-IgG-BV650 (G18-145, 1:600), anti-CD27-BV786 (L128, 1:100), anti-CD69-BV480 (FN50, 1:200) (BD Biosciences); anti-IgA-PerCP (polyclonal, 1:200) (Jackson ImmunoResearch); anti-CD3-SB-436 (OKT3, 1:200), anti-CD33-Super Bright 436 (WM-53, 1:50), anti-IgD-PerCP-eFluor 710 (IA6-2, 1:200) (Invitrogen). Dead cell exclusion was performed by Zombie NIR Fixable Viability Kit (Biolegend, 1:800). Multiparametric flow cytometry data was collected on Cytek Aurora with SpectroFlo Software version 2.2.0.3.

In vitro PBMCs activation and ELISA

PBMCs of vaccinated individuals and patients with a history of SARS-CoV-2 infection were plated at 0.5×10^6 cells ml $^{-1}$ and polyclonally stimulated for 9 days with thiol-modified CpG (0.25 μ M, TCGTCGTTTGTCTTTGTCGTT) and hIL-2 (100 ng/ml, Immunotools). At day 9, the supernatants of the in vitro culture were cleared from debris by centrifugation and used to determine the presence of SARS-CoV-2 spike-specific IgG antibodies (Anti-SARS-CoV-2-QuantiVac-ELISA (IgG), Euroimmun) according to the manufacturer's instructions. To detect S1 specific IgM, supernatant of the in vitro culture and serum of vaccinated individuals was incubated on a S1 pre-coated plate (Anti-SARS-CoV-2, Euroimmun). Bound IgM was detected with alkaline phosphatase-conjugated anti-human IgM (Jackson ImmunoResearch), and developed with p-nitrophenyl phosphate (Sigma-Aldrich) in DEA buffer.

Serum IgG determination

SARS-CoV-2-specific antibodies were determined by Anti-SARS-CoV-2-QuantiVac-ELISA (IgG) from Euroimmun detecting anti-SARS-CoV-2 spike IgG (anti-SARS-CoV-2 S IgG; <35.2 BAU ml $^{-1}$: negative, ≥ 35.2 BAU ml $^{-1}$: positive) according to the manufacturer's instructions.

Neutralization assay

Samples of vaccinated and convalescent individuals were tested in a plaque reduction neutralization assay. In brief, VeroE6 cells were seeded in 12-well plates at a density of 2.8×10^5 cells per well 24 h before infection. Serum samples were diluted at ratios

of 1:16, 1:32, 1:64, 1:128, 1:256, 1:512 and 1:1,024 in 50 µl PBS total volume. For each sample, one negative control was included (PBS without serum). Diluted sera and negative controls were subsequently mixed with 90 plaque-forming units (PFU) of authentic SARS-CoV-2 (either B.1, alpha or beta variant) in 50 µl PBS (1,600 PFU ml⁻¹) resulting in final sera dilution ratios of 1:32, 1:64, 1:128, 1:256, 1:512, 1:1,024 and 1:2,048. After incubation at room temperature for 1 h, 400 µl PBS was added to each sample and the mixture was subsequently used to infect VeroE6 cells. After 1.5 h of incubation at room temperature, inoculum was removed and the cells were overlaid with 0.6% Oxoid-agar in DMEM, 20 mM HEPES (pH 7.4), 0.1% NaHCO₃, 1% BSA and 0.01% DEAE-Dextran. Cells were fixed 72 h after infection using 4% formaldehyde for 30 min and stained with 1% crystal violet upon removal of the agar overlay. PFU were counted manually. Plaques counted for serum-treated wells were compared to the average number of plaques in the untreated negative controls, which were set to 100%. The PRNT₅₀ value was calculated using a linear regression model in GraphPad Prism 9 (GraphPad Prism Software).

Statistics

Statistical analysis was performed with GraphPad Prism 9 (GraphPad Prism Software). Statistical significance was assessed by one-way ANOVA with a mixed effects model, two-way ANOVA with main effects only, two-tailed Mann–Whitney test with Holm–Šídák multiple comparison, Wilcoxon test and Spearman correlation. Analyses were performed in independent experiments. Statistics was performed for Figs. 1a, b, d, e, 2, Extended Data Figs. 2d, e, 4d, e, f, 5c in n = 5 longitudinally analysed vaccines for A*01/S₈₆₅ and A*02/S₂₆₉ and n = 4 longitudinally analysed vaccines for A*03/S₃₇₈; for Fig. 3a, b, c, Extended Data Fig. 6e, g in n = 8 longitudinally analysed vaccinees for DRB1*15:01/S₂₃₆; for Fig. 3d, e in 8 longitudinally analysed vaccines; for Fig. 3f, g, Extended Data Fig. 7c in n = 8 longitudinally analysed vaccines and n = 8 donors with a history of natural SARS-CoV-2 infection cross-sectionally; for Fig. 4a, b, d, Extended Data Fig. 10 in n = 11 cross-sectionally analysed vaccinees for A*01/S₈₆₅ at 80–120 dpb, n = 9 cross-sectionally analysed vaccinees for A*02/S₂₆₉ at 80–120 dpb, n = 8 cross-sectionally analysed vaccinees for A*03/S₃₇₈ at 80–120 dpb, n = 10 donors with a history of natural SARS-CoV-2 infection cross-sectionally for A*01/S₈₆₅ 80–120 dpb, n = 10 donors with a history of natural SARS-CoV-2 infection cross-sectionally for A*02/S₂₆₉ 80–120 dpb and n = 10 donors with a history of natural SARS-CoV-2 infection cross-sectionally for A*03/S₃₇₈ 80–120 dpb; Extended Data Fig. 7b, h in n = 8 longitudinally analysed vaccines; Extended Data Fig. 7d in n = 7 longitudinally analysed vaccinees; for Extended Data Fig. 7e in n = 16 donors with a history of natural SARS-CoV-2 infection cross-sectionally/longitudinally; for Extended Data

Fig. 8b, 9b, c in $n = 5$ longitudinally analysed vaccinees for A*01/S865 ($n = 5$ at 20–40 dpb and 4 at 40–80 dpb), $n = 5$ longitudinally analysed vaccinees for A*02/S269 ($n = 5$ at 20–40 dpb and 4 at 40–80 dpb), $n = 4$ longitudinally analysed vaccinees for A*03/S378 ($n = 4$ at 20–40 dpb and 2 at 40–80 dpb), $n = 9$ donors with a history of natural SARS-CoV-2 infection cross-sectionally for A*01/S865 ($n = 5$ at 20–40 dpb, 4 at 40–80 dpb), $n = 8$ donors with a history of natural SARS-CoV-2 infection cross-sectionally for A*02/S269 ($n = 4$ at 20–40 dpb, 4 at 40–80 dpb), $n = 7$ donors with a history of natural SARS-CoV-2 infection cross-sectionally for A*03/S378 ($n = 4$ at 20–40 dpb, 3 at 40–80 dpb). * $P < 0.05$; ** $P < 0.01$; *** $P < 0.001$; **** $P < 0.0001$.

Reporting summary

Further information on research design is available in the [Nature Research Reporting Summary](#) linked to this paper.

Data availability

Patient-related data not included in the paper were generated as part of clinical examination and may be subject to patient confidentiality. Further raw and supporting data conflicting with patient confidential, are available from the corresponding authors upon request (response within two weeks). Requests for these data will be reviewed by the corresponding authors to verify if the request is subject to any intellectual property or confidentiality obligations. Reference viral sequences SARS-CoV-2 (MN908947.3) <https://www.ncbi.nlm.nih.gov/nuccore/MN908947>, 229E (NC_002645) https://www.ncbi.nlm.nih.gov/nuccore/NC_002645, HKU1 (NC_006577) https://www.ncbi.nlm.nih.gov/nuccore/NC_006577, NL63 (NC_005831) https://www.ncbi.nlm.nih.gov/nuccore/NC_005831, OC43 (NC_006213) https://www.ncbi.nlm.nih.gov/nuccore/NC_006213, MERS (NC_019843) https://www.ncbi.nlm.nih.gov/nuccore/NC_019843, SARS-CoV-1 (NC_004718) https://www.ncbi.nlm.nih.gov/nuccore/NC_004718) were downloaded from the NCBI database (<https://www.ncbi.nlm.nih.gov/>). Any data and materials that can be shared will be released via a Material Transfer Agreement. [Source data](#) are provided with this paper.

Code availability

R code to reproduce the analyses of multiparametric flow-cytometry data are available at https://github.com/sagar161286/SARSCoV2_specific_CD8_Tcells.

References

1. 1.

Krammer, F. SARS-CoV-2 vaccines in development. *Nature* **586**, 516–527 (2020).

2. 2.

Baden, L. R. et al. Efficacy and safety of the mRNA-1273 SARS-CoV-2 vaccine. *N. Engl. J. Med.* **384**, 403–416 (2021).

3. 3.

Polack, F. P. et al. Safety and efficacy of the BNT162b2 mRNA COVID-19 vaccine. *N. Engl. J. Med.* **383**, 2603–2615 (2020).

4. 4.

Sahin, U. et al. COVID-19 vaccine BNT162b1 elicits human antibody and T_H1 T cell responses. *Nature* **586**, 594–599 (2020).

5. 5.

Sahin, U. et al. BNT162b2 vaccine induces neutralizing antibodies and poly-specific T cells in humans. *Nature* **595**, 572–577 (2021).

6. 6.

Skelly, D. T. et al. Vaccine-induced immunity provides more robust heterotypic immunity than natural infection to emerging SARS-CoV-2 variants of concern. Preprint at <https://doi.org/10.21203/rs.3.rs-226857/v1> (2021).

7. 7.

Kalimuddin, S. et al. Early T cell and binding antibody responses are associated with COVID-19 RNA vaccine efficacy onset. *Med (NY)* **2**, 682–688 (2021).

8. 8.

Painter, M. M. et al. Rapid induction of antigen-specific CD4⁺ T cells guides coordinated humoral and cellular immune responses to SARS-CoV-2 mRNA vaccination. Preprint at <https://doi.org/10.1101/2021.04.21.440862> (2021).

9. 9.

Widge, A. T. et al. Durability of responses after SARS-CoV-2 mRNA-1273 vaccination. *N. Engl. J. Med.* **384**, 80–82 (2021).

10. 10.

Collier, D. A. et al. Sensitivity of SARS-CoV-2 B.1.1.7 to mRNA vaccine-elicited antibodies. *Nature* **593**, 136–141 (2021).

11. 11.

Wang, Z. et al. mRNA vaccine-elicited antibodies to SARS-CoV-2 and circulating variants. *Nature* **592**, 616–622 (2021).

12. 12.

Goel, R. R. et al. Distinct antibody and memory B cell responses in SARS-CoV-2 naïve and recovered individuals following mRNA vaccination. *Sci. Immunol.* **6**, eabi6950 (2021).

13. 13.

Joshi, N. S. et al. Inflammation directs memory precursor and short-lived effector CD8⁺ T cell fates via the graded expression of T-bet transcription factor. *Immunity* **27**, 281–295 (2007).

14. 14.

Boudousquié, C. et al. Differences in the transduction of canonical Wnt signals demarcate effector and memory CD8 T cells with distinct recall proliferation capacity. *J. Immunol.* **193**, 2784–2791 (2014).

15. 15.

Turner, J. S. et al. SARS-CoV-2 mRNA vaccines induce persistent human germinal centre responses. *Nature* <https://doi.org/10.1038/s41586-021-03738-2> (2021).

16. 16.

Ellebedy, A. H. et al. Defining antigen-specific plasmablast and memory B cell subsets in human blood after viral infection or vaccination. *Nat. Immunol.* **17**, 1226–1234 (2016).

17. 17.

Lederer, K. et al. SARS-CoV-2 mRNA vaccines foster potent antigen-specific germinal center responses associated with neutralizing antibody generation. *Immunity* **53**, 1281–1295 (2020).

18. 18.

Akondy, R. S. et al. Origin and differentiation of human memory CD8 T cells after vaccination. *Nature* **552**, 362–367 (2017).

19. 19.

Kaech, S. M. & Ahmed, R. Memory CD8⁺ T cell differentiation: initial antigen encounter triggers a developmental program in naïve cells. *Nat. Immunol.* **2**, 415–422 (2001).

20. 20.

Romero, P. et al. Four functionally distinct populations of human effector-memory CD8⁺ T lymphocytes. *J. Immunology* **178**, 4112–4119 (2007).

21. 21.

Schulien, I. et al. Characterization of pre-existing and induced SARS-CoV-2-specific CD8⁺ T cells. *Nat. Med.* **27**, 78–85 (2021).

22. 22.

Sievers, F. et al. Fast, scalable generation of high-quality protein multiple sequence alignments using Clustal Omega. *Mol. Syst. Biol.* **7**, 539 (2011)

23. 23.

Reynisson, B., Alvarez, B., Paul, S., Peters, B. & Nielsen, M. NetMHCpan-4.1 and NetMHCIIpan-4.0: improved predictions of MHC antigen presentation by concurrent motif deconvolution and integration of MS MHC eluted ligand data. *Nucleic Acids Res.* **48** (W1), W449–W454 (2020).

24. 24.

Wieland, D. et al. TCF1⁺ hepatitis C virus-specific CD8⁺ T cells are maintained after cessation of chronic antigen stimulation. *Nat. Commun.* **8**, 15050 (2017).

25. 25.

Alanio, C., Lemaitre, F., Law, H. K., Hasan, M. & Albert, M. L. Enumeration of human antigen-specific naive CD8⁺ T cells reveals conserved precursor frequencies. *Blood* **115**, 3718–3725 (2010).

Acknowledgements

We thank all donors for participating in the current study and the FREEZE-Biobank Center for biobanking (Freiburg University Medical Center) and the Medical Faculty for support. The study was funded by the Federal Ministry of Education and Research (grant number 01KI2077 to G.K., M.H., M.S. and R.T.) and by COVID-19 research grants of the Ministry of Science, Research and Art, State of Baden-Wuerttemberg (COVID-19/AZ.: AZ33-7533-6-10/89/8 to C.N.-H. and B.B.). The presented work was also supported by CRC/TRR 179-Project 01 and CRC 1160-Project A02 (to R.T.), CRC/TRR 179-Project 02 and CRC 1160-Project A06 (to C.N.-H.), CRC 1160-Project B02 (M.R.), CRC/TRR 179-Project 04 (to T.B.), CRC/TRR 179-Project 20 and CRC 1160-Project A02 (to M.H.), CRC/TRR 179-Project 21, CRC 1160-Project A03 and BE-5496/5-1 (to B.B.) of the German Research Foundation (DFG; TRR 179 project no. 272983813; CRC 1160 project no. 256073931). M.H. was supported by a Margarete von Wrangell fellowship (State of Baden-Wuerttemberg). T.B. was supported by the Berta-Ottenstein Programme, Faculty of Medicine, University of Freiburg. H.L. was supported by the IMM-PACT-Programme for Clinician Scientists, Department of Medicine II, Medical Center – University of Freiburg and Faculty of Medicine, University of Freiburg. The funding body had no role in the decision to write or submit the manuscript.

Author information

Author notes

1. These authors contributed equally: Valerie Oberhardt, Hendrik Luxenburger, Janine Kemming, Isabel Schulien
2. These authors jointly supervised this work: Robert Thimme, Christoph Neumann-Haefelin, Maike Hofmann

Affiliations

1. Department of Medicine II (Gastroenterology, Hepatology, Endocrinology and Infectious Diseases), Freiburg University Medical Center, Faculty of Medicine, University of Freiburg, Freiburg, Germany

Valerie Oberhardt, Hendrik Luxenburger, Janine Kemming, Isabel Schulien, Benedikt Csernalabics, Julia Lang-Meli, Katharina Wild, Kristi Basho, Mircea Stefan Marinescu, Oezlem Sogukpinar, Hanna Hilger, Katarina Stete, Bertram Bengsch, Siegbert Rieg, Sagar, Tobias Boettler, Katharina Zoldan, Robert Thimme, Christoph Neumann-Haefelin & Maike Hofmann

2. Faculty of Biology, University of Freiburg, Freiburg, Germany

Valerie Oberhardt, Janine Kemming & Julian Staniek

3. IMM-PACT, Faculty of Medicine, University of Freiburg, Freiburg, Germany

Hendrik Luxenburger & Julia Lang-Meli

4. Institute of Virology, Freiburg University Medical Center, Faculty of Medicine, University of Freiburg, Freiburg, Germany

Kevin Ciminski, Sebastian Giese, Jonas Fuchs, Georg Kochs & Martin Schwemmle

5. Department of Rheumatology and Clinical Immunology, Freiburg University Medical Center, Faculty of Medicine, University of Freiburg, Freiburg, Germany

Iga Janowska, Julian Staniek, Fernando Topfstedt & Marta Rizzi

6. Faculty of Chemistry and Pharmacy, University of Freiburg, Freiburg, Germany

Katharina Wild

7. Department of Pediatrics and Adolescent Medicine, Ulm University Medical Center, Ulm, Germany

Ales Janda

8. Institute for Transfusion Medicine and Gene Therapy, Freiburg University Medical Center, Faculty of Medicine, University of Freiburg, Freiburg, Germany

Florian Emmerich

9. Signalling Research Centres BIOSS and CIBSS, University of Freiburg, Freiburg, Germany

Bertram Bengsch

10. Department of Haematology, Oncology & Stem Cell Transplantation, Freiburg University Medical Center, Faculty of Medicine, University of Freiburg, Freiburg, Germany

Cornelius F. Waller

11. Berta-Ottenstein Programme, Faculty of Medicine, University of Freiburg, Freiburg, Germany

Tobias Boettler

Contributions

V.O., H.L., J.K. and I.S. planned, performed and analysed experiments with the help of K.C., S.G., B.C., I.J., J.S., K.W., S.M., J.L.M., J.M.L., K.B., J.F., F.T., A.J., K.Z. S. and O.S. H.L., J.L.M., B.B., C.W., H.H., K.S. and S.R. were responsible for donor recruitment. F.E. performed four-digit HLA typing by next-generation sequencing. T.B., K.Z., G.K., M.S., M.R., R.T., C.N.-H. and M.H. contributed to experimental design, planning and supervision. V.O., H.L., J.K., I.S., R.T., M.H. and C.N.-H. interpreted data and wrote the manuscript. M.H., C.N.-H. and R.T. designed the study and are joint last authors.

Corresponding authors

Correspondence to [Robert Thimme](#) or [Christoph Neumann-Haefelin](#) or [Maike Hofmann](#).

Ethics declarations

Competing interests

The authors declare no competing interests.

Additional information

Peer review information *Nature* thanks Antonio Bertoletti, Katherine Kedzierska and the other, anonymous, reviewer(s) for their contribution to the peer review of this work. Peer review reports are available.

Publisher's note Springer Nature remains neutral with regard to jurisdictional claims in published maps and institutional affiliations.

Extended data figures and tables

Extended Data Fig. 1 Spike-specific CD8+ T cell epitopes following vaccination.

(a) Timeline showing blood and serum collection before and after prime and boost vaccination. **(b)** Gating strategy of flow cytometry data. A*01/S₈₆₅-, A*02/S₂₆₉- and A*03/S₃₇₈-specific CD8+ T cells were identified via pMHC-I tetramer-based analysis. **(c)** Comparison of epitope sequences with amino acid sequences of SARS-CoV-1/2, MERS and common cold coronaviruses amino acid sequences (upper panel) and with circulating SARS-CoV-2 variants of concern (VOC) (middle panel), respectively for A*01/S₈₆₅, A*02/S₂₆₉ and A*03/S₃₇₈-specific CD8+ T cell epitopes. (Lower panel) A*01/S₈₆₅, A*02/S₂₆₉ and A*03/S₃₇₈ peptide characteristics, comparing different prediction methods for the estimation of MHC I binding affinity, half-life and processing. **(d)** Heatmap showing the percentage of patients with a CD8+ T cell response to spike overlapping peptides/fine-mapped minimal optimal epitope in relation to the total number of patients tested with the respective HLA type. $n = 16$ OLP: overlapping peptide. Parts of the figure were drawn by using pictures from Servier Medical Art (<http://smart.servier.com/>) and licensed under a Creative Common Attribution 3.0 Generic License (a).

Source data

Extended Data Fig. 2 Spike-specific CD8+ T cells before and after enrichment.

(a, b) Dot plots showing A*01/S₈₆₅-, A*02/S₂₆₉- and A*03/S₃₇₈-specific CD8+ T cells ex vivo without pMHC-I tetramer-based enrichment **(a)** and after pMHC-I tetramer-based enrichment **(b)** at BL, before and after boost vaccination. **(c)** Exemplary dot plots (5-6 dpb) depicting the expression levels of CD38, Ki-67, T-BET, GRZB, PD-1 and CXCR3 in A*02/S₂₆₉- (green) specific and bulk (grey) CD8+ T cells. **(d)** % of GRZB, PD-1 and CXCR3 expressing A*01/S₈₆₅-, A*02/S₂₆₉- and A*03/S₃₇₈-specific non-naïve CD8+ T cells. **(e)** Exemplary dot plot (5-6 dpb) depicting the expression levels of CD39 and TOX in A*02/S₂₆₉- (green) specific and bulk (grey) CD8+ T cells. % expression among A*01/S₈₆₅-, A*02/S₂₆₉-and A*03/S₃₇₈-specific non-naïve CD8+ T cells is shown on the right side. BL: baseline; dpp: days post prime; dpb: days post boost; GRZB: granzyme B. **(d-e)** Two-way ANOVA with main effects only comparing the effect of the different epitopes and of time course. All statistically significant results are marked with the respective exact p-value (p_e: epitope, p_t: time).

Source data

Extended Data Fig. 3 Expression levels of CD38, T-BET, TOX, PD-1 and BCL-2 after prime and boost vaccination.

(a) t-SNE representation of flow cytometry data comparing A*01/S₈₆₅-, A*02/S₂₆₉- and A*03/S₃₇₈-specific CD8+ T cells after prime and boost vaccination (prime 4, 3 and 5 and boost 3, 3 and 5 individuals for A*01/S₈₆₅, A*02/S₂₆₉ and A*03/S₃₇₈, respectively). Expression levels of TOX, PD-1 and T-BET are indicated for A*01/S₈₆₅, A*02/S₂₆₉ and A*03/S₃₇₈ (colour-code: blue, low expression; red, high expression). **(b)** Diffusion map showing flow cytometry data for A*01/S₈₆₅- and A*03/S₃₇₈-specific CD8+ T cells of one representative donor at dpp (shades of red) and dpb (shades of grey) with CD38, T-BET, TOX and BCL-2 expression levels plotted on the diffusion map (colour-code: blue, low expression; red, high expression). dpp: days post prime; dpb: days post boost; t-SNE: t-distributed stochastic neighbour embedding.

Extended Data Fig. 4 Spike-specific CD8+ T cells in SARS-CoV-2 convalescents after a single vaccination and expression of early memory marker after prime and boost vaccination.

(a-c) Data of two donors who recovered from SARS-CoV-2 infection >365 day ago and received a single dose Bnt162b2 vaccination. **(a)** The calculated ex vivo frequency for A*02/S₂₆₉-specific CD8+ T cells in two donors is indicated at baseline (cSARS-CoV-2) and days after single dose vaccination. % of CD38, Ki-67, T-BET^{hi} **(b)** and TOX^{hi} **(c)** expressing A*02/S₂₆₉- specific non-naïve CD8+ T cells. **(d-e)** Exemplary dot plots depicting the expression levels of CD127 **(d)** and TCF-1 **(e)** in A*02/S₂₆₉- (green) specific and bulk (grey) CD8+ T cells 6 dpb. % A*01/S₈₆₅-, A*02/S₂₆₉- and A*03/S₃₇₈-specific non-naïve CD8+ T cells expressing CD127 **(d)** and TCF-1 **(e)** were determined. Correlation of indicated marker with dpb is depicted on the right. **(f)** Exemplary dot plots depicting the expression levels of BCL-2 in A*02/S₂₆₉- (green) specific as well as on bulk (grey) CD8+ T cells 6 dpb. nMFI (MFI normalized to naïve CD8+ T cells) of A*01/S₈₆₅-, A*02/S₂₆₉- and A*03/S₃₇₈-specific non-naïve CD8+ T cells expressing BCL-2 was determined. Correlation of nMFI BCL-2 with dpb is depicted on the right. cSARS: convalescent SARS; dpv: days post vaccination; BL: baseline; dpp: days post prime; dpb: days post boost; nMFI: normalized Median Fluorescent Intensity, epi: epitope. **(d-f)** Two-way ANOVA with main effects only comparing the effect of the different epitopes and of time course (left) and Spearman

correlation (right) was performed. All statistically significant results are marked with the respective exact p-value (p_e : epitope, p_t : time).

[Source data](#)

Extended Data Fig. 5 Frequency and functional capacity of spike-specific CD8+ T cells following prime and boost vaccination.

(a) Gating strategy of flow cytometry data. Cytokine secretion of A*01/S₈₆₅-, A*02/S₂₆₉- and A*03/S₃₇₈-specific CD8+ T cells was determined after in vitro expansion. **(b)** Workflow depicting peptide-specific in vitro expansion of CD8+ T cells. **(c)** Frequency of A*01/S₈₆₅-, A*02/S₂₆₉- and A*03/S₃₇₈ -specific CD8+ T cells after 14 day of in vitro expansion. **(d-g)** Dot plots showing A*01/S₈₆₅-, A*02/S₂₆₉- and A*03/S₃₇₈ -specific CD8+ T cells after in vitro expansion **(d)** and IFN- γ - **(e)**, TNF- **(f)** and CD107a- **(g)** producing CD8+ T cells after in vitro expansion (5-6 dpb). **(c)** Two-way ANOVA with main effects only comparing the effect of the different epitopes and of time course. BL: baseline; dpp: days post prime; dpb: days post boost, epi: epitope. Two-way ANOVA with main effects only comparing the effect of the different epitopes and of time course. All statistically significant results are marked with the respective exact p-value (p_e : epitope, p_t : time).

[Source data](#)

Extended Data Fig. 6 Circulating spike-specific CD4+ T cells following prime and boost vaccination.

(a) Gating strategy of flow cytometry data. DRB1*15:01/S₂₃₆-specific CD4+ T cells were identified via pMHCII tetramer-based enrichment used in further analyses. **(b)** Dot plots showing DRB1*15:01/S₂₃₆-specific CD4+ T cells ex vivo after pMHCII tetramer-based enrichment at BL, before and after boost vaccination. **(c)** Comparison of DRB1*15:01/S₂₃₆ epitope sequence with amino acid sequences of SARS-CoV-1/2, MERS and common cold coronaviruses (left) and of circulating SARS-CoV-2 variants of concern (VOC) (right). **(d)** Number of responses (left) and the calculated ex vivo frequencies (middle) of DRB1*15:01/S₂₃₆-specific CD4+ T cells in historic controls (HC, $n = 8$). % naïve within total DRB1*15:01/S₂₃₆-specific CD4+ T cells in historic controls (right). Detection limit: 1.25×10^{-4} . **(e)** % naïve of total DRB1*15:01/S₂₃₆- specific CD4+ T cells. **(f)** Representative dot plots of ICOS+CD38++ and Ki-67+ expression (grey: bulk, black: DRB1*15:01/S₂₃₆-specific CD4+ T cells). **(g)** % CXCR5-CXCR3+ TH1 cells and of CXCR5+PD-1+ TFH within non-naïve

DRB1*15:01/S₂₃₆-specific CD4+ T cells with representative dot plots (grey: bulk, black: DRB1*15:01/S₂₃₆-specific CD4+ T cells). BL: baseline, dpp: days post prime, dpb: days post boost; TFH: follicular helper T cells; TH1: T helper cells 1-like cells. Bar charts show the median with IQR. (e, g) One-way ANOVA with a mixed effects model comparing the effect of the time course. All statistically significant results are marked with the respective exact p-value (p_t : time).

[Source data](#)

Extended Data Fig. 7 Circulating B cells, antibodies and antibody neutralization activity after prime and boost vaccination.

(a) Gating strategy of flow cytometry data for different B cell subpopulations. **(b)** % of CD19+, naïve, switched memory, ASCs, CD69+aN and CD95+ aN cells within bulk B cells was determined at BL, post prime/boost. Nonlinear fit was calculated in red. **(c)** Detection of spike IgM in serum at BL, post prime/boost by ELISA. Level of secreted IgM was determined in supernatant of PBMC from BL, post prime/boost and after natural infection after in vitro stimulation for 9 d with CpG and IL-2. Detection limit: O.D. 8.5×10^{-2} . **(d)** Antibody neutralization activity is depicted as PRNT₅₀ at BL, dpp and dpb vaccination for the SARS-CoV-2 VOC alpha and beta. **(e)** Antibody neutralization capacity is depicted as PRNT₅₀ at different dps in natural SARS-CoV-2 infection with SARS-CoV-2 ancestral variant B.1. (d-e) Numbers indicate non-logarithmic median value. Detection limit: $5 \log_2 \text{PRNT}_{50}$. **(f)** Dot plots showing double tetramer positive B cells for S1 and RBD epitope at 28-30 dpb. **(g)** Dot plots representing co-expression of IgD/IgM (left), IgG/CD27 (middle) and CD95/CD71 (right) on concatenated flies of S1-specific B cells at 28-30 dpb. **(h)** Donut plots representing co-expression of CD27/IgG (upper) and CD71/CD95 (lower) in concatenated analysis of S1-specific B cells populations (n indicated the number of individual files concatenated) after boost vaccination. sw memory: switched memory; aN: activated naïve; BL: baseline; dpp: days post prime; dpb: days post boost; dps: days post symptoms; O.D.: optical density; PRNT₅₀: plaque-reduction neutralization titer 50. Bar charts show the median with IQR. (c-e) One-way ANOVA with a mixed effects model comparing the effect the time course. All statistically significant results are marked with the respective exact p-value (p_t : time).

[Source data](#)

Extended Data Fig. 8 Comparison of spike-specific CD8+ T cells after vaccination and natural infection.

(a) Distribution of dpb and dps of donors analysed for A*01/S₈₆₅-, A*02/S₂₆₉- and A*03/S₃₇₈-specific CD8+ T cells after vaccination and natural infection. **(b)** Calculated frequency of A*01/S₈₆₅-, A*02/S₂₆₉- and A*03/S₃₇₈-specific CD8+ T cells ex vivo after pMHC1 tetramer-based enrichment at 20-39 and 40-80 dpb/dps. Detection limit: 5×10^{-6} . **(c)** Plotted expression levels of T-BET, TCF-1, BCL-2, CCR7, CD38 and PD1 on t-SNE depicting all spike-specific CD8+ T cells >80 dpb vaccination (upper) and >80 dps in natural SARS-CoV-2 infection (lower) are indicated for A*01/S₈₆₅, A*02/S₂₆₉ and A*03/S₃₇₈ (colour-code: blue, low expression; red, high expression). dpb: days post boost; dps: days post symptom onset; t-SNE: t-distributed stochastic neighbour embedding. Bar charts show the median with IQR. (a) 2-way ANOVA including Tukey's multiple comparisons test were performed. (b) Statistical analyses of vaccination vs. natural infection was performed by Mann-Whitney test with Holm-Šídák method. All statistically significant results are marked with the respective exact p-value.

[Source data](#)

[Extended Data Fig. 9 Subset distribution of spike-specific CD8+ T cell after vaccination and natural infection.](#)

(a) Gating strategy of memory CD8+ T cell populations among A*02/S₂₆₉- (green) (36 dps) specific CD8+ T cells, (grey/black: bulk CD8+ T cells). **(b)** Distribution of spike-specific CD8+ T-cell memory subsets TED, TCM, TTM and TEM1 at 20-39 and 40-80 dpb/dps. **(c)** Distribution of spike-specific CD8+ T-cell memory subsets TEM2, TEM3 and TEMRA at 20-39, 40-80 and >80 dpb/dps. dpb: days post boost; dps: days post symptoms; ; TED: early differentiated, TCM: central memory T cells and TEM1: effector memory T cells 1 ; TEM2: effector memory T cells 2; TEM3: effector memory T cells 3, TEMRA terminally differentiated effector memory cells re-expressing CD45RA. Bar charts show the median with IQR. (b-c) Statistical analyses of vaccination vs. natural infection was performed by Mann-Whitney test with Holm-Šídák method. All statistically significant results are marked with the respective exact p-value.

[Source data](#)

[Extended Data Fig. 10 Expression levels of BCL-2, TCF1 and CD38 and polyfunctionality of spike-specific CD8+ T cells after vaccination and natural infection.](#)

(a) Plotted expression levels of TCF-1 on t-SNE depicting spike-specific CD8+ T cells >80 dpb vaccination and dps of natural infection for A*01/S₈₆₅- (vaccination n = 9,

natural infection $n = 9$), A*02/S₂₆₉- (vaccination $n = 10$, natural infection $n = 8$) and A*03/S₃₇₈- (vaccination $n = 9$, natural infection $n = 9$) (colour-code: blue, low expression; red, high expression). **(b, c)** nMFI (normalized to naïve CD8+ T cells) of BCL-2 (b, upper), TCF1 (b, middle) and CD38 (c, lower) spike-specific non-naïve CD8+ T cells at 20-39, 40-80 and >80 dpb/dps. **(d)** % of TNF-producing CD8+ T cells in relation to the frequency of spike-specific CD8+ T cells after in vitro expansion. **(e)** Bar graphs depicting the polyfunctionality of the respective spike-specific CD8+ T cells comparing vaccination and natural infection. dpb: days post boost; dps: days post symptom onset. Bar charts show the median with IQR. (b-e) Statistical analyses of vaccination vs. natural infection was performed by Mann–Whitney test with Holm–Šídák method. All statistically significant results are marked with the respective exact p-value.

[Source data](#)

Supplementary information

[Supplementary Table 1](#)

This table lists donor characteristics.

[Reporting Summary](#)

[Peer Review File](#)

Source data

[Source Data Fig. 1](#)

[Source Data Fig. 2](#)

[Source Data Fig. 3](#)

[Source Data Fig. 4](#)

[Source Data Extended Data Fig. 1](#)

[Source Data Extended Data Fig. 2](#)

[Source Data Extended Data Fig. 4](#)

[**Source Data Extended Data Fig. 5**](#)

[**Source Data Extended Data Fig. 6**](#)

[**Source Data Extended Data Fig. 7**](#)

[**Source Data Extended Data Fig. 8**](#)

[**Source Data Extended Data Fig. 9**](#)

[**Source Data Extended Data Fig. 10**](#)

Rights and permissions

Open Access This article is licensed under a Creative Commons Attribution 4.0 International License, which permits use, sharing, adaptation, distribution and reproduction in any medium or format, as long as you give appropriate credit to the original author(s) and the source, provide a link to the Creative Commons license, and indicate if changes were made. The images or other third party material in this article are included in the article's Creative Commons license, unless indicated otherwise in a credit line to the material. If material is not included in the article's Creative Commons license and your intended use is not permitted by statutory regulation or exceeds the permitted use, you will need to obtain permission directly from the copyright holder. To view a copy of this license, visit <http://creativecommons.org/licenses/by/4.0/>.

[**Reprints and Permissions**](#)

About this article

Cite this article

Oberhardt, V., Luxenburger, H., Kemming, J. *et al.* Rapid and stable mobilization of CD8⁺ T cells by SARS-CoV-2 mRNA vaccine. *Nature* **597**, 268–273 (2021).
<https://doi.org/10.1038/s41586-021-03841-4>

- Received: 07 May 2021
- Accepted: 20 July 2021
- Published: 28 July 2021

- Issue Date: 09 September 2021
 - DOI: <https://doi.org/10.1038/s41586-021-03841-4>
-

This article was downloaded by **calibre** from <https://www.nature.com/articles/s41586-021-03841-4>

| [Section menu](#) | [Main menu](#) |

- Article
- [Published: 18 November 2020](#)

Defining HPV-specific B cell responses in patients with head and neck cancer

- [Andreas Wieland](#) [ORCID: orcid.org/0000-0001-9648-7922^{1,2}](#),
- [Mihir R. Patel^{3,4}](#),
- [Maria A. Cardenas⁵](#),
- [Christiane S. Eberhardt^{1,2}](#),
- [William H. Hudson](#) [ORCID: orcid.org/0000-0002-2513-1213^{1,2}](#),
- [Rebecca C. Obeng](#) [ORCID: orcid.org/0000-0001-8624-7108^{1,2,6}](#),
- [Christopher C. Griffith^{4,6}](#),
- [Xu Wang⁷](#),
- [Zhuo G. Chen^{4,7}](#),
- [Haydn T. Kissick](#) [ORCID: orcid.org/0000-0001-7624-5598^{1,2,4,5}](#),
- [Nabil F. Saba^{4,7}](#) &
- [Rafi Ahmed](#) [ORCID: orcid.org/0000-0002-9591-2621^{1,2,4}](#)

[Nature](#) volume 597, pages 274–278 (2021)

- 7596 Accesses
- 16 Citations
- 60 Altmetric
- [Metrics details](#)

Subjects

- [B cells](#)
- [Head and neck cancer](#)
- [Humoral immunity](#)
- [Tumour immunology](#)
- [Tumour virus infections](#)

Abstract

Tumours often contain B cells and plasma cells but the antigen specificity of these intratumoral B cells is not well understood^{1,2,3,4,5,6,7,8}. Here we show that human papillomavirus (HPV)-specific B cell responses are detectable in samples from patients with HPV-positive head and neck cancers, with active production of HPV-specific IgG antibodies *in situ*. HPV-specific antibody secreting cells (ASCs) were present in the tumour microenvironment, with minimal bystander recruitment of influenza-specific cells, suggesting a localized and antigen-specific ASC response. HPV-specific ASC responses correlated with titres of plasma IgG and were directed against the HPV proteins E2, E6 and E7, with the most dominant response against E2. Using intratumoral B cells and plasma cells, we generated several HPV-specific human monoclonal antibodies, which exhibited a high degree of somatic hypermutation, consistent with chronic antigen exposure. Single-cell RNA sequencing analyses detected activated B cells, germinal centre B cells and ASCs within the tumour microenvironment. Compared with the tumour parenchyma, B cells and ASCs were preferentially localized in the tumour stroma, with well-formed clusters of activated B cells indicating ongoing germinal centre reactions. Overall, we show that antigen-specific activated and germinal centre B cells as well as plasma cells can be found in the tumour microenvironment. Our findings provide a better understanding of humoral immune responses in human cancer and suggest that tumour-infiltrating B cells could be harnessed for the development of therapeutic agents.

Access options

Subscribe to Journal

Get full journal access for 1 year

\$199.00

only \$3.90 per issue

[Subscribe](#)

All prices are NET prices.

VAT will be added later in the checkout.

Tax calculation will be finalised during checkout.

Rent or Buy article

Get time limited or full article access on ReadCube.

from \$8.99

[Rent or Buy](#)

All prices are NET prices.

Additional access options:

- [Log in](#)
- [Access through your institution](#)
- [Learn about institutional subscriptions](#)

Fig. 1: HPV-specific antibody-secreting cells are present in the TME of patients with HPV-positive HNSCC.

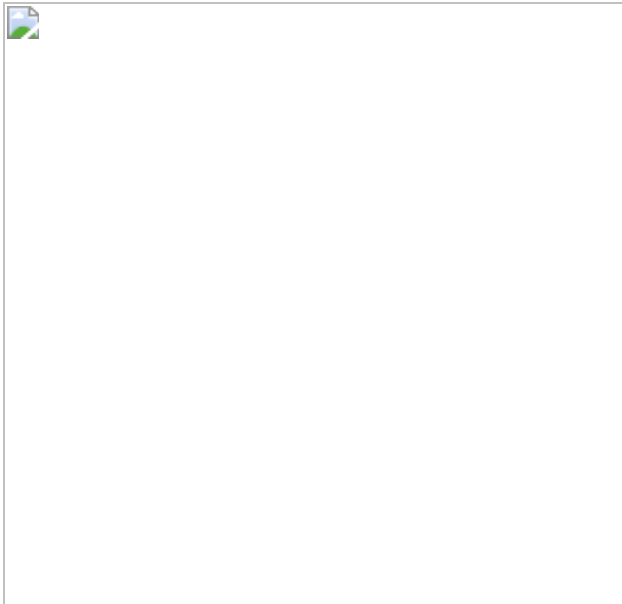


Fig. 2: HPV-specific IgG antibody titres correlate with HPV-specific IgG-secreting cells in the TME.

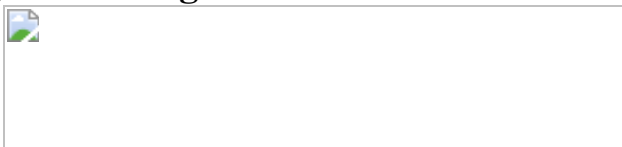


Fig. 3: Generation of human monoclonal antibodies against HPV from patients with HNSCC.

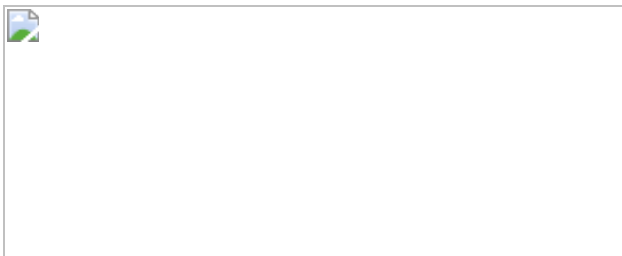
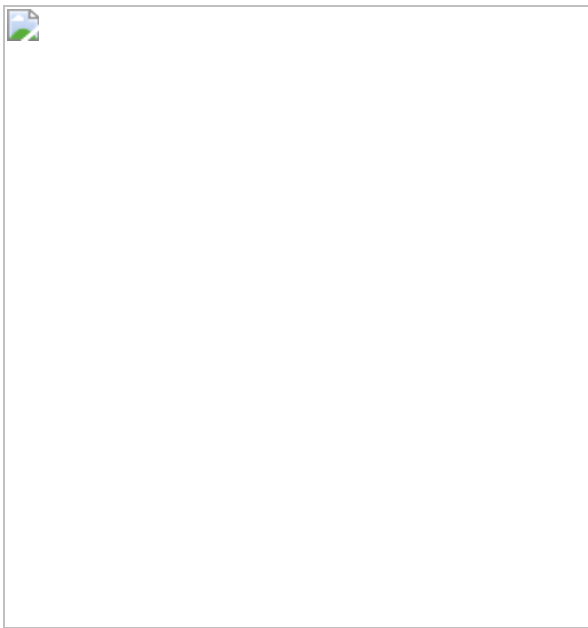


Fig. 4: The TME contains activated B cells, germinal centre B cells and ASCs.



Fig. 5: Transcriptomic and spatial characterization of B cells and plasma cells in the TME.



Data availability

The following protein sequences were used for generating recombinant HPV proteins: E2 (Uniprot P03120), E6 (Uniprot03126) and E7 (Uniprot P03129). RNA-seq and scRNA-seq data are available in the NCBI Gene Expression Omnibus (GEO) database under the SuperSeries accession

numbers [GSE149327](#) and [GSE153559](#), respectively. Normalized gene expression counts of sorted B cell subsets are available in Supplementary Table 1. HPV-specific monoclonal antibodies are available with a completed Material Transfer Agreement. Other relevant data are available from the corresponding authors upon reasonable request.

Code availability

Custom code for RNA-seq and scRNA-seq is available from the corresponding authors upon reasonable request.

References

1. 1.
Cabrita, R. et al. Tertiary lymphoid structures improve immunotherapy and survival in melanoma. *Nature* **577**, 561–565 (2020).
2. 2.
Helmink, B. A. et al. B cells and tertiary lymphoid structures promote immunotherapy response. *Nature* **577**, 549–555 (2020).
3. 3.
Petitprez, F. et al. B cells are associated with survival and immunotherapy response in sarcoma. *Nature* **577**, 556–560 (2020).
4. 4.
Flynn, N. J., Somasundaram, R., Arnold, K. M. & Sims-Mourtada, J. The multifaceted roles of B cells in solid tumors: emerging treatment opportunities. *Target. Oncol.* **12**, 139–152 (2017).
5. 5.

Yuen, G. J., Demissie, E. & Pillai, S. B lymphocytes and cancer: a love-hate relationship. *Trends Cancer* **2**, 747–757 (2016).

6. 6.

Shalapour, S. et al. Immunosuppressive plasma cells impede T-cell-dependent immunogenic chemotherapy. *Nature* **521**, 94–98 (2015).

7. 7.

Kroeger, D. R., Milne, K. & Nelson, B. H. Tumor-infiltrating plasma cells are associated with tertiary lymphoid structures, cytolytic T-cell responses, and superior prognosis in ovarian cancer. *Clin. Cancer Res.* **22**, 3005–3015 (2016).

8. 8.

Lechner, A. et al. Tumor-associated B cells and humoral immune response in head and neck squamous cell carcinoma. *OncoImmunology* **8**, 1535293 (2019).

9. 9.

Ang, K. K. et al. Human papillomavirus and survival of patients with oropharyngeal cancer. *N. Engl. J. Med.* **363**, 24–35 (2010).

10. 10.

Nulton, T. J., Olex, A. L., Dozmorov, M., Morgan, I. M. & Windle, B. Analysis of The Cancer Genome Atlas sequencing data reveals novel properties of the human papillomavirus 16 genome in head and neck squamous cell carcinoma. *Oncotarget* **8**, 17684–17699 (2017).

11. 11.

Marur, S., D’Souza, G., Westra, W. H. & Forastiere, A. A. HPV-associated head and neck cancer: a virus-related cancer epidemic. *Lancet Oncol.* **11**, 781–789 (2010).

12. 12.

Mei, H. E. et al. Blood-borne human plasma cells in steady state are derived from mucosal immune responses. *Blood* **113**, 2461–2469 (2009).

13. 13.

Ward, M. J. et al. Tumour-infiltrating lymphocytes predict for outcome in HPV-positive oropharyngeal cancer. *Br. J. Cancer* **110**, 489–500 (2014).

14. 14.

Lang Kuhs, K. A. et al. Characterization of human papillomavirus antibodies in individuals with head and neck cancer. *Cancer Epidemiol.* **42**, 46–52 (2016).

15. 15.

Lang Kuhs, K. A. et al. Human papillomavirus 16 E6 antibodies are sensitive for human papillomavirus-driven oropharyngeal cancer and are associated with recurrence. *Cancer* **123**, 4382–4390 (2017).

16. 16.

Dahlstrom, K. R. et al. Diagnostic accuracy of serum antibodies to human papillomavirus type 16 early antigens in the detection of human papillomavirus-related oropharyngeal cancer. *Cancer* **123**, 4886–4894 (2017).

17. 17.

Ellebedy, A. H. et al. Defining antigen-specific plasmablast and memory B cell subsets in human blood after viral infection or vaccination. *Nat. Immunol.* **17**, 1226–1234 (2016).

18. 18.

Davis, C. W. et al. Longitudinal analysis of the human B cell response to Ebola virus infection. *Cell* **177**, 1566–1582 (2019).

19. 19.

Sullivan, N. L. et al. Breadth and functionality of Varicella-Zoster virus glycoprotein-specific antibodies identified after Zostavax vaccination in humans. *J. Virol.* **92**, e00269-18 (2018).

20. 20.

Li, G. M. et al. Pandemic H1N1 influenza vaccine induces a recall response in humans that favors broadly cross-reactive memory B cells. *Proc. Natl Acad. Sci. USA* **109**, 9047–9052 (2012).

21. 21.

Scheid, J. F. et al. Broad diversity of neutralizing antibodies isolated from memory B cells in HIV-infected individuals. *Nature* **458**, 636–640 (2009).

22. 22.

Pereira, J. P., Kelly, L. M., Xu, Y. & Cyster, J. G. EBI2 mediates B cell segregation between the outer and centre follicle. *Nature* **460**, 1122–1126 (2009).

23. 23.

Barrena, S. et al. Aberrant expression of tetraspanin molecules in B-cell chronic lymphoproliferative disorders and its correlation with normal B-cell maturation. *Leukemia* **19**, 1376–1383 (2005).

24. 24.

Arce, S. et al. CD38 low IgG-secreting cells are precursors of various CD38 high-expressing plasma cell populations. *J. Leukoc. Biol.* **75**, 1022–1028 (2004).

25. 25.

Green, J. A. et al. The sphingosine 1-phosphate receptor S1P₂ maintains the homeostasis of germinal center B cells and promotes niche confinement. *Nat. Immunol.* **12**, 672–680 (2011).

26. 26.

Sharonov, G. V., Serebrovskaya, E. O., Yuzhakova, D. V., Britanova, O. V. & Chudakov, D. M. B cells, plasma cells and antibody repertoires in the tumour microenvironment. *Nat. Rev. Immunol.* **20**, 294–307 (2020).

27. 27.

Sautès-Fridman, C., Petitprez, F., Calderaro, J. & Fridman, W. H. Tertiary lymphoid structures in the era of cancer immunotherapy. *Nat. Rev. Cancer* **19**, 307–325 (2019).

28. 28.

Skeate, J. G., Woodham, A. W., Einstein, M. H., Da Silva, D. M. & Kast, W. M. Current therapeutic vaccination and immunotherapy strategies for HPV-related diseases. *Hum. Vaccin. Immunother.* **12**, 1418–1429 (2016).

29. 29.

Chaturvedi, A. K. et al. Human papillomavirus and rising oropharyngeal cancer incidence in the United States. *J. Clin. Oncol.* **29**, 4294–4301 (2011).

30. 30.

Krishna, S. et al. Human papilloma virus specific immunogenicity and dysfunction of CD8⁺ T cells in head and neck cancer. *Cancer Res.* **78**, 6159–6170 (2018).

31. 31.

Dahlstrom, K. R. et al. HPV serum antibodies as predictors of survival and disease progression in patients with HPV-positive squamous cell carcinoma of the oropharynx. *Clin. Cancer Res.* **21**, 2861–2869 (2015).

32. 32.

Wieland, A. & Ahmed, R. Fc receptors in antimicrobial protection. *Curr. Top. Microbiol. Immunol.* **423**, 119–150 (2019).

33. 33.

Kamphorst, A. O. et al. Rescue of exhausted CD8 T cells by PD-1-targeted therapies is CD28-dependent. *Science* **355**, 1423–1427 (2017).

34. 34.

de León, D. C. et al. Human papillomavirus (HPV) in breast tumors: prevalence in a group of Mexican patients. *BMC Cancer* **9**, 26 (2009).

35. 35.

Smith, K. et al. Rapid generation of fully human monoclonal antibodies specific to a vaccinating antigen. *Nat. Protocols* **4**, 372–384 (2009).

36. 36.

Satija, R., Farrell, J. A., Gennert, D., Schier, A. F. & Regev, A. Spatial reconstruction of single-cell gene expression data. *Nat. Biotechnol.* **33**, 495–502 (2015).

37. 37.

Stuart, T. et al. Comprehensive integration of single-cell data. *Cell* **177**, 1888–1902 (2019).

38. 38.

DeTomaso, D. & Yosef, N. FastProject: a tool for low-dimensional analysis of single-cell RNA-Seq data. *BMC Bioinformatics* **17**, 315 (2016).

39. 39.

Milpied, P. et al. Human germinal center transcriptional programs are de-synchronized in B cell lymphoma. *Nat. Immunol.* **19**, 1013–1024 (2018).

40. 40.

Hudson, W. H. et al. Expression of novel long noncoding RNAs defines virus-specific effector and memory CD8⁺ T cells. *Nat. Commun.* **10**, 196 (2019).

41. 41.

Zerbino, D. R. et al. Ensembl 2018. *Nucleic Acids Res.* **46**, D754–D761 (2018).

42. 42.

Kim, D., Langmead, B. & Salzberg, S. L. HISAT: a fast spliced aligner with low memory requirements. *Nat. Methods* **12**, 357–360 (2015).

43. 43.

Li, H. et al. The Sequence Alignment/Map format and SAMtools. *Bioinformatics* **25**, 2078–2079 (2009).

44. 44.

Liao, Y., Smyth, G. K. & Shi, W. featureCounts: an efficient general purpose program for assigning sequence reads to genomic features. *Bioinformatics* **30**, 923–930 (2014).

45. 45.

Love, M. I., Huber, W. & Anders, S. Moderated estimation of fold change and dispersion for RNA-seq data with DESeq2. *Genome Biol.* **15**, 550 (2014).

46. 46.

Lê, S., Josse, J. & Husson, F. FactoMineR: An R Package for Multivariate Analysis. *J. Stat. Softw.* **25**, 1–18 (2008).

47. 47.

Wilkerson, M. D. & Hayes, D. N. ConsensusClusterPlus: a class discovery tool with confidence assessments and item tracking. *Bioinformatics* **26**, 1572–1573 (2010).

Acknowledgements

This work was supported by funding from the Ambrose Monell Foundation (R.A.), a Winship Invest\$ Pilot grant (to R.A., Z.G.C. and N.F.S.), and NCI grant 1-R00-CA197891 (H.T.K.). W.H.H. is a Cancer Research Institute Irvington Fellow supported by the Cancer Research Institute. We would like to acknowledge the pathology personnel involved in sample handling, the Emory Flow Cytometry Core supported by the National Center for Georgia Clinical and Translational Science Alliance of the National Institutes of Health (NIH) under award number UL1TR002378, and the Yerkes NHP Genomics Core, which is supported in part by NIH P51 OD011132. We would also like to thank C. W. Davis and L. J. Sudmeier for feedback on the manuscript.

Author information

Affiliations

1. Emory Vaccine Center, Emory University School of Medicine, Atlanta, GA, USA

Andreas Wieland, Christiane S. Eberhardt, William H. Hudson, Rebecca C. Obeng, Haydn T. Kissick & Rafi Ahmed

2. Department of Microbiology and Immunology, Emory University School of Medicine, Atlanta, GA, USA

Andreas Wieland, Christiane S. Eberhardt, William H. Hudson, Rebecca C. Obeng, Haydn T. Kissick & Rafi Ahmed

3. Department of Otolaryngology, Emory University School of Medicine, Atlanta, GA, USA

Mihir R. Patel

4. Winship Cancer Institute of Emory University, Atlanta, GA, USA

Mihir R. Patel, Christopher C. Griffith, Zhus G. Chen, Haydn T. Kissick, Nabil F. Saba & Rafi Ahmed

5. Department of Urology, Emory University School of Medicine, Atlanta, GA, USA

Maria A. Cardenas & Haydn T. Kissick

6. Department of Pathology, Emory University School of Medicine, Atlanta, GA, USA

Rebecca C. Obeng & Christopher C. Griffith

7. Department of Hematology and Medical Oncology, Emory University School of Medicine, Atlanta, GA, USA

Xu Wang, Zhus G. Chen & Nabil F. Saba

Contributions

A.W. conceived and designed the project. A.W. and R.A. designed experiments and wrote the manuscript. A.W. performed most of the experiments (including cell isolation, ELISPOT, serology, flow cytometry

and monoclonal antibody generation) and analysed the generated data. C.S.E. performed MBC assays and helped with flow cytometry experiments. M.A.C. and H.T.K. analysed scRNA-seq data. W.H.H. analysed bulk RNA-seq data. R.C.O. performed and analysed multiplex immunohistochemistry experiments. M.R.P. collected and provided human specimens, and analysed patient data. C.C.G. and X.W. handled human specimens. N.F.S. and Z.G.C. initiated the clinical specimen protocol. All authors contributed to the revision of the manuscript.

Corresponding authors

Correspondence to [Andreas Wieland](#) or [Rafi Ahmed](#).

Ethics declarations

Competing interests

A.W. and R.A. are inventors on a patent (US patent application no. 16/971,627) filed by Emory University relating to HPV-specific monoclonal antibodies and HPV E2 as potential immunological target in HPV-positive cancers. All other authors declare no competing interests.

Additional information

Peer review information *Nature* thanks Shiv Pillai and the other, anonymous, reviewer(s) for their contribution to the peer review of this work.

Publisher's note Springer Nature remains neutral with regard to jurisdictional claims in published maps and institutional affiliations.

Extended data figures and tables

[**Extended Data Fig. 1 ASC responses in patients with HPV-positive HNSCC.**](#)

a, Sequencing-based HPV genotyping of p16⁺ HNSCC cases ($n = 32$). **b**, Representative ELISPOT showing total ASCs among lymphocytes from metLNs, primary tumours (TILs) and PBMCs of a patient with p16⁺ HNSCC. **c–e**, Summary graphs showing the frequency of ASCs producing IgG, IgA and IgM among lymphocytes from metLNs ($n = 37$) (**c**), TILs ($n = 22$) (**d**) or PBMCs ($n = 39$) of patients with p16⁺ HNSCC (**e**). Data are mean \pm s.e.m. *** $P = 0.0001$, **** $P < 0.0001$ (**c**); ** $P = 0.0021$, **** $P < 0.0001$ (**d**); **** $P < 0.0001$ (**e**), Friedman test with two-sided Dunn's multiple comparisons test. Not significant (ns) = 0.1720. **f**, Representative ELISPOT of E2/6/7-specific IgG-secreting ASCs in PBMCs, metLNs and TILs of a patient with p16⁺ HNSCC. MBP indicates negative control. **g**, Correlation (Spearman) of antigen-specific IgG-secreting ASCs in metLNs and TILs ($n = 18$ patients) with $r = 0.7536$ and $P < 0.0001$.

Extended Data Fig. 2 Patients with HPV-negative HNSCC exhibit reduced lymphocyte infiltration into the tumour and lack HPV-specific ASCs.

a, Number of isolated lymphocytes per gram primary tumour in patients with p16⁺ ($n = 35$) and p16⁻ ($n = 9$) HNSCC. *** $P = 0.0007$, two-tailed Mann–Whitney test. **b**, Frequency of ASCs producing IgG, IgA and IgM among lymphocytes from metLNs of patients with p16⁺ ($n = 37$) and p16⁻ ($n = 6$ for IgG, $n = 5$ for IgA and IgM) HNSCC. **c**, Frequency of E2/6/7-specific IgG-secreting ASCs among total IgG-secreting ASCs in metLNs ($n = 6$) and TILs ($n = 1$) of patients with p16⁻ HNSCC. **d**, Frequency of E2/6/7- and influenza-specific IgG⁺ MBCs among total IgG⁺ MBCs in the peripheral blood of patients with p16⁺ ($n = 27$) and p16⁻ ($n = 9$) HNSCC. Numbers indicate detected responses among tested samples. Data are mean \pm s.e.m.

Extended Data Fig. 3 Serological analyses.

a–c, IgG titres against E2 (**a**), E6 (**b**) and E7 (**c**) in plasma of healthy individuals ($n = 50$) and patients with p16⁺ HNSCC ($n = 39$). Data are median and quartiles. **** $P < 0.0001$, two-tailed Mann–Whitney test. **d, e**,

E2/6/7-specific IgA (**d**) and IgM (**e**) titres in plasma of patients with p16⁺ HNSCC ($n = 39$). **f**, E2/6/7-specific IgG titres in plasma of p16⁺ patients and graph demonstrating an IgG response against at least two HPV proteins in the vast majority of patients ($n = 39$). Data are median and quartiles.

*** $P = 0.0006$, Friedman test with two-sided Dunn's multiple comparisons test. ns, 0.1852. **g**, Heat map showing E2/6/7-specific IgG antibody titres in patients with p16⁺ HNSCC ($n = 39$) with each column representing a patient. **h**, Correlation (Spearman) between E2/6/7-specific IgG⁺ ASCs in primary tumour and E2/6/7-specific IgG titres in plasma ($n = 18$ patients) with $r = 0.7343$ and $P < 0.0001$.

Extended Data Fig. 4 Human monoclonal antibodies against HPV E antigens.

a, Clustered binding pattern of E2-specific monoclonal antibodies performed by competition ELISA. Recognition of linear epitopes was determined by western blot. **b**, ELISA of E6-specific antibodies (21E2, 21E11, 21H3) generated from single-cell sorted ASCs from metLNs of a patient with HPV⁺ HNSCC. An E2-specific monoclonal antibody 22B10) is shown as negative control. a.u., arbitrary units. **c**, Number of SHMs in the V_h and V_l chain of E6-specific monoclonal antibodies ($n = 3$) with indicated mean.

Extended Data Fig. 5 Activated cells of the B cell lineage from the TME are present in distinct clusters.

a, UMAP plots showing enrichment for ABC, ASC, GCB and proliferation gene sets. **b**, Violin plots showing gene set enrichment scores among the four clusters identified by scRNA-seq. P values determined by two-sided Pearson's Chi-squared test for binary variables with Yates continuity correction. **c**, UMAP plots showing expression of selected genes. **d**, UMAP plots showing distribution of cells of the indicated patient and tissue origin (in red) among the identified clusters. Bar graphs quantifying the composition of the respective sample in terms of frequency among the identified clusters: ASCs, ABCs, GCBs and transitory cells.

Extended Data Fig. 6 Gene expression of cytokines and other immunomodulators by B cells and plasma cells in the TME.

a, Flow plots showing the presence of ASCs and ABCs but absence of germinal centre (GC) B cells in the peripheral blood of a healthy volunteer 7 days after vaccination with Fluarix. **b**, ASC ELISPOT showing total IgG/A/M-secreting cells (top) and influenza-specific IgG/A/M-secreting cells (bottom) in PBMCs 7 days after vaccination with Fluarix. **c**, Representative histogram of ASCs from peripheral blood (red) or metLNs (blue) of patients with p16⁺ HNSCC showing Ki67 expression. Numbers indicate frequency of Ki67⁺ cells among total ASCs. Summary graph showing paired frequencies of Ki67-expressing ASCs in PBMCs, metLNs and TILs ($n = 14$). *** $P < 0.0001$, paired two-tailed t -test. **d**, Heat map showing gene expression (normalized reads) of selected cytokines and immunomodulators as well as CD19 and CXCR5 as reference. Immunomodulators related to B cells and previously described as negative regulators in the TME are highlighted in red. An expression threshold was set to 50 normalized reads, with reads less than 50 displayed in white.

Extended Data Fig. 7 Multiplex immunohistochemistry analysis of B cells and ASCs in the TME.

a, Representative multiplex immunohistochemistry (mIHC) section of HPV⁺ HNSCC tumour ($n = 7$) with B cell infiltrates and associated germinal centres (white arrows) (see also Fig. 5e). Seven-colour composite mIHC images of CD19, CD20, Ki67, IRF4, CD138, P16 and DAPI (left), individual images of CD20, CD19, Ki67, and IRF4 (middle), and high magnification (right) of a region of interest (white box). **b**, Frequency of Ki67⁺ and CD138⁺ ASCs (CD19⁺CD20⁻IRF4⁺) in mIHC sections of seven HPV⁺ HNSCC tumours. Data are mean \pm s.e.m. **c**, Quantification of B cells (CD19⁺CD20⁺), ABCs (CD19⁺CD20⁺Ki67⁺), and ASCs (CD19⁺CD20⁻IRF4⁺) in the stroma and tumour parenchyma of three patients with HPV⁻ HNSCC.

Extended Data Fig. 8 Gating strategy for isolation and analysis of B cell subsets.

Gating strategy for B cell subsets used for flow cytometric analyses, bulk RNA-seq analyses, scRNA-seq analyses or the generation of E2-specific monoclonal antibodies. B cell subsets used for bulk RNA-seq analyses are highlighted in red: ASCs, ABCs and GCBs.

Extended Data Table 1 Patient characteristics

Extended Data Table 2 List of antibodies and reagents

Supplementary information

Supplementary Table 1

RNA-seq data of B cell subsets. Normalized gene expression is shown.

Reporting Summary

Rights and permissions

Reprints and Permissions

About this article

Cite this article

Wieland, A., Patel, M.R., Cardenas, M.A. *et al.* Defining HPV-specific B cell responses in patients with head and neck cancer. *Nature* **597**, 274–278 (2021). <https://doi.org/10.1038/s41586-020-2931-3>

- Received: 26 December 2019
- Accepted: 23 July 2020

- Published: 18 November 2020
- Issue Date: 09 September 2021
- DOI: <https://doi.org/10.1038/s41586-020-2931-3>

Further reading

- [**Functional HPV-specific PD-1+ stem-like CD8 T cells in head and neck cancer**](#)
 - Christiane S. Eberhardt
 - , Haydn T. Kissick
 - , Mihir R. Patel
 - , Maria A. Cardenas
 - , Nataliya Prokhnevskaya
 - , Rebecca C. Obeng
 - , Tahseen H. Nasti
 - , Christopher C. Griffith
 - , Se Jin Im
 - , Xu Wang
 - , Dong M. Shin
 - , Mary Carrington
 - , Zhusuo G. Chen
 - , John Sidney
 - , Alessandro Sette
 - , Nabil F. Saba
 - , Andreas Wieland
 - & Rafi Ahmed

Nature (2021)

- [**A refined view of tumour-associated B cells**](#)
 - Sarah Seton-Rogers

Nature Reviews Cancer (2021)

- **A refined view of tumour-associated B cells**

- Sarah Seton-Rogers

Nature Reviews Immunology (2021)

This article was downloaded by **calibre** from <https://www.nature.com/articles/s41586-020-2931-3>

| [Section menu](#) | [Main menu](#) |

- Article
- [Published: 01 September 2021](#)

Functional HPV-specific PD-1⁺ stem-like CD8 T cells in head and neck cancer

- [Christiane S. Eberhardt](#)^{1,2,3,4 na1},
- [Haydn T. Kissick](#) [ORCID: orcid.org/0000-0001-7624-5598](#)^{1,2,5,6 na1},
- [Mihir R. Patel](#)^{5,7},
- [Maria A. Cardenas](#)⁶,
- [Nataliya Prokhnevskaya](#)⁶,
- [Rebecca C. Obeng](#) [ORCID: orcid.org/0000-0001-8624-7108](#)^{1,2,8,9},
- [Tahseen H. Nasti](#)^{1,2},
- [Christopher C. Griffith](#)^{5,8},
- [Se Jin Im](#)^{1,2,10},
- [Xu Wang](#)¹¹,
- [Dong M. Shin](#)^{4,11},
- [Mary Carrington](#) [ORCID: orcid.org/0000-0002-2692-2180](#)^{12,13},
- [Zhuo G. Chen](#)^{5,11},
- [John Sidney](#)¹⁴,
- [Alessandro Sette](#)^{14,15},
- [Nabil F. Saba](#)^{5,11},
- [Andreas Wieland](#) [ORCID: orcid.org/0000-0001-9648-7922](#)^{1,2 na2} &
- [Rafi Ahmed](#) [ORCID: orcid.org/0000-0002-9591-2621](#)^{1,2,5 na2}

[Nature](#) volume 597, pages 279–284 (2021)

- 5477 Accesses

- 134 Altmetric
- [Metrics details](#)

Subjects

- [Cytotoxic T cells](#)
- [Head and neck cancer](#)
- [Immunosurveillance](#)
- [Tumour virus infections](#)

Abstract

T cells are important in tumour immunity but a better understanding is needed of the differentiation of antigen-specific T cells in human cancer^{1,2}. Here we studied CD8 T cells in patients with human papillomavirus (HPV)-positive head and neck cancer and identified several epitopes derived from HPV E2, E5 and E6 proteins that allowed us to analyse virus-specific CD8 T cells using major histocompatibility complex (MHC) class I tetramers. HPV-specific CD8 T cells expressed PD-1 and were detectable in the tumour at levels that ranged from 0.1% to 10% of tumour-infiltrating CD8 T lymphocytes (TILs) for a given epitope. Single-cell RNA-sequencing analyses of tetramer-sorted HPV-specific PD-1⁺ CD8 TILs revealed three transcriptionally distinct subsets. One subset expressed *TCF7* and other genes associated with PD-1⁺ stem-like CD8 T cells that are critical for maintaining T cell responses in conditions of antigen persistence. The second subset expressed more effector molecules, representing a transitory cell population, and the third subset was characterized by a terminally differentiated gene signature. T cell receptor clonotypes were shared between the three subsets and pseudotime analysis suggested a hypothetical differentiation trajectory from stem-like to transitory to terminally differentiated cells. More notably, HPV-specific PD-1⁺*TCF-1*⁺ stem-like TILs proliferated and differentiated into more effector-like cells after *in vitro* stimulation with the cognate HPV peptide, whereas the more terminally differentiated cells did not proliferate. The presence of functional HPV-specific PD-1⁺*TCF-1*⁺*CD45RO*⁺ stem-like CD8 T cells with

proliferative capacity shows that the cellular machinery to respond to PD-1 blockade exists in HPV-positive head and neck cancer, supporting the further investigation of PD-1 targeted therapies in this malignancy. Furthermore, HPV therapeutic vaccination efforts have focused on E6 and E7 proteins; our results suggest that E2 and E5 should also be considered for inclusion as vaccine antigens to elicit tumour-reactive CD8 T cell responses of maximal breadth.

Access options

Subscribe to Journal

Get full journal access for 1 year

\$199.00

only \$3.90 per issue

[Subscribe](#)

All prices are NET prices.

VAT will be added later in the checkout.

Tax calculation will be finalised during checkout.

Rent or Buy article

Get time limited or full article access on ReadCube.

from \$8.99

[Rent or Buy](#)

All prices are NET prices.

Additional access options:

- [Log in](#)
- [Access through your institution](#)

- [Learn about institutional subscriptions](#)

Fig. 1: Intratumoral PD-1⁺ CD8 T cells are made up of distinct subsets with PD-1⁺TCF-1⁺ stem-like cells residing in lymphoid-like stromal areas.

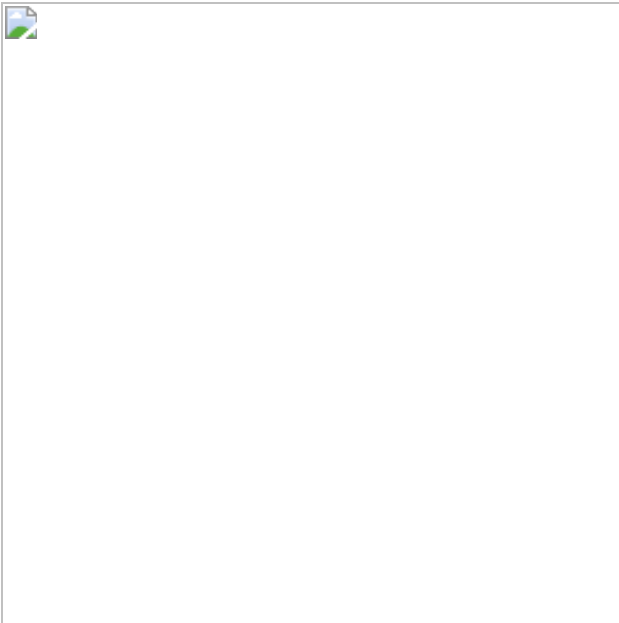


Fig. 2: Identification of HPV-specific CD8 T cells in PBMCs and tumours of patients with HPV-positive HNSCC.



Fig. 3: HPV-specific CD8 TILs are made up of three transcriptionally distinct clusters.

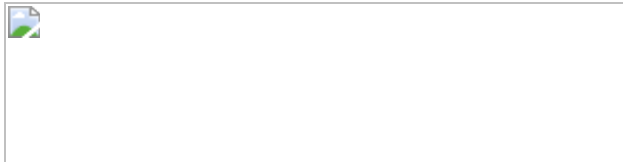


Fig. 4: The three HPV-specific transcriptionally distinct clusters share TCR clonotypes.

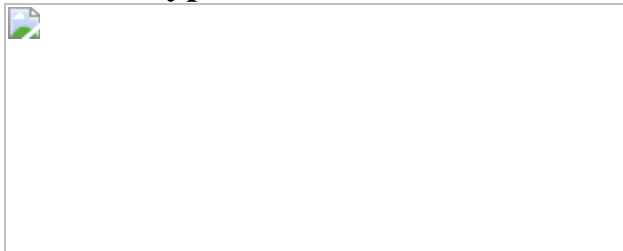
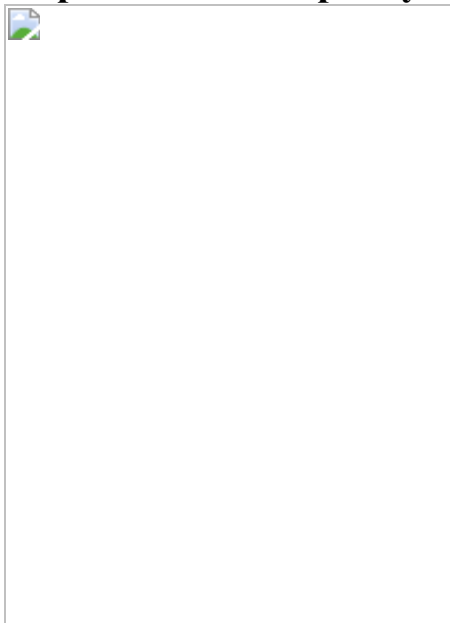


Fig. 5: HPV-specific PD-1⁺TCF-1⁺ stem-like CD8 T cells in the tumour have proliferative capacity and can differentiate into effector-like cells.



Data availability

The following protein sequences were used for predicting and generating HPV peptides: E2 (Uniprot P03120), E5 (Uniprot P06927), E6 (Uniprot P03126), and E7 (Uniprot P03129). scRNA-seq data are available in the NCBI Gene Expression Omnibus (GEO) database under the accession number [GSE180268](#). Other relevant data are available from the corresponding authors upon reasonable request.

Code availability

Custom code for scRNA-seq is available from the corresponding authors upon reasonable request.

References

1. 1.

Hashimoto, M. et al. CD8 T cell exhaustion in chronic infection and cancer: opportunities for interventions. *Annu. Rev. Med.* **69**, 301–318 (2018).

2. 2.

McLane, L. M., Abdel-Hakeem, M. S. & Wherry, E. J. CD8 T cell exhaustion during chronic viral infection and cancer. *Annu. Rev. Immunol.* **37**, 457–495 (2019).

3. 3.

Gallimore, A. et al. Induction and exhaustion of lymphocytic choriomeningitis virus-specific cytotoxic T lymphocytes visualized using soluble tetrameric major histocompatibility complex class I-peptide complexes. *J. Exp. Med.* **187**, 1383–1393 (1998).

4. 4.

Zajac, A. J. et al. Viral immune evasion due to persistence of activated T cells without effector function. *J. Exp. Med.* **188**, 2205–2213 (1998).

5. 5.

Barber, D. L. et al. Restoring function in exhausted CD8 T cells during chronic viral infection. *Nature* **439**, 682–687 (2006).

6. 6.

Im, S. J. et al. Defining CD8⁺ T cells that provide the proliferative burst after PD-1 therapy. *Nature* **537**, 417–421 (2016).

7. 7.

Utzschneider, D. T. et al. T cell factor 1-expressing memory-like CD8⁺ T cells sustain the immune response to chronic viral infections. *Immunity* **45**, 415–427 (2016).

8. 8.

He, R. et al. Follicular CXCR5- expressing CD8⁺ T cells curtail chronic viral infection. *Nature* **537**, 412–428 (2016).

9. 9.

Jadhav, R. R. et al. Epigenetic signature of PD-1⁺TCF1⁺CD8 T cells that act as resource cells during chronic viral infection and respond to PD-1 blockade. *Proc. Natl Acad. Sci. USA* **116**, 14113–14118 (2019).

10. 10.

Zander, R. et al. CD4⁺ T cell help is required for the formation of a cytolytic CD8⁺ T cell subset that protects against chronic infection and cancer. *Immunity* **51**, 1028–1042 (2019).

11. 11.

Hudson, W. H. et al. Proliferating transitory T cells with an effector-like transcriptional signature emerge from PD-1⁺ stem-like CD8⁺ T cells during chronic infection. *Immunity* **51**, 1043–1058 (2019).

12. 12.

Sade-Feldman, M. et al. Defining T cell states associated with response to checkpoint immunotherapy in melanoma. *Cell* **175**, 998–1013 (2018).

13. 13.

Brummelman, J. et al. High-dimensional single cell analysis identifies stem-like cytotoxic CD8⁺ T cells infiltrating human tumors. *J. Exp. Med.* **215**, 2520–2535 (2018).

14. 14.

Jansen, C. S. et al. An intra-tumoral niche maintains and differentiates stem-like CD8 T cells. *Nature* **576**, 465–470 (2019).

15. 15.

Mann, T. H. & Kaech, S. M. Tick-TOX, it's time for T cell exhaustion. *Nat. Immunol.* **20**, 1092–1094 (2019).

16. 16.

Bhatt, K. H. et al. Profiling HPV-16-specific T cell responses reveals broad antigen reactivities in oropharyngeal cancer patients. *J. Exp. Med.* **217**, e20200389 (2020).

17. 17.

Krishna, S. et al. Human papilloma virus specific immunogenicity and dysfunction of CD8⁺ T cells in head and neck cancer. *Cancer Res.* **78**, 6159–6170 (2018).

18. 18.

Bobisse, S. et al. Sensitive and frequent identification of high avidity neo-epitope specific CD8⁺ T cells in immunotherapy-naive ovarian cancer. *Nat. Commun.* **9**, 1092 (2018).

19. 19.

Wieland, A. et al. T cell receptor sequencing of activated CD8 T cells in the blood identifies tumor-infiltrating clones that expand after PD-1

therapy and radiation in a melanoma patient. *Cancer Immunol. Immunother.* **67**, 1767–1776 (2018).

20. 20.

Simoni, Y. et al. Bystander CD8⁺ T cells are abundant and phenotypically distinct in human tumour infiltrates. *Nature* **557**, 575–579 (2018).

21. 21.

Rosato, P. C. et al. Virus-specific memory T cells populate tumors and can be repurposed for tumor immunotherapy. *Nat. Commun.* **10**, 567 (2019).

22. 22.

Gattinoni, L. et al. A human memory T cell subset with stem cell-like properties. *Nat. Med.* **17**, 1290–1297 (2011).

23. 23.

Kamphorst, A. O. et al. Rescue of exhausted CD8 T cells by PD-1-targeted therapies is CD28-dependent. *Science* **355**, 1423–1427 (2017).

24. 24.

Patel, J. J., Levy, D. A., Nguyen, S. A., Knochelmann, H. M. & Day, T. A. Impact of PD-L1 expression and human papillomavirus status in anti-PD1/PDL1 immunotherapy for head and neck squamous cell carcinoma—systematic review and meta-analysis. *Head Neck* **42**, 774–786 (2020).

25. 25.

Skeate, J. G., Woodham, A. W., Einstein, M. H., Da Silva, D. M. & Kast, W. M. Current therapeutic vaccination and immunotherapy strategies for HPV-related diseases. *Hum. Vaccines Immunother.* **12**, 1418–1429 (2016).

26. 26.

Ha, S. J. et al. Enhancing therapeutic vaccination by blocking PD-1-mediated inhibitory signals during chronic infection. *J. Exp. Med.* **205**, 543–555 (2008).

27. 27.

de Martel, C., Georges, D., Bray, F., Ferlay, J. & Clifford, G. M. Global burden of cancer attributable to infections in 2018: a worldwide incidence analysis. *Lancet Glob. Health* **8**, e180–e190 (2020).

28. 28.

Wieland, A. et al. Defining HPV-specific B cell responses in patients with head and neck cancer. *Nature*, <https://doi.org/10.1038/s41586-020-2931-3> (2020).

29. 29.

NIH Tetramer Core Facility. *Production Protocols: Class I MHC Tetramer Preparation*
<https://tetramer.yerkes.emory.edu/support/protocols#10> (2006).

30. 30.

Vita, R. et al. The Immune Epitope Database (IEDB): 2018 update. *Nucleic Acids Res.* **47**, D339–D343 (2019).

31. 31.

Sidney, J. et al. Measurement of MHC/peptide interactions by gel filtration or monoclonal antibody capture. *Current Protoc. Immunol.* **100**, 18.3.1–18.3.36 (2013).

32. 32.

Satija, R., Farrell, J. A., Gennert, D., Schier, A. F. & Regev, A. Spatial reconstruction of single-cell gene expression data. *Nat. Biotechnol.* **33**,

495–502 (2015).

33. 33.

DeTomaso, D. & Yosef, N. FastProject: a tool for low-dimensional analysis of single-cell RNA-seq data. *BMC Bioinformatics* **17**, 315 (2016).

34. 34.

Trapnell, C. et al. The dynamics and regulators of cell fate decisions are revealed by pseudotemporal ordering of single cells. *Nat. Biotechnol.* **32**, 381–386 (2014).

Acknowledgements

This work was supported by funding from the Ambrose Monell Foundation (R.A.); the T. J. Martell Foundation (R.A.); NIH grants 5U19AI057266 and P01AI056299 (R.A.); the Oliver S. and Jennie R. Donaldson Charitable Trust (R.A.); a Winship Invest\$ Pilot grant (R.A., Z.G.C. and N.F.S.); Swiss National Science Foundation grant P300PB_174483 (C.S.E.); a Eugenio Litta Foundation grant (C.S.E.); NCI grant 1-R00-CA197891 (H.T.K.); the James M. Cox Foundation and James C. Kennedy (H.T.K.); the Prostate Cancer Foundation (H.T.K. and N.P.); and a Triological Society Research Career Development Award (M.R.P.). We thank H. Wu for technical assistance and M. Clayton for administrative support. We acknowledge the Emory Flow Cytometry Core supported by the National Center for Georgia Clinical and Translational Science Alliance of the NIH under award number UL1TR002378; the Integrated Cellular Imaging Microscopy Core of the Winship Cancer Institute of Emory University and the NIH–NCI under award number, 2P30CA138292-04; and the Yerkes NHP Genomics Core, which is supported in part by NIH P51 OD011132. This research was supported in part by the Intramural Research Program of the NIH, the Frederick National Laboratory for Cancer Research and the Center for Cancer Research. The project has been funded in part with federal funds from the Frederick National Laboratory for Cancer Research, under contract no. HHSN261200800001E. The content of this publication does

not necessarily reflect the views or policies of the Department of Health and Human Services, nor does mention of trade names, commercial products or organizations imply endorsement by the US Government.

Author information

Author notes

1. These authors contributed equally: Christiane S. Eberhardt, Haydn T. Kissick
2. These authors jointly supervised this work: Andreas Wieland, Rafi Ahmed

Affiliations

1. Emory Vaccine Center, Emory University School of Medicine, Atlanta, GA, USA

Christiane S. Eberhardt, Haydn T. Kissick, Rebecca C. Obeng, Tahseen H. Nasti, Se Jin Im, Andreas Wieland & Rafi Ahmed

2. Department of Microbiology and Immunology, Emory University School of Medicine, Atlanta, GA, USA

Christiane S. Eberhardt, Haydn T. Kissick, Rebecca C. Obeng, Tahseen H. Nasti, Se Jin Im, Andreas Wieland & Rafi Ahmed

3. Centre for Vaccinology, University Hospitals Geneva, Geneva, Switzerland

Christiane S. Eberhardt

4. Division of General Pediatrics, Department of Pediatrics, Gynecology & Obstetrics, Faculty of Medicine, University of Geneva, Geneva, Switzerland

Christiane S. Eberhardt & Dong M. Shin

5. Winship Cancer Institute of Emory University, Atlanta, GA, USA

Haydn T. Kissick, Mihir R. Patel, Christopher C. Griffith, Zhuo G. Chen, Nabil F. Saba & Rafi Ahmed

6. Department of Urology, Emory University School of Medicine, Atlanta, GA, USA

Haydn T. Kissick, Maria A. Cardenas & Nataliya Prokhnevskaya

7. Department of Otolaryngology, Emory University School of Medicine, Atlanta, GA, USA

Mihir R. Patel

8. Department of Pathology, Emory University School of Medicine, Atlanta, GA, USA

Rebecca C. Obeng & Christopher C. Griffith

9. Robert H. Lurie Comprehensive Cancer Center, Northwestern University Feinberg School of Medicine, Chicago, IL, USA

Rebecca C. Obeng

10. Department of Immunology, Sungkyunkwan University School of Medicine, Suwon, South Korea

Se Jin Im

11. Department of Hematology and Medical Oncology, Emory University School of Medicine, Atlanta, GA, USA

Xu Wang, Dong M. Shin, Zhuo G. Chen & Nabil F. Saba

12. Basic Science Program, Frederick National Laboratory for Cancer Research in the Laboratory of Integrative Cancer Immunology, National Cancer Institute, Bethesda, MD, USA

Mary Carrington

13. Ragon Institute of MGH, MIT and Harvard, Boston, MA, USA

Mary Carrington

14. Division of Vaccine Discovery, La Jolla Institute for Immunology, La Jolla, CA, USA

John Sidney & Alessandro Sette

15. Department of Medicine, University of California, San Diego, La Jolla, CA, USA

Alessandro Sette

Contributions

C.S.E. performed most of the experiments and analysed the data. H.T.K. analysed the scRNA-seq data. M.R.P. collected and provided human specimens, and analysed patient data. M.A.C. analysed scRNA-seq data. M.A.C., N.P. and A.W. performed in vitro proliferation experiments. R.C.O. performed and analysed multiplex immunohistochemistry experiments. T.H.N. performed flow cytometry experiments. C.C.G. and X.W., supervised by D.M.S., handled human specimens. M.C. performed HLA-typing analyses. J.S. and A.S. performed peptide–MHC affinity measurements. D.M.S., N.F.S. and Z.G.C. initiated the clinical specimen protocol. A.W. processed human specimens. A.W. and R.A. conceived, designed and supervised the project, and contributed equally to this work. C.S.E., H.T.K., A.W. and R.A. wrote the manuscript, with all authors contributing to the revision of the manuscript.

Corresponding authors

Correspondence to [Andreas Wieland](#) or [Rafi Ahmed](#).

Ethics declarations

Competing interests

R.A. holds patents related to the PD-1 inhibitory pathway. C.S.E., A.W. and R.A. are inventors on a patent application filed by Emory University relating to the use of HPV-specific TCR sequences. All other authors declare no competing interests.

Additional information

Peer review information *Nature* thanks Benny Chain, Evan Newell and the other, anonymous, reviewer(s) for their contribution to the peer review of this work.

Publisher's note Springer Nature remains neutral with regard to jurisdictional claims in published maps and institutional affiliations.

Extended data figures and tables

[Extended Data Fig. 1 Analysis of PD-1 \$\pm\$ CD8 TILs in patients with HPV-positive HNSCC.](#)

a, Frequency of CD8 T cells among TILs and number of CD8 $^{+}$ TILs per gram of HPV-positive HNSCC primary tumours (pink) and metastatic lymph nodes (metLN, grey), with mean and SD. **b**, Representative flow plots showing Granzyme B, Ki-67, and CD39 expression among TCF-1 $^{+}$ Tim-3 $^{-}$ and Tim-3 $^{+}$ TCF-1 $^{-}$ CD8 T cell subsets in TILs. **c**, Frequency of Granzyme B $^{+}$, Ki-67 $^{+}$ and CD39 $^{+}$ cells among PD-1 $^{+}$ CD8 TIL subsets, with means and SD. Two-sided Wilcoxon matched-pairs rank test. **d**, Geometric mean fluorescence intensity (MFI) of TOX in CD8 TIL subsets and patient-matched naive peripheral blood CD8 T cells (CD3 $^{+}$ CD4 $^{-}$ CD8 $^{+}$ CCR7 $^{+}$ CD45RA $^{+}$), with means and SD. Friedman test with two-sided Dunn's multiple comparisons test. **e, f**, Multiplex immunohistochemistry of primary tumour (**e**) and (**f**) metastatic lymph nodes (metLN) showing CD8 $^{+}$ (red) and PD-1 $^{+}$ (green) cells infiltrating the tumour parenchyma (cytokeratin $^{+}$; blue) and stroma (cytokeratin negative;

black areas highlighted by the orange dashed lines). TCF-1⁺ cells (white) are predominantly found in the stromal regions of the metastasis. Composite image on the right shows stem-like CD8 T cells (CD8⁺PD-1⁺TCF-1⁺; yellow membranous staining with white nuclear marker) within the stroma at a higher magnification of the area corresponding to the white rectangle. **g, h**, Frequency (**g**) and density (**h**) of PD-1⁺TCF-1⁻ CD8 TILs in the tumour parenchyma and stroma, with mean and SD. $n = 7$ (five primary tumours (pink) and two metastatic lymph nodes (grey)). ns = not significant, two-sided paired t-tests.

Extended Data Fig. 2 Mapping of HPV-specific CD8 T cell epitopes in patients with HNSCC.

a, Summary graph showing the numbers of positive peptides from HPV E2 (blue), E5 (green), E6 (red) and E7 (grey) proteins in expanded T cells of patients with HPV-positive HNSCC ($n = 17$) as measured by IFN γ ELISpot. **b**, Flow plots of expanded PBMC re-stimulated with the identified peptides and analysed by ICCS for IFN γ and TNF α . Gated on CD3⁺CD4⁻CD8⁺ cells. **c**, Flow plots of expanded PBMC stained with HPV-specific MHC-I tetramers. Gated on CD3⁺CD4⁻CD8⁺ cells. **d**, Table summarizing results of the HLA-binding assays (IC₅₀) of identified HPV epitopes. Indicated in bold are epitopes for which ex vivo tetramer staining was performed.

Extended Data Fig. 3 Direct ex vivo tetramer staining of TILs and PBMCs from patients with HNSCC.

TILs from primary tumours and metastatic lymph nodes as well as matched PBMC samples were tetramer-stained ex vivo with HPV-specific tetramers. Flow plots showing tetramer⁺ CD8 T cells in primary tumours, metastatic LN and PBMC. The cells were stained with the following tetramers: **a**, A01/E2 151-159. **b**, A01/E2 329-337, **c**, A02/E5 46-54 and **d**, B35/E6 52-61. Gated on CD3⁺CD4⁻CD8⁺ cells.

Extended Data Fig. 4 MHC-I tetramer sorting and scRNA-seq analysis of HPV-specific PD-1 \pm CD8 T cells from primary

tumour and metastatic lymph nodes.

a, b, Flow cytometry plots showing pre- and post-sorted tetramer-positive cells from primary and metastatic tumours. **c–f**, scRNA-seq data of the 13 tetramer-sorted samples showing the relative distribution among the three different clusters (stem-like, transitory and exhausted) in HPV-specific CD8 T cells in each sample.

Extended Data Fig. 5 Comparison of HPV-specific PD-1 \pm CD8 T cells in primary tumour and metastatic lymph nodes.

HPV tetramer-specific CD8 T cells from 13 samples including seven primary tumours and six metastatic lymph nodes were sorted and subjected to single cell RNAseq. **a**, UMAP clustering of HPV tetramer-specific CD8 T cells combined from all 13 samples, irrespective of tumour site, identified three distinct clusters; #1 stem-like, #2 transitory and #3 terminally differentiated/exhausted. **b**, Pairwise comparison of identified clusters among all HPV tetramer-specific CD8 T cells. Volcano plots show average fold-change by all cells in the cluster by $-\log_{10}$ p-value. The number of differentially expressed genes ($\geq 0.25 \text{ Log}_2$ fold-change in each pairwise comparison) are indicated in each plot. **c**, Heat map showing the top differentially expressed genes. The top 25 most significant genes from each cluster are shown. **d**, To assess gene expression differences of HPV-specific CD8 T cells in the two sites, we performed UMAP clustering of cells isolated from primary tumour and metastatic lymph node samples, respectively. We identified three clusters in primary tumours and four in metastatic lymph nodes. Gene expression was compared between the respective subsets (Green \rightarrow Green; Yellow \rightarrow Yellow; Blue \rightarrow Blue) in each tissue. Volcano plots highlight the differences between these clusters. The orange cluster identified in the metastatic lymph nodes consisted of very few cells and was thus not included in the comparisons. **e**, VISION analysis of HPV-specific CD8 T cells for enrichment of gene signatures associated with LCMV-specific stem-like and terminally differentiated/exhausted CD8 T cells. UMAP plots show the top quintile of cells enriched for the signature in blue. **f**, FACS analysis of various markers for HPV tetramer-specific intratumoral CD8 T cells. Plots are gated on PD-

1^+ HPV-specific CD8 T cells and show the respective marker versus TCF-1, the defining transcription factor of stem-like CD8 T cells. Summary plots show the frequency of TCF-1 $^+$ and TCF-1 $^-$ cells expressing the respective marker for six patient samples.

Extended Data Fig. 6 Comparing the transcriptional program of total PD-1 $^+$ CD8 T cells with HPV-specific PD-1 $^+$ CD8 T cells in the tumour.

To compare total PD-1 $^+$ CD8 T cells with HPV-specific PD-1 $^+$ CD8 T cells in the TME, we performed scRNA-seq of total PD-1 $^+$ CD8 T cells (depleted of identified HPV-specific CD8 T cell reactivities) and used analysis techniques similar to those in Fig. 3. **a**, UMAP clustering of PD-1 $^+$ CD8 T cells. Cells from six samples (three patients, primary tumour and metastatic lymph nodes) were computationally combined, and four distinct clusters were identified. **b**, Distribution of individual samples among the four identified clusters. **c**, Comparison of gene expression differences between total PD-1 $^+$ CD8 T cells and HPV tetramer-positive CD8 T cells. The corresponding clusters of cells from HPV tetramer-specific CD8 T cells were compared to the cells found among total PD-1 $^+$ CD8 T cells. Clusters 1-3 mapped very closely to what was found in the HPV-specific cells, with relatively few differentially expressed genes. **d**, Comparison of cluster 4 in PD-1 $^+$ cells to clusters of HPV-specific cells. Cluster 4 was compared to the other clusters to identify specific gene differences. Volcano plots show fold change versus -log(p-value) for each gene. **e**, UMAP plots show selected genes that are significantly up- or down-regulated in this cluster versus others from the PD-1 $^+$ cells.

Extended Data Fig. 7 HPV-specific CD8 T cell clonotypes exist in multiple differentiation states.

a, UMAP clustering of HPV tetramer-specific CD8 T cells. **b**, TCR repertoire of tetramer-positive CD8 TILs in primary tumours (Prim.) and metastatic lymph nodes (Met.) with the top four clonotypes highlighted. Colours do not indicate the same clonotype between patients or epitope

reactivities. **c**, TCR repertoire of tetramer-positive CD8 TILs in matched primary tumour and metastatic lymph node of the same patient with the top 4 clonotypes highlighted. Colours indicate the same clonotype within a patient and epitope reactivity. **d**, TCR frequency in patients with matched primary and metastatic tissue. **e**, TCR diversity of the identified clusters. **f**, Overlap between clusters for each patient as determined by Morisita Horn index. **g**, Distribution of the most frequent TCR clonotypes for each patient and epitope across gene expression clusters. UMAP plots show the distribution of the most frequent TCR clonotype across clusters. Accompanying bar charts showing the distribution of the eight most prominent TCR clonotypes across all clusters (clonotypes with less than 10 cells are not shown). The number of cells of the respective TCR clonotype is indicated below.

[Extended Data Fig. 8 Pseudotime analysis to investigate the lineage relationship of HPV-specific PD-1 \$\pm\$ CD8 T cell subsets.](#)

a–c, Pseudotime analysis of HPV tetramer-positive CD8 T cells showing a differentiation trajectory where cells start as stem-like PD-1 $^+$ TCF-1 $^+$ cells, transition through an intermediate stage, before taking on a terminally differentiated state. Selected genes (**b**) and enrichments for stem- and terminally differentiated gene signatures (**c**) are shown through this trajectory. **d**, Pseudotime analysis showing the distribution of the immunodominant clonotype of patients 7 and 51 in primary tumour and metastatic site through pseudotime.

[Extended Data Fig. 9 Proliferation and differentiation potential of HPV-specific stem-like CD8 T cells.](#)

a, Flow plots showing the gating strategy to isolate stem-like (CD39 $^-$ Tim-3 $^-$) and terminally differentiated cells (CD39 $^+$ Tim-3 $^+$) PD-1 $^+$ CD45RA $^-$ CD8 T cells. Histograms showing TCF-1 expression to validate that the sorting strategy using CD39 and Tim-3 as surrogate markers enriches for stem-like (green) and terminally differentiated (blue) cells. **b**, Representative plots showing CTV dilution and expression of CD45RO, CD25 and CD28 after five days of culturing stem-like and terminally

differentiated CD8 T cells alone or with peptide-pulsed PBMCs. Summary plots show percentage of cells positive for the indicated markers on day five. Means and their SD are represented, ** < 0.01 , ns = not significant, unpaired Mann-Whitney U test.

Extended Data Fig. 10 Gating strategies.

a, Flow plots showing the gating strategy for bulk TIL staining and gating on live CD3⁺CD8⁺PD-1⁺ (shown in Fig. 1a) and Tim-3/TCF-1⁺ cells (shown in Fig. 1b–d). **b**, Flow plots showing the gating strategy for ICCS of expanded T cells measuring IFN γ and TNF α expression of live CD3⁺CD4⁻CD8⁺ cells (shown in Fig. 2b). **c**, Flow plots showing the sort gating strategy for ex vivo TIL staining (shown in Fig. 2c). Tetramer-positive CD8 T cells were gated as live CD3⁺ CD4⁻ CD8⁺ double-tetramer⁺ cells.

Supplementary information

Reporting Summary

Supplementary Table 1

List of reagents.

Supplementary Table 2

Predicted HPV-peptides used for T cell expansion and epitope mapping.

Rights and permissions

Reprints and Permissions

About this article

Cite this article

Eberhardt, C.S., Kissick, H.T., Patel, M.R. *et al.* Functional HPV-specific PD-1⁺ stem-like CD8 T cells in head and neck cancer. *Nature* **597**, 279–284 (2021). <https://doi.org/10.1038/s41586-021-03862-z>

- Received: 31 August 2020
- Accepted: 28 July 2021
- Published: 01 September 2021
- Issue Date: 09 September 2021
- DOI: <https://doi.org/10.1038/s41586-021-03862-z>

This article was downloaded by **calibre** from <https://www.nature.com/articles/s41586-021-03862-z>

| [Section menu](#) | [Main menu](#) |

- Article
- [Published: 01 September 2021](#)

Structural basis for piRNA targeting

- [Todd A. Anzelon](#)¹ ✉ [ORCID: orcid.org/0000-0001-8043-5028](#)¹ nAff2
- [Saikat Chowdhury](#) [ORCID: orcid.org/0000-0001-8043-5028](#)¹ nAff2
- [Siobhan M. Hughes](#)¹ ✉
- [Yao Xiao](#)¹
- [Gabriel C. Lander](#) [ORCID: orcid.org/0000-0003-4921-1135](#)¹ &
- [Ian J. MacRae](#) [ORCID: orcid.org/0000-0002-5112-0294](#)¹

[Nature](#) volume 597, pages 285–289 (2021)

- 3885 Accesses
- 23 Altmetric
- [Metrics details](#)

Subjects

- [Cryoelectron microscopy](#)
- [Piwi RNAs](#)

Abstract

PIWI proteins use PIWI-interacting RNAs (piRNAs) to identify and silence transposable elements and thereby maintain genome integrity between metazoan generations¹. The targeting of transposable elements by PIWI has been compared to mRNA target recognition by Argonaute proteins^{2,3},

which use microRNA (miRNA) guides, but the extent to which piRNAs resemble miRNAs is not known. Here we present cryo-electron microscopy structures of a PIWI–piRNA complex from the sponge *Ephydatia fluviatilis* with and without target RNAs, and a biochemical analysis of target recognition. Mirroring Argonaute, PIWI identifies targets using the piRNA seed region. However, PIWI creates a much weaker seed so that stable target association requires further piRNA–target pairing, making piRNAs less promiscuous than miRNAs. Beyond the seed, the structure of PIWI facilitates piRNA–target pairing in a manner that is tolerant of mismatches, leading to long-lived PIWI–piRNA–target interactions that may accumulate on transposable-element transcripts. PIWI ensures targeting fidelity by physically blocking the propagation of piRNA–target interactions in the absence of faithful seed pairing, and by requiring an extended piRNA–target duplex to reach an endonucleolytically active conformation. PIWI proteins thereby minimize off-targeting cellular mRNAs while defending against evolving genomic threats.

Access options

Subscribe to Journal

Get full journal access for 1 year

\$199.00

only \$3.90 per issue

[Subscribe](#)

All prices are NET prices.

VAT will be added later in the checkout.

Tax calculation will be finalised during checkout.

Rent or Buy article

Get time limited or full article access on ReadCube.

from \$8.99

Rent or Buy

All prices are NET prices.

Additional access options:

- [Log in](#)
- [Access through your institution](#)
- [Learn about institutional subscriptions](#)

Fig. 1: Structural features unique to PIWIs.

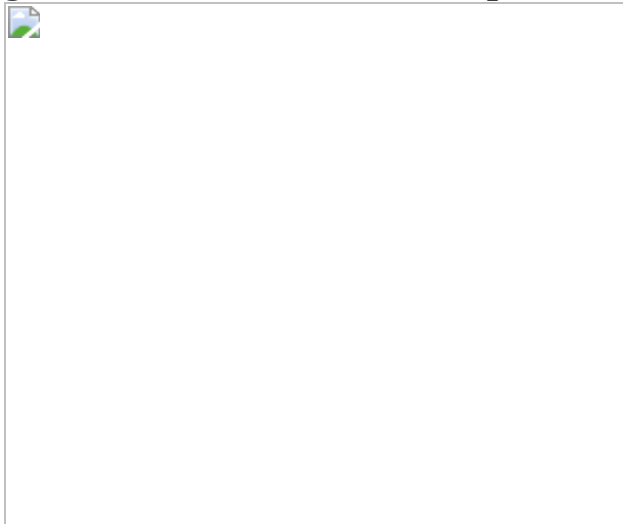


Fig. 2: piRNAs are more selective than miRNAs.

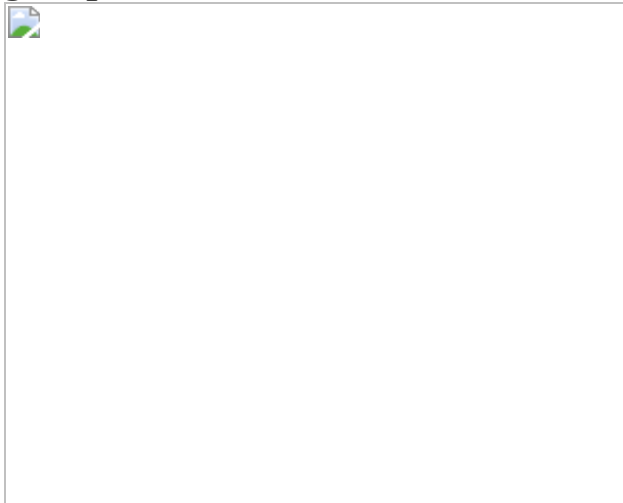


Fig. 3: Structural basis for piRNA target binding.

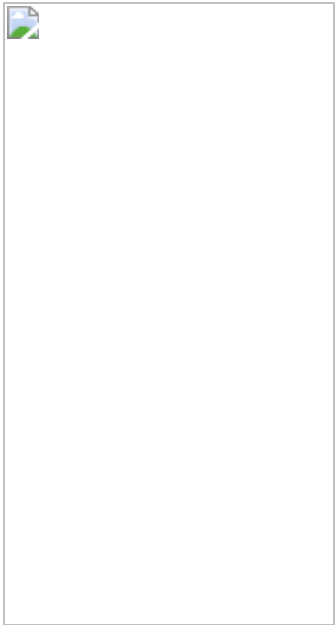


Fig. 4: Extensive pairing activates piRNA–target cleavage.



Data availability

Maps for the *Ef*Piwi–piRNA and *Ef*Piwi–piRNA-target complexes have been deposited in the EMDB under accession numbers [EMD-23061](#) and [EMD-23063](#), respectively. Corresponding atomic models have been deposited in the PDB under accession numbers [7KX7](#) and [7KX9](#). The *Ef*Piwi(MID/Piwi)–piRNA–long-target complex map has been deposited in the EMDB under accession number [EMD-23062](#). [Source data](#) are provided with this paper.

References

1. 1.

Ozata, D. M., Gainetdinov, I., Zoch, A., O'Carroll, D. & Zamore, P. D. PIWI-interacting RNAs: small RNAs with big functions. *Nat. Rev. Genet.* **20**, 89–108 (2019).

2. 2.

Shen, E. Z. et al. Identification of piRNA binding sites reveals the Argonaute regulatory landscape of the *C. elegans* germline. *Cell* **172**, 937–951.e18 (2018).

3. 3.

Gou, L. T. et al. Pachytene piRNAs instruct massive mRNA elimination during late spermiogenesis. *Cell Res.* **24**, 680–700 (2014).

4. 4.

Grimson, A. et al. Early origins and evolution of microRNAs and Piwi-interacting RNAs in animals. *Nature* **455**, 1193–1197 (2008).

5. 5.

Lewis, B. P., Shih, I. H., Jones-Rhoades, M. W., Bartel, D. P. & Burge, C. B. Prediction of mammalian microRNA targets. *Cell* **115**, 787–798 (2003).

6. 6.

Wee, L. M., Flores-Jasso, C. F., Salomon, W. E. & Zamore, P. D. Argonaute divides its RNA guide into domains with distinct functions and RNA-binding properties. *Cell* **151**, 1055–1067 (2012).

7. 7.

Salomon, W. E., Jolly, S. M., Moore, M. J., Zamore, P. D. & Serebrov, V. Single-molecule imaging reveals that Argonaute reshapes the binding properties of its nucleic acid guides. *Cell* **162**, 84–95 (2015).

8. 8.

Chandradoss, S. D., Schirle, N. T., Szczepaniak, M., MacRae, I. J. & Joo, C. A dynamic search process underlies microRNA targeting. *Cell* **162**, 96–107 (2015).

9. 9.

Parker, J. S., Parizotto, E. A., Wang, M., Roe, S. M. & Barford, D. Enhancement of the seed-target recognition step in RNA silencing by a PIWI/MID domain protein. *Mol. cell* **33**, 204–214 (2009).

10. 10.

Schirle, N. T. & MacRae, I. J. The crystal structure of human Argonaute2. *Science* **336**, 1037–1040 (2012).

11. 11.

Schirle, N. T., Sheu-Gruttaduria, J. & MacRae, I. J. Structural basis for microRNA targeting. *Science* **346**, 608–613 (2014).

12. 12.

Sheu-Gruttaduria, J., Xiao, Y., Gebert, L. F. & MacRae, I. J. Beyond the seed: structural basis for supplementary microRNA targeting by human Argonaute2. *EMBO J.* **38**, e101153 (2019).

13. 13.

Friedman, R. C., Farh, K. K., Burge, C. B. & Bartel, D. P. Most mammalian mRNAs are conserved targets of microRNAs. *Genome Res.* **19**, 92–105 (2009).

14. 14.

Zhang, D. et al. The piRNA targeting rules and the resistance to piRNA silencing in endogenous genes. *Science* **359**, 587–592 (2018).

15. 15.

Goh, W. S. et al. piRNA-directed cleavage of meiotic transcripts regulates spermatogenesis. *Genes Dev.* **29**, 1032–1044 (2015).

16. 16.

Halbach, R. et al. A satellite repeat-derived piRNA controls embryonic development of *Aedes*. *Nature* **580**, 274–277 (2020).

17. 17.

Zhang, P. et al. MIWI and piRNA-mediated cleavage of messenger RNAs in mouse testes. *Cell Res.* **25**, 193–207 (2015).

18. 18.

Nozawa, M. et al. Evolutionary transitions of microRNA–target pairs. *Genome Biol. Evol.* **8**, 1621–1633 (2016).

19. 19.

Brennecke, J. et al. Discrete small RNA-generating loci as master regulators of transposon activity in *Drosophila*. *Cell* **128**, 1089–1103 (2007).

20. 20.

Wang, J. et al. piRBase: a comprehensive database of piRNA sequences. *Nucleic Acids Res.* **47**, D175–D180 (2019).

21. 21.

Matsumoto, N. et al. Crystal structure of silkworm PIWI-clade Argonaute Siwi bound to piRNA. *Cell* **167**, 484–497.e9 (2016).

22. 22.

Yamaguchi, S. et al. Crystal structure of *Drosophila* Piwi. *Nat. Commun.* **11**, 858 (2020).

23. 23.

Funayama, N., Nakatsukasa, M., Mohri, K., Masuda, Y. & Agata, K. Piwi expression in archeocytes and choanocytes in demosponges: insights into the stem cell system in demosponges. *Evol. Dev.* **12**, 275–287 (2010).

24. 24.

Alie, A. et al. The ancestral gene repertoire of animal stem cells. *Proc. Natl Acad. Sci. USA* **112**, E7093–E7100 (2015).

25. 25.

Wynant, N., Santos, D. & Vanden Broeck, J. The evolution of animal Argonautes: evidence for the absence of antiviral AGO Argonautes in vertebrates. *Sci. Rep.* **7**, 9230 (2017).

26. 26.

Reuter, M. et al. Miwi catalysis is required for piRNA amplification-independent LINE1 transposon silencing. *Nature* **480**, 264–267 (2011).

27. 27.

Wu, P. H. et al. The evolutionarily conserved piRNA-producing locus *pi6* is required for male mouse fertility. *Nat. Genet.* **52**, 728–739 (2020).

28. 28.

Arif, A. et al. The tiny, conserved zinc-finger protein GTSF1 helps PIWI proteins achieve their full catalytic potential. Preprint at <https://doi.org/10.1101/2021.05.04.442675> (2021).

29. 29.

Herzog, V. A. et al. Thiol-linked alkylation of RNA to assess expression dynamics. *Nat. Methods* **14**, 1198–1204 (2017).

30. 30.

Sienski, G., Donertas, D. & Brennecke, J. Transcriptional silencing of transposons by Piwi and Maelstrom and its impact on chromatin state and gene expression. *Cell* **151**, 964–980 (2012).

31. 31.

Le Thomas, A. et al. Piwi induces piRNA-guided transcriptional silencing and establishment of a repressive chromatin state. *Genes Dev.* **27**, 390–399 (2013).

32. 32.

Aravin, A. A. et al. A piRNA pathway primed by individual transposons is linked to de novo DNA methylation in mice. *Mol. Cell* **31**, 785–799 (2008).

33. 33.

Kuramochi-Miyagawa, S. et al. DNA methylation of retrotransposon genes is regulated by Piwi family members MILI and MIWI2 in murine fetal testes. *Genes Dev.* **22**, 908–917 (2008).

34. 34.

Nott, T. J. et al. Phase transition of a disordered nuage protein generates environmentally responsive membraneless organelles. *Mol. Cell* **57**, 936–947 (2015).

35. 35.

Sheu-Gruttaduria, J. & MacRae, I. J. Phase transitions in the assembly and function of human miRISC. *Cell* **173**, 946–957.e16

(2018).

36. 36.

Flores-Jasso, C. F., Salomon, W. E. & Zamore, P. D. Rapid and specific purification of Argonaute–small RNA complexes from crude cell lysates. *RNA* **19**, 271–279 (2013).

37. 37.

Suloway, C. et al. Automated molecular microscopy: the new Leginon system. *J. Struct. Biol.* **151**, 41–60 (2005).

38. 38.

Zheng, S. Q. et al. MotionCor2: anisotropic correction of beam-induced motion for improved cryo-electron microscopy. *Nat. Methods* **14**, 331–332 (2017).

39. 39.

Lander, G. C. et al. Appion: an integrated, database-driven pipeline to facilitate EM image processing. *J. Struct. Biol.* **166**, 95–102 (2009).

40. 40.

Kimanius, D., Forsberg, B. O., Scheres, S. H. & Lindahl, E. Accelerated cryo-EM structure determination with parallelisation using GPUs in RELION-2. *eLife* **5**, e18722 (2016).

41. 41.

Rohou, A. & Grigorieff, N. CTFFIND4: Fast and accurate defocus estimation from electron micrographs. *J. Struct. Biol.* **192**, 216–221 (2015).

42. 42.

Goddard, T. D., Huang, C. C. & Ferrin, T. E. Visualizing density maps with UCSF Chimera. *J. Struct. Biol.* **157**, 281–287 (2007).

43. 43.

Pettersen, E. F. et al. UCSF Chimera—a visualization system for exploratory research and analysis. *J. Comput. Chem.* **25**, 1605–1612 (2004).

44. 44.

Punjani, A., Rubinstein, J. L., Fleet, D. J. & Brubaker, M. A. cryoSPARC: algorithms for rapid unsupervised cryo-EM structure determination. *Nat. Methods* **14**, 290–296 (2017).

45. 45.

Tan, Y. Z. et al. Addressing preferred specimen orientation in single-particle cryo-EM through tilting. *Nat. Methods* **14**, 793–796 (2017).

46. 46.

Waterhouse, A. et al. SWISS-MODEL: homology modelling of protein structures and complexes. *Nucleic Acids Res.* **46**, W296–W303 (2018).

47. 47.

Emsley, P., Lohkamp, B., Scott, W. G. & Cowtan, K. Features and development of Coot. *Acta Crystallogr. D* **66**, 486–501 (2010).

48. 48.

Liebschner, D. et al. Macromolecular structure determination using X-rays, neutrons and electrons: recent developments in Phenix. *Acta Crystallogr. D* **75**, 861–877 (2019).

49. 49.

Williams, C. J. et al. MolProbity: More and better reference data for improved all-atom structure validation. *Protein Sci.* **27**, 293–315 (2018).

50. 50.

Goddard, T. D. et al. UCSF ChimeraX: Meeting modern challenges in visualization and analysis. *Protein Sci.* **27**, 14–25 (2018).

51. 51.

Buchan, D. W. A. & Jones, D. T. The PSIPRED protein analysis workbench: 20 years on. *Nucleic Acids Res.* **47**, W402–W407 (2019).

52. 52.

Jones, D. T. Protein secondary structure prediction based on position-specific scoring matrices. *J. Mol. Biol.* **292**, 195–202 (1999).

53. 53.

Nakanishi, K. et al. Eukaryote-specific insertion elements control human ARGONAUTE slicer activity. *Cell Rep.* **3**, 1893–1900 (2013).

54. 54.

Park, M. S. et al. Human Argonaute3 has slicer activity. *Nucleic Acids Res.* **45**, 11867–11877 (2017).

55. 55.

Park, M. S. et al. Multidomain convergence of Argonaute during RISC assembly correlates with the formation of internal water clusters. *Mol. Cell* **75**, 725–740.e6 (2019).

56. 56.

Martin, M. Cutadapt removes adapter sequences from high-throughput sequencing reads. *EMBnet.journal* **17**, 10–12 (2011).

Acknowledgements

We thank N. Funayama for the *E. fluviatilis* *piwi-a* cDNA clone, Y. Tomari for the Siwi cDNA clone, and I. H. Segel for advice about measuring binding reactions with very slow off-rates. The research of G.C.L. is supported by NIH grant R21AG067594 and an Amgen Young Investigator Award. The research of I.J.M. is supported by NIH grant R35GM127090.

Author information

Author notes

1. Saikat Chowdhury

Present address: CSIR-Centre for Cellular and Molecular Biology,
Hyderabad, India

2. These authors contributed equally: Todd A. Anzelon, Saikat
Chowdhury, Siobhan M. Hughes

Affiliations

1. Department of Integrative Structural and Computational Biology, The Scripps Research Institute, La Jolla, CA, USA

Todd A. Anzelon, Saikat Chowdhury, Siobhan M. Hughes, Yao Xiao, Gabriel C. Lander & Ian J. MacRae

Contributions

T.A.A. prepared *EfPiwi*–piRNA, Siwi–piRNA, and hAGO2–miRNA samples, performed biochemical experiments, built *EfPiwi* models and co-wrote the manuscript. S.C. prepared cryo-EM samples, collected data, produced high-resolution reconstructions and assisted with model building. S.M.H. identified and developed *EfPiwi* as a source of active Piwi protein. Y.X. helped to develop *EfPiwi* and established purification protocols.

G.C.L. provided structural insights and guidance in cryo-EM data collection and analysis. I.J.M. provided structural and mechanistic insights and co-wrote the manuscript.

Corresponding author

Correspondence to [Ian J. MacRae](#).

Ethics declarations

Competing interests

The authors declare no competing interests.

Additional information

Peer review information *Nature* thanks Hong-Wei Wang and the other, anonymous, reviewer(s) for their contribution to the peer review of this work.

Publisher's note Springer Nature remains neutral with regard to jurisdictional claims in published maps and institutional affiliations.

Extended data figures and tables

[Extended Data Fig. 1 Piwi protein purification and extended Piwi family tree.](#)

a, Coomassie-stained SDS PAGE of piRNA-loaded PIWI proteins captured using an immobilized complementary oligonucleotide. Input shows partially purified protein samples that were incubated with capture resin. Unbound shows protein that did not bind the resin. Captured shows protein retained on the resin after washing (eluted by boiling in SDS). After elution shows protein retained on the resin after incubation with the competitor oligonucleotide (eluted by boiling in SDS). **b**, Capture-purified PIWI

proteins before and after anion exchange purification. Input fraction shows samples after elution by competitor oligonucleotide in capture-purification step. Purified indicates the final purification products. Note: Δseed-gate Siwi was captured at such low levels that it was unclear whether any active Siwi was obtained until observing the sample's ability to specifically bind ^{32}P -labeled target RNAs. **c**, Phylogenetic tree of PIWI proteins shows EfPiwi belongs to the ancient *Drosophila* Ago3-like branch.

Extended Data Fig. 2 Imaging and processing of the EfPiwi-piRNA complex (and EfPiwi-piRNA-long target complex).

a, Representative cryo-EM micrograph (1,765 micrographs collected in total). Input sample contained EfPiwi-piRNA and a long target RNA (complementary to piRNA nucleotides g2–g25). **b**, Cryo-EM data processing workflow. The data set contained two populations of well resolved particles, one for the binary EfPiwi-piRNA complex and another for the ternary EfPiwi-piRNA-long target complex. Particles isolated from micrographs were sorted by reference-free 2D classification. Only particles containing high-resolution features for the intact complex were selected for downstream processing. 3D classification was used to further remove low-resolution or damaged particles, and the remaining particles were refined to obtain a 3.8 Å reconstruction for the EfPiwi-guide complex, and 8.6 Å for the ternary EfPiwi-piRNA-long target complex. **c**, The final 3D map for the EfPiwi-piRNA complex coloured by local resolution values, where the majority of the map was resolved between 3.5 Å and 4 Å with the flexible PAZ and N domains having lower resolution. **d**, Angular distribution plot showing the Euler angle distribution of the EfPiwi-piRNA particles in the final reconstruction. The position of each cylinder corresponds to the 3D angular assignments and their height and colour (blue to red) corresponds to the number of particles in that angular orientation. **e**, Directional Fourier Shell Correlation (FSC) plot representing 3D resolution anisotropy in the reconstructed map, with the red line showing the global FSC, green dashed lines correspond to ± 1 standard deviation from mean of directional resolutions, and the blue histograms correspond to percentage of directional resolution over the 3D FSC. **f**, EM density quality of EfPiwi-piRNA complex. Individual domains of EfPiwi fit into the EM density, EM density shown in mesh; molecular models (coloured as in Fig. 2) shown in cartoon

representation with side chains shown as sticks; piRNA shown in stick representation.

Extended Data Fig. 3 Conserved structural features in extended Piwi family.

a, Surface of hAGO2 (left) and EfPiwi (right), highlighting g5-g6 nucleotide-binding loops. Superimposing g5-g6 nucleotides (red sticks) from hAGO2 onto EfPiwi results in steric clashes. **b**, g5-g6 loop in AGO structures (left) is kinked, enabling pre-organization of seed 3' end. Equivalent loop in Piwi structures (right) cannot kink due to bulky residues (labeled positions 1 and 2), conserved in Piwi family. **c**, Close up superposition of central-gate and seed-gate structures in AGO and PIWI proteins, respectively. **d**, Superposition of seed-gate regions from all known Piwi (left) and AGO (right) structures, with secondary structure schematics shown above. **e**, Secondary structure predictions indicate the α_6 extension is a defining feature of the Piwi family. Predictions were by PSIPRED 4.0. **f**, L1-L2 interface near seed-gate in EfPiwi. Hydrophobic residues buried at the L1-L2 interface are shown. **g**, Sequence alignment shows L1-L2 interface residues in EfPiwi are broadly conserved in Piwis (green) and distinct from the equivalent residues in AGOs (blue).

Extended Data Fig. 4 Target release from hAGO2 and EfPiwi loaded with identical guides.

a, Schematic of pairing between guide RNAs and seed-matched target RNAs used in main text Fig. [2b](#), [c](#). **b**, Schematic of pairing between 22 nt guide RNA and target RNAs spanning the seed and central regions. **c**, Release of ^{32}P -labeled target RNAs from EfPiwi-22 nt guide in the presence of excess unlabeled target RNA over time. **d**, Release rates of target RNAs from hAGO2-22 nt guide (data from Fig. [2d](#), left) and EfPiwi-22nt guide (**c**). Results show hAGO2 and EfPiwi create distinct binding properties for the same guide RNA. All plotted data are the mean values of triplicate measurements. Error bars indicate SD. **e**, Ribbon representation of hAGO2, EfPiwi, and an overlay illustrating relative positions of the central-gate and seed-gate. In **c**, **d**, $n = 3$ independent experiments, data are mean \pm s.d.

Extended Data Fig. 5 Imaging and processing of the EfPiwi-piRNA-target complex.

a, Representative cryo-EM micrograph of EfPiwi-piRNA-target complex (1,881 micrographs collected in total). **b**, Workflow for processing EfPiwi-piRNA-target complex dataset. Particles isolated from micrographs were sorted by reference-free 2D classification. Only particles containing high-resolution features for the intact complex were selected for downstream processing. 3D classification was used to further remove low-resolution or damaged particles, and the remaining particles were refined to obtain a 3.5 Å map. **c**, The EfPiwi-piRNA-target complex map coloured by local resolution. **d**, Euler angle distribution plot for the EfPiwi-piRNA-target complex particles. **e**, Directional Fourier Shell Correlation (FSC) plot representing 3D resolution anisotropy in the reconstructed map. Red line shows global FSC; green dashed lines ± 1 standard deviation from mean of directional resolutions; blue histograms indicate percentage of directional resolution over the 3D FSC. **f**, EM density quality of EfPiwi-piRNA-target complex. Individual domains of EfPiwi and RNAs fit into the EM density; EM density shown in mesh; protein models shown in cartoon representation (coloured as in Fig. 1) with side chains shown as sticks; RNAs shown in stick representation.

Extended Data Fig. 6 EfPiwi target binding data.

a, Raw data for k_{on} values shown in Fig. 3f. Plots of target RNAs with mismatches (sequences shown in Extended Data Fig. 6c) binding to EfPiwi-piRNA complexes over time. Protein concentrations used in each experiment are indicated at top of each graph. 95% confidence limits of observed association rates (k_{obs}) and k_{on} values indicated. WT EfPiwi (black), Δseed-gate EfPiwi (red). **b**, Raw data for k_{off} values shown in Extended Data Fig. 7e. Plots of target RNAs with mismatches (mm) dissociating from EfPiwi-piRNA complexes over time. All data were fit to a plateau value of 0.15. 95% confidence limits of k_{on} values indicated. All data points were measured three times. Error bars indicate SEM. Center line indicates best fit to data. Surrounding lines indicate 95% confidence limits. In all panels, $n = 3$ independent experiments, data are mean \pm s.d.

Extended Data Fig. 7 Target binding with mismatches.

a, Guide-target pairing schematic for select mismatched targets binding Siwi-piRNA complexes. Mismatches coloured gold. **b**, Association rates of target RNAs (shown in **a**) with wild-type Siwi (left) and Δ seed-gate Siwi. Indicated p-values from two-sided t-test are 6.11×10^{-5} and 0.205 for wild-type and Δ seed-gate Siwi, respectively. **c**, Guide-target pairing schematic for mismatched targets used in main text Fig. 3f, and panels d and e here. Mismatches coloured gold. **d**, Dissociation rates of ^{32}P -labeled target RNAs with three consecutive mismatches from wild-type EfPiwi. Most mismatched segments had moderate (~10-fold) effects on k_{off} , except 14–16 mismatches, which increased $k_{off} \sim 70$ fold. **e**, Dissociation constants (K_D) calculated from k_{on} and k_{off} values for target RNAs binding wild-type EfPiwi-guide complex. **f**, Surface representation of the modeled piRNA-target duplex. piRNA nucleotides numbered at the Watson-Crick face. Non-hydrogen RNA atoms positioned ≤ 4 Å from an EfPiwi atom coloured purple. In **b**, **d**, and **e**, $n = 3$ independent experiments, data are mean \pm s.d.

Extended Data Fig. 8 Target cleavage by EfPiwi and Siwi (part 1).

a, Denaturing gels showing cleavage of g2-g21 matched ^{32}P -labeled target RNA by EfPiwi, hAGO2 or Siwi in the presence of various divalent cations (2 mM each). Schematic of piRNA-target pairing shown (top). Gels are representative results for $n = 3$ independent experiments for EfPiwi and hAGO2, and $n = 2$ independent experiments for Siwi. **b**, Time course showing cleavage of g2-g21 paired ^{32}P -labeled target RNA by EfPiwi in the presence of Mg^{2+} , Mn^{2+} , or both at approximate physiological divalent cation concentrations. **c**, Cleavage of g2-g21 matched ^{32}P -labeled target RNA by EfPiwi at various temperatures shows activity over the full physiological range (17–30 °C). Gel is representative of $n = 3$ independent experiments. **d**, Quantification of results (and replicates) in **c**. **e**, Cleavage of target RNAs with varying degrees of 3' complementarity by EfPiwi at 30 °C. In **b**, **d** and **e**, $n = 3$ independent experiments, data are mean \pm s.d.

Source data

Extended Data Fig. 9 Fig. S8. Target cleavage by EfPiwi and Siwi (part 2).

a, Guide-target pairing schematic for targets with varying degrees of complementarity to piRNA 3' end used in Fig. 4a and b, e. **b**, Quantification target RNAs (1 nM) cleaved after treating with excess (100 nM) EfPiwi loaded with a 22 or 25 nt guide or hAGO2 loaded with a 22 nt guide for 1 h. $n = 3$ independent experiments, data are mean \pm s.d. **c**, Guide-target pairing schematic for targets with 3 nt mismatched regions. **d**, Quantification mismatched target RNAs (1 nM) cleaved after treating with excess (100 nM) EfPiwi loaded with a 22 or 25 nt guide or hAGO2 loaded with a 22 nt guide for 1 h. $n = 3$ independent experiments, data are mean \pm s.d. **e**, Cleavage of targets with varying degrees of complementarity to piRNA 3' end (shown panel a) by Siwi (2 mM MnCl₂, 37 °C). Gel is representative of $n = 3$ independent experiments, with data plotted as mean \pm s.d. shown below. **f**, From Fig. 4c: sequences of the 26 target RNAs, with 0–8 mismatches opposite piRNA nucleotides g11–g18, that were most readily cleaved by EfPiwi (listed in order of cleavage product abundance). Mismatched nucleotides coloured yellow. Greyed out sequences indicate constant regions shared by all target RNAs. Triangle indicates cleavage site.

[Source data](#)

Extended Data Table 1 Cryo-EM data collection, refinement, and validation statistics

Supplementary information

Supplementary Figure 1

Unprocessed and uncropped gel images. **a**, Unprocessed gel scans corresponding to gel in Fig. 4a and Extended Data Fig. 9b. Corresponding panels or data indicated above gels. Dotted lines indicate where the gel was cropped. **b**, Unprocessed gel scans corresponding to gels in Extended Data Fig. 8a. Corresponding panels indicated above gels. Dotted lines indicate where the gel was cropped. **c**, Unprocessed gel scan corresponding to data

in Extended Data Fig. 8b. Dotted lines indicate separation between samples. **d**, Unprocessed gel scan corresponding to gel in Extended Data Fig. 8c and data in Extended Data Fig. 8d. Dotted lines indicate where the gel was cropped. **e**, Unprocessed gel scan corresponding to data in Extended Data Fig. 8e. Dotted line indicates separation between samples. **f**, Unprocessed gel scan corresponding to gel and data in Extended Data Fig. 9e. Dotted lines indicate where the gel was cropped. **g**, Unprocessed gel scan corresponding to data in Extended Data Fig. 9d. Dotted line indicates separation between samples.

Reporting Summary

Peer Review File

Supplementary Table 1

A list of oligonucleotides used in this study.

Source data

Source Data Extended Data Fig. 8

Source Data Extended Data Fig. 9

Rights and permissions

Reprints and Permissions

About this article

Cite this article

Anzelon, T.A., Chowdhury, S., Hughes, S.M. *et al.* Structural basis for piRNA targeting. *Nature* **597**, 285–289 (2021).

<https://doi.org/10.1038/s41586-021-03856-x>

- Received: 20 February 2021
- Accepted: 28 July 2021
- Published: 01 September 2021
- Issue Date: 09 September 2021
- DOI: <https://doi.org/10.1038/s41586-021-03856-x>

Target practice: first Piwi structure with RNA

- Sara Osman

News & Views 06 Sept 2021

This article was downloaded by **calibre** from <https://www.nature.com/articles/s41586-021-03856-x>

| [Section menu](#) | [Main menu](#) |

Amendments & Corrections

- **Author Correction: Mechanisms of BRCA1–BARD1 nucleosome recognition and ubiquitylation** [17 August 2021]
Author Correction •
- **Author Correction: TP53 loss creates therapeutic vulnerability in colorectal cancer** [25 August 2021]
Author Correction •

- Author Correction
- [Published: 17 August 2021](#)

Author Correction: Mechanisms of BRCA1–BARD1 nucleosome recognition and ubiquitylation

- [Qi Hu ORCID: orcid.org/0000-0003-3647-8471¹](#)
- [Maria Victoria Botuyan ORCID: orcid.org/0000-0002-6466-7432¹](#)
- [Debiao Zhao¹](#)
- [Gaofeng Cui¹](#)
- [Elie Mer ORCID: orcid.org/0000-0003-2339-9547¹](#) &
- [Georges Mer ORCID: orcid.org/0000-0002-1900-1578^{1,2}](#)

[Nature](#) volume 597, page E5 (2021)

- 745 Accesses
- 3 Altmetric
- [Metrics details](#)

The [Original Article](#) was published on 28 July 2021

[Download PDF](#)

Correction to: *Nature* <https://doi.org/10.1038/s41586-021-03716-8>
Published online 28 July 2021

In this Article, a citation to Witus et al.¹ was inadvertently omitted, and has now been added as ref. 80 in the new sentence: “We note that the conformational flexibility of BRCA1^R–BARD1^R–UbcH5c–NCP highlighted in our work is consistent with a recent publication⁸⁰, giving us confidence that the structures and interactions revealed in the two studies are relevant.”. The original Article has been corrected online.

References

1. 1.

Witus, S. R. et al. BRCA1/BARD1 site-specific ubiquitylation of nucleosomal H2A is directed by BARD1. *Nat. Struct. Mol. Biol.* **28**, 268–277 (2021).

Author information

Author notes

1. These authors contributed equally: Qi Hu, Maria Victoria Botuyan, Debiao Zhao

Affiliations

1. Department of Biochemistry and Molecular Biology, Mayo Clinic, Rochester, MN, USA

Qi Hu, Maria Victoria Botuyan, Debiao Zhao, Gaofeng Cui, Elie Mer & Georges Mer

2. Department of Cancer Biology, Mayo Clinic, Rochester, MN, USA

Georges Mer

Corresponding author

Correspondence to [Georges Mer](#).

Rights and permissions

[Reprints and Permissions](#)

About this article

Cite this article

Hu, Q., Botuyan, M.V., Zhao, D. *et al.* Author Correction: Mechanisms of BRCA1–BARD1 nucleosome recognition and ubiquitylation. *Nature* **597**, E5 (2021). <https://doi.org/10.1038/s41586-021-03881-w>

- Published: 17 August 2021
- Issue Date: 09 September 2021
- DOI: <https://doi.org/10.1038/s41586-021-03881-w>

This article was downloaded by **calibre** from <https://www.nature.com/articles/s41586-021-03881-w>

- Author Correction
- [Published: 25 August 2021](#)

Author Correction: TP53 loss creates therapeutic vulnerability in colorectal cancer

- [Yunhua Liu¹](#),
- [Xinna Zhang^{2,3}](#),
- [Cecil Han¹](#),
- [Guohui Wan¹](#),
- [Xingxu Huang⁴](#),
- [Cristina Ivan^{2,3}](#),
- [Dahai Jiang^{2,3}](#),
- [Cristian Rodriguez-Aguayo^{3,5}](#),
- [Gabriel Lopez-Berestein^{3,5}](#),
- [Pulivarthi H. Rao⁶](#),
- [Dipen M. Maru⁷](#),
- [Andreas Pahl⁸](#),
- [Xiaoming He⁹](#),
- [Anil K. Sood^{1,2,3}](#),
- [Lee M. Ellis¹⁰](#),
- [Jan Anderl⁸](#) &
- [Xiongbin Lu^{1,3}](#)

[Nature](#) volume 597, page E6 (2021)

- 798 Accesses
- 5 Altmetric
- [Metrics details](#)

Subjects

- [Cancer genomics](#)

The [Original Article](#) was published on 22 April 2015

[Download PDF](#)

Correction to: *Nature* <https://doi.org/10.1038/nature14418> Published online 22 April 2015

In Extended Data Fig. 9a of this Article, the casp-3 immunohistochemical staining images in the HEA125 and Ama-3 treatment groups of POLR2A^{loss} tumours were inadvertently taken from serial tissue sections of a tumour in the Ama-3 treatment group of POLR2A^{neutral} tumours. In Fig. 1 of this Amendment, we have replaced these two images with corrected ones (highlighted by red boxes). All of the original casp-3 staining images from the POLR2A^{neutral} and POLR2A^{loss} tumours with indicated treatments are shown in [Supplementary Information](#) to this Amendment. The immunohistochemistry staining images were not used for quantitative analysis in the study, and this mistake does not affect the conclusions of the original Article. The original Article has not been corrected online.

Fig. 1: This is the original and corrected Extended Data Fig. 9a of the original Article.



The affected panels are highlighted by red boxes.

Supplementary information is available in the online version of this Amendment.

Author information

Affiliations

1. Department of Cancer Biology, The University of Texas MD Anderson Cancer Center, Houston, TX, USA

Yunhua Liu, Cecil Han, Guohui Wan, Anil K. Sood & Xiongbin Lu

2. Department of Gynaecologic Oncology and Reproductive Medicine, The University of Texas MD Anderson Cancer Center, Houston, USA

Xinna Zhang, Cristina Ivan, Dahai Jiang & Anil K. Sood

3. Center for RNA Interference and Non-coding RNAs, The University of Texas MD Anderson Cancer Center, Houston, TX, USA

Xinna Zhang, Cristina Ivan, Dahai Jiang, Cristian Rodriguez-Aguayo, Gabriel Lopez-Berestein, Anil K. Sood & Xiongbin Lu

4. School of Life Science and Technology, ShanghaiTech University, Shanghai, China

Xingxu Huang

5. Department of Experimental Therapeutics, The University of Texas MD Anderson Cancer Center, Houston, TX, USA

Cristian Rodriguez-Aguayo & Gabriel Lopez-Berestein

6. Department of Paediatrics, Baylor College of Medicine, Houston, TX, USA

Pulivarthi H. Rao

7. Department of Pathology, The University of Texas MD Anderson Cancer Center, Houston, TX, USA

Dipen M. Maru

8. Heidelberg Pharma GmbH, Ladenburg, Germany

Andreas Pahl & Jan Anderl

9. Department of Biomedical Engineering, The Ohio State University, Columbus, OH, USA

Xiaoming He

10. Department of Surgical Oncology, The University of Texas MD Anderson Cancer Center, Houston, TX, USA

Lee M. Ellis

Corresponding author

Correspondence to [Xiongbin Lu](#).

Supplementary information

[Supplementary Information](#)

This file shows the original casp-3 staining images from the POLR2A^{neutral} and POLR2A^{loss} tumours with indicated treatments in Extended Data Fig. 9a.

Rights and permissions

[Reprints and Permissions](#)

About this article

Cite this article

Liu, Y., Zhang, X., Han, C. *et al.* Author Correction: TP53 loss creates therapeutic vulnerability in colorectal cancer. *Nature* **597**, E6 (2021).

<https://doi.org/10.1038/s41586-021-03664-3>

- Published: 25 August 2021
- Issue Date: 09 September 2021
- DOI: <https://doi.org/10.1038/s41586-021-03664-3>

| [Section menu](#) | [Main menu](#) |